



# Modelling of high Karlovitz combustion in spark-ignition engines

Edouard Suillaud

## ► To cite this version:

Edouard Suillaud. Modelling of high Karlovitz combustion in spark-ignition engines. Chemical and Process Engineering. Université Paris-Saclay, 2021. English. NNT : 2021UPAST016 . tel-03279553

**HAL Id: tel-03279553**

**<https://theses.hal.science/tel-03279553>**

Submitted on 6 Jul 2021

**HAL** is a multi-disciplinary open access archive for the deposit and dissemination of scientific research documents, whether they are published or not. The documents may come from teaching and research institutions in France or abroad, or from public or private research centers.

L'archive ouverte pluridisciplinaire **HAL**, est destinée au dépôt et à la diffusion de documents scientifiques de niveau recherche, publiés ou non, émanant des établissements d'enseignement et de recherche français ou étrangers, des laboratoires publics ou privés.

# Modelling of high Karlovitz combustion in spark-ignition engines

Thèse de doctorat de l'Université Paris-Saclay

École doctorale n° 579, Sciences Mécaniques et Energétiques,  
Matériaux et Géosciences (SMEMaG)

Spécialité de doctorat: Combustion

Unité de recherche: IFP Energies nouvelles, 1 et 4 avenue de Bois-Préau, 92852  
Rueil-Malmaison, France ; Institut Carnot IFPEN Transports Energie

Référent: CentraleSupélec

Thèse présentée et soutenue en visio-conférence totale, le 12 mars 2021, par

Edouard SUILLAUD

## Composition du jury:

Benoit Fiorina	Président
Professeur, CentraleSupélec	
Pascale Domingo	Rapporteur & Examineur
Directeur de recherche CNRS, CORIA	
Nilanjan Chakraborty	Rapporteur & Examineur
Professeur, Université de Newcastle, UK	
Andreas Kempf	Examineur
Professeur, Université de Duisburg-Essen, Allemagne	
Frédéric Ravet	Examineur
Expert combustion, Renault SA	
Olivier Colin	Directeur
Docteur, HDR, IFPEN	
Denis Veynante	Co-directeur
Directeur de recherche, CentraleSupélec	
Karine Truffin	Encadrante
Docteur, IFPEN	

**Titre:** Modélisation de la combustion à haut Karlovitz dans les moteurs à allumage commandé

**Mots clés:** Haut Karlovitz, modélisation, moteur à allumage commandé, flamme de prémélange turbulente

**Résumé :** Les constructeurs automobiles ont pour objectif de développer de nouvelles technologies pour diminuer les émissions de  $\text{CO}_2$  des moteurs à allumage commandé (AC) parce que les réglementations en matière d'émissions deviennent de plus en plus strictes. Une possible solution est le concept de "downsizing" appliqué aux moteurs AC, consistant à réduire la cylindrée du moteur tout en augmentant la puissance spécifique. Néanmoins, cette solution augmente l'apparition de combustions anormales, comme le cliquetis. Pour éviter ces phénomènes la combustion est diluée par la recirculation des gaz d'échappement. Cependant, celle-ci augmente la variabilité cycle à cycle de la combustion. Aujourd'hui, la conception et l'optimisation des moteurs AC reposent sur des outils de mécanique des fluides numériques. Cependant, les modèles actuels de combustion turbulente perdent leur caractère prédictif lorsqu'ils sont utilisés pour simuler une combustion fortement diluée dans un écoulement turbulent. Ces modèles ont été conçus en faisant l'hypothèse d'une flamme dans le régime de flammelette. Or, la combustion dans un moteur AC suralimenté et dilué change de régime de combustion correspondant au régime de flamme épaissie (FE). Ainsi, dans cette thèse de doctorat une étude numérique avec le code AVBP est présentée pour mettre en évidence les différences entre les régimes de flammelette et FE. L'objectif de cette thèse est de déterminer un modèle adapté à la combustion dans le régime FE utilisant le formalisme du modèle de flamme cohérente (CFM). Des simulations numériques directes (DNS) d'une flamme de prémélange  $\text{C}_8\text{H}_{18}$ /air sont réalisées.

Une première série de DNS d'interactions flamme-vortex est effectuée dans l'optique de modéliser l'étirement tangentiel du front de flamme à travers la définition d'une fonction d'efficacité. Ensuite, les interactions entre une flamme plane et un champ turbulent 3D sont étudiées. Le champ tur-

bulent est généré et maintenu suivant une méthode spectrale de forçage. Ces simulations permettent d'évaluer la validité du concept de densité de surface de flamme (FSD) dans le régime FE grâce à des analyses de la surface de flamme, de sa structure et des caractéristiques de l'étirement du front de flamme et de la vitesse de déplacement. Ces deux dernières grandeurs sont considérées comme des facteurs clés pour la modélisation de la combustion turbulente fortement diluée. Premièrement, la zone de réaction reste fine pour chaque flamme étudiée, ce qui mène à analyser la flamme à travers une iso-surface particulière de cette zone de réaction. Deuxièmement, la vitesse de déplacement sur cette iso-surface présente des dépendances différentes à l'étirement tangentiel et à la courbure, qui sont modélisées à travers deux longueurs de Markstein effectives dépendant à la fois de l'intensité turbulente et de la diffusion différentielle. Des corrélations en fonction du nombre de Karlovitz sont données pour ces longueurs.

Cette analyse de DNS permet d'étendre le model CFM au régime FE à travers la définition de nouvelles variable de progrès et FSD. Les équations de transport de ces nouvelles variables sont ensuite déterminées. Leur fermeture est présentée en utilisant de nouveaux modèles ou existants pour les termes sources. Ces sous modèles sont comparés a priori aux résultats de DNS permettant de valider et d'ajuster les sous-modèles. Le modèle CFM étendu au régime FE est alors implémenté dans le code AVBP grâce au développement d'une nouvelle relation entre les variables de progrès filtrées au sens de Reynolds et de Favre. Une série de simulations de flamme turbulente monodimensionnelles est ensuite réalisée pour examiner le comportement de chaque sous-modèle lorsqu'ils interagissent entre eux. Une analyse de la sensibilité du modèle à certains paramètres permet de déduire quelques ajustements. Finalement, les résultats encourageant des tests a priori et a posteriori montrent le potentiel de l'extension du model CFM proposée.

**Title:** Modelling of high Karlovitz combustion in spark-ignition engines

**Keywords:** High Karlovitz, modelling, spark ignition engine, turbulent premixed flame

**Abstract:** Car manufacturers aim to develop new technologies for reducing the CO<sub>2</sub> emissions of Spark Ignition (SI) engines as emission regulations get increasingly stringent. One of the solutions found by the car manufacturers is the downsizing concept applied to SI engines, which is to reduce the displacement of the engine while increasing the specific power. Nonetheless, this concept increases the occurrence of abnormal combustions, like knock and super-knock. So, to avoid such phenomena, the combustion is diluted through exhaust gas recirculation (EGR), the rate of which is increased from 5% to 20% or even 30%. However, this recirculation increases the combustion cycle-to-cycle variability.

Nowadays, the car manufacturers rely on CFD tools for designing and optimizing SI engines. However, the current models of turbulent combustion lose their predictivity when they are used to simulate a highly diluted combustion involving high turbulent intensities. Indeed, the current models were built based on the assumptions of the flamelet regime. Yet, the combustion in a diluted boosted SI engine drifts from the flamelet regime to the thin reaction zone (TRZ) regime in a Peters diagram.

Thus, a numerical study using the AVBP code is proposed in this Ph.D thesis to highlight the differences between flames in the flamelet regime and flames in the TRZ regime, the aim of which is to determine a combustion model suitable for combustion in the TRZ regime based on the formalism of the coherent flame model (CFM). Direct numerical simulations (DNS) of a premixed C<sub>8</sub>H<sub>18</sub>/air flame are conducted. First, a set of flame-vortex interactions is performed to investigate the modelling of the tangential strain rate through the definition of an efficiency function.

Then, interactions between a planar flame and a three-dimensional turbulent field are studied considering a forced turbulent field using a spectral method. These simulations are analysed to investigate the validity of the flame surface density (FSD)

concept in the TRZ regime through the analyses of the fame surface, the flame structure, the characteristics of the flame stretch and of the displacement speed in the TRZ regime, which are considered as key factors in the modelling of highly diluted turbulent combustion. First the reaction zone is shown to remains thin for each flame, leading to focus this study on a specific iso-surface in the reaction zone and how it is affected by turbulence. Second, the displacement speed on this iso-surface shows a differentiate dependency on tangential strain rate and curvature. This dependency is modelled through two effective Markstein lengths, which depend on both turbulence intensity and preferential diffusion. Models for these lengths with respect to the Karlovitz number are proposed. This analysis of the DNS yields an extension of the CFM model to TRZ regime through the definition of a new progress variable and using a fine-grained flame surface density. Then, the transport equations of both the new progress variable and the fine-grained FSD are closed with existing models and new ones for the source terms involved. Each sub-model is compared to the DNS results through a specific post-processing method, leading to adjustment of the proposed models.

The model proposed is implemented in the AVBP code. Therefore, a new relationship between the filtered and the resolved progress variable is developed. Then, a set of one-dimensional turbulent flames is performed to evaluate the proposed model and the behaviour of the sub-models with each other. The results from these simulations are compared to the DNS through the previously proposed post-processing methodology. Adjustments of the models are deduced from this analysis. Finally, a discussion on the applicability of this model to engine application is drawn.

To conclude, the encouraging results from a priori and a posteriori validation show the potential of the extension of the CFM model proposed in this thesis.

Université Paris-Saclay

Espace Technologique / Immeuble Discovery

Route de l'Orme aux Merisiers RD 128 / 91190 Saint-Aubin, France



*“And I knew exactly what to do. But in a much more real sense, I had no idea what to do.”*

— Michael Gary Scott, *The Office*

# Remerciements

Je tiens à remercier tout d'abord le Professeur Benoit Fiorina d'avoir accepté la présidence de mon jury de thèse. Je remercie ensuite Pascale Domingo et Nilanjan Chakraborty d'avoir assuré, avec minutie et intérêt, le rôle de rapporteur de ce manuscrit. Je remercie également Andreas Kempf et Frederic Ravet qui ont accepté de participer à mon jury de thèse en tant qu'examineurs.

Je tiens à exprimer toute ma reconnaissance à Denis Veynante et Olivier Colin pour avoir dirigé ce travail de thèse et m'avoir fait profiter de leur grande expérience en combustion. Je remerci Denis Veynante pour sa grande sympathie et pour nous avoir fait confiance dans le pari d'étendre le modèle CFM à la combustion dans le régime des flammes épaissies. Il a toujours accueilli avec ouverture d'esprit nos idées et a suivi avec rigueur nos investigations. Ses conseils pour valoriser le travail réalisé pendant cette thèse de doctorat m'ont été très précieux.

Je souhaite également remercier Olivier Colin dont l'encadrement pendant ces trois années de thèse à l'IFPEN a été d'une très grande qualité scientifique m'ayant permis de surmonter de nombreuses difficultés grâce à un débit d'idées époustouflant.

Je souhaite remercier tout particulièrement Karine Truffin qui m'a encadré pendant ces trois années de thèse à l'IFPEN. Je suis persuadé que sans son encadrement nous n'aurions pas pu obtenir tant de résultats durant cette courte période, notamment grâce aux appels à projets (PRACE, DARI). De plus, ses questions et remarques m'ont permis de prendre du recul sur mon travail et d'enrichir mes compétences en présentation de mes résultats.

J'adresse aussi mes remerciements à tous les membres de l'équipe du projet MACDIL qui ont participé à l'amélioration de mon travail de thèse et à une prise de recul sur les résultats obtenus. Je remercie également Gilles Bruneaux pour tout ce qu'il a fait pour intégrer les doctorants à l'équipe R116 (anciennement R102), et ses actions lors des confinements successifs de la crise du COVID. Enfin je tiens à exprimer mon immense reconnaissance à Michel Guion pour sa bonne humeur en toutes circonstances et surtout pour s'être démené lors du confinement de mars 2020 pour trouver des solutions. J'exprime de vifs remerciements à tous les ingénieurs des départements R116 et R104 pour leur sympathie et leur disponibilité à mes questions. J'ai une pensée particulière pour Stéphane Jay et Christian Angelberger.

Je tiens également à remercier l'ensemble des thésards que j'ai côtoyés au cours des trois dernières années, pour la bonne ambiance qu'ils ont su mettre au troisième étage (la première année) puis au premier étage (la deuxième année) et enfin à Giroflées (lors de la trop courte dernière année). Je remercie très chaleureusement mes collègues de bureaux, Fabien Tagliante et

Maxime Tarrot, pour leur humour, leur disponibilité et les nombreuses discussions et échanges que nous avons pu avoir pendant ces trois années. Enfin, j'ai une pensée particulière pour Andreas, Hassan et Louise (ils se reconnaîtront) pour les dîners autour d'un **Feuerzangenbowle**, les tennis, les discussions et les fous rire.

Enfin, je remercie ma famille et mes amis, en particulier mes parents m'ayant permis de choisir ce parcours académique tout en m'insufflant les valeurs nécessaires à sa réussite. Pour conclure, je remercie Aurore qui fut le soutien indéfectible m'ayant permis d'aller au bout de cette aventure.

# Contents

<b>Introduction</b>	<b>i</b>
<b>1 Modelling of Premixed flames in SI engines</b>	<b>1</b>
1.1 The equations of aero-thermo-chemistry. . . . .	1
1.2 Physics of the laminar premixed flame. . . . .	3
1.3 Turbulent combustion . . . . .	7
1.3.1 Physics of turbulent flow . . . . .	7
1.3.2 Turbulence/combustion interaction mechanisms . . . . .	8
1.3.3 The classification of the interactions between flame and turbulence: Com- bustion regimes . . . . .	9
1.4 Computational fluid dynamics approaches for combustion modelling. . . . .	11
1.4.1 Direct numerical simulations approach . . . . .	12
1.4.2 Reynolds averaged Navier Stokes approach . . . . .	13
1.4.3 Large eddy simulations approach . . . . .	15
1.5 State of the art on computational fluid dynamics modelling of turbulent premixed flames. . . . .	17
1.5.1 Thickened flame for LES model . . . . .	17
1.5.2 $G$ -equation model . . . . .	19
1.5.3 Flame surface density based models . . . . .	21
1.5.4 Algebraic closure of the flame surface density . . . . .	23
1.5.5 The Coherent Flame Model: a flame surface density transport equation approach . . . . .	24
1.6 State of the art on high Karlovitz premixed flames. . . . .	28
1.6.1 Turbulent premixed flames at medium and high Karlovitz numbers . . .	28
1.6.2 Attempts to model premixed flame in the thin reaction zone regime . . .	39
1.7 Conclusions: Objectives and structure of the thesis . . . . .	44
<b>2 Turbulent strain rate modelling using 2D flame/vortex interactions</b>	<b>47</b>
2.1 The direct numerical simulations set-up . . . . .	47
2.1.1 Purpose of the analysis of flame-vortex interactions . . . . .	47
2.1.2 DNS implementation . . . . .	50

2.2	Discussion on the common assumptions in the context of the thin reaction zone regime . . . . .	54
2.3	Analysis of the efficiency function . . . . .	60
2.4	Conclusions . . . . .	64
<b>3</b>	<b>Analysis of 3D direct numerical simulations of premixed flames interacting with turbulence</b>	<b>67</b>
3.1	Direct numerical implementation . . . . .	67
3.1.1	Flow configuration and chemistry . . . . .	68
3.1.2	Turbulence forcing method . . . . .	72
3.1.3	Simulation parameters . . . . .	74
3.1.4	Post-processing methods . . . . .	75
3.2	Flame surface analysis: which approach for modelling ? . . . . .	76
3.2.1	Qualitative analysis of instantaneous flames . . . . .	77
3.2.2	Analysis of the temporal evolution of flame surfaces . . . . .	78
3.2.3	Analysis of the turbulent flame velocity and wrinkling . . . . .	79
3.2.4	Analysis of the inner flame structure . . . . .	81
3.2.5	Modelling implications . . . . .	84
3.3	Analysis of the displacement speed on an iso-surface . . . . .	88
3.3.1	Analysis of conditional means with curvature . . . . .	88
3.3.2	Analysis of conditional means with strain rate and curvature . . . . .	90
3.4	Conclusions . . . . .	97
<b>4</b>	<b><i>A priori</i> modelling for premixed flame in the thin reaction zone regime</b>	<b>99</b>
4.1	Discussion on the coherent flame model . . . . .	99
4.2	Post-processing methodology of DNS for <i>a priori</i> validation . . . . .	101
4.3	Closure of the transport equation of progress variable . . . . .	102
4.3.1	Closure of the turbulent flux . . . . .	102
4.3.2	Closure of the displacement speed . . . . .	106
4.4	Closure of the flame surface density transport equation . . . . .	114
4.4.1	Closure of the unresolved transport term . . . . .	115
4.4.2	Closure of the normal propagation . . . . .	116
4.4.3	Closure of the tangential strain rate . . . . .	118
4.4.4	Closure of the stretch due to curvature . . . . .	126
4.5	Discussion on the relationship between $\tilde{\mathcal{C}}$ and $\bar{\mathcal{C}}$ . . . . .	129
4.6	Conclusions . . . . .	133
<b>5</b>	<b>A first <i>a posteriori</i> validation in the thin reaction zone regime</b>	<b>135</b>
5.1	<i>A posteriori</i> simulations of one-dimensional turbulent flames . . . . .	135
5.1.1	Description of the one-dimensional turbulent flame method . . . . .	135
5.1.2	Description of the models tested . . . . .	137
5.2	Analysis of the one-dimensional turbulent flames – general behaviour of the models	138

5.2.1	Analysis of predicted fuel consumption . . . . .	139
5.2.2	Analysis of the predicted flame structure . . . . .	142
5.3	Analysis of the one-dimensional turbulent flames - Predictions of the sub-models	145
5.3.1	Closure of the filtered progress variable . . . . .	145
5.3.2	Closures of curvature and its variance . . . . .	147
5.3.3	Closures of stretch due to curvature and displacement speed . . . . .	150
5.4	Discussion on the application of the proposed approach to LES and engines simulations . . . . .	153
5.4.1	Discussion on the closure of the transport equation of progress variable .	154
5.4.2	Discussion on the modelling of flame surface production and destruction terms. . . . .	156
5.5	Conclusions . . . . .	161
<b>6</b>	<b>Conclusions and Perspectives</b>	<b>163</b>
6.1	Conclusions . . . . .	163
6.2	Perspectives for future works . . . . .	166
<b>A</b>	<b>Comparison of the convective schemes</b>	<b>171</b>
A.1	Numerical schemes description . . . . .	171
A.1.1	Equations and temporal discretization . . . . .	171
A.1.2	Spatial discretization . . . . .	172
A.1.3	DNS Set-up . . . . .	174
A.2	Comparison of the convective schemes . . . . .	174
A.2.1	Temporal evolutions . . . . .	175
A.2.2	Comparison of statistics of displacement speed on a progress variable iso-surface . . . . .	176
A.2.3	Comparison of statistics for Reynolds averaged Navier-Stokes modelling .	178
A.3	Conclusions . . . . .	179
<b>B</b>	<b>Discussion on turbulence forcing method</b>	<b>181</b>
B.1	Direct numerical simulation implementation . . . . .	181
B.2	Flame surface analysis . . . . .	183
B.2.1	Analysis of the temporal evolution of flame surfaces . . . . .	183
B.2.2	Analysis of the turbulent flame velocity and wrinkling . . . . .	184
B.2.3	Analysis of the inner flame structure . . . . .	186
B.3	Analysis of the displacement speed on an iso-surface . . . . .	187
B.3.1	Analysis of conditional means with curvature . . . . .	188
B.3.2	Analysis of conditional means with strain rate and curvature . . . . .	190
B.4	Statistics for <i>a priori</i> validation . . . . .	193
B.4.1	Statistics of curvature and its variance . . . . .	193
B.4.2	Statistics of stretch due to curvature and displacement speed . . . . .	194
B.5	Conclusions . . . . .	196

<b>C</b>	<b>Derivation of the fine grained flame surface density transport equation</b>	<b>197</b>
<b>D</b>	<b>Laminar stretched flames</b>	<b>199</b>
D.1	Spherical laminar premixed flame . . . . .	199
D.2	Counter-flow laminar premixed flame . . . . .	201
<b>E</b>	<b>Closure of the term due to heat release in the tangential strain rate</b>	<b>203</b>
<b>F</b>	<b>Synthèse en français</b>	<b>205</b>
	<b>List of Figures</b>	<b>209</b>
	<b>List of Tables</b>	<b>221</b>
	<b>Bibliography</b>	<b>223</b>



# Introduction

## Industrial Context

Nowadays, in the context of climate change, the transport sector is one of the main contributors to global anthropogenic CO<sub>2</sub> emissions, about 23%. From Fig. 1, the road transport, which is divided equally into heavy-duty and light-duty vehicles, is the main factor in term of emissions. Furthermore, Spark-Ignition (SI) engine, fuelled with gasoline, powers 70% of the light-duty vehicles worldwide and should still represent 50% in 2030. Thus, SI engines will remain the major energy source and CO<sub>2</sub> contributor for passenger cars. So, reducing CO<sub>2</sub> emissions of passenger cars seems to be one key factor to mitigating global warmings. For this purpose engine manufacturers aim at increasing the efficiency of SI engines.

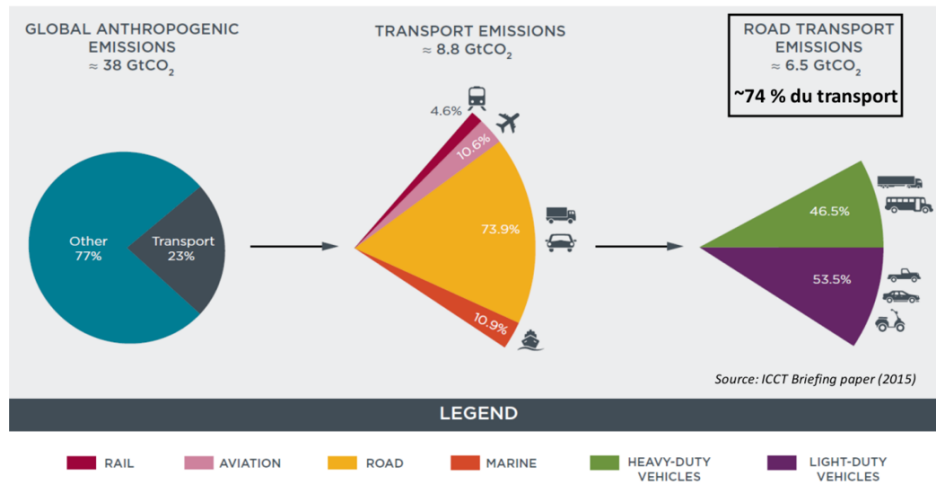


Figure 1: Diagram of anthropogenic emissions focusing on the transport sector

The trend in a route towards high efficiency SI engines is downsizing, which consists in reducing the piston displacement while increasing the specific power. This process is allowed by increasing the engine load using forced induction, through turbochargers or superchargers. This concept could lead potentially to 20% of fuel savings compared to standard engines. However, the use of turbocharger leads to higher temperatures and pressures during combustion, the consequence of which is higher occurrence of abnormal combustion as knock and super-knock. The latter are to be avoided for preserving the engine integrity.

An extensive selection of technologies are available for downsizing, from ultra-lean burn conditions (Benoit et al., 2019) to pre-chamber ignition system (Bozza et al., 2019). One solution investigated by car manufacturers is increasing the rate of diluent gases through exhaust

gas recirculation (EGR), from 5% to 20% or even up to 30%, which is the focus of the present thesis.

The design and optimisation of the complex strategies to be developed for the application of these technologies rely strongly on computational fluid dynamics (CFD). Indeed, the physical processes taking place in such complex devices can hardly be studied experimentally. Today, car manufacturers are mainly using Reynolds average Navier Stokes (RANS) CFD tools, which allow to make a ranking of different geometries and/or strategies. Nonetheless, RANS is unable to predict cycle-to-cycle variability and sporadic phenomena like abnormal combustion even at these standard conditions, because it simulates a phase averaged mean cycle. For this reason, large-eddy simulation (LES) approach was developed. This approach allows to simulate typically 10 to 20 consecutive individual cycles giving access to non-cyclic phenomena, allowing to predict the variance of indicated mean effective pressure (IMEP) of an engine and also the occurrences of knock (Chen et al., 2020).

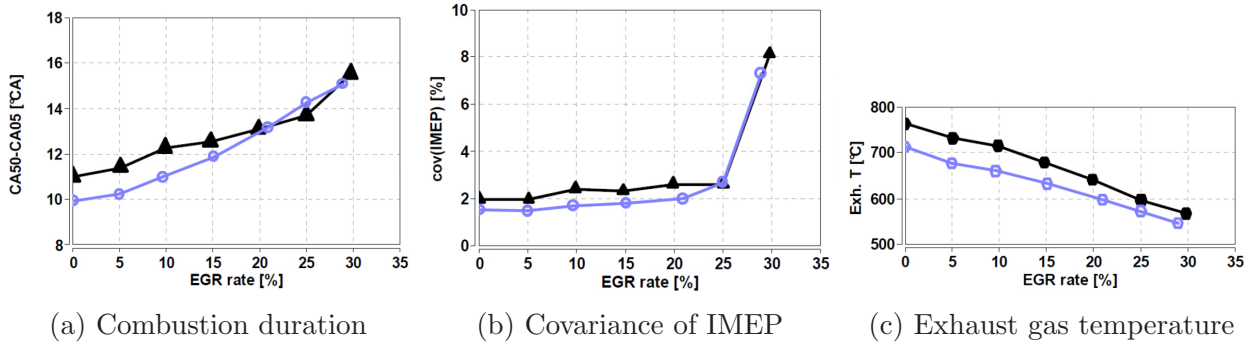


Figure 2: The impact of variation of exhaust gas recirculation (EGR) rate on the engine: (a) the evolution of combustion duration with EGR rate, (b) the evolution of fluctuations of indicated mean effective pressure (IMEP) with EGR rate and (c) the evolution of the exhaust gas temperature with EGR rate. (Francqueville and Michel, 2014)

The impacts of dilution on real boosted SI engines were evaluated in several experiments, such as the one conducted by Francqueville and Michel (2014). In this study, they performed a variation of the dilution rate with EGR in a single-cylinder engine.

The results of this study are summarized in Fig. 2, where the combustion duration is plotted against the EGR rate in Fig. 2a. This combustion time is computed with the difference  $CA_{50} - CA_{05}$ , where  $CA_{05}$  and  $CA_{50}$  correspond to crank angles when 5% and 50% of the fuel mass are burnt, respectively. In Fig. 2a, the combustion duration rises with EGR rate. Moreover, when EGR rate increases, the amount of inert gas to be heated increases, resulting in a decrease in the temperature of the exhaust gas after combustion, which could explain the decrease in exhaust gas temperature with the EGR rate in Fig. 2c. This decrease of temperature allows an increase in the auto-ignition delay of the fuel/air mixture (reducing abnormal combustion tendency).

Moreover, the evolution of the co-variance of IMEP with EGR rate is plotted in Fig. 2b,

which represents the combustion cycle-to-cycle variability of the engine. As seen in Fig. 2b, the covariance of IMEP increases slightly with a growth in EGR rate, for rates below 25%. However, when EGR rates are greater than 25%, the combustion cycle-to-cycle variability highly increases, exceeding the acceptable limit fixed at 5% co-variance of IMEP. In addition, this variability is mainly observed during the first moment after the ignition indicating that the flame is much more affected by the fluctuations of the turbulent flow.

To better understand how dilution affects combustion, Kobayashi et al. (2007) explored the behaviour of Bunsen-type turbulent premixed methane-air flames and propane-air flames at high pressure and temperature. In these experiments, the flames were diluted with CO<sub>2</sub> for a range of EGR rate (in mass) between 0% and 14%. The aim of such a study is to understand the effect of dilution with burnt gases on turbulent flame at different pressures and temperatures.

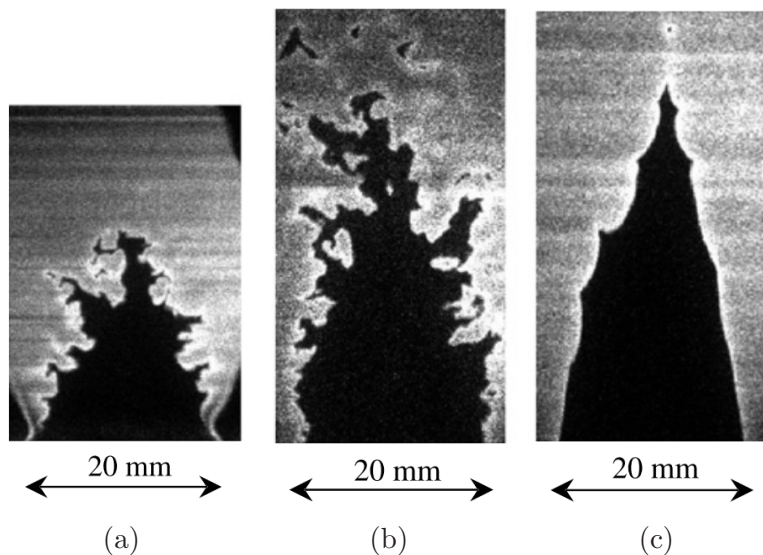


Figure 3: OH-planar Laser induced fluorescence (PLIF) images at 0.5 MPa and 573K: (a) EGR rate = 0% and  $u'_t/S_L^0 = 3$ , (b) EGR rate = 14% and  $u'_t/S_L^0 = 3$ , and (c) EGR rate = 7% and  $u'_t/S_L^0 \approx 0$ . (Kobayashi et al., 2007)

The pictures in Fig. 3 compare OH-planar Laser induced fluorescence (PLIF) of turbulent flames without dilution (Fig. 3a) and with an EGR rate of 14% (Fig. 3b), and a laminar flame diluted with an EGR rate of 7% (Fig. 3c). The turbulent flow fields involved in in Figs. 3a and 3b are similar with a velocity ratio of  $u'_t/S_L^0 = 3$ , where  $u'_t$  is the characteristic velocity of the largest turbulent scale and  $S_L^0$  is the laminar flame velocity.

First, the diluted flames present a larger height than the one without dilution, which corresponds to smaller reaction rate per surface unit. This phenomena indicate that dilution by EGR slows the flame. Second, the comparison of the two turbulent flames shows that the depth of the wrinkles of the flame region tends to increase, and the edge of each wrinkle tends to become sharper when air is diluted with EGR. Third, the laminar flame in Fig. 3c is wrinkled because of intrinsic flame instabilities. This suggests that the intrinsic flame instability also plays a significant role in the case of EGR dilution.

These phenomena may indicate change in the nature of the interaction between the flame and the turbulence. Indeed, when the laminar flame is diluted, the laminar flame velocity decreases, which is equivalent to an increase in the laminar flame thickness. Thus, the size of the vortices seen by the flame front are smaller, relatively to the flame thickness.

So, it seems that the main effect of dilution is to broaden the flame front leading to a more wrinkled front and a lower burning velocity, which are making the flame more passive in turbulent flow.

While this study highlights the effect of dilution on the flame front, the experiments are not representative of a real boosted SI engine with exhaust gas recirculation. In that respect, Mounaïm-Rousselle et al. (2013) conducted a set of experiments on a single-cylinder engine, the aim of which is to study the characteristics of the flame, which can explain the observations made by Francqueville and Michel (2014). The impact of dilution on a stoichiometric iso-octane-air premixed flame is observed from in-cylinder measurements. The operating conditions are summarized below:

- The intake pressure is 1.3 bars, which is representative of a boosted engine
- The intake gases temperature is 50 °C
- The exhaust gases are injected using a mixture of 73.5% of N<sub>2</sub>, 14% of H<sub>2</sub>O and 12.5% of CO<sub>2</sub> by volume
- The EGR rate is limited to 30% in mass

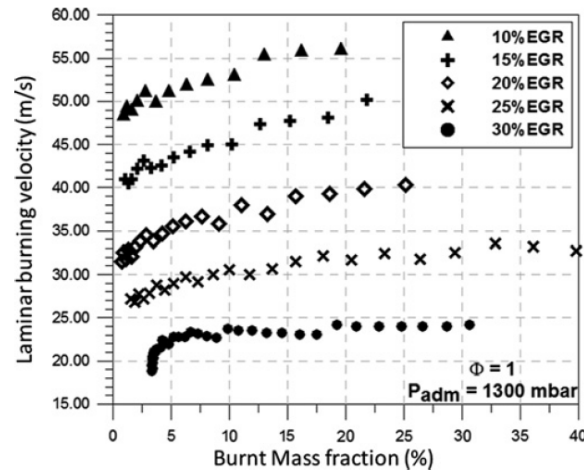


Figure 4: Evolution of laminar burning velocity (expressed in cm/s unlike displayed in the original figure), using the PREMIX code (CHEMKIN package), versus burnt mass fraction for all conditions. (Mounaïm-Rousselle et al., 2013)

When the dilution rate is increased, the authors observed a decrease in the turbulent flame velocity  $S_T$ , which is in agreement with the evolution of the combustion duration observed by Francqueville and Michel (2014). In order to understand this decrease, the impact of dilution



As already seen, dilution by burnt gases and the increase in turbulence, due to turbocharging, lead to an increase in the Karlovitz number. Yet, the current models of turbulent combustion were created based on combustions with low Karlovitz numbers. Thus, these models seem unsuitable for high Karlovitz number combustion, as seen by Gülder and Smallwood (2007) and Oijen et al. (2005).

Finally, from these observations, a project of French National Research Agency (ANR) has been set up to provide tools for engine designing at high EGR rates. This thesis is one of the steps of this project, the aim of which is to provide an accurate combustion model for LES approach.

## Aim of the thesis

The main objective of the ANR project MACDIL (Moteur à Allumage Commandé à forte DILution) is to provide a better understanding and description of the combustion resulting from high dilution rates and high turbulent intensities inside SI engines. This thesis investigates one of the scientific issues of this project.

In fact the modelling of combustion regimes with intermediate and high Karlovitz numbers have only been investigated recently and are the most difficult to describe. Indeed, they do not occur in the flamelet regime, where a local laminar structure hypothesis can be made. In this regime, the existing models should be re-evaluated.

The main challenge is to extend the existing combustion models to high Karlovitz combustion regimes while preserving their ability to describe the flamelet regime. Finally, the objective of this thesis is to assess the possibility to extend the validity of the approach of the flame surface density (FSD) concept to the TRZ regime. For this purpose, a series of iso-octane/air premixed flame direct numerical simulations (DNS) is used to model *a priori* major source terms of the progress variable and flame surface density (FSD) equation in the TRZ regime.

Works conducted in this thesis are organized as follow:

- **Chapter 1** describes the necessary notions and tools for reactive flow simulations. First, the phenomena governing laminar premixed flames are recalled. Then, notions about turbulence are introduced to better understand interactions between flame and turbulent flows. A classification of these interactions is described and different approaches for modelling and simulating turbulent combustion are presented. Then, a state of the art on the understanding and modelling of turbulent combustion with high Karlovitz number is drawn. Then, studies on DNS of combustion in the TRZ regime are analysed to highlight the phenomena involved with high turbulence intensities and their modelling implications. This chapter gives the detailed objectives of the present thesis.
- **Chapter 2** presents the analysis of a set of 2D DNS of flames interacting with a pair of counter-rotating vortices. First, the numerical implementation is described along with



the objective of such simulations, which is to provide elements for modelling the flame stretch. Second, a discussion of the commonly made assumptions is presented in order to understand the reason of the failure of current models to predict accurate flame stretch for high Karlovitz number combustion. Finally, the current models are compared to the results from DNS and a proposed efficiency function.

- **Chapter 3** analyses a set of 3D DNS of flames interacting with a statistically stationary turbulent flow generated using a spectral forcing method. The numerical implementation is first described along with the flow configuration and the forcing method. Second, a general analysis of the resulting turbulent flames is given allowing to propose an approach for modelling. Third, a focus is made on the analysis of the flame displacement speed leading to propose a model for this term on a specific iso-surface of the flame front.
- **Chapter 4** describes the *a priori* approach developed in this thesis to adapt the coherent flame model (CFM) to TRZ regime. First, a discussion on the CFM model is made based on the state of the art and the results from the 3D DNS in Chapters 1 and 3, respectively. Second, the modified transport equations of the CFM model are presented. Third, the different models used and developed during this thesis to close the modified transported equations are presented and *a priori* tested against DNS.
- **Chapter 5** is dedicated to the analysis of statistically 1D turbulent flames, in order to perform *a posteriori* validation of the model proposed in this thesis. First, the proposed model is implemented in the AVBP code. Then, the different closures presented in Chapter 4 are evaluated. Finally, the application of the proposed approach to LES of automotive engines is discussed.
- The conclusions and the perspectives for this work are drawn in Chapter 6.





# Chapter 1

## Modelling of Premixed flames in spark-ignition engines

### 1.1 The equations of aero-thermo-chemistry.

The equations of aero-thermo-chemistry are the traditional Navier-Stokes equations used in fluid mechanics combined to the specific balance equations for reacting flows. The latter are used for the transport of total energy and chemical species. Many books report these equations, such as the one by Poinso and Veynante (2012).

In the rest of this study, Soret and Dufour's effects are not taken into account and the diffusion coefficients are considered as constant for all the species transported. So, the equation system of aero-thermo-chemistry is written as follows:

#### Continuity equation for incompressible fluid

$$\frac{\partial \rho}{\partial t} + \frac{\partial \rho u_i}{\partial x_i} = 0, \quad (1.1.1)$$

where  $\rho$  is the density and  $u_i$  is the  $i^{\text{th}}$  component of the flow velocity field  $\mathbf{u}$ .

#### Conservation of the chemical species

The mass conservation equation for species  $k$  is written:

$$\frac{\partial \rho Y_k}{\partial t} + \frac{\partial \rho (u_i + V_{k,i}) Y_k}{\partial x_i} = \dot{\omega}_k, \quad (1.1.2)$$

where  $Y_k$  is the mass fraction of species  $k$ ,  $V_{k,i}$  is the  $i^{\text{th}}$  component of the diffusion velocity  $\mathbf{V}_k$  of species  $k$  and  $\dot{\omega}_k$  its reaction rate. Due to the total mass conservation and by summing all species equations, given in Eq. (1.1.2), a necessary condition is defined for the diffusion velocity:

$$\sum_{k=1}^N Y_k V_{k,i} = 0. \quad (1.1.3)$$

Using the Hirschfelder and Curtiss approximation for multispecies gas (reported by Poinot and Veynante (2012)), the diffusion velocity of each species might be expressed as follows:

$$\mathbf{V}_k X_k = -D_k \nabla X_k, \quad (1.1.4)$$

where  $X_k$  is the mole fraction of species  $k$  and  $D_k$  is an equivalent diffusion coefficient of species  $k$  in the rest of the mixture, which is defined using the Schmidt number  $S_{ck}$  of species  $k$  and the kinematic viscosity  $\nu$ :

$$D_k = \frac{\nu}{S_{ck}}. \quad (1.1.5)$$

### Conservation of momentum

$$\frac{\partial \rho u_i}{\partial t} + \frac{\partial \rho u_j u_i}{\partial x_j} = -\frac{\partial P}{\partial x_i} + \frac{\partial \tau_{ij}}{\partial x_j}, \quad (1.1.6)$$

where  $P$  is the pressure and  $\tau$  is the viscous tensor. The latter is expressed by Eq. (1.1.7) assuming Newtonian fluid.

$$\tau_{ij} = \mu \left( \frac{\partial u_i}{\partial x_j} + \frac{\partial u_j}{\partial x_i} \right) - \frac{2}{3} \mu \frac{\partial u_j}{\partial x_j} \delta_{ij}, \quad (1.1.7)$$

where  $\mu$  is the dynamic viscosity and  $\delta_{ij}$  is the Kronecker delta. The former allows to define the kinematic viscosity as:  $\mu = \rho \nu$ .

### Conservation of the total energy

$$\frac{\partial \rho e_t}{\partial t} + \frac{\partial (\rho e_t + P) u_j}{\partial x_j} = \frac{\partial u_i \tau_{ij}}{\partial x_j} - \frac{\partial J_j^e}{\partial x_j} + \dot{\omega}_T, \quad (1.1.8)$$

where  $e_t$  is the total energy,  $\dot{\omega}_T$  the heat release due to combustion and  $J_j^e$  the heat flux in the direction  $j$ . The latter is expressed, using Fourier's law, as:

$$J_j^e = -\lambda \frac{\partial T}{\partial x_j}, \quad (1.1.9)$$

where  $\lambda$  is the thermal diffusivity and  $T$  is the temperature.

When the pressure is assumed constant and the viscous heating negligible, the energy balance equation given in Eq. (1.1.8) can be simplified and expressed with temperature, as follows:

$$\rho C_p \left( \frac{\partial T}{\partial t} + \frac{\partial T u_i}{\partial x_i} \right) = \dot{\omega}'_T + \frac{\partial}{\partial x_i} \left( \lambda \frac{\partial T}{\partial x_i} \right) - \rho \frac{\partial T}{\partial x_i} \left( \sum_{k=1}^N C_{p,k} Y_k V_{k,i} \right), \quad (1.1.10)$$

where  $C_p$  and  $C_{p,k}$  are the mass heat capacities at constant pressure of the mixture and of the species  $k$ , respectively, and  $\dot{\omega}'_T$  is the reaction term. The latter differs from the heat release  $\dot{\omega}_T$  and is defined as:

$$\dot{\omega}'_T = \dot{\omega}_T - \sum_{k=1}^N h_{sk} \dot{\omega}_k, \quad (1.1.11)$$

where  $h_{sk} = \int_{T_0}^T C_{p,k} dT$  is the sensible enthalpy of the species  $k$ . Thus, when all heat capacities are equal  $C_{p,k} = C_p$ , the terms  $\dot{\omega}'_T$  and  $\dot{\omega}_T$  are equal.

In the case of premixed combustion, the flame is often described using a **progress variable**  $c$ , such as  $c = 0$  in the fresh gases and  $c = 1$  in the fully burnt gases. There are several ways to define this variable, for example as a reduced temperature using Eq.(1.1.12a) or a reduced mass fraction using Eq.(1.1.12b):

$$c = \frac{T - T_u}{T_b - T_u}, \quad (1.1.12a)$$

$$c = \frac{\sum Y_k - \sum Y_{k_u}}{\sum Y_{k_b} - \sum Y_{k_u}}, \quad (1.1.12b)$$

where the indices  $u$  and  $b$  are used to designate variables in the fresh gases and in the burnt gases, respectively.

From the formulas in Eq.(1.1.12) and from the conservation of total energy in Eq. (1.1.10), a balance equation is defined for the progress variable  $c$ :

$$\frac{\partial \rho c}{\partial t} + \nabla \cdot (\rho c \mathbf{u}) = \nabla \cdot (\rho D_c \nabla c) + \dot{\omega}_c, \quad (1.1.13)$$

where  $D_c$  is a diffusion coefficient and  $\dot{\omega}_c$  is a source term.

### Ideal gas law

$$P = \rho r T, \quad (1.1.14)$$

where  $r$  is the density weight ideal gas constant. This quantity can be computed following:

- from the universal gas constant  $R = 8.314 \text{ J/mol/K}$  and the molar mass  $W = (\sum Y_k / W_k)^{-1}$ , where  $W_k$  is the molar mass of species  $k$ , of the mixture:

$$r = \frac{R}{W}, \quad (1.1.15)$$

- from the mass heat capacities  $C_p$  and  $C_v$  at constant pressure and volume, respectively:

$$r = C_p - C_v. \quad (1.1.16)$$

## 1.2 Physics of the laminar premixed flame.

The one-dimensional laminar flame propagating into a premixed gas is the basic configuration, both for theory and for numerical solving. This flame is usually described as a wave propagating from the burnt to the fresh gases at a speed which reaches a constant value  $S_L$  after a transient phase, as illustrated in Fig. 1.2.1.

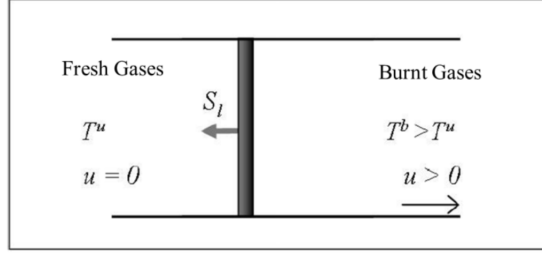


Figure 1.2.1: Propagation of a laminar premixed flame in a duct. (Richard, 2005).

When the laminar flame is considered as steady, the conservation equations presented in Section 1.1 are written as follows:

$$\rho u = \text{constant} = \rho_u S_L, \quad (1.2.1)$$

$$\frac{\partial}{\partial x} (\rho (u + V_k) Y_k) = \dot{\omega}_k, \quad (1.2.2)$$

$$\rho C_p u \frac{\partial T}{\partial x} = \dot{\omega}'_T + \frac{\partial}{\partial x} \left( \lambda \frac{\partial T}{\partial x} \right) - \rho \frac{\partial T}{\partial x} \sum_{k=1}^N C_{p,k} Y_k V_k. \quad (1.2.3)$$

The reaction terms  $\dot{\omega}_k$  in this set of equations are determined through the chemical mechanism, which can be first approximated with the following general model:



where  $\text{O}_x$  and  $P$  are the oxidant and the reaction's products, respectively. The reaction rate  $\dot{\omega}$  of this general reaction is usually modelled through an Arrhenius law:

$$\dot{\omega} = \rho A Y_F^m Y_{O_x}^n \exp \left( -\frac{E_a}{RT} \right), \quad (1.2.5)$$

where  $A$  is a pre-exponential factor,  $E_a$  the activation energy for the reaction,  $Y_F$  and  $Y_{O_x}$  the mass fractions of the fuel and the oxidant, respectively,  $m$  and  $n$  the partial orders of reaction for the fuel and the oxidant, respectively.

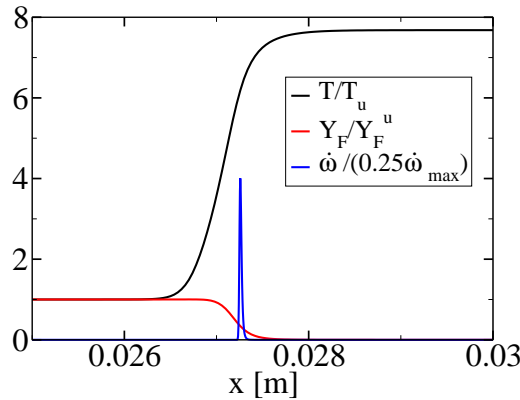


Figure 1.2.2: Spatial profiles of normalized temperature, normalized fuel mass fraction and the normalized reaction rate of a steady 1D laminar premixed flame.

Thus, from the knowledge of a chemical mechanism Eqs. (1.2.1) to (1.2.3) can be solved. A typical solution of this set of equation is given in Fig. 1.2.2, where the spatial profile of the normalized temperature  $T/T_u$  is plotted along with the normalized reaction rate  $\dot{\omega}/(0.25\dot{\omega}_{max})$  and the normalized fuel mass fraction. The normalizations of the temperature and the fuel mass fraction are done with their respective values in the fresh gases,  $T_u$  and  $Y_F^u$ . The reaction rate is normalized with 0.25 of its maximum value for visual purpose.

### Laminar Flame Velocity

Considering the simple case of a 1D stationary laminar flame configuration, the laminar flame velocity  $S_L^0$  is deduced from the fuel mass conservation described by Eq. (1.2.2):

$$\rho_u S_L^0 Y_F^u = - \int_{-\infty}^{+\infty} \dot{\omega}_F dx = \dot{\Omega}_F, \quad (1.2.6)$$

where  $\dot{\Omega}_F$  is the total fuel consumption rate in the domain and  $\dot{\omega}_F$  is the local fuel reaction rate.

### Laminar Flame Thickness

One key feature of premixed laminar flames is that they have a specific thickness which can be characterized by the **thermal thickness** defined as:

$$\delta_L^0 = \frac{T_b - T_u}{\max(|\nabla T|)}, \quad (1.2.7)$$

where  $T_b$  is the temperature of the burnt gases.

By observing the temperature and species profiles and the reaction rate evolution through the flame, two zones can be distinguished in Fig. 1.2.2: a preheating zone and a reaction zone of thickness  $\delta_r$ . The former is a zone where the temperature of the fresh gases increases; the latter is the zone where the reactions actually occur. So, different ways exist to compute the flame thickness, several of them are presented here:

- The **total thickness**  $\delta_L^t$  corresponds to the distance over which the temperature changes from  $T_u(1 + \epsilon)$  to  $T_b(1 - \epsilon)$
- The **diffusion thickness**  $\delta_L$  is usually dimensionally defined using the kinematic viscosity in the fresh gases  $\nu_u$  and the laminar flame velocity  $S_L^0$ :

$$\delta_L = \frac{\nu_u}{S_L^0}. \quad (1.2.8)$$

- **Reaction thickness**  $\delta_r$  is generally defined by a proportional law with the diffusion thickness. For most premixed flames,  $\delta_r/\delta_L^0 \approx 0.1$  (Poinsot and Veynante, 2012).

The main drawback of the previous expressions is that they require a first computation of the flame. Thus, correlations are mainly used for simulation purpose, like the correlation

proposed by Blint (1986):

$$\delta_L^{Blint} = 2 \frac{\lambda}{\rho C_p S_L^0} \left( \frac{T_b}{T_u} \right)^{0.7}, \quad (1.2.9)$$

where  $T_u$  is the temperature of the fresh gases and  $T_b$  is the adiabatic flame temperature. Note that this equation requires the knowledge of the laminar flame speed, which can be determined from phenomenological correlations as the one proposed by Metghalchi and Keck (1982) for iso-octane.

Finally, because in the flame front occur different competitive phenomena (for example, thermal conduction, species diffusion, chemical reaction), some non dimensional numbers are introduced:

- The flame Reynolds number  $Re_f$  compares the characteristic time associated with diffusion and the time it takes for the flame front to propagate over a distance corresponding to its thickness:

$$Re_f = \frac{S_L^0 \delta}{\nu_u}, \quad (1.2.10)$$

where  $\delta$  is the laminar flame thickness and  $\nu_u$  is the kinematic viscosity of the fresh gases. Thus, the value of the flame Reynolds number is strongly dependent on the definition of the flame thickness chosen. When the diffusive flame thickness is used in Eq. (1.2.10),  $Re_f$  is equal to 1.

- The Prandtl number  $Pr$  compares the kinematic viscosity to the thermal conductivity:

$$Pr = \frac{\nu \rho C_p}{\lambda}. \quad (1.2.11)$$

- The Lewis number of each species  $Le_k$  compares the thermal diffusivity to the molar diffusivity of the species  $k$ :

$$Le_k = \frac{\lambda}{\rho C_p D_k} = \frac{Sc_k}{Pr}. \quad (1.2.12)$$

The thermal diffusivity is mainly controlled by the major species, which is typically nitrogen for reactions occurring in the air.

To conclude, a characteristic time of the flame  $\tau_f$  is defined as:

$$\tau_f = \frac{\delta_L}{S_L^0}. \quad (1.2.13)$$

$\tau_f$  represents the time needed by the laminar flame to travel a distance equal to the laminar flame thickness  $\delta_L$



## 1.3 Turbulent combustion

. In spark ignition (SI) engines, the flow is strongly turbulent (Heywood, 1988; Lacour and Pera, 2011; Lorenzo et al., 2020; Mahendar et al., 2019; Prucka et al., 2010).

### 1.3.1 Physics of turbulent flow

First, turbulence is highly chaotic and stochastic. These characteristics associated with the fluctuating processes defining turbulence make the response of the flow highly dependent on initial and boundary conditions. A statistic approach is often chosen to describe turbulent flows. The main idea is to split any quantity  $Q$  into a mean part  $\bar{Q}$  and a fluctuating part  $Q'$  as:

$$Q = \bar{Q} + Q'. \quad (1.3.1)$$

An important issue is how the turbulence energy is distributed over the different length scales present in the flow field. As proposed by Kolmogorov (1940), turbulent fluctuations are associated with different scales ranging from the largest, the **integral length scale**  $l_t$ , to the smallest one, the **Kolmogorov length scale**  $\eta$ . The former scale represents the most energetic turbulent structures, while the latter corresponds to the structures where all the energy has been dissipated. From this theory the flow is considered as a collection of vortices with different characteristic lengths  $r$  and characteristic velocities  $u'(r)$ , allowing to define the eddy turnover time and wave-number as  $\tau_r = r/u'(r)$  and  $k_r = 2\pi/r$ , respectively. To characterize each turbulent scales a Reynolds number  $Re(r)$  is introduced as:

$$Re(r) = \frac{u'(r)r}{\nu}, \quad (1.3.2)$$

where  $u'(r)$  is the characteristic velocity of the motion of size  $r$ . When  $r$  corresponds to the integral scale  $l_t$ , the corresponding Reynolds number is the integral Reynolds number:

$$Re_t = \frac{u'_t l_t}{\nu}, \quad (1.3.3)$$

where  $u'_t$  is the characteristic velocity of the integral scale.

Figure 1.3.1 shows the Kolmogorov energetic cascade in a homogeneous isotropic turbulence (HIT) fully developed and maintained.

Three zones are defined in Fig. 1.3.1 from this spectral representation:

1. The **integral zone**, which corresponds to the largest and the most energetic structures (small wave-numbers).
2. The **inertial zone**, which corresponds to the range of scales where the energy exchanges are achieved without losses. According to Kolmogorov's theory (Kolmogorov, 1940) the energy transfer from the large eddies of size  $l_t$  is equal to the dissipation of energy at

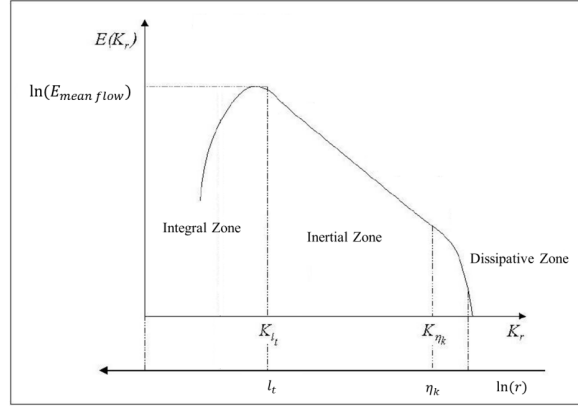


Figure 1.3.1: Turbulence spectrum

the Kolmogorov scale  $\eta$ . Since the dissipation rate  $\varepsilon$  is constant in the inertial zone, dimensional analysis relates the eddy turnover time  $\tau_r$  and the characteristic velocity  $u'(r)$  of the  $r$  length scale to  $\varepsilon$ :

$$\varepsilon \sim \frac{u'(r)^2}{\tau_r} \sim \frac{u'(r)^3}{r}. \quad (1.3.4)$$

Therefore, the dissipation rate  $\varepsilon$  is directly related to the characteristic velocity and the length of the integral scale eddies through:

$$\varepsilon \sim \frac{u_t^3}{l_t}. \quad (1.3.5)$$

The kinetic energy  $u'(r)^2$  at scale  $r$  is then  $\varepsilon^{2/3} k_r^{-2/3}$  leading to the following kinetic energy density in wave number space  $E(k_r)$ :

$$E(k_r) = \frac{du'(r)^2}{dk} \sim \varepsilon^{2/3} k_r^{-5/3}. \quad (1.3.6)$$

This is the well-known  $k^{-5/3}$  law for the kinetic energy spectrum in the inertial subrange.

3. The **dissipative zone** represents the smallest structures with scales lower than the Kolmogorov length. At this scale all the energy is dissipated into heat, and the Reynolds number verifies:

$$Re_\eta = \frac{u'(\eta)\eta}{\nu} = 1. \quad (1.3.7)$$

### 1.3.2 Turbulence/combustion interaction mechanisms

Combustion and turbulent flow are affected by each other within the turbulent reactive flow. First, by crossing the flame front the turbulent field is perturbed, as described by (Poinot and Veynante, 2012, p.196). On the one hand, a relaminarization of the flow can occur as an effect of the increase in the kinematic viscosity  $\nu$  with the high temperatures involved in the burnt gases. On the other hand, the increase in temperature can lead to an acceleration

of the burnt gases caused by their dilatation enhancing the turbulence intensity. Another phenomenon due to the increase of temperature is observed on the turbulent transport. The previous mechanism enhancing the turbulence intensity is usually oriented in the opposite direction of the gradients of the transported variables (typically toward the fresh gases for temperature). However, as mentioned because of thermal expansion, the pressure gradient in flames tends to accelerate the pockets of burnt gas downstream leading to induce vorticity. This phenomenon known as the baroclinic effect (Batley et al., 1996) generates a counter-gradient transport, as observed by Veynante and Poinso (1997). These complexes phenomena competing with each other are studied in detail by Mueller (1998) through the observation of vorticity generation in experiments. This study shows how gas expansion and flame stretching can influence the turbulent flow. As a result, the flame behaviour is clearly not isotropic, and the assumption of isotropic turbulence cannot be considered any more, although in practice turbulent combustion models do not take into account this anisotropy.

Second, the flame front by propagating through the turbulent flow is perturbed by the large and the small eddies. On the one hand, the large scales of turbulence, compared to the laminar flame thickness, are mostly wrinkling the flame. On the other hand, the small eddies are penetrating the flame front which allows them to interact directly with chemistry and to increase turbulent mixing and diffusive effects. However, from a macroscopic point of view the main effect of turbulence on the flame is to increase the propagation speed  $S_T$ . Damköhler (1940) attributed this acceleration to the increase in the flame front surface  $\mathcal{A}_T$  by wrinkling, leading to:

$$\frac{S_T}{S_L^0} \propto \frac{\mathcal{A}_T}{\mathcal{A}_L}, \quad (1.3.8)$$

where  $\mathcal{A}_L$  represents the flame surface of the laminar flame. From Eq.(1.3.8) the wrinkling factor is defined as the right hand side term  $\Xi = \frac{\mathcal{A}_T}{\mathcal{A}_L}$ . In addition, some experimental studies conducted by Abdel-Gayed et al. (1984, 1989) allowed to determine a simple expression for the wrinkling, through  $S_T/S_L$ :

$$\frac{S_T}{S_L^0} = 1 + \alpha \left( \frac{u'_t}{S_L^0} \right)^n, \quad (1.3.9)$$

where  $\alpha$  and  $n$  are constants close to unity. This approximation is valid for weak turbulence (Peters, 1999). Finally, the wrinkling of the flame by turbulence can lead to quenching.

### 1.3.3 The classification of the interactions between flame and turbulence: Combustion regimes

With regards to numerical simulation, it is important to know which of the previous phenomena described takes over. The classification of the combustion regimes of a turbulent premixed flame was the subject of many studies, some of them are based on phenomenological interactions analysis (Borghi, 1985; Peters, 1999). They allow plotting combustion diagrams like Peters-Borghi diagram in Fig. 1.3.2, which is mainly based on non-dimensional numbers, such as the Karlovitz number and the Damköhler number. The latter compares the characteristic time of

the integral scale to the chemical time,  $Da = \tau_t/\tau_f$ ; the former compares the chemical time with the Kolmogorov time,  $Ka = \tau_f/\tau_\eta$ .

These two numbers are often expressed as functions of the laminar flame thickness, the laminar flame velocity and the characteristic lengths and velocities of turbulence:

$$Da = \left( \frac{l_t}{\delta_L} \right) \left( \frac{S_L^0}{u_t'} \right), \quad (1.3.10)$$

$$Ka = \left( \frac{l_t}{\delta_L} \right)^{-1/2} \left( \frac{u_t'}{S_L^0} \right)^{3/2}. \quad (1.3.11)$$

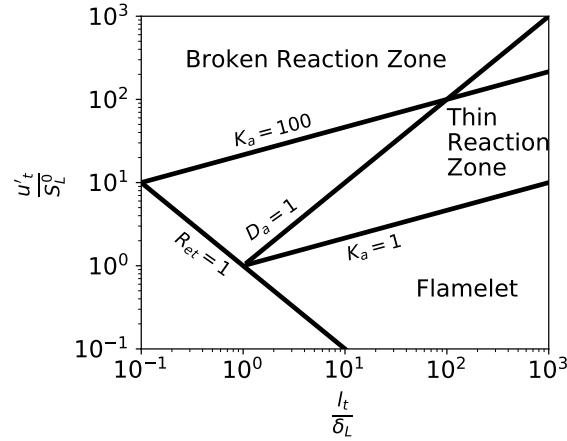


Figure 1.3.2: Combustion regimes using Peters-Borghi diagram (Peters, 1999)

Peters (1999) proposed to classify turbulent premixed flames using the Karlovitz number. This classification, illustrated in Fig. 1.3.2, is based on the Klimov-Williams criterion, which corresponds to the line separating the flamelet and the distributed reaction zones with the condition  $Ka = 1$ :

- When  $Ka < 1$ , the Kolmogorov scale  $\eta_k$  is larger than the laminar flame thickness. Thus, none of the structures of turbulence are penetrating the flame front. The flame is seen as a collection of flamelets, which are 1D thin reactive-diffusive layers locally propagating at the laminar flame speed, and is wrinkled by turbulence, this is the **flamelet regime**.
- When  $Ka > 1$ , the Kolmogorov scale is smaller than  $\delta_L$ , it means that some of the turbulent structures might penetrate the flame front. However, only few of them will affect the flame because the small scales are strongly dissipative. Peters refined the analysis of this zone by proposing a new criterion allowing to identify the structures penetrating the reaction zone. By considering the reaction thickness instead of  $\delta_L$ , the Karlovitz number becomes  $K_{ar} = (\delta_r/\eta_k)^2$ . When  $K_{ar}$  is larger than 1, corresponding to  $Ka = 100$  by assuming  $\delta_r/\delta_L \approx 0.1$ , the smallest turbulent structures penetrate the reaction zone. Thus, this zone is divided into two regimes:
  - When  $1 < Ka < 100$ , the Kolmogorov scale is smaller than the laminar flame thickness but larger than the reaction zone. Therefore, the smallest turbulent structures

are only penetrating the preheat zone. This zone is called the **Thin Reaction Zone (TRZ) regime**.

- When  $Ka > 100$ , the smallest turbulent structures penetrate the reaction zone. Thus, the turbulence is perturbing chemical reactions that can locally lead to quenching. This zone is known as the **Broken Reaction Zone (BRZ) regime**.

### Combustion in IC engines

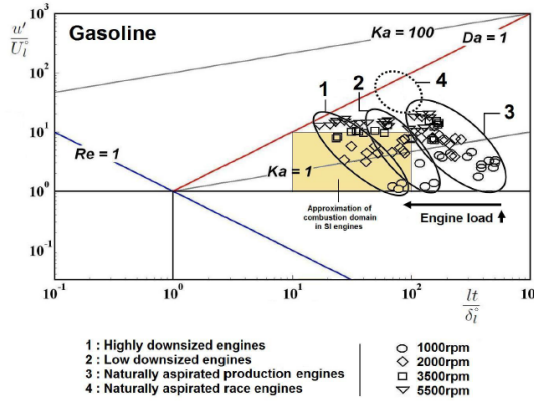


Figure 1.3.3: Operating domain of a IFPEN's SI engine burning gasoline at different engine speeds and loads, from the work of Bougrine (2012).

In IC engines, flow in the chamber is generated by aerodynamic motions induced by the intake, the piston movements and the spray, when direct injection is used. These motions are therefore controlled by air-paths and chamber geometries. Thus, from global geometrical considerations, the length and velocity of the integral scale involved in SI engines are typically in the range:  $1 < l_t/\delta_L < 100$  and  $1 < u'_t/S_L^0 < 50$ . According to the Peters-Borghi diagram in Fig. 1.3.2, it corresponds to a zone in both the flamelet regime and the TRZ regime, as displayed in Fig. 1.3.3. This figure proposed by Bougrine (2012) shows the levels of  $l_t/\delta_L$  and  $u'_t/S_L^0$  for an IFPEN SI engine. It appears that combustion regime involved in SI engines are strongly dependent on the engine load and engine speeds. However, for naturally aspired engines the combustion is mainly in the flamelet regime, while for downsized engines the flames drift from flamelet regime to the TRZ regime.

## 1.4 Computational fluid dynamics approaches for combustion modelling.

Simulations of IC engines require to resolve the equations of aero-thermo-chemistry presented in Section 1.1. For this purpose, there are three different approaches, the concepts of which are derived from the spectral representation of the turbulence presented in Section 1.3. These approaches are: the direct numerical simulations (DNS), the Reynolds averaged Navier Stokes (RANS) and the large eddy simulations (LES).

The principle of these three approaches, described below, are illustrated in Fig. 1.4.1.

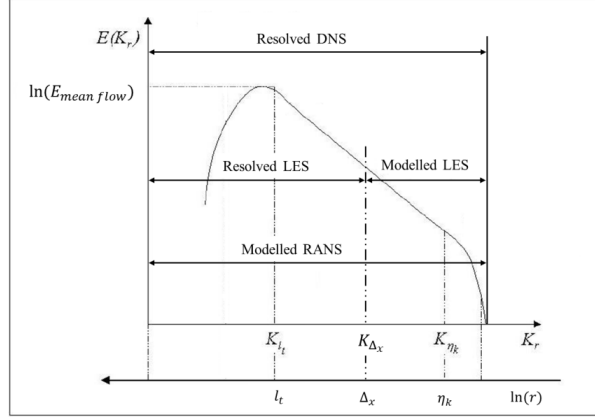


Figure 1.4.1: Turbulence spectrum with resolution methods domain

### 1.4.1 Direct numerical simulations approach

This first method is the most natural one and consists in solving directly the equations of aero-thermo-chemistry. The idea behind DNS is to resolve all scales of the turbulence (presented in Fig. 1.3.1). To achieve this objective, the mesh used to numerically solve the equations in Section 1.1 is subjected to constraints concerning both its size and its cells size. In DNS, to resolve simultaneously the large scales  $l_t$  and the small scales  $\eta$  of turbulence, a mesh with  $N$  cells in each spatial direction, the size of which is  $\Delta$ , should respect the following constraints:

$$N\Delta \geq l_t, \quad (1.4.1)$$

$$\Delta \leq \eta. \quad (1.4.2)$$

Furthermore, the size of the system studied, like the combustion chamber of a piston engine, is larger than the integral length. The characteristic length of the system  $L$ , which is the diameter of the chamber combustion in a piston engine, is expressed as  $L = N\Delta$ . So from this relationship and Eq. (1.4.2), the following relationship is defined between  $N$ , the size of the system and the Kolmogorov length:

$$N \geq \frac{L}{\eta}, \quad \text{or equivalently, } Re_t < N^{4/3}. \quad (1.4.3)$$

However, in the case of a reactive flow the inner flame structure must be fully resolved to compute correctly the chemical reactions. The proper resolution of chemical scales depends strongly on the type of chemical scheme used. For simple description of the chemistry, a minimum of  $N_f \approx 20$  grid points are required to fully resolved the inner flame structure (Poinsot and Veynante, 2012). This leads to an upper limit for the turbulence integrale length scale  $l_t$  which must be smaller than  $L$  to provide converged statistics:

$$\frac{l_t}{\delta_L^0} < \frac{L}{\delta_L^0} < \frac{N}{N_f}. \quad (1.4.4)$$

Equation (1.4.4) can be expressed using the non-dimensional numbers  $Re_t$  and  $Da$ , leading to the following computation grid condition:

$$Re_t Da < \left( \frac{N}{N_f} \right)^2. \quad (1.4.5)$$

For example, considering a piston engine, like the one used by Mounaïm-Rousselle et al. (2013), whose combustion chamber has a diameter of  $L = 85$  mm, a typical Kolmogorov length in this chamber of  $\eta = 0.0047$  mm and a flame whose thickness is approximately  $\delta_L^0 = 0.1$  mm, the number of nodes in the mesh in each direction must be  $N \geq 18000$ . Thus, in this case the total number of cells for computing the flow in the domain is larger than  $10^{12}$ . This example illustrates the difficulties linked to the use of DNS. Indeed, to perform this simulation the computer resources required would be too high for an industrial application. That is why the DNS method is mainly used for academic purpose and simple cases to investigate fundamental aspects which can not be experimentally studied. This approach is the one used in this study to analyse different flames interacting with turbulence in Chapters 2 and 3 .

### 1.4.2 Reynolds averaged Navier Stokes approach

This second method is the most used in industrial processes because of the computing time-savings. Because of the complexity and the large range of scales involved in a turbulent flow, as presented in Section 1.3, this method is focused on the averaged component in Eq. (1.3.1).

Usually, the averaged component is interpreted as an ensemble average. In practice, in IC engines, it is a statistic average of  $N_t$  engine cycles:

$$\overline{Q(\mathbf{x}, \theta)} = \frac{1}{N_t} \lim_{N_t \rightarrow +\infty} \sum_{i=1}^{N_t} Q_i(\mathbf{x}, \theta), \quad (1.4.6)$$

where  $Q$  is any quantity of interest and  $\theta$  is the time during an engine cycle expressed in crank angle. The averaged fluctuations of any quantity is zero,  $\overline{Q'} = 0$ .

This ensemble average is known as the Reynolds average, to be opposed to the Favre average, which is a density weighted average defined as:

$$\tilde{Q} = \frac{\overline{\rho Q}}{\bar{\rho}}. \quad (1.4.7)$$

Analogically to the Reynolds average, any quantity may be decomposed into a Favre average and the associated fluctuations  $Q''$  as  $Q = \tilde{Q} + Q''$ . As for the Reynolds average, the Favre average of the associated fluctuations is zero (*i.e.*,  $\tilde{Q''} = 0$  but the Reynolds average of these fluctuation is non-zero,  $\overline{Q''} \neq 0$ ).

Using these averaged operators, defined in Eqs. (1.4.6) and (1.4.7), the equations of the



aero-thermo-chemistry in Section 1.1 are averaged and become:

$$\frac{\partial \bar{\rho}}{\partial t} + \frac{\partial \bar{\rho} u_i}{\partial x_i} = 0, \quad (1.4.8)$$

$$\frac{\partial \bar{\rho} \tilde{Y}_k}{\partial t} + \frac{\partial \bar{\rho} \tilde{u}_i \tilde{Y}_k}{\partial x_i} + \frac{\partial \bar{\rho} \widetilde{u_i'' Y_k''}}{\partial x_i} = - \frac{\partial}{\partial x_i} \left( \bar{\rho} D_k \frac{\partial \tilde{Y}_k}{\partial x_i} \right) + \bar{\omega}_k, \quad (1.4.9)$$

$$\frac{\partial \bar{\rho} \tilde{u}_i}{\partial t} + \frac{\partial \bar{\rho} \tilde{u}_i \tilde{u}_j}{\partial x_j} + \frac{\partial \bar{\rho} \widetilde{u_i'' u_j''}}{\partial x_j} = - \frac{\partial \bar{P}}{\partial x_j} + \frac{\partial \bar{\tau}_{ij}}{\partial x_j}, \quad (1.4.10)$$

$$\bar{\rho} C_p \left( \frac{\partial \tilde{T}}{\partial t} + \frac{\partial \tilde{T} \tilde{u}_i}{\partial x_i} + \frac{\partial \widetilde{T u_i''}}{\partial x_i} \right) = \bar{\omega}'_T + \frac{\partial}{\partial x_i} \left( \lambda \frac{\partial \tilde{T}}{\partial x_i} \right) - \rho \frac{\partial T}{\partial x_i} \left( \sum_{k=1}^N C_{p,k} Y_k V_{k,i} \right). \quad (1.4.11)$$

Assuming that all the heat capacities  $C_{p,k}$  are equal, using Eq. (1.1.3), Eq. (1.4.11) becomes:

$$\bar{\rho} C_p \left( \frac{\partial \tilde{T}}{\partial t} + \frac{\partial \tilde{T} \tilde{u}_i}{\partial x_i} + \frac{\partial \widetilde{T u_i''}}{\partial x_i} \right) = \bar{\omega}'_T + \frac{\partial}{\partial x_i} \left( \lambda \frac{\partial \tilde{T}}{\partial x_i} \right). \quad (1.4.12)$$

Finally, in this system of averaged equation, some unknown terms appear corresponding to the fluctuations of the quantities involved due to the turbulent structures smaller than  $l_t$ . So, in the RANS approach models for these terms are needed to close the system and enable its solving. The main closures are:

- The **Reynolds stress tensor**  $\widetilde{u_k'' u_i''}$ , which is usually model using Boussinesq's assumption (Boussinesq, 1897) introducing a turbulent viscosity  $\mu_t$ :

$$\bar{\rho} \widetilde{u_k'' u_i''} = -\mu_t \left( \frac{\partial \tilde{u}_i}{\partial x_j} + \frac{\partial \tilde{u}_j}{\partial x_i} - \frac{2}{3} \delta_{ij} \frac{\partial \tilde{u}_i}{\partial x_i} \right) + \frac{2}{3} \bar{\rho} k, \quad (1.4.13)$$

where  $k$  is the turbulent kinetic energy. Many models exist for this tensor, from algebraic models (for example, using a mixing length (Prandtl, 1925)) to models with two transport equations (for example, for  $k$  and  $\varepsilon$  known as the  $k$ - $\varepsilon$  model (Jones and Launder, 1972)).

- The **thermal flux**  $\widetilde{T'' u_i''}$ , which is modelled with a gradient approach introducing a turbulent Prandtl number  $P_{rt}$ :

$$\widetilde{T'' u_i''} = - \frac{\nu_t}{P_{rt}} \frac{\partial \tilde{T}}{\partial x_i}. \quad (1.4.14)$$

- The **turbulent species flux**  $\widetilde{Y_k'' u_i''}$ , which are usually modelled with gradient approach introducing a turbulent Schmidt number  $S_{ct}$ :

$$\bar{\rho} \widetilde{Y_k'' u_i''} = - \frac{\mu_t}{S_{ct}} \frac{\partial \tilde{Y}_k}{\partial x_i}. \quad (1.4.15)$$

- The **mean reaction rate**  $\bar{\omega}_k$  or  $\bar{\omega}'_T$ . Numerous studies propose models for this quan-

tity and are well documented (Kuo, 2005; Poinso and Veynante, 2012; Veynante and Vervisch, 2002). Some of these models are: the eddy break up (EBU) model (Spalding, 1977), the Bray-Moss-Libby (BML) model (Bray and Moss, 1977), flame surface density models (Marble and Broadwell, 1977; Pope, 1988; Trouvé and Poinso, 1994) or probability density functions models (Pope, 1985).

### 1.4.3 Large eddy simulations approach

The large eddy simulations approach can be seen as a hybrid method combining DNS and RANS approaches. Indeed, the objective in LES is to explicitly compute the largest structures of the flow field, whereas the effects of the smallest ones are modelled (as illustrated in Fig. 1.4.1).

Analogously to RANS approach, variables are spatially filtered to distinguish the largest and the smallest scales in LES. The filtered quantity  $\overline{Q}$  is then defined as:

$$\overline{Q(\mathbf{x}, t)} = \int_{\mathcal{V}} Q(\mathbf{x}', t) G_{\Delta}(\mathbf{x} - \mathbf{x}') d\mathbf{x}', \quad (1.4.16)$$

where  $\mathcal{V}$  is the domain of simulation,  $\Delta$  is the filter width and  $\mathbf{x}$  is the position vector. The functions used as filter need to respect essential properties, which are:

- the filter is normalized:

$$\int_{\mathcal{V}} G_{\Delta}(\mathbf{x} - \mathbf{x}') d\mathbf{x}' = 1. \quad (1.4.17)$$

- the filter is linear:

$$\overline{Q_1 + Q_2} = \overline{Q_1} + \overline{Q_2}. \quad (1.4.18)$$

- the filter commutes with the derivation operators:

$$\frac{\partial \overline{Q}}{\partial t} = \overline{\frac{\partial Q}{\partial t}}, \quad (1.4.19)$$

$$\frac{\partial \overline{Q}}{\partial x_i} = \overline{\frac{\partial Q}{\partial x_i}}. \quad (1.4.20)$$

This commutation is only valid under restrictive assumptions and often wrong in IC engines, where the filter size varies with spatial location. However, the uncertainties due to this commutation are neglected and their effects are assumed to be incorporated in the subgrid scale models (Poinso and Veynante, 2012).

Some of the usual filters in LES are given below:

- **The box filter:**

$$G_{\Delta}(\mathbf{x}) = \begin{cases} \frac{1}{\Delta^n} & \text{if } |\mathbf{x}| \leq \frac{\Delta}{2}, \\ 0 & \text{otherwise.} \end{cases} \quad (1.4.21)$$

- **The Gaussian filter:**

$$G_{\Delta}(\mathbf{x}) = \left( \frac{1}{\Delta} \sqrt{\frac{6}{\pi}} \right)^n \exp \left( -\frac{6}{\Delta^2} \mathbf{x}^2 \right). \quad (1.4.22)$$

- **The spectral filter:**

$$G_{\Delta}(\mathbf{x}) = \frac{\sin \left( \frac{\pi}{\Delta} \mathbf{x} \right)}{\mathbf{x} \pi}. \quad (1.4.23)$$

In Eqs. (1.4.21) and (1.4.22),  $n$  represents the number of dimensions of the studied domain.

Finally, a Favre filter is defined in LES analogously to the Favre average in RANS approach:

$$\tilde{Q} = \frac{\overline{\rho Q}}{\bar{\rho}}. \quad (1.4.24)$$

In practice, the filtering is done through the mesh of size  $\Delta_x$ . Consequently, the apparent filtering is assimilated to a Gaussian filter or a box filter, the width of which is close to  $\Delta_x$ .

The following system of the filtered equations of the aero-thermo-chemistry is analogous to the RANS averaged system in Eqs. (1.4.8) to (1.4.11).

Finally, in this system of filtered equations, some unknown terms appear corresponding to the effects of unresolved motions. The main closures of these terms in LES are:

- The **subgrid scale Reynolds stress tensor**  $\widetilde{u_k u_i} - \tilde{u}_k \tilde{u}_i$ , which is usually model through a kinematic turbulent sub-grid scale viscosity  $\nu_t$  and Boussinesq's assumption:

$$\widetilde{u_i u_j} - \tilde{u}_i \tilde{u}_j = -\nu_t \left( \frac{\partial \tilde{u}_i}{\partial x_j} + \frac{\partial \tilde{u}_j}{\partial x_i} - \frac{2}{3} \delta_{ij} \frac{\partial \tilde{u}_i}{\partial x_i} \right) + \frac{2}{3} k_{sgs}, \quad (1.4.25)$$

where  $k_{sgs}$  is the turbulent sub-grid scale kinetic energy. Many models exist for this tensor, from algebraic models (such as Smagorinsky's model (Smagorinsky, 1963)) to models with a transport equation for  $k_{sgs}$ , reported by Richard (2005).

- The **sub-grid scale thermal and species flux**  $\widetilde{u_i T} - \tilde{u}_i \tilde{T}$  and  $\widetilde{u_i Y_k} - \tilde{u}_i \tilde{Y}_k$  are usually modelled with a gradient approach like for RANS modelling:

$$\bar{\rho} C_p \left( \widetilde{u_i T} - \tilde{u}_i \tilde{T} \right) = -\bar{\rho} C_p \frac{\nu_t}{P_{rt}} \frac{\partial \tilde{T}}{\partial x_i}, \quad (1.4.26)$$

$$\bar{\rho} \left( \widetilde{u_i Y_k} - \tilde{u}_i \tilde{Y}_k \right) = -\bar{\rho} \frac{\nu_t}{S_{ct}} \frac{\partial \tilde{Y}_k}{\partial x_i}, \quad (1.4.27)$$

where  $S_{ct}$  and  $P_{rt}$  are turbulent Schmidt and Prandtl numbers, respectively.

- The **mean reaction rate**  $\bar{\omega}_k$  or  $\bar{\omega}'_T$ . As for the RANS approach, numerous studies were conducted to propose models for this quantity and are well documented (Poinot and Veynante, 2012; Veynante and Vervisch, 2002). A non-exhaustive list of models is further described in the next section.

To conclude, the potential of the LES can be illustrated on a piston engine application, where typical values of the mesh size  $\Delta_x$  are approximately 0.5 mm. Using this magnitude to define a LES filter width for the piston engine cited in Section 1.4.1 (Mounaïm-Rousselle et al., 2013) leads to a mesh using 170 cells in each direction. Thus, the 3D LES mesh for the combustion chamber would have approximately 4,000,000 cells, which is much smaller than the DNS mesh presented in Section 1.4.1. Nevertheless, with this approach only the largest structures of turbulence are resolved.

## 1.5 State of the art on computational fluid dynamics modelling of turbulent premixed flames.

As told in the previous section, applying an LES filter allows to define a coarse mesh. However, with such mesh the front flame is usually not resolved. Indeed, the flame thickness is approximately 0.05 mm while a typical cell size for an engine LES simulation is about 0.5 mm. Yet, the heat release that occurs in the flame front is usually large and the other relevant variables are evolving in the flame front along a steep slope.

To overcome these issues, three main approaches have been proposed: simulation of an artificially thickened flame, use of a flame front tracking technique (*G*-equation), or filtering with a Gaussian filter larger than the mesh size as proposed by Boger (1998; 2000). Some RANS approaches, such as probability density function formulations or developing sub-grid scale models for filtered reaction rates and unresolved scalar transport, can be used to avoid the aforementioned theoretical problems as reported by Poinso and Veynante (2012).

The present section is dedicated to the description of the three main LES approaches cited beginning with artificially thickened flames. Then, the level-set approach is presented following by the description of models based on flame surface density.

### 1.5.1 Thickened flame for LES model

The thickened flame for LES (TFLES) model is based on a kinetic description of the flame. This model first introduced by Butler and O'Rourke (1977) and O'Rourke and Bracco (1979) for laminar flame simulations consists in thickening artificially the flame front by a factor  $F$ . This thickening affects only the thickness of the flame front.

Indeed, as presented in Section 1.2 the flame thickness  $\delta_L^0$  and the laminar flame speed  $S_L^0$  are given by:

$$\delta_L^0 \propto \frac{D}{S_L^0}, \quad (1.5.1)$$

$$S_L^0 \propto \sqrt{D\dot{\omega}}, \quad (1.5.2)$$

where  $D$  is a diffusivity coefficient (either thermal or molar) of the fresh gases and  $\dot{\omega}$  is the mean reaction rate. Thus, multiplying the diffusivity by  $F$  while dividing the  $\dot{\omega}$  by this same

factor thickens the flame by a factor  $F$ .

Nevertheless, artificially thickening the flame by a factor  $F$  leads to decrease the Damköhler number by this same factor:

$$Da^F = \frac{lt}{F\delta_L^0} \frac{S_L^0}{u_t'} = \frac{1}{F} Da, \quad (1.5.3)$$

where  $Da$  and  $Da^F$  are the real Damköhler number and the one after thickening, respectively. This decrease in the Damköhler number leads to strongly change the turbulence/flame interactions. Indeed, some studies from DNS (Angelberger et al., 1998; Veynante and Poinso, 1997) show that by thickening artificially the flame, the turbulence is not disturbing the flame as much as it should, in particular the small vortices, the scales of which are larger than the LES filter width  $\Delta$  but smaller than flame thickness  $F\delta_L^0$ . Veynante and Poinso (1997) and Angelberger et al. (1998) show that these vortices are no longer affecting the flame front, while vortices of scales larger than  $F\delta_L^0$  are less efficient. Thus, the creation of flame surface by turbulence through the wrinkling of the flame front is largely underestimated using an artificially thickened flame.

Based on these observations, some studies such as the one conducted by Colin et al. (2000) proposed the use of an efficiency function  $E$ , the aim of which is to evaluate the real wrinkling  $\Xi_0$  compared to the wrinkling of the resolved flame front  $\Xi_1$ . The wrinkling is defined as the ratio  $\mathcal{A}_T/\mathcal{A}_0$ , where  $\mathcal{A}_T$  is the turbulent flame surface and  $\mathcal{A}_0$  is the projection of  $\mathcal{A}_T$  on the normal propagation direction.

$$E = \frac{\Xi_0}{\Xi_1}. \quad (1.5.4)$$

The spectral analysis of DNS similar to those conducted by Meneveau and Poinso (1991) lead Angelberger et al. (1998) to the following expression for the sub-grid scale wrinkling  $\Xi$  generated by a homogeneous isotropic turbulence:

$$\Xi = 1 + \alpha \Gamma \left( \frac{\Delta}{\delta_L^0}, \frac{u_{\Delta}'}{S_L^0} \right) \frac{u_{\Delta}'}{S_L^0}, \quad (1.5.5)$$

where  $u_{\Delta}'$  is the fluctuation velocity associated to the turbulent scales  $\Delta$ , and  $\Gamma$  is an efficiency function. Studies (Bougrine et al., 2014; Charlette et al., 2002a; Colin et al., 2000; Meneveau and Poinso, 1991) are dedicated to the modelling of this function, some of them are reported in Table 1.1. The model constant  $\alpha$  is written by Colin et al. (2000) to get a turbulent flame speed  $S_T = \Xi S_L^0$  with the form  $S_T = S_L^0 + u_t'$ :

$$\alpha = \beta \frac{2 \ln(2)}{3c_{ms}(Re_t^{1/2} - 1)}, \quad (1.5.6)$$

where  $c_{ms} = 0.28$  and  $\beta$  is equal to unity. This expression involves the turbulent Reynolds number  $Re_t = l_t u_t'/\nu$ , which is rarely known *a priori* in the context of LES. To overcome this issue, the efficiency function proposed by Charlette et al. (2002a) can be used, which does not involve integral quantities.

In practice, the effects of the thickening on the resolved wrinkling are implemented in LES code by multiplying the reaction rate and the diffusivities by  $E$ . Thus, this model may be summarized with the following relationships:

$$\delta_{L,resolved} \propto \frac{EFD}{ES_L^0} = F\delta_L^0, \quad (1.5.7)$$

$$S_T \propto \sqrt{(EFD)\frac{E\dot{\omega}}{F}} = ES_L^0. \quad (1.5.8)$$

To conclude, this approach presents many advantages mainly due to its simplicity. For example:

- it allows to control easily the thickening of the flame front given by  $F\delta_L^0$ ,
- its form, which does not depend on combustion regime assumptions, seems universal.
- this model naturally converges to the laminar flame when the turbulence intensity sufficiently decreases.

Nevertheless, the drawbacks of this model are drags to its application for new IC engines:

- The needed thickening factor  $F$  for IC engines configurations are very large, approximately 50 to 100. These levels of  $F$  might affect the evaluation of the wall heat flux, or the simulation of the sparking phase. These issues are well documented by Richard (2005).
- The thickening changes the turbulence/combustion interactions due to the change in the characteristic flame time involved, leading to a modified Damköhler number.
- The efficiency function is developed based on flamelet assumptions and is probably not valid in the TRZ regime.
- The main issue concerns the equilibrium assumption between production and destruction of sub-grid scale flame surface, which is needed for the use of an algebraic closure of the sub-grid scale wrinkling.

### 1.5.2 $G$ -equation model

Contrary to the TFLES model, the “ $G$ -equation” approach is purely kinematic, where the flame thickness is set to zero and the flame front is described as a propagating surface. To track this surface, Kerstein et al. (1988) introduced a variable  $G$ , the field of which is resolved on the LES mesh as illustrated in Fig. 1.5.1.

Thereby, the flame is spotted with an iso-surface  $G = G^*$  and the  $G$  field is obtained with the transport equation 1.5.9.

$$\frac{\partial G}{\partial t} + u_i \frac{\partial G}{\partial x_i} = w \left| \frac{\partial G}{\partial x_i} \right|, \quad (1.5.9)$$

where  $w$  is the propagation velocity of the iso-surface  $G = G^*$ .

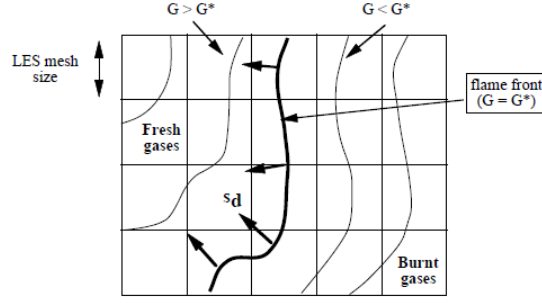


Figure 1.5.1: Flame front and  $G$  field (Poinsot and Veynante, 2012)

When the  $G$ -equation is filtered the term  $\overline{w|\frac{\partial G}{\partial x_i}|}$  appears and needs to be modelled. Usually, a similar transport equation for the resolved field  $\overline{G}$  as the  $G$  equation given in Eq. (1.5.9) is defined (Peters, 1999; Pitsch, 2005):

$$\frac{\partial \overline{G}}{\partial t} + \overline{u_i} \frac{\partial \overline{G}}{\partial x_i} = S_T \left| \frac{\partial \overline{G}}{\partial x_i} \right|, \quad (1.5.10)$$

where  $S_T$  is the propagation speed of the resolved field  $\overline{G}$ . This velocity can be seen as a sub-grid scale turbulent flame speed. To close Eq. (1.5.10), this velocity must be modelled. The commonly used model for  $S_T$  proposed by Pitsch (2005) is based on a similar relationship as Eq. (1.3.9):

$$\frac{S_T}{S_L} = 1 + \alpha \left( \frac{u'_\Delta}{S_L^0} \right)^n, \quad (1.5.11)$$

where the model constants  $\alpha$  and  $n$  are close to unity. The main drawback of this approach is that  $S_T$  is a global variable difficult to measure and the model of which depends strongly on the modelling of the velocity fluctuations  $u'_\Delta$ .

Finally, the main advantage of this approach is that it does not depend on combustion regimes. Nevertheless, many issues might make difficult its use in new IC engines simulations, such as:

- From a numerical point of view, the absence of diffusion term in the transport equation of  $G$  might lead to very large gradient of each variables. Consequently, the simulations could diverge. Therefore, front-tracking techniques are needed, as well as cusp removal techniques.
- As for the TFLES model, the sub-grid scale wrinkling is introduced through the turbulent flame speed in Eq. (1.5.11) leading to the same limit for this approach.
- The correlations for the turbulent flame speed are based on flamelet assumptions making them difficult to use in TRZ regime.

### 1.5.3 Flame surface density based models

When Eq.(1.1.13) is filtered with a LES filter following the approach defined in Section 1.4.3, the filtered equation is:

$$\frac{\partial \overline{\rho c}}{\partial t} + \nabla \cdot (\overline{\rho c \mathbf{u}}) + \nabla \cdot [\overline{\rho}(\widetilde{c\mathbf{u}} - \widetilde{c}\widetilde{\mathbf{u}})] = \nabla \cdot (\overline{\rho D_c \nabla c}) + \overline{\dot{\omega}_c}. \quad (1.5.12)$$

There are three terms to model in Eq.(1.5.12):

1. **The unresolved turbulent transport**  $\widetilde{c\mathbf{u}} - \widetilde{c}\widetilde{\mathbf{u}}$ .
2. **The filtered molecular diffusion fluxes**  $\nabla \cdot (\overline{\rho D_c \nabla c})$ .
3. **The filtered reaction rate**  $\overline{\dot{\omega}_c}$ .

The unresolved turbulent transport is generally modelled using a simple gradient assumption, as proposed by Boger (1998; 2000):

$$\widetilde{c\mathbf{u}} - \widetilde{c}\widetilde{\mathbf{u}} = -\frac{\nu_t}{S_{ct}} \nabla \widetilde{c}, \quad (1.5.13)$$

where  $S_{ct}$  is a sub-grid scale turbulent Schmidt number, and  $\nu_t$  is the sub-grid scale viscosity estimated from turbulence models. Richard et al. (2005; 2007) suggested to take into account a laminar contribution, due to thermal expansion, in LES in the unresolved turbulent transport leading to:

$$\nabla \cdot [\overline{\rho}(\widetilde{c\mathbf{u}} - \widetilde{c}\widetilde{\mathbf{u}})] = -\nabla \cdot \left[ \overline{\rho} \frac{\nu_t}{S_{ct}} \nabla \widetilde{c} \right] - \rho_u S_L^0 \nabla \cdot [(\bar{c} - \widetilde{c}) \bar{\mathbf{n}}], \quad (1.5.14)$$

where  $\bar{\mathbf{n}} = -\nabla \bar{c} / |\nabla \bar{c}|$  is the normal vector to the filtered flame surface pointing toward the fresh gases.

In order to model the two other terms, the G-equation and the progress variable approaches are compared. These two approaches are equivalent, when the variable  $G$  is chosen as the progress variable  $c$ :

$$\nabla \cdot (\rho D_c \nabla c) + \dot{\omega}_c = \rho S_d |\nabla c|, \quad (1.5.15)$$

where  $S_d$  is the displacement speed of the iso-surface of the progress variable  $c$  relatively to the local flow velocity. The velocity  $S_d$  is defined using Eq.(1.5.16), deduced from the exact balance equation of the progress variable  $c$  in Eq.(1.1.13).

$$S_d = \frac{1}{|\nabla c|} \frac{Dc}{Dt}, \quad (1.5.16)$$

where  $Dc/Dt$  is the material derivative of the progress variable defined as  $Dc/Dt = \partial c / \partial t + \mathbf{u} \cdot \nabla c$ .

Then, the flame surface density (FSD) is defined as the amount of flame surface in a volume. This FSD is first defined from the area of the iso-surface of  $c^*$  with  $\Sigma^* = \delta \mathcal{A}^* / \delta V = |\nabla c|_{c=c^*}$ , which corresponds to the fine-grained FSD (Vervisch et al., 1995). However, this approach



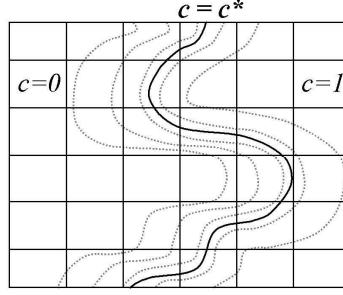


Figure 1.5.2: Schematic iso-surface  $c = c^*$ . A flame surface density  $\bar{\Sigma}^*$  and a surface averaged reaction rate  $\langle \rho S_d \rangle_s^*$  are associated with each iso-surface. The generalized flame surface density and the generalized surface averaged reaction rate  $\langle \rho S_d \rangle_s$  allow to take into account all the iso-surfaces in the flame front. (Richard, 2005)

depends strongly on the choice of  $c^*$ . Assuming the flame infinitely thin,  $\Sigma^*$  does not depend on the choice of  $c^*$  leading to consider  $\bar{\Sigma}^* = \bar{\Sigma}$ , where  $\bar{\Sigma} = \int_0^1 \bar{\Sigma}^* dc^*$  is the **generalized** flame surface density (see Figure 1.5.2).

When Eq. (1.5.15) is filtered,  $\overline{\rho S_d |\nabla c|}$  should be modelled. For this purpose, Boger (1998; 2000) proposed to introduce a Dirac function, following Gao's approach (Gao and O'Brien, 1993), and wrote:

$$\overline{\rho S_d |\nabla c|} = \int_V \rho S_d |\nabla c| G_\Delta(\mathbf{x}') d\mathbf{x}', \quad (1.5.17)$$

$$= \int_V \int_0^1 \rho S_d |\nabla c| \delta(c - c^*) G_\Delta(\mathbf{x}') dc^* d\mathbf{x}', \quad (1.5.18)$$

$$= \int_0^1 \langle \rho S_d \rangle_s^* \bar{\Sigma}^* dc^*, \quad (1.5.19)$$

$$= \langle \rho S_d \rangle_s \bar{\Sigma}, \quad (1.5.20)$$

where  $\langle \rho S_d \rangle_s^* = \overline{\rho S_d |\nabla c| \delta(c - c^*)} / |\nabla c| \delta(c - c^*)$  is the surface averaged of  $\rho S_d$  on the iso-surface  $c = c^*$  and  $\bar{\Sigma}^* = |\nabla c| \delta(c - c^*)$  is the sub-grid flame surface density of the iso-surface  $c = c^*$ . Equation 1.5.20 defines the generalized surface averaged  $\langle \rho S_d \rangle_s$ , which is generally modelled with Eq.(1.5.21) in the flamelet regime assuming the flame locally propagates at the laminar flame speed:

$$\langle \rho S_d \rangle_s = \rho_u S_L. \quad (1.5.21)$$

Finally, the filtered balance equation of progress variable Eq.(1.5.12) becomes a filtered transport equation involving the flame surface density:

$$\frac{\partial \bar{\rho c}}{\partial t} + \nabla \cdot (\bar{\rho c} \bar{\mathbf{u}}) = \rho_u S_L \bar{\Sigma}. \quad (1.5.22)$$

The main advantages of this approach are:

- It allows to decouple the chemistry and the turbulence by introducing the laminar flame

velocity, which allows to adapt the chemistry to a large range of conditions, like in the  $G$ -equation approach.

- The progress variable  $c$  is a well defined physical variable, which allows to easily compare results from simulations and from experiments.

The issue here is to evaluate the flame surface density  $\bar{\Sigma}$ . There are two main approaches to model the FSD, through an algebraic model or through a transported equation for  $\bar{\Sigma}$ , described in Sections 1.5.4 and 1.5.5, respectively.

#### 1.5.4 Algebraic closure of the flame surface density

The concept of algebraic model of flame surface density is a simple approach. The idea is to express  $\bar{\Sigma}$  using a sub-grid scale wrinkling factor  $\Xi$ . This wrinkling factor is the ratio between the subgrid scale flame surface and its projection in the propagating direction. It is computed as proposed by Boger (2000):

$$\Xi = \frac{|\nabla c|}{|\nabla \bar{c}|}. \quad (1.5.23)$$

An expression for flame surface density is deduced from Eq.(1.5.23):

$$\bar{\Sigma} = \Xi |\nabla \bar{c}|, \quad (1.5.24)$$

where  $\nabla \bar{c}$  is the gradient of the resolved progress variable.

Boger et al. (1998; 2000) proposed to use the BML model (well described by Poinso and Veynante (2012)) combined with TFLES approach to model  $\Xi$ , leading to:

$$\bar{\Sigma} \approx 4\sqrt{\frac{6}{\pi}} \Xi \frac{\bar{c}(1 - \bar{c})}{\Delta}, \quad (1.5.25)$$

where  $\Delta$  is the width of the LES filter. Note that  $\Delta/\Xi$  represents a wrinkling scale.

First, the model proposed for  $\Xi$  in Eq. (1.5.5) for TFLES model is commonly used. Charlette et al. (2002a) proposed an algebraic closure of the flame surface density through:

$$\Xi = 1 = \min \left( \frac{\Delta}{\delta_L^0}, \Gamma \frac{u'}{S_L^0} \right)^\beta, \quad (1.5.26)$$

where  $\beta$  is a model constant that can be evaluated using a dynamic approach (Charlette et al., 2002b).

An alternative model, based on the fractal approach by Gouldin et al. (1989), was applied by Wang et al. (2011). With this approach, the wrinkling is similar to:

$$\Xi = \left( \frac{\Delta}{\delta_c} \right)^\beta, \quad (1.5.27)$$

where  $\delta_c$  is the inner cut-off scale estimated as twice the laminar flame thickness, and  $\beta$  is a model parameter determined using the dynamic evaluation proposed by Charlette et al. (2002b). This model, tested using jet flames, has been adapted to simulations of IC engines by Mouriaux et al. (2017).

The main drawback of this method lies in the equilibrium assumption between production and destruction of sub-grid scale flame surface, as reported by Rymer (2001). Indeed, the wrinkling  $\Xi$  is given by a similar relationship as the ones involved in TFLES model and  $G$ -equation models.

### 1.5.5 The Coherent Flame Model: a flame surface density transport equation approach

The second approach was first introduced by Marble and Broadwell (1977) corresponding to an empirical transport equation for the flame surface density. Pope (1988) and Candel and Poinso (1990) proposed a more rigorous approach based on the use of conservation equations for elementary volumes and surfaces embedded in a turbulent flow field leading to define an exact balance equation for the flame surface-to-volume ratio,  $\Sigma$ :

$$\frac{\partial \Sigma}{\partial t} + \nabla \cdot (\mathbf{u} \Sigma) = (\nabla \cdot \mathbf{u} - \mathbf{nn} : \nabla \mathbf{u}) \Sigma - \mathbf{n} \cdot \nabla (S_d \Sigma), \quad (1.5.28)$$

where  $S_d$  is the displacement speed defined in Eq. (1.5.16) and  $\mathbf{n} = -\nabla c / |\nabla c|$  is the local normal vector to the flame surface. Similarly to the work of Trouvé and Poinso (1994) for RANS approach, several authors (Boger et al., 1998; Boger, 2000; Hawkes and Cant, 2000; Veynante and Vervisch, 2002) filtered Eq. (1.5.28) leading to the following LES filtered transport equation for FSD:

$$\underbrace{\frac{\partial \bar{\Sigma}}{\partial t}}_{T_0} + \underbrace{\nabla \cdot (\langle \mathbf{u} \rangle_s \bar{\Sigma})}_T = \underbrace{\langle \nabla \cdot \mathbf{u} - \mathbf{nn} : \nabla \mathbf{u} \rangle_s \bar{\Sigma}}_S + \underbrace{\langle S_d \nabla \cdot \mathbf{n} \rangle_s \bar{\Sigma}}_C - \underbrace{\nabla \cdot (\langle S_d \mathbf{n} \rangle_s \bar{\Sigma})}_P, \quad (1.5.29)$$

where  $\langle \rangle_s$  is the generalized surface average operator introduced in Eq. (1.5.20). This operator corresponds to a filtering operator on the flame front for any quantity of interest  $Q$ :

$$\langle Q \rangle_s = \frac{\overline{Q \Sigma}}{\bar{\Sigma}}. \quad (1.5.30)$$

Richard et al. (2005; 2007) introduced the ECFM-LES model consisting in closure of the different terms of Eq. (1.5.29) described below:

- $T_0$  is the time dependent component.
- $T$  is the convective transport of the FSD  $\bar{\Sigma}$ .
- $S$  represents the tangential strain rate induced by all turbulent structures.

- $C$  represents the flame stretching due to curvature.
- $P$  is a term of normal propagation of the flame front.

The closure of each term proposed by Richard et al. (2005; 2007) is based on the decomposition into resolved and sub-grid scale parts presented below.

### The convective transport term

The convective transport term  $T$  is decomposed as follows:

$$\nabla \cdot (\langle \mathbf{u} \rangle_s \bar{\Sigma}) = \nabla \cdot (\tilde{\mathbf{u}} \bar{\Sigma}) + [\nabla \cdot (\langle \mathbf{u} \rangle_s \bar{\Sigma}) - \nabla \cdot (\tilde{\mathbf{u}} \bar{\Sigma})]. \quad (1.5.31)$$

The first term in Eq. (1.5.31) corresponds to the resolved transport of the FSD. The second term is the unresolved transport term, which is modelled by Richard et al. (2005; 2007) with a simple gradient approach, neglecting  $\nabla \cdot (\tau S_L^0 \tilde{\mathbf{c}} \bar{\mathbf{n}} \bar{\Sigma})$ , the contribution due to flame-induced thermal expansion, not related to turbulent structures:

$$[\nabla \cdot (\langle \mathbf{u} \rangle_s \bar{\Sigma}) - \nabla \cdot (\tilde{\mathbf{u}} \bar{\Sigma})] = -\nabla \cdot \left( \frac{\nu_t}{S_{ct}} \nabla \bar{\Sigma} \right), \quad (1.5.32)$$

where  $\nu_t$  and  $S_{ct}$  are the turbulent kinematic viscosity and a turbulent Schmidt number, respectively.

### The tangential strain rate

The tangential strain rate, also noted  $\langle a_T \rangle_s$ , is decomposed as follows:

$$\langle a_T \rangle_s = \langle \nabla \cdot \mathbf{u} - \mathbf{nn} : \nabla \mathbf{u} \rangle_s, \quad (1.5.33)$$

$$= \langle A_T \rangle_s + \langle a_T \rangle_s^{sgs}. \quad (1.5.34)$$

The first term in Eq. (1.5.34) is the tangential strain rate induced by the resolved velocity field that is defined as  $\nabla \cdot \tilde{\mathbf{u}} - \langle \mathbf{nn} \rangle_s : \nabla \tilde{\mathbf{u}}$ . Hawkes and Cant (2000) proposed to express  $\langle A_T \rangle_s$  using the surface averaged flame normal vector  $\langle \mathbf{n} \rangle_s = -\nabla \bar{c} / \bar{\Sigma}$ , leading to:

$$\langle A_T \rangle_s = \left( \delta_{ij} - (\langle \mathbf{n} \rangle_s)_i (\langle \mathbf{n} \rangle_s)_j - \frac{1}{3} \alpha \delta_{ij} \right) \frac{\partial \tilde{u}_i}{\partial x_j}, \quad (1.5.35)$$

where  $\alpha$  is a term introduced to nullify the isotropic part of the orientation tensor when the flow becomes laminar. This term is given by  $\alpha = 1 - |\langle \mathbf{n} \rangle_s|^2$ .

The second term of Eq. (1.5.34) is the tangential strain rate induced by the sub-grid scale velocity field that should be modelled. As Richard et al. (2005; 2007) proposed, this term is classically modelled as:

$$\langle a_T \rangle_{s,c^*} = \alpha_{a_T} \Gamma \frac{u'}{\Delta}, \quad (1.5.36)$$

where  $\alpha_{aT}$  is a model constant,  $u'$  is the turbulent velocity fluctuation at scale  $\Delta$ , which is the mesh size.  $\Gamma$  is an efficiency function which takes into account the ability of all vortices to wrinkle the flame.

In LES, the flame front is partly wrinkled by the resolved structures of the turbulent flow, consequently only the strain due to the unresolved turbulent scales shall be modelled. Nevertheless, as Colin et al. (2000) suggested, only the turbulent structures with a size larger than the resolved flame thickness  $\widehat{\Delta}$  are able to efficiently wrinkle the resolved flame front. Thus, the turbulent structures, the size of which are smaller than  $\widehat{\Delta}$ , must be taken into account in the modelling of the sub-grid scale tangential strain rate. These structures of scale  $\widehat{\Delta}$  have a characteristic velocity  $\widehat{u}'$  that is related to the velocity of the sub-grid scale turbulent structure  $u'$  considering a homogeneous isotropic turbulence:

$$\widehat{u}' = u' \left( \frac{\widehat{\Delta}}{\Delta} \right)^{1/3}. \quad (1.5.37)$$

The issue is to evaluate the sub-grid scale fluctuation velocity  $u'$ . Using Smagorinsky's model for turbulence leads to evaluate  $u'$  using the turbulent kinematic viscosity:

$$u' = \frac{\nu_t}{C\Delta}, \quad (1.5.38)$$

where  $C$  is a model constant, often chosen equal to 0.12 as suggested by Richard et al. (2007).

The efficiency function  $\Gamma$  can be evaluated following the intermittent turbulent net flame stretch (ITNFS) function proposed by Meneveau and Poinso (1991), but Richard et al. (2007) retained the spectral approach proposed by Charlette et al. (2002a), which has been specifically developed in a LES context and is theoretically more adapted to estimate the sub-grid scale tangential strain rate. This spectral approach involves an adimensional wavenumber  $k_+$  associated to the wavenumber  $k$  defined as follows:

$$k_+ = \frac{k\widehat{\Delta}}{\pi}. \quad (1.5.39)$$

This adimensional wavenumber is used in the relationship that exists between the strain-rate and the energy spectrum in homogeneous turbulence allowing to compute  $\Gamma$  as:

$$\left( \Gamma \frac{\widehat{u}'}{\widehat{\Delta}} \right)^2 = \left( \frac{\pi}{\widehat{\Delta}} \right)^3 \int_1^\infty [C_r(k_+)]^2 k_+^2 E_{11}(k_+) dk_+, \quad (1.5.40)$$

where  $C_r(k_+)$  is a correction function, which takes into account the ability of the turbulent eddies at scale  $\pi/k$  to stretch the flame.  $E_{11}(k_+)$  is the one-dimensional (longitudinal) energy spectrum in the direction of the wavenumber  $k$ , defined using the standard longitudinal Kolmogorov spectrum with the Pao correction to account for the viscous cut-off :

$$E_{11}(k_+) = \frac{18}{55} \left( \frac{\pi}{\widehat{\Delta}} \right)^{-5/3} k_+^{-5/3} \varepsilon^{2/3} \exp \left( -\frac{3}{2} C_k \pi^{4/3} k_+^{4/3} \left( \frac{\eta}{\widehat{\Delta}} \right)^{4/3} \right), \quad (1.5.41)$$

where  $C_k \approx 1.5$  is the universal Kolmogorov constant,  $\eta$  is the Kolmogorov scale and  $\varepsilon$  is the rate of dissipation of turbulent kinetic energy.

In this approach to evaluate the efficiency function, the key parameter to model is the correction function  $C_r(k_+)$ , which is determined using the 2D DNS configuration described by Meneveau and Poinso (1991). The most common correction functions are reported in Table 1.1.

Table 1.1: The most common correction functions taking into account the ability of the turbulent eddies at scale  $r_c = \pi/k$  to stretch the flame.  $u_c$  is the characteristic velocity of the turbulent eddies at scale  $r_c$

References	Validity domain	Model
Meneveau and Poinso (1991)	$\frac{r_c}{\delta_L^0} \in [0.8; 10]$	$C_{r,MP} = 10^{-\frac{0.545}{\log\left(4\frac{r_c}{\delta_L^0}\right)+0.364}}$
Colin et al. (2000)	$\frac{r_c}{\delta_L^0} \in [3; 6]$	$C_{r,CDVP} = \frac{1}{2} \left[ 1 + \operatorname{erf} \left( 0.6 \left( \ln \left( \frac{r_c}{\delta_L^0} \right) - \sqrt{\frac{S_L^0}{u_c}} \right) \right) \right]$
Charlette et al. (2002a)	$\frac{r_c}{\delta_L^0} \in [3; 6]$	$C_{r,CMV} = C_{r,CDVP} \times \frac{1}{2} \left[ 1 + \operatorname{erf} \left( 3 \log \left( 2 \frac{u_c}{S_L^0} \right) \right) \right]$
Bougrine et al. (2014)	$\frac{r_c}{\delta_L^0} \in [3; 30]$	$C_{r,B} = \frac{1 + \operatorname{erf}[0.9 \ln(\frac{r_c}{\delta_L^0}) - 2]}{1 + 0.3 \frac{u_c}{S_L^0} (1 + \operatorname{erf}[0.9 \ln(\frac{r_c}{\delta_L^0}) - 2])} \times \left[ \frac{1}{Le} (1.76 + \tanh(Le - 2)) \right]$

### Normal propagation and stretch due to curvature

Richard et al. (2005; 2007) proposed to decomposed the stretch due to curvature,  $C$ , into resolved and sub-grid scale parts. From the analysis of a 1D steady laminar flame, Richard (2005) shows that normal propagation and resolved stretch due to curvature are physically linked to ensure the laminar flame propagation when the sub-grid scale turbulence is low.

Richard et al. (2005; 2007) proposed a formulation for these terms based on the normal to the iso-surface of the progress variable,  $\bar{\mathbf{n}}$ . When the surface averaged flame curvature is decomposed as  $\langle \nabla \cdot \mathbf{n} \rangle_s = \nabla \cdot \bar{\mathbf{n}} + [\langle \nabla \cdot \mathbf{n} \rangle_s - \nabla \cdot \bar{\mathbf{n}}]$ , the proposed formulation (Richard, 2005; Richard et al., 2007) leads to the following expression:

$$-\nabla \cdot (\langle S_d \mathbf{n} \rangle_s \bar{\Sigma}) + \langle S_d \nabla \cdot \mathbf{n} \rangle_s \bar{\Sigma} = \underbrace{-\nabla \cdot (S_d \bar{\mathbf{n}} \bar{\Sigma})}_{P_{res}} + \underbrace{S_d \nabla \cdot \bar{\mathbf{n}} \bar{\Sigma}}_{C_{res}} + \underbrace{[\bar{\mathbf{n}} \cdot \nabla (S_d \bar{\Sigma}) - \nabla \cdot \langle S_d \mathbf{n} \rangle_s \bar{\Sigma}]}_{(P+C)_{sgs}}, \quad (1.5.42)$$

where  $P_{res}$  and  $C_{res}$  are the resolved normal propagation and stretch due to curvature terms, respectively, and  $(P + C)_{sgs}$  is a sub-grid scale term.

To close the resolved terms  $P_{res}$  and  $C_{res}$ , the displacement speed  $S_d$  must be evaluated. From the mass conservation in the case of a 1D steady laminar flame, the displacement speed is modelled as:

$$S_d = \frac{\rho_u}{\bar{\rho}} S_L^0. \quad (1.5.43)$$

The sub-grid scale term  $(P + C)_{sgs}$  is closed as a sub-grid scale curvature term. This term is often modelled as a destruction term:

$$(P + C)_{sgs} = -\beta_0 S_L^0 \frac{\bar{\Sigma}^2}{1 - \bar{c}}, \quad (1.5.44)$$

where  $\beta_0$  is a constant model. Analysis of DNS simulations (Trouvé and Poinso, 1994) have shown that the sub-grid scale curvature acts not only as a sink term towards burned gases but also as a source term towards fresh gases. Hence, Veynante et al. (1996) proposed the following expression to take into account both effects:

$$(P + C)_{sgs} = \beta_c S_L^0 \frac{c^* - \bar{c}}{\bar{c}(1 - \bar{c})} \bar{\Sigma}^2, \quad (1.5.45)$$

where  $\beta_c$  and  $c^*$  are model constants. Equation (1.5.45) is the sub-model used in ECFM-LES model (Richard et al., 2007).

## 1.6 State of the art on high Karlovitz premixed flames.

Combustion regimes involved in IC engines are flamelet and TRZ regime, corresponding to turbulent flames characterized by medium and high Karlovitz numbers. Thus, all efforts for modelling turbulent combustion should be made on the understanding of a flame in TRZ regime.

In this section is presented the main phenomena involved in the thin reaction zone regime. Then, the attempts to model turbulent flames in the TRZ regime are described.

### 1.6.1 Turbulent premixed flames at medium and high Karlovitz numbers

Peters (1999) defined a theoretical approach describing the flame characteristics in the thin reaction zone regime. For a flame in the TRZ regime the small eddies of turbulence are entering the preheat zone and increase the mixing, destroying the quasi-steady laminar flame structure identified in the corrugated flamelet regime.

The idea behind the model is that small eddies penetrating the preheat zone will transport preheat fluid from a region near the reaction zone over a distance corresponding to its own size, as illustrated in Fig. 1.6.1. This mechanism is supposed to lead to a thickening of the preheat zone.

Peters (1999) proposed to use the level-set approach to model the premixed combustion with the  $G$ -equation model in Eq. (1.5.9). Peters used asymptotic analysis on the flame speed

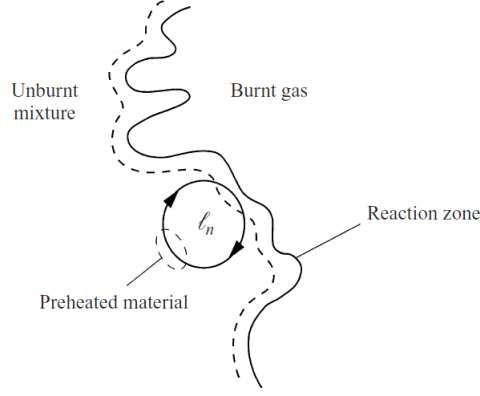


Figure 1.6.1: Transport of preheated material from a region of thickness  $\delta_L$ , the flame thickness, by an eddy of size  $l_n$  during half a turnover time. (Peters, 1999)

(Matalon and Creta, 2012; Matalon and Matkowsky, 1982; Pelce and Clavin, 1982) to propose closure for the velocity  $w$  involved in Eq. (1.5.9) leading to:

$$w = S_L^0 - S_L^0 \mathcal{L} \kappa + \mathcal{L} \mathbf{n}_G \cdot \nabla \mathbf{u} \cdot \mathbf{n}_G, \quad (1.6.1)$$

where  $\mathcal{L} = D_{\mathcal{L}}/S_L^0$  and  $D_{\mathcal{L}}$  are the Markstein length and the Markstein diffusivity, respectively.  $\mathbf{n}_G = -\nabla G/|\nabla G|$  is the unit normal vector to the flame surface pointing to the fresh gases and  $\kappa = \nabla \cdot \mathbf{n}_G$  is the flame curvature. Equation (1.6.1) associates the phenomenon described in Fig. 1.6.1 to effects of the flame front curvature and strain rate on the velocity  $w$  through the Markstein length. The author suggested to rather use the mass diffusivity of the deficient species in the expression of  $\mathcal{L}$ .

Then, by combining Eq. (1.6.1) with the G-equation (Eq. 1.5.9), the flame in the TRZ regime can be modelled with the following filtered equation:

$$\bar{\rho} \frac{\partial \widetilde{G}}{\partial t} + \bar{\rho} \widetilde{\mathbf{u} \cdot \nabla G} = \bar{\rho} S_L^0 |\widetilde{\nabla G}| - \bar{\rho} D \langle \kappa \rangle_G |\widetilde{\nabla G}| + \bar{\rho} \langle \mathcal{L} \mathbf{n}_G \cdot \nabla \mathbf{u} \cdot \mathbf{n}_G \rangle_G |\widetilde{\nabla G}|, \quad (1.6.2)$$

where  $\langle \rangle_G$  is an averaging operator defined for any quantity of interest  $Q$  as:

$$\langle Q \rangle_G = \frac{\widetilde{Q |\nabla G|}}{|\widetilde{\nabla G}|}. \quad (1.6.3)$$

This work is considered as the starting point for modelling flames in the TRZ regime. Indeed, lots of works were conducted in order to examine, experimentally or numerically, the assumptions made by Peters (1999). From all these studies a large range of experiments and direct numerical simulations are available for the TRZ regime and the BRZ regime and reported recently by Driscoll et al. (2020). The present study only focused on some of them, as summarized in the Peters-Borghi diagram in Fig. 1.6.2. The present section first focuses on the experimental data, then on the numerical observations.



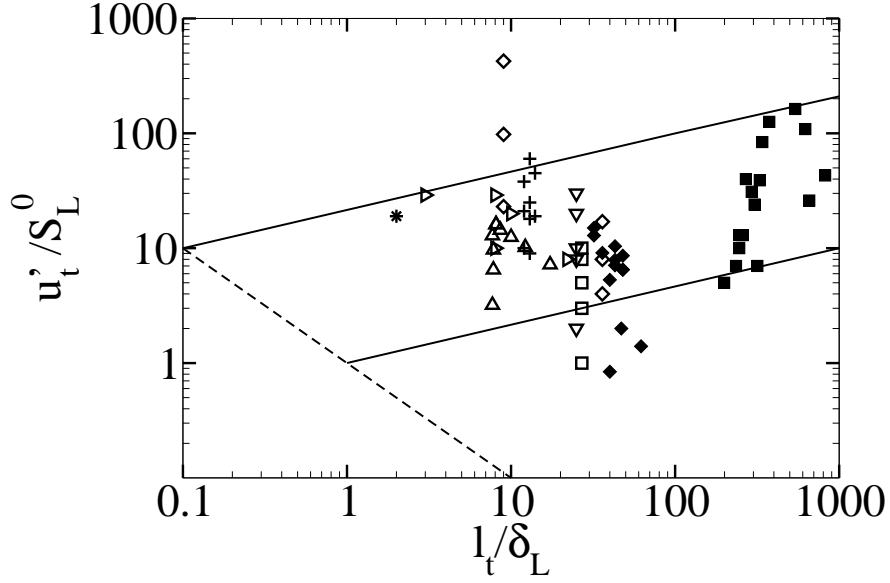


Figure 1.6.2: Some studies of high Karlovitz turbulent premixed flames:  $\blacklozenge$  experiments by Gülder (2007) and Yuen and Gülder (2013),  $\blacksquare$  experiments by Wabel et al. (2017),  $\square$  DNS by Ahmed et al. (2019),  $\diamond$  DNS by Aspden et al. (2011a,b, 2015, 2016, 2017, 2019),  $\triangle$  DNS by Han and Huh (2009),  $\triangleright$  DNS by Hawkes and Chen (2005),  $\nabla$  DNS by Nivarti and Cant (2017),  $*$  DNS by Poludnenko and Oran (2010, 2011), and  $+$  DNS by Lapointe and Blanquart (2017; 2015) and Savard et al. (2014; 2015; 2017; 2015).

### Experimental observations

First, de Goey et al. (2005) conducted experiments to verify the assumptions made by Peters (1999) on the structure of a flame in the TRZ regime. They analysed methane-air premixed flames in a weak swirled burner using Rayleigh and OH-laser-induced predissociative fluorescence (LIPF) to observe instantaneous flame thickness. The measurements from this study seem to confirm the theory proposed by Peters (1999). Indeed, the measurement highlighted that the turbulent motions only affect the preheat layers of the flame front. At the boundary of the BRZ regime (defined in Section 1.3.3), the Kolmogorov scale turbulent structures are of comparable size as the reaction zone thickness,  $\delta_r$ , allowing these structures to sufficiently penetrate the flame to enhance mixing near the reaction zone. Nevertheless, it seems that the small eddies are not able to penetrate in the flame zone all the way up to the reaction zone suggesting that extreme turbulence does not significantly alter the state relations that describe the chemistry, as concluded in the review by Driscoll et al. (2020).

Further experiments on the impact of turbulence on the flame front for flames in the TRZ regime were conducted by Gülder (2007) and Yuen and Gülder (2013)) using methane-air and propane-air flames in a Bunsen type burner. In these studies, the focus is made on the macroscopic impacts through the analysis of the fuel consumption using the turbulent flame speed  $S_T$ . This turbulent flame speed was evaluated using two methods. The first method

corresponds to the conventional consumption speed measured using:

$$S_{T,1} = \frac{\dot{m}_r}{\rho_r \mathcal{A}_f}, \quad (1.6.4)$$

where  $\dot{m}_r$  and  $\rho_r$  are the mass flow rate and the density of reactants, respectively.  $\mathcal{A}_f$  is the surface area of  $\bar{c} = 0.5$  contour. The second method is based on Damköhler's relationship presented in Eq. (1.3.8):

$$\frac{S_{T,F}}{S_L^0} = I_0 \frac{\mathcal{A}_T}{\mathcal{A}_L}, \quad (1.6.5)$$

where  $I_0 \approx 1$  is a factor introduced to take into account the effect of stretch on the laminar flame speed (Matalon and Matkowsky, 1982), and the flame surface  $\mathcal{A}_T$  is computed as the integral of the FSD using a two-dimensional estimate of  $\Sigma$ :

$$\Sigma(c) = \frac{L(c)}{\mathcal{A}(c)}, \quad (1.6.6)$$

where  $L(c)$  is the flame front length and  $\mathcal{A}(c)$  is the flame zone area. Halter et al. (2009) and Veynante et al. (2010) showed that this 2D method to estimate the FSD from experiment data underestimates the burning speed and even propose corrections. Nevertheless, these corrections are limited, for example the factor is  $4/\pi \approx 1.27$  using an isotropic assumption. So, the method presented in Eq. (1.6.6) still gives insight on the general behaviour of turbulent flames with Karlovitz number.

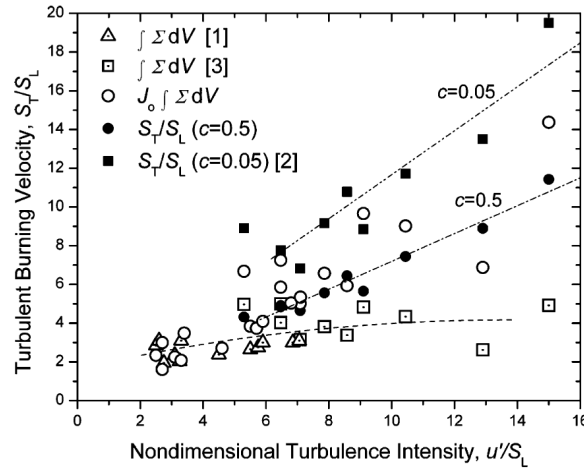


Figure 1.6.3: Integrated flame surface density data. Also shown are the experimentally determined turbulent burning velocities evaluated at  $\bar{c} = 0.5$  (full circles) and  $\bar{c} = 0.05$  (full squares). Two dotted-dashed straight lines are approximate linear fits to experimental turbulent burning velocity data. Empty circles represent the product of  $J_0$ , defined in Eq. (1.6.7) and integrated flame surface density. (Gülder, 2007)

The comparison of the ratios  $S_{T,1}/S_L^0$  and  $S_{T,F}/S_L^0$  in Fig. 1.6.3 shows that for “weak” turbulent intensities,  $u'_t/S_L^0 < 6$ , the increase of both ratios are proportional, confirming Damköhler's assumption. Nevertheless, when the turbulence intensity is sufficiently high, both the fractal approach proposed by Gouldin (1987) and the FSD approach fail to reproduce the discrepancies

between  $S_{T,1}/S_L^0$  and  $\mathcal{A}_T/\mathcal{A}_L$ . The authors explain these discrepancies with the mixing generated by the small eddies of the turbulent flow increasing the effective transport, in agreement with the theory of Peters (1999) and the results of de Goey et al. (2005). So, because of the mixing induced by the small eddies, Gülder proposed to introduced a new factor  $J_0$  in Damköhler's relationship (Eq. 1.3.8) to take into account the enhancement in transport induced by the active eddies penetrating into the preheat zone of the flame. This factor is evaluated assuming that active eddies of size of the Taylor microscale penetrate the preheat layer. The factor  $J_0$  might be evaluated using an effective diffusivity due to the Taylor microscale. Therefore, by using the definition of the Karlovitz number, the factor  $J_0$  is written:

$$J_0 \approx \left[1 + S_c Re_{\lambda_c}^{-1/2}\right] \left(\frac{u'_t}{S_L^0}\right)^{-1} Ka, \quad (1.6.7)$$

where  $S_c$  is the Schmidt number of the mixture and  $Re_{\lambda_c} \approx Re_t^{1/2}$  is the Reynolds number associated to the Taylor micro-scale  $\lambda_c$ . This expression suggests that  $J_0$  becomes widely larger than unity, when the turbulence intensity increases. The author then estimates values of  $S_T/S_L^0$  close to  $S_{T,1}/S_L^0$  using:

$$\frac{S_T}{S_L^0} = I_0 J_0 \frac{\mathcal{A}_T}{\mathcal{A}_L}, \quad (1.6.8)$$

where  $I_0$  is the stretch factor approximately equal to 1.

Wabel et al. (2017) analysed results from an experiment on an axisymmetric Bunsen burner involving methane-air flame. The authors explored the behaviour of the turbulent flame speed with  $u'_t/S_L^0$  following three definitions for  $S_T$ :

- the conventional speed  $S_{T,1}$  given in Eq. (1.6.4) using the area of the  $\bar{c} = 0.5$  contour,
- a speed  $S_{T,2}$  computed using Eq. (1.6.4) using the area of the  $\bar{c} = 0.2$  contour instead of  $\bar{c} = 0.5$ ,
- the turbulent speed computed from the flamelet FSD  $S_{T,F} = (S_L^0/\mathcal{A}_L) \int_V \Sigma dV$ .

As observed by Gülder (2007); Gülder and Smallwood (2007) and Yuen and Gülder (2013), the turbulent speed presents a “bending” effect regardless of the definition used, reported in Fig. 1.6.4. This “bending” occurs when the preheat layers become thick, suggesting that the thickened preheat layers play a role in the bending. It is assumed that at extreme turbulence intensity the preheat zone is so thick that eddies passing through the layer cannot survive. Therefore, burning velocity no longer increases linearly resulting in the bending effect. These observations are in agreement with the theory proposed by Peters (1999).

Finally, a recent study by Nivarti et al. (2018) analyses further the experimental results by Yuen and Gülder (2013) and Wabel et al. (2017). The discrepancies observed between  $S_T/S_L^0$  and  $\mathcal{A}_T/\mathcal{A}_L$  are explained by the arising diffusivity from the small scales of the turbulent flow, of size smaller than the laminar flame thickness,  $r < \delta_L^0$ . This leads the author to modify

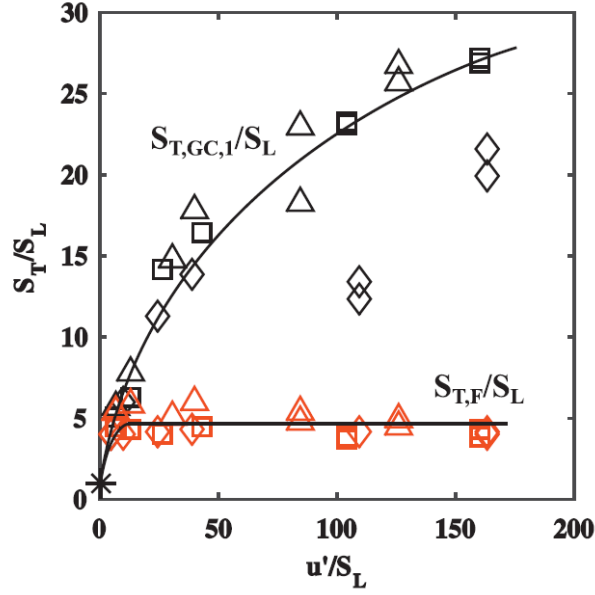


Figure 1.6.4: Mean flamelet velocity,  $S_{T,F}$  in red symbols, compared to global consumption speed based on  $\bar{c} = 0.5$ ,  $S_{T,1}$  in black symbols. (Wabel et al., 2017)

Damköhler's relationship Eq. (1.3.8) into:

$$\frac{S_T}{S_L^0} = \left(1 + \frac{\Delta\mathcal{A}}{\mathcal{A}}\right) \left(1 + \frac{\Delta D}{D}\right)^{1/2}, \quad (1.6.9)$$

where  $(1 + \Delta\mathcal{A}/\mathcal{A}) = \mathcal{A}_T/\mathcal{A}_L$  is attributed to the large scales of turbulence, of size larger than  $\delta_L^0$ , while the enhancement factor  $\Delta D/D$  is attributed to the small scales  $r < \delta_L^0$ . This second term in Eq. (1.6.9) corresponds to Damkhöler's second hypothesis reported by Driscoll et al. (2020), which is: if all of the upstream eddies are smaller than the laminar flame thickness, then their only influence is to increase the diffusivity from the molecular diffusivity  $D$  to the new value  $D + \Delta D$ . A simple model is given for this factor by Nivarti et al. (2018):

$$\frac{\Delta D}{D} \approx Ka^{2/3}. \quad (1.6.10)$$

The combination of Eqs. (1.6.9) and (1.6.10) shows a good agreement with experiments in Fig.1.6.5 and confirms that turbulence affects mixing in the preheat layer through diffusion effects. Thus, the results suggest to further investigate the effects of turbulence on diffusion.

### Numerical studies

Two DNS studies by Nivarti and Cant (2017) and Ahmed et al. (2019), were conducted to further explore the “bending” effect observed in experimental studies. The former is the analysis of 3D-DNS of a statistically planar methane-air premixed flame propagating in a turbulent flow field. The turbulent flow field is a decaying homogeneous isotropic turbulence. The latter is the analysis of 3D-DNS of a statistically planar methane-air premixed flame interacting with a forced turbulent flow field. In both studies the ratio  $S_T/S_L^0$  remains close to the ratio  $\mathcal{A}_T/\mathcal{A}_L$

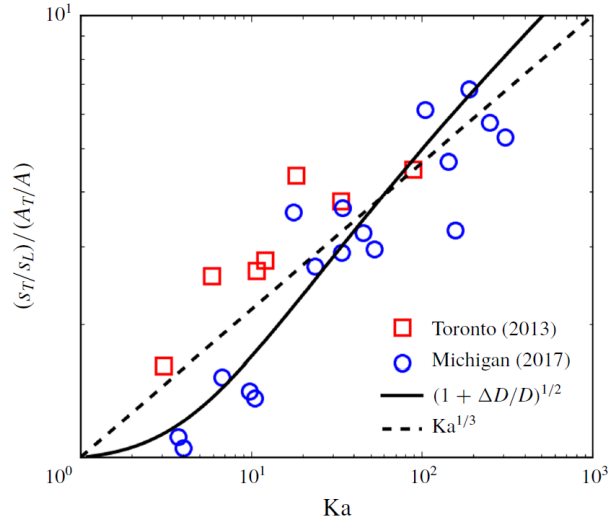


Figure 1.6.5: Measured disparity  $(S_T/S_L^0)/(\mathcal{A}_T/\mathcal{A}_L)$  in the profiles of burning velocity enhancement and flame surface area enhancement as observed in experiments (Wabel et al., 2017; Yuen and Gülder, 2013) (symbols) and the enhancement factor (solid line) obtained from a numerical evaluation of  $(1 + \Delta D/D)^{1/2}$ . Also shown is the leading-order term  $Ka^{1/3}$  (dashed line). (Nivarti et al., 2018)

even for high values of  $u'_t/S_L^0$  as seen in Fig. 1.6.6. This figure shows that the ratio  $S_T/S_L^0$  presents a bending, in agreement with experimental studies. However,  $\mathcal{A}_T/\mathcal{A}_L$  also presents a bending. Thus, in DNS the bending effect on the turbulent flame speed is associated in the first-order to the bending on the flame surface. Note that in the DNS conducted by Nivarti and Cant (2017) the balance between strain and curvature is not reached, questioning the conclusions drawn. However, the observations from the DNS conducted by Ahmed et al. (2019), where the strain/curvature balance is reached, confirm the conclusions drawn by Nivarti and Cant (2017). This suggests that, contrary to the experimental studies, Damköhler's relationship in Eq. (1.3.8) is sufficient to evaluate the turbulent flame speed.

Note that the integral length scales involved in these simulations (Ahmed et al., 2019; Nivarti and Cant, 2017) are much smaller than the integral scales of the experiments (Gülder, 2007; Wabel et al., 2017; Yuen and Gülder, 2013), by approximately a factor 10 to 100. Nonetheless, all these works show that turbulent flames with high Karlovitz number present a bending. On the one hand, the reason of this bending is associated to a saturation of the flame surface combined to an increase of the local propagation speed in the experiments. On the other hand, DNS suggest that the bending is mainly due to a bending effect on the flame surface because the stretch factor  $I_0$  is close to 1. Both the experimental and numerical studies suggest to analyse the inner flame structure to better understand the origin of this “bending”.

In that respect, many direct numerical simulations of premixed flames interacting with a homogeneous isotropic turbulence generated and forced in all the domain with spectral methods were conducted to investigate the impact of turbulence on the inner flame structure. Poludnenko and Oran (2010, 2011) analysed DNS of interaction of a premixed  $H_2$ -air flame with a subsonic, homogeneous isotropic turbulence considering a simplified reaction-diffusion model based on

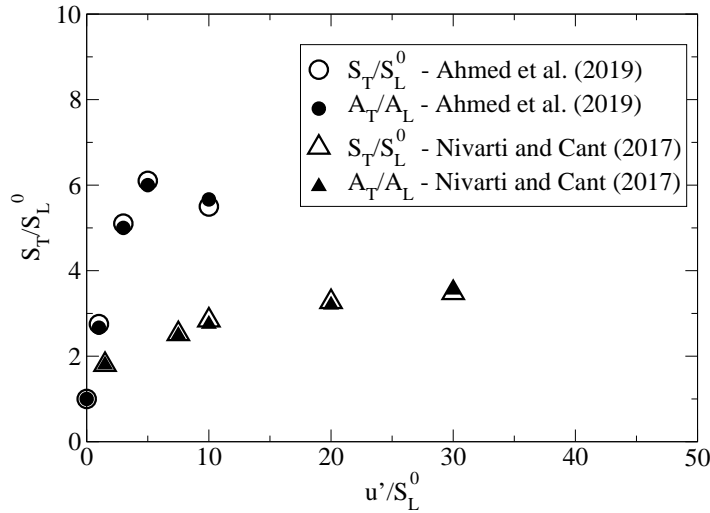


Figure 1.6.6: Evolution of  $S_T/S_L^0$  and  $A_T/A_L$  with the velocity ratio  $u'/S_L^0$  from two DNS studies (Ahmed et al., 2019; Nivarti and Cant, 2017).

one-step Arrhenius kinetics and assuming unity Lewis numbers.

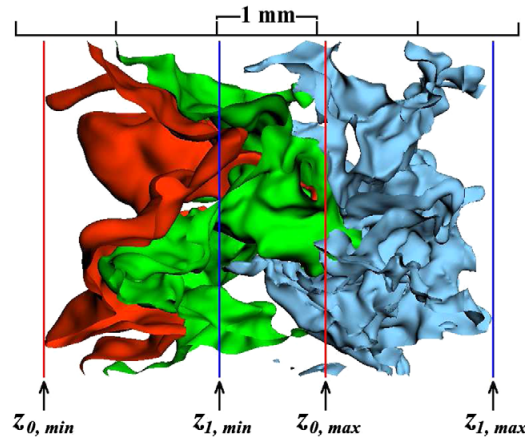


Figure 1.6.7: Iso-surfaces of fuel mass fraction, the values of which are 0.05 (red), 0.6 (green) and 0.95 (blue). The red and green iso-surfaces bound the flamelet reaction zone. The green and blue iso-surfaces bound the preheat zone.  $z_{0,min}$  and  $z_{1,max}$  mark the flame brush bounds. (Poludnenko and Oran, 2010, 2011)

They observed that the time-averaged internal structure of the flame is close to that of a planar laminar flame, especially in the reaction zone. However, the preheat zone shows evidence of broadening. This thickening, associated with disturbance in the flame front due to turbulence, makes the flame surface difficult to define as seen in Fig. 1.6.7. The evolution of the temporal averaged area  $\overline{A}_Y$  normalized with the laminar flame surface  $L^2$ , computed for each iso-surface of the fuel mass fraction, against fuel mass fraction was analysed by the authors. It appeared that this area was much smaller near the burnt gases ( $Y_{fuel}$  close to 0) than in the fresh gases.

Then, Aspden et al. (2011a,b, 2015, 2016, 2017, 2019) conducted 3D-DNS of lean premixed

hydrogen and methane flames. Simulations were performed using a chemical mechanism including 9 species and 27 reactions for hydrogen flames, and a chemical mechanism with 19 species and 84 reactions for  $\text{CH}_4$  flames. A very large range of Karlovitz numbers was considered, from  $Ka = 4$  to 8767. Moreover, the diffusion effects were investigated through a variation of the equivalence ratio at a constant Karlovitz number  $Ka = 266$ .

The authors observed an increase in the flame surface area, because of the wrinkles generated, and the flame is broadened when the turbulence intensity grows. The higher Karlovitz numbers, the sharper the wrinkles are observed. At constant  $Ka$ , these wrinkles become less pronounced when the lean flame gets richer, which is in agreement with the observations by Kobayashi et al. (2007).

This broadening of the flame was evaluated using a thickening factor  $\Theta$  defined as:

$$\Theta(T) = \frac{\langle \nabla T(\xi) |_{\xi=T} \rangle_{Ka=1}}{\langle \nabla T(\xi) |_{\xi=T} \rangle_{Ka=n}}, \quad (1.6.11)$$

where  $\langle \nabla T(\xi) |_{\xi=T} \rangle$  is the conditional means of the temperature gradient. The normalization by the conditional mean at  $Ka = 1$ , instead of the laminar flame, is used to account for the thermo-diffusive instability in the hydrogen flames (Aspden et al., 2016).

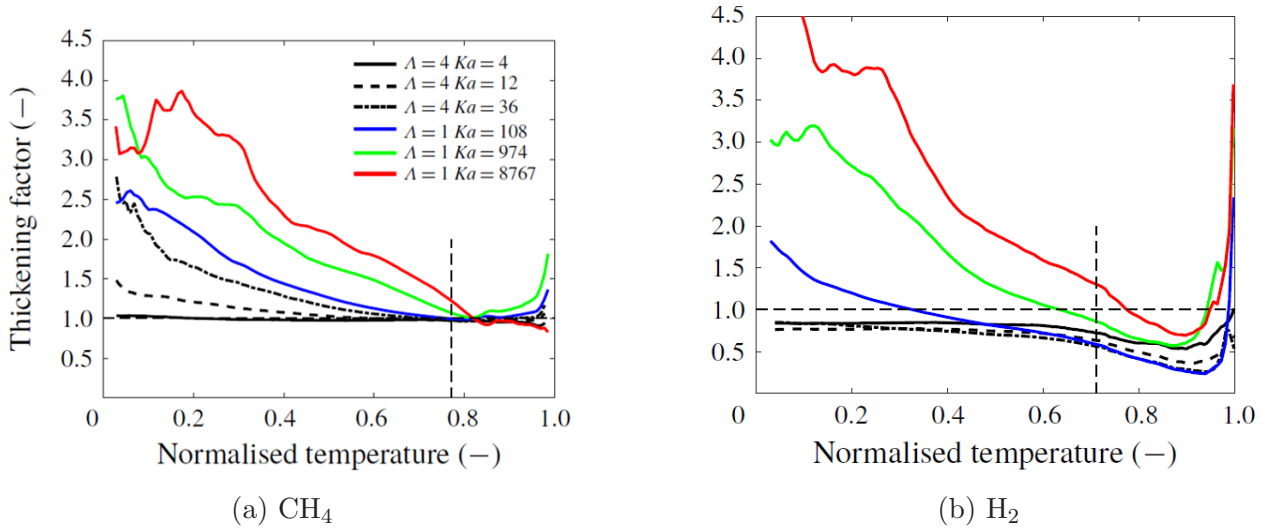


Figure 1.6.8: Thickening factor  $\Theta(c)$  as a function of the normalized temperature (a) for  $\text{CH}_4$  and (b) for  $\text{H}_2$ . (Aspden et al., 2019)

Figure 1.6.8 shows the evolution of  $\Theta$  with the normalized temperature for both methane and hydrogen flames at different Karlovitz numbers. When  $Ka$  increases,  $\Theta$  increases strongly for normalised temperature smaller than 0.5. This increase is greater for hydrogen flames, which have non-unity Lewis numbers unlike methane flames. These observations are in agreement with the theory proposed by Peters (Peters, 1999), which suggests that small eddies enhanced diffusion through turbulent mixing. However, the observed stretch factor  $I_0$  remains close to 1 suggesting that the bending is mainly due to the flame surface.

In addition, another set of DNS was conducted by Lapointe and Blanquart (2017; 2015)



and Savard et al. (2014; 2015; 2017; 2015) to evaluate the impact of turbulence on the inner flame structure. Unlike previous studies, the fuel used, which was n-heptane, was closer to real automotive engine fuels. The Karlovitz number was varied in a range between 75 and 1050. The corresponding combustion regimes, defined by Peters (1999), are the TRZ and the BRZ regimes<sup>1</sup>. Furthermore, all these simulations were computed twice, first with all the Lewis numbers equal to unity, and second with non-unity Lewis numbers. Some of the numerical parameters of the cases simulated (Lapointe and Blanquart, 2017; Lapointe et al., 2015; Savard and Blanquart, 2014, 2015, 2017; Savard et al., 2015) are reported in Table 1.2

Table 1.2: Parameters of the simulations conducted in (Lapointe et al., 2015).  $Ka$  is the Karlovitz number in the unburnt gases computed as  $Ka = (\delta_L^0/S_L^0)\sqrt{u_t'^3/(\nu l_t)}$ .

Case	$S_L^0$ [m/s]	$\delta_L^0$ [mm]	$l_t/\delta_L$	$u'/S_L^0$	$Ka$	$Re_t$
A	0.36	0.39	1.1	9.0	78	83
B	0.36	0.39	1.1	18.0	220	190
C	0.86	0.32	1.0	38	648	290
D	2.3	0.25	1.2	45	740	380

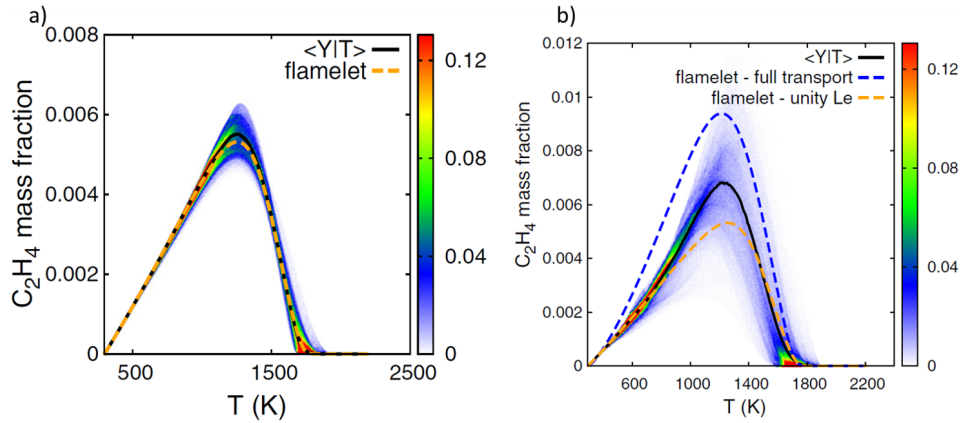


Figure 1.6.9: Joint probability density function (PDF) and conditional mean  $\langle Y|T \rangle$  (in black solid line) of  $C_2H_4$  mass fraction vs temperature (a) from the unity Lewis number and (b) from the non-unity Lewis number. Dashed lines are flamelet solutions for non-unity Lewis number in blue and for unity Lewis number in orange. (Savard et al., 2015)

Figure 1.6.9a shows the joint probability density function (PDF) and the conditional mean of  $C_2H_4$  mass fraction against temperature for a case with all the Lewis numbers equal to 1 compared to a flamelet evolution in dashed line. Tracking  $C_2H_4$  allows to ensure to analyse the flame structure, because  $C_2H_4$  is an intermediate species only existing in the flame front. The flame structure observed in this case is in average close to a flamelet structure, while when differential diffusion is taken into account in Fig. 1.6.9b, the turbulent flame structure lies between that of a full transport and a unity Lewis number flamelet.

<sup>1</sup>Driscoll et al. (2020) proposed a modified combustion regimes diagram resulting from measure data. Using this diagram, the set of DNS (Lapointe and Blanquart, 2017; Lapointe et al., 2015; Savard and Blanquart, 2014, 2015, 2017; Savard et al., 2015) corresponds to the wrinkled corrugated flamelet regime. However, the present study focuses on the effect of increasing Karlovitz number on the flame behaviour.



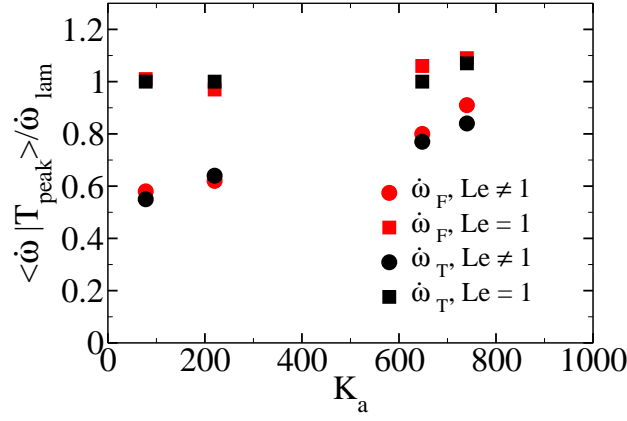


Figure 1.6.10: Conditional mean of fuel consumption  $\langle \dot{\omega}_F | T \rangle$  and heat release  $\langle \dot{\omega}_T | T \rangle$  corresponding to temperature of peak source term using data from (Lapointe et al., 2015). The values are normalized by the corresponding laminar flame.

Even if both  $Le = 1$  and  $Le \neq 1$  cases have a mean flame structure similar to a laminar flame structure, the differential diffusion has a non negligible impact on the flame. This is illustrated through an alternative definition of the stretch factor  $I_{0,S}$ :

$$I_{0,S} = \frac{\langle \dot{\omega}(T_{peak}) \rangle}{\dot{\omega}_{lam}}, \quad (1.6.12)$$

where  $\langle \dot{\omega}(T_{peak}) \rangle$  is the conditional mean of reaction rate corresponding to temperature of peak source term, and  $\dot{\omega}_{lam}$  is the maximum reaction rate of the corresponding 1D laminar flame. This factor corresponds to a stretch factor of the isotherm  $T = T_{peak}$ . Contrary to the common definition of the stretch factor, Eq. (1.6.12) only evaluate the effect of flame stretch on the reaction zone identified as the isotherm  $T = T_{peak}$ . Even if this factor does not take into account the thickening of the preheat zone, it shows how the reaction zone behave to highly turbulent flows.

Figure 1.6.10 shows the evolution of the stretch factor with the Karlovitz number for the simulations of flames with  $Le = 1$  and  $Le \neq 1$ . The evolution of  $I_{0,S}$  with  $Ka$  is close to constant for the simulations where  $Le = 1$ , suggesting that turbulence weakly affects the inner structure of the flame. While for  $Le \neq 1$  cases, case A presents a significantly smaller stretch factor ( $I_{0,S} = 0.6$ ) than the laminar flame. Yet, case A has already a significantly large Karlovitz number suggesting that when  $Le \neq 1$ ,  $I_{0,S}$  first decreases with  $Ka$ . This decrease is attributed to stretching effects leading to local extinctions, which participate to a decrease of the heat release. Then, the increase of  $Ka$  (from 78 to 740) leads to an increase of  $I_{0,S}$  to values close to the ones encountered with  $Le = 1$  for the highest Karlovitz numbers. So, Figure 1.6.10 suggests that the turbulent diffusivity due to turbulent mixing becomes dominant when a sufficiently high Karlovitz number is reached.

The effect of turbulence on the flame front structure for  $Le \neq 1$  cases is further analysed in Fig. 1.6.11, where the profiles of fuel consumption rate with temperature are plotted. Only the mean source terms are shown but it should be noted that, as turbulence intensity is increased,

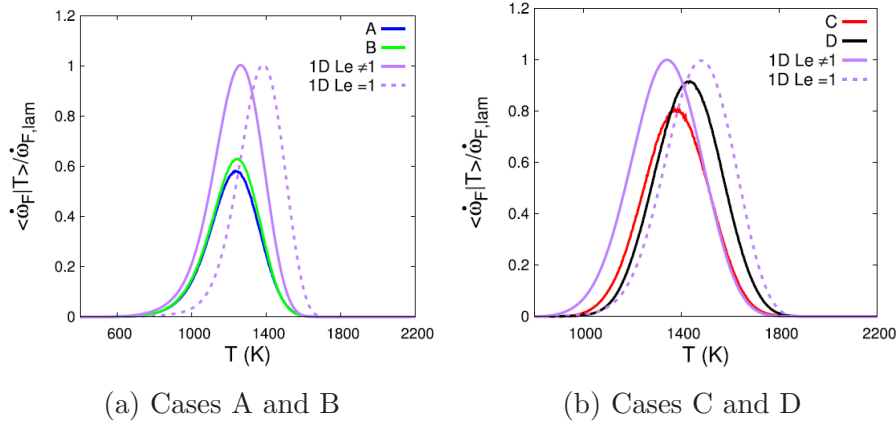


Figure 1.6.11: Conditional means of normalized fuel consumption rate for non-unity Lewis number simulations. The fuel consumption rates are normalized by the peak value in the corresponding laminar flame. (Lapointe et al., 2015)

the fluctuations of the fuel consumption rate are enhanced significantly. It can be seen that fuel consumption rate, first, decreases relatively to a 1D laminar flame with case A, which is in agreement with the analysis of Fig. 1.6.10. As explained previously, this decrease is mainly due to stretching effect leading to local flame extinctions. In Fig. 1.6.11, the fuel consumption rate tends to the profile of a 1D laminar flame with unity Lewis numbers when  $Ka$  increases.

As a consequence, the authors proposed to explain the impact of the turbulence on the flame front through diffusion, as suggested by Peters (1999), by introducing a turbulent diffusivity  $D_T$  to define an effective diffusivity, as suggested by Damkhöler's second hypothesis:

$$D_{eff} = D_i + D_T, \quad (1.6.13)$$

where  $D_i$  is the mass diffusivity of the species  $i$ . Equation (1.6.13) leads to introduce an effective Lewis number  $Le_{i,eff}$ :

$$Le_{i,eff} = \frac{1 + a_{Ka} Ka}{\frac{1}{Le_i} + a_{Ka} Ka}, \quad (1.6.14)$$

where  $a_{Ka}$  is a coefficient adjusted to best fit the data from DNS conducted by Savard and Blanquart (2014), the value proposed is 0.05.

### 1.6.2 Attempts to model premixed flame in the thin reaction zone regime

The starting point of TRZ modelling is the work of Peters (1999), where the author proposed an adaptation of the level-set approach in Eq. (1.6.2) by assuming that the propagating velocity  $w$  is expressed with Eq (1.6.1).

The difference with the models in the flamelet regime in this equation relies in the terms linked to the curvature  $\kappa$  and the strain rate  $\mathbf{n} \cdot \nabla \mathbf{v} \cdot \mathbf{n}$ . Indeed, it is assumed that these two terms are preponderant compared to the propagative term  $S_L^0 |\nabla G|$ . Furthermore, Peters

defined a filtered transport equation for the variable  $\sigma = |\nabla G|$ , where the curvature and the strain rate are involved. Thus, efforts should be made in the modelling of these two terms.

Finally, considering  $G$  as the equivalent of a progress variable and  $\sigma = |\nabla G|$  as an equivalent to the FSD, the model proposed by Peters is close to a model based on the transport of the flame surface density (such as the Coherent Flame Model).

A study of 2D-DNS of lean methane-air and hydrogen-air flames was conducted by Hawkes and Chen (2005), focusing on the main assumptions used to model the stretch rate acting on turbulent flame speed. In this study, the approach proposed by Peters (1999) is applied considering  $G$  as the progress variable and  $\sigma$  as the FSD.

Three models for computing stretch rate related to curvature  $S_d \nabla \cdot \mathbf{n}$  were compared in this study from the analysis of a set of DNS. The models rely on different estimations of the displacement speed:

1.  $S_d$  is equal to the speed of the considered iso-surface in the case of an unstrained laminar flame, corresponding to a flamelet approach. This model for  $S_d$  leads to write the stretch due to curvature as:

$$S_d \nabla \cdot \mathbf{n} \approx \frac{\rho_u}{\rho} S_L^0 \nabla \cdot \mathbf{n}. \quad (1.6.15)$$

2.  $S_d$  is considered linearly dependent on the Markstein number  $M_a$ , the tangential strain rate  $a_t$  and the curvature  $\nabla \cdot \mathbf{n}$  with  $\kappa_a = (a_t + S_L^0 \nabla \cdot \mathbf{n}) \delta_L / S_L^0$  the total dimensionless stretch, corresponding to asymptotic analysis. The stretch due to curvature deduced from this model is expressed as:

$$S_d \nabla \cdot \mathbf{n} \approx \frac{\rho_u}{\rho} S_L^0 (1 - M_a \kappa_a) \nabla \cdot \mathbf{n}. \quad (1.6.16)$$

3.  $S_d$  is decomposed as:

$$S_d = S_r + S_n - D \nabla \cdot \mathbf{n}, \quad (1.6.17)$$

where  $S_r$  is the reaction rate related speed defined in Eq.(1.6.18),  $S_n$  is the normal propagation related speed defined in Eq.(1.6.19) and  $D \nabla \cdot \mathbf{n}$  is the tangential diffusion related speed.  $D$  is the mass diffusivity of the fuel.

$$S_r = -\frac{\dot{\omega}_c}{\rho |\nabla c|}, \quad (1.6.18)$$

$$S_n = -\frac{\mathbf{n} \cdot \nabla (\rho D |\nabla c|)}{\rho |\nabla c|}. \quad (1.6.19)$$

Then, Eq.(1.6.17) is directly used in the definition of the stretch rate due to curvature leading to:

$$S_d \nabla \cdot \mathbf{n} = (S_r + S_n) \nabla \cdot \mathbf{n} - D (\nabla \cdot \mathbf{n})^2. \quad (1.6.20)$$

Tangential diffusion effects due to large curvature are assumed dominant in the TRZ regime. Moreover, the sum of the reaction rate and normal propagation contributions is

considered of the order of magnitude of the displacement speed of a planar laminar flame,  $(\rho_u/\rho)S_L^0$ , leading to:

$$S_d \nabla \cdot \mathbf{n} \approx -D(\nabla \cdot \mathbf{n})^2 + \frac{\rho_u}{\rho} S_L^0 \nabla \cdot \mathbf{n}. \quad (1.6.21)$$

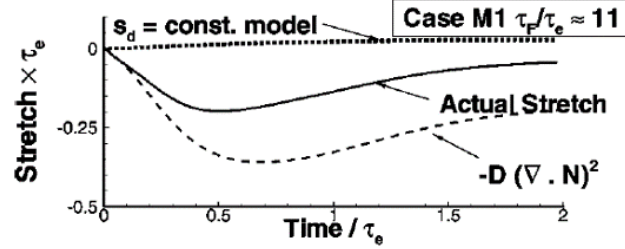
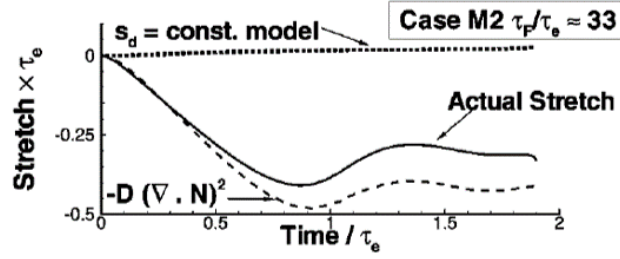
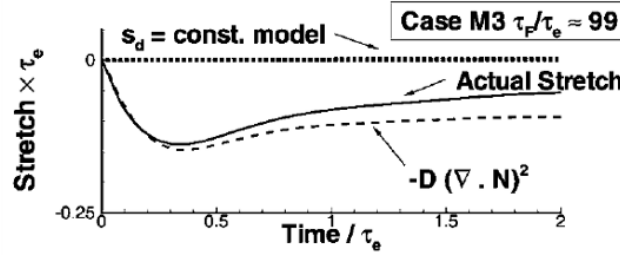
(a)  $Ka = 30$ (b)  $Ka = 165$ (c)  $Ka = 290$ 

Figure 1.6.12: Stretch rate due to curvature,  $S_d \nabla \cdot \mathbf{n}$ , and models versus time - normalized by the eddy turnover time of integral scale  $\tau_e$ , for methane-air premixed flame: for (a)  $Ka = 30$ , for (b)  $Ka = 165$  and for (c)  $Ka = 290$ . (Hawkes and Chen, 2005)

Figure 1.6.12 shows the temporal evolution of the area-weighted mean stretch rate due to curvature,  $S_d \nabla \cdot \mathbf{n}$  predicted with the first model described above ( $S_d$  as a constant) and with Eq.(1.6.21), for a methane-air flame for three levels of Karlovitz number ( $Ka = 30$ ,  $Ka = 165$  and  $Ka = 290$ ). When  $S_d$  is considered equal to  $(\rho_u/\rho)S_L^0$ , the predicted  $S_d \nabla \cdot \mathbf{n}$  is equal to zero, because curvature is zero in average. The evolution of  $S_d \nabla \cdot \mathbf{n}$  in Fig. 1.6.12a is over-predicted by the model using Eq.(1.6.21), while in Figs. 1.6.12b and 1.6.12c the accuracy of the model seems to increase with the Karlovitz number. So the results in Fig. 1.6.12 show that the flamelet model (Eq. 1.6.15) is too approximative to compute correctly the stretch rate due to curvature, while the model taking into account tangential diffusion effects (Eq. 1.6.21) seems to reproduce more correctly  $S_d \nabla \cdot \mathbf{n}$ . Furthermore, the difference between the actual stretch due to curvature and  $-D(\nabla \cdot \mathbf{n})^2$  cannot be explain with the flamelet component of  $S_d \nabla \cdot \mathbf{n}$ ,

which is zero. So, even if the model proposed by Peters shows a clear improvement, choosing  $D$  as the species mass diffusivity does not seem enough.

To conclude on this study, even if the results show the improvement brought by considering additional terms suggested by Peters (1999) in Eq. (1.6.21), the use of two-dimensional DNS is limiting the evaluation of a model for curvature and displacement speed because some 3D geometrical stretch effects are not taken into account and turbulence is not representative of a real turbulent flame.

Then, Trisjono et al. (2016) and Wang et al. (2017) focused on the displacement speed and the flame stretch by observing 3D-DNS of hydrogen-air and methane-air premixed flames, respectively. In both works the displacement speed is decomposed according to Eq.(1.6.17).

They first observed that turbulence seems to locally slow down the flame, with a generalized flame speed with respect to the unburnt gases of about  $0.66S_L^0$  (Trisjono et al., 2016). This phenomenon was explained by Trisjono et al. (2016) with the evolution of the reaction related speed  $S_r$  with the tangential strain rate plotted in Fig. 1.6.13a. In this study (Trisjono et al., 2016),  $a_T$  is in average positive, which implies a decrease in  $S_r$ .

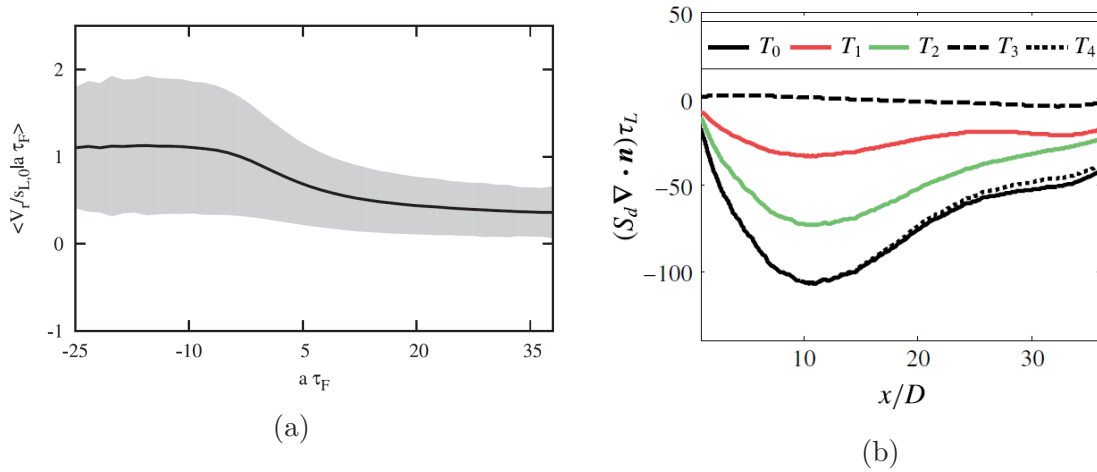


Figure 1.6.13: (a) Response of reaction related speed  $V_r = S_r$  normalized with  $S_L^0$  to strain. (Trisjono et al., 2016) (b) The axial evolution of the integrated generalized surface averaged curvature stretch term:  $T_0 = \langle S_d \nabla \cdot \mathbf{n} \rangle$ ;  $T_1 = \langle (S_r + S_n) \nabla \cdot \mathbf{n} \rangle$ ;  $T_2 = -\langle D(\nabla \cdot \mathbf{n})^2 \rangle$ ;  $T_3 = \langle S_d \rangle \langle \nabla \cdot \mathbf{n} \rangle$ ;  $T_4 = \langle S_d \nabla \cdot \mathbf{n} \rangle - \langle S_d \rangle \langle \nabla \cdot \mathbf{n} \rangle$ . (Wang et al., 2017)

Finally, the curvature term  $\langle S_d \nabla \cdot \mathbf{n} \rangle$  and the different components according to the equations 1.6.22 and 1.6.23 are plotted through the flame front in Fig. 1.6.13b.

$$\underbrace{\langle S_d \nabla \cdot \mathbf{n} \rangle}_{T_0} = \underbrace{\langle (S_r + S_n) \nabla \cdot \mathbf{n} \rangle}_{T_1} - \underbrace{\langle D(\nabla \cdot \mathbf{n})^2 \rangle}_{T_2}, \quad (1.6.22)$$

$$= \underbrace{\langle S_d \rangle \langle \nabla \cdot \mathbf{n} \rangle}_{T_3} + \underbrace{(\langle S_d \nabla \cdot \mathbf{n} \rangle - \langle S_d \rangle \langle \nabla \cdot \mathbf{n} \rangle)}_{T_4}. \quad (1.6.23)$$

This graph shows that  $\langle S_d \rangle \langle \nabla \cdot \mathbf{n} \rangle$  is close to zero. So, the flamelet assumption considering  $\langle S_d \nabla \cdot \mathbf{n} \rangle = \langle S_d \rangle \langle \nabla \cdot \mathbf{n} \rangle$  is wrong. The evolution of  $\langle S_d \nabla \cdot \mathbf{n} \rangle - \langle S_d \rangle \langle \nabla \cdot \mathbf{n} \rangle$  compared to  $\langle S_d \nabla \cdot \mathbf{n} \rangle$

shows that the spatial average of the product of the fluctuations is dominant. Furthermore, by considering the decomposition of the displacement speed (Eq. 1.6.17) the results confirm Peters's theory (Peters, 1999) and the observations in 2D simulation of Hawkes and Chen (2005) on the term  $D(\nabla \cdot \mathbf{n})^2$ , which becomes the dominant term in the curvature term  $S_d \nabla \mathbf{n}$ .

The study by Han and Huh (2009), along with others (Sankaran et al., 2015; Wang et al., 2017), highlighted the curvature effects on the displacement speed, through the sum  $S_r + S_n$ . Nevertheless, Chakraborty and Cant (2006, 2011, 2005a,b) highlighted that both tangential strain rate and curvature are correlated to  $S_r + S_n$ . In addition, they also observe that these correlations are strongly dependent on the Lewis number of the fuel. To evaluate the influence of the Lewis number on the correlation between  $S_r + S_n$  and curvature, they defined a Markstein length due to curvature  $\mathcal{L}_{rn}$ :

$$S_r + S_n = \frac{\rho_u}{\rho} S_L^0 - S_L^0 \mathcal{L}_{rn} \kappa. \quad (1.6.24)$$

The analysis of the joint PDF of  $S_r + S_n$  and curvature shows that  $\mathcal{L}_{rn} < 0$  when  $Le < 1$  and  $\mathcal{L}_{rn} > 0$  when  $Le > 1$ .

Peters (1999) argued that the dominant curvature effect on displacement speed in the thin reaction zones regime arises through the tangential diffusion component  $-D \nabla \cdot \mathbf{n}$ , but studies (Chakraborty and Cant, 2006, 2011, 2005a,b; Chakraborty and Klein, 2008) reveal that in the case of non-unity Lewis number the curvature effects on the combined reaction and normal diffusion components  $S_r + S_n$  cannot be ignored. This indicates that modelling of curvature effects on  $S_r + S_n$  is required in order to address differential diffusion effects on turbulent premixed flame propagation. In addition, this study can be compared to the analysis of Hawkes and Chen (2005). Indeed, they defined an effective diffusivity  $D_{eff}$  to be modelled, which can be related to the Markstein length defined by Chakraborty and Cant (2006, 2011, 2005a,b) when Eq. (1.6.24) is combined with both the decomposition of the stretch due to curvature in Eq. (1.6.20):

$$\langle S_d \kappa \rangle_s = \left\langle \frac{\rho_u}{\rho} S_L^0 \kappa \right\rangle_s - \langle (D + S_L^0 \mathcal{L}_{rn}) \kappa^2 \rangle_s. \quad (1.6.25)$$

When  $Le = 0.8$ , Eq. (1.6.25) suggests that the term  $S_L^0 \mathcal{L}_{rn}$  decreases the effective diffusivity defined as  $D_{eff} = D + S_L^0 \mathcal{L}_{rn}$ . This is in agreement with the work of Hawkes and Chen (2005).

So, studies conducted by Chakraborty and Cant (2006, 2011, 2005a,b) suggest that the correlation between  $a_T$  and  $S_r + S_n$ , and the one between  $\kappa$  and  $S_r + S_n$  should be modelled in LES and should take into account differential diffusion.

Finally, as suggested by Peters (1999) and Hawkes and Chen (2005), Katragadda et al. (2012; 2014a; 2014b) proposed a model for the stretch due to curvature in the context of generalized FSD transport equation. This model was developed in the context of TRZ regime,

and is given below:

$$\begin{aligned} \langle S_d \kappa \rangle_s \bar{\Sigma} = & -\beta_1 S_L^0 \left(1 - \overline{\langle \mathbf{N} \rangle}_s \overline{\langle \mathbf{N} \rangle}_s\right) (\bar{c} - c^*) f(\bar{c}, \tilde{c}) \bar{\Sigma} \\ & - D_{eff} \beta_H \left(1 - \overline{\langle \mathbf{N} \rangle}_s \overline{\langle \mathbf{N} \rangle}_s\right)^2 \frac{1}{\bar{c}^2 (1 - \bar{c})^2} \bar{\Sigma}, \end{aligned} \quad (1.6.26)$$

where  $\overline{\langle \mathbf{N} \rangle}_s = -\nabla \bar{c} / \bar{\Sigma}$  is the surface averaged flame normal vector,  $D_{eff}$  is an effective diffusivity which is expected to approach the mass diffusivity for low  $Da$  combustion, and  $\beta_1$ ,  $c^*$ ,  $f(\bar{c}, \tilde{c})$  and  $\beta_H$  are model parameters defined as follows:

$$\beta_1 = (7.24 Le^{-0.68}) (1 + Ka)^{-0.25}, \quad (1.6.27a)$$

$$c^* = \frac{1.27 \exp(-0.77 Le)}{\text{erf}[(1 + Ka)^{1.1}/4.85]} \left[ 1 + \frac{f_2(Re_t) - 1.0}{[1.0 + \exp(-5.0(Ka - 1.9))]^5} \right], \quad (1.6.27b)$$

$$f_2(Re_t) = 0.49 \frac{Re_t^{0.41} + 0.69}{0.46 Re_t^{0.46} + 0.56}, \quad (1.6.27c)$$

$$f(\bar{c}, \tilde{c}) = 1.0 - \frac{\exp(-9.0(1 - \tilde{c}))}{\bar{c}(1.0 - \bar{c})^m}, \quad (1.6.27d)$$

$$m = 1.56 \frac{\exp(-0.24 Le)}{\text{erf}[(1.0 + Ka)/1.5]}, \quad (1.6.27e)$$

$$\beta_H = 2.24 Le^{-0.85} \frac{0.5}{1 + \exp[-(Re_t - 20)]}. \quad (1.6.27f)$$

This model presents some encouraging results allowing to reproduce the stretch due to curvature for different turbulent intensities. However, this model includes numerous constants directly fitted from the DNS results. Besides, these constants are obtained for light hydrocarbons, while fuels used in automotive engine are heavy hydrocarbons. Thus, the universality of Eqs. (1.6.26) and (1.6.27) remains to be verified. In Chapter 4, this model (Eqs. 1.6.26 to 1.6.27f) is compared to a model proposed in the present study and to DNS.

Finally, a small number of LES were performed at high Karlovitz numbers. Duwig et al. (2011) performed a well resolved LES using reduced chemistry of an experimental pilot premixed jet burner with Karlovitz numbers up to 1600. The grid resolution was fine enough to resolve the reacting layer assuming perfect mixing at the sub-grid scale and neglecting sub-grid scale fluctuations, this LES is in fact very close to a DNS as sub-grid scale contributions are expected to be negligible. It is therefore not very surprising that good results were obtained against the experiment. Such an approach is impractical for SI engines due to the extremely small flame thickness.

## 1.7 Conclusions: Objectives and structure of the thesis

In this chapter, the physics of laminar and turbulent flames is presented along with the different approaches for numerical simulations of turbulent reactive flows. A focus is made on a LES



model based on the definition of a flame surface density, the coherent flame model (CFM). The CFM model was developed based on the flamelet assumptions.

The first assumption of the flamelet regime, considering the flame as a collection of parallel infinitely thin flamelets, was seen to be invalid in the TRZ regime. Indeed, numerous studies (Aspden et al., 2011a,b, 2015, 2016, 2017, 2019; de Goey et al., 2005; Gülder, 2007; Poludnenko and Oran, 2010, 2011; Yuen and Gülder, 2013) show that a thickening of the preheat zone occurs, when the turbulence intensity is increased. This thickening is generally associated to a strong distortion of the progress variable iso-surface towards  $c = 0$ . Thus, in the TRZ regime the iso-surfaces of progress variable are not parallel questioning the validity of the concept of FSD in this regime.

In addition, the second assumption of the flamelet regime, considering that each flamelet propagates locally at the laminar flame velocity, appears to be invalid for high Karlovitz numbers. Consequently, the model commonly used to evaluate the propagation speed in Eq. (1.5.21) cannot be used in the TRZ regime. Indeed, as Peters (1999) suggested and confirmed in numerous studies (Chakraborty and Cant, 2006, 2011, 2005a,b; Chakraborty and Klein, 2008; Han and Huh, 2009; Poludnenko and Oran, 2010, 2011; Sankaran et al., 2015; Trisjono et al., 2016; Wang et al., 2017) the propagation speed of the flame front is highly impacted by turbulence through the effect of stretch. The focus was made on the stretch due to curvature  $S_d\kappa$  in many studies. Furthermore, different studies (Chakraborty and Cant, 2006, 2011, 2005a,b; Chakraborty and Klein, 2008; Lapointe and Blanquart, 2017; Lapointe et al., 2015; Savard and Blanquart, 2014, 2015, 2017; Savard et al., 2015) suggest that some effects of preferential diffusion shall be taken into account in models of  $S_d$  and  $S_d\kappa$ .

Thus, the main purpose of this PhD, which is to extend the CFM approach to highly diluted and turbulent premixed flames, can be decomposed into secondary objectives:

1. to propose an adaptation of the concept of the flame surface density to flames in the TRZ regime,
2. to propose a model for the tangential strain rate valid in the TRZ regime,
3. to propose a model for the stretch due to curvature,
4. to propose a model for the flame displacement speed,
5. to take into account differential diffusion effects in the models.

To reach these objectives, the present PhD thesis is organized as follows:

- **Chapter 2** is dedicated to the analysis of two-dimensional flames interacting with pairs of counter rotating vortices, in order to develop a new efficiency function to be used in the approach proposed by Charlette et al. (2002a) (Eq. 1.5.36) for tangential strain rate modelling.



- **Chapter 3** is dedicated to the analysis of 3D DNS of flames interacting with a forced turbulent field. This analysis is conducted in order to better understand the phenomena involved in the TRZ regime to propose a path for adapting the concept of flame surface density. Then, a specific focus is made on the effect of turbulence on the flame displacement speed, through its response to tangential strain rate and curvature, in order to propose a model for this quantity. These 3D DNS are also used to explore the effects of differential diffusion on the flame front and on the displacement speed.
- **Chapter 4** is dedicated to describe an *a priori* model proposed for flames in the TRZ regime. In this chapter, the adaptation of the flame surface density approach is explicitly presented along with the models for the tangential strain rate, the stretch due to curvature and the displacement speed, including preferential diffusion effects. This *a priori* model is tested using the results from the 3D DNS.
- **Chapter 5** is dedicated to complete the *a priori* model of the previous chapter. It presents *a posteriori* validation using one-dimensional turbulent premixed flames compared to the 3D DNS. Finally, the application of the proposed model to SI engines simulation is discussed.

# Chapter 2

## Turbulent strain rate modelling using 2D flame/vortex interactions

In the previous chapter, it is suggested that in the thin reaction zone (TRZ) regime the smallest scales of turbulence strongly disturb the flame front. In premixed combustion framework, some authors (Bougrine et al., 2014; Candel and Poinso, 1990; Charlette et al., 2002a; Colin et al., 2000; Meneveau and Poinso, 1991; Poinso et al., 1991) proposed to study how specific scales of turbulence affect the flame front through the flame stretch rate using 2D direct numerical simulations (DNS) of isolated pair of vortices interacting with planar flames.

This chapter is dedicated to the analysis of 2D DNS of a premixed  $C_8H_{18}$ -air flame interacting with various pair of vortices corresponding to turbulent structures encountered in the TRZ regime. So, the main purpose of the present study is to develop a new function  $C_r$  involved in tangential strain rate model (see Section 1.5.5) valid for the TRZ regime.

In this chapter, the purpose and the set-up of these 2D-DNS are first described in Section 2.1. Then, the assumptions commonly made to evaluate an efficiency function in tangential strain rate modelling are investigated in Section 2.2. Finally, a new function  $C_r$  is proposed from the analysis of the 2D-DNS of flame-vortex interactions in Section 2.3.

Note that this chapter is only dedicated to 2D-DNS analysis. Consequently, the accuracy of the tangential strain rate model based on the efficiency function derived from these flame/vortex interactions will be evaluated and compared to other models against 3D-DNS of turbulent flames at various Karlovitz numbers in Section 4.4.3.

### 2.1 The direct numerical simulations set-up

#### 2.1.1 Purpose of the analysis of flame-vortex interactions

As presented in Section 1.5.5, the tangential strain rate involved in the filtered transport equation of flame surface density (FSD) (Eq. 1.5.29) is modelled based on the intermittent turbulent net flame stretch (ITNFS) approach introduced by Meneveau and Poinso (1991). This approach, first introduced for Reynold averaged Navier-Stokes (RANS) modelling, consists in

assuming that each scale of turbulence acts independently on the flame front. Consequently, the resulting total turbulent strain rate is computed by summing strain rates induced by each turbulent scale, from Kolmogorov to integral length scales. This leads to write the total turbulent strain rate as:

$$a_T = \alpha_0 \Gamma \frac{\varepsilon}{k_t}, \quad (2.1.1)$$

where  $\alpha_0$  is a model constant,  $\varepsilon$  and  $k_t$  are the turbulent dissipation rate and the turbulent kinetic energy, respectively.  $\Gamma$  is an efficiency function to take into account the reduced ability of small vortices to wrinkle the flame front. Charlette et al. (2002a) proposed in a large-eddy simulation (LES) context a spectral description of the turbulence leading to:

$$\left( \Gamma \frac{u'}{\Delta} \right)^2 = \left( \frac{\pi}{\Delta} \right)^3 \int_1^\infty [C_r(k_+)]^2 k_+^2 E_{11}(k_+) dk_+, \quad (2.1.2)$$

where  $k_+ = k\hat{\Delta}/\pi$  is an adimensional wavenumber associated to the wavenumber  $k = \pi/r$  with  $r$  the size of the structures of the turbulent flow and  $E_{11}(k_+)$  is the one-dimensional (longitudinal) energy spectrum in the direction of the wavenumber  $k$  (Eq. 1.5.41). As presented in Chapter 1, the key parameter in Eq. (2.1.2) is the correction function  $C_r(k_+)$ , which takes into account the ability of the turbulent eddies at scale  $r$  to stretch the flame. In this chapter, the correction function  $C_r$  will also be referred to as the efficiency function.

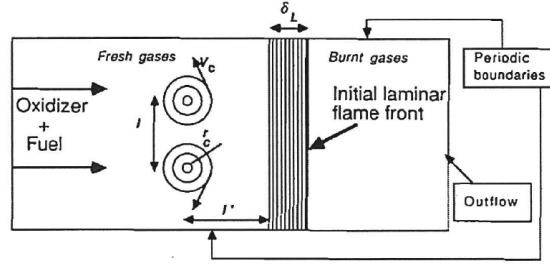


Figure 2.1.1: Initial geometry of the flame-vortex interaction (Candel and Poinso, 1990). A pair of counter-rotating vortices, of radius  $r$  and velocity  $u'_r$ , is initially located at a distance  $l'$  from the flame front. The centres of the two vortices are at a distance  $l$  from each other.

The challenge in evaluating this correction function is to isolate the effect each scale on the flame stretch. Recently, Doan et al. (2017) suggests to use the bandpass filtering method described by Leung et al. (2012). The results from these DNS (Doan et al., 2017) are encouraging but is focused on turbulent scales larger than the flame thickness, which does not correspond to the scope of the present study. Nevertheless, the effect of each turbulent scale is isolated through 2D DNS of a planar flame interacting with a pair of counter rotating vortices, as described by Meneveau and Poinso (1991). The initial configuration is displayed in Fig. 2.1.1. Note that these two dimensional simulations of flame/vortex interactions strongly approximate the eddies involved in a 3D turbulent flow field.

Because  $C_r$  quantifies the ability of the turbulent eddies of size  $r$  and velocity  $u'_r$  to stretch the flame, the flame stretch is extracted from the DNS. Usually this quantity is evaluated from the flame surface variation assumed to be proportional to the total reaction rate. Thus, the

flame stretch  $K(t)$  during a simulation is approximated as the rate of change of total heat release  $Q$ :

$$K(t) = \frac{1}{\mathcal{A}(t)} \frac{d\mathcal{A}}{dt} \approx \frac{1}{Q(t)} \frac{dQ}{dt}, \quad (2.1.3)$$

where  $\mathcal{A}$  is the flame surface. The approximation in Eq. (2.1.3) is based on the assumption that under stretching effects the local flame speed does not change, which could be accurate for mixtures with unity Lewis numbers in the flamelet regime. For this reason and because previous studies (Lapointe et al., 2015; Savard and Blanquart, 2015; Savard et al., 2015) highlight the strong impact of the flame stretch on the local speed, this assumption should be re-investigated.

During the interaction between a flame and vortices, three phases are observed in Fig. 2.1.2.

1. An induction phase during which the pair of vortices moves toward the flame front without perturbing it.
2. A stretching phase during which the pair of vortices is interacting with the flame front by stretching it.
3. An annihilation phase during which the flame fronts interact and merge, leading to flame surface destruction. This phase is not always observed because the vortices can be dissipated before flame surface destruction occurs.

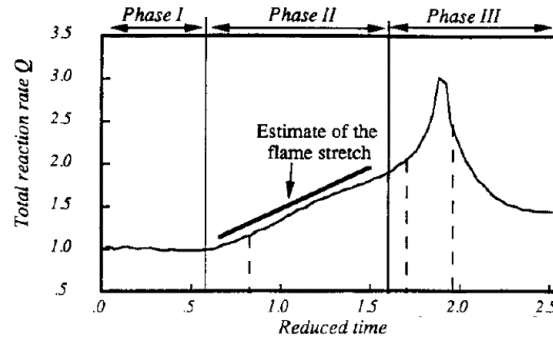


Figure 2.1.2: An example of the temporal evolution of the total heat release during a flame-vortex interaction ( $u'_r/S_L^0 = 28$  and  $r_c/\delta_L^0 = 5$ ). (Meneveau and Poinso, 1991)

The function  $C_r$  is deduced from the second phase where the reaction rate grows exponentially, corresponding to a constant  $(1/Q(t))dQ/dt$  and consequently to a constant flame stretch  $K_r$ . In previous studies (Bougrine et al., 2014; Charlette et al., 2002a; Meneveau and Poinso, 1991),  $K_r$  is deduced from the estimation of the maximum slope of the second phase:

$$K_r = \max \left( \frac{1}{Q} \frac{dQ}{dt} \right). \quad (2.1.4)$$

Finally, the efficiency  $C_r$  of a pair of vortices of size  $r$  and velocity  $u'_r$  to stretch the flame is evaluated as:

$$C_r(r, u'_r) = K_r \frac{r}{u'_r}, \quad (2.1.5)$$

where  $u'_r/r$  is the theoretical strain rate induced by them. To develop a model for  $C_r$  depending on the characteristics of the structures involved in a turbulent flow, the 2D DNS of interactions flame-vortex are usually conducted by varying both the size  $r$  of the vortices and their velocity  $u'_r$ . The ranges of variation of the size and the velocities of the vortices already conducted in previous studies (Bougrine et al., 2014; Colin et al., 2000) correspond to flames in the flamelet regime focusing on large vortices compared to the flame thickness, *i.e.*,  $r > \delta_L$ . These conditions are reported in Fig. 2.1.3.

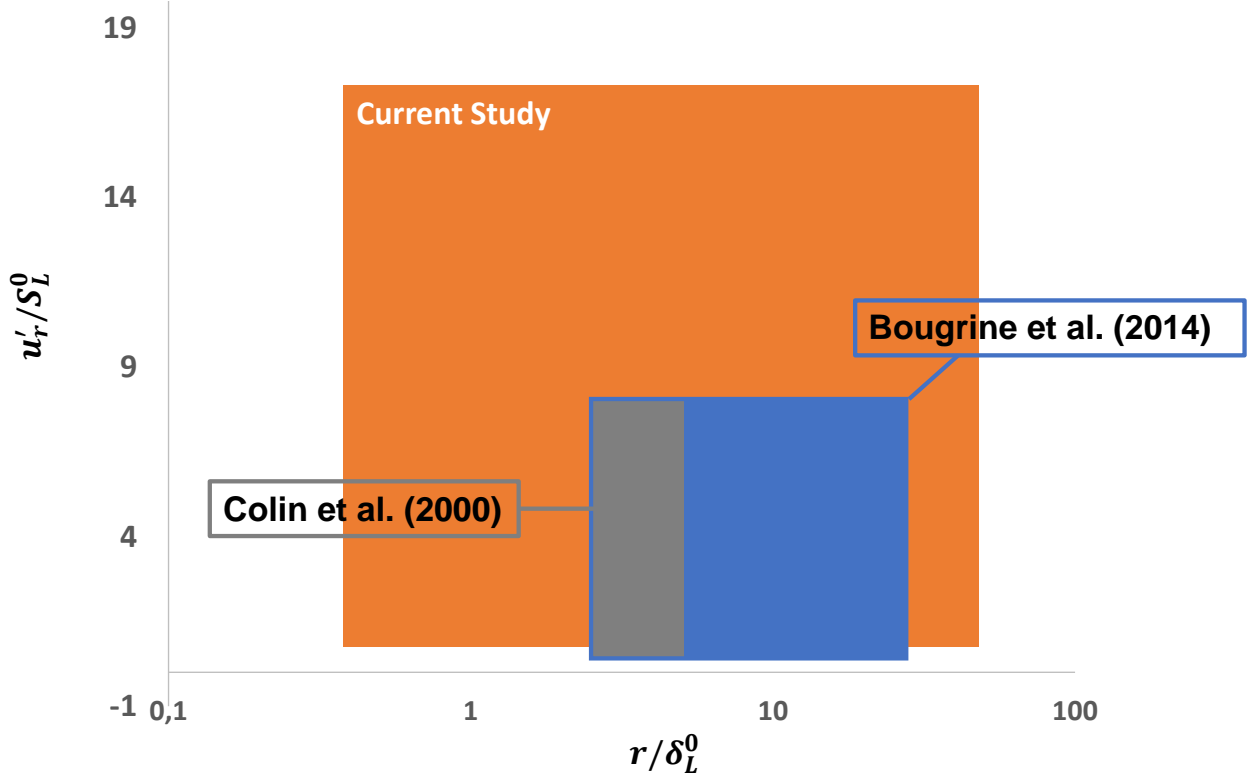


Figure 2.1.3: Diagram presenting the range of operating conditions from the works of Colin et al. (2000), Bougrine et al. (2014) and from this study with grey, blue and orange areas, respectively.

### 2.1.2 DNS implementation

Because the present study is focused on turbulent flames in the TRZ regime, 2D DNS of flame/vortex interactions are conducted to:

1. Explore the effects of small vortices on the flame stretch, because in the TRZ regime the small structures of turbulence penetrate the preheat zone and perturb the flame front. This is made possible by extending the range of sizes and velocities of the vortices, compared to previous studies (Bougrine et al., 2014; Colin et al., 2000).
2. Re-investigate the approximations commonly made for computing the flame stretch in flame-vortex interactions based on flamelet assumptions:
  - approximating the stretch flame as the rate of change of total heat release  $Q$  (Eq. 2.1.3),

- approximating the strain rate with the flame stretch ( $K_r \approx a_T$ ).

The AVBP code (Moureau et al., 2005) was used to simulate a 2D steady planar laminar pre-mixed iso-octane/air flame in a square domain using a two-steps Taylor-Galerkin type scheme (TTGC) (Colin and Rudgyard, 2000), which is 3<sup>rd</sup> order in time and space. The iso-octane/air kinetics are described by a two-step Arrhenius mechanism with 6 species:



This scheme was developed for piston engine simulations and validated using both the laminar flame speed  $S_L^0$  and the laminar flame thickness  $\delta_L^0$  for the following conditions: 323 K, a constant pressure of 1 atm and an equivalence ratio ranging between 0.5 and 1.2 (Bonhomme et al., 2013). The forward reaction rates  $k_{f1}$  and  $k_{f2}$  for  $\text{C}_8\text{H}_{18}$  oxidation and for  $\text{CO}-\text{CO}_2$  equilibrium, respectively, are expressed below.

$$k_{f1} = A_1 T^{b_1} e^{-\frac{E_{a,1}}{RT}} [\text{C}_8\text{H}_{18}]^{n_{\text{C}_8\text{H}_{18}}} [\text{O}_2]^{n_{\text{O}_2,1}}, \quad (2.1.8)$$

$$k_{f2} = A_2 T^{b_2} e^{-\frac{E_{a,2}}{RT}} [\text{CO}]^{n_{\text{CO}}} [\text{O}_2]^{n_{\text{O}_2,2}}. \quad (2.1.9)$$

$A_i$  is the pre-exponential factor,  $b_i$  is the temperature exponent,  $E_{a,i}$  is the activation energy of reaction  $i$ , and  $n_{k,i}$  are the reaction exponents for species  $k$  in reaction  $i$  (Table 2.1).  $R$  is the ideal gas constant equal to  $8.314 \text{ J.K}^{-1}.\text{mol}^{-1}$ . The viscosity  $\mu$  follows a power law defined as:

$$\mu = \mu_{ref} \left( \frac{T}{T_{ref}} \right)^b, \quad (2.1.10)$$

where  $\mu_{ref} = 7.17 \cdot 10^{-5} \text{ kg.m}^{-1}.\text{s}^{-1}$  is the viscosity of the unburnt gases at the reference temperature  $T_{ref} = 2240 \text{ K}$ , and  $b = 0.66$ .

For the whole study, a stoichiometric ( $\Phi = 1$ )  $\text{C}_8\text{H}_{18}$ /air mixture is considered, at a temperature  $T_u = 300 \text{ K}$  and a pressure  $P_u = 1 \text{ atm}$ , leading to a laminar flame speed  $S_L^0 = 0.366 \text{ m/s}$  and a flame thickness  $\delta_L^0 = 385 \text{ }\mu\text{m}$ .

Table 2.1: Arrhenius parameters for the  $\text{C}_8\text{H}_{18}$  2-step mechanism.

Case	$\text{Le}_{\text{Fuel}}$	reaction	$A_i$	$b_i$	$E_{a,i} [\text{cal/mol}]$	$n_k$
$\text{Le}_k \neq 1$	2.9	$\text{C}_8\text{H}_{18}$ oxidation	$5.443 \cdot 10^{12}$	0.1	$3.6 \cdot 10^4$	$n_{\text{C}_8\text{H}_{18}} = 1.1$
						$n_{\text{O}_2,1} = 0.54$
		$\text{CO} - \text{CO}_2$ equilibrium	$2.0 \cdot 10^9$	0	$1.4 \cdot 10^4$	$n_{\text{CO}} = 1.0$
						$n_{\text{O}_2,2} = 0.5$
$\text{Le}_k = 1$	1.0	$\text{C}_8\text{H}_{18}$ oxidation	$9.150 \cdot 10^{12}$	0.1	$3.6 \cdot 10^4$	$n_{\text{C}_8\text{H}_{18}} = 1.1$
						$n_{\text{O}_2,1} = 0.54$
		$\text{CO} - \text{CO}_2$ equilibrium	$3.327 \cdot 10^9$	0	$1.4 \cdot 10^4$	$n_{\text{CO}} = 1.0$
						$n_{\text{O}_2,2} = 0.5$

Because in Section 1.6.1 numerous studies (Chakraborty and Cant, 2006, 2011, 2005a,b;

Chakraborty and Klein, 2008; Lapointe and Blanquart, 2017; Lapointe et al., 2015; Savard and Blanquart, 2014, 2015, 2017; Savard et al., 2015) suggest that preferential diffusion has a significant impact on the flame front, all the simulations were performed twice, once considering differential diffusion with non unity Lewis numbers and once with all the Lewis numbers equal to unity. The Arrhenius coefficients of the 2-step mechanism were adapted for  $Le_k = 1$  case as shown in Table 3.1, in order to get the same laminar flame speed and thickness for both cases.

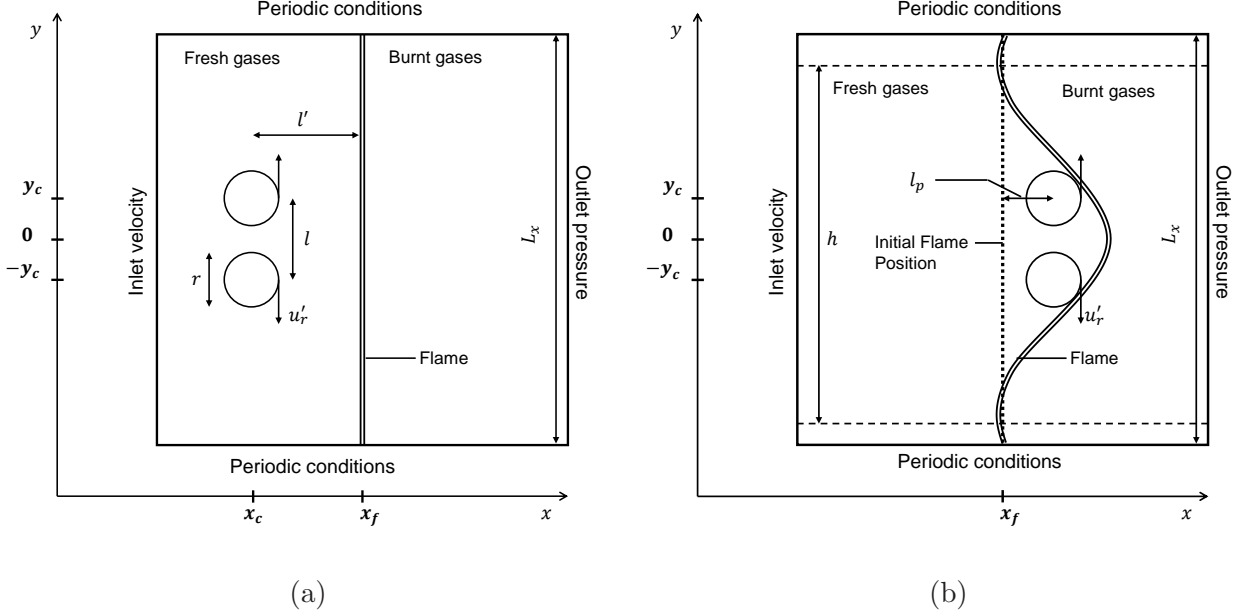


Figure 2.1.4: DNS configuration of flame-vortex interactions. A pair of counter-rotating vortices interacts with an initially planar premixed flame. (a) the schematic configuration of the initial solution. (b) The schematic configuration corresponding to the moment when the flame stretch is evaluated.

The size  $L_x \times L_y$  of the domain presented in Fig. 2.1.4a is defined as a function of the size  $r$  of the counter-rotating vortices:  $L_x = 6r$ . The vortices are defined through the stream function  $\Psi$ :

$$\Psi(x, y) = \Theta \exp \left[ -\frac{(x - x_c)^2 + (y - y_c)^2}{2r^2} \right], \quad (2.1.11)$$

where  $\Theta$  is the vortex strength and  $(x - x_c)^2 + (y - y_c)^2$  is the square of the distance to the centre of the vortex. The initial position of the pair of vortices is arbitrary. The vortices should not be too close together to prevent them from interacting with each other, but not too far apart to allow them to move towards the flame. In practice, we chose  $x_c = x_f - 3r$ , where  $r$  is the radius of the vortex and the flame position is  $x_f$ , and  $y_c = \pm 3r/2$ .

In this study, similar configurations as (Bougrine et al., 2014; Colin et al., 2000; Meneveau and Poinso, 1991) are simulated but extending the range of vortices both in size and in velocity. Thus, to represent a flame in the flamelet regime and two flames in the TRZ regime, the turbulent characteristics of cases A, C and D from the 3D DNS, presented in Chapter 3, were chosen to evaluate  $u'_r$  of the vortices. Three sets of DNS are performed with a constant  $u'_r$  for each of them. The velocity for each set of DNS is chosen to correspond to the characteristic velocity of the turbulent structures with a scale of  $\delta_L^0$  in the 3D DNS.

Nevertheless, extending the range of size of vortices to small scales compared to the laminar flame thickness is limited by the dissipation of the vortices. To evaluate this dissipation, the enstrophy  $\mathcal{E}$  of each configuration reported in Table 2.2 is computed. First, the vorticity of the vortices must be defined as:

$$\boldsymbol{\Omega} = \nabla \otimes \mathbf{u}. \quad (2.1.12)$$

The enstrophy is then deduced from the vorticity following:

$$\mathcal{E} = \frac{1}{2} \int_V |\boldsymbol{\Omega}|^2 d\mathbf{x}. \quad (2.1.13)$$

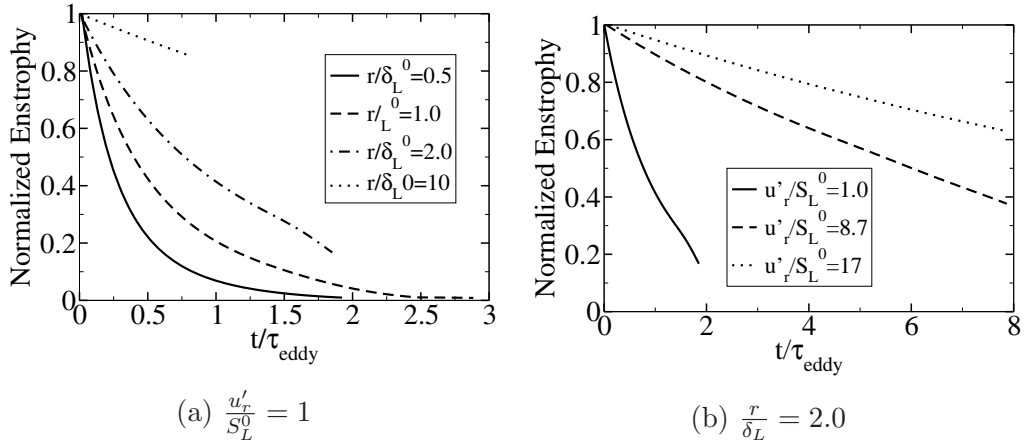


Figure 2.1.5: Evolution of the normalized enstrophy  $\mathcal{E}/\mathcal{E}_{t=0}$ , with  $\mathcal{E}_{t=0}$  the initial enstrophy, against time normalized with the eddy turnover time  $\tau_{eddy}$  for: (a) vortices with the same velocity ratio,  $u'_r/S_L^0 = 1$  and (b) vortices with the same size  $r/\delta_L = 2$ .

Figure 2.1.5 shows the evolution of  $\mathcal{E}/\mathcal{E}_{t=0}$  with time normalized with the eddy turnover time  $\tau_{eddy} = r/u'_r$  for different pair of vortices. In Fig. 2.1.5a, this temporal evolution is plotted for vortices with the same velocity ratio ( $u'_r/S_L^0 = 1$ ). In this figure, the smaller is the vortex, the quicker its enstrophy reaches zero. When  $r/\delta_L = 0.5$ , the vortices are dissipated after approximately 1 eddy turnover avoiding them to interact with the flame front. Indeed, interaction with flame front occurs after a time at least larger than  $\tau_{eddy}$ .

In Fig. 2.1.5b, the temporal evolution of enstrophy is plotted for vortices of size  $r/\delta_L = 2$  but for three different velocities. The impact of the velocity on dissipation is significant. Indeed, the smaller  $u'_r/S_L^0$  is, the quicker the vortices are dissipated relatively to the eddy turnover time.

In order to simulate the maximum vortices interacting with the flame front, the size ratio is chosen in a range between 0.5 and 50 allowing to simulate the effects of small structures as well as larger vortices on the flame stretch.

A total of 38 flame-vortex interactions were computed, including 28 non-diluted flames and 10 diluted flames. The latter are diluted with a 20% EGR rate. The exhaust gas used for dilution is a mixture of  $\text{CO}_2$  and  $\text{H}_2\text{O}$ . The numerical parameters for these 38 simulations are summarized in Table 2.2. These operating conditions are compared to previous works by Colin



et al. (2000) and Bougrine et al. (2014) in Fig.2.1.3. The range of vortices is significantly larger for both size and strength.

Finally, the existing models (Bougrine et al., 2014; Charlette et al., 2002a; Colin et al., 2000; Meneveau and Poinso, 1991) are based on the evaluation of  $C_r$  using the flame stretch  $K_r$  with Eq. (2.1.5), which includes both tangential strain rate and stretch due curvature. However, as presented in Section 1.6.1, in the TRZ regime the stretch due to curvature becomes much more important in the total stretch. Thus, in the present study, we propose to evaluate the impact of this definition by computing the function  $C_r$  considering only the strain rate:

$$C_r = \langle a_T \rangle_s \frac{r}{u'_r}, \quad (2.1.14)$$

where  $\langle a_T \rangle_s$  is the surface averaged tangential strain rate defined as:

$$\langle a_T \rangle_s = \frac{\int_{\mathcal{V}} a_T |\nabla c| dV}{\int_{\mathcal{V}} |\nabla c| dV}, \quad (2.1.15)$$

where  $\mathcal{V}$  is the computation domain and  $c$  is the progress variable. Unfortunately, Eq. (2.1.15) depends on the domain size and the length of the flame affected by the vortices. To minimize the impacts on the evaluation of  $\langle a_T \rangle_s$ , the domain  $\mathcal{V}$  was limited to the zone of height  $h$  (see Fig. 2.1.4b) containing only the part of the flame affected by the vortices. Despite these major drawbacks,  $\langle a_T \rangle_s$  (Eq. 2.1.15) was chosen because in the FSD transport equation (Eq. 1.5.29) the tangential strain rate involved is surface averaged.

## 2.2 Discussion on the common assumptions in the context of the thin reaction zone regime

The progress variable is defined as the reduced temperature :

$$c = \frac{T - T_u}{T_b - T_u}, \quad (2.2.1)$$

where  $T_u$  and  $T_b$  are the temperature of the fresh and the burnt gases, respectively. The common approximations made for analysing flame-vortex interactions are discussed in this section.

As mentioned in the previous section, the analysis of 2D DNS of flame-vortex interactions relies on the evolution of the flame surface  $\mathcal{A}$ . This surface in the flamelet regime is either the generalized surface  $\mathcal{A} = \int_{\mathcal{V}} |\nabla c| dV$  or  $\mathcal{A}^* = \int_{\mathcal{V}} |\nabla c| \delta(c - c^*) dV$  the surface associated to the progress variable iso-surface  $c = c^*$ , because the flame is a collection of parallel iso-surfaces. Nevertheless, the observations made in different studies presented in Section 1.6.1 on the inner structure of the flame suggest that the definition of the flame surface must have a significant impact on the flame modelling. A detailed discussion on the issue of the definition of the flame surface is proposed in Chapter 3.

In the context of 2D-DNS, the flame stretch rate is first computed, in the present study,

Table 2.2: The DNS set-up of the flame-vortex interactions

Case	EGR rate	$Le_{fuel}$	<b>Ka</b>	$\mathbf{u}'_r/\mathbf{S}^0_L$	$\mathbf{r}/\delta_L$	$N_x$
A1	0%	2.9	3	1	0.5	320
A2	0%	2.9	3	1	1.0	480
A3	0%	2.9	3	1	2.0	960
A4	0%	2.9	3	1	10.0	1800
C1	0%	2.9	89	8.7	0.5	320
C2	0%	2.9	89	8.7	1.0	480
C3	0%	2.9	89	8.7	2.0	960
C4	0%	2.9	89	8.7	10.0	1800
C5	0%	2.9	89	8.7	50.0	1800
D1	0%	2.9	250	17	0.5	320
D2	0%	2.9	250	17	1.0	480
D3	0%	2.9	250	17	2.0	960
D4	0%	2.9	250	17	10.0	1800
D5	0%	2.9	250	17	50.0	1800
A1u	0%	1.0	3	1	0.5	320
A2u	0%	1.0	3	1	1.0	480
A3u	0%	1.0	3	1	2.0	960
A4u	0%	1.0	3	1	10.0	1800
C1u	0%	1.0	89	8.7	0.5	320
C2u	0%	1.0	89	8.7	1.0	480
C3u	0%	1.0	89	8.7	2.0	960
C4u	0%	1.0	89	8.7	10.0	1800
C5u	0%	1.0	89	8.7	50.0	1800
D1u	0%	1.0	250	17	0.5	320
D2u	0%	1.0	250	17	1.0	480
D3u	0%	1.0	250	17	2.0	960
D4u	0%	1.0	250	17	10.0	1800
D5u	0%	1.0	250	17	50.0	1800
C1 <sub>EGR</sub>	20%	2.9	89	8.7	0.5	320
C2 <sub>EGR</sub>	20%	2.9	89	8.7	1.0	480
C3 <sub>EGR</sub>	20%	2.9	89	8.7	2.0	960
C4 <sub>EGR</sub>	20%	2.9	89	8.7	10.0	1800
C5 <sub>EGR</sub>	20%	2.9	89	8.7	50.0	1800
D1 <sub>EGR</sub>	20%	2.9	250	17	0.5	320
D2 <sub>EGR</sub>	20%	2.9	250	17	1.0	480
D3 <sub>EGR</sub>	20%	2.9	250	17	2.0	960
D4 <sub>EGR</sub>	20%	2.9	250	17	10.0	1800
D5 <sub>EGR</sub>	20%	2.9	250	17	50.0	1800

using the generalized flame surface and an iso-surface at  $c^* = 0.8$ . The latter corresponds to the peak of reaction rate of the laminar flame.

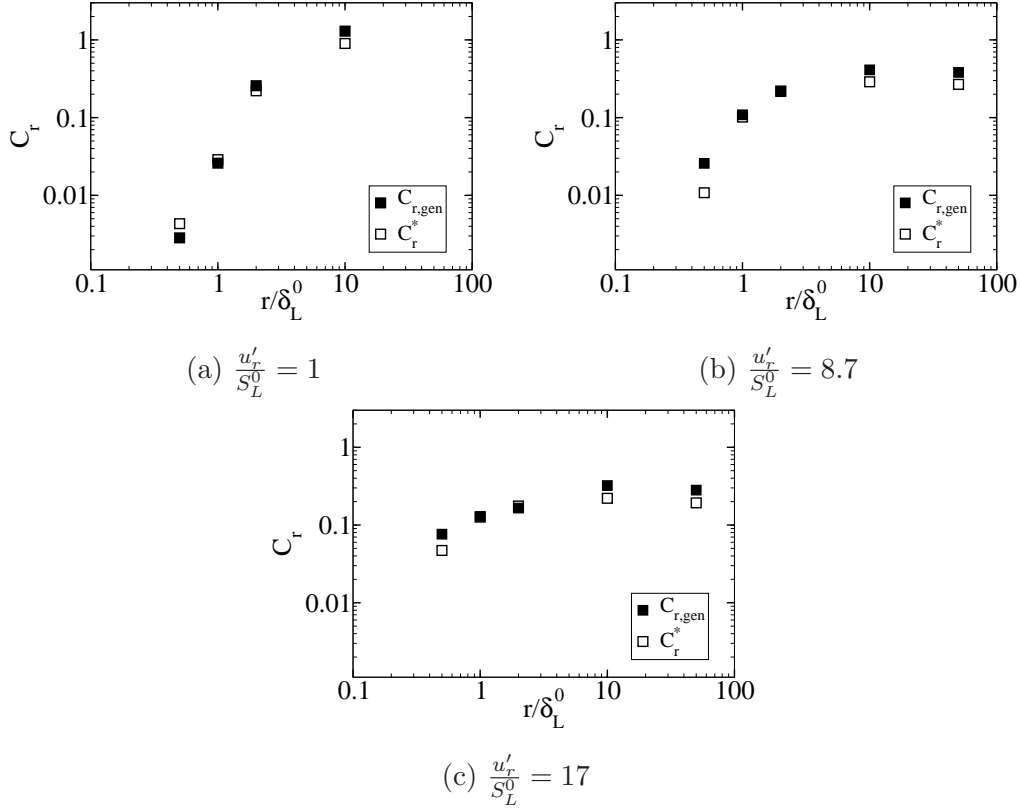


Figure 2.2.1: Comparison of the efficiency functions computed from a stretch rate defined using the generalized flame surface (■) and using an iso-surface at  $c^* = 0.8$  (□), for the velocity ratios: (a)  $u'/S_L^0 = 1$ , (b)  $u'/S_L^0 = 8.7$  and (c)  $u'/S_L^0 = 17$ .

Figure 2.2.1 compares the efficiency  $C_{r,gen}$  computed with a flame stretch rate deduced from the generalized flame surface (in plain symbols) and the efficiency  $C_r^*$  deduced from an iso-surface at  $c^* = 0.8$  (in empty symbols). For each velocity ratio,  $C_{r,gen}$  and  $C_r^*$  present similar evolutions with a growing size ratio  $r/\delta_L^0$ . Nevertheless, the efficiency  $C_r^*$  differs from the generalized definition  $C_{r,gen}$  by 40 to 45% for large vortices ( $r/\delta_L^0 > 2$ ), while for small vortices the two efficiencies are of similar magnitudes.

Thus, for simplicity in post-processing, the definition for the efficiency using the generalized surface is preferred, because both definitions present the same tendency and their magnitudes are similar for small vortices, which correspond to the turbulent scales involved in the TRZ regime investigated in this study. The discrepancies observed for large vortices in Fig. 2.2.1 can be taken into account in engines application by tuning the model constant  $\alpha_{aT}$ .

The first hypothesis commonly made is to compute the flame stretch as the rate of change of the total reaction rate. Thus, from this 2D-DNS the impact of the definition of the flame stretch is studied. The efficiency functions computed from  $(1/\mathcal{A})d\mathcal{A}/dt$  and from  $(1/Q)dQ/dt$  for the three different velocity ratios are compared in Fig. 2.2.2. When the vortices are large ( $r/\delta_L^0 > 2$ ), the two definitions lead to the same  $C_r$ . When the vortices get smaller, a slight

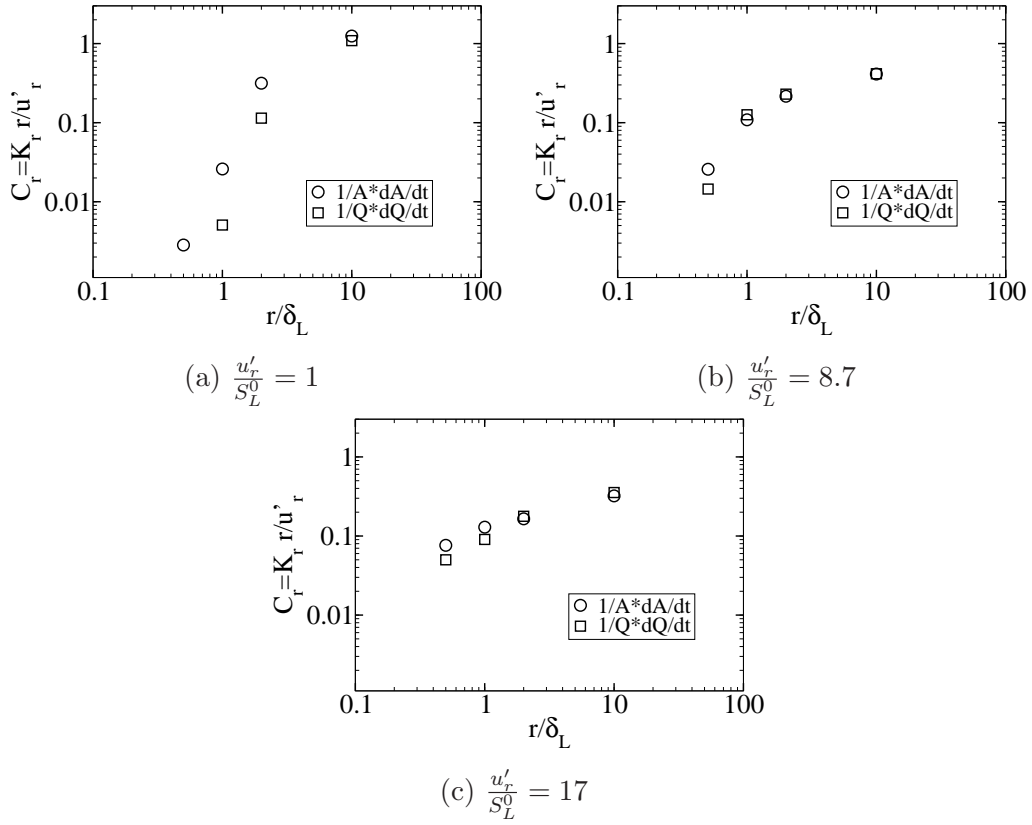


Figure 2.2.2: Comparison of the efficiency functions computed from a stretch defined with  $(1/\mathcal{A})d\mathcal{A}/dt$  and with  $(1/Q)dQ/dt$ , for the velocity ratios: (a)  $u'_r/S_L^0 = 1$ , (b)  $u'_r/S_L^0 = 8.7$  and (c)  $u'_r/S_L^0 = 17$ .

difference appears between  $C_r$  defined with  $(1/\mathcal{A})d\mathcal{A}/dt$  and  $C_r$  defined with  $(1/Q)dQ/dt$  in Figs. 2.2.2b and 2.2.2c. However, for large velocities this difference decreases and becomes negligible for  $r/\delta_L^0 > 1$ , while this gap is more important for  $u'_r/S_L^0 = 1$  in Fig. 2.2.2a. For  $u'_r/S_L^0 = 1$  and  $r/\delta_L^0 \leq 1$ , the estimated efficiency function reaches values smaller than 0.1, which indicates a very weak ability of these vortices to stretch the flame. Indeed, their energy dissipates too quickly to sufficiently stretch the flame and thus to sufficiently disturb the heat release, as shown in Fig. 2.1.5a, leading to insignificant efficiency  $C_r$ . Thus, this case defines a lower boundary for the efficiency function that corresponds to the turbulent scales non-affecting the flame.

The second common assumption, which allows to compute the effective stretch using the theoretical strain and an efficiency function, is investigated. The flame stretch rate is often decomposed into stretch due to curvature and tangential strain rate as:

$$K = \underbrace{\nabla \cdot \mathbf{u} - \mathbf{nn} : \nabla \mathbf{u}}_{a_T} + \underbrace{S_d \nabla \cdot \mathbf{n}}_{\kappa}, \quad (2.2.2)$$

where  $\mathbf{n}$  is the local normal vector to the flame surface oriented toward the fresh gases. The second common approximation made in 2D flame/vortex interactions is to neglect the stretch due to curvature compared to the strain rate, leading to the idea that the stretch is fully

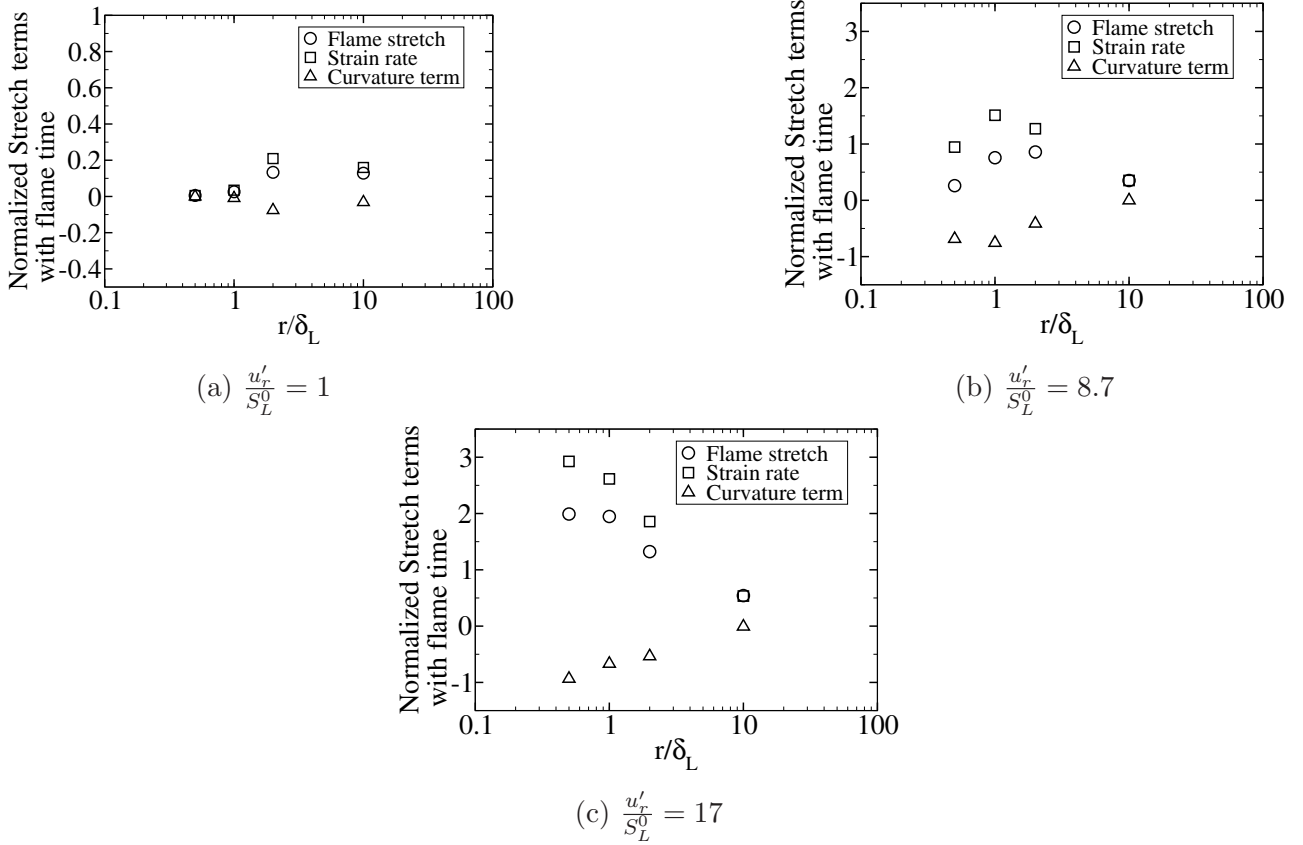


Figure 2.2.3: The balance on the flame stretch terms normalized with the flame time  $\tau_F = \delta_L/S_L^0$ , allowing evaluations of the roles of the strain rate  $\langle a_T \rangle_s$  and the stretch due to curvature  $\langle S_d \kappa \rangle_s$ , for the velocity ratios: (a)  $u'_r/S_L^0 = 1$ , (b)  $u'_r/S_L^0 = 8.7$  and (c)  $u'_r/S_L^0 = 17$ .

determined with the strain rate  $a_T$ :

$$K \approx a_T. \quad (2.2.3)$$

Thus, to verify the validity of this approximation, the balance of the curvature term and the strain rate is shown in Fig. 2.2.3.

The case corresponding to the flamelet regime ( $u'_r/S_L^0 = 1$ ) is presented in Fig. 2.2.3a, where it is observed that  $\langle a_T \rangle_s \approx K_r$ . This is consistent with the assumption that stretch due to curvature weakly affects the production of flame surface in the flamelet regime. Note that the smallest vortices ( $r/\delta_L^0 = 0.5$  and  $r/\delta_L^0 = 1$ ) are not relevant because the flame stretch rate, the strain rate and the curvature are zero. Nonetheless, when high velocities  $u'_r/S_L^0 = 8.7$  and  $u'_r/S_L^0 = 17$  are considered in Figs. 2.2.3b and 2.2.3c, respectively, the effect of stretch due to curvature becomes more significant for the smallest vortices. Indeed, the difference observed between the total stretch and the tangential strain rate increases, when  $r/\delta_L^0$  decreases, up to 50% relative error for  $r/\delta_L^0 < 5$ . This effect is logically reduced when  $r/\delta_L^0$  increases because the curvature reduces with the size of the vortices.

So, this investigation suggests that the large scales of turbulence affect the flame front like in the flamelet regime by enhancing the tangential strain rate, while the small scales affect the strain rate and the curvature simultaneously. The latter might be affected through effects of the small vortices on the displacement speed.

Thus, the efficiency  $C_r$  is computed using the flame stretch  $K_r$  (Eq. 2.1.5) and using the tangential strain rate  $\langle a_T \rangle_s$  (Eq. 2.1.14). A comparison of these two definitions is plotted in Fig. 2.2.4. The efficiency functions computed with  $\langle a_T \rangle_s$  are close to those calculated with

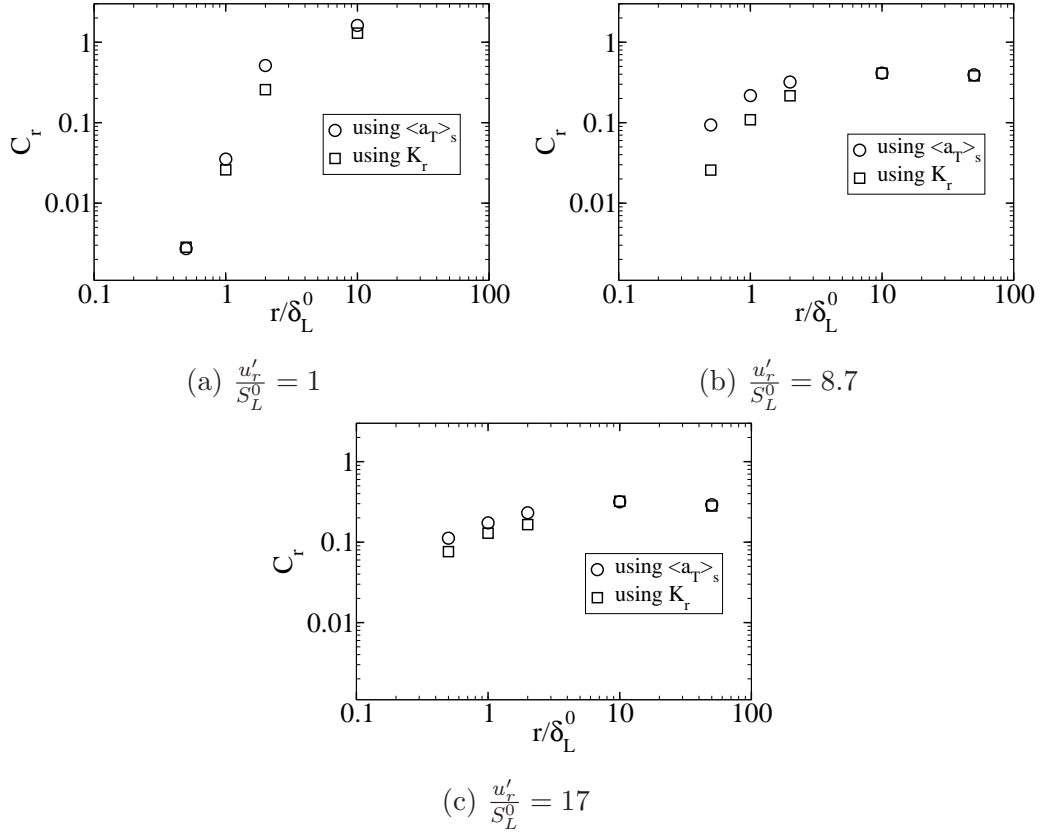


Figure 2.2.4: Comparison of the efficiency functions computed from the stretch  $K_r$  (Eq. 2.1.5) and from the tangential strain rate  $\langle a_T \rangle_s$  (Eq. 2.1.14) for the velocity ratios: (a)  $u'_r/S_L^0 = 1$ , (b)  $u'_r/S_L^0 = 8.7$  and (c)  $u'_r/S_L^0 = 17$ .

$K_r$  for the unit velocity ratio in Fig. 2.2.4a, consistent with the flame stretching balance in Fig. 2.2.3a. As expected from the flame stretching balance for  $u'_r/S_L^0 = 8.7$  and  $u'_r/S_L^0 = 17$  cases, both methods present identical efficiency functions for the largest vortices ( $r/\delta_L \gg 1$ ) in Figs. 2.2.4b and 2.2.4c. Differences by a factor up to 2 are observed for  $r/\delta_L < 5$ , consistent with the analysis of Figs. 2.2.3b and 2.2.3c.

The deviations observed are quantified using Eq.(2.2.4) and are reported in Table 2.3.

$$\varepsilon = \left| \frac{C_r^{a_T} - C_r^K}{C_r^K} \right|. \quad (2.2.4)$$

In Table 2.3, two values are extreme. First, at  $u'_r/S_L^0 = 1$  and  $r/\delta_L = 0.5$ , the deviation is surprisingly low, while at  $u'_r/S_L^0 = 8.7$  and  $r/\delta_L = 0.5$ , the deviation is extremely large. Nevertheless, the efficiencies involved in these two cases are close to zero. The former presents an efficiency of approximately 0.002, and the latter has an efficiency smaller than 0.1, corresponding to the lower boundary defined in the analysis of Fig. 2.2.2. The efficiency functions being close to zero, these discrepancies are not relevant.

Table 2.3: Deviation of the efficiency  $C_r$  for each pair of vortices using  $a_T^r$  instead of  $K_r$ .

$u_r'/S_L^0 \backslash r/\delta_L$	0.5	1.0	2.0	10.0	50.0
1.0	3.9%	36%	100%	25%	
8.7	263%	100%	48%	0.2%	3.2%
17.0	46%	35%	41%	1.5%	3.7%

Finally, this comparison suggests that the efficiency estimated from strain rate only can be sensibly smaller than the one estimated from total stretch. As we want to evaluate the tangential strain rate independently from the stretch due to curvature in the FSD equation, we choose to estimate the efficiency of eddies considering only the tangential strain rate in the rest of this study (Eq. 2.1.14).

## 2.3 Analysis of the efficiency function

In this section, the effect of the Lewis number and of dilution with burnt gases on the efficiency function is first evaluated. Then, the efficiency functions computed from DNS are compared to the current models.

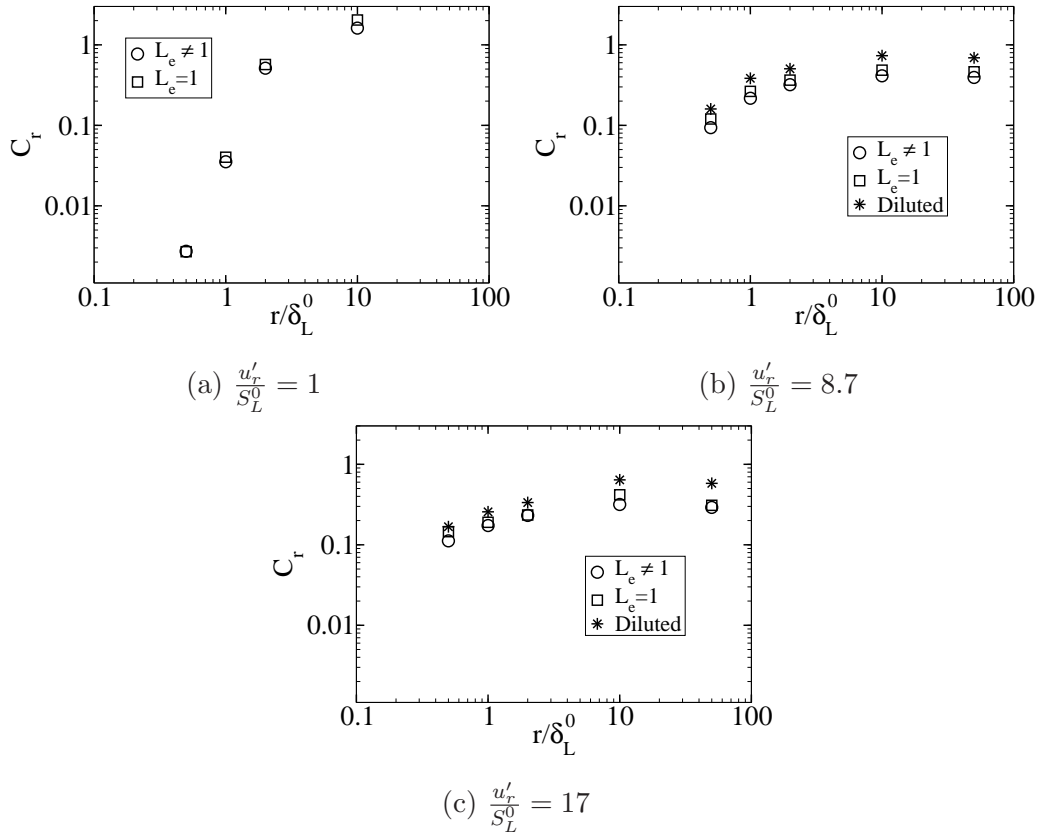


Figure 2.3.1: Comparison of the efficiency functions computed from unity Lewis numbers, non unity Lewis numbers and diluted cases for the following velocity ratios: (a)  $u'/S_L^0 = 1$ , (b)  $u'/S_L^0 = 8.7$  and (c)  $u'/S_L^0 = 17$ .

Figure 2.3.1 compares the efficiency functions computed from non-unity and unity Lewis number simulations and diluted cases. Whatever the velocity ratio, the general behaviour of the efficiency  $\langle a_T \rangle_s r / u'_r$  of  $Le_k \neq 1$ ,  $Le_k = 1$  and diluted flames are similar.

For  $u'_r/S_L^0 = 8.7$  and  $u'_r/S_L^0 = 17.0$  in Figs. 2.3.1b and 2.3.1c, respectively, the efficiencies in  $Le_k \neq 1$  cases are smaller than the ones in  $Le_k = 1$  cases. When  $u'_r/S_L^0 = 8.7$ , the factor between efficiencies in  $Le_k \neq 1$  and  $Le_k = 1$  cases is approximately 0.85, which is close to the factor predicted by Bougrine et al. (2014) defined as:

$$\frac{C_r(Le \neq 1)}{C_r(Le = 1)} = \frac{1}{Le} [1.76 + \tanh(Le - 2)], \quad (2.3.1)$$

where  $Le$  is the Lewis number of the fuel species.

When dilution with  $\text{CO}_2$  and  $\text{H}_2\text{O}$  is applied, the efficiencies  $C_r$  are larger than those of unity Lewis numbers cases by approximately 45% and 20% for  $u'_r/S_L^0 = 8.7$  and  $u'_r/S_L^0 = 17.0$ , respectively. This suggests that a dependence on the EGR rate should be taken into account. This issue was not further explored and should be investigated in future works.

In the rest of this study, the efficiency computed from  $Le_k = 1$  and  $Le_k \neq 1$  cases are analysed to investigate existing efficiency functions and to propose a new formulation of this function. The existing functions investigated are the followings:

- Cant et al. (1991) proposed to modelled the turbulent tangential strain rate, in the context of RANS modelling, as  $\langle a_T \rangle_s \propto C_A / \tau_\eta$ , where  $C_A$  is a constant equals to 0.28 and  $\tau_\eta$  is the eddy turnover time of the Kolmogorov scale. This model is equivalent to Eq. (2.1.1) when the efficiency function  $C_r$  involved in Eq. (2.1.2) is a constant:

$$C_{r,C} \left( \frac{r}{\delta_L^0}, \frac{u'_r}{S_L^0} \right) = 1. \quad (2.3.2)$$

- The model proposed by Charlette et al. (2002a):

$$C_{r,CMV} \left( \frac{r}{\delta_L^0}, \frac{u'_r}{S_L^0} \right) = \frac{1}{4} \left[ 1 + \operatorname{erf} \left( 0.6 \left( \ln \left( \frac{r_c}{\delta_L^0} \right) - \sqrt{\frac{S_L^0}{u_c}} \right) \right) \right] \times \left[ 1 + \operatorname{erf} \left( 3 \log \left( 2 \frac{u_c}{S_L^0} \right) \right) \right]. \quad (2.3.3)$$

- The model proposed by Bougrine et al. (2014):

$$C_{r,B} \left( \frac{r}{\delta_L^0}, \frac{u'_r}{S_L^0} \right) = \frac{1 + \operatorname{erf}[0.9 \ln(\frac{r_c}{\delta_L^0}) - 2]}{1 + 0.3 \frac{u_c}{S_L^0} (1 + \operatorname{erf}[0.9 \ln(\frac{r_c}{\delta_L^0}) - 2])} \left[ \frac{1}{Le} (1.76 + \tanh(Le - 2)) \right]. \quad (2.3.4)$$

The results from the present 2D-DNS are compared to Bougrine's (Eq. 2.3.4), Charlette's (Eq. 2.3.3) and Cant's (Eq. 2.3.2) functions in Fig. 2.3.2. As expected, the model proposed by Cant et al. (1991) overestimates the effect of the small vortices. For large velocity ratios



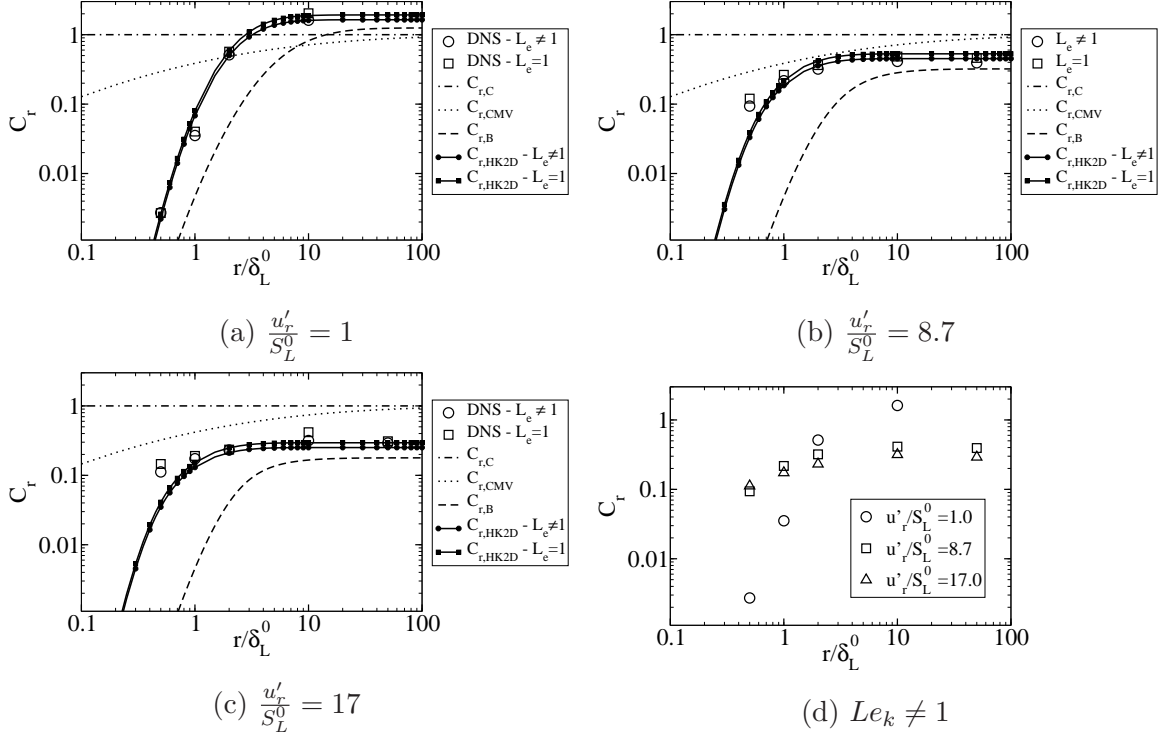


Figure 2.3.2: Evolutions of the efficiency functions with  $r/\delta_L$  from the DNS compared to Cant's model, Bougrine's model (Bougrine et al., 2014), Charlette's model (Charlette et al., 2002a) and the proposed model (Eq. 2.3.5) for the following velocity ratios: (a)  $u'_r/S_L^0 = 1$ , (b)  $u'_r/S_L^0 = 8.7$  and (c)  $u'_r/S_L^0 = 17$ . (d) Comparisons of the efficiencies from the different velocity ratios for  $Le_k \neq 1$  cases.

( $u'_r/S_L^0 = 8.7$  and  $u'_r/S_L^0 = 17$ ), Cant's function overestimates the efficiency function even with bigger scales of turbulence.

Whatever the velocity ratio considered, the functions proposed by Charlette et al. (2002a) and Bougrine et al. (2014) reproduce the decrease in efficiency when  $r/\delta_L^0$  is reduced. However, Charlette's function (Eq. 2.3.3) underestimates this decrease, whereas Bougrine's function (Eq. 2.3.4) overestimates it. Furthermore, only Bougrine's function predicts the decrease of  $C_r$  with  $u'_r$  for the largest vortices, but the predicted reduction is exaggerated. In addition, none of these functions reproduce the increase in efficiency at small scales when  $u'_r/S_L^0$  increases, as shown in Fig. 2.3.2d for  $Le_k \neq 1$  cases.

All these observations are hints on the shape that the efficiency function should have to correctly predict the flame stretch for combustion in the TRZ regime, leading to propose a new efficiency function by combining the functions proposed by Charlette et al. (2002a) and Bougrine et al. (2014) as follows:

$$C_{r,HK2D} \left( \frac{r}{\delta_L^0}, \frac{u'_r}{S_L^0}, Le \right) = C_{r,1} \left( \frac{r}{\delta_L^0}, \frac{u'_r}{S_L^0} \right) \left[ \frac{1}{Le} (1.76 + \tanh(Le - 2)) \right], \quad (2.3.5)$$

with:

$$C_{r,1} \left( \frac{r}{\delta_L^0}, \frac{u_r'}{S_L^0} \right) = \frac{\left[ 1 + \operatorname{erf} \left( a \log \left( \frac{r}{\delta_L^0} \right) - c \sqrt{\frac{S_L^0}{u_r'}} \right) \right]^e}{\left[ 1 + b \frac{u_r'}{S_L^0} \left( 1 + \operatorname{erf} \left( a \log \left( \frac{r}{\delta_L^0} \right) - c \sqrt{\frac{S_L^0}{u_r'}} \right) \right) \right]^d}, \quad (2.3.6)$$

where  $a$ ,  $b$ ,  $c$ ,  $d$  and  $e$  are model parameters. In this study, the model parameters of the new efficiency function are determined using a least square method to best fit the DNS results. The values of these parameters are reported in Table 2.4.

Table 2.4: Fitted parameters of the proposed efficiency function.

$a$	$b$	$c$	$d$	$e$
1.05	0.24	0.91	1.03	1.53

Figure 2.3.2 also shows the efficiencies predicted by the function in Eq. (2.3.5). This function improves the accuracy of the predicted efficiencies compared to the existing functions (Bougrine et al., 2014; Cant et al., 1991; Charlette et al., 2002a), especially for the small vortices. These improvements are illustrated in Fig. 2.3.3, where the predicted tangential strain rate of the different models are plotted against the effective tangential strain rate of the 28 DNS of non-diluted flames reported in Table 2.2. As expected, the proposed correlation fits very well the DNS. So, to quantify the improvements, the global relative error  $\varepsilon_{a_T}$  on the effective tangential strain rate is computed for each model as:

$$\varepsilon_{a_T} = \frac{\sqrt{\sum \left| \langle a_T \rangle_s - \frac{u_r'}{r} C_r \right|^2}}{\sum \langle a_T \rangle_s}, \quad (2.3.7)$$

where  $\langle a_T \rangle_s$  is the tangential strain rate extracted from the DNS and  $C_r$  is the efficiency function. Table 2.5, reporting the global relative errors of the models investigated, confirms the observations made with Figs. 2.3.2 and 2.3.3. The new function proposed in Eq. (2.3.5) reduces by a factor 7 the error induced by Charlette's function (Charlette et al., 2002a) and by 4 the error induced by the function of Bougrine et al. (2014).

Table 2.5: Mean error on the effective tangential strain rate (Eq. 2.3.7) for the 28 non-diluted flames of Table 2.2.

Efficiency function	Relative error $\varepsilon_{a_T}$
Cant et al. (1991)	116.9%
Charlette et al. (2002a)	39.2%
Bougrine et al. (2014)	24.5%
Present function (Eq. 2.3.5)	5.7%

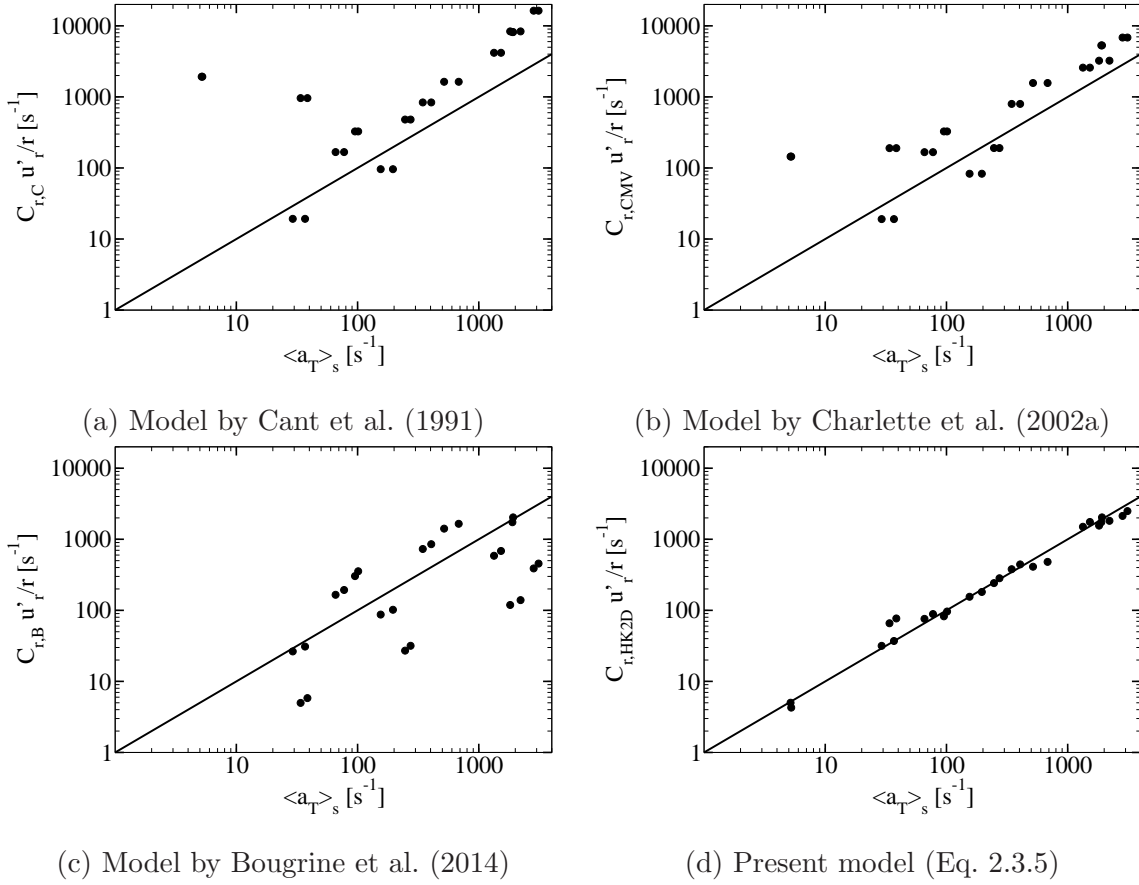


Figure 2.3.3: Comparisons between effective tangential strain rate from DNS ( $\langle a_T \rangle_s$ ) from the 28 non-diluted flames of Table 2.2 and from several  $C_r$  functions following Eq. (2.1.14): (a) Cant et al. (1991), (b) Charlette et al. (2002a), (c) Bougrine et al. (2014) and (d) Present work (Eq. 2.3.5).

## 2.4 Conclusions

In this chapter, a set of two-dimensional direct numerical simulations of flame-vortex interactions was conducted in order to evaluate a model for the flame stretch in the thin reaction zone regime. The vortices size range computed in this study was extended to small scales compared to previous studies (Bougrine et al., 2014; Charlette et al., 2002a; Meneveau and Poinso, 1991), in order to compute conditions close to the TRZ regime. The analysis of the set of DNS was dedicated to re-investigate the assumptions commonly made in the previous studies in order to highlight what could have lead to the inability of the current models to predict the flame stretch in the TRZ regime. Despite a stretch defined with the rate of change of the total reaction rate (instead of the rate of change of the flame surface), the strongest approximation is to neglect the effect of curvature on the flame stretch.

Three set of DNS are performed in order to evaluate the effect of differential diffusion on the tangential strain rate. The comparison between non-unity and unity Lewis numbers cases shows that the factor introduced by Bougrine et al. (2014) well captures the impact of differential diffusion on the tangential strain rate.

Then, the resulting efficiency functions from the DNS were compared to the existing func-

tions in order to highlight the differences for the small vortices. From these results, a new efficiency function fitted on the set of DNS with  $Le_k \neq 1$  is defined and presents results close to Bougrine's function.

Nevertheless, even if some drawbacks in the tangential strain rate estimation from flame/vortex interactions were corrected, other assumptions have not been investigated, like the 2D configuration and the transient interaction with a single pair of vortices. Thus, the efficiency function deduced from this analysis might be insufficient to predict the tangential strain rate of a flame interacting with a fully developed turbulent field, especially in 3D. Consequently, the behaviour of this model for the tangential strain rate is evaluated using 3D-DNS of quasi-stationary turbulent flames in Chapter 4.



# Chapter 3

## Analysis of 3D direct numerical simulations of premixed flames interacting with turbulence

Three-dimensional direct numerical simulations (DNS) of statistically stationary turbulent premixed flames are performed to further explore the impact of turbulence on the flame front, especially on the source terms involved in the coherent flame model (CFM). Most of the fuels that were considered in the previous studies were hydrogen, methane and propane, while only a few works focused on representative fuels of gasoline as n-heptane (Lapointe et al., 2015; Savard and Blanquart, 2015; Savard et al., 2015). In this study the fuel considered is iso-octane,  $C_8H_{18}$ .

In this chapter, the set-up for 3D-DNS is first described in Section 3.1. Then, the 3D-DNS are analysed in Section 3.2 to define an approach for modelling the premixed flame in the thin reaction zone (TRZ) regime. The response of the displacement speed to turbulence is analysed on a specific iso-surface of the progress variable in Section 3.3, allowing to propose an adequate *a priori* model.

### 3.1 Direct numerical implementation

The aim of the 3D DNS conducted in this work is to investigate the characteristics of a premixed flame interacting with a turbulent flow in the TRZ regime. Three kinds of simulations were conducted to take into account differential diffusion effects, as suggested in (Lapointe et al., 2015; Savard and Blanquart, 2015; Savard et al., 2015), and dilution effects:

1. simulations with unity Lewis numbers for all species,
2. simulations with non unity Lewis numbers for all species,
3. a simulation with dilution of the fresh gases by burnt gases, to verify that the increase of the Karlovitz number induced by dilution is sufficient to explain the impacts of EGR dilution on the flame front.

For this study, the DNS computations were conducted using the AVBP code (Moureau et al., 2005), which was recently used for DNS by Tagliante et al. (2019). It solves the three-dimensional compressible Navier-Stokes equations on unstructured and hybrid grids. The AVBP numerical schemes are based on the cell-vertex method. Two convective schemes are available :

1. a finite-volume Lax-Wendroff type scheme (LW), which is 2<sup>nd</sup> order in time and space,
2. a two-steps Taylor-Galerkin type scheme (TTGC) (Colin and Rudgyard, 2000), which is 3<sup>rd</sup> order in time and space.

A comparison of the two schemes is given in Appendix A to evaluate the benefit of one over the other by conducting twice the same set-up. LW-scheme is preferred to TTGC-scheme for the purpose of computational economy for all the present study.

The flow configuration is first introduced with a description of the chemistry followed by the presentation of the turbulence forcing method. Finally, the different cases simulated and analysed in this chapter are described.

### 3.1.1 Flow configuration and chemistry

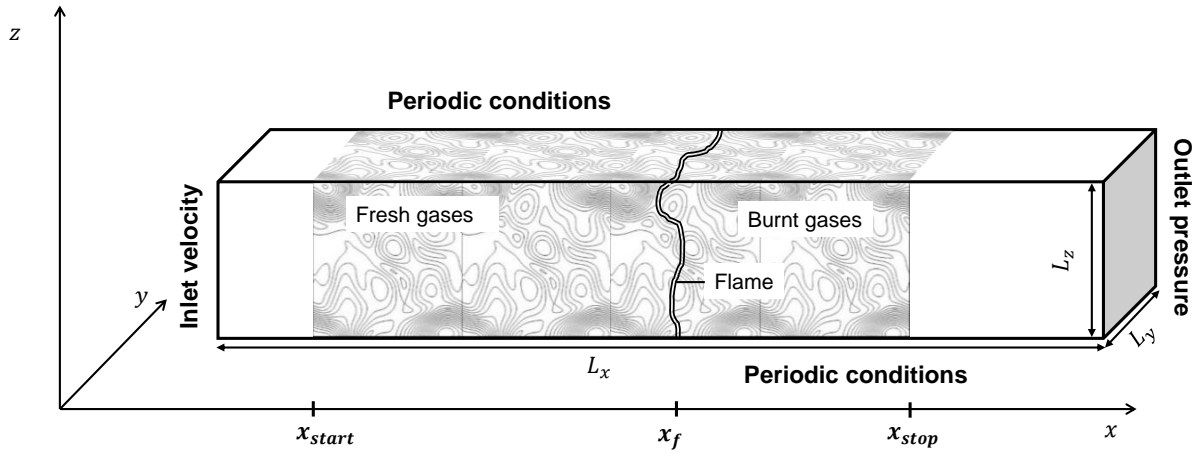


Figure 3.1.1: Schematic view of the flow configuration of the DNS with turbulence forced in a defined volume including fresh and burnt gases. The turbulence is forced between  $x_{start}$  and  $x_{stop}$ . The domain width is  $L_y = L_z = L$  and the domain length is  $L_x = 6L$ . The position of the flame front on this view is given by  $x_f$ .

Figure 3.1.1 presents a schematic view of the computational domain, which is similar to that of numerous studies (Aspden et al., 2011a,b, 2015, 2016, 2017, 2019; Savard and Blanquart, 2014, 2015, 2017). A statistically-flat flame interacting with a turbulent field is chosen, using a turbulence forcing method described later (Section 3.2). In this configuration the inlet and outlet boundaries are specified in the direction of the mean flame propagation. The transverse boundaries are considered to be periodic. The outflow boundary is taken to be partially non-reflecting and specified according to the Navier-Stokes Characteristic Boundary Conditions

(NSCBC) technique (Poinsot and Lele, 1992). For each simulation, the inflow velocity  $U_{in}$  is constant throughout the simulation and selected to match the turbulent flame speed  $S_T$ , defined as:

$$S_T = \frac{1}{\rho_u \mathcal{A}_0} \int_V \dot{\omega}_c dV, \quad (3.1.1)$$

where  $\dot{\omega}_c = \dot{\omega}'_T / (C_p(T_b - T_u))$  is the chemical source term with  $\dot{\omega}'_T$  the heat release rate,  $\rho_u$  the density of the fresh gases and  $\mathcal{A}_0$  the laminar flame surface corresponding to the y-z cross section of surface  $L^2$  in Fig. 3.1.1.  $L_y = L_z = L$  is the domain width. In practice, the flame drifts slightly, but the velocity of the drift  $U_{in} - S_T$  is small and constant in average. This allows to compute the flame statistics considering at each instant  $t$  the space origin as  $x_0(t) = x_0(t=0) + (U_{in} - S_T)t$ .

The domain width is chosen as  $L \approx 15\delta_L^0$ , where  $\delta_L^0 = (T_b - T_u) / \max(|\nabla T|)$  is the thermal flame thickness with  $T_u$  and  $T_b$  the temperature in the fresh and burnt gases, respectively. The cell size  $\Delta_x$  used is chosen for each simulation as the minimum length allowing to get at least 20 grid points within the thermal thickness and to get at least a length scale ratio  $\eta_k / \Delta_x \geq 0.5$  (where  $\eta_k$  is the Kolmogorov length scale).

The iso-octane/air kinetics are described by a two-step Arrhenius mechanism with 6 species:



This scheme was developed for piston engine simulations and validated using both the laminar flame speed  $S_L^0$  and the laminar flame thickness  $\delta_L^0$  for the following conditions: 323 K, a constant pressure of 1 atm and an equivalence ratio ranging between 0.5 and 1.2 (Bonhomme et al., 2013). The forward reaction rates  $k_{f1}$  and  $k_{f2}$  for  $\text{C}_8\text{H}_{18}$  oxidation and for  $\text{CO}-\text{CO}_2$  equilibrium, respectively, are expressed below.

$$k_{f1} = A_1 T^{b_1} e^{-\frac{E_{a,1}}{RT}} [\text{C}_8\text{H}_{18}]^{n_{\text{C}_8\text{H}_{18}}} [\text{O}_2]^{n_{\text{O}_2,1}}, \quad (3.1.4)$$

$$k_{f2} = A_2 T^{b_2} e^{-\frac{E_{a,2}}{RT}} [\text{CO}]^{n_{\text{CO}}} [\text{O}_2]^{n_{\text{O}_2,2}}. \quad (3.1.5)$$

$A_i$  is the pre-exponential factor,  $b_i$  is the temperature exponent,  $E_{a,i}$  is the activation energy of reaction  $i$ , and  $n_{k,i}$  are the reaction exponents for species  $k$  in reaction  $i$  (Table 3.1).  $R$  is the ideal gas constant equal to  $8.314 \text{ J.K}^{-1}.\text{mol}^{-1}$ . The viscosity  $\mu$  follows a power law defined as:

$$\mu = \mu_{ref} \left( \frac{T}{T_{ref}} \right)^b, \quad (3.1.6)$$

where  $\mu_{ref} = 7.17 \cdot 10^{-5} \text{ kg.m}^{-1}.\text{s}^{-1}$  is the viscosity of the unburnt gases at the reference temperature  $T_{ref} = 2240 \text{ K}$ , and  $b = 0.66$ .

Using a simplified mechanism with only few species might alter the effect of differential diffusion. For this reason, the influence of the chemical mechanism was investigated by performing a simulation of case C (see Section 3.1.3 for cases description) with an analytically



Table 3.1: Arrhenius parameters for the  $C_8H_{18}$  2-step mechanism.

Case	$Le_{Fuel}$	reaction	$A_i$	$b_i$	$E_{a,i}$ [cal/mol]	$n_k$
$Le_k \neq 1$	2.9	$C_8H_{18}$ oxidation	$5.443 \cdot 10^{12}$	0.1	$3.6 \cdot 10^4$	$n_{C_8H_{18}} = 1.1$
		$CO - CO_2$ equilibrium	$2.0 \cdot 10^9$	0	$1.4 \cdot 10^4$	$n_{O_2,1} = 0.54$
						$n_{CO} = 1.0$
						$n_{O_2,2} = 0.5$
$Le_k = 1$	1.0	$C_8H_{18}$ oxidation	$9.150 \cdot 10^{12}$	0.1	$3.6 \cdot 10^4$	$n_{C_8H_{18}} = 1.1$
		$CO - CO_2$ equilibrium	$3.327 \cdot 10^9$	0	$1.4 \cdot 10^4$	$n_{O_2,1} = 0.54$
						$n_{CO} = 1.0$
						$n_{O_2,2} = 0.5$

reduced chemistry (ARC) mechanism (Felden et al., 2018, 2019). From a reduced synthetic paraffinic kerosene (SPK) mechanism (48 species and 416 reactions) offering the possibility to model lean premixed combustion of air and iso-octane, a reduction procedure was applied using the Yark tool (Pepiot-Desjardins and Pitsch, 2008) which includes skeletal reductions and quasi-steady state (QSS) approximations. The final mechanism, called ISOOCT18, contains 18 transported species and 13 QSS species, which are reported in Table 3.2. It has been validated for the following conditions: initial temperature of 300-450 K, equivalent ratios of 0.7-1.0 and a constant pressure of 1 atm (Lapeyre et al., 2016) .

Table 3.2: ISOOCT18 scheme: 18 transported species, and 13 as QSS species to compute source terms.

Transported			QSS	
$N_2$	$H_2O_2$	$iC_8H_{18}$	$HO_2$	$CH_2CHO$
$O$	$C_2H_6$	$CH_4$	$CH_2$	$C_2H_5$
$H$	$CO$	$C_2H_2$	$CH_3$	$C_3H_5$
$OH$	$C_3H_6$	$C_2H_4$	$HCO$	$iC_4H_7$
$H_2$	$CH_2O$		$HCCO$	$tC_4H_9$
$H_2O$	$iC_4H_8$		$C_2H_3$	$iC_8H_{17}$
$O_2$	$CO_2$		$C_3H_4$	

For the whole study, a stoichiometric ( $\Phi = 1$ )  $C_8H_{18}$ /air mixture is considered, at a temperature  $T_u = 300$  K and a pressure  $P_u = 1$  atm, leading to a laminar flame speed  $S_L^0 = 0.366$  m/s and a flame thickness  $\delta_L^0 = 385$   $\mu m$ .

The effect of preferential diffusion in the TRZ regime is investigated conducting the simulations twice for each turbulence level, as proposed by Lapointe et al. (2015); Savard and Blanquart (2014, 2015, 2017) and Savard et al. (2015): once considering differential diffusion with non-unity Lewis numbers ( $Le_k \neq 1$ ) and once with the Lewis number for all the species set to unity ( $Le_k = 1$ ). The Lewis number  $Le_k$  of each species  $k$  is defined as:

$$Le_k = \frac{S_{ck}}{P_r}, \quad (3.1.7)$$

where  $P_r$  and  $S_{ck}$  are the Prandtl number and the Schmidt number of the species  $k$ , respectively. The former is equal to 0.69 in this study and the Schmidt numbers are reported in Table 3.3.

Table 3.3: Schmidt number of each species of the two-step mechanism for  $Le_k \neq 1$  and  $Le_k = 1$  cases. The Prandtl number is  $P_r = 0.69$ .

Species	$Le_k \neq 1$	$Le_k = 1$
$C_8H_{18}$	2.0167	0.69
$O_2$	0.7343	0.69
$N_2$	0.6950	0.69
$CO_2$	0.9461	0.69
$H_2O$	0.5432	0.69
$CO$	0.7444	0.69

The Arrhenius coefficients of the 2-step mechanism were adapted for the  $Le_k = 1$  case as shown in Table 3.1, in order to get the same laminar flame speed and thickness for both cases.

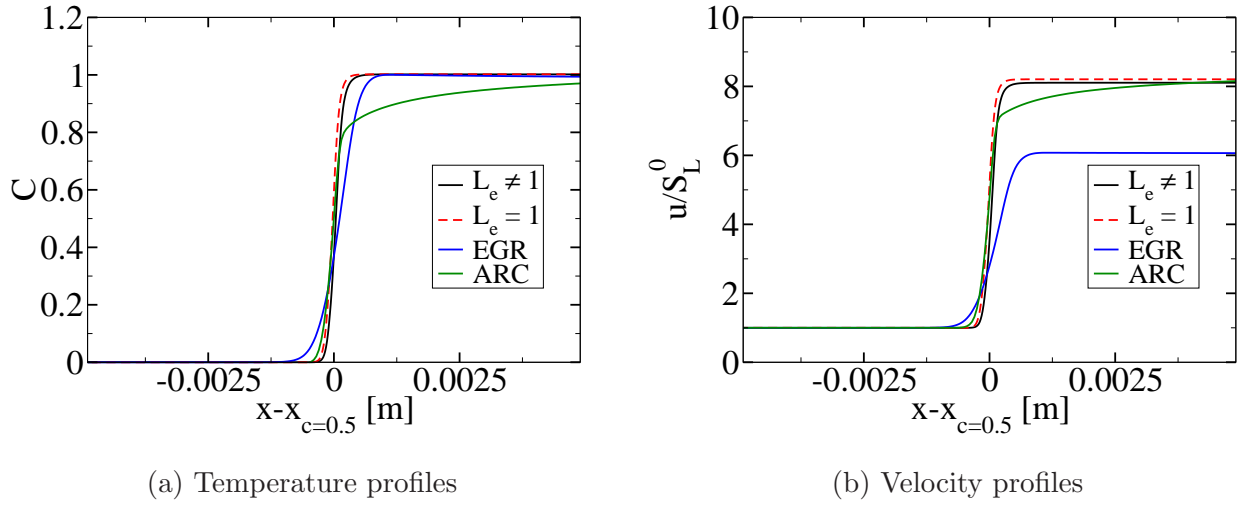


Figure 3.1.2: Comparisons of the one dimensional laminar flames spatial profiles of (a) progress variable and (b) velocity centred on  $c = 0.5$ .

Figure 3.1.2 shows the progress variable based on the temperature, Eq. (1.1.12a), and velocity profiles along the  $x$ -axis of 1D laminar flames using non-unity Lewis numbers in black solid line, unity Lewis numbers in red dashed line with the respective Arrhenius coefficient given in Table 3.1, and the ARC mechanism in green solid line. Both the progress variable and the velocity profiles of non unity Lewis and unity Lewis cases are superimposed indicating that both the laminar flame speed and the laminar flame thickness are similar (as seen in Table 3.4) whether differential diffusion is deactivated or not.

Figure 3.1.2a illustrates the impact of the ARC mechanism. ARC case presents a progress variable profile much smoother in the burnt gases side than with the 2-step mechanism. This difference is also observed on the velocity profile in Fig. 3.1.2b. However, the heat release is weakly impacted by the mechanism because  $u_b^{2step} \approx u_b^{ARC}$ , where  $u_b^{2step}$  and  $u_b^{ARC}$  are the flow velocities in the burnt gases of the cases using the 2-step and the ARC mechanisms, respectively. Thus, it is expected that the two mechanisms will present similar results. Note, the laminar flame velocity of the ARC mechanism reported in Table 3.4 is close to  $S_L^0$  computed with the 2-step mechanism.

As already mentioned, a flame diluted with burned gases is also simulated. The chemistry

use in this case is the 2-step mechanism with non-unity Lewis numbers. A 20% dilution mass ratio is carried out with a mixture of  $\text{CO}_2$  and  $\text{H}_2\text{O}$ . The progress variable and velocity profiles of this case are displayed with blue lines in Fig. 3.1.2. When the flame is diluted with burned gases (with a 20% EGR rate), the flame appears slightly thickened on the progress variable profiles in Fig. 3.1.2a, confirmed in Table 3.4. The main impact is observed on the velocity profiles, where  $u_b/S_L^0$  is approximately 6 with dilution, while this ratio is about 8 for non-diluted case. This illustrates the impact of dilution on the heat release through the heat release factor  $\tau = u_b/u_u - 1$ , where  $u_b$  and  $u_u$  are the flow velocities in the burnt and the fresh gases, respectively. Note that the laminar flame speed, reported in Table 3.4, is significantly reduced with dilution, and the diluted thermal laminar flame thickness is approximately twice the non-diluted  $\delta_L^0$ .

Table 3.4: Laminar flame velocity  $S_L^0 = -(1/\rho_u Y_F^u) \int_{-\infty}^{+\infty} \dot{\omega}_F dx$ , where  $\dot{\omega}_F$ ,  $\rho_u$  and  $Y_F^u$  are the local fuel reaction rate, the density and the fuel mass fraction in the fresh gases, respectively, and thermal diluted laminar flame thickness  $\delta_L^0 = (T_b - T_u)/\max(|\nabla T|)$  for the different flames simulated.

		2-step mechanism		ARC mechanism
	$Le_k \neq 1$	$Le_k = 1$	EGR rate = 20%	
$S_L^0$ [m/s <sup>-1</sup> ]	0.366	0.37	0.15	0.36
$\delta_L^0$ [ $\mu\text{m}$ ]	385	385	791	560

### 3.1.2 Turbulence forcing method

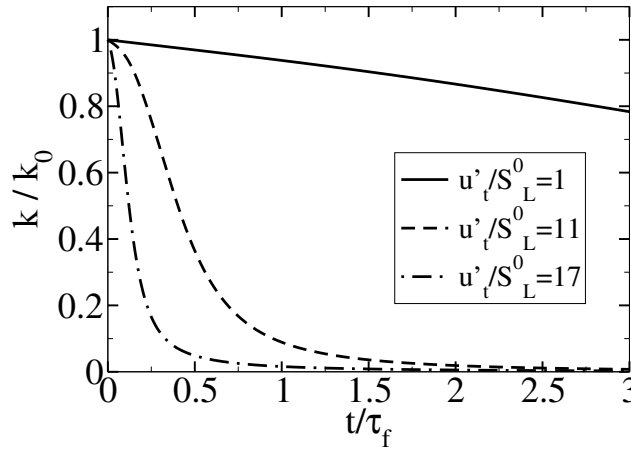


Figure 3.1.3: The temporal evolution of the turbulent kinetic energy  $k$  normalized by its initial value  $k_0$  for three different turbulent intensities. Two of these cases correspond to turbulent flows encountered in the TRZ regime. The time in x-axis is normalized with the characterized time of the flame  $\tau_f = \delta_L^0/S_L^0$ .

In numerical simulations with an initial homogeneous isotropic turbulence (HIT), the decay of the turbulent kinetic energy (TKE),  $k$ , in the absence of velocity field forcing can be estimated from theory considering  $dk/dt = -k/\tau_t$ , with  $\tau_t$  the eddy turnover time ( $\tau_t = l_t/u'_t$  with  $u'_t$  the

characteristic velocity of the integral scale and  $l_t$  the integral length scale of turbulence). The temporal evolutions of TKE in decaying HIT is plotted in Fig. 3.1.3 for three levels of turbulence intensity. The more intense is the turbulence, the faster the decay occurs. Indeed, TKE reaches zero after a significantly large time compared to the characteristic flame time  $\tau_f = S_L^0/\delta_L^0$  for a turbulence intensity of  $u_t'/S_L^0 = 1$ . While for turbulent intensities of  $u_t'/S_L^0 = 11$  and  $u_t'/S_L^0 = 17$ , corresponding to flames in the TRZ regime, TKE reaches zero after one  $\tau_f$  for the former and even less for the latter. As a consequence, a decaying turbulence set-up would not allow the flame to adapt to turbulence, therefore leading to unrealistic statistics.

To overcome this issue, different methods exist, reported by Klein et al. (2017):

- The use of a turbulent inflow condition in order to maintain the desired turbulence level in the computational domain. With this method the temporal decay of the decaying HIT is replaced by a spatial decay. This gives rise to new complications such as Landau-Darrieus or Rayleigh-Taylor instabilities. Moreover, planar flames with a turbulent inflow conditions are rather unsteady. In practice, to overcome this issue a control loop must be implemented to adjust the inflow velocity.
- The use of volume forcing within the whole computational domain, as illustrated in Fig. 3.1.1, in order to ensure a constant turbulence level. In previous works, many methods were used (from linear forcing method (Savard and Blanquart, 2014, 2015, 2017) to spectral forcing techniques (Aspden et al., 2011a,b, 2015, 2016, 2017, 2019)).

In this study, a spectral forcing method proposed by Eswaran and Pope (1988) is used to offset the decay of TKE and maintain the turbulence characteristics. This method generates a stochastic time-evolving forcing vector  $\mathbf{f}$ . This vector is used as a source term in the momentum conservation equation of the Navier-Stokes equations, as  $\rho\mathbf{f}$ . This stochastic forcing term introduces energy in the largest scales of the domain. A turbulent energy spectrum is established, with the largest scales cascading toward smaller scales and these being dissipated by viscosity. When the rate of energy introduced by the forcing technique equals the rate of dissipation, a statistically steady state is reached. However, this forcing term introduces some heating by viscous dissipation of the turbulent kinetic energy, which should be avoided. For this purpose a new energy source term is defined, according to the study of Paoli and Shariff (2009), with :

$$S_e = \rho\mathbf{f} \cdot \mathbf{u} - \langle \rho\mathbf{f} \cdot \mathbf{u} \rangle, \quad (3.1.8)$$

where  $\langle \rangle$  is the averaging operator over the whole domain and  $S_e$  is the energy source term due to the forcing method.

In practice, Eswaran and Pope (1988) added a forcing acceleration in the momentum conservation equation of the Navier-Stokes equations in wavenumber space. According to them, the dissipation rate  $\varepsilon$  can be estimated from forcing parameters as:

$$\varepsilon = \frac{4\tau_g\sigma_g^2 N_g}{1 + \tau_g(k_0^2\varepsilon)^{1/3}}, \quad (3.1.9)$$

where  $\sigma_g$  and  $\tau_g$  are a characteristic forcing acceleration and a characteristic forcing time, respectively. The latter controlled the time to reach a statistically steady state. Moreover, this method requires two other parameters: the size of the computational domain  $L$ , such that  $2\pi/L$  is the first forced wave number, and the number of forced modes  $N_g$ , which has been set to 92 from the work of Paoli and Shariff (2009).

With the forcing method used, HIT is imposed in the volume defined in Fig. 3.1.1 where the flame is contained. It can be argued that this forcing term being artificial and imposed at the flame location, this approach might lead to erroneous flame statistics. For this purpose, additional simulations were performed conditioning the forcing source term with the progress variable, as suggested by Klein et al. (2017). These cases are analysed in Appendix B.

### 3.1.3 Simulation parameters

Four cases A, B, C and D are investigated with increasing Karlovitz number while keeping a nearly constant integral length scale. This point is important as it means that the flame will see the same largest scales, while the Kolmogorov scale decreases from A to D, therefore increasing both the range of scales interacting with the flame structure and their intensities. This way, the evolution of flame statistics with increasing turbulence intensity can be unambiguously attributed to small scales influence.

The Karlovitz number, defined as  $Ka = (\delta_L^0/l_t)^{1/2}(S_L^0/u_t')^{-3/2}$ , varies from 2.9 to 46.2 as seen in Table 3.5. Case A is expected to be representative of the upper part of the flamelet regime. Cases B, C and D were selected to fall inside the TRZ regime. These cases are performed with differential diffusion ( $Le_k \neq 1$ ) and the 2-step chemistry presented in previous section. As seen in Table 3.5, the turbulence intensity and integral length scale slightly differ between unity and non-unity Lewis number cases, which is attributed to the modified species diffusivities leading to the need to adjust the forcing parameters. However, these adjustments were not conducted in this study, and the exact same forcing parameters were used for non-unity and unity Lewis numbers cases.

Case C-ARC is identical to case C but performed with the ARC mechanism in place of the simplified 2-step mechanism in order to evaluate the importance of the chemistry description on flame statistics. Case C-EGR is performed using turbulence forcing parameters allowing the same Karlovitz number as case C, but with a diluted mixture. Dilution is made with burned products composed of  $H_2O$  and  $CO_2$  at  $T = T_u$ .

All these cases are displayed in the Peters-Borghi diagram in Fig. 3.1.4 and their numerical parameters are reported in Table 3.5.

Table 3.5: The DNS set-up for the simulations of the interaction between a planar flame and forced homogeneous isotropic turbulence. The Karlovitz number  $Ka$  and the Damköhler number  $Da$  are defined with Eqs. (1.3.11) and (1.3.10), respectively. The laminar flame thickness used to evaluate these numbers is the thermal laminar flame thickness  $\delta_L^0 = (T_b - T_u)/\max(|\nabla T|)$ .  $N_{cell}$  is the number of cells in the mesh used for simulating the flames.

Case	$l_t/\delta_L$	$u'/S_L^0$	$Ka$	$Da$	$Re_t$	$Le_{Fuel}$	$\delta_L^0/\Delta_x$	$\eta_k/\Delta_x$	$N_{cell}$
A	3.3	3.0	2.9	9.9	89.6	2.9	20	1.7	$83e^6$
B	4.4	8.2	11.2	4.8	325.0	2.9	20	0.9	$83e^6$
C	4.3	12.5	21.4	3.1	489.0	2.9	20	0.6	$83e^6$
D	4.4	21.1	46.2	1.9	833.2	2.9	31	0.7	$254e^6$
C-EGR	4.1	14.5	27.1	2.2	452.5	2.9	21	0.6	$83e^6$
A <sub>1</sub>	5.1	2.5	1.7	18.7	74.8	1.0	20	2.0	$83e^6$
C <sub>1</sub>	4.9	11.9	18.5	3.7	530.7	1.0	20	0.7	$83e^6$
D <sub>1</sub>	5.1	22.1	46.2	2.1	1016.1	1.0	31	0.7	$254e^6$
C-ARC	4.3	12.5	21.4	3.1	489.0	2.9	20	0.6	$83e^6$

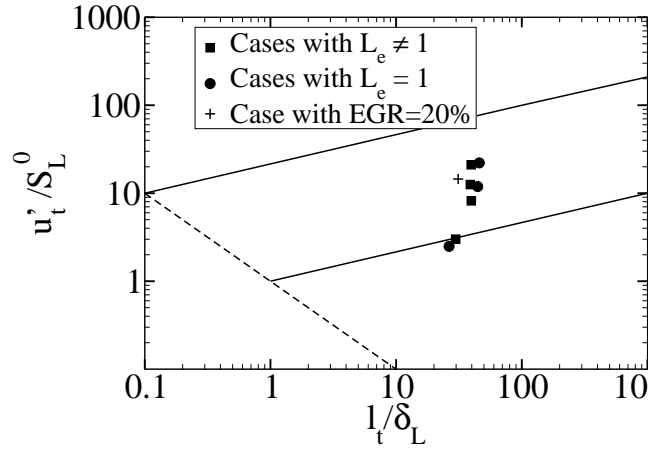


Figure 3.1.4: Direct Numerical Simulations of High Karlovitz turbulent premixed flame.

### 3.1.4 Post-processing methods

In this study, results from 3D DNS simulations of interactions between premixed flames and turbulence are post-processed using two approaches :

1. The **generalized** approach consists in computing the quantity of interest through the whole flame, which means considering all the values of the progress variable. For some variables the surface average is computed as:

$$\langle Q \rangle_s(t) = \frac{\int_{\mathcal{V}} Q(t, \mathbf{x}) |\nabla c(t, \mathbf{x})| dV}{\mathcal{A}_T(t)}, \quad (3.1.10)$$

where  $Q$  is a quantity of interest,  $\mathcal{A}_T(t) = \int_{\mathcal{V}} |\nabla c(t, \mathbf{x})| dV$  is the generalized flame surface,  $\mathcal{V}$  is the simulation domain,  $t$  is the time and  $\mathbf{x}$  is the position vector.

2. The **iso-surface** approach consists in extracting a specified iso-surface of progress variable  $c^*$ , and then computing the surface average of the variables of interest on this iso-surface

following:

$$\langle Q \rangle_s^*(t) = \frac{\int_V Q(t, \mathbf{x}) |\nabla c(t, \mathbf{x})| \delta(c(t, \mathbf{x}) - c^*) dV}{\mathcal{A}_T^*(t)}, \quad (3.1.11)$$

where  $Q$  is a quantity of interest,  $\mathcal{A}_T^*(t) = \int_V |\nabla c(t, \mathbf{x})| \delta(c(t, \mathbf{x}) - c^*) dV$  is the area of the iso-surface at  $c^*$  and  $\delta(c)$  is the Dirac function.

Finally, in both approaches the different surface averaging operations are then temporally averaged as:

$$\overline{\langle Q \rangle} = \frac{\sum \langle Q \rangle(t) \mathcal{A}(t)}{\overline{\mathcal{A}}}, \quad (3.1.12)$$

where  $\langle Q \rangle$  is either the instantaneous generalized surface averaged quantity of interest (Eq. 3.1.10) or the instantaneous  $c^*$  iso-surface averaged quantity of interest (Eq. 3.1.11) depending on the approach chosen. Similarly,  $\mathcal{A}(t)$  is either the instantaneous generalized flame surface or the instantaneous area of the  $c^*$  iso-surface, and  $\overline{\mathcal{A}}$  is the time averaged flame surface (either generalized flame surface or  $c^*$  iso-surface) defined as:

$$\overline{\mathcal{A}} = \frac{\sum \mathcal{A}(t)}{N_t}, \quad (3.1.13)$$

where  $N_t$  is the number of instantaneous solutions. Note that for reasons of simplicity, the notation used in Eq. (3.1.12) is not retained in the rest of this study. The various results presented in the following sections are therefore time averages according to Eq. (3.1.12).

The DNS reported in Table 3.5 present a transient phase and a quasi-steady phase, as illustrated with the evolution of the generalized flame surface in Fig. 3.2.2. Thus, the flames simulated are temporally averaged over their steady-state period, which is defined as the period over which the mean and variance of the signal are time-invariant, corresponding to the phase where the fluctuations of the TKE become constant. It is noteworthy that the levels of fluctuation of TKE depend strongly on the turbulence intensity. Indeed, the levels of TKE fluctuations of cases with low Karlovitz number ( $A$  and  $A_1$ ) are higher than the others because the levels of dissipation rate  $\varepsilon$  are very low, causing difficulty to stabilize with the forcing method used. Statistics are computed after the transient phase using at least 15 eddy turnover times  $\tau_t = l_t/u'_t$ , to get sufficient convergence. The physical time needed to reach convergence  $\tau_{conv}$  and the physical time needed to compute statistics  $\tau_{stat}$  are reported in Table 3.6 with the CPU time  $\tau_{tot}$  for each simulations.

## 3.2 Flame surface analysis: which approach for modelling ?

This section presents the results obtained from the 3D-DNS, and is organized as follows. First, instantaneous slices of the flames are described. Second, the general flame properties are presented. Third, the effect of the high turbulence intensity is highlighted through a bending



Table 3.6: Characteristic times for each simulations.

Case	$Ka$	$\tau_{conv}/\tau_f$	$\tau_{stat}/\tau_t$	$\tau_{tot}$ in [hCPU]
A	2.9	5.2	18.2	690,000
B	11.2	4.8	25.2	502,000
C	21.4	5.2	30.7	431,000
D	46.2	5.0	16.0	658,000
C-EGR	27.1	1.5	7.3	99,000
A <sub>1</sub>	1.7	5.2	15.0	797,000
C <sub>1</sub>	18.5	3.8	21.6	350,000
D <sub>1</sub>	46.2	5.3	23.2	840,000

effect on the wrinkling before analysing the thickening of the flame. Finally, the modelling implications are discussed. In the present study the progress variable is defined as the reduced temperature, Eq. (1.1.12a).

### 3.2.1 Qualitative analysis of instantaneous flames

Figure 3.2.1 presents instantaneous colour fields of the heat release rate and iso-contours of  $c$  on two-dimensional slices in the x-y mid-plane. For the unity Lewis number simulations, the heat release rate shows weak fluctuations along the flame front, even for cases C<sub>1</sub> and D<sub>1</sub>. At the same time these cases present  $c$  iso-contours that are not parallel to each other in the preheat zone, corresponding to  $c$  values approximately smaller than 0.4. An increase of the Karlovitz number (case A<sub>1</sub> to D<sub>1</sub>) seems to slightly thicken the preheat zone when preferential diffusion is not accounted for.

When differential diffusion is taken into account, the thickening of the flame front with increasing  $Ka$  is much more pronounced than in unity Lewis number cases. Indeed, for case A, which is at the upper limit of the flamelet regime ( $Ka = 2.9$ ), the contours of progress variable are wrinkled but remain parallel to each other. For cases C and D, which are in the TRZ regime ( $Ka = 21.4$  and  $Ka = 46.2$ , respectively),  $c$  iso-contours on the unburned gases side of the flame are qualitatively more wrinkled than the ones close to the burnt gases side. Moreover, they remain globally parallel to each other for  $c$  values approximately larger than 0.7, i.e., in the heat release region. In addition, the fluctuations of heat release rate in cases C and D are much larger than in cases C<sub>1</sub>, D<sub>1</sub> and A. It means that there might be more local extinctions in the TRZ regime than in the flamelet regime, as already suggested by Lapointe et al. (2015) and Savard and Blanquart (2015, 2017).

Thus, this qualitative analysis shows that an increase of the turbulence intensity first increases the wrinkling of the flame. As already observed by many authors (Aspden et al., 2011a,b, 2015, 2016, 2017, 2019; Savard and Blanquart, 2014, 2015, 2017), the second consequence is a thickening of the preheat zone of the flame, which appears more important when the differential diffusion is taken into account. In addition, turbulence also seems to impact the heat release rate by increasing its fluctuations, also observed by Lapointe et al. (2015) and



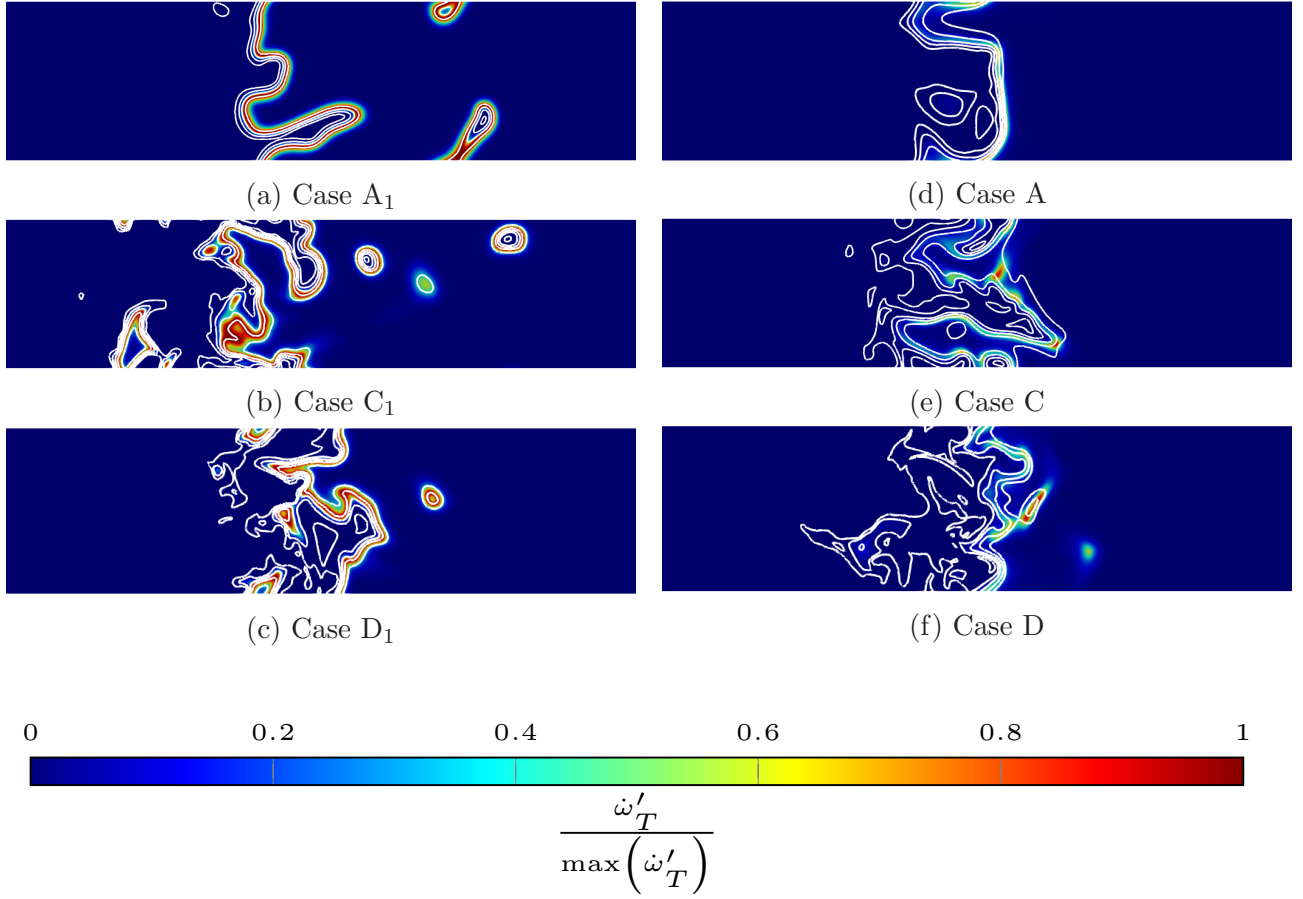


Figure 3.2.1: Two-dimensional slices in x-y mid-plane of the flames coloured with the heat release rate and with contours of the progress variable (white lines), defined as the reduced temperature: (a) to (c) for unity Lewis number cases and (d) to (f) for non-unity Lewis number cases.

Savard and Blanquart (2015, 2017). As for the thickening, this last effect is less important when the Lewis numbers are equal to one.

### 3.2.2 Analysis of the temporal evolution of flame surfaces

Figure 3.2.2 shows the temporal evolution of the flame surface defined as  $\mathcal{A}_T(t) = \int_{\mathcal{V}} |\nabla c|(t) dV$ , with  $\mathcal{V}$  the whole domain. This surface is well defined and commonly used to compute the total flame surface in the flamelet regime. Its relevance in the TRZ regime is questionable but  $\mathcal{A}_T$  is used in the present study as a reference allowing comparison of flames in the flamelet and TRZ regimes.

As expected, each case shows a transitory phase followed by a quasi steady-state with  $\mathcal{A}_T(t)$  oscillating around an average value. Note that the diluted turbulent flame C-EGR (red dashed line) reaches a stationary phase in Fig. 3.2.2a but the simulation ends shortly after, which might lead to a sample too small to compute sufficiently relevant statistics. However, to verify that the flames are stationary, the temporal averaged rate of change of the flame surface  $(1/\mathcal{A}_T)d\mathcal{A}_T/dt$  was verified to be close to zero.

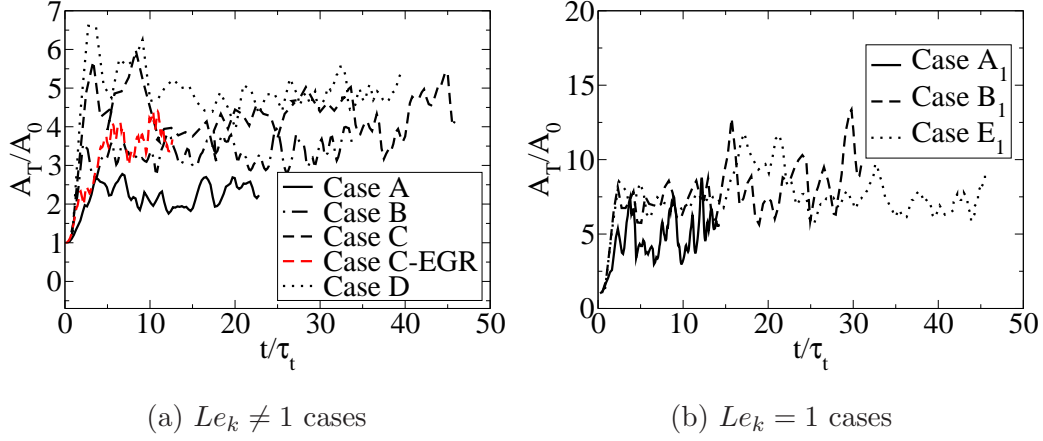


Figure 3.2.2: Temporal evolution of the turbulent flame surface  $\mathcal{A}_T$  normalized with the laminar flame surface  $\mathcal{A}_0$  (a) for cases with  $Le_k \neq 1$ , (b) for cases with  $Le_k = 1$ .

### 3.2.3 Analysis of the turbulent flame velocity and wrinkling

From a macroscopic point of view the main effect of turbulence on the flame is to increase the propagation speed  $S_T$  defined as:

$$S_T = \frac{1}{\rho_u \mathcal{A}_0} \int_V \dot{\omega}_c dV, \quad (3.2.1)$$

where  $\dot{\omega}_c = \dot{\omega}'_T / (C_p(T_b - T_u))$  is the chemical source term with  $\dot{\omega}'_T$  the heat release rate,  $\rho_u$  the density of the fresh gases and  $\mathcal{A}_0$  the laminar flame surface corresponding to the y-z cross section of surface  $L^2$ . Damköhler attributed this acceleration to the increase in the flame front surface  $\mathcal{A}_T$  by wrinkling, leading to:

$$\frac{S_T}{S_L^0} \propto \frac{\mathcal{A}_T}{\mathcal{A}_0}, \quad (3.2.2)$$

The proportionality between the increase of the propagation speed and the flame wrinkling  $\Xi = \mathcal{A}_T/\mathcal{A}_0$ , is often quantified through the effect of the flame stretch using the stretch factor defined by:

$$I_0 = \frac{S_T}{S_L^0 \Xi}, \quad (3.2.3)$$

The evolution of the flame wrinkling (circles) and propagation speed (plain triangles) are plotted as functions of  $Ka$  in Figs. 3.2.3a and 3.2.3b, for  $Le_k \neq 1$  and  $Le_k = 1$  cases, respectively. For  $Le_k \neq 1$  cases,  $\Xi$  and  $S_T$  reach saturation simultaneously at a  $Ka$  corresponding to case C, while for  $Le_k = 1$  cases the quantities even decrease between C and D. This saturation is known as the bending effect, a phenomenon well documented in the literature (Ahmed et al., 2019; Driscoll et al., 2020; Gülder, 2007; Gülder and Smallwood, 2007; Nivarti and Cant, 2017; Nivarti et al., 2018; Wabel et al., 2017). At the same time, the maximum wrinkling and turbulent flame speed of  $Le_k = 1$  cases are approximately 3.5 larger than that of  $Le_k \neq 1$  cases. This can be considered the major impact of preferential diffusion on turbulent flames in the TRZ regime, and justifies the need to include preferential diffusion in the modelling of this regime. Note that case C-EGR (dashed symbols) presents values for  $\Xi$  and  $S_T/S_L^0$  consistent with the evolution

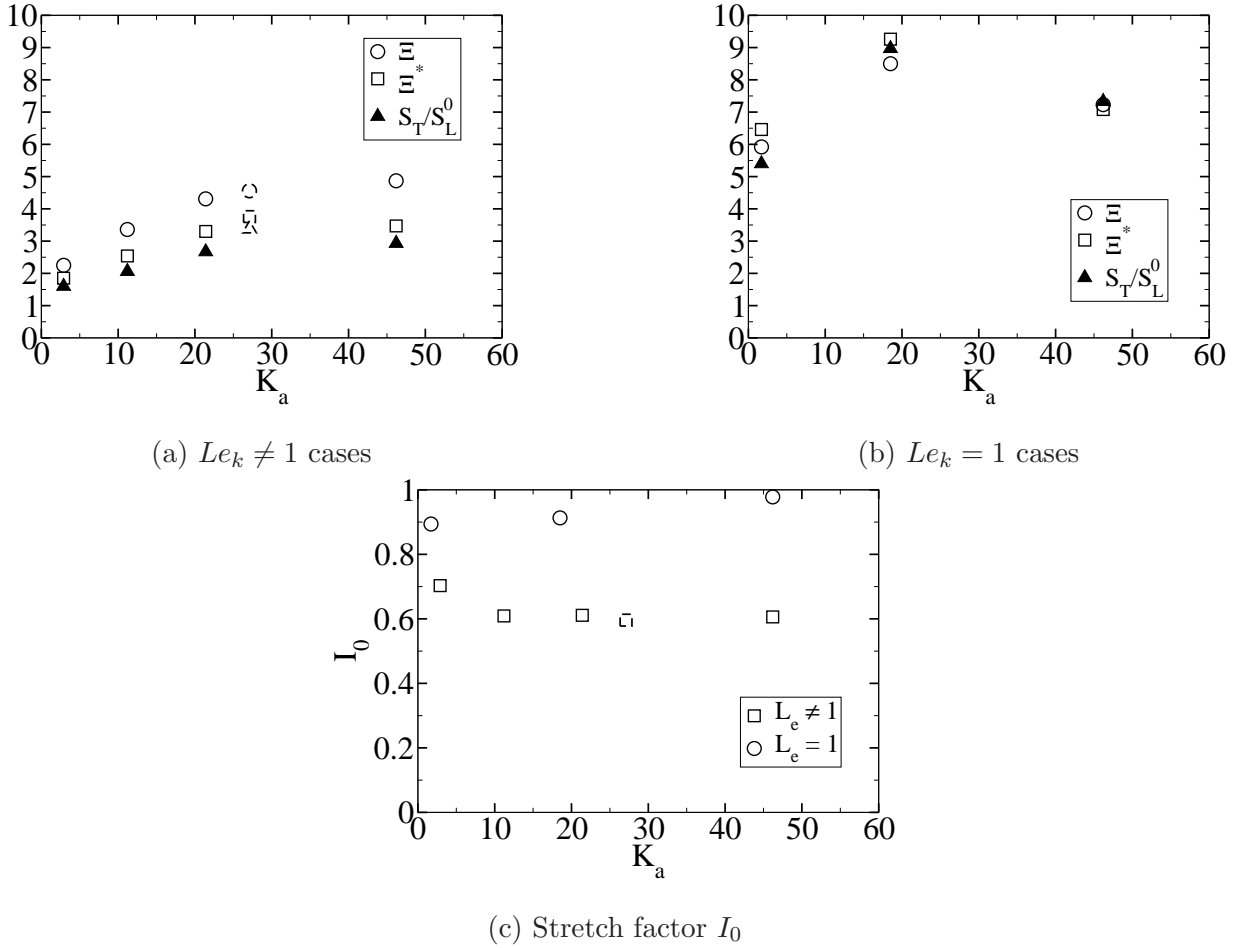


Figure 3.2.3: Evolutions of  $\Xi = \mathcal{A}_T/\mathcal{A}_0$ ,  $\Xi^* = \mathcal{A}_T^*/\mathcal{A}_0$  and  $S_T/S_L^0$  with  $Ka$ , (a) for  $Le_k \neq 1$  cases, (b) for cases with  $Le_k = 1$  and (c) Evolution of the stretch factor  $I_0$ . Dashed symbols are used for case C-EGR.

observed for non-diluted cases in Fig. 3.2.3a suggesting that dilution with burned gases does not impact the bending effect.

The evolution of the stretch factor  $I_0$  with  $Ka$  is shown in Fig. 3.2.3c. For unity Lewis number cases,  $I_0$  remains close to unity, even at the largest  $Ka$ , which corresponds to the proximity of  $\Xi$  and  $S_T/S_L^0$  in Fig. 3.2.3b. For non-unity Lewis cases,  $I_0$  is already smaller than unity (0.7) for case A and decreases only slightly down to 0.6 for case D. Note that case C-EGR (dashed symbol) presents a stretch factor  $I_0$  consistent with the evolution observed for non-diluted cases. These results indicate, in line with previous DNS (Aspden et al., 2011b; Lapointe et al., 2015; Savard and Blanquart, 2015; Savard et al., 2015) that the local consumption speed of unity Lewis number flames is weakly affected by stretch, even in the TRZ regime, while flames showing preferential diffusion are affected in a larger extent. This difference of behaviour is illustrated by the larger fluctuations of the heat release rate for  $Le_k \neq 1$  cases compared to  $Le_k = 1$  cases, as observed in Fig. 3.2.1. These fluctuations indicate that local strain and stretch rates strongly impact the consumption speed. This aspect will be studied in the present thesis considering the statistics of the displacement speed  $S_d$ .

The evolution of the wrinkling  $\Xi^*$  on an iso-surface  $c^* = 0.8$ , corresponding to the maximum reaction rates of the laminar flame (see Fig. 3.2.4), is also plotted in Figs. 3.2.3a and 3.2.3b.

This wrinkling is defined as:

$$\Xi^* = \frac{\mathcal{A}_T^*}{\mathcal{A}_0}, \quad (3.2.4)$$

where  $\mathcal{A}_T^*$  is the area of the iso-surface  $c^* = 0.8$ .

As expected from previous DNS (Aspden et al., 2011b; Lapointe et al., 2015; Savard and Blanquart, 2015; Savard et al., 2015), when  $Le_k = 1$ ,  $\Xi^*$  and  $\Xi$  are almost similar, which is a consequence of the weak effect of stretch on the local consumption speed. Similarly,  $\Xi^*$  is almost equal to  $\Xi$  for case A. This is in agreement with the flamelet assumption considering the flame as a collection of parallel flamelets leading to a generalized flame surface  $\mathcal{A}_T$  close to the area of any iso-surface of progress variable. Figure 3.2.3a shows a much better agreement of  $\Xi^*$  with  $S_T$  than  $\Xi$  for high  $Ka$ , which suggests that the surface of the reaction zone remains an accurate measure of the turbulent flame speed and, consequently, of the total reaction rate.

Unlike in the present and previous DNS studies (Ahmed et al., 2019; Nivarti and Cant, 2017; Nivarti et al., 2018), Gülder and Smallwood (2007) observed experimentally that the flame wrinkling reaches a saturation, while the turbulent flame speed still increases with increasing  $Ka$ . Consequently, the factor  $I_0$  increases with  $Ka$  leading to values much larger than unity in the TRZ regime. They attributed this increase of the local burning velocity in the TRZ regime by the enhancement of the species and heat transport in the preheat zone by small-scale turbulent eddies.

This difference between DNS and experiments is still not well understood. It could be explained by the difficulty to accurately measure flame surface and speed in such highly turbulent experiments, but it could also be explained by the artificial nature of turbulence forcing technics in DNS.

### 3.2.4 Analysis of the inner flame structure

To evaluate the effect of both turbulence and differential diffusion on the inner structure of the flame, the profile of the conditional mean of the chemical source term  $\dot{\omega}_c = \dot{\omega}'_T / (C_p(T_b - T_u))$  with the progress variable is plotted for each case in Fig. 3.2.4.

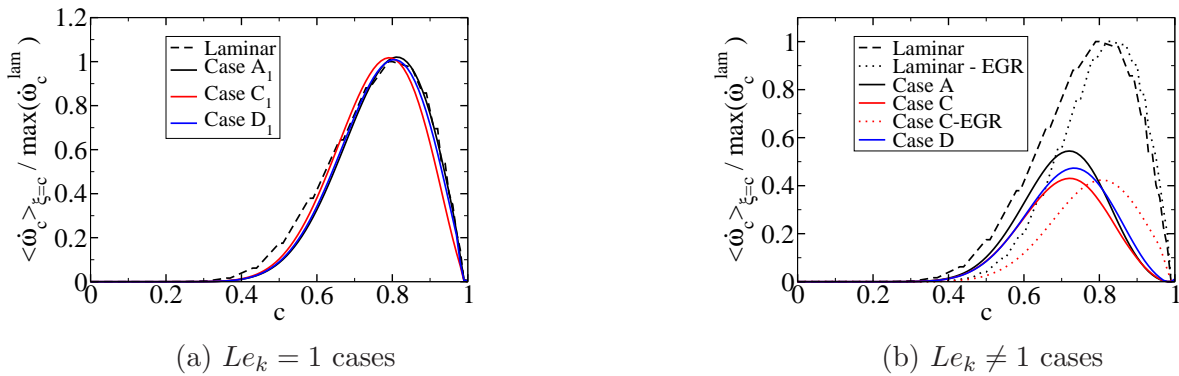


Figure 3.2.4: Conditional mean of the chemical source term  $\langle \dot{\omega}_c(c) \rangle_{\xi=c}$  as a function of progress variable: (a) for cases with  $Le_k = 1$ , and (b) for  $Le_k \neq 1$  cases. Dotted lines are used to represent flames diluted with burned gases.

Figure 3.2.4 shows the conditional mean of the progress variable chemical source term  $\langle \dot{\omega}_c(c) \rangle_{\xi=c}$ , normalized by the peak chemical source term of the 1D laminar flame, as a function of the progress variable  $c$  for each case. As described in Section 3.1.1, the flames with unity Lewis numbers and non-unity Lewis numbers have the same  $S_L^0$  and  $\delta_L^0$ . As a consequence, the laminar flames with unity Lewis numbers and non-unity Lewis numbers present similar chemical source term profiles as seen in Fig. 3.2.4 in black dashed lines. The profiles of cases A<sub>1</sub>, C<sub>1</sub> and D<sub>1</sub> are very close to those of the 1D laminar flame, as observed in previous DNS studies. This suggests that with unity Lewis numbers, although the flame is slightly thickened, turbulence does not impact the inner flame structure significantly. It is noteworthy that, as turbulence intensity is increased, the fluctuations of the progress variable chemical source term are significantly enhanced, as observed in Fig. 3.2.1.

On the contrary, the non-unity Lewis number cases show a decrease of the chemical source term when  $Ka$  increases, from a maximum of 0.55 for case A down to 0.43 for case C. However, when  $Ka$  increases further, the inverse tendency is observed with an increase of  $\dot{\omega}_c / \max(\dot{\omega}_c^{lam})$  up to 0.48 for case D. But the number of studied cases here is too low to provide a clear view on the evolution of this maximum as a function of  $Ka$ . This phenomenon was also observed by Lapointe et al. (2015), who suggested that as turbulent mixing is enhanced, differential diffusion effects are reduced. It can also be remarked that although peak values are slightly different for cases A, C and D, the chemical source term assumes very similar shapes for the three cases when  $c > c_{peak}$ , with  $c_{peak} \approx 0.7$  corresponding to the maximum reaction rate. As observed by Lapointe et al. (2015),  $c_{peak}$  of the turbulent flames shifts from 0.8 to 0.7 for  $Le_k \neq 1$ , which is due to preferential diffusion effects. This suggests that the inner structure of high Karlovitz flames C and D remains close to the structure of a flame in the flamelet regime (case A) on the burnt gases side, in line with the definition of the TRZ regime. These quantitative analysis confirm the preliminary observations in Fig. 3.2.1.

Note that the laminar flame diluted with burned gases has a very similar chemical source term as the non-diluted flame, except that the peak is slightly shifted toward the burned gases side (with  $c_{peak} = 0.85$  compared to  $c_{peak} = 0.8$  for non-diluted case). The diluted turbulent flame C-EGR has a very similar conditional mean chemical source term as the non-diluted case C. As for the laminar flames, the peak of mean conditional chemical source term for case C-EGR is significantly shifted toward the burned gases side. Even if dilution with burned gases change the location of the peak of conditional chemical source term, it seems to weakly affect the inner flame structure compared to the corresponding laminar flame.

To quantify the apparent thickening of the flame, the thickening factor  $\Theta$  introduced by Aspden et al. (2019) is examined.

$$\Theta = \frac{\langle |\nabla c|(\xi) \rangle_{\xi=c}^{ref}}{\langle |\nabla c|(\xi) \rangle_{\xi=c}}, \quad (3.2.5)$$

where  $\langle |\nabla c|(\xi) \rangle_{\xi=c}$  is the mean value of the progress variable gradient conditioned on the progress variable value  $\xi$ . In this study the normalization is made using the gradient of the laminar flame for both non-unity and unity Lewis number cases, while Aspden et al. (2019) performed the normalisation using the conditional mean of the gradient for the case  $Ka = 1$ .

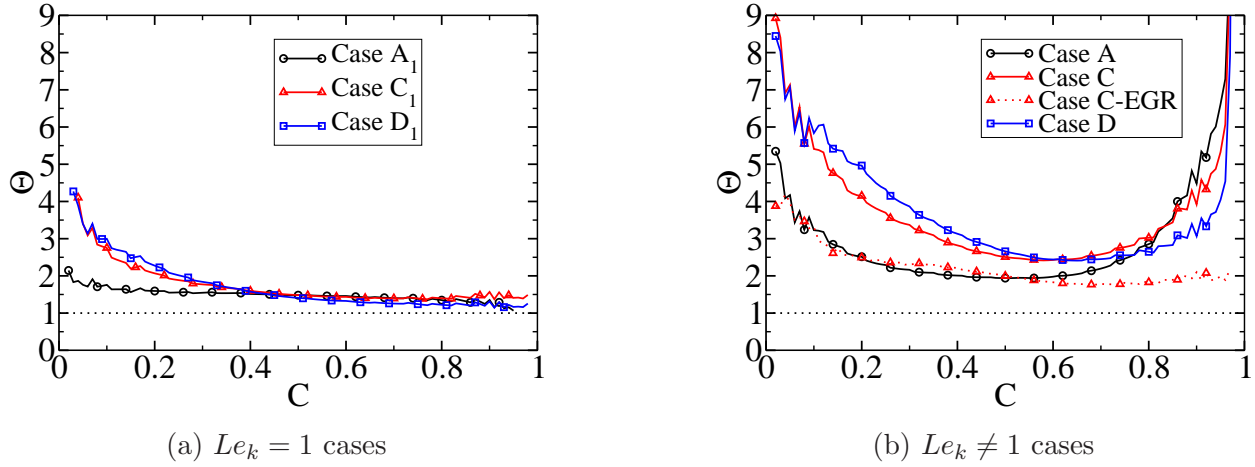


Figure 3.2.5: Thickening factor  $\Theta(c)$  (a) for cases with  $Le_k = 1$ , and (b) for  $Le_k \neq 1$  cases. Dotted lines are used to represent flames diluted with burned gases.

In Fig. 3.2.5a, the evolution of  $\Theta$  with the progress variable is shown for unity Lewis number cases. Case A<sub>1</sub> presents a constant value equal to 1.5, which indicates that the flame is uniformly thickened compared to the laminar flame. Cases C<sub>1</sub> and D<sub>1</sub> present a thickening on the fresh gases side ( $c < 0.5$ ) up to a factor 2 compared to case A<sub>1</sub>, but  $\Theta$  converges to the value of case A<sub>1</sub> when  $c \geq 0.5$ . This observation was already made by Aspden et al. (2019), where the thickening factor of a methane flame collapsed to that of a flame in the flamelet regime. So, when  $Ka$  increases, the flame is thickened on the fresh gases side but remains thin for  $c \geq 0.5$  for unity Lewis number cases.

The same quantity is shown for non-unity Lewis number simulations in Fig. 3.2.5b. For case A,  $\Theta$  reaches values close to 5-6 for  $c < 0.3$  and  $c > 0.7$ , but remains close to 2 elsewhere. The unexpected thickening observed in the fresh gases side might be due to the fact that case A is at the upper limit of the flamelet regime. Compared to case A, cases C and D present an even larger thickening on the fresh and burnt gases sides, which is consistent with the observed non-parallel progress variable iso-surfaces in the preheat zone in Fig. 3.2.1. However, in the reaction zone ( $0.5 < c < 0.9$  as seen in Fig. 3.2.4) the increase of the thickening compared to case A is relatively low, approximately 2.4 for case C and 2.6 for case D. The broadening of the thickening factor on the burnt gases side, in Fig. 3.2.5b, may be due to the normalization by the laminar case for which the reaction zone extends further towards  $c = 1$  in Fig. 3.2.4b, resulting in higher  $\Theta$  values. Note that the thickness factor of the diluted case C-EGR (red dotted line) is close to those of cases A and C<sub>1</sub>. These similitudes between cases C-EGR and C<sub>1</sub> suggest that dilution with burned gases affects the inner flame structure similarly as setting all the Lewis numbers to unity.

These results seem to confirm that the inner structure of flames with  $Le_k = 1$  are weakly

affected by an increase of  $Ka$ , while the thickening strongly increases with  $Ka$  in the fresh gases side for flames with  $Le_k \neq 1$ . This is consistent with the observation in Fig. 3.2.1 showing strongly wrinkled and non-parallel iso-surfaces in the preheat zone. So, the inner structure is no longer the same as a laminar flame. However, whether the Lewis numbers are unity or not, Figs. 3.2.4 and 3.2.5 show that the structures of the reaction zone of high Karlovitz number flames are similar to those of the flamelet regime, suggesting that the reaction zone is a good tracker to capture the general behaviour of the flame.

The analysis proposed by Peters (1999) considering a thin reaction zone for the TRZ regime is globally verified in the present DNS, but the impact of the Lewis number needs to be added: when  $Le_k = 1$  perturbations of the reaction zone can be neglected, while the flame is strongly thickened for  $Le_k \neq 1$ .

### 3.2.5 Modelling implications

The progress variable source term involved in the right hand side (RHS) of Eq. (1.5.12) is the first quantity of interest for modelling. Its integral over the whole domain  $\Omega_{tot} = \int_{\mathcal{V}} \dot{\omega}_c dV$  is evaluated by integrating the RHS of Eq. (1.5.15) because the integral of the diffusive contribution  $\nabla \cdot (\rho D \nabla c)$  in Eq. (1.5.15) is zero. Thus,  $\Omega_{tot}$  can be related to the displacement speed by integrating the RHS of Eq. (1.5.12):

$$\Omega_{tot} = \int_{\mathcal{V}} [\dot{\omega}_c + \nabla \cdot (\rho D \nabla c)] dV = \int_{\mathcal{V}} \rho S_d |\nabla c| dV = \langle \rho S_d \rangle_s \mathcal{A}_T, \quad (3.2.6)$$

where  $\mathcal{V}$  is the whole simulation domain,  $\langle \rho S_d \rangle_s$  is the surface averaged displacement speed and  $\mathcal{A}_T$  is the flame surface, both defined with the generalized approach of the CFM model:

$$\mathcal{A}_T = \int_{\mathcal{V}} |\nabla c| dV, \quad (3.2.7)$$

$$\langle \rho S_d \rangle_s = \frac{\int_{\mathcal{V}} \rho S_d |\nabla c| dV}{\mathcal{A}_T}. \quad (3.2.8)$$

As shown in previous sections, for  $Le_k \neq 1$  cases, the flame structure is very perturbed in the preheat zone while only moderately in the reaction zone. This suggests that referring the reaction rate to an iso-surface in the reaction zone might be easier than considering all iso-surfaces. This is why we compare  $\Omega_{tot}$  to the integrated RHS term  $\Omega_{c^*}$  conditioned on a  $c^*$  iso-surface:

$$\Omega_{c^*} = \int_{\mathcal{V}} \rho S_d |\nabla c| \delta(c - c^*) dV = \langle \rho S_d \rangle_s^* \mathcal{A}_T^*. \quad (3.2.9)$$

In Eq. (3.2.9),  $\delta(c)$  is the Dirac function,  $\langle \rho S_d \rangle_s^*$  and  $\mathcal{A}_T^*$  are the surface averaged displacement speed at  $c = c^*$  and the area of the  $c^*$  iso-surface, respectively. Note that  $\Omega_{c^*}$  is not equal to the reaction rate on the iso-surface  $c = c^*$ ,  $\int_{\mathcal{V}} \dot{\omega}_c \delta(c - c^*) dV$ .

Figure 3.2.6 presents the evolutions of  $\Omega_{c^*}$ ,  $\langle \rho S_d \rangle_s^*$  and  $\mathcal{A}_T^*$  normalized by  $\Omega_{tot}$ ,  $\langle \rho S_d \rangle_s$  and  $\mathcal{A}_T$ , respectively, as functions of  $c^*$  for case C. In Fig. 3.2.6 is also plotted the stretch factor  $I_0^*$



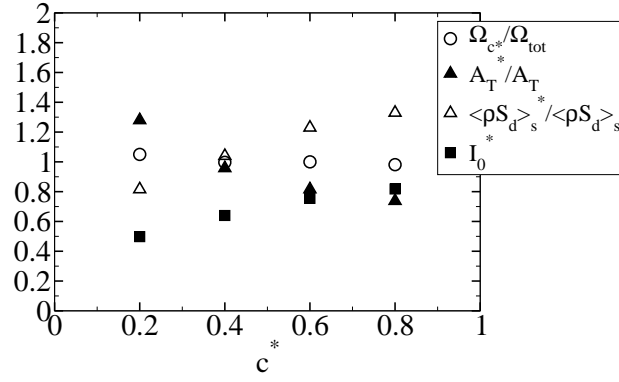


Figure 3.2.6: The evolution  $\Omega_{c^*}$ ,  $\langle \rho S_d \rangle_s^*$  and  $\mathcal{A}_T^*$  normalized by  $\Omega_{tot}$ ,  $\langle \rho S_d \rangle_s$  and  $\mathcal{A}_T$ , respectively, and  $I_0^*$  as functions of the progress variable for case C.

at  $c^*$ , defined as:

$$I_0^* = \frac{\langle \rho S_d \rangle_s^*}{\rho_u S_L^0}. \quad (3.2.10)$$

On the one hand,  $\Omega_{c^*}$  is equal to  $\Omega_{tot}$  for all iso-surfaces. This result is in fact expected because the flame being statistically stationary, all iso-surfaces need to advance at the same velocity. On the other hand,  $\mathcal{A}_T^*$  decreases substantially with increasing  $c^*$ . This result is consistent with Fig. 3.2.1 which shows a strong distortion of  $c^*$  iso-surfaces towards  $c^* = 0$ , corresponding to a strong increase of the flame surface  $\mathcal{A}_T^*$ . This illustrates once again that in the TRZ regimes,  $c^*$  iso-surfaces are not parallel to each other for low values of  $c^*$ . As shown by Eq. (3.2.9) larger values of  $\mathcal{A}_T^*$  at small  $c^*$  need to be compensated by smaller displacement speeds, *i.e.*, by smaller values of  $I_0^*$ .

These results show that the modelling of  $\mathcal{A}_T^*$  and  $\langle \rho S_d \rangle_s^*$  will depend on the choice of  $c^*$  in the TRZ regime. Figure 3.2.6 shows that  $I_0^*$  increases significantly when  $c^*$  increases from 0.2 to 0.8 and that it seems to reach a plateau, indicating again that in the reaction zone, progress variable iso-surfaces remains approximately parallel, unlike in the preheat zone. This is why in the rest of this study the flame will be studied through an iso-surface  $c^* = 0.8$ , close to the maximum of heat release rate iso-surface.

To check the equilibrium state on this particular iso-surface, the flame stretch balance at  $c^* = 0.8$  is shown in Fig. 3.2.7. For each simulation the rate of change of  $\mathcal{A}^*$ ,  $\langle K \rangle_s^*$ , is close to zero. This figure shows the absolute values of the tangential strain rate,  $\langle a_T \rangle_s^* = \langle \nabla \cdot \mathbf{u} - \mathbf{nn} : \nabla \mathbf{u} \rangle_s^*$ , and the stretch rate due to curvature,  $\langle S_d \kappa \rangle_s^* = \langle S_d \nabla \cdot \mathbf{n} \rangle_s^*$ , where  $\mathbf{n} = -\nabla c / |\nabla c|$  is the local normal vector to the flame,  $\mathbf{u}$  is the flow velocity and  $\langle \rangle_s^*$  is the surface averaging operator defined with Eq. (3.1.11). Both evolutions increase quasi linearly with  $Ka$ . Note that the tangential strain rate and the stretch due to curvature are significantly smaller, when the flame is diluted with burned gases (dashed symbols). These reduced values for cases C-EGR are explained by much less intense turbulence of this case compared to case C. Indeed, even if their Karlovitz numbers are close because of the reduction of the laminar flame speed by dilution with burned gases, the velocity of the integral scales involved in case C-EGR is half the one involved in case C ( $u'_t = 2.2$  m/s and  $u'_t = 4.6$  m/s, respectively). These reduced tangential strain rate and stretch due to curvature combined with the observations made previously show



that a diluted flame is much more sensitive to turbulence than non-diluted one.

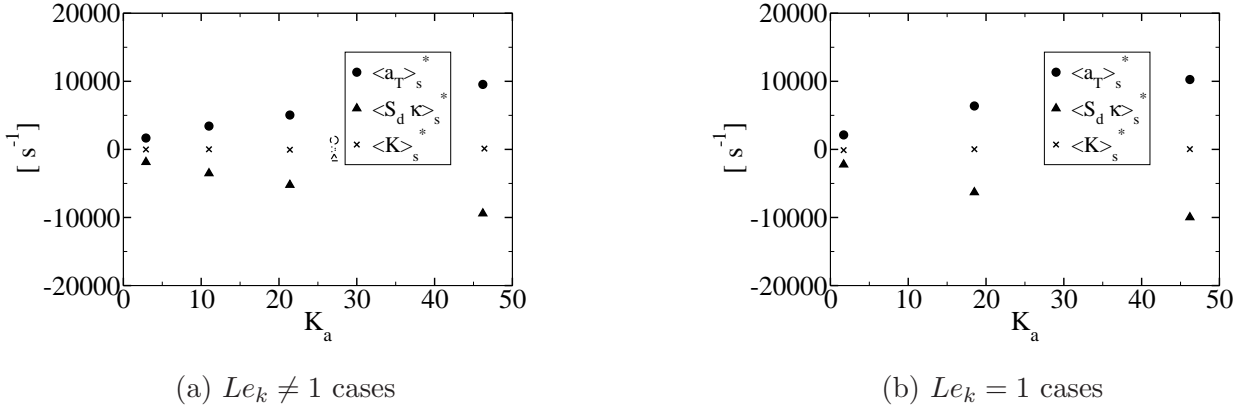


Figure 3.2.7: Evolutions of  $\langle K \rangle_s^* = (1/\mathcal{A}_T^*) (d\mathcal{A}_T^*/dt) = \langle a_T \rangle_s^* + \langle S_d \kappa \rangle_s^*$ ,  $\langle a_T \rangle_s^* = \langle \nabla \cdot \mathbf{u} - \mathbf{nn} : \nabla \mathbf{u} \rangle_s^*$  and  $\langle S_d \kappa \rangle_s^* = \langle S_d \nabla \cdot \mathbf{n} \rangle_s^*$ , where  $\mathbf{n} = -\nabla c/|\nabla c|$  is the local normal vector to the flame,  $\mathbf{u}$  is the flow velocity and  $\langle \cdot \rangle_s^*$  is the surface averaging operator defined with Eq. (3.1.11): (a) for cases with  $Le_k \neq 1$  and (b) for cases with  $Le_k = 1$ . Dashed symbols are used for case C-EGR.

Figure 3.2.8 summarizes the results about the bending effect on the iso-surface  $c^* = 0.8$ . As for the generalized approach (Fig. 3.2.3), the wrinkling  $\Xi^* = \mathcal{A}_T^*/\mathcal{A}_0$  presents a bending when the Karlovitz increases, for each set of simulations in Fig. 3.2.8a. As expected, the stretch factor  $I_0^*$  is almost constant close to 1 with an increase of  $Ka$  in Fig. 3.2.8b. The wrinkling  $\Xi^*$  of the iso-surface  $c^* = 0.8$  is also reported in Fig. 3.2.3 by square symbols. As for the generalized approach,  $\Xi^*$  presents a bending for each set of simulations. However, its values are smaller and closer to  $S_T/S_L^0$ . This reflects the fact that  $I_0^*$  is closer to unity than  $I_0$ . All these observations indicate that the iso-surface  $c^*$  allows to well predict the turbulent flame speed and, therefore, suggests that a flame surface density (FSD) based model is still appropriate.

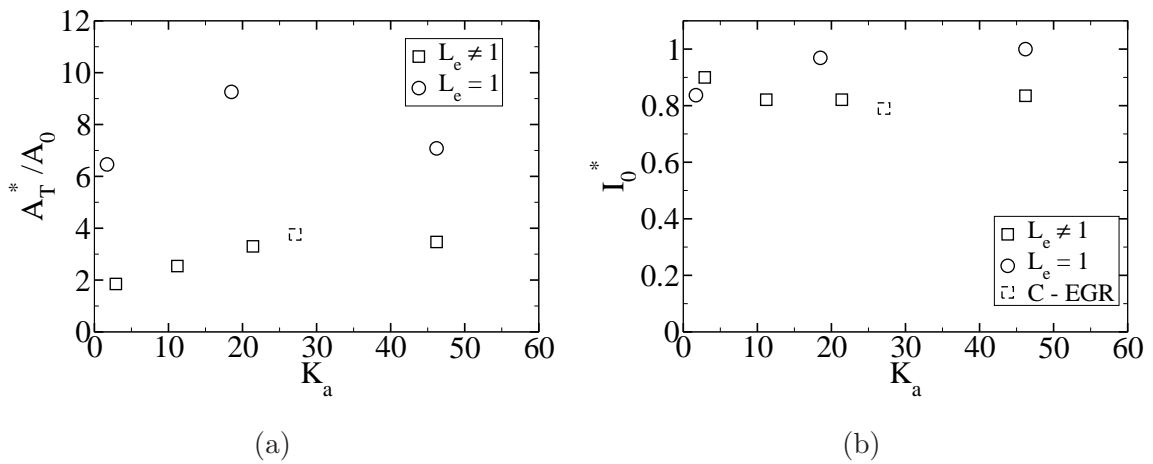


Figure 3.2.8: Evolutions of: (a) area of the iso-surface  $c^* = 0.8$  normalized with the laminar flame surface and (b) the stretch factor  $I_0^* = \langle \rho S_d \rangle_s^* / (\rho_u S_L^0)$ . Non-unity Lewis number cases, unity Lewis number cases and cases with turbulence forced only in the fresh gases are plotted in square, circle and cross symbols, respectively.

Finally, in this section it has been seen that flames interacting with a forced turbulent field

reach a quasi-steady state. The influence of the turbulence on the flame front has two main effects:

1. It thickens the flame front, especially the preheat zone. The reaction zone is also thickened but the iso-surfaces of progress variable remain parallel to each other.
2. It increases the total flame surface by increasing the wrinkling of the flame front. However, a bending effect occurs both on the wrinkling and the propagation speed.

As a consequence, by increasing the Karlovitz number, the consumption speed is increased until a sufficiently high  $Ka$  is reached. For higher  $Ka$  values, a decrease of the consumption speed is observed. The inner structure of  $Le = 1$  cases suggests that this bending effect on the consumption speed is mainly due to the bending of the surface. Moreover, the inner structure of the flames remains close to the structure of a flame in the flamelet regime in the burnt gas side. To conclude, the analysis of the chemical source term through the flame front of a high Karlovitz case has shown that it seems reasonable to evaluate the overall fuel consumption from a reaction zone surface density formalism.

Therefore, the purpose of this study being to adapt the CFM model to TRZ regime, the definition of the progress variable is modified as follows:

$$\mathcal{C} = \mathcal{H}(c - c^*), \quad (3.2.11)$$

where  $\mathcal{H}(c)$  is the Heaviside function giving  $\mathcal{C} = 0$  when  $c < c^*$  and  $\mathcal{C} = 1$  otherwise. Using the same progress variable, Knudsen and Pitsch (2008) modified the balance equation of the progress variable leading to, when filtered:

$$\frac{\partial \bar{\rho} \tilde{\mathcal{C}}}{\partial t} + \nabla \cdot (\bar{\rho} \tilde{\mathbf{u}} \tilde{\mathcal{C}}) = -\nabla \cdot (\overline{\rho \mathbf{u} \mathcal{C}} - \bar{\rho} \tilde{\mathbf{u}} \tilde{\mathcal{C}}) + \langle \rho S_d \rangle_{s,c^*} \bar{\Sigma}^*, \quad (3.2.12)$$

where  $\bar{\Sigma}^* = \overline{|\nabla \mathcal{C}|} = \overline{|\nabla c| \delta(c - c^*)}$  is the surface density of the iso-surface  $c = c^*$  corresponding to the fine-grained FSD (Vervisch et al., 1995) and  $\langle \cdot \rangle_{s,c^*}$  is the surface averaging operation on the iso-surface  $c = c^*$ :

$$\langle Q \rangle_{s,c^*} = \frac{\overline{Q |\nabla c| \delta(c - c^*)}}{\bar{\Sigma}^*} = \frac{\int_V Q |\nabla c| \delta(c - c^*) G_\Delta(\mathbf{x} - \mathbf{x}') d\mathbf{x}'}{\int_V |\nabla c| \delta(c - c^*) G_\Delta(\mathbf{x} - \mathbf{x}') d\mathbf{x}'}, \quad (3.2.13)$$

where  $Q$  is a quantity of interest.

As for the generalized approach of CFM, the surface density of the iso-surface  $c = c^*$  is evaluated through a transport equation. This equation is determined by deriving the exact balance equation of  $\mathcal{C}$  and then filtering (as presented in Appendix C), leading to:

$$\begin{aligned} \frac{\partial \bar{\Sigma}^*}{\partial t} + \nabla \cdot (\tilde{\mathbf{u}} \bar{\Sigma}^*) = & -\nabla \cdot (\overline{\mathbf{u} \Sigma^*} - \tilde{\mathbf{u}} \bar{\Sigma}^*) + \langle \nabla \cdot \mathbf{u} - \mathbf{nn} : \nabla \mathbf{u} \rangle_{s,c^*} \bar{\Sigma}^* \\ & + \langle S_d \kappa \rangle_{s,c^*} \bar{\Sigma}^* - \nabla \cdot (\langle S_d \mathbf{n} \rangle_{s,c^*} \bar{\Sigma}^*), \end{aligned} \quad (3.2.14)$$

where  $\langle \nabla \cdot \mathbf{u} - \mathbf{nn} : \nabla \mathbf{u} \rangle_{s,c^*}$  is the surface averaged tangential strain rate and  $\langle S_d \kappa \rangle_{s,c^*}$  is the surface averaged stretch rate due to curvature, where  $\kappa = \nabla \cdot \mathbf{n}$  is the curvature.

### 3.3 Analysis of the displacement speed on an iso-surface

A more thorough analysis of the displacement speed is now presented with a modelling objective. In the rest of the present study, the exponent  $*$  refers to the value of the variables on the iso-surface  $c = c^*$ .

#### 3.3.1 Analysis of conditional means with curvature

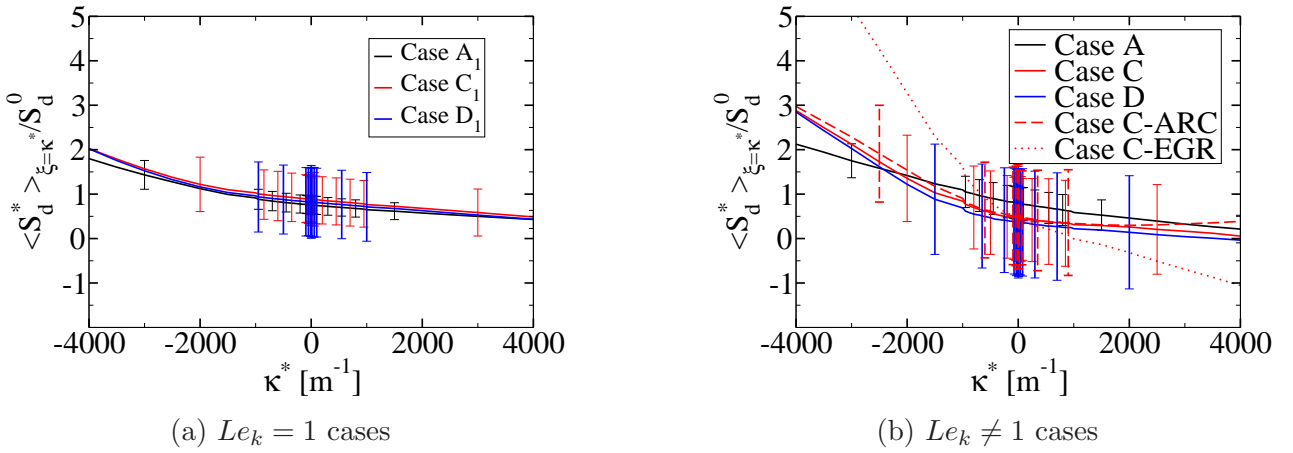


Figure 3.3.1: Evolution of the conditional mean of displacement speed  $\langle S_d^*(\xi) \rangle_{\xi=\kappa^*}$ , normalized with the laminar flame speed at  $c = c^*$ ,  $S_d^0$ , with curvature  $\kappa^*$ : (a) for cases with  $Le_k = 1$  and (b) for  $Le_k \neq 1$  cases. The error bars represent the standard deviation.

Figure 3.3.1 presents the mean displacement speed  $\langle S_d^*(\xi) \rangle_{\xi=\kappa^*}$  conditioned on  $\kappa^*$ , the flame curvature. The displacement speed is normalized with  $S_d^0 = \rho_u S_L^0 / \rho^*$ , the displacement speed of the planar laminar flame at  $c = c^*$ . The standard deviation is also reported by error bars. As observed in previous studies for  $Le_k \neq 1$  (Han and Huh, 2009; Hawkes and Chen, 2005; Nivarti et al., 2018; Sankaran et al., 2015), Fig. 3.3.1b shows a negative correlation between displacement speed and curvature. It also shows an increase of the slope with the Karlovitz number. Case C-ARC performed using an ARC mechanism is seen to be very close to case C performed with the 2-step mechanism. This indicates that the influence of curvature on the displacement speed is hardly sensitive to the level of chemistry description. In Fig. 3.3.1a, the same results are presented for  $Le_k = 1$  cases: the negative correlation is also observed but the slope is smaller, and is marginally affected by the increase of the turbulence intensity.

To further analyse the displacement speed, the conditional statistics of the different components of  $S_d^*$ , as defined in Eqs. (1.6.17) to (1.6.19), are plotted as functions of curvature in Fig. 3.3.2. The thermal diffusivity  $D_{th}^*$  depends on the mixture composition and the temperature but is assumed to be the same for  $Le_k = 1$  and  $Le_k \neq 1$  flames, as shown in Fig. 3.3.2a

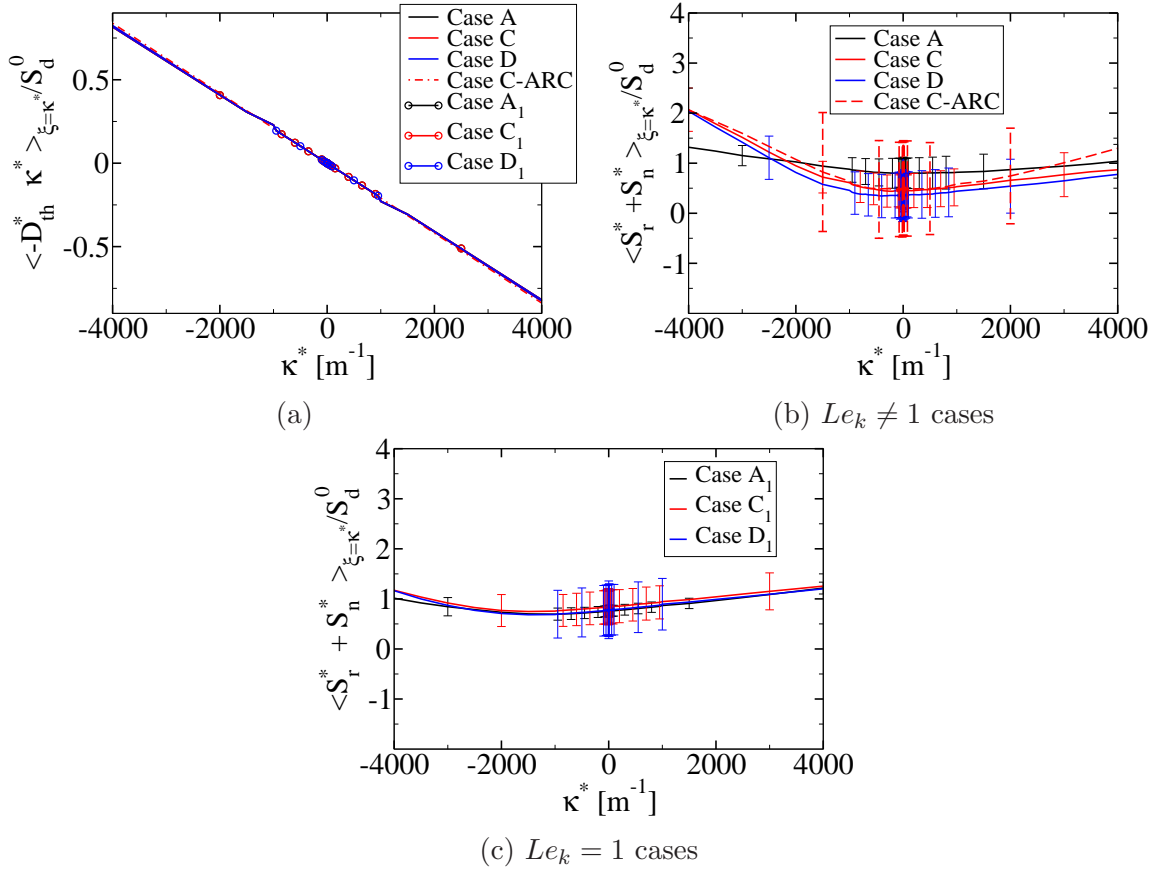


Figure 3.3.2: Evolution of the conditional mean of the components of the displacement speed, normalized with the laminar flame speed at  $c = c^*$ ,  $S_d^0$ , with curvature  $\kappa^*$  : (a)  $\langle -D_{th}^* \kappa(\xi) \rangle_{\xi=\kappa^*}$  for all the cases (b)  $\langle S_r^* + S_n^*(\xi) \rangle_{\xi=\kappa^*}$  for cases with  $Le_k \neq 1$  and (c)  $\langle S_r^* + S_n^*(\xi) \rangle_{\xi=\kappa^*}$  for cases with  $Le_k = 1$ . The error bars represent the standard deviation.

where the tangential diffusions  $\langle S_t^* \rangle_{\xi=\kappa^*} = -D_{th}^* \kappa^*$  of each case are identical. With this reasonable hypothesis, differences observed on  $\langle S_d^* \rangle_{\xi=\kappa^*}$  are only due to the sum of  $\langle S_r^* \rangle_{\xi=\kappa^*}$  and  $\langle S_n^* \rangle_{\xi=\kappa^*}$ .

Figures 3.3.2b and 3.3.2c present the sum  $\langle S_r^* + S_n^* \rangle_{\xi=\kappa^*}$  as a function of the curvature for the same flames. The evolution of  $\langle S_r^* + S_n^* \rangle_{\xi=\kappa^*}$  differs from  $\langle S_d^* \rangle_{\xi=\kappa^*}$  mainly for positive curvature where the correlation is positive between  $\langle S_r^* + S_n^* \rangle_{\xi=\kappa^*}$  and  $\kappa^*$ . However, it can be observed that as for  $\langle S_d^* \rangle_{\xi=\kappa^*}$ , non-unity Lewis number flames show increasing slopes for increasing  $Ka$ , while  $Le_k = 1$  flames show weak sensitivity to  $Ka$ .

At  $\kappa^* = 0$ , we could expect  $\langle S_d^* \rangle_{\xi=\kappa^*} / S_d^0$  to be close to unity, which is not the case: for  $Le_k \neq 1$ , it ranges between 0.37 and 0.8, while for  $Le_k = 1$  flames, it takes larger values close to 0.85. Figure 3.3.3 shows that the mean tangential strain rate conditioned with curvature,  $\langle a_T^* \rangle_{\xi=\kappa^*}$ , is not zero at  $\kappa^* = 0$  meaning that the flame is positively strained. Moreover, the standard deviations reported as error bars in Fig. 3.3.3 are very large, particularly for cases D and D<sub>1</sub>, and might also be a reason for  $\langle S_d^* \rangle_{\xi=\kappa^*}$  to be far from  $S_d^0$  at  $\kappa^* = 0$ .

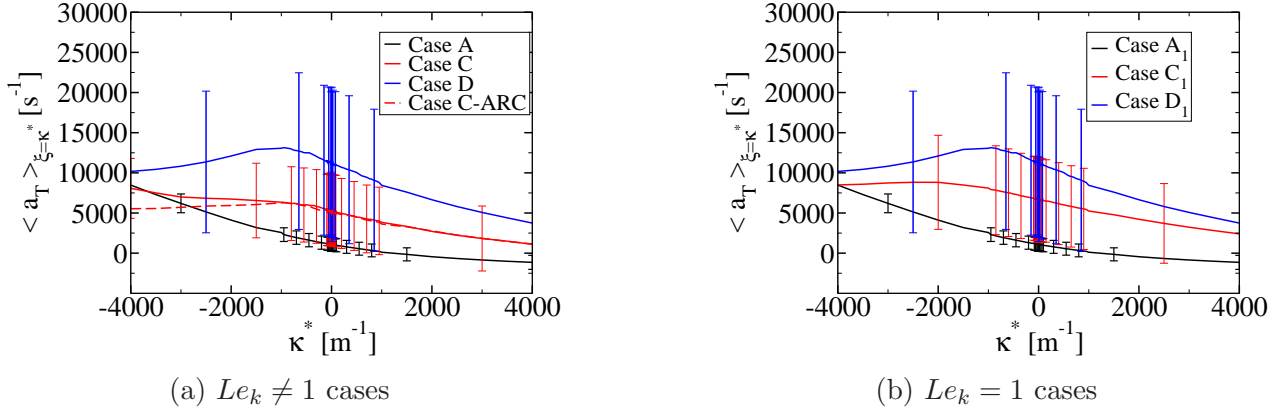


Figure 3.3.3: Evolution of the conditional mean of tangential strain rate  $\langle a_T^*(\xi) \rangle_{\xi=\kappa^*}$  with curvature  $\kappa^*$  : (a) for cases with  $Le_k \neq 1$  and (b) for cases with  $Le_k = 1$ . The error bars represent the standard deviation.

### 3.3.2 Analysis of conditional means with strain rate and curvature

This dependency of  $\langle S_r^* + S_n^* \rangle_{\xi=\kappa^*}$  to turbulence intensity is in agreement with previous studies (Han and Huh, 2009; Hawkes and Chen, 2005; Sankaran et al., 2015; Wang et al., 2017). Figure 3.3.2 suggests that analysing the response of curvature alone is not sufficient and a double conditioning on both curvature and strain rate is required, as presented in Fig. 3.3.4. The joint probability density function (PDF) of curvature and strain rate is also plotted in this figure by black solid lines corresponding to 10% (outer line), 50% and 90% (inner line) of the maximum values of the joint PDF.

The correlation of  $a_T^*$  and  $\kappa^*$  is evaluated using Pearson's correlation coefficient (Pearson, 1895), defined in Eq. (3.3.1), and listed in Table 3.7.

$$r_{X,Y} = \frac{\sum_{i=1}^n (X_i - \langle X \rangle) (Y_i - \langle Y \rangle)}{\sqrt{(X_i - \langle X \rangle)^2} \sqrt{(Y_i - \langle Y \rangle)^2}}, \quad (3.3.1)$$

where  $(X_i, Y_i)$  is a sample pair of data,  $\langle \rangle$  denotes the sample mean, and  $n$  is the sample size.

Table 3.7: Pearson's correlation coefficient,  $r_{a_T^*, \kappa^*}$ , between strain rate  $a_T^*$  and curvature  $\kappa^*$  for the flames presented in this paper.

Case	A	C	D	A <sub>1</sub>	C <sub>1</sub>	D <sub>1</sub>
$Ka$	2.9	21.4	46.2	2.7	18.5	46.2
$r_{a_T^*, \kappa^*}$	-0.65	-0.40	-0.28	-0.56	-0.28	-0.18

As already observed in the literature (Chakraborty and Cant, 2005a), the correlation of  $a_T^*$  and  $\kappa^*$  is negative and decreases as  $Ka$  increases. At low  $Ka$ , the correlation is strong for case A and weaker for case A<sub>1</sub>. As the Karlovitz number increases, the correlation decreases similarly for  $Le_k = 1$  and  $Le_k \neq 1$  flames.

Figure 3.3.4 illustrates the complexity of the dependency of the displacement speed with strain rate and curvature. The evolution of  $\langle S_r^* + S_n^* \rangle_{(a_T^*, \kappa^*)}$  with  $\kappa^*$  (not displayed) presents the same trend as the evolution of the conditional mean  $\langle S_r^* + S_n^* \rangle_{\xi=\kappa^*}$  in Figs. 3.3.2b and 3.3.2c

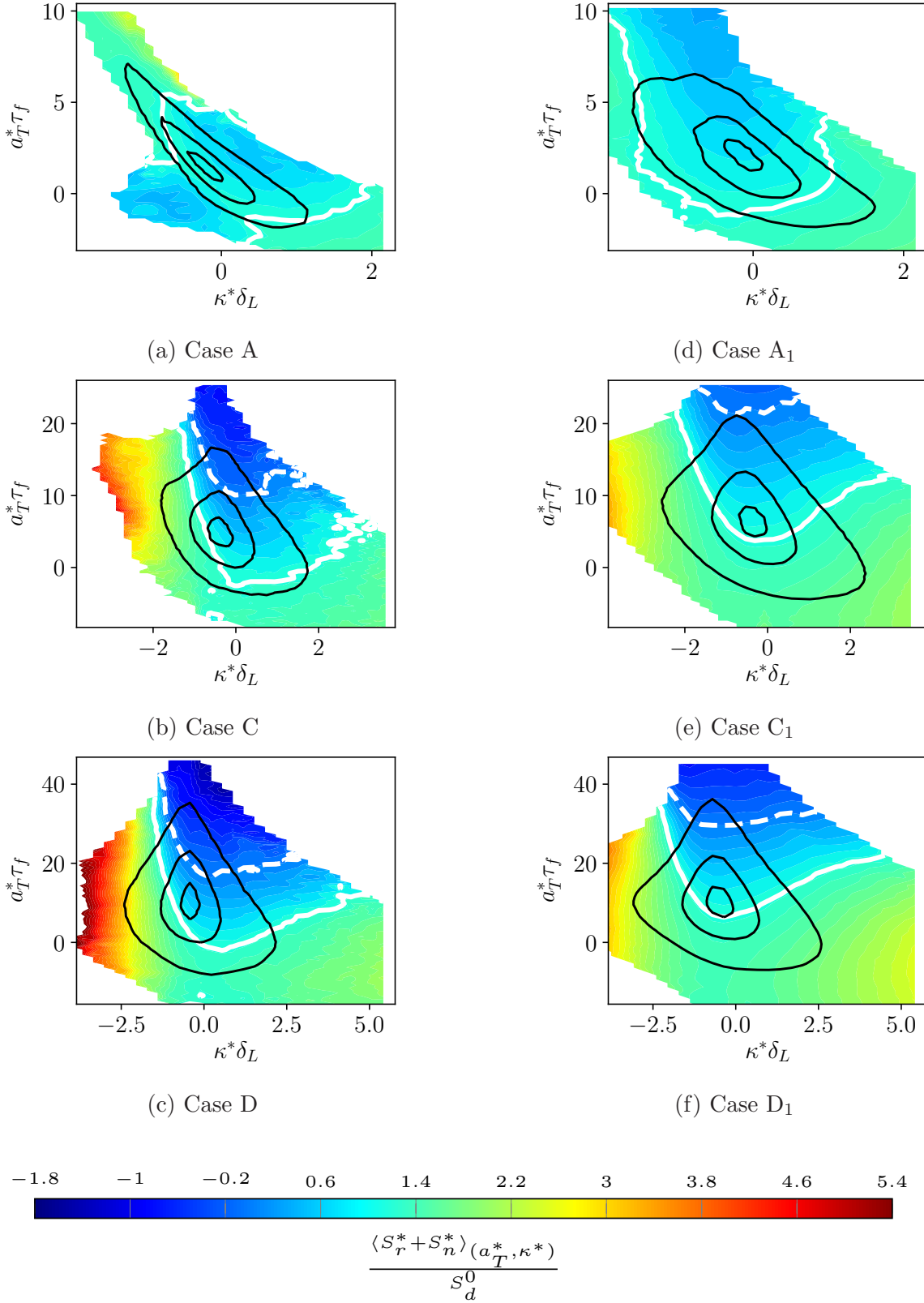


Figure 3.3.4: Evolution of the conditional mean of  $\langle S_r^* + S_n^* \rangle_{(a_T^*, \kappa^*)}$  with  $a_T^*$  and  $\kappa^*$  for: (a) to (c) the cases with  $Le_k \neq 1$  and (d) to (f) the cases with  $Le_k = 1$ . Black lines are contours of the joint probability density function (PDF) of  $a_T^*$  and  $\kappa^*$  corresponding to 10% (outer line), 50% and 90% (inner line) of its maximum value. The solid white line is the iso-contour  $\langle S_r^* + S_n^* \rangle_{(a_T^*, \kappa^*)} = \rho_u S_L / \rho^*$  and the dashed white line is the iso-contour  $\langle S_r^* + S_n^* \rangle_{(a_T^*, \kappa^*)} = 0$ .

but the slopes depend on the value of  $a_T^*$ . The evolution of  $\langle S_r^* + S_n^* \rangle_{(a_T^*, \kappa^*)}$  with  $a_T^*$  seems linear with a slope that depends on  $Ka$  and differential diffusion (through the Lewis number). Thus, when the flame is stretched, the displacement speed responds differently to tangential strain rate and curvature.

Figure 3.3.4 shows that a model for  $S_d^*$  needs to account for both strain rate  $a_T^*$  and curvature  $\kappa^*$ . To our knowledge, no such expression of  $S_d^*$  was proposed up to now for the TRZ regimes. We propose here a model for  $S_d^*$  that is based on an expression originally proposed from laminar asymptotic theories (Matalon and Matkowsky, 1982). Although there is no theoretical justification for that, previous studies (Chakraborty and Cant, 2006, 2011, 2005b; Lapointe et al., 2015; Savard and Blanquart, 2015, 2017) developed the idea that the flame structure under strong turbulent conditions might be represented in average as that of a laminar flame with modified diffusivities and Markstein lengths. Following this idea, the following expression for  $S_d^* = S_r^* + S_n^* - D^* \kappa^*$  is retained:

$$S_d^* = S_d^0 - \mathcal{L}_{a_T} a_T^* - \mathcal{L}_\kappa S_d^* \kappa^* - D^* \kappa^*, \quad (3.3.2)$$

where  $\mathcal{L}_{a_T}$  and  $\mathcal{L}_\kappa$  are turbulent Markstein lengths for strain rate and curvature that need to be defined. Equation (3.3.2) is implicit as the stretch rate due to curvature is  $S_d^* \kappa^*$  involving the displacement speed. It can be rearranged in an explicit form as:

$$S_d^* = \frac{S_d^0 - \mathcal{L}_{a_T} a_T^* - D^* \kappa^*}{1 + \mathcal{L}_\kappa \kappa^*}. \quad (3.3.3)$$

In this study, values for  $(\mathcal{L}_{a_T}, \mathcal{L}_\kappa)$  are first determined from DNS using a least square method to best fit the results of Fig 3.3.4 for each case. This fit is done by minimizing the difference  $\varepsilon$  between the DNS and the model values (Eq. 3.3.2) weighted by the joint PDF of  $a_T^*$  and  $\kappa^*$  following Eq. (3.3.4) to avoid edge effects and to give more importance to the most probable strain rate and curvature values:

$$\varepsilon = [\langle S_r^* + S_n^* \rangle_{(a_T^*, \kappa^*)} - (S_d^0 - \mathcal{L}_{a_T} a_T^* - \mathcal{L}_\kappa S_d^* \kappa^*)] p(a_T^*, \kappa^*), \quad (3.3.4)$$

where  $p(a_T^*, \kappa^*)$  is the joint PDF of  $a_T^*$  and  $\kappa^*$ .

The evolution of  $\mathcal{M}_{a_T} = \mathcal{L}_{a_T} / \delta_L^0$  and  $\mathcal{M}_\kappa = \mathcal{L}_\kappa / \delta_L^0$  with turbulence intensity are plotted in Fig. 3.3.5 for all cases. The values of  $\mathcal{L}_{a_T}$  and  $\mathcal{L}_\kappa$  for  $Ka = 0$  are obtained using stretched laminar flames simulations (detailed in Appendix D): a counter-flow premixed flame to evaluate  $\mathcal{L}_{a_T}$  using the open-source solver Cantera, and a spherical flame for  $\mathcal{L}_\kappa$  using the AVBP code.

For  $Le_k \neq 1$  flames, it can be first observed that  $\mathcal{M}_{a_T}$  and  $\mathcal{M}_\kappa$  strongly decrease with increasing  $Ka$  number, as expected from the work of Lapointe and Blanquart (2017); Lapointe et al. (2015); Savard and Blanquart (2014, 2015, 2017) and Savard et al. (2015). Indeed, they suggest that when turbulence is sufficiently intense, the turbulent diffusivity  $D_T$  becomes dominant compared to thermal or mass diffusivities. This leads to define an effective Lewis number converging toward 1 with an increasing Karlovitz number. This can be taken into



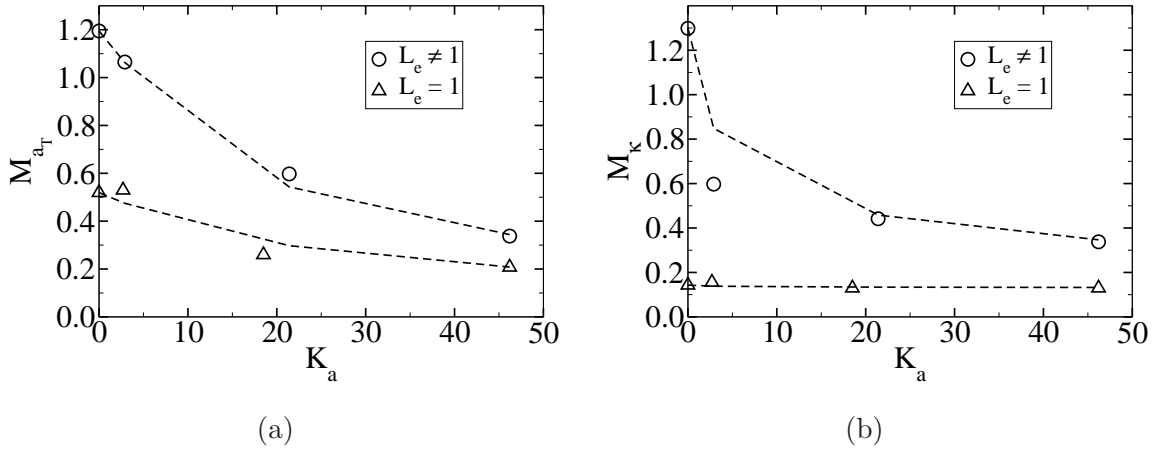


Figure 3.3.5: Evolution of effective Markstein numbers with  $Ka$ : (a) for  $\mathcal{M}_{a_T} = \mathcal{L}_{a_T} / \delta_L^0$  and (b) for  $\mathcal{M}_\kappa = \mathcal{L}_\kappa / \delta_L^0$ . The values computed from stretched laminar flame and from the optimization methods are shown with dots and the dashed lines represent the models in Eqs. (3.3.5) and (3.3.6).

account with a Markstein number tending toward zero with an increase of  $Ka$ . The values obtained for case A are also seen to be still quite far from laminar values ( $Ka = 0$ ) for curvature.

The effect of the Lewis number is first observed for a laminar flame.  $\mathcal{L}_{a_T}(Le_k = 1)$  is approximately half the value of  $\mathcal{L}_{a_T}(Le_k \neq 1)$ , which means that its sensitivity to strain rate cannot be neglected. The Markstein length  $\mathcal{L}_\kappa$  of  $Le_k = 1$  cases being lower than  $\mathcal{L}_\kappa$  of  $Le_k \neq 1$  cases and almost constant with  $Ka$  indicates a very low sensitivity to curvature.

Consistently, when the Karlovitz number increases, the decrease of  $\mathcal{L}_{a_T}$  observed for unity Lewis number flames has a very similar shape to that of non-unity Lewis number cases, while  $\mathcal{L}_\kappa$  remains very close to its laminar value, when  $Le_k = 1$ . These observations might be specific to the present fuel, thermodynamic conditions and chemical mechanism and cannot be generalized to all unity and larger than unity Lewis number flames.

However a similar evolution was described by Savard and Blanquart (2014) for the effective Lewis numbers they introduced. Using DNS of lean premixed turbulent hydrogen flames they observed that the flame tends to behave like a unity Lewis number flame when the turbulence intensity increases sufficiently. From this observation, they proposed an expression for the effective Lewis numbers (Eq. 1.6.14). In the present study, expressions for  $\mathcal{L}_{a_T}$  and  $\mathcal{L}_\kappa$  depending on the Karlovitz number are proposed inspired from Eq. (1.6.14):

$$\frac{\mathcal{L}_{a_T}}{\delta_L^0} = \frac{1}{1 + \alpha Ka^a} \frac{\mathcal{L}_{a_T}^0}{\delta_L^0} + \left(1 - \frac{1}{1 + \alpha Ka^a}\right) \mathcal{M}_{a_T}^\infty, \quad (3.3.5)$$

$$\frac{\mathcal{L}_\kappa}{\delta_L^0} = \frac{1}{1 + \beta Ka^b} \frac{\mathcal{L}_\kappa^0}{\delta_L^0} + \left(1 - \frac{1}{1 + \beta Ka^b}\right) \mathcal{M}_\kappa^\infty, \quad (3.3.6)$$

where  $\mathcal{L}_{a_T}^0$  and  $\mathcal{L}_\kappa^0$  are the laminar Markstein lengths,  $\mathcal{M}_{a_T}^\infty$  and  $\mathcal{M}_\kappa^\infty$  are asymptotic Markstein numbers at the upper range of the TRZ regime, and  $\alpha$ ,  $\beta$ ,  $a$  and  $b$  are model parameters. These parameters, reported in Table 3.8, are chosen using a least square method to best fit the evolutions of  $\mathcal{L}_{a_T}$  and  $\mathcal{L}_\kappa$ . Note that  $\mathcal{M}_{a_T}^\infty$  and  $\mathcal{M}_\kappa^\infty$  take small values in the present DNS.



As observed in Fig. 3.3.5, the proposed correlation recovers qualitatively the evolution of  $\mathcal{L}_{a_T}$  and  $\mathcal{L}_\kappa$  with  $Ka$ , although at low  $Ka$  the error is quite important for  $\mathcal{L}_\kappa$ . The behaviour

Table 3.8: Fitted parameters for modelling the Markstein numbers with Eqs.(3.3.5) and (3.3.6).

$\alpha$	$a$	$\beta$	$b$	$\mathcal{M}_{a_T}^\infty$	$\mathcal{M}_\kappa^\infty$
0.04	1.2	0.3	0.7	0.08	0.14

of Eq. (3.3.2) is assessed on  $\langle S_r^* + S_n^* \rangle_{(a_T^*, \kappa^*)}$ , using the correlations in Eqs. (3.3.5) and (3.3.6) for the turbulent Markstein lengths, for each case in Figs. 3.3.6 and 3.3.7.

Figure 3.3.6 shows the evolution of  $\langle S_r^* + S_n^* \rangle_{(a_T^*, \kappa^*)}$  with  $a_T^*$  considering a fixed  $\kappa^*$  corresponding to the maximum of joint PDF of  $a_T^*$  and  $\kappa^*$ , for DNS and Eq. (3.3.2). In the same figure is plotted the PDF of  $a_T^*$  when  $\kappa^*$  is fixed. Equation (3.3.2) well reproduces the behaviour of  $\langle S_r^* + S_n^* \rangle_{(a_T^*, \kappa^*)}$  for  $Le_k \neq 1$  cases in Figs. 3.3.6a to 3.3.6c. However,  $\langle S_r^* + S_n^* \rangle_{(a_T^*, \kappa^*)}$  is overestimated (underestimated), when the tangential strain rate is strongly negative (positive). Fortunately, these overestimations and underestimations occur at extreme values of  $a_T^*$  corresponding to very low probabilities according to the joint PDF. For  $Le_k = 1$  cases in Figs. 3.3.6d to 3.3.6f, the predictions of Eq. (3.3.2) reproduce very well the evolutions observed in DNS.

Figure 3.3.6 shows the evolution of  $\langle S_r^* + S_n^* \rangle_{(a_T^*, \kappa^*)}$  with  $\kappa^*$  considering a fixed  $a_T^*$  corresponding to the maximum of joint PDF of  $a_T^*$  and  $\kappa^*$ , for DNS and Eq. (3.3.2). In the same figure is plotted the PDF of  $\kappa^*$  when  $a_T^*$  is fixed. For  $Le_k \neq 1$  cases in Figs. 3.3.7a to 3.3.7c, Eq. (3.3.2) is in good agreement with DNS except for strongly negative and positive curvatures. For these extreme curvatures, Eq. (3.3.2) overestimates the velocity  $\langle S_r^* + S_n^* \rangle_{(a_T^*, \kappa^*)}$ . However, these overestimations occur at extreme values of  $\kappa^*$ , corresponding to very low probabilities according to the joint PDF of  $a_T^*$  and  $\kappa^*$ . Thus, these marginal values are rare and do not impact significantly the statistics of the displacement speed.

For  $Le_k = 1$  cases in Figs. 3.3.7d and 3.3.7f, the predictions of Eq. (3.3.2) are in good agreement with the DNS for negative curvatures. However, when the curvature becomes positive, Eq. (3.3.2) underpredicts the increase observed in the DNS. This leads to an underprediction of  $\langle S_r^* + S_n^* \rangle_{(a_T^*, \kappa^*)}$  by a factor close to 2 for  $\kappa^* \delta_L \geq 2$ . Note that these values correspond to highly curved front justifying, therefore, that the model is unable to reproduce accurately the observed  $\langle S_r^* + S_n^* \rangle_{(a_T^*, \kappa^*)}$ . Even if these underpredictions are observed for curvature values corresponding to relatively low probabilities of  $p(a_T, \kappa)$ , it is expected that their impact on the mean prediction of  $S_d^*$  by Eq. (3.3.2) will not be negligible.

Finally, note that  $\mathcal{L}_{a_T}$  and  $\mathcal{L}_\kappa$  have close values for non-unity Lewis numbers cases, suggesting that a single effective Markstein length should be sufficient for modelling. The use of a single length simplifies the modelling process because only one length needs to be tabulated. Here a correlation for a single effective Markstein length  $\mathcal{L}_{rn}$  is deduced from the work of Savard and Blanquart (2014) on an effective Lewis number, Eq. (1.6.14):

$$\frac{\mathcal{L}_{rn}}{\delta_L^0} = \frac{1}{1 + \alpha Ka} \frac{\mathcal{L}_{rn}^0}{\delta_L^0}, \quad (3.3.7)$$

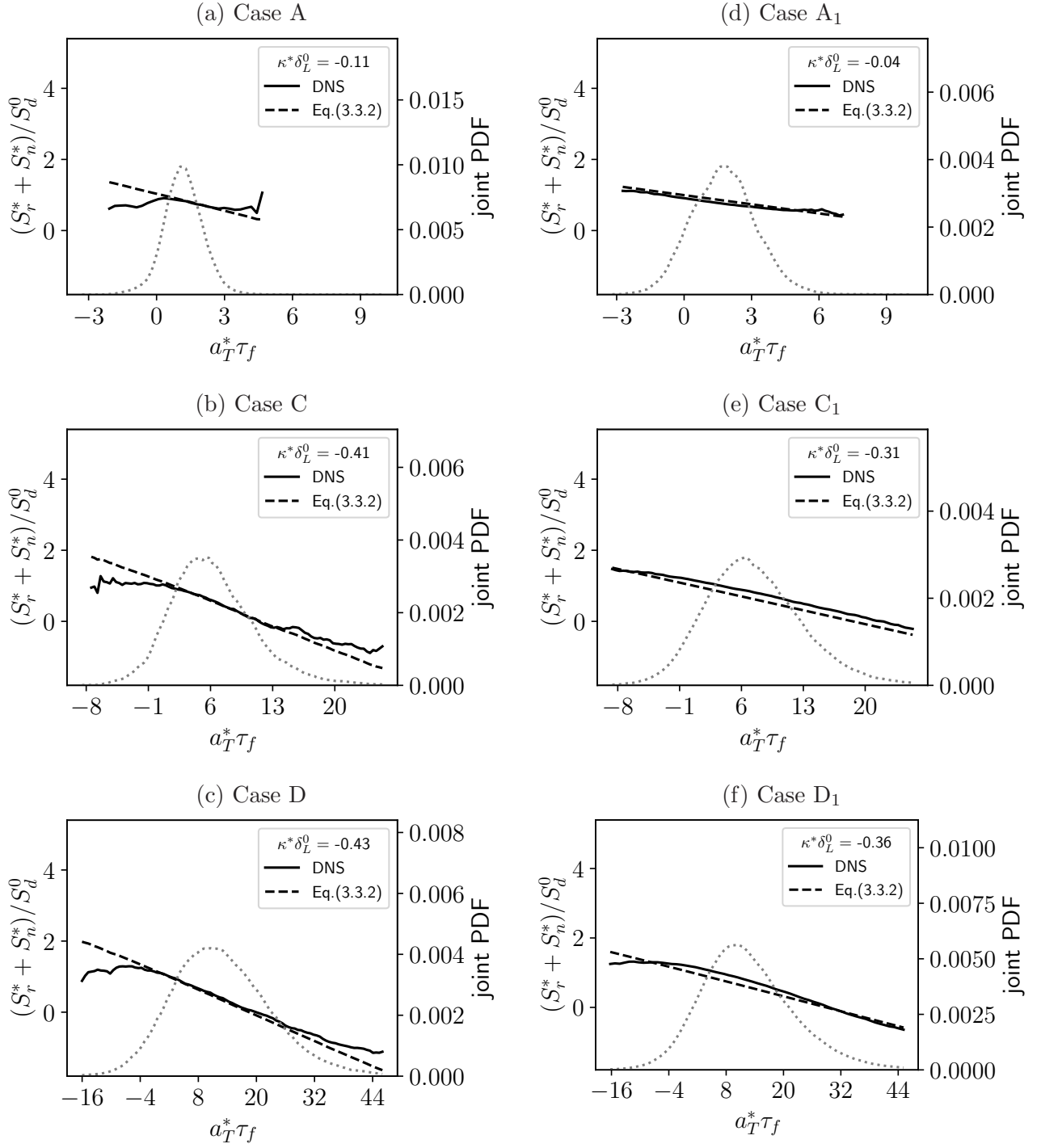


Figure 3.3.6: Evolution of  $\langle S_r^* + S_n^* \rangle_{(a_T^*, \kappa^*)}$  from DNS and predicted by Eq. (3.3.2) with  $a_T^*$  at fixed  $\kappa^*$  values for: (a) to (c) the cases with  $Le_k \neq 1$  and (d) to (f) the cases with  $Le_k = 1$ . The values of  $\kappa^*$  chosen correspond to the maxima of joint PDF. The PDF of  $a_T^*$  is shown in grey dot lines.

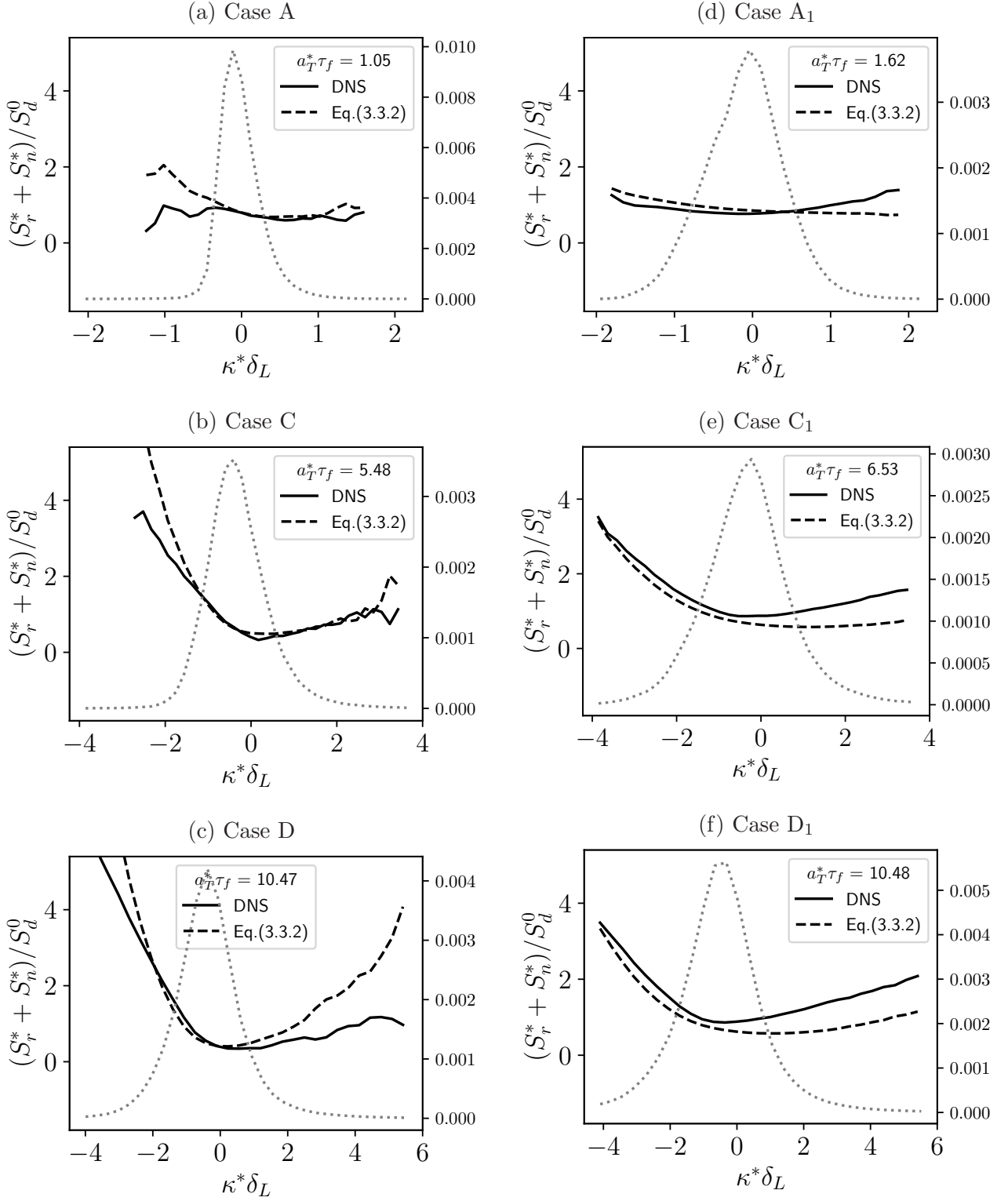


Figure 3.3.7: Evolution of  $\langle S_r^* + S_n^* \rangle_{(a_T^*, \kappa^*)}$  from DNS and predicted by Eq. (3.3.2) with  $\kappa^*$  at fixed  $a_T^*$  values for: (a) to (c) the cases with  $Le_k \neq 1$  and (d) to (f) the cases with  $Le_k = 1$ . The values of  $a_T^*$  chosen correspond to the maxima of joint PDF. The PDF of  $\kappa^*$  is shown in grey dot lines.

where  $\alpha$  is set to 0.1 to best fit both  $\mathcal{L}_{aT}$  and  $\mathcal{L}_\kappa$  through a least square method.  $\mathcal{L}_{rn}^0$  is the Markstein length of the laminar flame. Equation (3.3.7) well reproduces  $\mathcal{L}_{aT}$  and  $\mathcal{L}_\kappa$  for  $Le_k \neq 1$  cases in Fig. 3.3.8. On the contrary, this correlation strongly underestimates  $\mathcal{L}_{aT}$  and  $\mathcal{L}_\kappa$  for  $Le_k = 1$  cases, which is expected to generate non negligible errors on the predictions of  $\langle S_d \rangle_{s,c^*}$ . These errors are expected to be mainly due to the discrepancies on  $\mathcal{L}_{aT}$  because this length is not negligible compared to  $\delta_L^0$  ( $\mathcal{L}_{aT}/\delta_L^0 \approx 0.5$ ). The errors on  $\mathcal{L}_\kappa$  can be neglected because this length is very small compared to  $\delta_L^0$  ( $\mathcal{L}_\kappa/\delta_L^0 < 0.2$ ). The impact of this approach compared to the use of two distinct effective Markstein lengths will be assessed in Chapter 5.

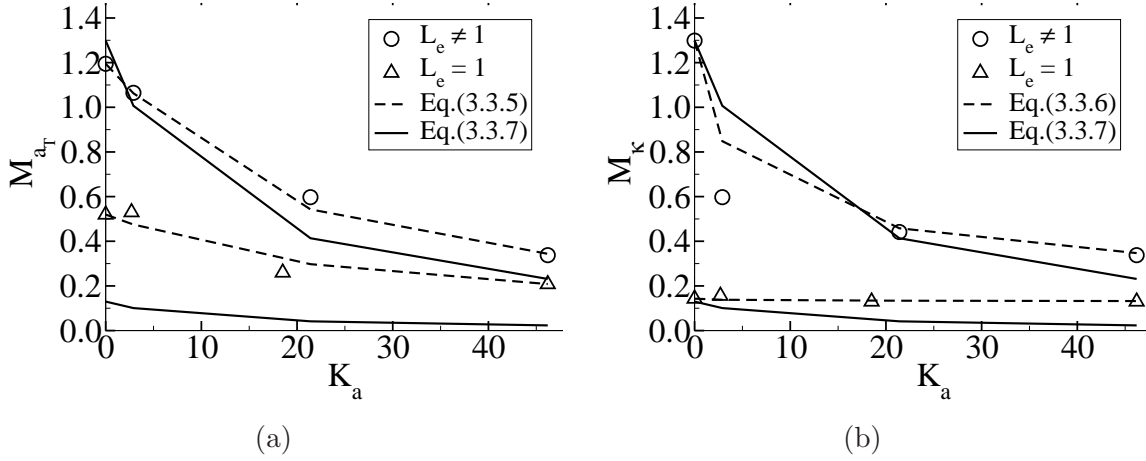


Figure 3.3.8: Evolution of the effective Markstein numbers with  $Ka$ : (a) for  $\mathcal{M}_{aT} = \mathcal{L}_{aT}/\delta_L^0$  and (b) for  $\mathcal{M}_\kappa = \mathcal{L}_\kappa/\delta_L^0$ . The values computed from stretched laminar flame and from the optimization methods are shown with symbols, the dashed lines represent the models in Eqs. (3.3.5) and (3.3.6) and the solid lines correspond to the model in Eq. (3.3.7).

### 3.4 Conclusions

In this chapter 3D-DNS of flames interacting with turbulence were examined. From this 3D-DNS, several observations were made in agreement with literature:

- When  $Ka$  increases sufficiently, a bending effect is observed on both the flame surface and the turbulent flame speed.
- When  $Ka$  increases, the flame is thickened mostly in the preheat zone. It was shown that when differential diffusion is taken into account, the flame front is also thickened in the reaction zone. Nevertheless, this thickening is relatively small compared to the one occurring in the preheat zone.
- The inner flame structure appears close to the structure of a flame in the flamelet regime in the reaction zone, whatever the turbulence intensity.

From these observations, the most relevant result toward the modelling of the FSD is that the fuel consumption can be evaluated through a particular iso-surface of progress variable. This lead to the analysis of an iso-surface of  $c = 0.8$ , which corresponds to the progress variable

of the peak of the laminar heat release rate. This specific study allows us to evaluate the impact of turbulence on the displacement speed and to propose a formulation to evaluate this speed from the knowledge of strain rate  $a_T^*$ , stretch rate due to curvature  $S_d^* \kappa^*$  and two turbulent Markstein lengths  $\mathcal{L}_{a_T}$  and  $\mathcal{L}_\kappa$ . The latter showed a decreasing evolution as the Karlovitz number increased. Models are also proposed in Eqs.(3.3.5) and (3.3.6) to evaluate these lengths knowing  $Ka$ .

Finally, these analysis provide a basis for the development of new closures in the equations of the CFM approach, as presented in Chapters 4 and 5.

# Chapter 4

## *A priori* modelling for premixed flame in the thin reaction zone regime

In this chapter, the extension of the range of applicability of the coherent flame model (CFM) approach to thin reaction zone (TRZ) regime is presented, using a large-eddy simulation (LES) formalism. Closures for each term are presented and assessed against the direct numerical simulations (DNS) presented in Chapter 3. To allow these comparisons the quantity of interests are extracted from DNS using a Reynolds averaged Navier-Stokes (RANS) approach. This RANS procedure was chosen because of the simplicity in extracting statistics from DNS, and because it allows to dispense with additional parameters such as filter size dependency. This *a priori* analysis, which enlightens on the relevance of the proposed closures, is a first step toward validation of the LES model proposed.

Thus, the present chapter is organised as follows. First, discussion on the CFM model (Richard et al., 2007) is presented leading to the description of the adapted equations of the proposed model in Section 4.1. Then, the post-processing methodology using a RANS approach is described in Section 4.2. The closures for the progress variable and the flame surface density (FSD) equations are presented and assessed against DNS in Sections 4.3 and 4.4, respectively. Finally, a discussion on the Bray-Moss-Libby (BML) model is presented leading to a new relationship between the filtered and resolved progress variable in Section 4.5.

### 4.1 Discussion on the coherent flame model

The coherent flame model is based on the concept of flame surface density (FSD), as described in Section 1.5.3. This concept of flame surface density was developed based on the assumptions of the flamelet regime:

- The flame is considered to remain infinitely thin, when it interacts with a turbulent flow. Thus, the flame front is defined as a surface separating burnt and fresh gases.
- The flame is a collection of flamelets locally propagating at the laminar flame velocity.

From these assumptions, the filtered balance equation of progress variable is written in a propagative form:

$$\frac{d\bar{\rho}\tilde{c}}{dt} + \nabla \cdot (\bar{\rho}\tilde{\mathbf{u}}\tilde{c}) + \nabla \cdot (\overline{\rho\mathbf{u}c} - \bar{\rho}\tilde{\mathbf{u}}\tilde{c}) = \rho_u S_L^0 \bar{\Sigma}, \quad (4.1.1)$$

where  $\bar{\Sigma}$  is the generalized flame surface density defined as:

$$\bar{\Sigma} = \int_0^1 \int |\nabla c| \delta(c - c^*) G_\Delta(\mathbf{x} - \mathbf{x}') d\mathbf{x}' dc^*, \quad (4.1.2)$$

where  $G_\Delta$  is the LES filter,  $\Delta$  is the width of the filter,  $\mathbf{x}$  is the position vector and  $\delta(c)$  is the Dirac function. From Eq. (4.1.2), the flame surface density along the iso-surface of the progress variable at  $c = c^*$  is defined as:

$$\bar{\Sigma}^* = \int |\nabla c| \delta(c - c^*) G_\Delta(\mathbf{x} - \mathbf{x}') d\mathbf{x}'. \quad (4.1.3)$$

When the first hypothesis of the flamelet regime is verified, the density of iso-surface  $c = c^*$  does not depend on the choice of  $c^*$  and  $\bar{\Sigma} = \bar{\Sigma}^*$ . However, as shown in Sections 1.6.1 and 3.2, one of the main characteristics of a flame in the TRZ regime is a broadening of the flame front due to intense turbulence. This observation directly invalidates the first assumption of the flamelet regime. Moreover, the thickening of the flame might be the consequence of different propagation velocities of each iso-surface of the progress variable, which are illustrated in Fig. 3.2.6 displaying for case C, large fluctuations of  $\langle \rho S_d \rangle_s^*$ , from  $0.22 \text{ kg/m}^2/\text{s}$  at  $c^* = 0.2$  to  $0.37 \text{ kg/m}^2/\text{s}$  at  $c^* = 0.8$ . Thus, the second assumption of the flamelet regime is not verified either.

Nevertheless, in the TRZ regime the reaction zone remains thin, as seen in Sections 1.6.1 and 3.2. This suggests that the surface of the reaction zone seems a relevant tracker to describe the general behaviour of the flame, in particular the flame propagation speed. Thus, the challenge is to adapt the concept of FSD to the reaction zone and, consequently, to modify the equations of the coherent flame model. The proposed approach, first presented in Section 3.2.5, consists in defining a new progress variable  $\mathcal{C}$  as:

$$\mathcal{C} = \mathcal{H}(c - c^*), \quad (4.1.4)$$

where  $\mathcal{H}(c)$  is the Heaviside function giving  $\mathcal{C} = 0$  when  $c < c^*$  and  $\mathcal{C} = 1$  otherwise. Following the work of Knudsen and Pitsch (2008) and the derivation of the balance equation of  $\mathcal{C}$  given in Appendix C, the filtered transport equations of the CFM approach become:

$$\frac{\partial \bar{\rho}\tilde{\mathcal{C}}}{\partial t} + \nabla \cdot (\bar{\rho}\tilde{\mathbf{u}}\tilde{\mathcal{C}}) = \underbrace{-\nabla \cdot (\overline{\rho\mathbf{u}\mathcal{C}} - \bar{\rho}\tilde{\mathbf{u}}\tilde{\mathcal{C}})}_{T_1} + \underbrace{\langle \rho S_d \rangle_{s,c^*} \bar{\Sigma}^*}_{T_2}, \quad (4.1.5)$$

$$\frac{\partial \bar{\Sigma}^*}{\partial t} + \nabla \cdot (\tilde{\mathbf{u}} \bar{\Sigma}^*) = - \underbrace{\nabla \cdot (\bar{\mathbf{u}} \bar{\Sigma}^* - \tilde{\mathbf{u}} \bar{\Sigma}^*)}_T + \underbrace{\langle \nabla \cdot \mathbf{u} - \mathbf{nn} : \nabla \mathbf{u} \rangle_{s,c^*} \bar{\Sigma}^*}_S + \underbrace{\langle S_d \kappa \rangle_{s,c^*} \bar{\Sigma}^*}_C - \underbrace{\nabla \cdot (\langle S_d \mathbf{n} \rangle_{s,c^*} \bar{\Sigma}^*)}_P, \quad (4.1.6)$$

where  $\bar{\Sigma}^*$  is the FSD along the iso-surface of the progress variable at  $c = c^*$  (Eq. 4.1.3). In these equations, 6 terms need to be closed:

1. The unresolved turbulent transport  $T_1 = \nabla \cdot (\bar{\rho} \mathbf{u} \bar{\mathcal{C}} - \bar{\rho} \tilde{\mathbf{u}} \tilde{\mathcal{C}})$  in Eq. (4.1.5),
2. The surface averaged displacement speed weighted with density  $\langle \rho S_d \rangle_{s,c^*}$  involved in  $T_2$  (Eq. 4.1.5),
3. The unresolved turbulent transport  $T = \nabla \cdot (\bar{\mathbf{u}} \bar{\Sigma}^* - \tilde{\mathbf{u}} \bar{\Sigma}^*)$  in Eq. (4.1.6),
4. The normal propagation term  $P = \nabla \cdot (\langle S_d \mathbf{n} \rangle_{s,c^*} \bar{\Sigma}^*)$  in Eq. (4.1.6),
5. The tangential strain rate  $\langle a_T \rangle_{s,c^*}$  involved in  $S$  (Eq. 4.1.6),
6. The stretch due to curvature  $\langle S_d \kappa \rangle_{s,c^*}$  involved in  $C$  (Eq. 4.1.6).

The next section describes the post-processing method. In Sections 4.3 and 4.4, closures following LES formalism for these terms are proposed and compared to the DNS presented in Chapter 3.

## 4.2 Post-processing methodology of DNS for *a priori* validation

As mentioned previously, the closures presented in Sections 4.3 and 4.4 are expressed following LES formalism. However, for the sake of simplicity, the post-processing procedure used to analyse the flame for *a priori* model development consists in a RANS validation. This procedure allows, as a first step, to verify the relevance of the closures proposed in this work.

The analysis of the flame consists in extracting the mean part and the fluctuating part of quantities of interest in RANS. In this study we discretize the simulation domain along the propagation axis, as illustrated in Fig. 4.2.1. The flames being statistically uniform in the y and z directions, a spatial averaging of  $\mathcal{C}$  in each slices of thickness  $\delta_x$  is performed allowing to get profiles of  $\bar{\mathcal{C}}$  and  $\tilde{\mathcal{C}}$  against the propagation axis  $x$ . The value of  $\delta_x$  is chosen as  $\delta_x = 2\Delta_x$ , where  $\Delta_x$  is the cell size of the DNS.

Then, from the extraction of the iso-surface  $c = c^*$ , the surface averaging operation, defined in Eq. (4.2.1), is applied to each variable of interest. Finally, from the profiles of  $\tilde{\mathcal{C}}$  and of



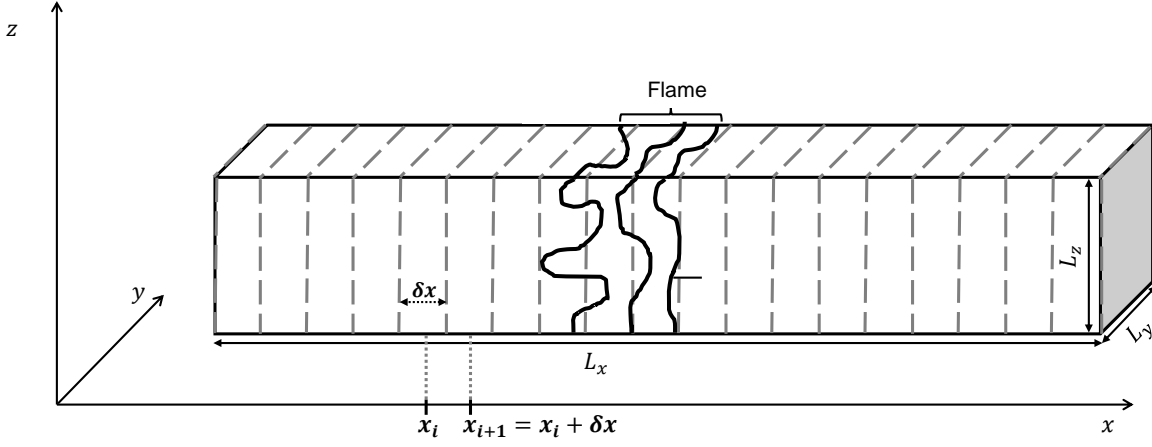


Figure 4.2.1: Schematic view of the post-processing method.

$\langle Q \rangle_{s,c^*}$  versus  $x$ , the RANS profiles of  $\langle Q \rangle_{s,c^*}$  against  $\tilde{\mathcal{C}}$  are deduced.

$$\langle Q \rangle_{s,c^*} = \frac{\int_{V_x} Q \delta \mathcal{A}^*}{\mathcal{A}^*}, \quad (4.2.1)$$

where  $Q$  is a general quantity,  $V_x$  is the volume of the slice at position  $x$ ,  $\mathcal{A}^*$  is the area of flame surface contained in the slice and  $\delta \mathcal{A}^*$  is an element of flame surface. In this approach, the quantities of interest are time averaged because the flames reach a quasi steady state.

### 4.3 Closure of the transport equation of progress variable

In this section, the closure of terms involved in the transport equation of progress variable  $\mathcal{C}$  (Eq. 4.1.5) are presented.

#### 4.3.1 Closure of the turbulent flux

Figure 4.3.1 shows the unresolved transport term  $T_1$  in Eq. (4.1.5), extracted from DNS using the procedure presented in Section 4.2, as a function of  $\tilde{\mathcal{C}}$  for cases A, C and D. This term is also compared with the progress variable propagation term  $T_2 = \langle \rho S_d \rangle_{s,c^*} \bar{\Sigma}^*$  in the same figure. In Fig. 4.3.1, for each case  $T_1$  remains significantly smaller than  $T_2$ . This suggests that effort should be spent on modelling the progress variable propagation term. Thus, for this unresolved transport term, the model proposed by Richard et al. (2007) appears sufficient. A simple gradient assumption combined to a turbulent diffusive mechanism is used, as proposed by Boger (2000):

$$\nabla \cdot (\overline{\rho \mathbf{u} \mathcal{C}} - \bar{\rho} \tilde{\mathbf{u}} \tilde{\mathcal{C}}) = -\nabla \cdot \left( \bar{\rho} \frac{\nu_t}{S_{ct}} \nabla \tilde{\mathcal{C}} \right) \quad (4.3.1)$$

where  $S_{ct}$  is a sub-grid scale Schmidt number, and  $\nu_t$  is the sub-grid scale viscosity estimated as:

$$\nu_t = C u'_\Delta \Delta, \quad (4.3.2)$$

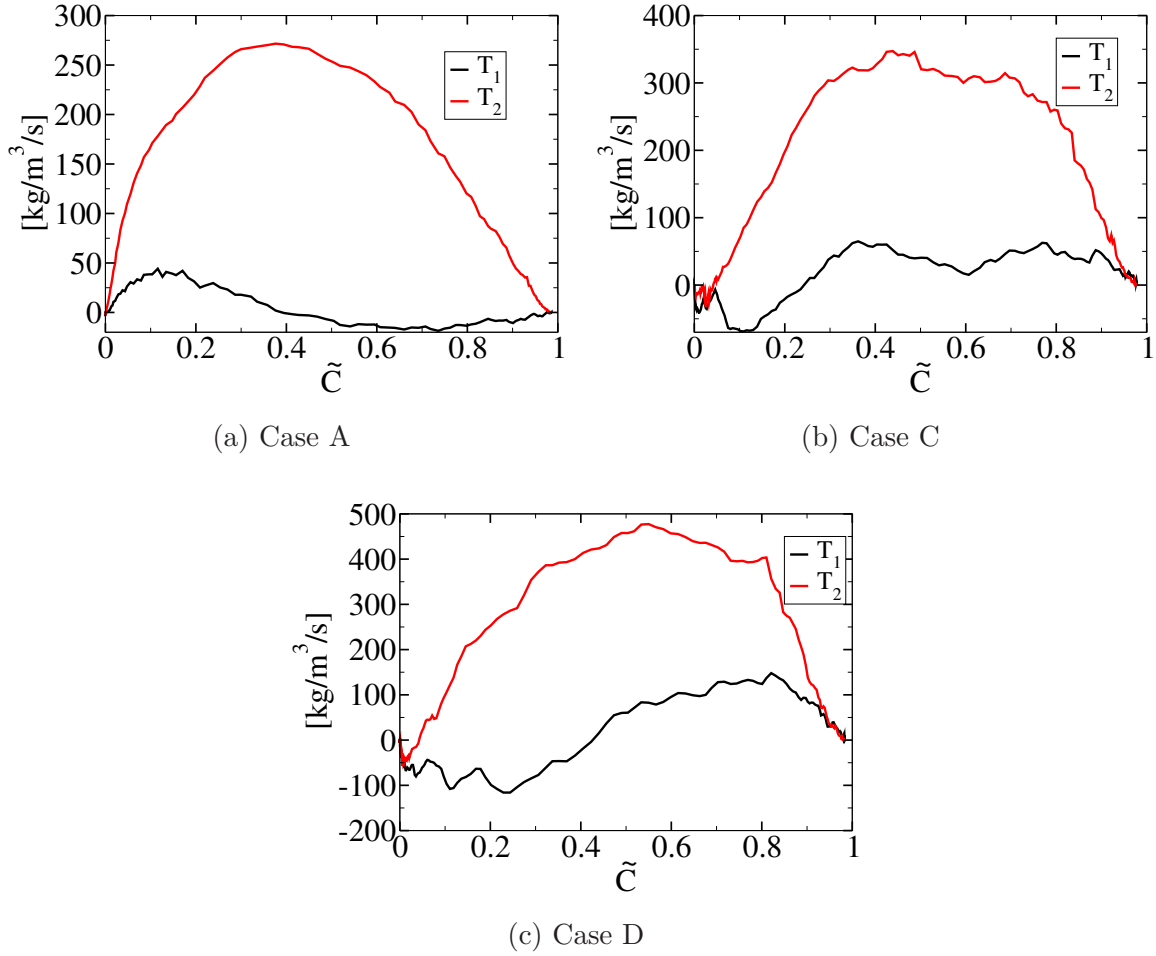


Figure 4.3.1: Comparison of the source terms involved in Eq. (4.1.5) as functions of  $\tilde{C}$ .  $T_1$  is the unresolved transport term  $\nabla \cdot (\overline{\rho \mathbf{u} \tilde{C}} - \tilde{\rho} \tilde{\mathbf{u}} \tilde{C})$  and  $T_2$  is the propagation term  $\langle \rho S_d \rangle_{s,c^*} \tilde{\Sigma}^*$ .

where  $u'_\Delta$  of the turbulent structures of size  $\Delta$  (the LES filter width),  $C$  is a constant, which is usually fixed to 0.12 in the absence of mean velocity gradient in the flow (corresponding to homogeneous isotropic turbulence). Equation (4.3.2) becomes in RANS modeling:

$$\nu_t = C u'_t l_t, \quad (4.3.3)$$

As suggested by Rymer (2001), for RANS modelling, and Richard et al. (2007), for LES modelling, a contribution corresponding to thermal expansion should be taken into account. In this study the model proposed by Richard et al. (2007) is chosen, and as suggested the simple case of a one-dimensional steady laminar flame is analysed to evaluate this contribution.

When a one-dimensional steady laminar flame is considered, the flux passing through the flame front,  $\rho \mathbf{u}$ , is constant leading to:

$$\overline{\rho \mathbf{u} \tilde{C}} = \tilde{\rho} \tilde{\mathbf{u}} \tilde{C} = \tilde{\rho} \tilde{\mathbf{u}} \tilde{C}. \quad (4.3.4)$$

In a steady laminar flame, the relationship between the flow velocity  $\mathbf{u}$  and the displacement speed of the flame is  $\mathbf{u} = -S_d \mathbf{n}$ , where  $\rho S_d = \rho_u S_L^0$  because the flame is steady. The former

and the latter relationships combined with Eq. (4.3.4) leads to:

$$\overline{\rho \mathbf{u} \tilde{C}} - \bar{\rho} \tilde{\mathbf{u}} \tilde{C} = -\rho_u S_L^0 (\bar{C} - \tilde{C}) \bar{\mathbf{n}}, \quad (4.3.5)$$

where  $\bar{\mathbf{n}} = -\nabla \bar{C} / |\nabla \bar{C}|$  is the normal vector to the filtered iso-surface of progress variable pointing toward the fresh gases. Finally, the complete model for the unresolved transport term is:

$$\nabla \cdot (\overline{\rho \mathbf{u} \tilde{C}} - \bar{\rho} \tilde{\mathbf{u}} \tilde{C}) = -\nabla \cdot \left( \bar{\rho} \frac{\nu_t}{S_{ct}} \nabla \tilde{C} \right) - \rho_u S_L^0 \nabla \cdot ((\bar{C} - \tilde{C}) \bar{\mathbf{n}}) \quad (4.3.6)$$

Figure 4.3.2 compares the simple gradient model (Eq. 4.3.1) and the model completed with the thermal expansion contribution (Eq. 4.3.6) to the DNS following the procedure presented in Section 4.2.

For high Karlovitz number cases (case C, C<sub>1</sub>, D and D<sub>1</sub>), the simple gradient model is in good agreement with the DNS. However, for low Karlovitz number the simple gradient model is unable to reproduce the evolution observed. Indeed, the DNS results suggest that for cases A and A<sub>1</sub> the unresolved transport corresponds to counter-gradient turbulent diffusion. The model taking into account thermal expansion (given in Eq. (4.3.6) is plotted in this same figure. For low Karlovitz number cases, this model improves significantly the predictions of the unresolved transport term  $T_1$ . In addition, this model presents a similar evolution with the filtered progress variable for high Karlovitz numbers cases as the simple gradient model.

Veynante et al. (1997) proposed a criterion to determine whether a turbulent flame is in the counter-gradient regime or in the simple gradient regime. Counter-gradient diffusion is observed when:

$$N_B \equiv \frac{\tau S_L^0}{2\alpha u'} > 1, \quad (4.3.7)$$

where  $\alpha$  is an efficiency function introduced by Veynante et al. (1997) to take into account the variable ability of turbulent eddies to act on the flame front. This efficiency proposed by Veynante et al. (1997) is similar to the efficiency function introduced by Meneveau and Poinso (1991) in their intermittent turbulent net flame stretch (ITNFS) model.

Table 4.1: Estimated values of the efficiency function  $\alpha$  using ITNFS model (Meneveau and Poinso, 1991) and of  $N_B$  defined in Eq. (4.3.7) for each case.

Case	$u'_t / S_L^0$	$l_t / \delta_L^0$	$\alpha$	$N_B$
A	2.9	3.3	0.48	2.5
C	12.5	4.3	0.7	0.4
D	21.1	4.4	0.72	0.2
A <sub>1</sub>	2.5	5.1	0.8	1.9
C <sub>1</sub>	11.9	4.9	0.82	0.4
D <sub>1</sub>	22.1	5.1	0.86	0.2

The magnitudes of  $\alpha$  are evaluated using the ITNFS model (Meneveau and Poinso, 1991), and are reported in Table 4.1. In this table is also reported  $N_B$  for each DNS case. For case A and A<sub>1</sub>  $N_B$  is 2.5 and 1.9, respectively, confirming that for low Karlovitz cases the flames are in a counter-gradient turbulent diffusion regime.

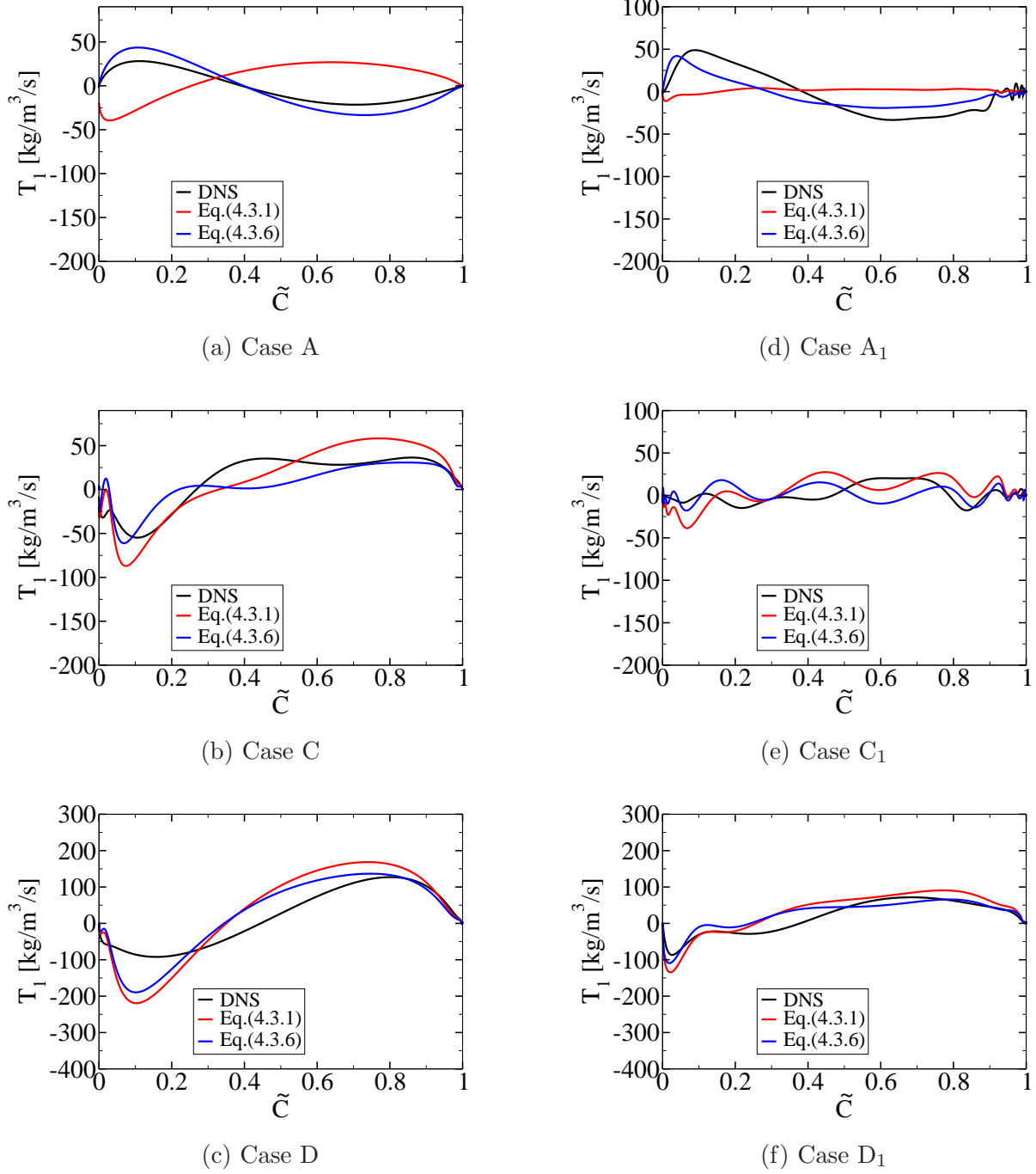


Figure 4.3.2: Comparison  $T_1 = \nabla \cdot (\overline{\rho u \tilde{C}} - \tilde{\rho} \tilde{u} \tilde{C})$  extracted from the DNS with both the simple gradient model (Eq. 4.3.1) and the model including the thermal expansion (Eq. 4.3.6) as functions of  $\tilde{C}$  for: (a) to (c) the cases with  $Le_k \neq 1$  and (d) to (f) the cases with  $Le_k = 1$ .

### 4.3.2 Closure of the displacement speed

As suggested in Fig. 4.3.1, the most important term to close in Eq. (4.1.5) is the progress variable propagation term  $\langle \rho S_d \rangle_{s,c^*} \bar{\Sigma}^*$ .

We assume that  $\langle \rho S_d \rangle_{s,c^*}$  is equal to  $\rho^* \langle S_d \rangle_{s,c^*}$ , where  $\rho^*$  is the density at  $c = c^*$  of the laminar flame. This assumption seems reasonable because on a  $c^*$  iso-surface  $\rho$  is expected to weakly fluctuate. So, the term to model is the displacement speed.

Starting from Eq. (3.3.3) we propose to express the mean displacement speed as the average over all possible curvature values.

$$\langle \rho S_d \rangle_{s,c^*} = \rho^* \int_{-\frac{1}{\mathcal{L}_\kappa} + \varepsilon}^{+\infty} \frac{S_d^0 - \mathcal{L}_{a_T} \langle a_T \rangle_{s,c^*} - D^* \kappa}{1 + \mathcal{L}_\kappa \kappa} p(\kappa) d\kappa \quad (4.3.8)$$

where  $p(\kappa)$  is the probability density function (PDF) of  $\kappa$ . The lower limit of the integral is chosen as  $-1/\mathcal{L}_\kappa + \varepsilon$  to ensure the denominator remains larger than  $\varepsilon$ . In Fig. 4.3.3, this limit is plotted as a vertical line which is shown to correspond to very small probabilities of  $\kappa$ . For case C for instance, the integral of the PDF of  $\kappa$  using the lower limit  $-1/\mathcal{L}_\kappa + \varepsilon$  is equal to 0.998, 0.993 and 0.986 for  $\tilde{\mathcal{C}} = 0.2, 0.5$  and  $0.8$ , respectively. This confirms that the lower limit  $-1/\mathcal{L}_\kappa + \varepsilon$  includes the essential part of the PDF of  $\kappa$  and as a consequence the integral in Eq. (4.3.8) covers the most significant curvatures contributing to the displacement speed.

At high Karlovitz numbers, strain rate and curvature become decorrelated as shown in Section 3.3.2. So, we assume that  $\langle a_T \rangle_{s,c^*}$  does not depend on curvature in Eq. (4.3.8). At low Karlovitz numbers on the other hand, the impact of strain rate on the displacement speed becomes small as it becomes nearly uniform and close to  $S_d^0$ .

The PDF  $p(\kappa)$  is modelled presuming a Gaussian shape:

$$p(\kappa) = \frac{1}{\sqrt{2\sigma^2\pi}} \exp\left(-\frac{(\kappa - \mu)^2}{2\sigma^2}\right), \quad (4.3.9)$$

where  $\mu = \langle \kappa \rangle_{s,c^*}$  is the surface average of  $\kappa$  and  $\sigma^2$  is the variance of  $\kappa$ , defined as:

$$\sigma^2 = \langle \kappa^2 \rangle_{s,c^*} - \langle \kappa \rangle_{s,c^*}^2. \quad (4.3.10)$$

Figure 4.3.3 presents the PDF extracted from the DNS and the modelled one for cases C and C<sub>1</sub> at three positions in the flame front corresponding to  $\tilde{\mathcal{C}} = 0.2, 0.5$  and  $0.8$ . The agreement is good although the model tends to over-predict the PDF width. This could induce some larger discrepancies in *a posteriori* testing than in *a priori* because all sub-models interact with each other, which might enhance errors. To better reproduce the PDF observed in DNS, the presumed PDF can be modified through the variance  $\sigma^2$ . Figure 4.3.4 compares the PDF extracted from case C to the presumed PDF (Eq. 4.3.9) using Eq. (4.3.10) to compute the variance of  $\kappa$  and using half the variance:

$$\sigma^2 = \frac{\langle \kappa^2 \rangle_{s,c^*} - \langle \kappa \rangle_{s,c^*}^2}{2}. \quad (4.3.11)$$

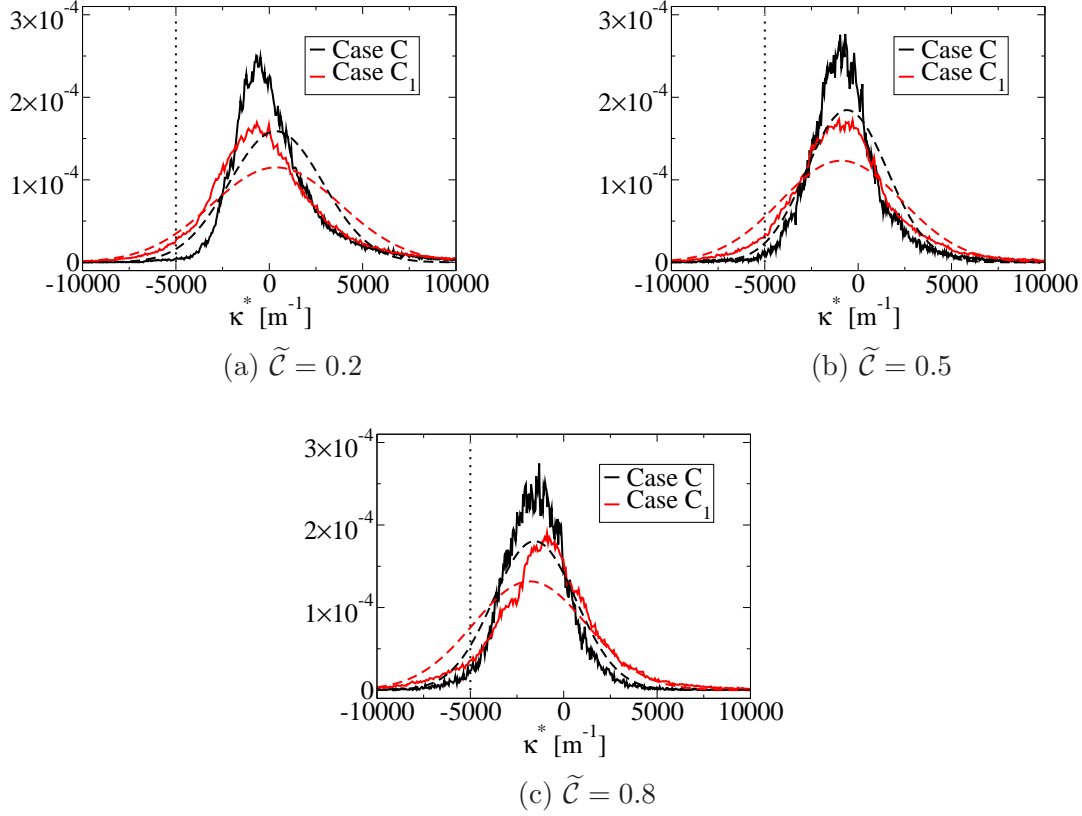


Figure 4.3.3: Probability density function (PDF) of  $\kappa$  in solid line compared to a presumed Gaussian PDF, defined in Eq. (4.3.9) in dashed line: (a) for  $\tilde{\mathcal{C}} = 0.2$ , (b) for  $\tilde{\mathcal{C}} = 0.5$  and (c) for  $\tilde{\mathcal{C}} = 0.8$ . The vertical dotted line represents the value of  $\kappa$  where  $1 + \mathcal{L}_\kappa \kappa$  is zero for the case C (for the case  $C_1$  this value is approximately  $-20000 \text{ m}^{-1}$ ).

In the rest of this chapter, the variance for curvature extracted from DNS (Eq. 4.3.10) is used to evaluate the potential of the model for displacement speed. Nevertheless, the impact of the width of the presumed PDF will be assessed in Chapter 5.

To complete the closure of the displacement speed, models for curvature  $\langle \kappa \rangle_{s,c^*}$  and its variance, involved in the PDF  $p(\kappa)$  (Eq. 4.3.9), are needed. Mechanisms linked to curvature are propagative phenomena (Trouvé and Poinso, 1994). This means that they are positive in the fresh gases side and negative in the burned gases side. Thus, Rymer (2001) proposed a model, that is adapted to the approach presented in this study using  $\bar{\mathcal{C}}$ :

$$\langle \kappa \rangle_{s,c^*} = \beta_1 \frac{c_1 - \bar{\mathcal{C}}}{\bar{\mathcal{C}}(1 - \bar{\mathcal{C}})} \bar{\Sigma}^*, \quad (4.3.12)$$

where  $\beta_1$  and  $c_1$  are model parameters. Moreover, Rymer (2001) also proposed a closure for curvature vanishing for planar laminar flames by introducing  $|\nabla \bar{\mathcal{C}}|$ . The retained model for the rest of this study is then:

$$\langle \kappa \rangle_{s,c^*} = \beta_1 \frac{c_1 - \bar{\mathcal{C}}}{\bar{\mathcal{C}}(1 - \bar{\mathcal{C}})} (\bar{\Sigma}^* - |\nabla \bar{\mathcal{C}}|). \quad (4.3.13)$$

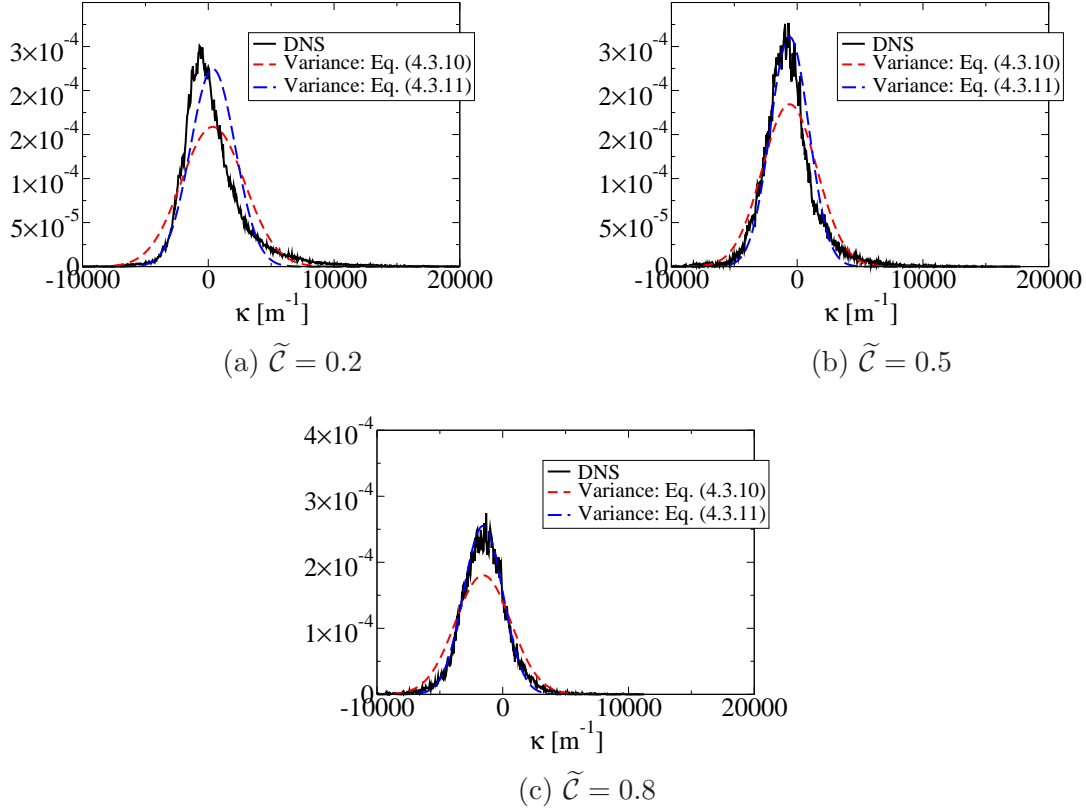


Figure 4.3.4: Probability density function (PDF) of  $\kappa$  in solid line compared to presumed PDF for case C: (a) for  $\tilde{C} = 0.2$ , (b) for  $\tilde{C} = 0.5$  and (c) for  $\tilde{C} = 0.8$ . The presumed PDF tested are the Gaussian presumed PDF defined in Eq. (4.3.9) using the variance of curvature extracted from DNS (Eq. 4.3.10) and using half the variance (Eq. 4.3.11) in red and blue dashed lines, respectively.

The parameters in Eq. (4.3.13) are chosen as  $\beta_1 = 4/3$  and  $c_1 = 0.5$  (values suggested by Rymer (2001)). The closure of the curvature term in Eq. (4.3.13) is compared to DNS results in Fig. 4.3.5, following the procedure presented in Section 4.2. It is noteworthy that  $\bar{C}$ ,  $\bar{\Sigma}^*$  and  $|\nabla \bar{C}|$  used to compute  $\langle \kappa \rangle_{s,c^*}$  are the exact values from the DNS. The comparison in Fig. 4.3.5 shows a good agreement between the model and the DNS, especially for the  $Le_k = 1$  cases. In addition, although this closure was proposed for the flamelet regime, it becomes even more accurate as the Karlovitz number increases.

In Fig. 4.3.5b the DNS results using the ARC mechanism for case C is also presented in dashed line. Being very close to that obtained with the 2-step scheme, we can conclude that flame curvature statistics are hardly affected by the chemistry description.

Another important component to model is the variance of the curvature,  $\sigma_\kappa^2$ , which is involved in the models for displacement speed and stretch due to curvature through the presumed PDF of curvature. The variance of curvature is defined with Eq. (4.3.10) involving  $\langle \kappa^2 \rangle_{s,c^*}$ . A model of  $\langle \kappa^2 \rangle_{s,c^*}$  is then needed. Hawkes et al. (2009) proposed a model given by the following

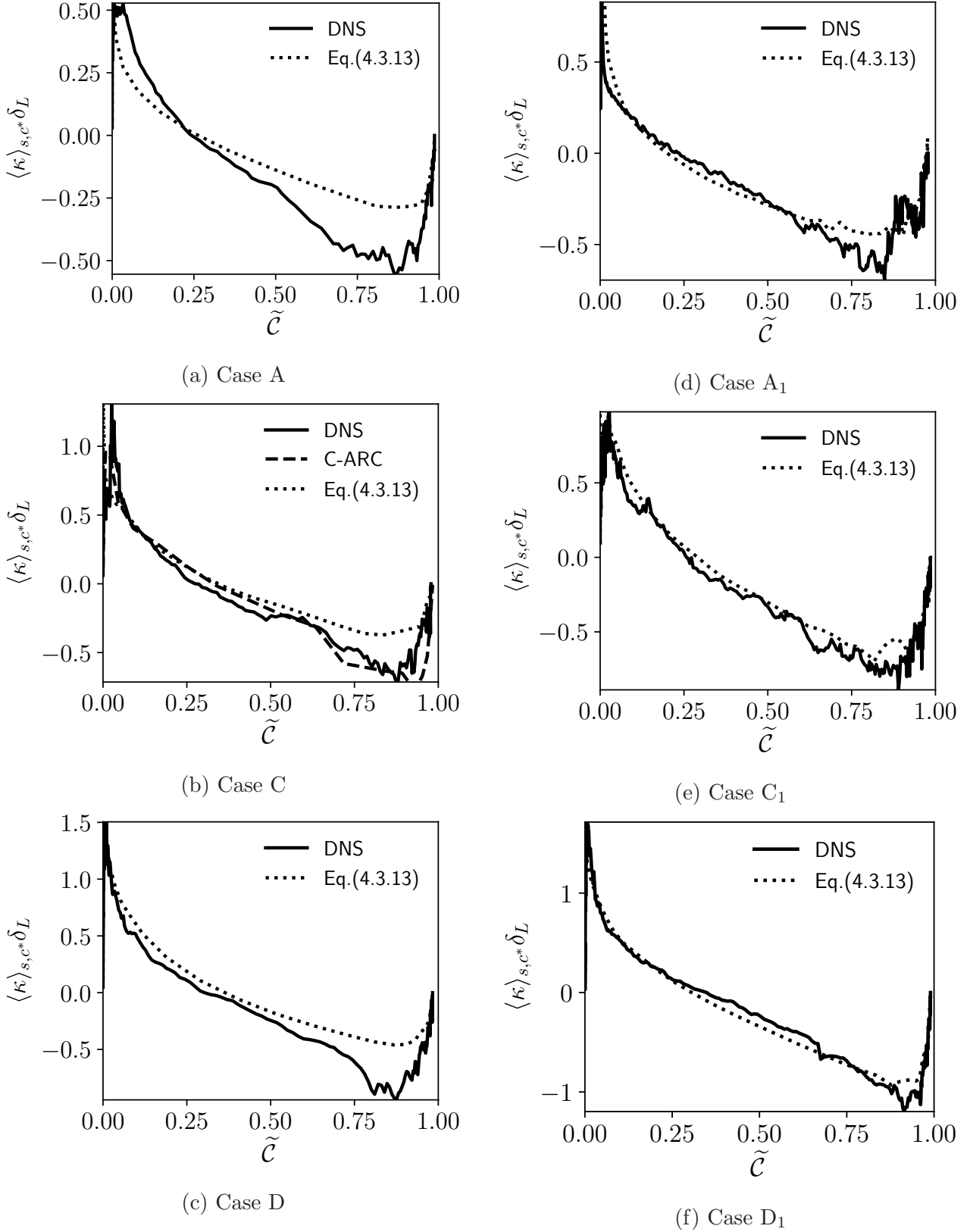
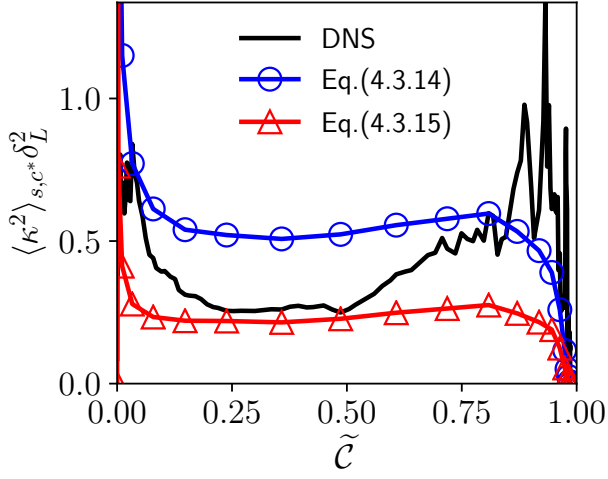
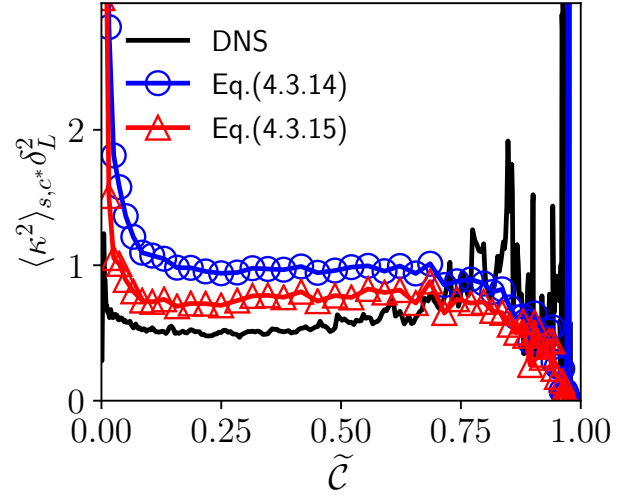
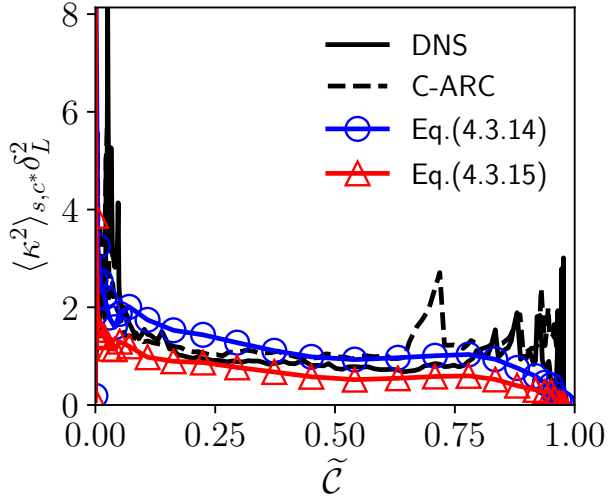


Figure 4.3.5: Comparison of the model for the curvature  $\langle \kappa \rangle_{s,c^*}$  given in Eq. (4.3.13) with the data from the DNS versus  $\tilde{C}$  for : (a) to (c) the cases with  $Le_k \neq 1$  and (d) to (f) the cases with  $Le_k = 1$ . Dashed line in (b) represents the curvature extracted from the simulation using ARC mechanism (case C-ARC).

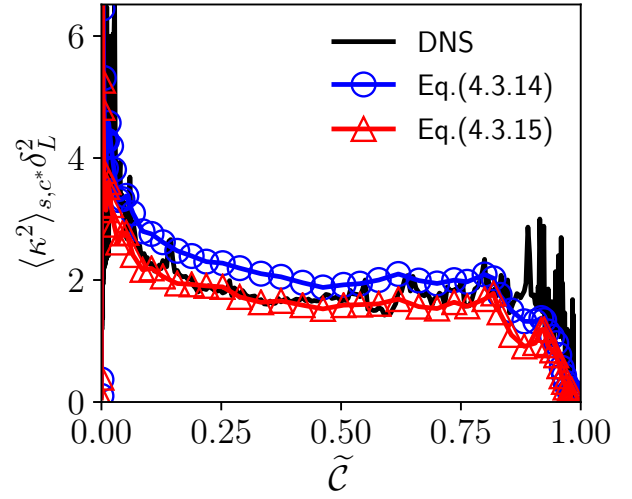
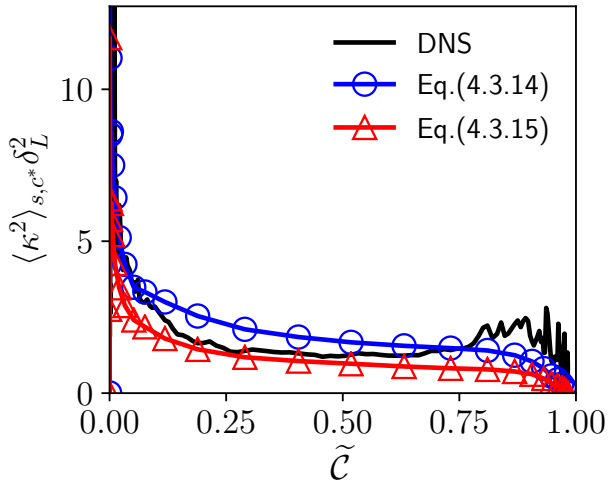




(a) Case A

(d) Case A<sub>1</sub>

(b) Case C

(e) Case C<sub>1</sub>

(c) Case D

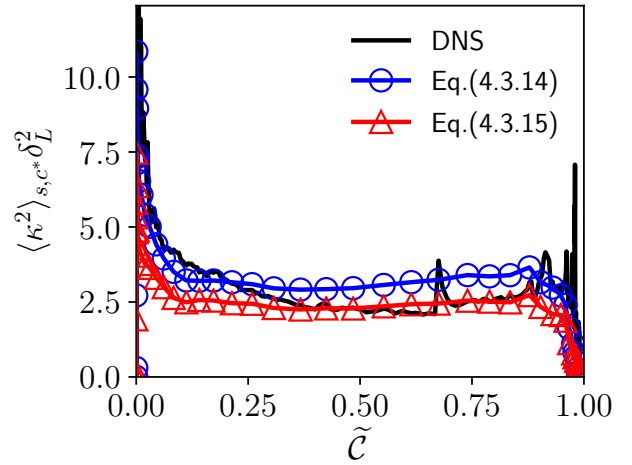
(f) Case D<sub>1</sub>

Figure 4.3.6: Comparison of the model for  $\langle \kappa^2 \rangle_{s,c^*}$  (Eq.4.3.15) with the data from the DNS and the model proposed by Hawkes et al. (2009) (Eq. 4.3.14) versus  $\tilde{C}$  for: (a) to (c) the cases with  $Le_k \neq 1$  and (d) to (f) the cases with  $Le_k = 1$ . Dashed line in (b) represents  $\langle \kappa^2 \rangle_{s,c^*}$  extracted from the simulation using ARC mechanism (case C-ARC).

equation:

$$\langle \kappa^2 \rangle_{s,c^*} = (1 - \langle n_i \rangle_{s,c^*} \langle n_i \rangle_{s,c^*})^2 \frac{\bar{\Sigma}^{*2}}{\bar{\mathcal{C}}^2 (1 - \bar{\mathcal{C}})^2}, \quad (4.3.14)$$

where  $\langle n_i \rangle_{s,c^*}$  is the  $i^{th}$  component of surface averaged flame normal vector,  $\langle \mathbf{n} \rangle_{s,c^*}$ . The factor  $1 - \langle n_i \rangle_{s,c^*} \langle n_i \rangle_{s,c^*}$  is a resolution factor introduced by Cant et al. (1991) for vanishing the net destruction of FSD when the flame is fully resolved.

To take into account this vanishing, we chose to introduce the resolved FSD  $|\nabla \bar{\mathcal{C}}|$  by analogy with the model for  $\langle \kappa \rangle_{s,c^*}$ :

$$\langle \kappa^2 \rangle_{s,c^*} = \beta_2 \frac{1}{\bar{\mathcal{C}}^2 (1 - \bar{\mathcal{C}})^2} (\bar{\Sigma}^* - |\nabla \bar{\mathcal{C}}|)^2, \quad (4.3.15)$$

where  $\beta_2$  is a model parameter fixed to one in the rest of this study.

Both models presented in Eqs. (4.3.14) and (4.3.15) are compared to the DNS in Fig. 4.3.6. As for curvature, the values used for  $\bar{\mathcal{C}}$ ,  $\bar{\Sigma}^*$  and  $|\nabla \bar{\mathcal{C}}|$  in the model are the ones extracted from the DNS. For non-unity Lewis number cases, the order of magnitude of  $\langle \kappa^2 \rangle_{s,c^*}$  is well reproduced by Eq. (4.3.15). For case A, the model tends to under-predict the strong increase of  $\langle \kappa^2 \rangle_{s,c^*}$  towards  $\bar{\mathcal{C}} = 0$  and nearly fails to predict the increase of  $\langle \kappa^2 \rangle_{s,c^*}$  when  $\bar{\mathcal{C}} \rightarrow 1$ . For cases C and D, the agreement with the DNS is much better. Note that the oscillations observed on the DNS results for  $\bar{\mathcal{C}}$  close to zero and 1 might be due to the very large curvatures observed in the regions. For the unity Lewis number cases, the agreement with the DNS is very good at all Karlovitz numbers.

Model proposed by Hawkes et al. (2009) presents similar results at large Karlovitz numbers, which is not surprising as both models assume similar expressions. At the same time, Hawkes model tends to over-predict  $\langle \kappa^2 \rangle_{s,c^*}$  by a factor of three for case A, unlike Eq. (4.3.15).

In Fig. 4.3.6b,  $\langle \kappa^2 \rangle_{s,c^*}$  obtained for the DNS using the ARC mechanism is also presented. Being very close to that obtained with the 2-step scheme, we can conclude that flame curvature statistics are hardly affected by the chemistry description and that the 2-step description remains an acceptable approximation of chemistry on this aspect.

Predictions of  $\langle S_d \rangle_{s,c^*}$  by the proposed model, Eq. (4.3.8), are now assessed against the DNS and the constant  $\langle S_d \rangle_{s,c^*}$  model adopted in the standard flamelet models ( $\langle \rho S_d \rangle_{s,c^*} = \rho_u S_L^0$ ). Figure 4.3.7a presents  $\langle S_d \rangle_{s,c^*}$  given by the proposed model for case A, using both the Markstein lengths fitted from the DNS (in plain symbols and dashed line) and those given by Eqs. (3.3.5) and (3.3.6). It can be seen that  $\langle S_d \rangle_{s,c^*}$  is over-predicted when correlations are used, while it closely follows the DNS for  $\bar{\mathcal{C}} > 0.1$  when the fitted values are used. This result confirms the strong impact of Markstein length evaluations. Note that the error observed with the Markstein length correlation is maximum for case A, which is the case where the correlation shows the poorest agreement with the fitted values as seen in Fig. 3.3.5. On the contrary for cases C and D, a much smaller difference is observed between fitted and correlation values (not shown).

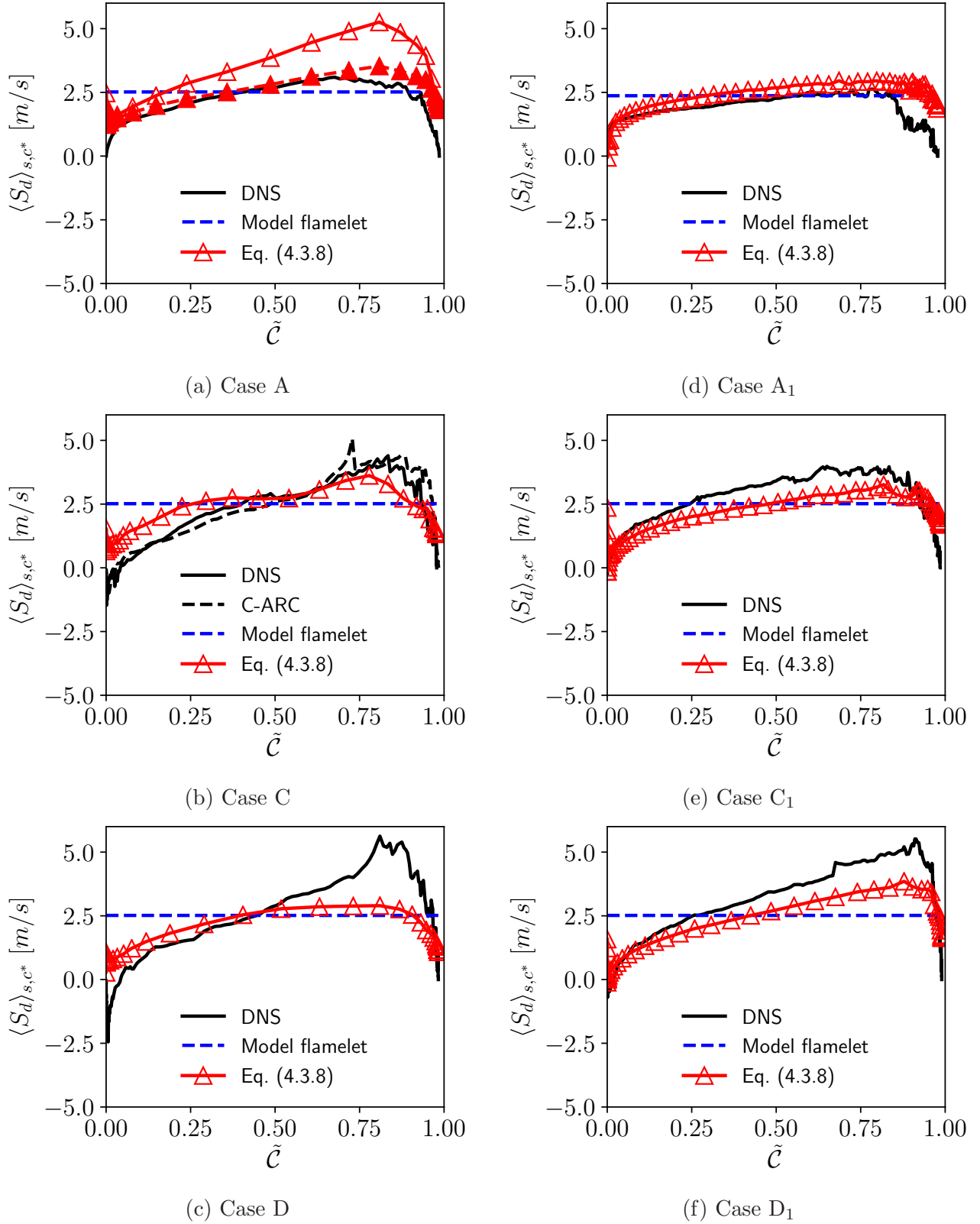


Figure 4.3.7: Comparison of the displacement speed  $\langle S_d \rangle_{s,c^*}$  for the proposed model (Eq. 4.3.8) with the DNS versus  $\tilde{C}$  for: (a) to (c) cases with  $Le_k \neq 1$  and (d) to (f) cases with  $Le_k = 1$ . Plain symbols and dashed line represent predictions from Eq. (4.3.8) using Markstein lengths fitted from the DNS. Black dashed line represents  $\langle S_d \rangle_{s,c^*}$  extracted from the simulation using ARC mechanism (case C-ARC).

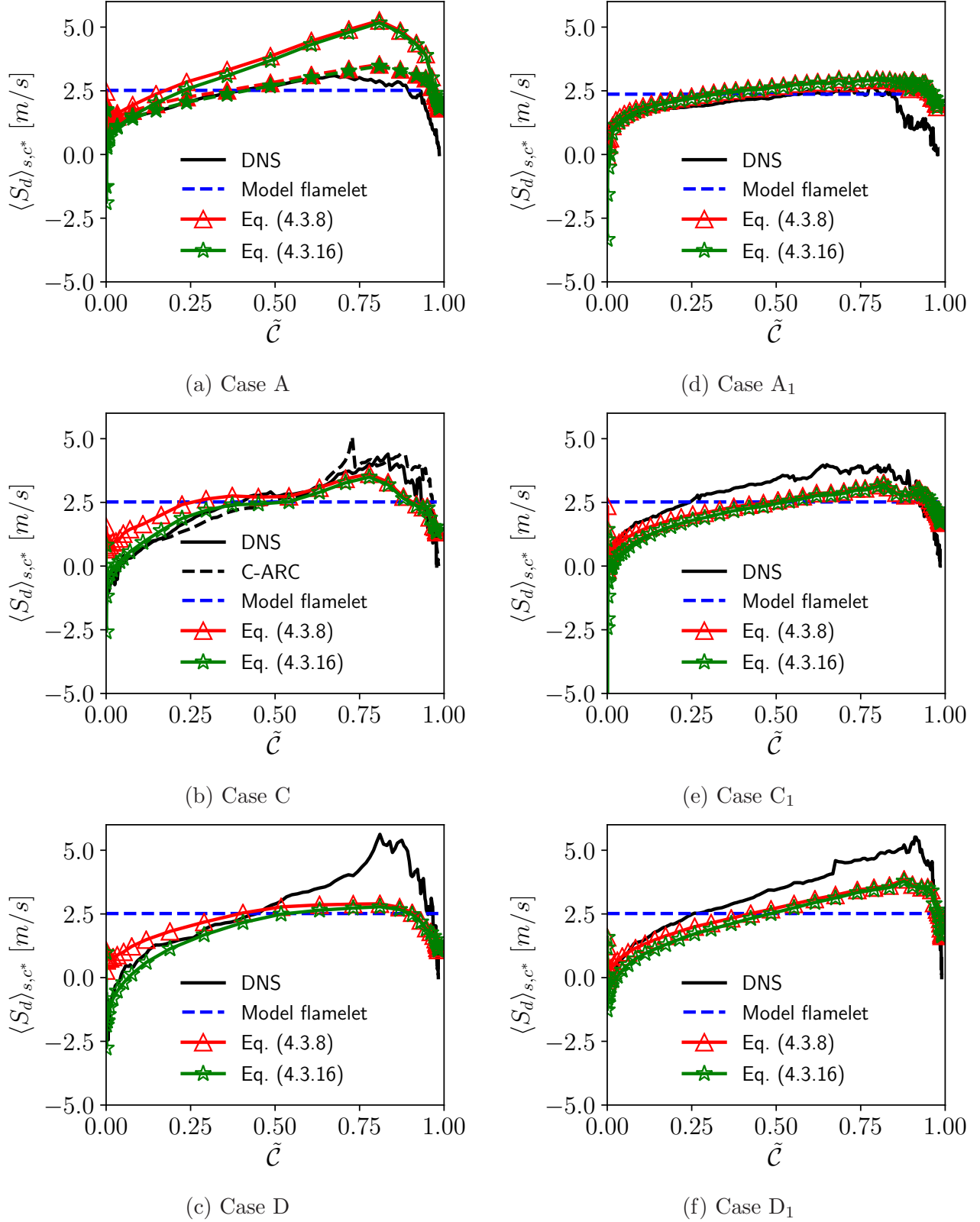


Figure 4.3.8: Comparison of the displacement speed  $\langle S_d \rangle_{s,c^*}$  for the proposed models in Eqs. (4.3.8) and (4.3.16) with the DNS versus  $\tilde{C}$  for: (a) to (c) cases with  $Le_k \neq 1$  and (d) to (f) cases with  $Le_k = 1$ . Plain symbols and dashed line represent predictions from Eqs. (4.3.8) and (4.3.16) using Markstein lengths fitted from the DNS. Black dashed line represents  $\langle S_d \rangle_{s,c^*}$  extracted from the simulation using ARC mechanism (case C-ARC).

For all six DNS cases, the proposed model predicts globally the increase of  $\langle S_d \rangle_{s,c^*}$  with  $\tilde{\mathcal{C}}$  observed in the DNS, unlike the flamelet model which remains constant, making a substantial improvement. At the same time this increase can be substantially over (case D) or under (cases C<sub>1</sub> and D<sub>1</sub>) predicted on the burned gases side.

More importantly from a modelling perspective, the proposed model does not capture the strong decrease of  $\langle S_d \rangle_{s,c^*}$  when  $\tilde{\mathcal{C}}$  tends toward zero for non-unity Lewis number cases: for case A,  $\langle S_d \rangle_{s,c^*}$  approaches zero in this zone and becomes even negative for cases C and D. A possible explanation might be that the proposed model relies on Eq. (3.3.2) for the displacement speed, which is directly taken from laminar flame analysis. This expression assumes that the displacement speed is locally in equilibrium with the local stretch. However, all the cases considered here present a Karlovitz number larger than unity which means that the smallest turbulent scales characteristic time is smaller than the flame time scale. In this condition, this equilibrium assumption might not be valid any more and the flame responds to stretch in a delayed and attenuated way (Poinsot and Veynante, 2012).

In order to improve the proposed model prediction towards  $\tilde{\mathcal{C}} = 0$ , the above remark suggests as a first very simple correction, to replace  $S_d$  by  $S_d^0$  in Eq. (4.3.8) when  $\kappa > 0$ . Mathematically, this is equivalent to introduce a factor  $\gamma$  in the proposed model expression of the displacement speed, such that  $\gamma = 0$  when  $\kappa > 0$  and  $\gamma = 1$  when  $\kappa < 0$ , leading to the corrected model below:

$$\langle \rho S_d \rangle_{s,c^*} = \rho^* \int_{-\frac{1}{\mathcal{L}_\kappa} + \varepsilon}^{+\infty} \frac{S_d^0 - \mathcal{L}_{a_T} \langle a_T \rangle_{s,c^*} - (D^* + (1 - \gamma) \mathcal{L}_\kappa S_d^0) \kappa}{1 + \gamma \mathcal{L}_\kappa \kappa} p(\kappa) d\kappa. \quad (4.3.16)$$

In Figs. 4.3.8a to 4.3.8c, the corrected model (in green star symbols) is found to be in much better agreement with the DNS data compared to the proposed model in Eq. (4.3.8) on the fresh gases side. For  $Le_k = 1$  cases, the models based on Eqs. (4.3.8) and (4.3.16) are nearly identical as in this case, the curvature Markstein lengths are much smaller.

## 4.4 Closure of the flame surface density transport equation

In this section, the closure of terms involved in the transport equation of flame surface density  $\overline{\Sigma^*}$  (Eq. 4.1.6) are presented. These terms are:

- The unresolved turbulent transport  $T = \nabla \cdot (\overline{\mathbf{u} \Sigma^*} - \tilde{\mathbf{u}} \overline{\Sigma^*})$  in Eq. (4.1.6),
- The normal propagation term  $P = \nabla \cdot (\langle S_d \mathbf{n} \rangle_{s,c^*} \overline{\Sigma^*})$  in Eq. (4.1.6),
- The tangential strain rate  $\langle a_T \rangle_{s,c^*} = \langle \nabla \cdot \mathbf{u} - \mathbf{nn} : \nabla \mathbf{u} \rangle_{s,c^*}$  (term  $S$  in Eq. 4.1.6),
- The stretch due to curvature  $\langle S_d \kappa \rangle_{s,c^*}$  (term  $C$  in Eq. 4.1.6).

Figure 4.4.1 shows the unresolved transport term  $T$ , the normal propagation  $P$  and the flame surface density source terms  $S$  and  $C$  as functions of  $\tilde{\mathcal{C}}$  for cases A, C and D, extracted

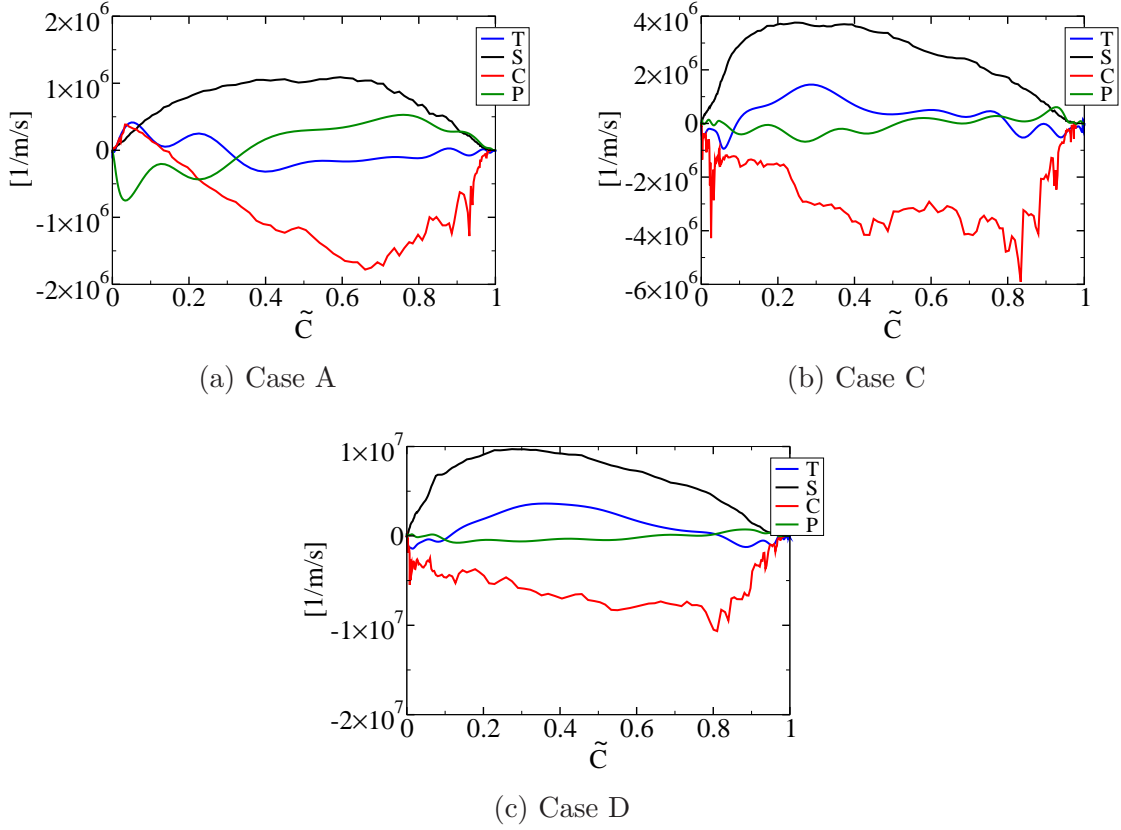


Figure 4.4.1: Comparison of the source terms involved in Eq. (3.2.14) as functions of  $\tilde{C}$ .  $T$  is the unresolved transport term  $\nabla \cdot (\overline{\mathbf{u}\Sigma^*} - \tilde{\mathbf{u}}\Sigma^*)$ ,  $S$  is the source term related to tangential strain rate and  $C$  is the source term related to stretch due to curvature  $\langle S_d \kappa \rangle_{s,c^*}$  and  $P$  is the normal propagation term  $\nabla \cdot (\langle S_d \mathbf{n} \rangle_{s,c^*} \Sigma^*)$ .

from DNS using the procedure presented in Section 4.2. In Fig. 4.4.1, the terms  $T$  and  $P$  are approximately one order of magnitude smaller than  $S$  and  $C$  for each case.

#### 4.4.1 Closure of the unresolved transport term

The unresolved transport term of FSD,  $T$ , is modelled with a simple gradient assumption following Richard et al. (2007):

$$\nabla \cdot (\overline{\mathbf{u}\Sigma^*} - \tilde{\mathbf{u}}\Sigma^*) = -\nabla \cdot \left( \frac{\nu_t}{S_{ct}} \nabla \Sigma^* \right). \quad (4.4.1)$$

As suggested by Rymer (2001), for RANS modelling, and Richard (2005), for LES modelling, a contribution corresponding to thermal expansion should be taken into account. Similarly to the term  $T_1$  (Eq. 4.1.5), this thermal expansion contribution is determined from the analysis of the simple case of a one-dimensional steady laminar flame. Because the flame is steady, Eq. (4.1.6) becomes:

$$\nabla \cdot (\overline{(\mathbf{u} + S_d \mathbf{n})\Sigma^*}) = 0, \quad (4.4.2)$$

where  $\overline{(\mathbf{u} + S_d \mathbf{n})\Sigma^*}$  is equal to  $(\langle \mathbf{u} \rangle_{s,c^*} + \langle S_d \mathbf{n} \rangle_{s,c^*})\Sigma^*$ . Yet, the displacement speed at  $c^*$  in a laminar flame is equal to  $(\rho_u/\rho^*)S_L^0$ , which leads to Eq. (4.4.3) when combined with the

following relationship:  $\mathbf{u} = -S_d \mathbf{n}$  (presented in Section 4.3).

$$\langle \mathbf{u} \rangle_{s,c^*} = -\frac{\rho_u}{\rho^*} S_L^0 \langle \mathbf{n} \rangle_{s,c^*}, \quad (4.4.3)$$

where  $\langle \mathbf{n} \rangle_{s,c^*} = -\nabla \bar{C} / \bar{\Sigma}^*$  is the surface averaged normal vector to the iso-surface  $c = c^*$  pointing toward the fresh gases.

Furthermore, the surface averaged velocity is modelled, using the Favre averaged velocity, as  $\langle \mathbf{u} \rangle_{s,c^*} = \tilde{\mathbf{u}} + \langle \mathbf{u}'' \rangle_{s,c^*}$ , where  $\langle \mathbf{u}'' \rangle_{s,c^*}$  corresponds to the difference between the Favre filtered velocity and the surface averaged velocity.

Similarly to the term  $T_1$ , the Favre filtered velocity field is modelled as:

$$\tilde{\mathbf{u}} = \frac{\rho_u}{\bar{\rho}} S_L^0 \langle \mathbf{n} \rangle_{s,c^*}. \quad (4.4.4)$$

Note that the normal vector used in Eq. (4.4.4) is  $\langle \mathbf{n} \rangle_{s,c^*}$ , while the normal vector is  $\bar{\mathbf{n}}$  in the model for  $\tilde{\mathbf{u}}$  (Eq. 4.3.5) used for modelling  $T_1$ . Then, combining the previous decomposition of  $\langle \mathbf{u} \rangle_{s,c^*}$  and Eq. (4.4.4) leads to:

$$\langle \mathbf{u}'' \rangle_{s,c^*} = \left( \frac{\rho_u}{\bar{\rho}} - \frac{\rho_u}{\rho^*} \right) S_L^0 \langle \mathbf{n} \rangle_{s,c^*}. \quad (4.4.5)$$

Equation (4.4.5) corresponds to a thermal expansion term added to the unresolved transport term of the flame surface density, as proposed by Rymer (2001), allowing to converge to a laminar flame when turbulence is sufficiently low. Equation (4.4.1) then becomes:

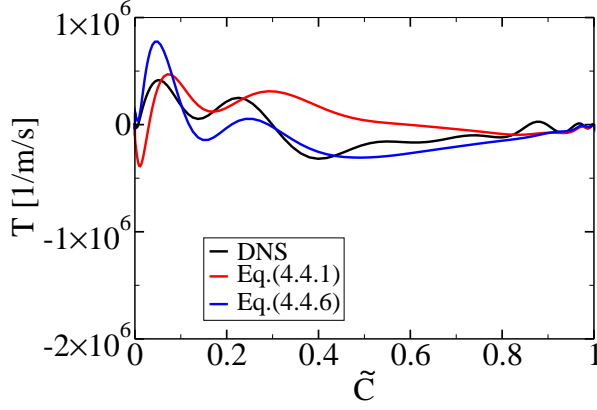
$$\nabla \cdot (\bar{\mathbf{u}} \bar{\Sigma}^* - \tilde{\mathbf{u}} \bar{\Sigma}^*) = -\nabla \cdot \left( \frac{\nu_t}{S_{ct}} \nabla \bar{\Sigma}^* \right) + \nabla \cdot \left[ \left( \frac{\rho_u}{\bar{\rho}} - \frac{\rho_u}{\rho^*} \right) S_L^0 \langle \mathbf{n} \rangle_{s,c^*} \bar{\Sigma}^* \right]. \quad (4.4.6)$$

The model given in Eq. (4.4.6) is compared to the unresolved term of the flame surface density extracted from the DNS and to the simple gradient model (Eq. 4.4.1) in Fig. 4.4.2. The model in Eq. (4.4.6) well predicts the unresolved term of FSD, both in terms of evolution with  $\tilde{C}$  and in magnitude, for each case. As for the term  $T_1$  the simple gradient model gives results similar to Eq. (4.4.6) for high Karlovitz numbers (cases C, D, C<sub>1</sub> and D<sub>1</sub>), while for cases A and A<sub>1</sub> the evolution predicted by the simple gradient model seems to be inaccurate, especially on the burnt gases side.

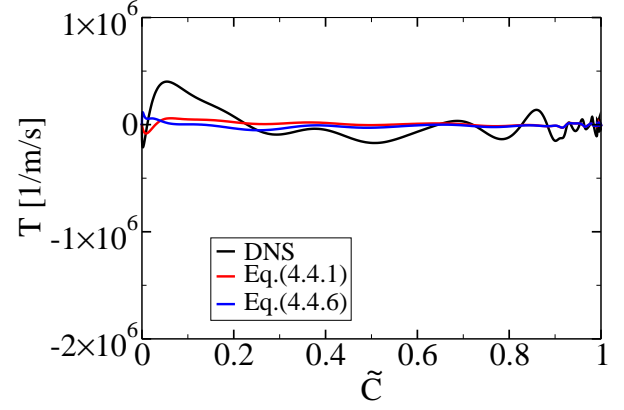
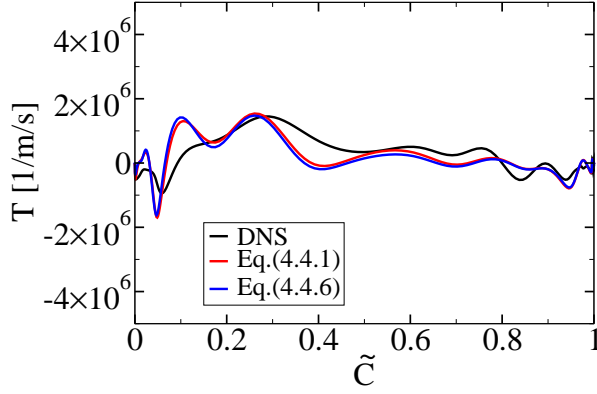
#### 4.4.2 Closure of the normal propagation

The normal propagation terms is usually modelled using the following relationship between the laminar flame speed and the displacement speed:

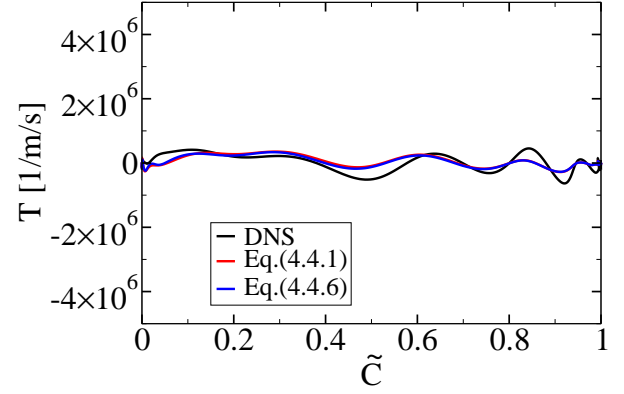
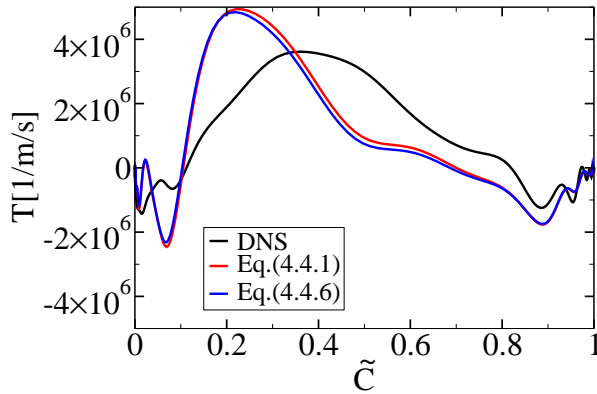
$$\rho S_d = \rho_u S_L^0. \quad (4.4.7)$$



(a) Case A

(d) Case A<sub>1</sub>

(b) Case C

(e) Case C<sub>1</sub>

(c) Case D

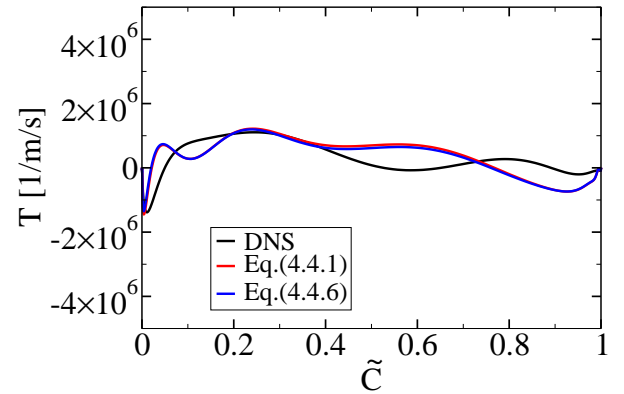
(f) Case D<sub>1</sub>

Figure 4.4.2: Comparison  $T = \nabla \cdot (\overline{\mathbf{u}\Sigma^*} - \widetilde{\mathbf{u}\Sigma^*})$  extracted from the DNS with the models given in Eqs. (4.4.1) and (4.4.6) as functions of  $\tilde{C}$  for: (a) to (c) the cases with  $Le_k \neq 1$  and (d) to (f) the cases with  $Le_k = 1$ .



This relationship is then used in the normal propagation speed:

$$\langle S_d \mathbf{n} \rangle_{s,c^*} \bar{\Sigma}^* = \frac{\rho_u}{\rho^*} S_L^0 \langle \mathbf{n} \rangle_{s,c^*} \bar{\Sigma}^*. \quad (4.4.8)$$

Even if in the TRZ regime this flamelet model is not valid, Eq. (4.4.8) is used for high Karlovitz number because the propagation term appears negligible (as seen in Fig. 4.4.1).

Finally, the sum of the unresolved transport term and the normal propagation is given as follows:

$$\nabla \cdot [(\langle \mathbf{u} \rangle_{s,c^*} - \tilde{\mathbf{u}} + \langle S_d \mathbf{n} \rangle_{s,c^*}) \bar{\Sigma}^*] = -\nabla \cdot \left( \frac{\nu_t}{S_{ct}} \nabla \bar{\Sigma}^* \right) + \nabla \cdot \left( \frac{\rho_u}{\bar{\rho}} S_L^0 \langle \mathbf{n} \rangle_{s,c^*} \bar{\Sigma}^* \right). \quad (4.4.9)$$

Figure 4.4.3 shows  $\langle S_d \mathbf{n} \rangle_{s,c^*} \bar{\Sigma}^*$  and the model presented in Eq. (4.4.8) as functions of the filtered progress variable  $\tilde{\mathcal{C}}$ . For each case, the model is in good agreement with the DNS results, except for  $\tilde{\mathcal{C}} < 0.4$  for  $Le_k \neq 1$  cases (up to values approximately 4 times larger than DNS for case D). These large discrepancies are due to the flamelet assumption  $I_0 \approx 1$ . Therefore, in the same figure is plotted the following model:

$$\langle S_d \mathbf{n} \rangle_{s,c^*} \bar{\Sigma}^* = I_0^* \frac{\rho_u}{\rho^*} S_L^0 \langle \mathbf{n} \rangle_{s,c^*} \bar{\Sigma}^*, \quad (4.4.10)$$

where  $I_0^*$  is the stretch factor on the iso-surface  $c = c^*$  defined as:

$$I_0^* = \frac{\langle \rho S_d \rangle_{s,c^*}}{\rho_u S_L^0}. \quad (4.4.11)$$

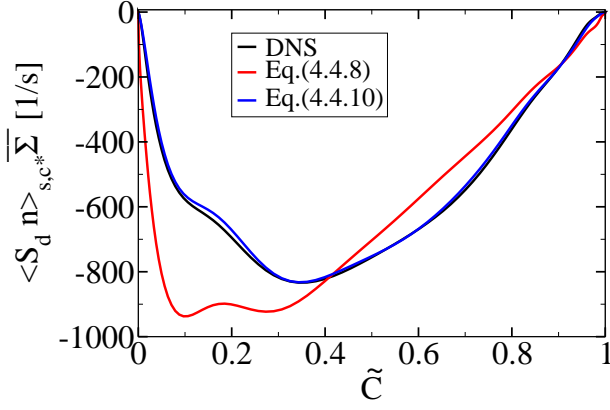
Equation (4.4.10) improves significantly the predictions for  $\langle S_d \mathbf{n} \rangle_{s,c^*} \bar{\Sigma}^*$  in Fig 4.4.3 for  $\tilde{\mathcal{C}} < 0.4$ . However, significant discrepancies remain on the fresh gases side when  $Ka$  increases. Indeed, for case C when  $\tilde{\mathcal{C}} \geq 0.4$  Eq. (4.4.10) is superimposed with the DNS results, elsewhere it overestimates  $\langle S_d \mathbf{n} \rangle_{s,c^*} \bar{\Sigma}^*$  by a factor 2. For  $\tilde{\mathcal{C}} \leq 0.1$  DNS results show small positive values, which Eq. (4.4.10) cannot reproduce.

Even if the model proposed in Eq. (4.4.8) overestimates strongly the normal propagation on the fresh gases side, this model is sufficient because it captures the overall evolutions of  $\langle S_d \mathbf{n} \rangle_{s,c^*} \bar{\Sigma}^*$ .

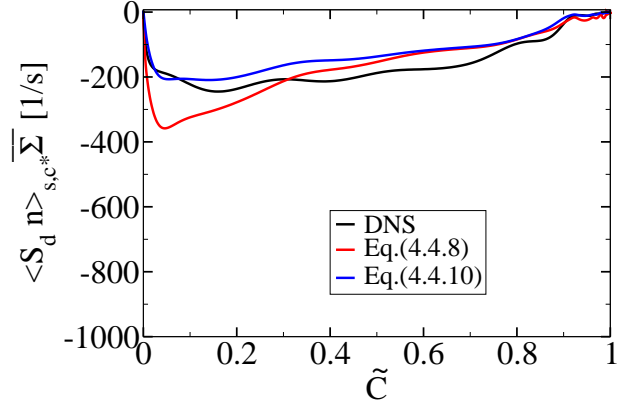
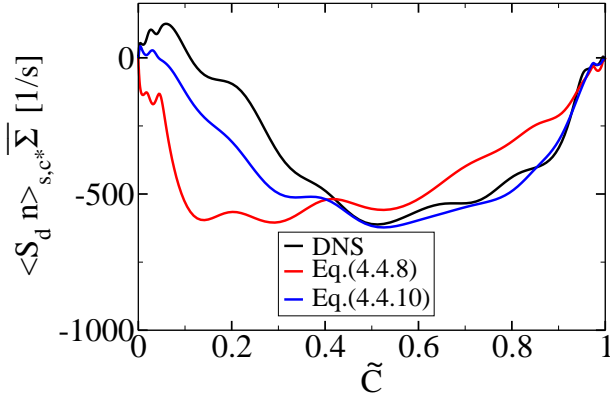
### 4.4.3 Closure of the tangential strain rate

Hawkes and Cant (2000) decomposed the tangential strain rate due to the surrounding fluid  $\langle a_T \rangle_{s,c^*} = \langle \nabla \cdot \mathbf{u} - \mathbf{nn} : \nabla \mathbf{u} \rangle_{s,c^*}$  as:

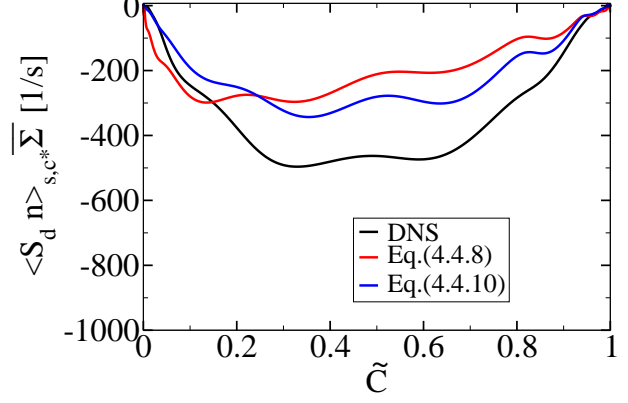
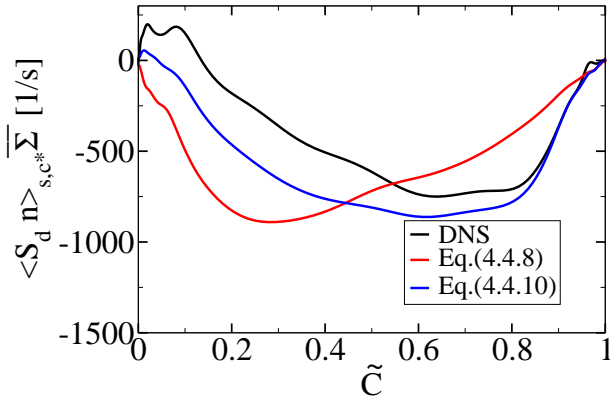
$$\langle a_T \rangle_{s,c^*} = \underbrace{\nabla \cdot \tilde{\mathbf{u}} - \langle \mathbf{nn} \rangle_{s,c^*} : \nabla \tilde{\mathbf{u}}}_{\langle A_T \rangle_{s,c^*}} + \langle a_T \rangle_{s,c^*}^{sgs} + S_{hr}, \quad (4.4.12)$$



(a) Case A

(d) Case A<sub>1</sub>

(b) Case C

(e) Case C<sub>1</sub>

(c) Case D

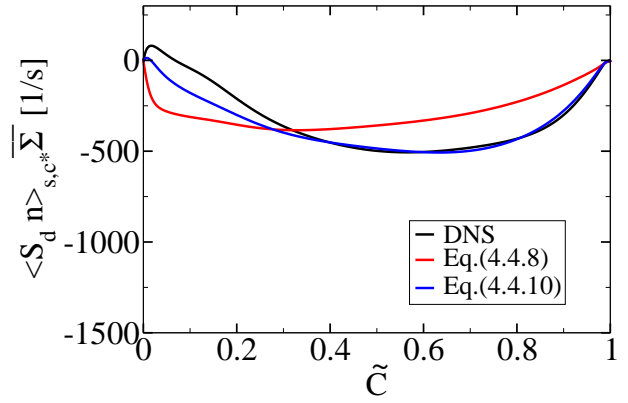
(f) Case D<sub>1</sub>

Figure 4.4.3: Comparison of  $\langle S_d \mathbf{n} \rangle_{s,c^*} \bar{\Sigma}^*$  extracted from the DNS with the models given by Eqs. (4.4.8) and (4.4.10) as functions of  $\tilde{C}$  for: (a) to (c) the cases with  $Le_k \neq 1$  and (d) to (f) the cases with  $Le_k = 1$ .

where  $\langle A_T \rangle_{s,c^*}$  is the tangential strain rate due to the resolved flow motions,  $\langle a_T \rangle_{s,c^*}^{sgs}$  is the tangential strain rate due to unresolved flow motions and  $S_{hr}$  is a term that accounts for the heat release effects. Due to expansion across the flame, the velocity gradients at the flame surface are different from the velocity gradients of the mean flow. The term  $S_{hr}$  is discussed in Section 4.4.4 dedicated to the stretch rate due to curvature. The term  $\langle A_T \rangle_{s,c^*}$  involves an orientation factor  $\langle \mathbf{nn} \rangle_{s,c^*}$ , which is not known. Consequently, the closures for the tangential strain rate due to resolved flow motions in Eq. (4.4.12) and tangential strain rate due to unresolved flow motions are presented in this section.

### Closure of the tangential strain rate due to resolved flow motions

The tangential strain rate due to resolved flow motions  $\langle A_T \rangle_{s,c^*}$  is evaluated adapting the model proposed by Hawkes and Cant (2000) in Chapter 1:

$$\langle A_T \rangle_{s,c^*} = \nabla \cdot \tilde{\mathbf{u}} - \left( \langle \mathbf{n} \rangle_{s,c^*} \langle \mathbf{n} \rangle_{s,c^*} + \frac{1}{3} \alpha \mathcal{I}_3 \right) : \nabla \tilde{\mathbf{u}}, \quad (4.4.13)$$

where  $\mathcal{I}_3$  is the identity matrix and  $\alpha = 1 - |\langle \mathbf{n} \rangle_{s,c^*}|^2$  is a resolution factor introduced by Cant et al. (1991) for vanishing the net destruction of FSD when the flame is fully resolved.

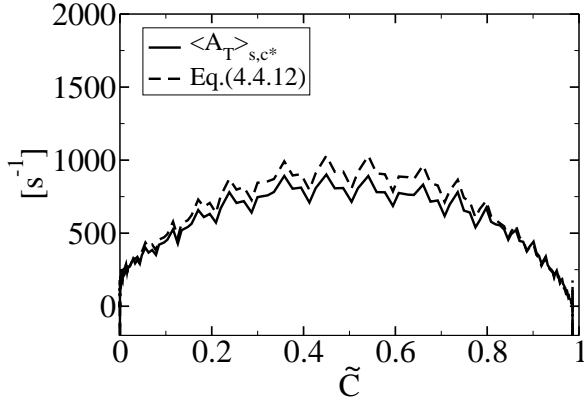
Figure 4.4.4 compares the model proposed by Hawkes and Cant (2000) (Eq. 4.4.13) and the tangential strain rate due to resolved flow motions in Eq. (4.4.12) extracted from DNS following the procedure presented in Section 4.2. For all six DNS cases, the proposed model reproduces the general evolution of  $\langle A_T \rangle_{s,c^*}$  through the flame front. The predictions of Eq. (4.4.13) are very accurate for case A and all three  $Le_k = 1$  cases. However, the model significantly overpredicts  $\langle A_T \rangle_{s,c^*}$  for cases C and D. These discrepancies should be further analysed, but because  $\langle A_T \rangle_{s,c^*}$  represents 20% and 10% of the total tangential strain rate for cases C and D, respectively, the model proposed by Hawkes and Cant (2000) (Eq. 4.4.13) is considered sufficient in the present study.

### Closure of the tangential strain rate due to unresolved flow motions

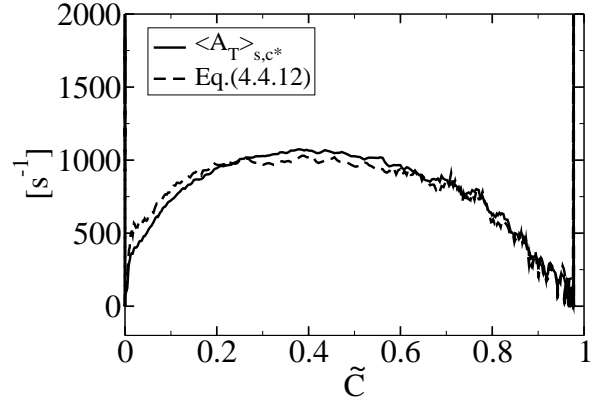
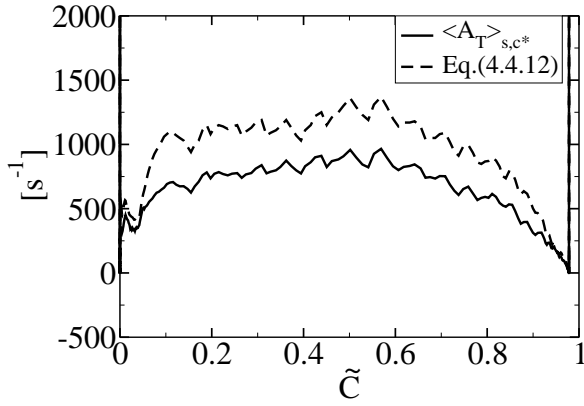
The tangential strain rate due to unresolved flow motions,  $\langle a_T \rangle_{s,c^*}^{sgs}$ , is modelled using the same approach proposed in the generalized CFM, presented in Sections 1.5.3. In this approach, the tangential strain rate is modelled using the approximated strain rate due to the turbulent structures smaller than the resolved flame thickness  $\hat{\Delta}$ :

$$\langle a_T \rangle_{s,c^*}^{sgs} = \alpha_{a_T} \Gamma \frac{\hat{u}'}{\hat{\Delta}}, \quad (4.4.14)$$

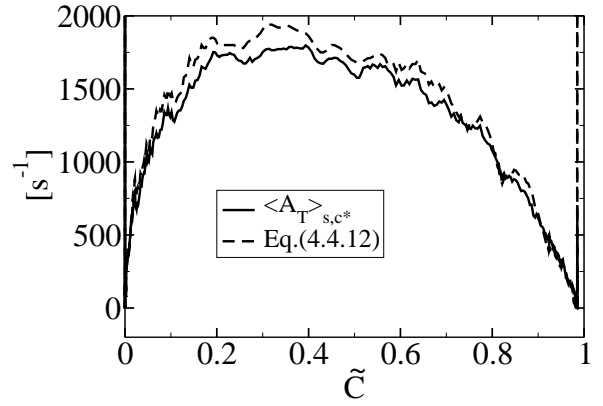
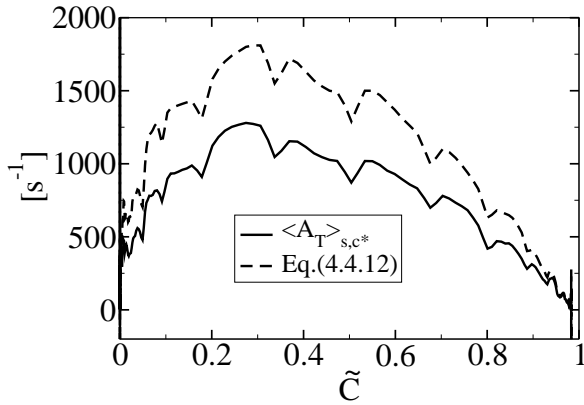
where  $\alpha_{a_T}$  is a model parameter,  $\Gamma$  is an efficiency function applied to differentiate the effect of the different turbulent scales on the flame straining and  $\hat{u}'$  is the characteristic velocity of the turbulent structures at scale  $\hat{\Delta}$ . The latter is estimated from the sub-grid scale fluctuation



(a) Case A

(d) Case A<sub>1</sub>

(b) Case C

(e) Case C<sub>1</sub>

(c) Case D

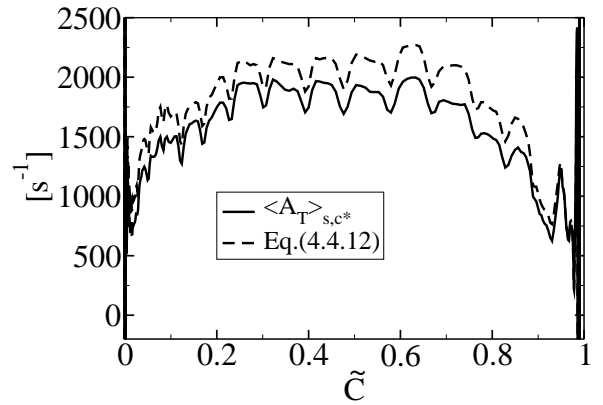
(f) Case D<sub>1</sub>

Figure 4.4.4: Evolutions of the tangential strain rate due to resolved flow motions  $\langle A_T \rangle_{s,c^*}$  in Eq. (4.4.12) with the filtered progress variable  $\tilde{C}$  for: (a) to (c) the cases with  $Le_k \neq 1$  and (d) to (f) the cases with  $Le_k = 1$ .

velocity  $u'$  and the mesh size  $\Delta$ :

$$\widehat{u'} = u' \left( \frac{\widehat{\Delta}}{\Delta} \right)^{1/3}. \quad (4.4.15)$$

The efficiency function  $\Gamma$ , introduced in Section 1.5.5, is recalled below:

$$\left( \Gamma \frac{\widehat{u'}}{\widehat{\Delta}} \right)^2 = \left( \frac{\pi}{\widehat{\Delta}} \right)^3 \int_0^\infty [C_r(k_+)]^2 k_+^2 E_{11}(k_+) dk_+, \quad (4.4.16)$$

where  $k_+ = k\widehat{\Delta}/\pi$  is the dimensionless wavenumber and  $C_r(k_+)$  is the efficiency function introduced in Chapter 2.  $E_{11}(k_+)$  is the one-dimensional (longitudinal) energy spectrum in the direction of the wavenumber  $k$  (Eq. 1.5.41).

As presented in Chapter 1, the key parameter in this model is the efficiency function  $C_r(k_+)$ . The five following functions are considered and tested:

1. As presented in Chapter 2, Cant et al. (1991) proposed to modelled the turbulent tangential strain rate, in the context of RANS modelling, as  $\langle a_T \rangle_s \propto C_A/\tau_\eta$ , where  $C_A$  is a constant equals to 0.28 and  $\tau_\eta$  is the eddy turnover time of the Kolmogorov scale. When a unit constant function  $C_r$  is introduced in Eq. (4.4.16), the model for  $\langle a_T \rangle_{s,c^*}^{sgs}$  (Eq. 4.4.14) and imposing  $\widehat{\Delta} = l_t$  and  $\widehat{u'} = u'_t$  becomes:

$$\langle a_T \rangle_{s,c^*} = \alpha_{a_T} \frac{3}{\sqrt{55}} Ka \frac{S_L^0}{\delta_L}. \quad (4.4.17)$$

This equation shows that the model proposed by Cant et al. (1991) is equivalent to the model proposed by Charlette et al. (2002a) using the unit constant efficiency function. This model is designated in the rest of this study as Cant model.

2. A Heaviside function defined as follows:

$$C_r(k_+) = \begin{cases} 1 & \text{if } k_+ < \frac{\widehat{\Delta}}{\delta_c} \\ 0 & \text{otherwise,} \end{cases} \quad (4.4.18)$$

where  $\delta_c$  is a cut-off scale. We assume here that the flame behaves as a low-pass filter (LPF) in term of wavenumber, the cut-off scale  $\delta_c$  of being identified here to the laminar flame thickness  $\delta_L^0$ . This assumption combined to the Heaviside's function allows an analytical integration of Eq. (4.4.16) leading to:

$$\left( \Gamma \frac{\widehat{u'}}{\widehat{\Delta}} \right)^2 = \frac{9}{55} Re_{\widehat{\Delta}} \left[ 1 - \exp \left( -\frac{3}{2} C_k \frac{1}{Re_{\widehat{\Delta}}} \left( \frac{\pi \widehat{\Delta}}{\delta_c} \right)^{4/3} \right) \right]. \quad (4.4.19)$$

Equation (4.4.19) leads to the following expression for  $\langle a_T \rangle_{s,c^*}^{sgs}$  when  $\widehat{\Delta} = l_t$  and  $\widehat{u'} = u'_t$ :

$$\langle a_T \rangle_{s,c^*} = \alpha_{a_T} \frac{3}{\sqrt{55}} Ka \frac{S_L^0}{\delta_L^0} \left[ 1 - \exp \left( -\frac{3}{2} C_k \frac{1}{Re_t} \left( \frac{\pi l_t}{\delta_c} \right)^{4/3} \right) \right]^{1/2}. \quad (4.4.20)$$

Equation (4.4.20) is referred to the LPF model in the rest of this study.

3. The model given by Eqs. (4.4.14) and (4.4.16) considering the function  $C_r$  proposed by Charlette et al. (2002a).
4. The model given by Eqs. (4.4.14) and (4.4.16) considering the function  $C_r$  proposed by Bougrine et al. (2014).
5. The model given by Eqs. (4.4.14) and (4.4.16) considering the function  $C_r$  proposed in Chapter 2 (Eq. 2.3.5). This function is designated as the HK<sub>2D</sub> model.

All these functions are reported in Table 4.2.

Table 4.2: The efficiency functions of the models compared to the DNS.

Model name	Efficiency function
Cant	$C_r \left( \frac{r_k}{\delta_L^0}, \frac{u_k}{S_L^0} \right) = 1$
LPF	$C_r \left( \frac{r_k}{\delta_L^0}, \frac{u_k}{S_L^0} \right) = \begin{cases} 1 & \text{if } k_+ < \frac{\hat{\Delta}}{\delta_L^0} \\ 0 & \text{otherwise} \end{cases}$
Charlette	$C_r \left( \frac{r_k}{\delta_L^0}, \frac{u_k}{S_L^0} \right) = \frac{1}{4} \left[ 1 + \operatorname{erf} \left( 0.6 \left( \ln \left( \frac{r_k}{\delta_L^0} \right) - \sqrt{\frac{S_L^0}{u_k}} \right) \right) \right] \left[ 1 + \operatorname{erf} \left( 3 \log \left( 2 \frac{u_k}{S_L^0} \right) \right) \right]$
Bougrine	$C_r \left( \frac{r_k}{\delta_L^0}, \frac{u_k}{S_L^0} \right) = \frac{1 + \operatorname{erf}[0.9 \ln(\frac{r_k}{\delta_L^0}) - 2]}{1 + 0.3 \frac{u_k}{S_L^0} (1 + \operatorname{erf}[0.9 \ln(\frac{r_k}{\delta_L^0}) - 2])} \left[ \frac{1}{Le} (1.76 + \tanh(Le - 2)) \right]$
HK <sub>2D</sub>	$C_r \left( \frac{r_k}{\delta_L^0}, \frac{u_k}{S_L^0} \right) = \frac{\left[ 1 + \operatorname{erf} \left( 1.05 \log \left( \frac{r_k}{\delta_L^0} \right) - 0.91 \sqrt{\frac{S_L^0}{u_k}} \right) \right]^{1.53}}{\left[ 1 + 0.24 \frac{u_k}{S_L^0} \left( 1 + \operatorname{erf} \left( 1.05 \log \left( \frac{r_k}{\delta_L^0} \right) - 0.91 \sqrt{\frac{S_L^0}{u_k}} \right) \right) \right]^{1.03}} \left[ \frac{1}{Le} (1.76 + \tanh(Le - 2)) \right]$

Equation (4.4.14) does not depend on the filtered progress variable leading to a constant profile of  $\langle a_T \rangle_{s,c^*}^{sgs}$  with  $\tilde{\mathcal{C}}$ . So, to compare the prediction of each model, the integrated tangential strain rate due to unresolved flow motions  $\langle a_T \rangle_s^*$  is computed from the DNS as:

$$\langle a_T \rangle_s^* = \frac{\int_{\mathcal{V}} \langle a_T \rangle_{s,c^*}^{sgs} \bar{\Sigma}^* d\mathbf{x}}{\int_{\mathcal{V}} \bar{\Sigma}^* d\mathbf{x}} = \frac{\int_{\mathcal{V}} (\langle a_T \rangle_{s,c^*} - \langle A_T \rangle_{s,c^*}) \bar{\Sigma}^* d\mathbf{x}}{\int_{\mathcal{V}} \bar{\Sigma}^* d\mathbf{x}}. \quad (4.4.21)$$

The tangential strain rates predicted by the different models are corrected using a model parameter  $\alpha_{a_T}$  for each model. This parameter is adjusted to fit the strain rates predicted by the Charlette et al. (2002a) model to DNS for the lowest Karlovitz numbers (*i.e.*, cases A and A<sub>1</sub>). Its use for the other models allows to evaluate differences between them. The values of  $\alpha_{a_T}$  used are 1.65 and 2.81 for  $Le_k \neq 1$  and  $Le_k = 1$ , respectively. The model constant adjusted for Charlette on case A<sub>1</sub> is retained for the Bougrine's model which is the only one to include

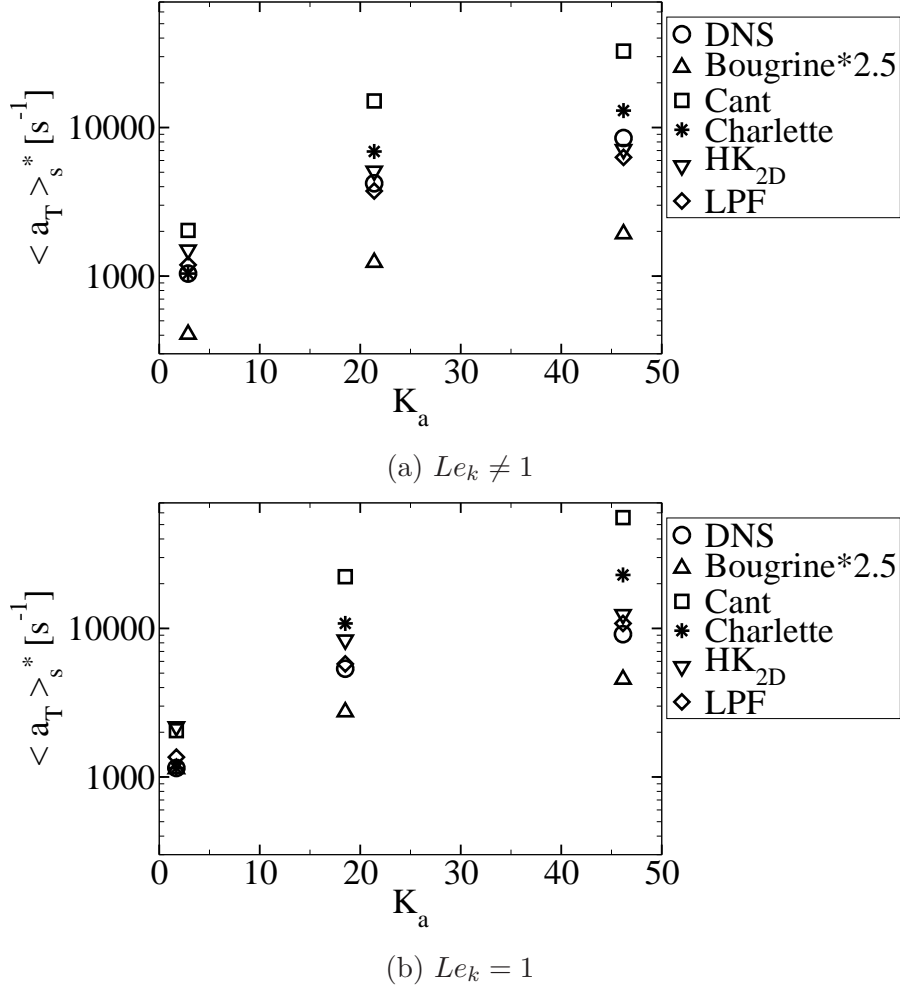


Figure 4.4.5: Tangential strain rate  $\langle a_T \rangle_s^* = \langle a_T \rangle_{s,c}^{sgs}$  from DNS compared to Bougrine’s model (Bougrine et al., 2014), Cant’s model (Cant et al., 1991), Charlette’s model (Charlette et al., 2002a), HK<sub>2D</sub> (Eq. 2.3.5) and LPF models (Eq. 4.4.20): (a) for cases with  $Le_k \neq 1$  and (b) for cases with  $Le_k = 1$ .

a correction for Lewis number effects (coefficient equal to 0.85 for our non-unity Lewis cases, leading to a model constant  $2.81.85 = 2.39$ ).

Since the values predicted by the Bougrine’s function are much smaller than the other models, they are plotted in Fig. 4.4.5 by multiplying them by a factor 2.5. Figure 4.4.5 compares model predictions and tangential strain rates extracted from the DNS, plotted as functions of  $Ka$ .

First looking at  $Le_k \neq 1$  cases in Fig. 4.4.5a, Cant’s model presents a linear increase of  $\langle a_T \rangle_{s,c}^{sgs}$  with  $Ka$ , as expected from Eq. (4.4.17), in agreement with the DNS. The turbulent strain predicts for case A is twice as large as that of the DNS. In addition, the slope of this line is too steep compared to the DNS. As a consequence, very large discrepancies are observed for high Karlovitz numbers. For instance, the predicted strain rate for case D is almost four times larger than that of the DNS. Thus, the Cant’s model clearly overestimates the effect of small structures of the turbulence on the tangential strain rate.

Charlette’s model over-predicts the turbulent strain rate for high Karlovitz numbers, with up to 64% relative error for case C. Nevertheless, the general trend with  $Ka$  seems to be well

reproduced, contrary to Cant's model. Surprisingly, Bougrine's model deteriorates significantly strain rate predictions: for each cases the predicted strain rate is about half the DNS values. This might be due to the strong decrease of the efficiency function for small turbulent structures, as observed by Bougrine et al. (2014). Nevertheless, the relative evolution of Bougrine's model is in good agreement with the DNS. Note that Bougrine's turbulent strain rate flattens with increasing  $Ka$ , while the DNS strain rate remains quasi-linear with  $Ka$ . This might be explained by a too strong decrease of Bougrine's efficiency function with the vortex velocity (Bougrine et al., 2014). HK<sub>2D</sub> model presents similar results as Bougrine's model multiplied by 10. This is mainly explained by the similar shape of the efficiency function of the two models, displayed in Fig. 2.3.2. LPF model is the only one to accurately predicts the turbulent strain rate for each case, with a maximum relative error of 25% for case D.

For  $Le_k = 1$  cases shown in Fig. 4.4.5b, the predictions of each model are similar to non-unity Lewis number cases. As for  $Le_k \neq 1$  cases, Bougrine's model strongly underestimates  $\langle a_T \rangle_{s,c^*}$  by a factor 2.5 and up to a factor 5 for cases A<sub>1</sub> and D<sub>1</sub>, respectively. Note that predictions of Cant's and Charlette's models are deteriorated compared to  $Le_k \neq 1$  cases. The latter presents a relative error of 150% for the highest Karlovitz number. Nevertheless, the main conclusions here are the same as for the non-unity Lewis number simulations.

Charlette's and Bougrine's functions were not developed for high Karlovitz number flames and, consequently, have never been validated for these conditions. Thus, the results observed on Cant's model confirm that the inability of small eddies to stretch the flame needs to be included in a turbulent strain rate model. The Charlette's and Bougrine's functions take into account the lower capacity of small vortices to stretch the flame, but the predictions of the LPF model show that this inability introduced in the Charlette's and Bougrine functions is not sufficient. It also shows that choosing  $\delta_L^0$  as the cut-off scale seems appropriate for the LPF model. From these cases, the LPF model seems to give the better prediction for  $\langle a_T \rangle_s^*$  with a maximum error always smaller than 25%. Nevertheless, this cut-off length might also be dependent on  $Ka$ , as already suggested for low  $Ka$  by Gülder (1995).

A comparison of  $\langle a_T \rangle_s^*$  extracted from the DNS with the models is then presented in Fig. 4.4.6 for all DNS cases but by tuning for each model the parameter  $\alpha_{a_T}$  to fit the strain rate obtained at the lowest Karlovitz numbers (i.e., cases A and A<sub>1</sub>). This tuned parameter is reported in Table 4.3 for each model.

Table 4.3: Tuned model parameter  $\alpha_{a_T}$  for each model.

Model	Bougrine	Cant	Charlette	HK <sub>2D</sub>	LPF
Case					
$Le_k \neq 1$	10.6	0.8	1.7	1.2	1.4
$Le_k = 1$	7.1	1.6	2.8	1.1	2.4

Figure 4.4.6 shows that tuning  $\alpha_{a_T}$  for each model improves significantly the predictions. The conclusions drawn in the analysis of Fig. 4.4.5 are still valid when  $\alpha_{a_T}$  is tuned for each model. Figure 4.4.6 shows that the best model is the LPF model and choosing  $\delta_L^0$  as the cut-off scale seems appropriate. Note that both Bougrine's and HK<sub>2D</sub> models present very similar



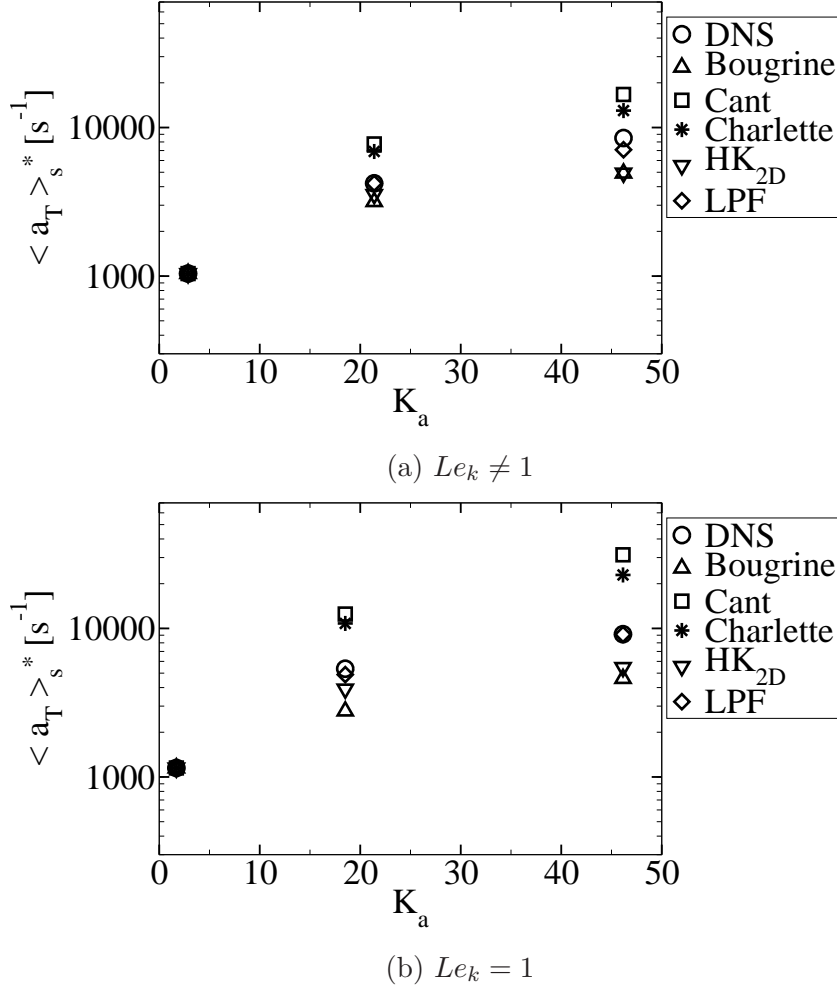


Figure 4.4.6: Tangential strain rate  $\langle a_T \rangle_s^* = \langle a_T \rangle_{s,c^*}^{sgs}$  from DNS compared to Bougrine’s model (Bougrine et al., 2014), Cant’s model (Cant et al., 1991), Charlette’s model (Charlette et al., 2002a), HK<sub>2D</sub> (Eq. 2.3.5) and LPF model (Eq. 4.4.20): (a) for cases with  $Le_k \neq 1$  and (b) for cases with  $Le_k = 1$ . Each model is tuned to fit the lowest Karlovitz number case.

results showing that the efficiency function proposed in Chapter 2 does not significantly improve predictions of  $\langle a_T \rangle_s^*$ .

#### 4.4.4 Closure of the stretch due to curvature

Similarly to the tangential strain rate in Section 4.4.3, the stretch rate due to curvature  $\langle S_d \kappa \rangle_{s,c^*}$  is decomposed as:

$$\langle S_d \kappa \rangle_{s,c^*} = \underbrace{\frac{\rho_u}{\rho^*} S_L^0 \nabla \cdot \langle \mathbf{n} \rangle_{s,c^*}}_{\langle S_d \kappa \rangle_{s,c^*}^{res}} + \underbrace{\left[ \langle S_d \kappa \rangle_{s,c^*} - \frac{\rho_u}{\rho^*} S_L^0 \nabla \cdot \langle \mathbf{n} \rangle_{s,c^*} \right]}_{\langle S_d \kappa \rangle_{s,c^*}^{sgs}}, \quad (4.4.22)$$

where  $\langle S_d \kappa \rangle_{s,c^*}^{res}$  and  $\langle S_d \kappa \rangle_{s,c^*}^{sgs}$  are the stretch rates due to curvature caused by resolved and unresolved flow motions, respectively. The latter is modelled using the approach used for the displacement speed. First, an expression for  $(S_d \kappa)^*$  is deduced from Eq. (3.3.3) by multiplying

it with  $\kappa^*$ :

$$(S_d\kappa)^* = \frac{\frac{\rho_u}{\rho^*} S_L^0 \kappa^* - \mathcal{L}_{a_T} a_T^* \kappa^* - D^* \kappa^{*2}}{1 + \mathcal{L}_\kappa \kappa^*}. \quad (4.4.23)$$

Equation (4.4.23) is then filtered with the operator  $\langle \rangle_{s,c^*}$  using the presumed PDF of the curvature, given in Eq. (4.3.9), leading to the following model:

$$\langle S_d\kappa \rangle_{s,c^*}^{sgs} = \int_{-\frac{1}{\mathcal{L}_\kappa} + \varepsilon}^{+\infty} \frac{S_d^0 \kappa - \mathcal{L}_{a_T} \langle a_T \rangle_{s,c^*} \kappa - D^* \kappa^2}{1 + \mathcal{L}_\kappa \kappa} p(\kappa) d\kappa. \quad (4.4.24)$$

The same assumptions are made here as for the model of displacement speed in Eq. (4.3.8).

The proposed model for the stretch due to curvature, defined by Eq. (4.4.24), is compared to the DNS in Fig. 4.4.7. It is computed using the Markstein lengths correlations for  $\mathcal{L}_{a_T}$  and  $\mathcal{L}_\kappa$  given by Eq. (3.3.5) and Eq. (3.3.6), respectively. In this figure is also presented a model proposed by Katragadda et al. (2014a) (Eqs. (1.6.26) to (1.6.27f)), using their suggested values for the model parameters. Although developed for the generalized approach, Katragadda's model is here computed using quantities  $\overline{\Sigma}^*$  and  $\overline{\mathcal{C}}$  on the iso-surface  $c^*$ .

For cases A to D, the proposed model reproduces qualitatively the evolution of  $\langle S_d\kappa \rangle_{s,c^*}$  as seen in Fig. 4.4.7a to 4.4.7c. In particular, the model is in good agreement with the DNS towards  $\tilde{\mathcal{C}} = 0$  and the decrease of  $\langle S_d\kappa \rangle_{s,c^*}$  with  $\tilde{\mathcal{C}}$  up to 0.8 approximately is correctly reproduced. On the contrary, above this value, the model goes back to zero too quickly compared to the DNS. This discrepancy can partly be explained by the strong numerical noise observed on the DNS on the burned gases side. Katragadda's model also recovers the order of magnitude of  $\langle S_d\kappa \rangle_{s,c^*}$  but it is less accurate than the proposed model and shows a too flat profile compared to the DNS. In Fig. 4.4.7a, the proposed model for case A is also presented using the Markstein lengths directly fitted on DNS case A in Section 3.3.2 (in plain symbols and dashed line). It can be seen that the proposed model prediction improves remarkably on the burnt gases side with the fitted Markstein lengths. For instance, at  $\tilde{\mathcal{C}} = 0.8$  the proposed model using the correlation over-estimates  $\langle S_d\kappa \rangle_{s,c^*}$  by a factor two while when using the fitted value, the error goes to nearly zero. This result shows that the proposed model has the ability to correctly recover the DNS results but it also shows that unfortunately, the model prediction is highly sensitive to the turbulent Markstein length employed. Future work is certainly needed to better assess how these lengths could be modelled in a more reliable and possibly universal manner.

For the cases with  $Le_k = 1$ , the proposed model presents the same type of agreement with the DNS although on case A it strongly under-estimates  $\langle S_d\kappa \rangle_{s,c^*}$ . For  $Le_k = 1$  cases, Eq. (4.4.24) and Katragadda's model are equivalent for  $\tilde{\mathcal{C}} < 0.7$ . However, on the burned gases side the proposed model (Eq. 4.4.24) better predicts  $\langle S_d\kappa \rangle_{s,c^*}$  than Katragadda's model, which presents large positive values while  $\langle S_d\kappa \rangle_{s,c^*}$  remains negative in the DNS. DNS case C using the ARC mechanism is also presented in Fig. 4.4.7b: as for previous flame statistics, it presents a very similar  $\langle S_d\kappa \rangle_{s,c^*}$  profile as the 2-step mechanism.

Finally, the stretch rate due to curvature caused by resolved flow motions  $\langle S_d\kappa \rangle_{s,c^*}^{res}$  can be

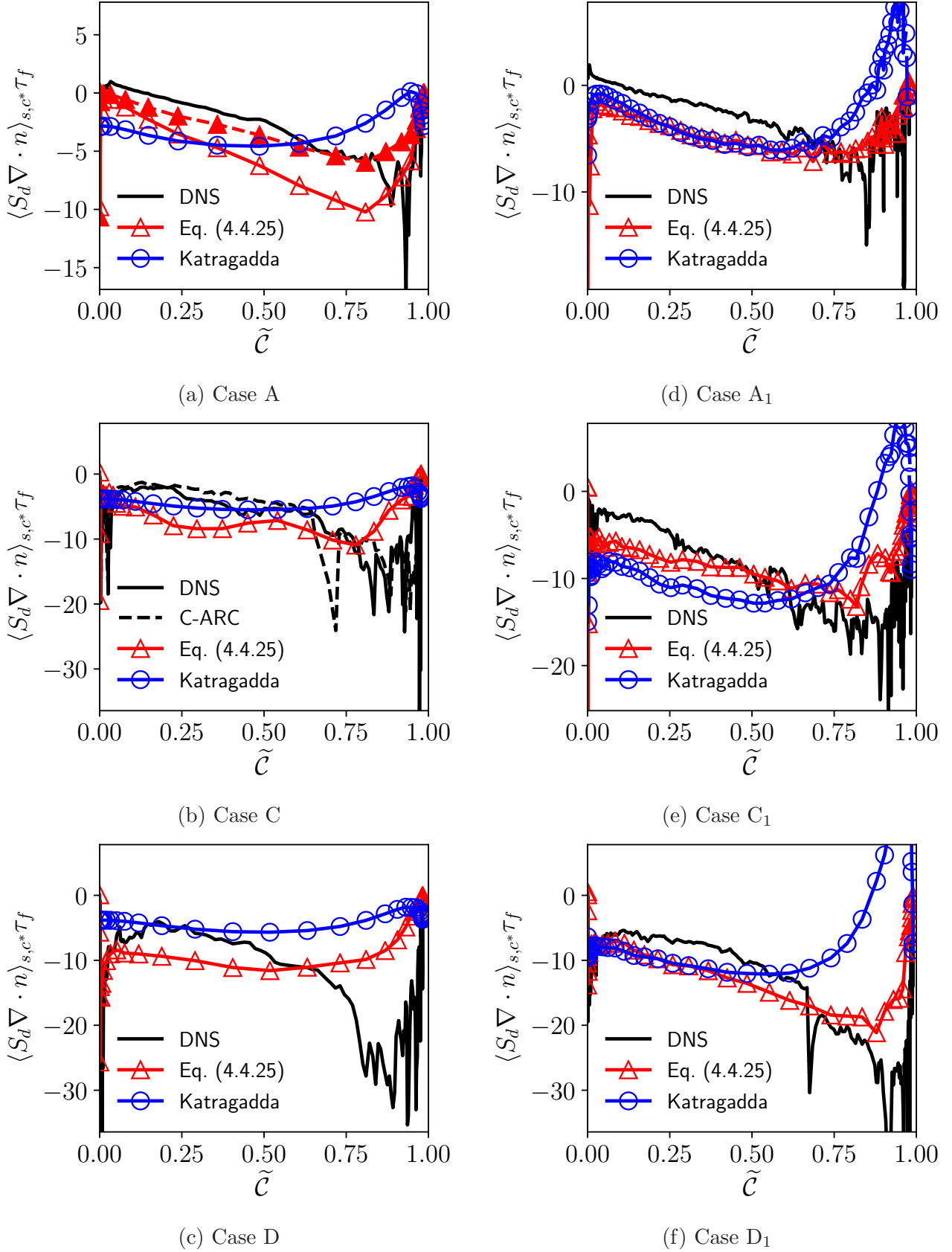


Figure 4.4.7: Comparison of the stretch due to curvature  $\langle S_d \kappa \rangle_{s,c^*}$  normalized with the chemical time  $\tau_f = \delta_L^0 / S_L^0$  for Katragadda's model (Katragadda et al., 2014a) and the proposed model (Eq. 4.4.24) with the DNS versus  $\tilde{C}$  for : (a) to (c) cases with  $Le_k \neq 1$  and (d) to (f) cases with  $Le_k = 1$ . Plain symbols and dashed line represent predictions from Eq. (4.4.24) using Markstein lengths fitted from the DNS in (a). Black dashed line represents  $\langle S_d \kappa \rangle_{s,c^*}$  extracted from the simulation using ARC mechanism (case C-ARC).

combined with the term that accounts for the heat release effects  $S_{hr}$  in the the tangential strain rate. The latter can be expressed (see Appendix E) as:

$$S_{hr} = \left( \frac{\rho_u}{\bar{\rho}} - \frac{\rho_u}{\rho^*} \right) S_L^0 \nabla \cdot \langle \mathbf{n} \rangle_{s,c^*}. \quad (4.4.25)$$

Equation (4.4.25) is similar to the expression proposed by Hawkes and Cant (2000). Thus, the sum of  $\langle S_d \kappa \rangle_{s,c^*}^{res}$  and  $S_{hr}$  is:

$$\langle S_d \kappa \rangle_{s,c^*}^{res} + S_{hr} = \frac{\rho_u}{\bar{\rho}} S_L^0 \nabla \cdot \langle \mathbf{n} \rangle_{s,c^*}. \quad (4.4.26)$$

Equation 4.4.26 corresponds to the stretch rate due to curvature caused by resolved flow motions introduced by Richard (2005).

## 4.5 Discussion on the relationship between $\tilde{\mathcal{C}}$ and $\bar{\mathcal{C}}$

Accurate predictions of the models presented in the previous section rely on the closure of the curvature and its variance, which involve  $\bar{\mathcal{C}}$ , as presented in Section 4.3.2. Unfortunately, the available variable, from Eq. (4.1.5), is  $\tilde{\mathcal{C}}$ . So,  $\bar{\mathcal{C}}$  should be expressed as a function of the resolved progress variable  $\tilde{\mathcal{C}}$ .

The usual relationship used is based on the Bray-Moss-Libby (BML) analysis (Bray and Moss, 1977). The BML model combines a statistical approach using probability density functions and a physical analysis. The PDF of the progress variable  $\mathcal{C}$  at a given location  $\mathbf{x}$  is expressed as the sum of fresh, fully burnt and burning gases contributions:

$$p(\mathcal{C}, \mathbf{x}) = \alpha(\mathbf{x})\delta(\mathcal{C}) + \beta(\mathbf{x})\delta(1 - \mathcal{C}) + \gamma(\mathbf{x})f(\mathcal{C}, \mathbf{x}), \quad (4.5.1)$$

where  $\alpha$ ,  $\beta$  and  $\gamma$  denotes the probability to have fresh gases, burnt gases and reacting mixture at location  $\mathbf{x}$ , respectively.  $\delta(\mathcal{C})$  and  $\delta(1 - \mathcal{C})$  are the Dirac functions corresponding to fresh and fully burnt gases, respectively. This model is developed assuming large Reynolds and Damköhler numbers, and is based on some strong assumptions, such as unity Lewis numbers, adiabatic flame, isobar or flamelet assumptions.

The flame front is considered as infinitely thin, which implies that the probability to be in the reactive zone is low ( $\gamma \ll 1$ ). Thus, Eq. (4.5.1) reduces to:

$$p(\mathcal{C}) = \alpha\delta(\mathcal{C}) + \beta\delta(1 - \mathcal{C}). \quad (4.5.2)$$

Bray and Moss (1977) express  $\bar{\rho}$  as:

$$\bar{\rho} = \frac{\rho_u}{1 + \tau\tilde{\mathcal{C}}}, \quad (4.5.3)$$

where  $\tau$  is the heat release factor defined as  $\tau = \rho_u/\rho_b - 1$ . Finally, the relationship between  $\tilde{\mathcal{C}}$

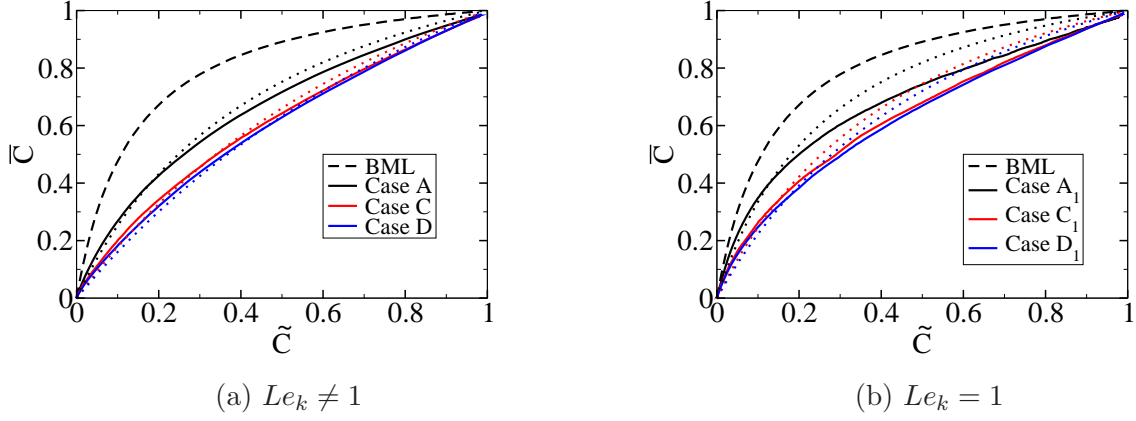


Figure 4.5.1: Evolutions of  $\bar{\mathcal{C}}$  as a function of  $\tilde{\mathcal{C}}$  for: (a) non-unity Lewis numbers cases and (b) unity Lewis numbers cases. The BML relationship is plotted in dashed line. The model proposed by Chakraborty and Cant (2011) is plotted in dotted lines.

and  $\bar{\mathcal{C}}$  is deduced from Eq. (4.5.3):

$$\bar{\mathcal{C}} = \frac{(1 + \tau)\tilde{\mathcal{C}}}{(1 + \tau\tilde{\mathcal{C}})}. \quad (4.5.4)$$

Figure 4.5.1 shows the evolution of  $\bar{\mathcal{C}}$  as a function of  $\tilde{\mathcal{C}}$  extracted from the DNS, as well as the BML relationship given in Eq. (4.5.4). Even for low Karlovitz cases (A and A<sub>1</sub>), the profiles of  $\bar{\mathcal{C}}$  with  $\tilde{\mathcal{C}}$  differs significantly from the profile predicted by the BML analysis. When the Karlovitz number is increased, the relationship between  $\bar{\mathcal{C}}$  and  $\tilde{\mathcal{C}}$  tends to the identity function. As expected, the BML relationship is not adapted to TRZ regime.

Chakraborty and Cant (2011) adapted the BML relationship given in Eq. (4.5.4) to take into account the effect of the Lewis number and that the flame is not infinitely thin:

$$\bar{\mathcal{C}} = \frac{(1 + \tau g^a Le^{-b})\tilde{\mathcal{C}}}{(1 + \tau g^a Le^{-b}\tilde{\mathcal{C}})}, \quad (4.5.5)$$

where  $g = \overline{\rho\mathcal{C}''^2}/\bar{\rho}\tilde{\mathcal{C}}(1 - \tilde{\mathcal{C}})$  is the segregation factor, and  $a$  and  $b$  are positive model constants, with the suggested values  $a = 0.26$  and  $b = 1.5$  (Chakraborty and Cant, 2011). The factor  $Le^{-b}$  accounts for the strengthening of thermal expansion effects with decreasing Lewis number. This expression better captures the variations of  $\bar{\mathcal{C}}$  with  $\tilde{\mathcal{C}}$  in dotted lines in Fig. 4.5.1, when the segregation factor is well fitted. The corresponding segregation factors are reported in Table 4.4. Nevertheless, to use this expression, a model for  $\overline{\rho\mathcal{C}''^2}$  is needed, which is not straightforward, especially in the TRZ regime.

Table 4.4: Segregation factor involved in Eq. (4.5.5) fitted to best reproduce  $\bar{\mathcal{C}}$  of each DNS.

Case A	Case C	Case D	Case A <sub>1</sub>	Case C <sub>1</sub>	Case D <sub>1</sub>
0.5	0.3	0.25	0.6	0.4	0.35

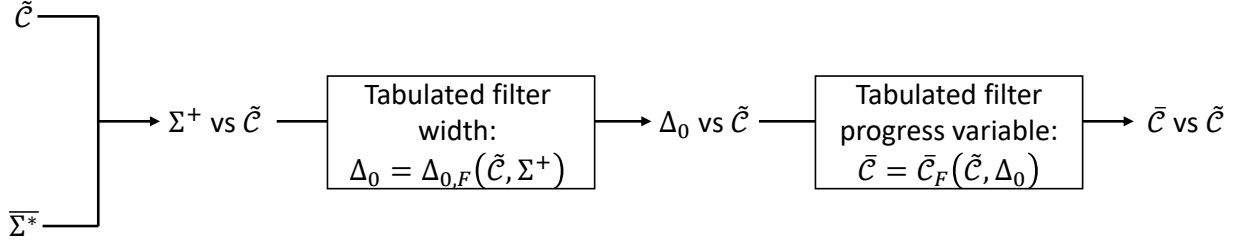


Figure 4.5.2: Schematic explanation for the determination of  $\bar{\mathcal{C}}$  from  $\Sigma^+$  and  $\tilde{\mathcal{C}}$ .

Even if the model proposed by Chakraborty and Cant (2011) improves significantly the prediction of  $\bar{\mathcal{C}}$ , the issue of evaluating the segregation factor motivates to explore, in this study, another model for  $\bar{\mathcal{C}}$  from the knowledge of  $\tilde{\mathcal{C}}$ . The idea of this new model was developed originally in the filtered laminar flame-PDF (FLF-PDF) by Moureau et al. (2011).

The FLF-PDF model is based on the sub-filter PDF analysis conducted by Moureau et al. (2011). The main idea is to filter laminar flames with a filter width  $\Delta_0$ , smaller or equal to the LES filter  $\Delta$ , to take into account the decrease of the PDF segregation due to the wrinkling and the thickening of the flame. In practice, lookup table of filtered quantities is obtained using spatial filtering of laminar flames. These lookup tables can be reorganized versus  $\tilde{\mathcal{C}}$  for every  $\Delta_0$  considered:

$$\tilde{\varphi} = \tilde{\varphi}_F(\tilde{\mathcal{C}}, \Delta_0), \quad (4.5.6)$$

where  $\varphi$  denotes any thermo-chemical quantity of interest. Equation (4.5.6) can be inverted into:

$$\Delta_0 = \Delta_{0,F}(\tilde{\mathcal{C}}, \tilde{\varphi}). \quad (4.5.7)$$

This idea is applied in this study to the modelling of the filtered progress variable  $\bar{\mathcal{C}}$  from the knowledge of the filtered FSD  $\bar{\Sigma}^*$ , which is normalized with the flame thickness  $\delta_F$ :

$$\Sigma^+ = \delta_F \bar{\Sigma}^*. \quad (4.5.8)$$

The procedure described by Moureau et al. (2011) becomes (illustrated in Fig. 4.5.2):

1. From the knowledge of  $\tilde{\mathcal{C}}$  and  $\Sigma^+$ , select the filter width  $\Delta_0 = \Delta_{0,F}(\tilde{\mathcal{C}}, \Sigma^+)$  that results in the same normalized FSD for the same filtered progress variable value, when the reference laminar flame is filtered at  $\Delta_0$  (as seen in Fig. 4.5.3a).
2. Filter the laminar flame progress variable in physical space at  $\Delta_0$  to obtain the value for the given parameters  $\tilde{\mathcal{C}}$  and  $\Sigma^+$ , i.e.  $\bar{\mathcal{C}} = \bar{\mathcal{C}}_F(\tilde{\mathcal{C}}, \Delta_0)$  (see Fig. 4.5.3b).

So, a filtered premixed laminar flames library is needed to complete this model. This library can be built by space filtering a laminar progress variable, for a wide range of filter width ( $\Delta_0$ ).

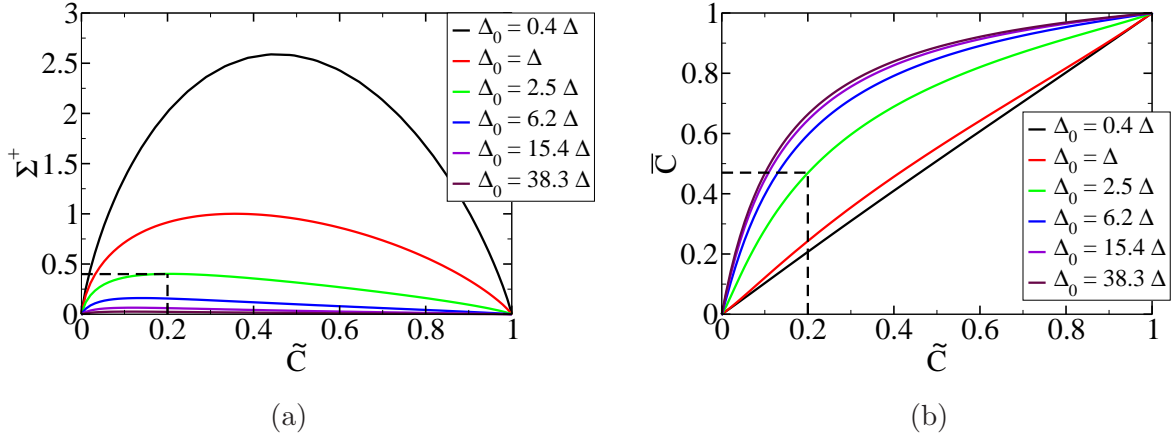


Figure 4.5.3: Schematic view of the look-up tables for the determination of  $\bar{C}$  from  $\Sigma^+$  and  $\tilde{C}$ : (a)  $\Sigma^+$  versus  $\tilde{C}$  and  $\Delta_0$  and (b)  $\bar{C}$  versus  $\tilde{C}$  and  $\Delta_0$

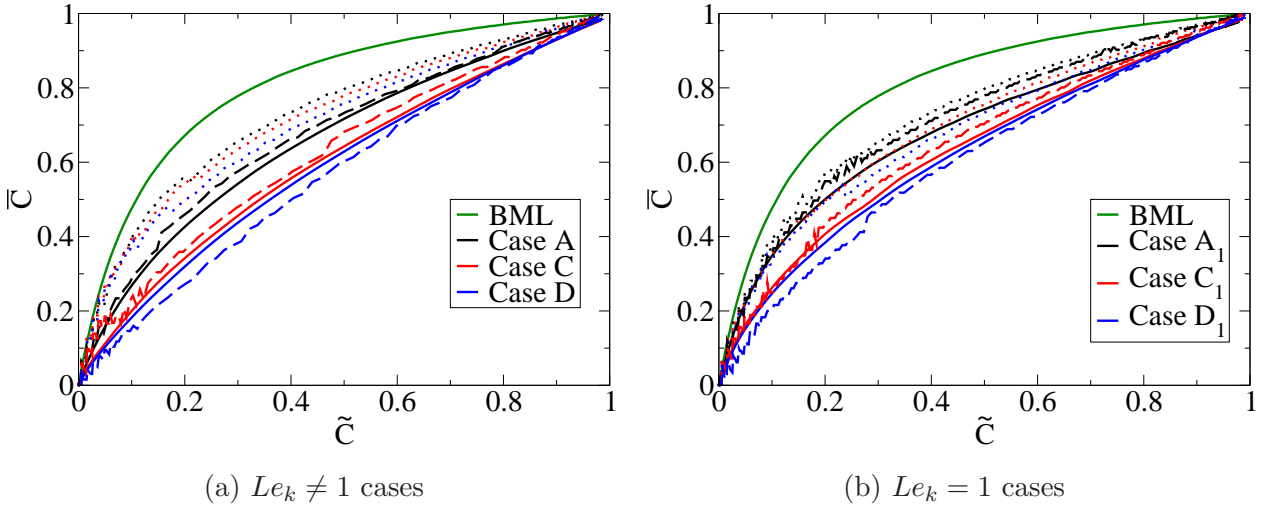


Figure 4.5.4: Comparisons of the profiles of filtered progress variable  $\bar{C}$  extracted from DNS (solid lines), from the FLF-PDF based model using the laminar flame thickness in Eq. (4.5.8) (dotted lines) and from the FLF-PDF based model using the effective flame thickness  $\delta_L^{eff}$  in Eq. (4.5.8) (dashed lines) for: (a)  $Le_k \neq 1$  cases and (b)  $Le_k = 1$  cases.

This progress variable is approximated by a hyperbolic tangent function of width  $\delta_F$ , which is the thermal flame thickness. From the DNS results presented in Section 3.2.1, the thermal thickness is nearly constant for unity Lewis number cases, while it strongly increases with the Karlovitz number for non-unity Lewis number cases. A simple dimensional model is proposed to take into account the thickening of the flame front observed for high Karlovitz number in Chapter 3 through an effective laminar flame thickness  $\delta_L^{eff}$ :

$$\delta_L^{eff} = \delta_L^0 \left( 1 + \alpha \frac{\mathcal{L}_\kappa}{S_L^0} \langle a_T \rangle_{s,c^*} \right), \quad (4.5.9)$$

where  $\alpha$  is a model constant set to 0.75 to recover the thickening observed in Chapter 3.  $\mathcal{L}_\kappa$  is the Markstein length linked to curvature defined in Section 3.3.2. Equation (4.5.9) allows to recover  $\delta_L^{eff} = \delta_L^0$  when  $Ka \ll 1$  and  $\delta_L^{eff} \approx \delta_L^0$  for unity Lewis number cases, because  $\mathcal{L}_\kappa$  is close to zero in these cases.



Figure 4.5.4 compares the profiles of filtered progress variable  $\bar{\mathcal{C}}$  extracted from DNS to those predicted by the FLF-PDF based model presented previously. First, when the effective flame thickness involved in the definition of  $\Sigma_+$  is set to the laminar flame thickness, the FLF-PDF based model improves slightly the predictions from the BML model. Indeed, this model (in dotted lines) reproduces the evolution with an increase of  $Ka$ , i.e. the profiles of  $\bar{\mathcal{C}}$  with  $\tilde{\mathcal{C}}$  tend to the identity function when  $Ka$  increases.

Then, the flame thickness involved in the FLF-PDF based model is computed using Eq. (4.5.9) in order to take into account the thickening observed in the TRZ regime (even in the reaction zone as seen in Section 3.2.1). The resulting profiles of filtered progress variable  $\bar{\mathcal{C}}$  are plotted in dashed lines in Fig. 4.5.4. These profiles are in good agreement with the profiles extracted from DNS. So, the FLF-PDF based model combined with an estimation of the effective flame thickness due to the overall thickening of the flame front (see Section 3.2.1) allows to accurately predict the relationship between  $\bar{\mathcal{C}}$  and  $\tilde{\mathcal{C}}$ .

## 4.6 Conclusions

In this chapter, a new approach is proposed to adapt the CFM model to flames in both flamelet and TRZ regimes. This approach is based on the analysis of the DNS presented in Chapters 2 and 3. This adaptation is based on the simulation of a particular iso-surface of progress variable  $c^*$  in the reaction zone. This is made possible by defining an adapted progress variable  $\mathcal{C} = \mathcal{H}(c - c^*)$ , where  $\mathcal{H}(c)$  is the Heaviside function and an adapted flame surface density  $\Sigma^* = |\nabla \mathcal{C}| = \Sigma \delta(c - c^*)$ , where  $\delta(c)$  is the Dirac function. Using these two variables, the equations of the CFM model are modified into the transport equations presented in Eqs. (4.1.5) and (4.1.6).

To complete the adaptation of the CFM model, closures are proposed for each term:

- A simple gradient model combined with a term that accounts for thermal expansion is chosen to model the unresolved transport term of the progress variable in Eq. (4.3.6).
- A model based on DNS analysis is defined for the displacement speed  $\langle S_d \rangle_{s,c^*}$  in Eq. (4.3.16). This model is based on the definition of a presumed Gaussian PDF of the flame curvature in Eq. (4.3.9) and on the definition of two distinct effective Markstein lengths,  $\mathcal{L}_{a_T}$  and  $\mathcal{L}_\kappa$ . The latter are estimated from the correlations given in Chapter 3 in Eqs. (3.3.5) and (3.3.6).
- As in the currently used CFM model, the tangential strain rate is decomposed into tangential strain rates due to resolved and unresolved flow motions. The former is modelled with a well known model proposed by Hawkes and Cant (2000) and given in Eq. (4.4.13). While the tangential strain rate due to sub-grid scale flow motions,  $\langle a_T \rangle_{s,c^*}^{sgs}$  is modelled using the approach defined in Sections 1.5.3 and 2.3, where the efficiency function used is either  $\text{HK}_{2D}$ , LPF or Bougrine's functions, reported in Section 4.4.
- The stretch rate due to curvature is also decomposed into contributions due to resolved and unresolved flow motions. The latter is modelled in Eq. (4.4.24) based on the DNS



analysis presented in Chapter 3. While the stretch rate due to curvature caused by resolved flow motions is modelled as  $(\rho_u/\rho^*)S_L^0 \nabla \cdot \langle \mathbf{n} \rangle_{s,c^*}$ , but when it is combined with the terms  $S_{hr}$  that accounts for the effect of heat release on the tangential strain rate, it becomes similar to term due to resolved flow motion in ECFM-LES model (Richard, 2005).

- The normal propagation term and the unresolved transport term of the FSD are modelled together in Eq. (4.4.9).

These closures depends strongly on the flame curvature  $\langle \kappa \rangle_{s,c^*}$  and its variance  $\sigma^2 = \langle \kappa^2 \rangle_{s,c^*} - \langle \kappa \rangle_{s,c^*}^2$ . The former is modelled following the model proposed by Rymer (2001) and reported in Eq. (4.3.13). The latter is evaluated through a model for  $\langle \kappa^2 \rangle_{s,c^*}$  given in Eq. (4.3.15). Both models depend strongly on the evaluation of the filtered progress variable  $\bar{\mathcal{C}}$ , which is not known. Traditionally,  $\bar{\mathcal{C}}$  is computed using the BML relationship, which is shown to poorly predicts the profile of  $\bar{\mathcal{C}}$  with  $\tilde{\mathcal{C}}$  for flames in the TRZ regime. Thus, a model based on the FLF-PDF approach (Moureau et al., 2011) is proposed in this chapter showing encouraging results.

This adaptation of the CFM model is compared to DNS in *a priori* tests, and shows encouraging results with good agreement with DNS for each sub-model. Further analysis are needed to enable the use of this model in engine applications. The first step is to evaluate the behaviour of this model in *a posteriori* tests, which is the focus of the next chapter.

# Chapter 5

## A first *a posteriori* validation in the thin reaction zone regime

The previous chapter shows an *a priori* adaptation of the coherent flame model (CFM) presented in Chapter 1 to flames in the thin reaction zone (TRZ) regime. Each sub-model presents encouraging results. In this chapter, a further step toward SI engines applications is proposed through the implementation of the model presented in Chapter 4 in the AVBP code.

In this chapter, one-dimensional turbulent flame simulations are first presented in Section 5.1 with the different models tested. Then, the predictions of the models are compared to direct numerical simulations (DNS) by evaluating the general behaviour of the flames in Section 5.2. Then, the predictions of each closures are compared to DNS in Section 5.3. Finally, the application of the model to large eddy simulations (LES) of spark-ignition (SI) engines is discussed in Section 5.4.

### 5.1 *A posteriori* simulations of one-dimensional turbulent flames

The objective here is to assess how the complete model, including each sub-models, behaves with an increase of the turbulence intensity and with differential diffusion. First, the method and the set up used to perform *a posteriori* validation is described. Then, the different models evaluated are presented.

#### 5.1.1 Description of the one-dimensional turbulent flame method

One-dimensional flames were simulated in Reynolds averaged Navier-Stokes (RANS) using the AVBP code corresponding to the flames in the 3D-DNS presented in Chapter 3. The results from these RANS simulations are then compared to the results extracted from the DNS with the procedure defined in Section 4.2.

In this section, we define the parameters of the RANS simulations. Turbulence is a three-dimensional phenomenon that needs to be modelled. In these one-dimensional turbulent flames,

effects of turbulence are taken into account as follows:

- The turbulent flow is modelled through an imposed turbulent viscosity, given by:

$$\nu_t = Cu'_t l_t, \quad (5.1.1)$$

where  $u'_t$  is the velocity of the turbulent structures at the integral scale of length  $l_t$ .  $u'_t$  and  $l_t$  are parameters of the simulations set to the values found in DNS and reported in Table 5.2.  $C$  is a constant determined following a Prandtl-Kolmogorov model (Launder and Spalding, 1972), where the turbulent viscosity is defined as:

$$\nu_t = C_k l_t k^{1/2}. \quad (5.1.2)$$

$C_k$  is a constant and  $k$  is the turbulent kinematic energy (TKE), defined as  $k = \sqrt{(3/2)u_t'^2}$  because the turbulence is supposed to be homogeneous and isotropic. Equation (5.1.2) becomes:

$$\nu_t = C_k \sqrt{\frac{3}{2}} u'_t l_t. \quad (5.1.3)$$

Finally, from Eq. (5.1.3) the constant  $C$  in Eq. (5.1.1) is set to 0.12, because  $C_k = 0.1$  in a homogeneous isotropic turbulence (HIT) without mean gradient of velocity.

- The stirring of the flame due to turbulence is imposed through the tangential strain rate due to unresolved flow motions  $\langle a_T \rangle_{s,c^*}^{sgs}$ , which is considered constant through the flame front and defined as presented in Section 4.4:

$$\langle a_T \rangle_{s,c^*}^{sgs} = \alpha_{a_T} \Gamma \frac{u'_t}{l_t}, \quad (5.1.4)$$

where  $\Gamma$  is an efficiency function modelled with Eq. (4.4.16) and one of the functions presented in Table 4.2 and  $\alpha_{a_T}$  is a constant to be fixed. In these RANS simulations, the constant  $\alpha_{a_T}$  is chosen to fit the DNS tangential strain rate due to unresolved flow motions of case A ( $\langle a_T \rangle_s^* = \int_V \langle a_T \rangle_{s,c^*} \bar{\Sigma}^* dV / \int_V \bar{\Sigma}^* dV$ ):

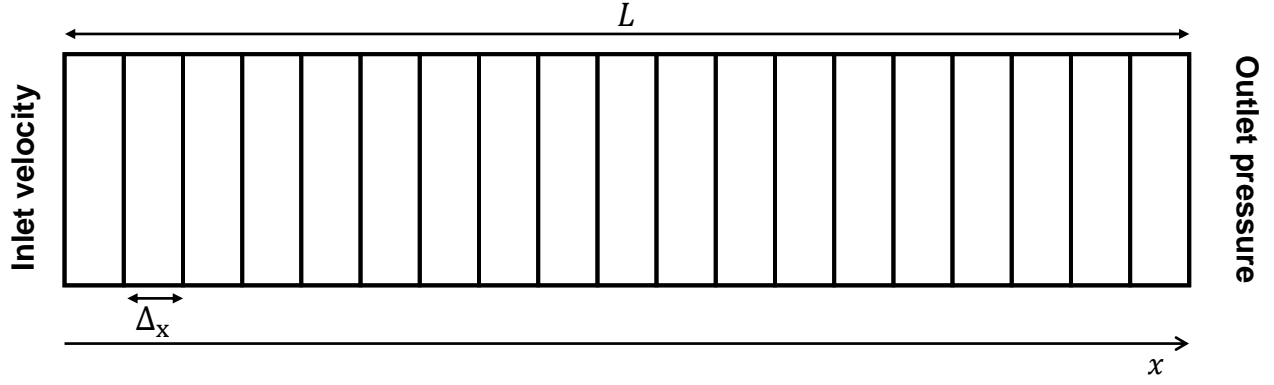
$$\alpha_{a_T} = \frac{l_{t,A} \langle a_T \rangle_{s,A}^*}{\Gamma_A u'_{t,A}}, \quad (5.1.5)$$

where the subscript  $A$  designates case A. The value of  $\alpha_{a_T}$  for each model presented in this study are reported in Table 5.1.

Table 5.1: Tuned model parameter  $\alpha_{a_T}$  for each model.

Models:	Bougrine	Cant	Charlette	HK <sub>2D</sub>	LPF
$\alpha_{a_T}$	10.6	0.8	1.7	1.2	1.4

Figure 5.1.1 presents a schematic view of the computational domain. As for the DNS presented in Chapter 3, the inflow and outflow boundaries are taken to be partially non-reflecting

Figure 5.1.1: Schematic view of the flow configuration of *a posteriori* simulations.

and specified according to the Navier-Stokes Characteristic Boundary Conditions (NSCBC) technique (Poinsot and Lelef, 1992). For each simulation, the inflow velocity  $U_{in}$  is constant throughout the simulation and selected to match the turbulent flame speed  $S_T$  of DNS cases (given in Section 3.2.3). To ensure convergence of the RANS simulations, the length of the  $L$  domain is defined broadly enough to prevent flames from coming out of it. The numerical parameters of the cases chosen to validate the model are reported in Table 5.2.

Table 5.2: Set-up for the simulations of one-dimensional turbulent flame.

Case	$l_t/\delta_L$	$u'_t/S_L^0$	Ka	Da	Re <sub>t</sub>	$\nu_t$ [m <sup>2</sup> /s]	$\Delta_x/\delta_L^0$	$S_T/S_L^0$
A	3.3	3.0	2.9	9.9	89.6	$16.9e^{-5}$	0.75	1.06
B	4.4	8.2	11.2	4.8	325.0	$61.7e^{-5}$	1.50	2.06
C	4.3	12.5	21.4	3.1	489.0	$91.9e^{-5}$	1.50	2.67
D	4.4	21.1	46.2	1.9	833.2	$158.7e^{-5}$	1.50	2.93
A <sub>1</sub>	5.1	2.5	1.7	18.7	74.8	$21.8e^{-5}$	0.75	5.4
C <sub>1</sub>	4.9	11.9	18.5	3.7	530.7	$99.7e^{-5}$	1.50	8.97
D <sub>1</sub>	5.1	22.1	46.2	2.1	1016.1	$192.7e^{-5}$	1.50	7.33

### 5.1.2 Description of the models tested

The model proposed in the present study is compared to the standard ECFM-LES model proposed by Richard et al. (2007). The closures of this model differing from the proposed model of this study, despite the difference in the approach as presented in Section 4.1, are:

- For the density weighted displacement speed:

$$\langle \rho S_d \rangle_s = \rho_u S_L^0, \quad (5.1.6)$$

where  $\langle \rangle_s$  is the surface averaging operator defined in Section 1.5.5.

- The model based on an efficiency function is used for the unresolved **tangential strain rate**  $\langle a_T \rangle_s^{sgs}$ , where the function  $C_r$  used is the one proposed by Bougrine et al. (2014) (see Eq. 2.3.4).

- The model for the unresolved **stretch rate due to curvature** is given in Section 1.5.5 by Eq. (1.5.45)

The model proposed in Chapter 4 referred to HK model is tested using different versions to evaluate the impact of different key parameters. In all the versions tested of HK model, the sub-models for  $\langle A_T \rangle_{s,c^*}$  and  $T + P$ , are those used by Richard et al. (2007) involving  $\bar{\mathbf{n}} = -\nabla \bar{\mathcal{C}}/|\nabla \bar{\mathcal{C}}|$  instead of  $\langle \mathbf{n} \rangle_{s,c^*} = -\nabla \bar{\mathcal{C}}/\bar{\Sigma}^*$  avoiding potential numerical instabilities. For all the versions tested in this chapter, the tangential strain rate due to unresolved flow motions is modelled by the LPF model introduced in Section 4.4.3, as suggested by the results from *a priori* tests in Fig. 4.4.6. All the versions of HK model use Eqs. (4.3.16) and (4.4.24) to model displacement speed and stretch rate due to curvature, respectively.

To differentiate the versions of HK model tested, the subscripts  $\alpha$  and  $\gamma$  are used to differentiate the variance involved in the presumed probability density function (PDF) curvature  $p(\kappa)$ :

- $\alpha$  corresponds to the presumed PDF for curvature defined using Eq. (4.3.9) with  $\sigma = \langle \kappa^2 \rangle_{s,c^*} - \langle \kappa \rangle_{s,c^*}^2$ , where the model parameter  $\beta_2$  involved in Eq. (4.3.15) is set to 1, as suggested in Chapter 4.
- $\gamma$  version differs from  $\alpha$  through the definition of the variance  $\sigma^2$  in the presumed PDF of curvature. In this version,  $\sigma^2$  is defined as half the curvature variance as discussed in Section 4.3.2 with Eq. (4.3.11).

The exponents  $2L$  and  $1L$  are used to differentiate the correlations used for the Markstein lengths. The former represents the approach using two distinct effective Markstein lengths, with Eqs. (3.3.5) and (3.3.6). The latter uses a single effective Markstein length  $\mathcal{L}_{rn}$  with Eq. (3.3.7). The main characteristics of each model tested are reported in Table 5.3. Note that  $\text{HK}_\alpha$  models correspond to the exact configuration of the model presented in *a priori* evaluations.

Table 5.3: The different models characteristics

Name	$\langle S_d \rangle_{s,c^*}$	$\langle S_d \kappa \rangle_{s,c^*}$	$\sigma^2$	Marstkein lengths	$\langle a_T \rangle_{s,c^*}^{sgs}$
$\text{HK}_\alpha$	Eq. (4.3.16)	Eq. (4.4.24)	Eq. (4.3.10)	Eqs. (3.3.5) and (3.3.6)	LPF
$\text{HK}_\gamma^{2L}$	Eq. (4.3.16)	Eq. (4.4.24)	Eq. (4.3.11)	Eqs. (3.3.5) and (3.3.6)	LPF
$\text{HK}_\gamma^{1L}$	Eq. (4.3.16)	Eq. (4.4.24)	Eq. (4.3.11)	Eq. (3.3.7)	LPF
ECFM-LES	Eq. 5.1.6	Eq. (1.5.45)	-	-	Bougrine

## 5.2 Analysis of the one-dimensional turbulent flames – general behaviour of the models

In this section, the general behaviour of each model tested is compared to DNS. The two criteria chosen to evaluate the potential of each model are:

- the prediction of the **fuel consumption**,
- the prediction of the **flame structure**.

### 5.2.1 Analysis of predicted fuel consumption

The accuracy of the different models for the prediction of the turbulent flame speed is evaluated in this section. Two criteria are used to determine the efficiency of a model:

1. the ability of the model to reproduce the bending observed on  $S_T$ ,
2. the ability of the model to take into account the effect of differential diffusion on the fuel consumption.

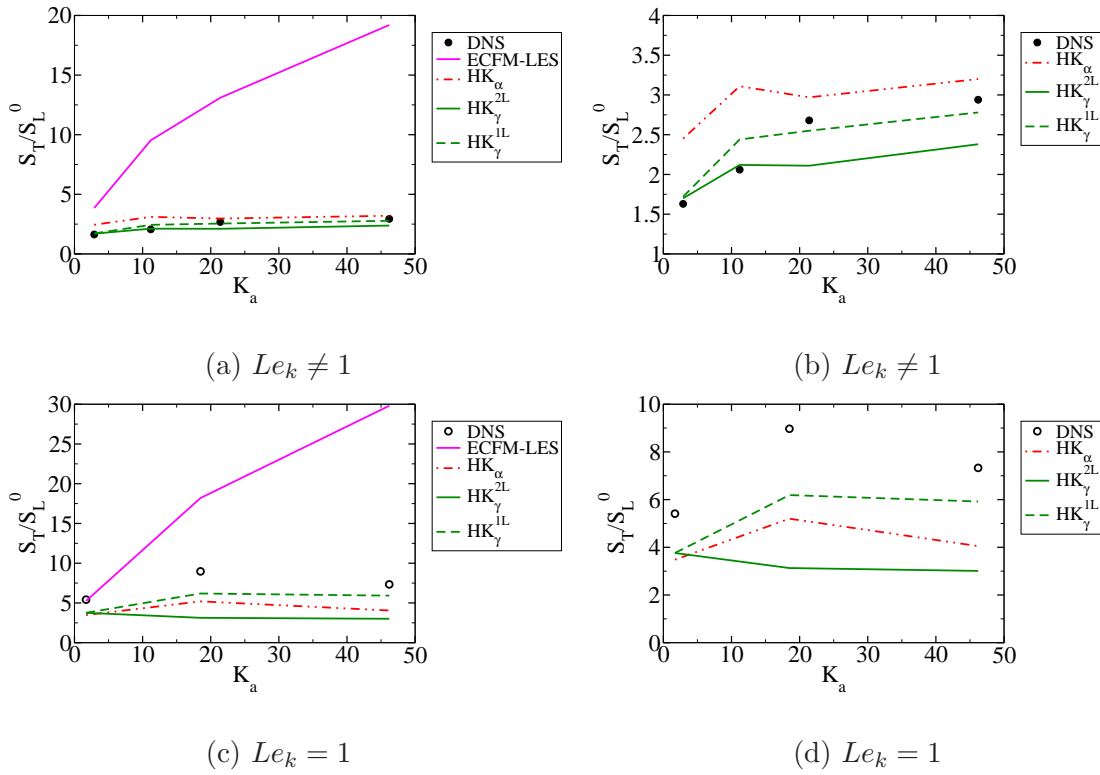


Figure 5.2.1: Evolutions of the predictions of  $S_T/S_L^0$  compared to DNS for: (a)  $Le_k \neq 1$  cases and (c) for  $Le_k = 1$  cases. (b) and (d) show a focus on the versions of HK model and DNS.

Figure 5.2.1 shows the ratio  $S_T/S_L^0$  predicted by each model as functions of  $Ka$ . First of all, each version of the proposed model presents a bending for  $Le_k \neq 1$  cases, except ECFM-LES. The latter increases too steeply with  $Ka$  leading to huge discrepancies for high Karlovitz number, up to 550% relative error for  $Ka = 46.2$ .

Even if  $HK_\alpha$  presents a bending, this model over-predicts  $S_T$ , especially for  $Ka < 20$  in Fig. 5.2.1b. In Fig. 5.2.1b,  $HK_\gamma^{2L}$  predicts turbulent flame speed with the same bending as  $HK_\alpha$  but are approximately 25% smaller. So, it seems that the presumed PDF defined in Eq. (4.3.9) evaluating the variance with Eq. (4.3.10) leads to an overestimation of the turbulent flame speed, especially for low Karlovitz number cases ( $Ka = 2.9$  and  $Ka = 11.2$ ). This

might be explained with the large width of the PDF, which gives weight to extreme values of curvature that are not observed in cases A ( $Ka = 2.9$ ) and B ( $Ka = 11.2$ ). These results confirm the need to well model the curvature PDF in the proposed approach.  $\text{HK}_\gamma^{1\text{L}}$  well reproduces the bending observed in DNS and predict accurate values of  $S_T/S_L^0$ , unlike  $\text{HK}_\gamma^{2\text{L}}$ . Note that  $\text{HK}_\alpha$  and  $\text{HK}_\gamma^{2\text{L}}$  models present an unexpected change of slope between low and high Karlovitz numbers (between cases B and C). It should be noted that this phenomenon is only observed when two distinct effective Markstein lengths are used. In addition, when a single effective Markstein length is used ( $\text{HK}_\gamma^{1\text{L}}$  model), the slope for low Karlovitz numbers ( $Ka < 15$ ) is overestimates. At this point, we are unable to propose a proper explanation and further analysis should be conducted to better understand the impact and evolution of the Markstein lengths. For high Karlovitz numbers, both  $\text{HK}_\gamma^{2\text{L}}$  and  $\text{HK}_\gamma^{1\text{L}}$  present the same slope between cases C and D, but the latter predicts larger  $S_T$  than the former suggesting that using two distinct effective Markstein lengths overestimates the effect of strain rate on the flame front, especially for high Karlovitz numbers. This is illustrated in Fig. 3.3.8, where the values of  $\mathcal{L}_{rn}$  are significantly smaller than  $\mathcal{L}_{aT}$  predicted by Eq. (3.3.5), approximately 30% smaller for  $Ka > 20$ . So, as a first step, using  $\mathcal{L}_{rn}$  better reproduces the trend on the turbulent flames.

As for  $Le_k \neq 1$  cases, the turbulent flame speed observed for  $Le_k = 1$  cases presents a bending, which is not predicted by ECFM-LES model. Contrary to non unity Lewis number cases,  $\text{HK}_\gamma^{2\text{L}}$  model does not have an increasing evolution in Fig. 5.2.1c. Indeed,  $S_T/S_L^0$  is reduced from 3.76 to 3.01, when  $Ka$  increases from 1.7 to 46.2. As for  $Le_k \neq 1$  cases,  $\text{HK}_\gamma^{2\text{L}}$  model, using two distinct effective Markstein lengths, has a worst behaviour than the model using  $\mathcal{L}_{rn}$ . In Fig. 5.2.1d,  $\text{HK}_\alpha$  and  $\text{HK}_\gamma^{1\text{L}}$  models are the models with the smallest errors in terms of  $S_T/S_L^0$ . But these models strongly underestimate the turbulent flame speed found in DNS with maximum relative errors of 45%, 40% and 30% for cases A<sub>1</sub>, C<sub>1</sub> and D<sub>1</sub>, respectively. Finally, only  $\text{HK}_\alpha$  and  $\text{HK}_\gamma^{1\text{L}}$  models are able to reproduce the decrease of  $S_T/S_L^0$  from case C<sub>1</sub> ( $Ka = 18.5$ ) to D<sub>1</sub> ( $Ka = 46.2$ ).

To understand the large discrepancies observed for  $Le_k = 1$  cases, the propagation term  $\langle \rho S_d \rangle_{s,c^*} \bar{\Sigma}^*$  is displayed in Fig. 5.2.2.  $Le_k \neq 1$  cases in Figs. 5.2.2a to 5.2.2d show that the spatial profiles of  $\langle \rho S_d \rangle_{s,c^*} \bar{\Sigma}^*$  predicted by  $\text{HK}_\gamma^{1\text{L}}$  are almost superimposed with those from the DNS. On the contrary, the spatial profiles predicted by ECFM-LES and  $\text{HK}_\alpha$  models are very different than those from DNS.  $\text{HK}_\gamma^{2\text{L}}$  predicts similar spatial profiles than  $\text{HK}_\gamma^{1\text{L}}$  but differing on the fresh gases side in particular for high  $Ka$  (cases C and D). These spatial profiles are related to the turbulent flame speed  $S_T$  through:

$$S_T = \frac{1}{\rho_u \mathcal{A}_0} \int_{\mathcal{V}} \langle \rho S_d \rangle_{s,c^*} \bar{\Sigma}^* dV, \quad (5.2.1)$$

where  $\mathcal{A}_0$  is the area of the flame projected in the propagation direction and  $\mathcal{V}$  is the domain of computation. Thus, the differences between the models in term of turbulent speed come from the integral of the spatial profiles.  $\text{HK}_\gamma^{2\text{L}}$  model predicts slightly smaller integrated propagation terms at high  $Ka$  than  $\text{HK}_\gamma^{1\text{L}}$  model showing a strong sensitivity to the spatial profiles of both

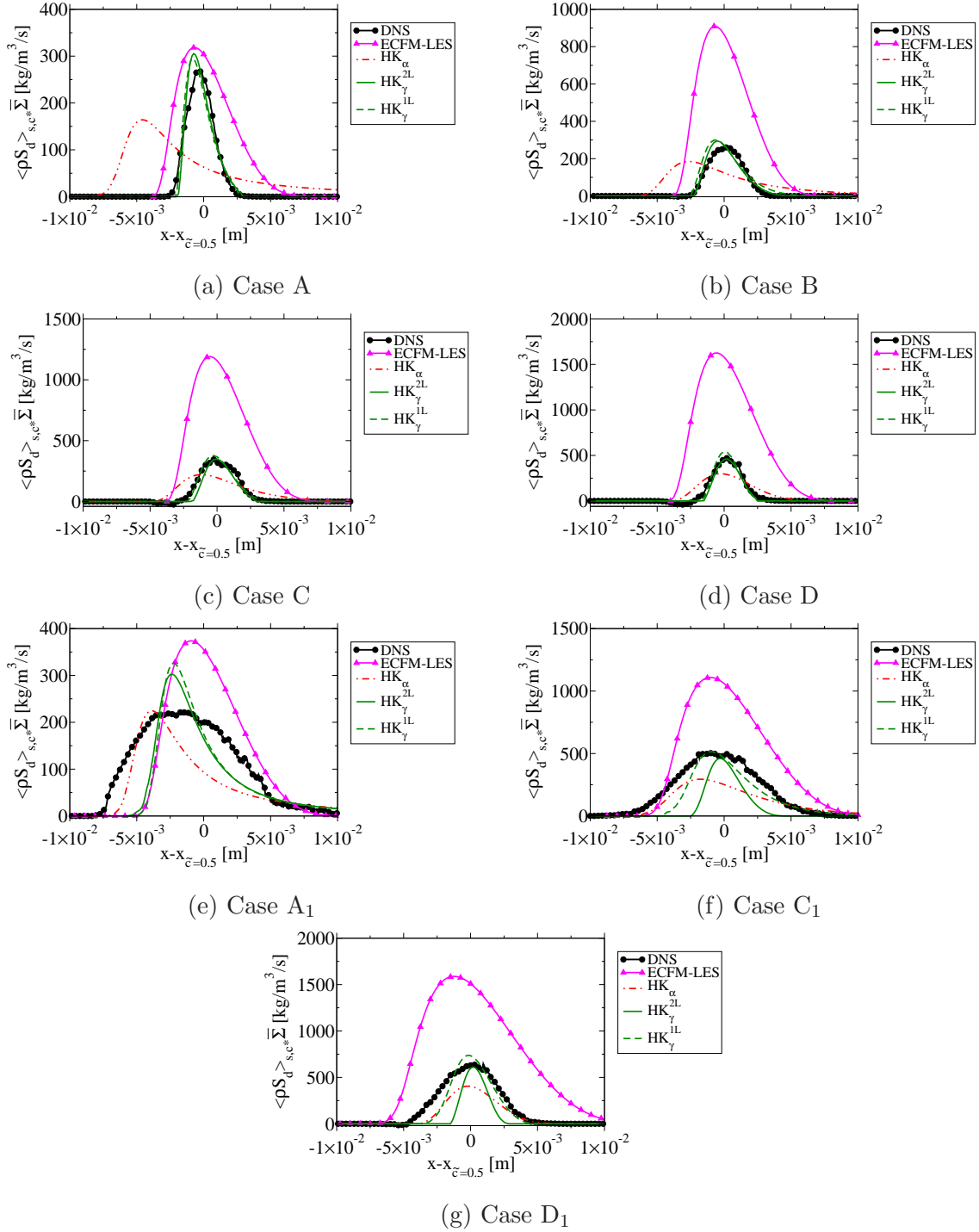


Figure 5.2.2: Predictions of the spatial profile of propagation term  $\langle \rho S_d \rangle_{s,c^*} \bar{\Sigma}^*$  centred on  $\tilde{c} = 0.5$  from the proposed model compared to ECFM-LES model and DNS, for : (a) to (d) cases with  $Le_k \neq 1$  and (e) to (g) cases with  $Le_k = 1$ .



$\langle S_d \rangle_{s,c^*}$  and  $\overline{\Sigma^*}$ .

Figures 5.2.2e to 5.2.2g show the spatial profiles of the propagation term for  $Le_k = 1$  cases. In these figures, the spatial profiles predicted by all the models tested are strongly different from DNS leading to very small integrated propagation terms compared to DNS. At this point, it is difficult to say whether these spatial profiles are due to the iso-surface approach or to the closures proposed based on Markstein lengths.

Finally, the model that best respects the criteria defined on the fuel consumption is  $HK_\gamma^{1L}$ . However, to further analyse the behaviour of each model, both the flame structure and the closures should be evaluated. The former is proposed in the next subsection, while Section 5.3 is dedicated to the latter.

## 5.2.2 Analysis of the predicted flame structure

A further step in the validation of the proposed model is to verify that the flame structure is well reproduced. The flame structure is evaluated through:

1. the spatial profile of the resolved progress variable  $\tilde{C}$ ,
2. the spatial profile of flame surface density (FSD)  $\overline{\Sigma^*}$ .

Figure 5.2.3 shows the spatial profiles of the resolved progress variable  $\tilde{C}$  obtained with the different models and compared with the DNS for each case. For  $Le_k \neq 1$  cases, ECFM-LES and  $HK_\alpha$  models predict larger spatial profiles of resolved progress variable, while  $HK_\gamma^{2L}$  and  $HK_\gamma^{1L}$  models accurately reproduce the profiles of  $\tilde{C}$ . Case A shows particular discrepancies between predictions from  $HK_\alpha$  and DNS confirming that computing the curvature variance  $\sigma^2$  with Eq. (4.3.10) in the presumed PDF of curvature (Eq. 4.3.9) leads to large discrepancies due to large values of  $\kappa$  taken into account that are not observed in case A.

For  $Le_k = 1$  cases in Figs. 5.2.3e to 5.2.3g, none of the models presented accurately reproduces the spatial profiles of  $\tilde{C}$ , except  $HK_\alpha$  model for high  $Ka$  (cases C<sub>1</sub> and D<sub>1</sub>). However, the predictions of this model for case A<sub>1</sub> present large discrepancies on the burned gases side ( $x - x_{\tilde{C}=0.5} > 0$ ).  $HK_\gamma^{2L}$  and  $HK_\gamma^{1L}$  models predict spatial profiles of  $\tilde{C}$  too steep for high Karlovitz numbers, while the profiles predicted have smoother slopes on the burned gases side for case A<sub>1</sub>. These observations suggest that the evaluation of the Markstein lengths does not explain that the proposed model is worst for  $Le_k = 1$  cases.

To further investigate these discrepancies, the behaviour of the models on the predictions of the FSD are displayed in Fig. 5.2.4. This figure shows the spatial profiles of the flame surface density centred on the position where  $\tilde{C} = 0.5$  for each case. The profiles predicted by each model present the same behaviours with  $Ka$  than the profiles of the progress variable in Fig. 5.2.3.  $HK_\gamma^{2L}$  and  $HK_\gamma^{1L}$  models are in very good agreement with DNS.

Figure 5.2.4 shows that for cases A, A<sub>1</sub> and B,  $HK_\alpha$  model presents a long tail on the burnt gases side, which is not in agreement with DNS.

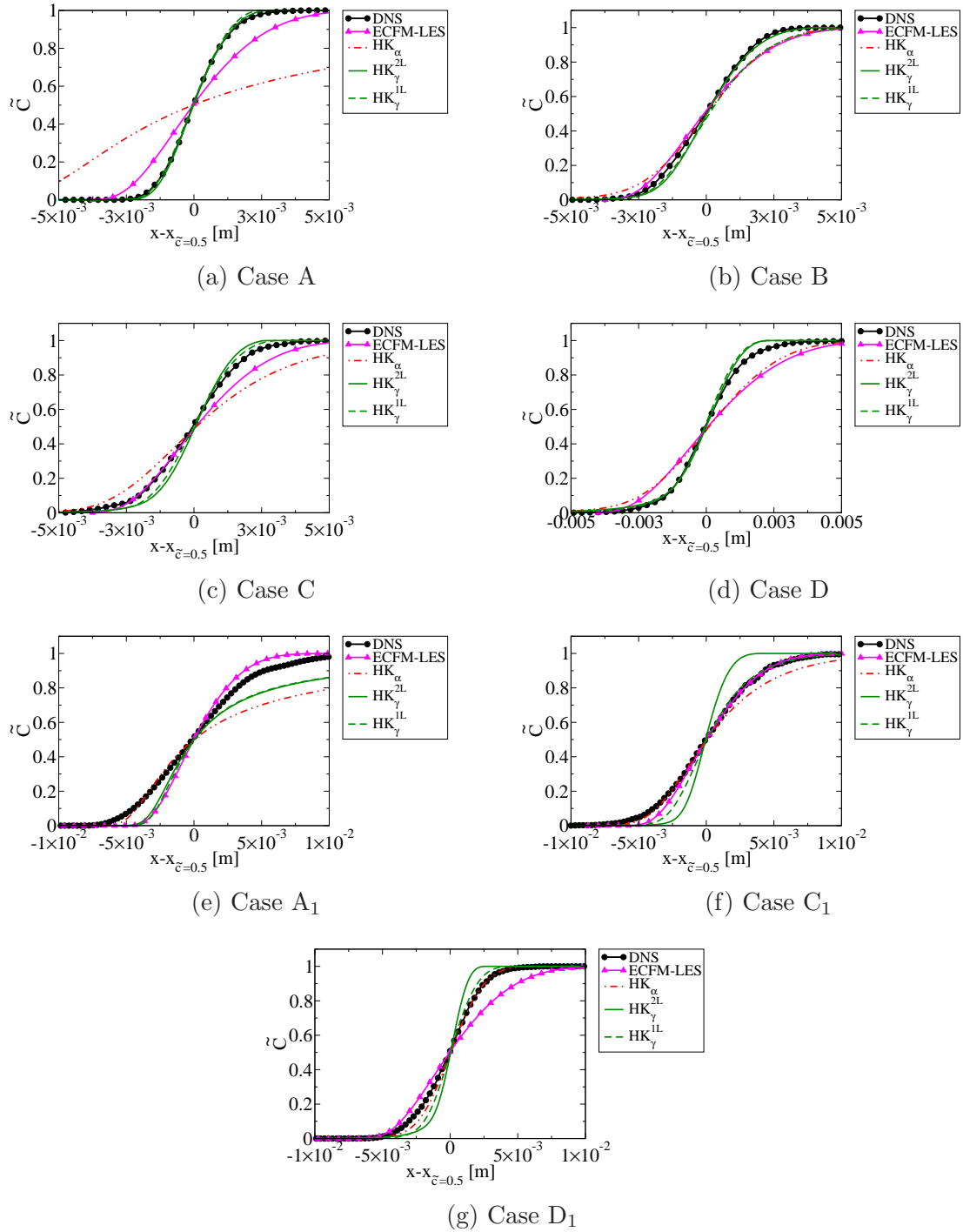


Figure 5.2.3: Predictions of the spatial profile of  $\tilde{\mathcal{C}}$  centred on the spatial location corresponding to  $\tilde{\mathcal{C}} = 0.5$  from the proposed model compared to ECFM-LES model and DNS, for (a) to (d) cases with  $Le_k \neq 1$  and (e) to (g) cases with  $Le_k = 1$ .

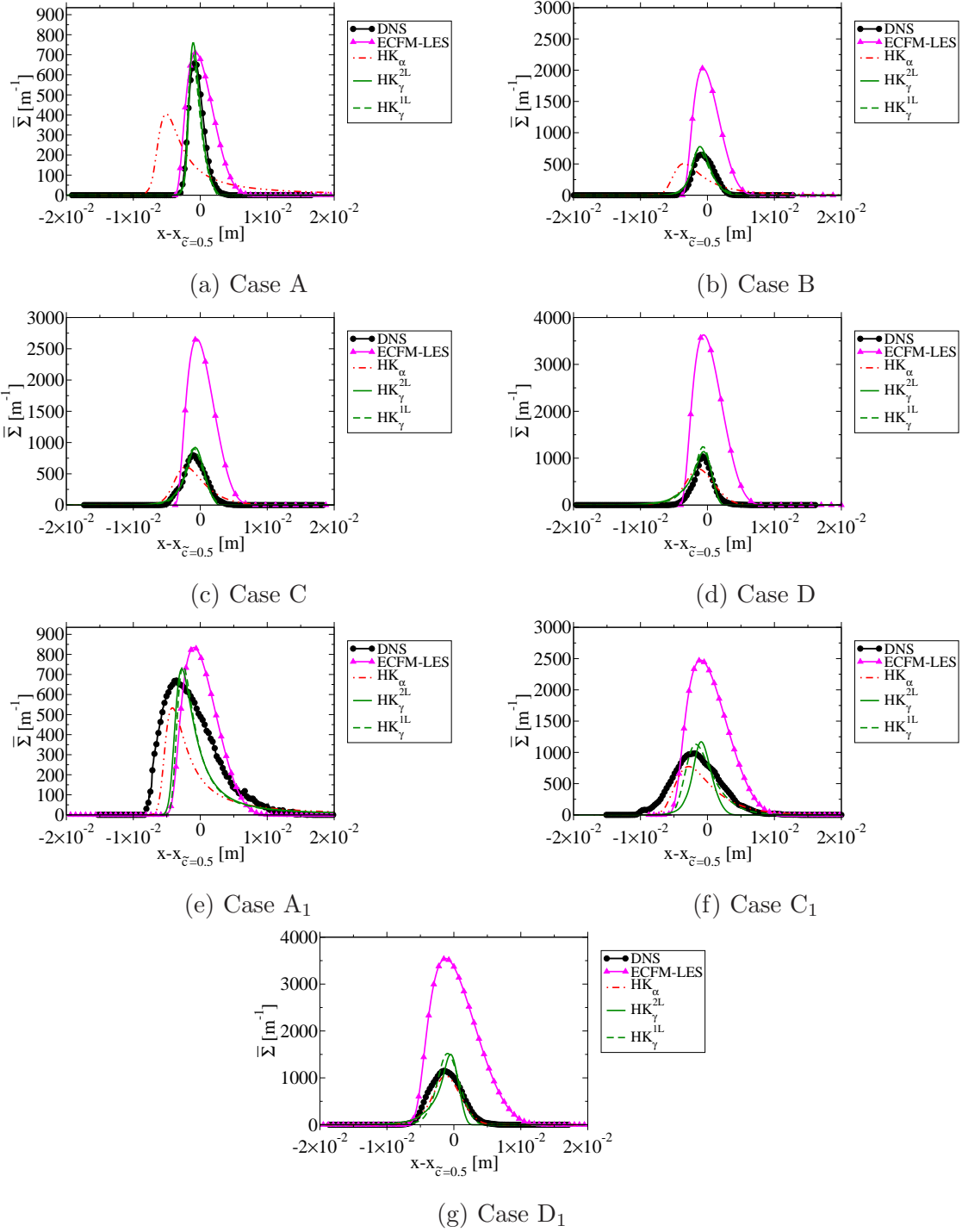


Figure 5.2.4: Predictions of the spatial profile of FSD  $\bar{\Sigma}^*$  centred on the spatial location corresponding to  $\tilde{c} = 0.5$  from the proposed model compared to ECFM-LES model and DNS, for : (a) to (d) cases with  $Le_k \neq 1$  and (e) to (g) cases with  $Le_k = 1$ .

The spatial profiles of FSD for  $Le_k = 1$  cases predicted by the proposed models, reported in Table 5.3, have the same shape as the one observed in DNS. Nevertheless, the turbulent flame width predicted by the models is much smaller than in DNS, from half the thickness down to a quarter for case A<sub>1</sub>. These thinner FSD profiles are consistent with the reduced turbulent flame speeds in Fig. 5.2.1c compared to DNS. These observations show that the proposed model behaves poorly at low  $Ka$ . At this point, it is difficult to propose an explanation for these surprising behaviours. The reasons can be due to the iso-surface approach or to the closures of the FSD production and destruction terms ( $\langle a_T \rangle_{s,c^*}^{sgs}$  and  $\langle S_d \kappa \rangle_{s,c^*}^{sgs}$ ), and consequently to Markstein length correlations. Thus, investigation of the closures proposed in Chapter 4 are needed, which is the focus of the next section.

Finally, this first analysis of the behaviour of the models with various Karlovitz number and Lewis numbers shows that  $HK_\gamma$  models present the highest potential to simulate flames in the TRZ regime because they reproduce the bending on the turbulent flame speed and accurately predict the flame structure. Even if the correlations used for the effective Markstein lengths have little impact on the flame structure predicted by the models, they are in fact crucial to accurately estimate the fuel consumption. The results from the models using  $\mathcal{L}_{a_T}$  and  $\mathcal{L}_\kappa$  highlight that the strong assumptions made lead to large discrepancies with the DNS. Furthermore, the results suggest that these discrepancies might be compensated using a single Markstein length  $\mathcal{L}_{rn}$ . Nevertheless, this observation should be verified through the simulations of a larger range of conditions.

## 5.3 Analysis of the one-dimensional turbulent flames - Predictions of the sub-models

To complete the analysis and validation of the proposed models, the sub-models used to close Eqs. (4.1.5) and (4.1.6) are compared to the DNS.

### 5.3.1 Closure of the filtered progress variable

As a first step, the model proposed in Section 4.5 to evaluate the filtered progress variable  $\bar{\mathcal{C}}$  is assessed against DNS. Figure 5.3.1 shows the profiles of  $\bar{\mathcal{C}}$  against  $\tilde{\mathcal{C}}$  obtained with the different models and compared to the DNS for each case. As already noticed, ECFM-LES model does not reproduce accurately the profile of  $\bar{\mathcal{C}}$  against  $\tilde{\mathcal{C}}$  for high Karlovitz numbers because the relationship between  $\bar{\mathcal{C}}$  and  $\tilde{\mathcal{C}}$  is the one proposed in the Bray-Moss-Libby (BML) model. For large values of  $Ka$ , the assumptions of the BML model are not valid leading to the discrepancies observed in Fig. 5.3.1. The other models use the approach presented in Section 4.5 to determine the relationship between  $\bar{\mathcal{C}}$  and  $\tilde{\mathcal{C}}$ . Figures 5.3.1a to 5.3.1d show that the proposed approach improves significantly the prediction of  $\bar{\mathcal{C}}(\tilde{\mathcal{C}})$  for non-unity Lewis numbers cases. However, some discrepancies are observed between the different versions of the proposed model.

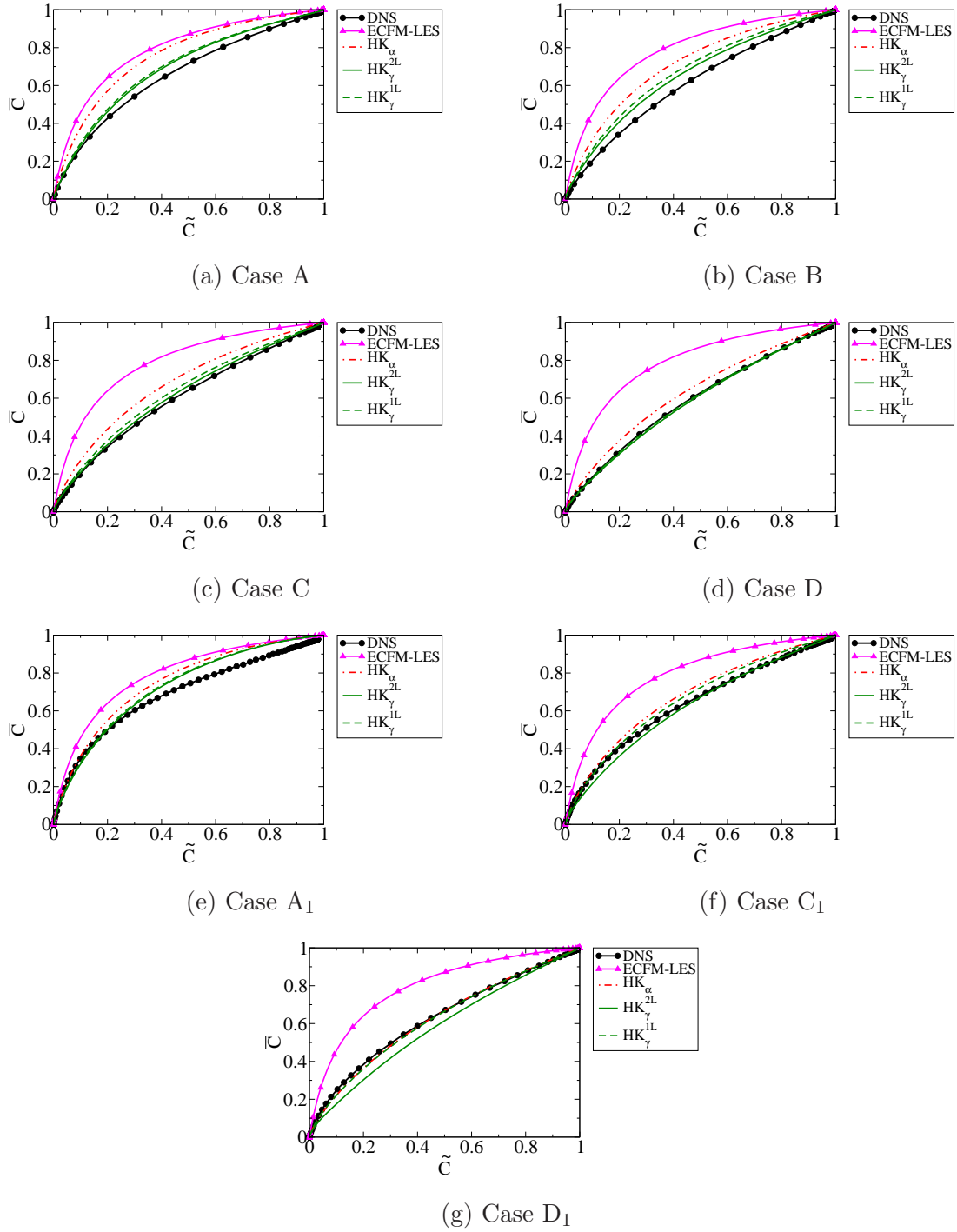


Figure 5.3.1: Predictions of  $\bar{C}$  from the proposed model as functions of  $\tilde{C}$  compared to ECFM-LES model and DNS, for : (a) to (d) cases with  $Le_k \neq 1$  and (e) to (g) cases with  $Le_k = 1$ .

$\text{HK}_\gamma^{2\text{L}}$  and  $\text{HK}_\gamma^{1\text{L}}$  models present, as expected, very similar profiles, while  $\text{HK}_\alpha$  model is less accurate especially for low  $Ka$ . Indeed, for case A the profile of  $\bar{\mathcal{C}}$  using  $\text{HK}_\alpha$  model is closer to the result of ECFM-LES model.

In Figs. 5.3.1e to 5.3.1g, all the models reproduce globally the profile of  $\bar{\mathcal{C}}$  against  $\tilde{\mathcal{C}}$  for unity Lewis number cases, except ECFM-LES and models using two distinct effective Markstein lengths, especially for case D<sub>1</sub>. Finally, these observations do not show any clue to explain the poor results of the proposed model on the flame structure for  $Le_k = 1$  cases.

### 5.3.2 Closures of curvature and its variance

Figure 5.3.2 compares the proposed model with DNS for the mean curvature. As for *a priori* modelling, this comparison shows a good agreement between the models and DNS for  $Le_k = 1$  cases and for cases C and D. However, for cases A and B the curvatures predicted by the models have weaker slopes than in DNS. This is particularly pronounced in case A, where  $\text{HK}_\alpha$  model even tends to a constant value on the burnt gases side, while the other versions of the proposed model keep a decreasing evolution in the burnt gases. These results suggest that the model proposed by Rymer (2001) and presented in Eq. (4.3.13) is accurate enough to reproduce the flame curvature. Cases A and B suggest that the presumed curvature PDF is one of the key elements in this model, which is strongly dependent on the variance of the curvature.

So, the model in Eq. (4.3.15) for  $\langle \kappa^2 \rangle_{s,c^*}$  is compared in Fig. 5.3.3 to the DNS for each version reported in Table 5.3. Figures 5.3.3a to 5.3.3d show this comparison for  $Le_k \neq 1$  cases. Surprisingly,  $\text{HK}_\alpha$  model predicts  $\langle \kappa^2 \rangle_{s,c^*}$  much smaller values than in *a priori* modelling, approximately half the value observed in DNS and down to a third for case A.

$\text{HK}_\gamma^{1\text{L}}$  and  $\text{HK}_\gamma^{2\text{L}}$  models accurately predict  $\langle \kappa^2 \rangle_{s,c^*}$  for cases C, D and C<sub>1</sub>. For low Karlovitz cases, these models under-predict  $\langle \kappa^2 \rangle_{s,c^*}$ , but still improve the prediction compared to  $\text{HK}_\alpha$  model. These results suggest that using half the curvature variance (Eq. 4.3.11) in the presumed PDF for curvature, given in Eq. (4.3.9), is a better suited model to compute the flame curvature variance. This questions the presumed PDF chosen for curvature in Eq. (4.3.9); a Gaussian PDF might not be the most suitable function for  $p(\kappa)$  and should be the focus of future work.

In addition, all the models present poor prediction of the profile of  $\langle \kappa^2 \rangle_{s,c^*}$  for cases A and A<sub>1</sub>, with the predicted  $\langle \kappa^2 \rangle_{s,c^*}$  decreasing toward zero when  $\tilde{\mathcal{C}} > 0.5$ , while DNS results show an increase. So, the model proposed in Eq. (4.3.15) behaves poorly at low  $Ka$ . It is difficult to explain here the cause of these discrepancies, which can be caused by the other closures because both  $\bar{\mathcal{C}}$  and  $\bar{\Sigma}^*$  are involved in Eq. (4.3.15). The investigation on the behaviour of this model at low  $Ka$  should be the focus of future work.

Finally, the analysis of the flame curvature and its variance suggests that  $\text{HK}_\gamma^{1\text{L}}$  and  $\text{HK}_\gamma^{2\text{L}}$  models present the best potential for modelling both the surface averaged curvature and its variance.

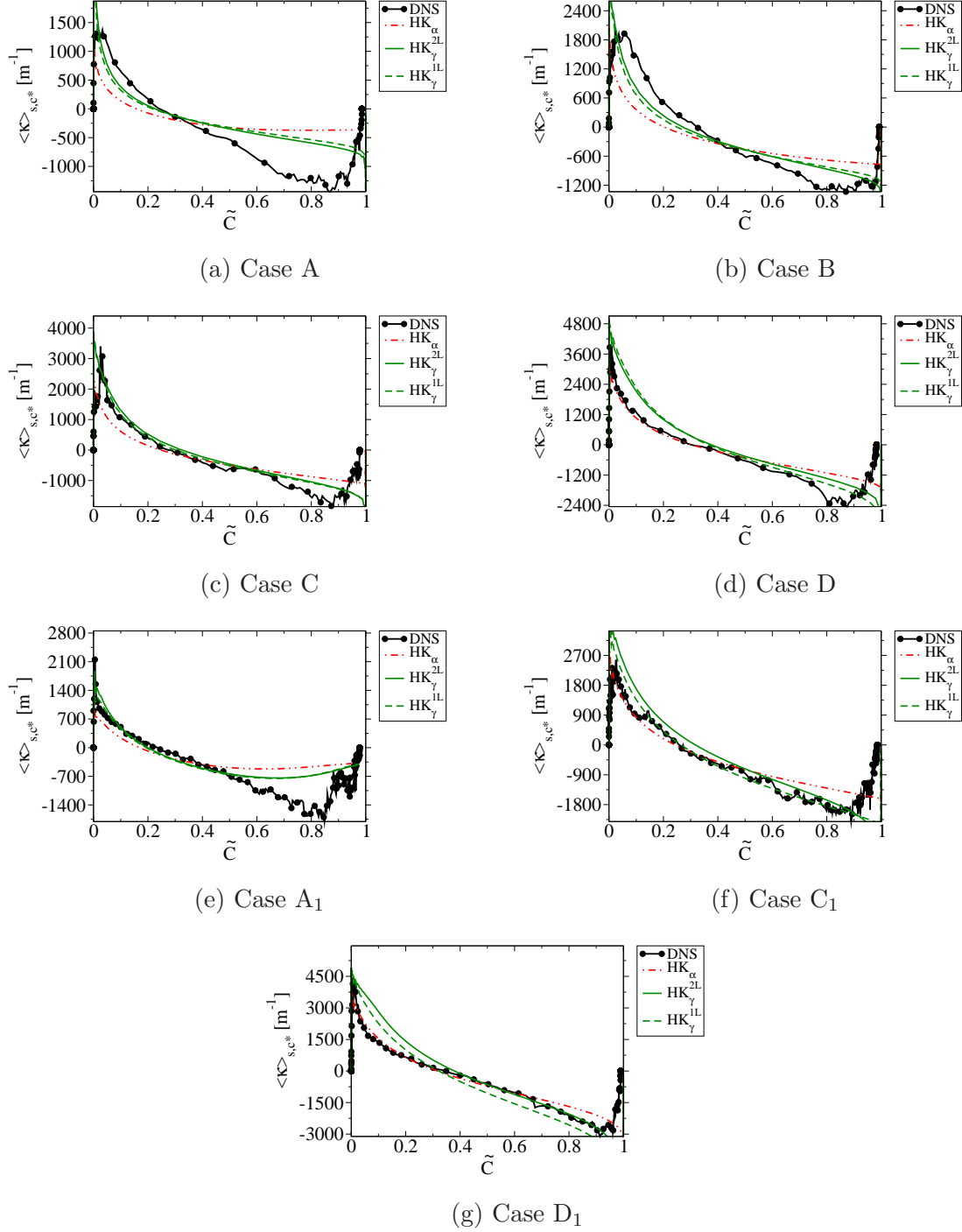


Figure 5.3.2: Predictions of  $\langle \kappa \rangle_{s,c^*}$  from the proposed model as functions of  $\tilde{C}$  compared to DNS, for (a) to (d) cases with  $Le_k \neq 1$  and (e) to (g) cases with  $Le_k = 1$ .

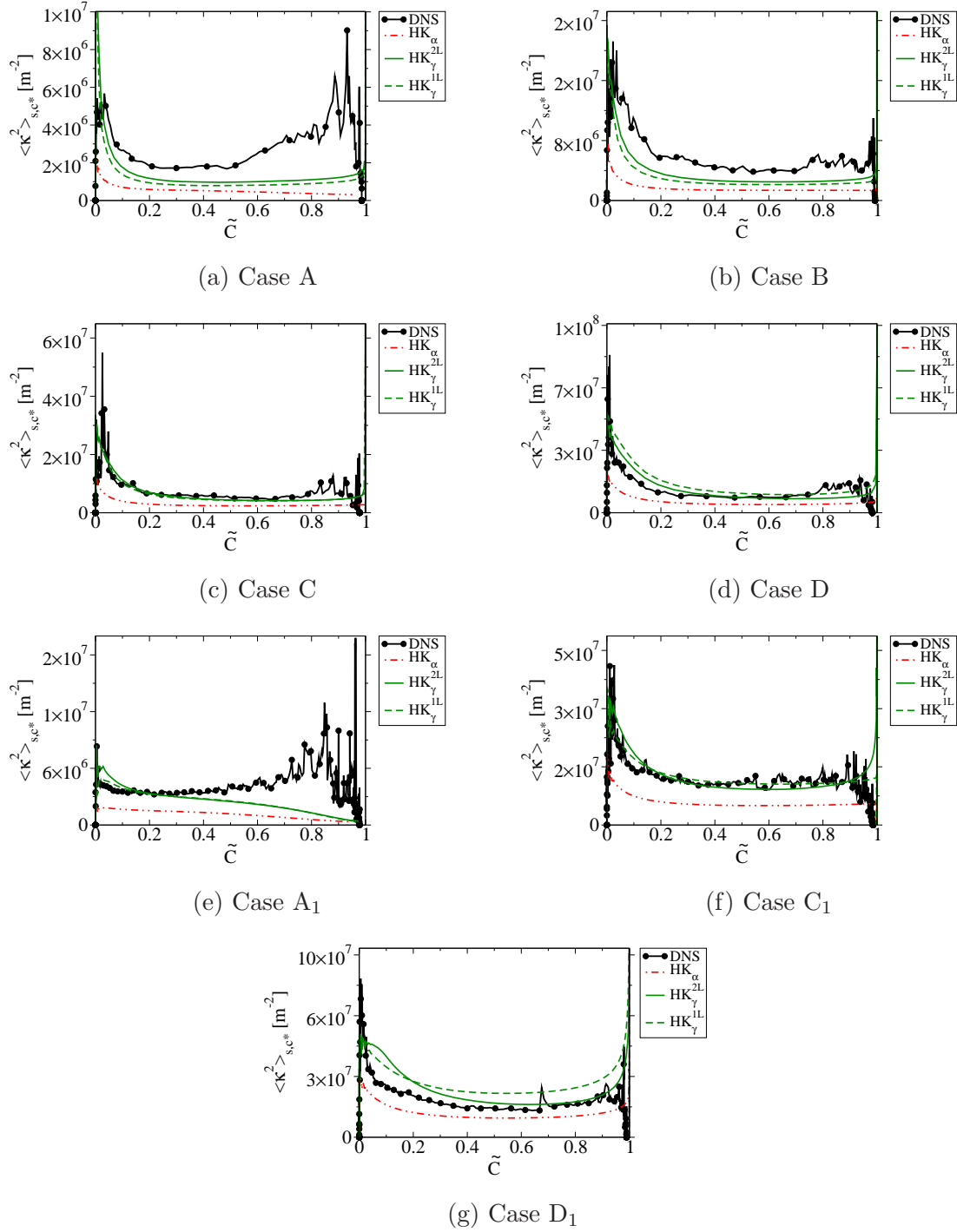


Figure 5.3.3: Predictions of  $\langle \kappa^2 \rangle_{s,c^*}$  from the proposed model as functions of  $\tilde{c}$  compared to DNS, for : (a) to (d) cases with  $Le_k \neq 1$  and (e) to (g) cases with  $Le_k = 1$ .



### 5.3.3 Closures of stretch due to curvature and displacement speed

The proposed model for the stretch due to curvature, defined by Eq. (4.4.24), is compared to the DNS and to ECFM-LES model (Richard et al., 2007) in Fig. 5.3.4.

For cases A to D,  $HK_\gamma$  models reproduce qualitatively the evolution of  $\langle S_d \kappa \rangle_{s,c^*}$ , regardless of the correlations chosen for the effective Markstein lengths, as seen in Figs. 5.3.4a to 5.3.4d, while ECFM-LES model only reproduces the stretch due to curvature for case A, as expected. When the flame is in the thin reaction zone regime (cases B to D), ECFM-LES predicts a decreasing  $\langle S_d \kappa \rangle_{s,c^*}$  from highly positive values, when  $\tilde{C}$  tends to zero, to negative values when  $\tilde{C} \rightarrow 1$ . The spatial profiles of FSD with ECFM-LES (Fig. 5.2.4) are explained by these positive values of  $\langle S_d \kappa \rangle_{s,c^*}$  on the fresh gases side. Indeed, positive values of  $\langle S_d \kappa \rangle_{s,c^*}$  enhance the production of flame surface, which leads to a production of flame surface largely overestimated when combined to the tangential strain rate.

$HK_\alpha$  model presents similar results as  $HK_\gamma$  models for cases B to D. Nevertheless, the profiles of stretch due to curvature predicted by the former are slightly flatter than those estimated from the latter, leading to slightly weaker flame surface destruction (negative values with smaller magnitudes) on the burnt gases side. This reduced destruction term explains the occurrence of a tail behind the flame front in Figs. 5.2.4b to 5.2.4d with  $HK_\alpha$ . This difference is more pronounced in case A, where  $HK_\alpha$  model even predicts  $\langle S_d \kappa \rangle_{s,c^*}$  slightly increasing when  $\tilde{C}$  tends to 1. This is in agreement with the tail observed on the FSD in Fig. 5.2.4a. However, because all the sub-models interact with each other, it is difficult to establish if this result on  $\langle S_d \kappa \rangle_{s,c^*}$  is caused by the profile of  $\langle \kappa \rangle_{s,c^*}$  in Fig. 5.3.2a or if it generates the curvature profile observed. This issue might be explored in future work, in order to better understand the model behaviour.

Note that the results of each model for  $Le_k = 1$  cases are very similar to  $Le_k \neq 1$  cases, except for low  $Ka$ . Contrary to case A,  $HK_\gamma$  models present the same profiles of  $\langle S_d \kappa \rangle_{s,c^*}$  than  $HK_\alpha$  model in case A<sub>1</sub>. This is in agreement with the results observed on the profiles of  $\langle \kappa \rangle_{s,c^*}$ ,  $\langle \kappa^2 \rangle_{s,c^*}$  and  $\overline{\Sigma^*}$ . These results on  $\langle S_d \kappa \rangle_{s,c^*}$  for  $Le_k = 1$  cases do not explain the thin spatial profiles observed for  $\overline{\Sigma^*}$ .

Predictions of  $\langle S_d \rangle_{s,c^*}$  by the proposed model, Eq. (4.3.16), are now assessed against the DNS. It is noteworthy that  $\langle S_d \rangle_{s,c^*}$  in the models is forced to remain positive in order to avoid a negative source term  $\rho^* \langle S_d \rangle_{s,c^*} \overline{\Sigma^*}$  in Eq. (3.2.12), which would not be physical. This clipping is a limitation of the proposed approach based on the flame displacement speed. At low to intermediate  $Ka$  values, the clipping remains limited and presumably does not significantly affect results. This is no more true for the largest Karlovitz of case D, where a substantial part of the flame front experiences negative displacement speeds. For  $Le_k \neq 1$  cases, the *a posteriori* models presented in Table 5.3 predict similar profiles as the *a priori* model in Fig. 4.3.8, which are globally in agreement with the displacement speed observed in the DNS.

For  $Le_k = 1$  cases in the TRZ regime (cases C<sub>1</sub> and D<sub>1</sub>),  $HK_\gamma^{1L}$  model predicts displacement speed almost superimposed with the one extracted from DNS, while predictions from  $HK_\gamma^{2L}$

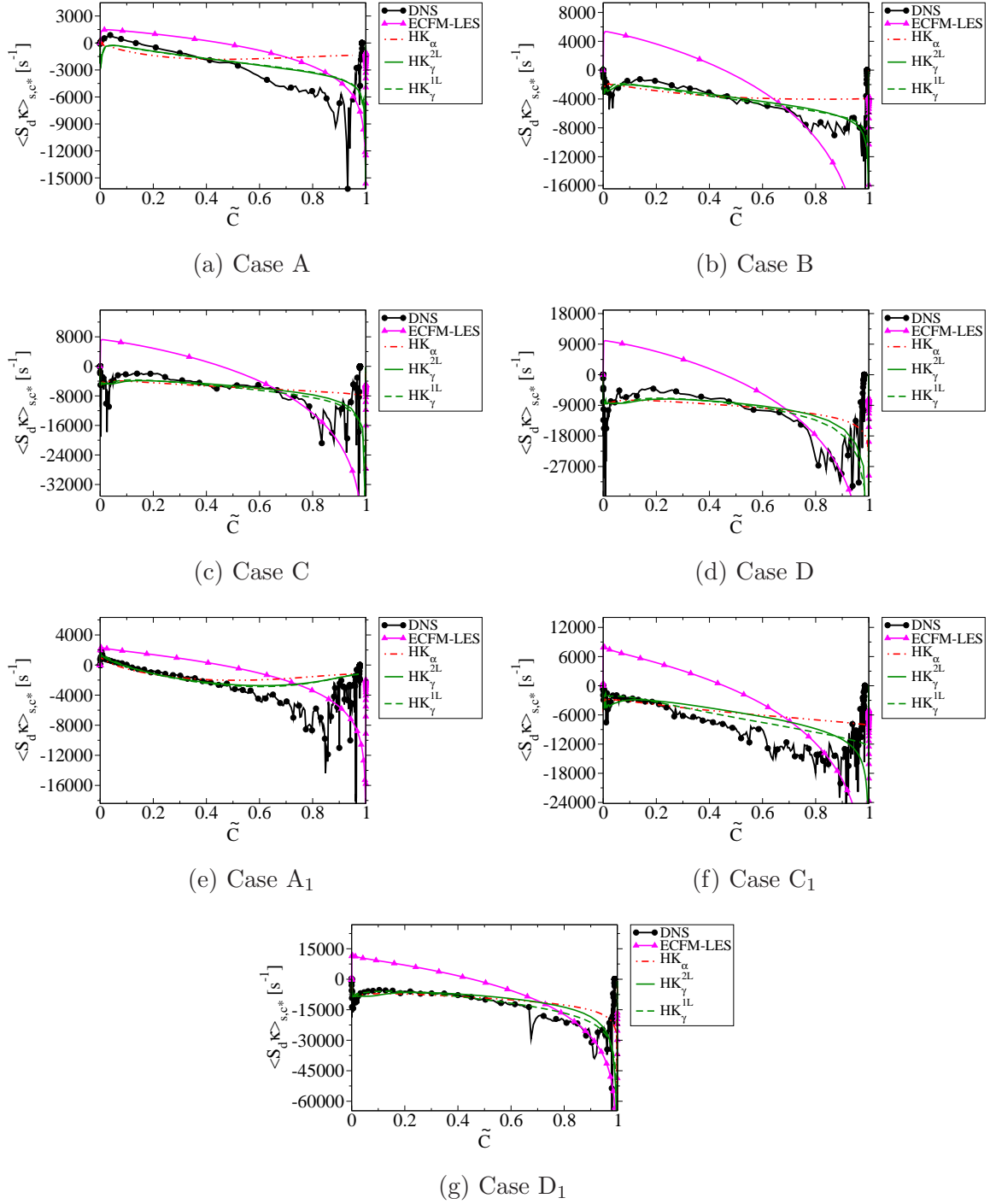


Figure 5.3.4: Predictions of  $\langle S_d \kappa \rangle_{s,c^*}$  from the proposed model as functions of  $\tilde{C}$  compared to DNS, for : (a) to (d) cases with  $Le_k \neq 1$  and (e) to (g) cases with  $Le_k = 1$ .

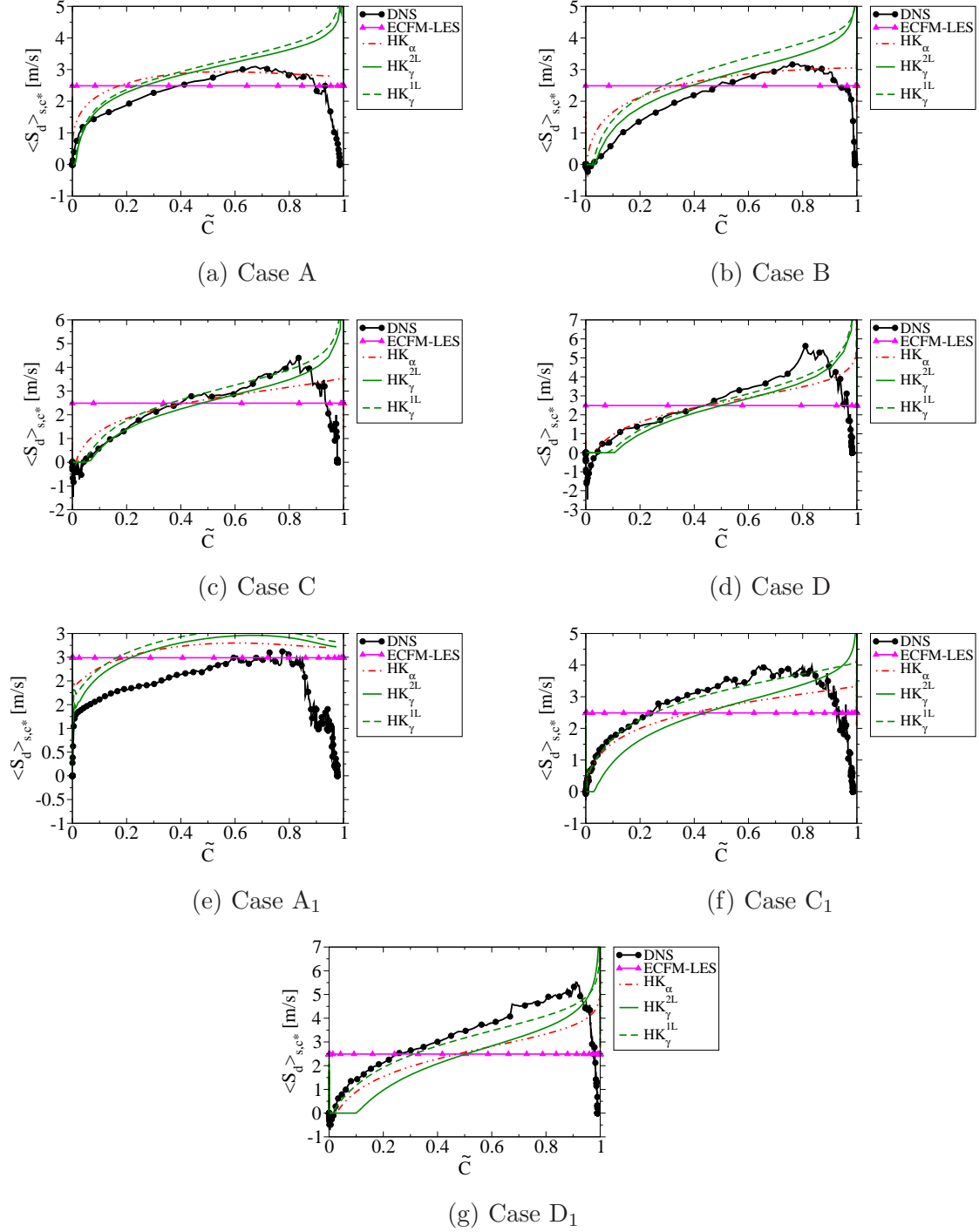


Figure 5.3.5: Predictions of  $\langle S_d \rangle_{s,c^*}$  from the proposed model as functions of  $\tilde{C}$  compared to DNS, for (a) to (d) cases with  $Le_k \neq 1$  and (e) to (g) cases with  $Le_k = 1$ .

model have the same evolution with  $\tilde{\mathcal{C}}$  but shifted down explaining the lower turbulent speed observed in Fig. 5.2.1c. This shift is due to the effective Markstein length  $\mathcal{L}_{a_T}$ , which is much larger using Eq. (3.3.5) than  $\mathcal{L}_{r_n}$  using Eq. (3.3.7) as observed in Fig. 3.3.8a. These larger values of the effective Markstein lengths lead to a largely negative component due to strain in the displacement speed. When compared to the results from  $\text{HK}_\gamma^{1\text{L}}$  model, it suggests that the tangential strain rate has a very weak effect on the displacement speed, unlike observed in the DNS analysis in Section 3.3.2. In addition, the predictions of  $\text{HK}_\alpha$  model are slightly less accurate in tendency than  $\text{HK}_\gamma^{2\text{L}}$  with a weaker slope.

However, in case A<sub>1</sub> the models present similar evolutions for  $\langle S_d \rangle_{s,c^*}$ , which flatten compared to high Karlovitz number cases and seem to converge toward the constant  $\langle S_d \rangle_{s,c^*}$  model ( $\langle \rho S_d \rangle_{s,c^*} = \rho_u S_L$ ).

To conclude, all proposed versions of HK model reproduce reasonably well  $\langle \kappa \rangle_{s,c^*}$ ,  $\langle \kappa^2 \rangle_{s,c^*}$ ,  $\langle S_d \kappa \rangle_{s,c^*}$ ,  $\langle S_d \rangle_{s,c^*}$  and  $\bar{\mathcal{C}}$  found in DNS. Unfortunately,  $\bar{\Sigma}^*$  and  $\tilde{\mathcal{C}}$  for low  $Ka$  cases and  $Le_k = 1$  cases are poorly predicted showing the limits of the model proposed in this study. The investigation conducted in this chapter shows that the following sub-models have a great effect on these results and above all on the turbulent flame speed which is in definitive the main characteristic to reproduce:

- the model for the **presumed PDF**  $p(\kappa)$ : reference model  $\alpha$  gives surprisingly the poorest results. The use of half the variance in  $\text{HK}_\gamma$  models give many improvements, suggesting that a presumed Gaussian PDF might not be adapted to capture the curvature PDF.
- the model for **effective Markstein lengths**: the 2L model based on the DNS analysis gives the poorest results, probably because it over-estimates the effect of tangential strain rate. Even if better results are obtained with the single Markstein length approach ( $\text{HK}_\gamma^{1\text{L}}$  model), the models based on Markstein lengths are limited. Indeed, in these models the concept of Markstein length, inspired from laminar flames concept where the flame stretch is small, is applied to highly turbulent flames with large flame stretch.
- the model for the **turbulent tangential strain rate**  $\langle a_T \rangle_{s,c^*}^{sgs}$ , expected to be one of the major sub-models controlling  $S_T$ . LPF model is found to bring much better results than the other models tested.

## 5.4 Discussion on the application of the proposed approach to LES and engines simulations

In this section is discussed two issues that can lead to numerical problems when the proposed model is applied to engine LES simulations. The first issue, discussed in Subsection 5.4.1, was first pointed out by Rymer (2001), for RANS modelling, and by Richard et al. (2007), for LES modelling. The second problem investigated in Subsection 5.4.2 is about the approximation made on the model for tangential strain rate due to unresolved flow motions.

### 5.4.1 Discussion on the closure of the transport equation of progress variable

Here is reminded the filtered transport equation for progress variable:

$$\frac{\partial \bar{\rho} \tilde{\mathcal{C}}}{\partial t} + \nabla \cdot (\bar{\rho} \tilde{\mathbf{u}} \tilde{\mathcal{C}}) = -\nabla \cdot (\overline{\rho \mathbf{u} \mathcal{C}} - \bar{\rho} \tilde{\mathbf{u}} \tilde{\mathcal{C}}) + \langle \rho S_d \rangle_{s,c^*} \bar{\Sigma}^*, \quad (5.4.1)$$

where  $\nabla \cdot (\overline{\rho \mathbf{u} \mathcal{C}})$  is the unresolved turbulent transport term modelled with a simple gradient approach combined with a thermal expansion term in Eq. (4.3.6). This equation can be expanded using the property  $\bar{\mathbf{n}} = -\nabla \bar{\mathcal{C}} / |\nabla \bar{\mathcal{C}}| = -\nabla \tilde{\mathcal{C}} / |\nabla \tilde{\mathcal{C}}|$ :

$$\nabla \cdot (\overline{\rho \mathbf{u} \mathcal{C}} - \bar{\rho} \tilde{\mathbf{u}} \tilde{\mathcal{C}}) = -\nabla \cdot \left( \bar{\rho} \frac{\nu_t}{S_{ct}} \nabla \tilde{\mathcal{C}} \right) + \rho_u S_L^0 (|\nabla \bar{\mathcal{C}}| - |\nabla \tilde{\mathcal{C}}| - (\bar{\mathcal{C}} - \tilde{\mathcal{C}}) \nabla \cdot \bar{\mathbf{n}}). \quad (5.4.2)$$

As already pointed out by Rymer (2001) and Richard et al. (2007), using Eq. (5.4.2) can cause some numerical difficulties. Indeed, the transported variables  $\bar{\Sigma}^*$  and  $\tilde{\mathcal{C}}$  are no longer explicitly linked but implicitly, because of the introduction of  $\bar{\mathcal{C}}$  in the transport equation of progress variable (Eq. 5.4.1). These issues were not encountered in present 1D simulations because  $\nabla \cdot \bar{\mathbf{n}} = 0$ .

Thus, for this reason the thermal expansion contribution of the unresolved turbulent transport term is taken into account to define a modified FSD, analogically to Richard's work (Richard, 2005):

$$\bar{\Sigma}^*_{\tilde{\mathcal{C}}} = \bar{\Sigma}^* - |\nabla \bar{\mathcal{C}}| + |\nabla \tilde{\mathcal{C}}| - (\bar{\mathcal{C}} - \tilde{\mathcal{C}}) \nabla \cdot \bar{\mathbf{n}}. \quad (5.4.3)$$

This definition leads to write Eq. (5.4.1) as:

$$\frac{\partial \bar{\rho} \tilde{\mathcal{C}}}{\partial t} + \nabla \cdot (\overline{\rho \mathbf{u} \mathcal{C}}) = -\nabla \cdot \left( \bar{\rho} \frac{\nu_t}{S_{ct}} \nabla \tilde{\mathcal{C}} \right) + \langle \rho S_d \rangle_{s,c^*} \bar{\Sigma}^*_{\tilde{\mathcal{C}}}. \quad (5.4.4)$$

As in Richard's work (Richard, 2005), we do not try to derive an exact transport equation for  $\bar{\Sigma}^*_{\tilde{\mathcal{C}}}$  but a similar equation to Eq. (4.1.6) is chosen for  $\bar{\Sigma}^*_{\tilde{\mathcal{C}}}$ . The closure terms of this new transport equation are modified following the same methodology as Richard et al. (2007).

Even if the flame surface densities  $\bar{\Sigma}^*$  and  $\bar{\Sigma}^*_{\tilde{\mathcal{C}}}$  are different, the transported total flame surfaces are the same, as demonstrated below and because  $\bar{\mathcal{C}} = \tilde{\mathcal{C}}$  on the border of the domain containing the whole flame.

$$\int_V \bar{\Sigma}^*_{\tilde{\mathcal{C}}} dV = \int_V \bar{\Sigma}^* dV + \int_V (\bar{\mathcal{C}} - \tilde{\mathcal{C}}) \nabla \cdot \bar{\mathbf{n}} dV \quad (5.4.5)$$

$$= \int_V \bar{\Sigma}^* dV + \int_{dV} (\bar{\mathcal{C}} - \tilde{\mathcal{C}}) \bar{\mathbf{n}} dS \quad (5.4.6)$$

$$= \int_V \bar{\Sigma}^* dV + 0 \quad (5.4.7)$$

Figure 5.4.1 compares the spatial profiles of both FSD  $\bar{\Sigma}^*$  and  $\bar{\Sigma}^*_{\tilde{\mathcal{C}}}$  extracted from DNS following the procedure presented in Section 4.2. At high Karlovitz numbers (cases B to D) both

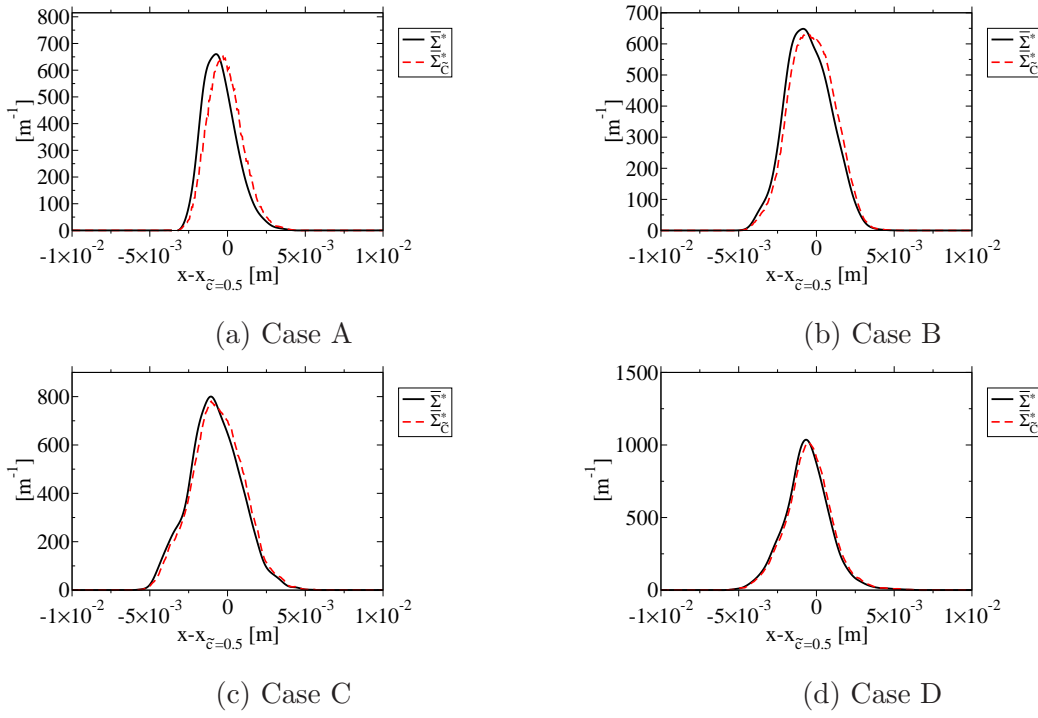


Figure 5.4.1: Spatial profiles of FSD  $\bar{\Sigma}^*$  and  $\bar{\Sigma}_{\tilde{C}}^*$  (Eq. 5.4.4) centred on  $\tilde{C} = 0.5$  extracted from the DNS for (a) to (d) cases with  $Le_k \neq 1$ .

FSD are equivalent in Figs. 5.4.1b to 5.4.1d, while at low  $Ka$  (case A)  $\bar{\Sigma}_{\tilde{C}}^*$  differs slightly from  $\bar{\Sigma}^*$ . Indeed,  $\bar{\Sigma}_{\tilde{C}}^*$  is slightly shifted toward the burned gases and its spatial profile seems more symmetrical than  $\bar{\Sigma}^*$ . Thus, changing the transport FSD to  $\bar{\Sigma}_{\tilde{C}}^*$  is expected to have little impact on the predictions of the proposed model.

In this section, the proposed model is tested using the variable  $\bar{\Sigma}_{\tilde{C}}^*$  instead of the filtered FSD  $\bar{\Sigma}^*$ .  $\text{HK}_{\gamma}^{\text{1L}}$  model is retained as considered to be the best one in the previous sections. When the transported variable  $\bar{\Sigma}_{\tilde{C}}^*$  is used, the model is called “ $\text{HK}_{\gamma}^{\text{1L}}\text{-}\bar{\Sigma}_{\tilde{C}}^*$ ”. Finally, the equations resolved using  $\text{HK}_{\gamma}^{\text{1L}}\text{-}\bar{\Sigma}_{\tilde{C}}^*$  model are:

$$\frac{\partial \rho \tilde{C}}{\partial t} + \nabla \cdot (\rho \mathbf{u} \tilde{C}) = -\nabla \cdot \left( \bar{\rho} \frac{\nu_t}{S_{ct}} \nabla \tilde{C} \right) + \langle \rho S_d \rangle_{s,c^*} \bar{\Sigma}_{\tilde{C}}^* \tilde{C}, \quad (5.4.8)$$

$$\begin{aligned} \frac{\partial \bar{\Sigma}_{\tilde{C}}^*}{\partial t} + \nabla \cdot (\tilde{\mathbf{u}} \bar{\Sigma}_{\tilde{C}}^*) = & -\nabla \cdot \left( \frac{\nu_t}{S_{ct}} \nabla \bar{\Sigma}_{\tilde{C}}^* \right) + \langle a_T \rangle_{s,c^*} \bar{\Sigma}_{\tilde{C}}^* \tilde{C} + \langle S_d \kappa \rangle_{s,c^*} \bar{\Sigma}_{\tilde{C}}^* \tilde{C} \\ & - \nabla \cdot \left( \frac{\rho_u}{\bar{\rho}} S_L^0 \langle \mathbf{n} \rangle_{s,c^*} \bar{\Sigma}_{\tilde{C}}^* \tilde{C} \right), \end{aligned} \quad (5.4.9)$$

where  $\langle \rho S_d \rangle_{s,c^*}$ , and  $\langle S_d \kappa \rangle_{s,c^*}$  are modelled with Eqs. (4.3.16) and (4.4.24), respectively. The tangential strain rate due to unresolved flow motions  $\langle a_T \rangle_{s,c^*}^{sgs}$  is modelled following the approach defined in Section 4.4.3 using the LPF model (Eq. 4.4.18) for the efficiency function. However,

the models for  $\langle \kappa \rangle_{s,c^*}$  and  $\langle \kappa^2 \rangle_{s,c^*}$  needed for Eqs. (4.3.16) and (4.4.24) are modified as follows:

$$\langle \kappa \rangle_{s,c^*} = \beta_1 \frac{c_1 - \bar{\mathcal{C}}}{\bar{\mathcal{C}}(1 - \bar{\mathcal{C}})} \left( \bar{\Sigma}_{\tilde{\mathcal{C}}}^* - \bar{\Sigma}_{\tilde{\mathcal{C}}}^{*lam} \right), \quad (5.4.10)$$

$$\langle \kappa^2 \rangle_{s,c^*} = \beta_2 \frac{1}{\bar{\mathcal{C}}^2(1 - \bar{\mathcal{C}})^2} \left( \bar{\Sigma}_{\tilde{\mathcal{C}}}^* - \bar{\Sigma}_{\tilde{\mathcal{C}}}^{*lam} \right)^2, \quad (5.4.11)$$

where  $\bar{\Sigma}_{\tilde{\mathcal{C}}}^{*lam} = |\nabla \tilde{\mathcal{C}}| + (\bar{\mathcal{C}} - \tilde{\mathcal{C}}) \nabla \cdot \bar{\mathbf{n}}$  is the laminar part of  $\bar{\Sigma}_{\tilde{\mathcal{C}}}^*$ , as introduced by Richard et al. (2007).  $Le_k \neq 1$  cases were simulated using model  $\text{HK}_{\gamma}^{1L} - \bar{\Sigma}_{\tilde{\mathcal{C}}}^*$  comparing to DNS and to

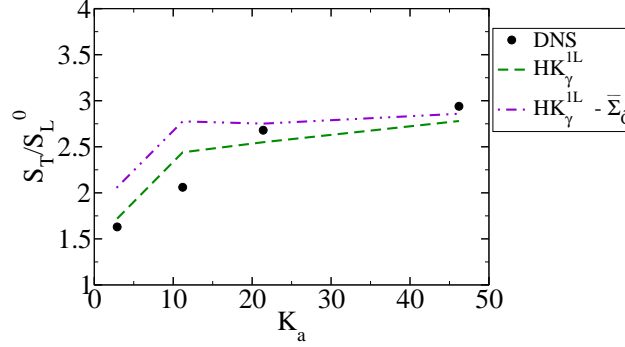


Figure 5.4.2: Evolution of the predictions of  $S_T/S_L^0$  when the transported FSD is  $\bar{\Sigma}_{\tilde{\mathcal{C}}}^*$  compared to DNS and to  $\text{HK}_{\gamma}^{1L}$  model using  $\bar{\Sigma}^*$  as the transported FSD.

$\text{HK}_{\gamma}^{1L}$  model. First, the evolutions of the turbulent flame speed are compared in Fig. 5.4.2. Both transported FSD models reproduce a bending on the turbulent flame speed. However, while for  $Ka = 21$  and  $Ka = 46$ ,  $\text{HK}_{\gamma}^{1L} - \bar{\Sigma}_{\tilde{\mathcal{C}}}^*$  model accurately predicts the turbulent flame speed, it overestimates  $S_T$  by approximately 30% for low Karlovitz number (i.e.,  $Ka = 2.9$  and  $Ka = 11.2$ ). Thus, the bending effect is too strong using the transported variable  $\bar{\Sigma}_{\tilde{\mathcal{C}}}^*$ .

Then, to better understand the effect of this change in the transported variable, the flame structure is plotted in Fig. 5.4.3. For high Karlovitz numbers (i.e., cases C and D), the spatial profiles of flame surface density predicted are very similar regardless of the transported variable chosen. While for low Karlovitz number cases (cases A and B), the profiles differ strongly. Indeed, when  $\bar{\Sigma}_{\tilde{\mathcal{C}}}^*$  is chosen, a tail appears after the flame front for cases A and B. This profile of flame surface density is similar to the one obtained with  $\text{HK}_{\alpha}$  model. This similarity between the two models suggests that the issue lies in the modelling of production and destruction of FSD, which is the focus of the next subsection.

## 5.4.2 Discussion on the modelling of flame surface production and destruction terms.

One issue of the proposed model based on an iso-surface approach can be understood when looking at the asymptotic shape of the FSD equation when going to the flamelet regime. In this regime,  $S_d^*$  tends toward  $(\rho_u/\rho^*)S_L^0$  and  $\langle S_d \kappa \rangle_{s,c^*}$  becomes close to  $(\rho_u/\rho^*)S_L^0 \langle \kappa \rangle_{s,c^*}$ . Con-

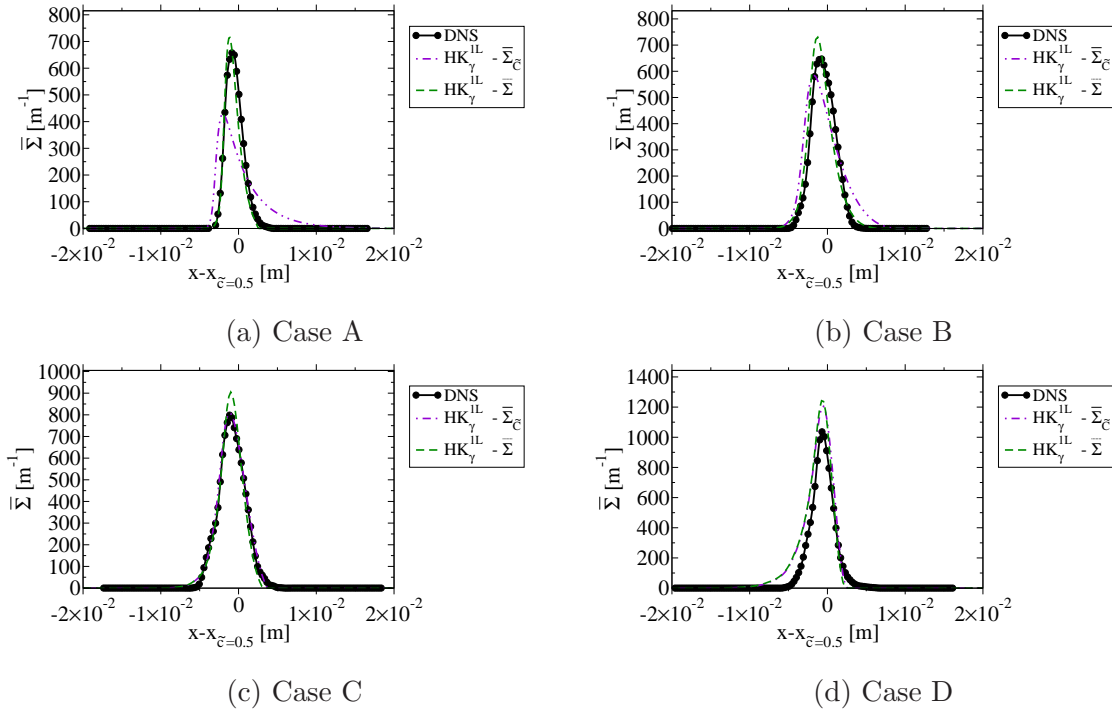


Figure 5.4.3: Predictions of the spatial profile of FSD  $\bar{\Sigma}^*$  centred on  $\tilde{\mathcal{C}} = 0.5$  when the transported FSD is  $\bar{\Sigma}_{\tilde{\mathcal{C}}}^*$  compared to DNS and  $\text{HK}_{\gamma}^{IL}$  model using  $\bar{\Sigma}^*$  as the transported FSD, for (a) to (d) cases with  $Le_k \neq 1$ .

sequently, the FSD transport equation can be simplified as follows:

$$\frac{\partial \bar{\Sigma}^*}{\partial t} + \nabla \cdot (\langle \mathbf{u} \rangle_{s,c^*} \bar{\Sigma}^*) = (\langle A_T \rangle_{s,c^*} + \langle a_T \rangle_{s,c^*}^{sgs}) \bar{\Sigma}^* + \frac{\rho_u}{\rho^*} S_L^0 \langle \kappa \rangle_{s,c^*} \bar{\Sigma}^*. \quad (5.4.12)$$

Equation (5.4.12) is almost the same equation developed by Richard et al. (2007). It only differs for the stretch due to curvature by a factor  $\rho_u/\rho^*$ . Yet, following the flamelet assumptions the iso-surfaces shall be equivalent. So, the flame surface density should not depend on the choice of  $c^*$ , which is not the case in Eq. (5.4.12) where  $c^*$  appears through the factor  $\rho_u/\rho^*$ . This factor causes the large “thickening” of the flame front on the burnt gases side, but it is determinant to model accurately the flame in the TRZ regime (i.e., for cases C and D).

This observation on Eq. (5.4.12) questions the modelling of the balance between tangential strain rate and stretch due to curvature. One of the strongest assumption made in the closures of the FSD transport equation is to consider that the tangential strain rate due to unresolved flow motions is driven by the fresh gases, leading to model  $\langle a_T \rangle_{s,c^*}^{sgs}$  as independent on  $\tilde{\mathcal{C}}$ . We propose here to verify this approximation by plotting  $\langle a_T \rangle_{s,c^*}^{sgs} = \langle a_T \rangle_{s,c^*} - \langle A_T \rangle_{s,c^*}$ , where  $\langle a_T \rangle_{s,c^*}$  and  $\langle A_T \rangle_{s,c^*}$  are the total and the resolved tangential strain rates, respectively, as a function of  $\tilde{\mathcal{C}}$ . Figure 5.4.4 shows the profiles of total tangential strain rate and tangential strain rates due to resolved and unresolved flow motions as functions of the filtered progress variable  $\tilde{\mathcal{C}}$ . Note that when  $Ka$  increases,  $\langle a_T \rangle_{s,c^*}^{sgs}$  tends to become constant with  $\tilde{\mathcal{C}}$ . So at high Karlovitz numbers, the approximation made on the tangential strain rate due to unresolved flow motions appears reasonable, explaining the agreement between DNS and predictions from the model



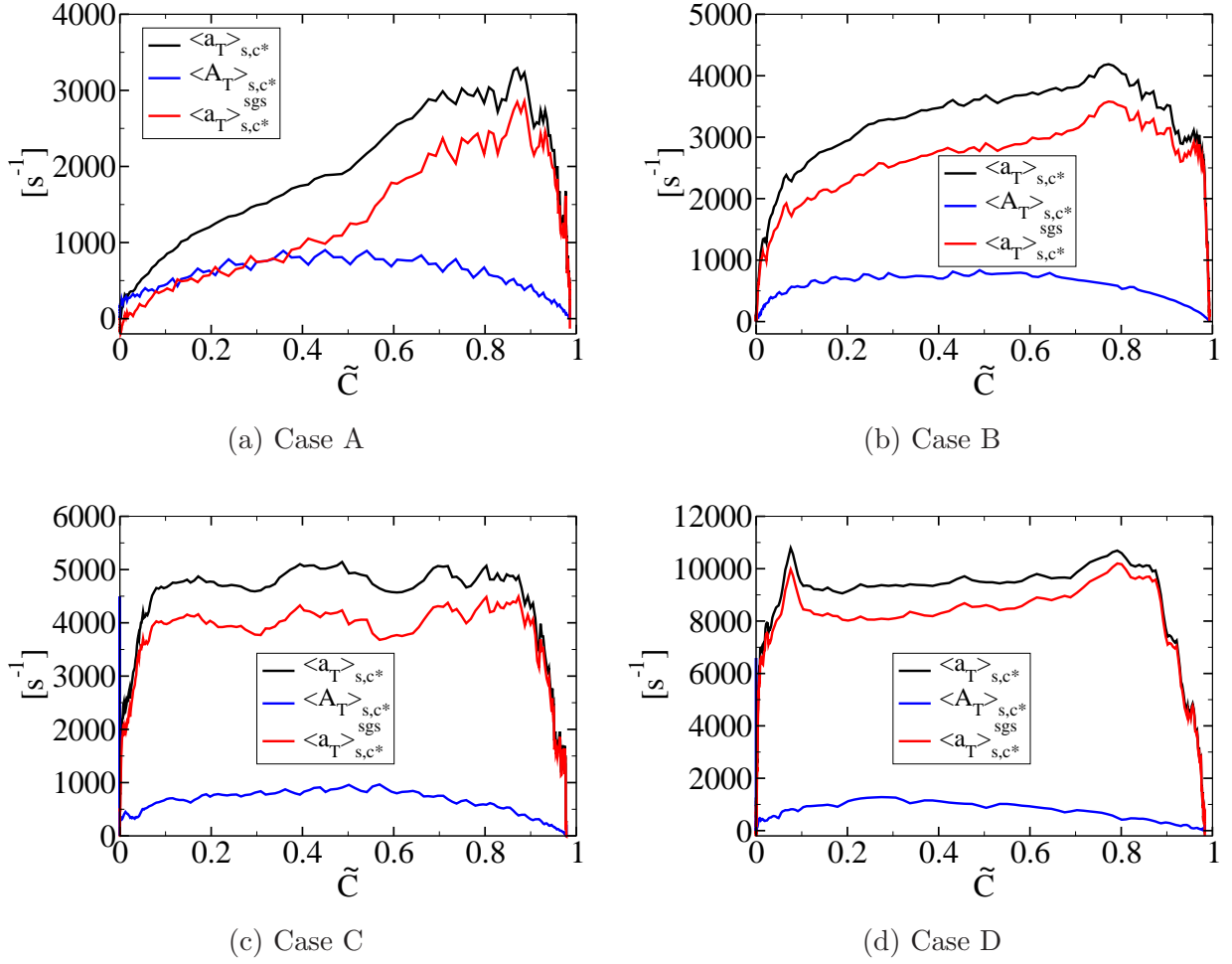


Figure 5.4.4: Evolutions of total, resolved and sub-grid scale tangential strain rate with the filtered progress variable  $\tilde{c}$  for (a) to (c) the cases with  $Le_k \neq 1$ .

in Sections 5.2 and 5.3. However, cases A and B do not present a constant value through the flame of the total tangential strain rate, which might explains the discrepancies observed for these low  $Ka$  cases in comparisons with DNS. These results motivate to adapt the tangential strain rate model from a 1D analysis.

In the 1D RANS simulations presented in this chapter,  $\langle a_T \rangle_{s,c^*}^{sgs}$  being assumed constant through the flame front, it is evaluated using the unburned gases turbulence properties  $u'_t$  and  $l_t$  from the DNS. However, the tangential strain rate (Fig. 5.4.4) is not constant and should be evaluated right on the iso-surface  $c = c^*$ . The adaptation we propose is based on the schematic view of the flame front displayed in Fig. 5.4.5. The idea here is that in the iso-surface approach, the tangential strain rate on the iso-surface  $c = c^*$ ,  $a_T^*$  should be defined using velocity field  $\mathbf{u}^*$  just in front of the chosen iso-surface:

$$a_T^* = \nabla \cdot \mathbf{u}^* + \mathbf{nn} : \nabla \mathbf{u}^*, \quad (5.4.13)$$

where  $\mathbf{n}$  is the local normal vector to the iso-surface  $c = c^*$ . Nevertheless,  $\mathbf{u}^*$  is not expected to be equal to the velocity field  $\mathbf{u}$  ahead of the flame front, mainly because of dilatation effects on

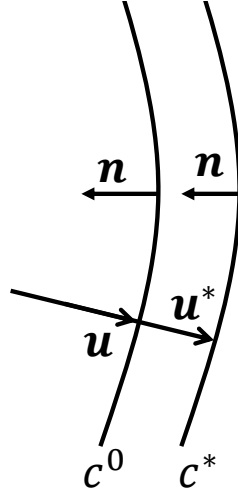


Figure 5.4.5: Schematic view of the flame front using two progress variable iso-surfaces at  $c^0$  and  $c^*$ .

the flow field due to flame. However, a relationship can be deduced between those two velocity fields using the definition of the flame displacement speed:

$$\mathbf{u}^* = \mathbf{u} + (S_{d,c^0}^0 - S_{d,c^*}^0) \mathbf{n}, \quad (5.4.14)$$

where  $S_{d,c^0}^0$  and  $S_{d,c^*}^0$  are the laminar displacement speeds of the iso-surfaces  $c = c^0$  and  $c = c^*$ , respectively. This relation is only valid in the flamelet regime and for a planar and steady flame. It is therefore a very rough estimation of the velocity in general. Then, Eq. (5.4.14) is injected in the definition of the tangential strain rate (Eq. 5.4.13) combined to surface averaging leading to:

$$\langle a_T \rangle_{s,c^*} = \langle \mathcal{A}(\mathbf{u}) \rangle_{s,c^*} + \langle \mathcal{A}((S_{d,c^0}^0 - S_{d,c^*}^0) \mathbf{n}) \rangle_{s,c^*}, \quad (5.4.15)$$

where  $\mathcal{A}(\phi)$  is the following operator:  $\mathcal{A}(\phi) = \nabla \cdot \phi - \mathbf{nn} : \nabla \phi$ . This operator applied to  $\mathbf{u}$ ,  $\langle \mathcal{A}(\mathbf{u}) \rangle_{s,c^*}$ , corresponds to the tangential strain rate on the iso-surface  $c = c^0$ , where  $c^0$  is close to zero. Equation (5.4.15) suggests that the tangential strain rate can be decomposed into a tangential strain rate evaluated from the unburned gases velocity  $\mathbf{u}$ ,  $\langle a_T \rangle_{s,c^0}$ , and a corrective strain rate taking into account dilatation effects on the flow:

$$\langle a_T \rangle_{s,c^*} = \langle a_T \rangle_{s,c^0} + (\langle a_T \rangle_{s,c^*} - \langle a_T \rangle_{s,c^0}). \quad (5.4.16)$$

By comparing Eqs. (5.4.15) and (5.4.16), the corrective strain rate  $(\langle a_T \rangle_{s,c^*} - \langle a_T \rangle_{s,c^0})$  is modelled by  $\langle \mathcal{A}((S_{d,c^0}^0 - S_{d,c^*}^0) \mathbf{n}) \rangle_{s,c^*}$ . When the operator  $\mathcal{A}(\phi)$  is applied to the unit normal vector

$\mathbf{n}$ , it can be written as:

$$\mathcal{A}(\mathbf{n}) = \frac{\partial n_i}{\partial x_i} - n_i n_j \frac{\partial n_i}{\partial x_j}, \quad (5.4.17)$$

$$= \frac{\partial n_i}{\partial x_i} - \frac{1}{2} n_j \frac{\partial n_i^2}{\partial x_j} \quad (5.4.18)$$

$$= \frac{\partial n_i}{\partial x_i} - 0, \quad (5.4.19)$$

because  $\sum n_i^2 = 1$ . Therefore the corrective strain is  $(S_{d,c^0}^0 - S_{d,c^*}^0) \langle \kappa \rangle_{s,c^*}$ . Thus, the balance of stretch due to curvature with tangential strain rate becomes:

$$\langle a_T \rangle_{s,c^*} + \langle S_d \kappa \rangle_{s,c^*} = \langle a_T \rangle_{s,c^0} + (\langle a_T \rangle_{s,c^*} - \langle a_T \rangle_{s,c^0}) + \langle S_d \kappa \rangle_{s,c^*}, \quad (5.4.20)$$

$$= \langle \mathcal{A}(\mathbf{u}) \rangle_{s,c^*} + (S_{d,c^0}^0 - S_{d,c^*}^0) \langle \kappa \rangle_{s,c^*} + \langle S_d \kappa \rangle_{s,c^*}. \quad (5.4.21)$$

Figure 5.4.6 compares a priori Eqs. (5.4.15) and (5.4.16) to the tangential strain rates  $\langle a_T \rangle_{s,c^*}$  and  $\langle a_T \rangle_{s,c^0}$ . The objectives of this comparison is to assess the impact of the corrective strain rate and verify that Eqs. (5.4.15) and (5.4.16) are equivalent.

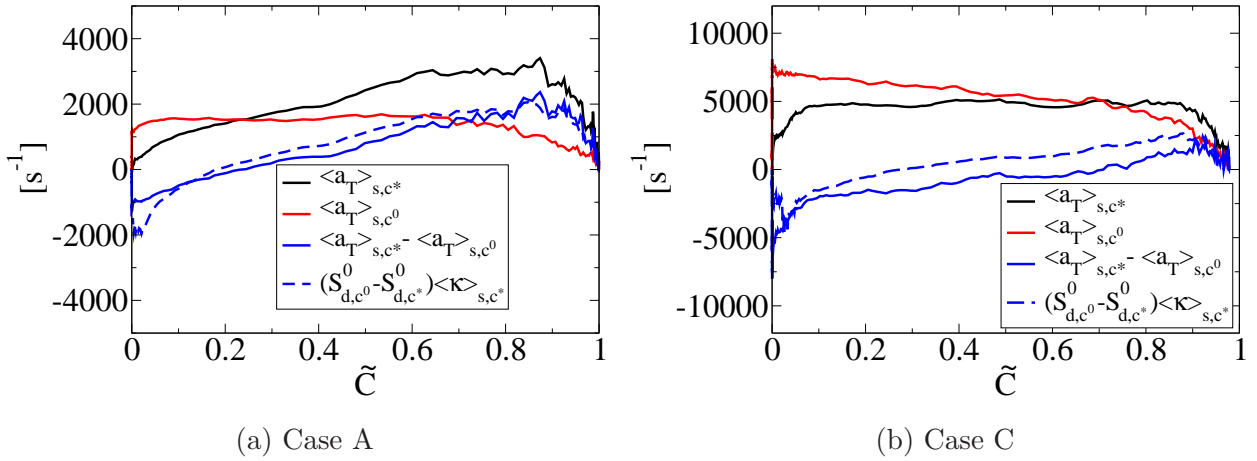


Figure 5.4.6: Comparison of the tangential strain rates  $\langle a_T \rangle_{s,c^*}$  and  $\langle a_T \rangle_{s,c^0}$  with the corrective strain rate  $(\langle a_T \rangle_{s,c^*} - \langle a_T \rangle_{s,c^0})$  and the modelled corrective strain rate  $(S_{d,c^0}^0 - S_{d,c^*}^0) \langle \kappa \rangle_{s,c^*}$ , for: (a) case A and (b) case C.

This approach is evaluated for cases A and C, in order to compare the differences between low and high Karlovitz number cases, where  $c^0 = 0.2$  and  $c^* = 0.8$ . The value of  $c^0$  was chosen to 0.2 because for smaller values the samples are not sufficient to extract relevant statistics. Figure 5.4.6 shows the profiles of  $\langle a_T \rangle_{s,c^*}$ ,  $\langle a_T \rangle_{s,c^0}$ ,  $(\langle a_T \rangle_{s,c^*} - \langle a_T \rangle_{s,c^0})$  and  $(S_{d,c^0}^0 - S_{d,c^*}^0) \langle \kappa \rangle_{s,c^*}$  against  $\tilde{C}$ . For the TRZ regime, Fig. 5.4.6b shows that  $\langle a_T \rangle_{s,c^*}$  and  $\langle a_T \rangle_{s,c^0}$  are close, which is in good agreement with the behaviour of the proposed model for high Karlovitz number (see Fig. 5.4.2). However, the profiles of  $\langle a_T \rangle_{s,c^*}$  and  $\langle a_T \rangle_{s,c^0}$  in Fig. 5.4.6a are significantly different for case A. Note that  $\langle a_T \rangle_{s,c^0}$  is almost constant, allowing to use a model based on a constant tangential strain rate due to unresolved flow motions.

For both cases A and C,  $(S_{d,c^0}^0 - S_{d,c^*}^0) \langle \kappa \rangle_{s,c^*}$  is similar to  $(\langle a_T \rangle_{s,c^*} - \langle a_T \rangle_{s,c^0})$  suggesting

that this rough model might be sufficient to compute the corrective strain rate involved in Eq. (5.4.16). Even if this model is theoretically valid only for planar and steady flames, it is expected to weakly affect the prediction of the proposed model (Chapter 4) in the TRZ regime.

## 5.5 Conclusions

In this chapter, a set of one-dimensional turbulent flames using different versions of the proposed model. The results from these simulations are compared to DNS. The closures of the first version tested ( $\text{HK}_\alpha$  model) are those presented in Chapter 4. Even if *a priori* tests in Chapter 4 present very encouraging results, the 1D turbulent flames simulations show that  $\text{HK}_\alpha$  model does not accurately predict the fuel consumption and assumes a too strong bending effect. It appears that the discrepancies observed between the *a priori* model ( $\text{HK}_\alpha$  model) and DNS are due to the too large width of the Gaussian presumed PDF modelling the distribution of flame curvature. Thus, thinner presumed PDF, retained in other versions of the model, significantly improves predictions.

Moreover, the introduction of two Markstein lengths following Eqs. (3.3.5) and (3.3.6) is found to deteriorate the predictions of the model, especially for unity Lewis numbers cases. Thus, the single effective Markstein length  $\mathcal{L}_{rn}$  modelled with Eq. (3.3.7) is preferred, and predicts the most accurate fuel consumption and bending.

Nevertheless, the accuracy of the model on the flame structure is gradually falling when the Karlovitz number decreases toward values of the flamelet regime. For this low Karlovitz number, the modelled flame structure is thicker in the burnt gases side than the one of the DNS, which is the consequence of a bad modelling of the balance between tangential strain rate and stretch due to curvature, as seen in Section 5.4. The mechanisms involved here are not well understood and should be further investigated.

Finally, the final proposed model presents encouraging results, but is strongly sensitive to the correlation used for  $\mathcal{L}_{rn}$  and the width of the presumed PDF  $p(\kappa)$ .



# Chapter 6

## Conclusions and Perspectives

### 6.1 Conclusions

The objective of this thesis is to develop a highly diluted combustion model for large eddy simulations (LES) of new generations of spark-ignition (SI) engine. The review of existing work on diluted combustion shows that highly diluted turbulent flames correspond to the thin reaction zone (TRZ) regime. Then, three specific objectives are addressed. The first one is to adapt the flame surface density (FSD) concept to the TRZ regime. The second objective is to propose models for source terms involved in the transport equations of progress variable and FSD, especially the displacement speed. In parallel, the third objective is to include the effect of differential diffusion in the models of the source terms, as suggested in the literature.

In order to reach these goals, the first chapter of this thesis reviews the physics involved and the existing studies on both diluted premixed flames and TRZ regime. This review highlights the main characteristics of a diluted flame interacting with a highly turbulent flow. These flames present mainly a thickening of the preheat zone and a bending effect on the fuel consumption when the Karlovitz number increases. In addition, a review of the existing works on the modelling of flames in the TRZ regime is also presented. Most of the existing attempts are based on the work of Peters (1999), suggesting that the small eddies penetrate the preheat zone and transport fluid near the reaction zone over a distance corresponding to its own size. From this assumption Peters (1999) proposes to model the flame through a level set approach and by modelling the displacement speed using asymptotic analysis. This suggests that one key element to model is the stretch due to curvature  $S_d\kappa$ . Numerous studies (Hawkes and Chen, 2005; Katragadda et al., 2014a; Trisjono et al., 2016; Wang et al., 2017) then analyse this term resulting to models involving the tangential diffusion through the diffusivity coefficient. Studies (Chakraborty and Cant, 2006, 2011, 2005a,b; Chakraborty and Klein, 2008; Savard and Blanquart, 2014) suggest to take into account differential diffusion in displacement speed modelling through the definition of an effective Lewis number or Markstein length.

Then, a study of two-dimensional direct numerical simulation (DNS) of flames interacting

with a pair of counter-rotating vortices is analysed using the AVBP code. The main objective of this analysis is to isolate the effect of one specific turbulent structure on the stirring of the flame front. These simulations are largely studied in the literature (Bougrine et al., 2014; Candel and Poinso, 1990; Charlette et al., 2002a; Colin et al., 2000; Meneveau and Poinso, 1991; Poinso et al., 1991) resulting in the definition of models for the tangential strain rate  $a_T$  in the flamelet regime. The study conducted in this thesis aims to re-evaluate some common approximations made and to extend the operating conditions to TRZ regime. This is done by analysing small vortices compared to the thermal laminar flame thickness and highly intense vortices. The common approximations made, which are to approximate the tangential strain rate with the total flame stretch evaluated from the rate of change of total heat release, appear to be insufficient to explain that the current models for  $a_T$  fail to predict accurately the strain rate in the TRZ regime. Moreover, this analysis leads to define a new efficiency function, which is close to the one proposed by Bougrine et al. (2014). Thus, no significant improvements are expected with this efficiency function. Finally, other characteristics of this kind of simulations are not investigated such as the transitory aspects of interactions between a flame front and a single pair of counter-rotating vortices.

Third, the interactions between a statistically planar flame and a turbulent flow are analysed using 3D DNS. The aims of these simulations are to further analyse the different source terms involved in the CFM model, in particular the displacement speed  $S_d$ , and the effects of differential diffusion on the flame front. To get sufficiently long interactions between turbulence and flame, a spectral method to force a turbulent field is applied. The simulations were chosen to cover a range of Karlovitz numbers ranging from the flamelet to the TRZ regimes. They are performed with  $Le_k \neq 1$  and  $Le_k = 1$  in order to evaluate the effect of preferential diffusion. The resulting turbulent flames present a thickened preheat zone with or without preferential diffusion. Nevertheless, the thickening is much larger for  $Le_k \neq 1$  cases. The resulting turbulent flames also present a bending on the fuel consumption through the evolution of the turbulent flame speed  $S_T$ . Unlike previous experimental studies (de Goey et al., 2005; Gülder, 2007; Wabel et al., 2017; Yuen and Gülder, 2013), both turbulent flame speed and turbulent flame surface present this bending in a similar way. These results suggest that preferential diffusion enhances the effect of turbulence on the flame front, in particular the thickening. Moreover, this analysis suggests to study the flame front through a particular iso-surface of the progress variable in the reaction zone, mainly because in this zone the flame structure is still close to the structure of a flame in the flamelet regime. Thus, the iso-surface  $c = 0.8$  is analysed and particularly the displacement speed on this surface. It has been observed that  $S_d$  on the iso-surface selected presents strong dependencies on both tangential strain rate and curvature. These dependencies are modelled based on asymptotic theories by defining two distinct Markstein lengths. These Markstein lengths allow to differentiate the effects of tangential strain rate and curvature, which seem to be correlated to differential diffusion. Indeed, the Markstein lengths computed using the DNS of  $Le_k = 1$  flames are much smaller than those

of  $Le_k \neq 1$  cases. In addition, these lengths decrease when the Karlovitz number increases. This observation is in agreement with studies of an effective Lewis number. Finally, correlations are proposed to use these Markstein lengths in a model for  $S_d$  deduced from asymptotic theories.

In the fourth chapter, the adaptation of the CFM model to flames in the TRZ regime is presented. This formalism is based on the definition of a new progress variable  $\mathcal{C} = \mathcal{H}(c^*)$ , where  $\mathcal{H}(c)$  is the Heaviside function. Then, transport equations for this progress variable (Eq. 4.1.5) and for the fine grained FSD,  $\Sigma^* = \Sigma\delta(c - c^*)$ , (Eq. 4.1.6) are derived. The source terms involved in these equations are closed with the following models:

- The unresolved transport term of the progress variable is modelled with a simple-gradient approach including a thermal expansion contribution (Eq. 4.3.6).
- The displacement speed is modelled as a function of the tangential strain rate and curvature involving Markstein lengths (Eq. 4.3.16). The effect of the curvature fluctuations is taken into account through a Gaussian presumed probability density function (PDF) of the curvature.
- The unresolved FSD transport is modelled with a simple-gradient approach including a contribution due to thermal expansion (Eq. 4.4.6).
- The model for normal propagation is similar to ECFM-LES model (Richard et al., 2007) (Eq. 4.4.8).
- The tangential strain rate is decomposed into contributions due to resolved and unresolved flow motions. The former is evaluated following a model (Eq. 4.4.13) proposed by Hawkes and Cant (2000). The approach proposed by Charlette et al. (2002a) is used to model the latter (Eqs. 4.4.14 and 4.4.16). Different efficiency functions can be used, for instance, the function proposed by Bougrine et al. (2014) or the one developed in Chapter 2 (Eq. 2.3.5).
- The model (Eq. 4.4.24) for the stretch due to curvature is deduced from the model of displacement speed and the curvature distribution.

Additionally, closures are proposed for both the curvature  $\langle \kappa \rangle_{s,c^*}$  and its variance in Eqs. (4.3.13) and (4.3.15), respectively. These submodels involve the filtered progress variable  $\bar{\mathcal{C}}$ , which is not *a priori* known. Thus, a new relationship between  $\bar{\mathcal{C}}$  and  $\tilde{\mathcal{C}}$  is defined based on the filtered laminar flame-PDF (FLF-PDF) model (Moureau et al., 2011). Then, each closure is *a priori* tested by comparing their predictions to DNS. These tests show a good agreement of the proposed closures with DNS. Moreover, a simple analysis of the tangential strain rate suggests that an efficiency function based on a low pass filter (LPF) using a Heaviside function and a cut-off lengths equal to  $\delta_L^0$  might be sufficient to reproduce the tangential strain rate due to unresolved flow motions in the TRZ regime.



The last chapter of this thesis is dedicated to a further step toward LES of spark-ignition engines. *A posteriori* tests are conducted using 1D turbulent flames to assess the general behaviour of the proposed model. These tests show that the formulation of the model proposed in Chapter 4 does not well predict the fuel consumption evolution with  $Ka$ , when all the closures interact with each other. However, a variation of different model parameters suggests to use a single effective Markstein length and half the variance of the curvature. The former show that modelling the effect of tangential strain rate and curvature on the displacement speed is not sufficient and should be further investigated; the latter suggest that a Gaussian presumed PDF is not well suited to model the curvature distribution. However, using these parameters allows the model to well reproduce the fuel consumption, the spatial profiles of progress variable and flame surface density, as well as source term profiles. Nevertheless, a discussion on the FSD transported highlights the limits of the proposed model. Indeed, the model predicts poorly the flame structure, when the flame is in the flamelet regime. A potential correction is proposed through a theoretical analysis of the tangential strain rate  $a_T$  on the iso-surface  $c = c^*$ . This correction should be further investigated in future work.

Finally, in this thesis we propose a new formalism of the CFM model valid in the TRZ regime, through solving transport equations of a specific iso-surface in the reaction zone. Even if both *a priori* and *a posteriori* tests present encouraging results, the model is not complete and need further analysis before being applied to LES of spark-ignition engines.

## 6.2 Perspectives for future works

Future works are required to adapt the model to SI engines applications. The further analyses needed can be organised into model improvement studies and validation works.

### Improvements of the model

First, the model for tangential strain rate due to unresolved flow motions is based on strong assumptions. The first hypothesis that needs to be investigate is the independence on  $\tilde{C}$ , as presented in Section 5.4.2. One potential solution lies in adding a corrective strain rate as proposed with Eq. (5.4.15). However, even if this solution is theoretically interesting, its application remains to be investigated *a priori* and *a posteriori*. The second point to investigate is the model based on intermittency turbulence. Indeed, the intermittent turbulent net flame stretch (ITNFS) model (Meneveau and Poinso, 1991) assumes that each scale of turbulence stretch the flame independently, *i.e.*, without interacting with other turbulent scales. One way to reinvestigate this assumption is to adapt the 2D-DNS of flame/vortex interactions by simulating the interactions between a flame front and multiple vortices. The idea is still to isolate the effect of one scale of turbulence on the stirring of the flame front but using a method to simulate statistically stationary flame/vortex interactions with a mean frequency of the dipole occurrence depending on its size, illustrated in Fig. 6.2.1. However, this method only

takes into account interactions between turbulent structures of the same scale and many issues are induced with this approach, such as the physical relevance .

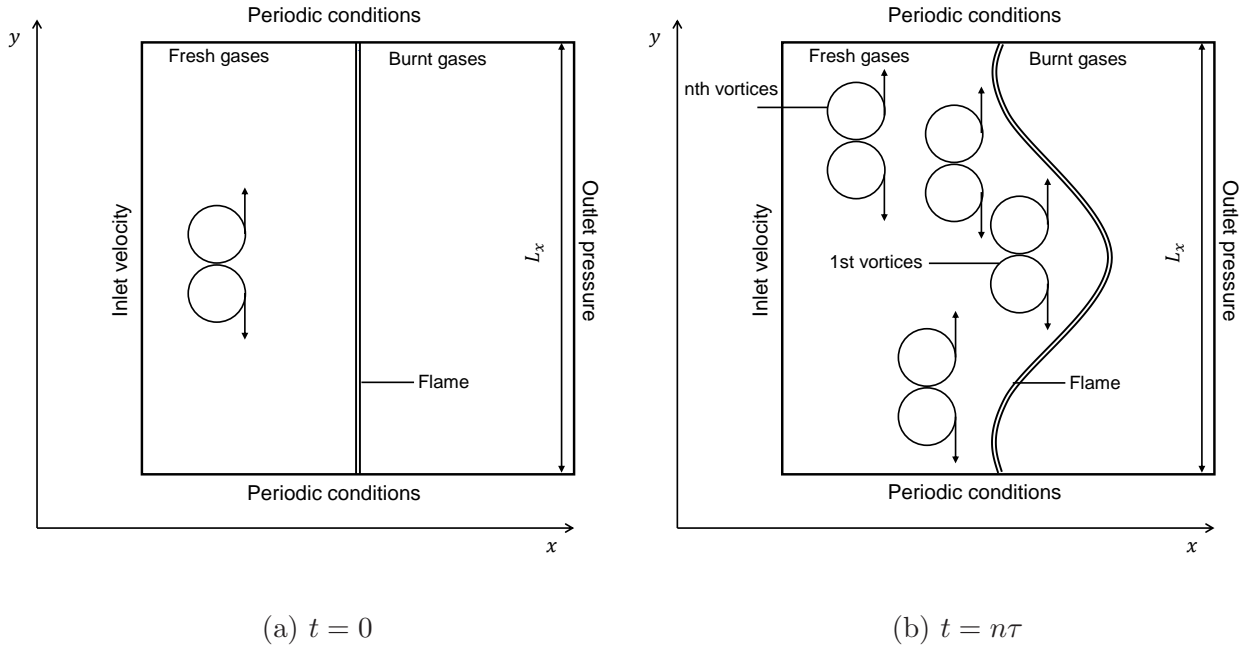


Figure 6.2.1: Schematic view of pulsed interactions flame-vortex: (a) Initial configuration with the creation of the first pair of vortices and (b) creation of the  $n^{\text{th}}$  pair of vortices after  $n\tau$ , where  $\tau$  is the period to be defined.

On the other hand, interpreting the flame front as a low-pass filter (LPF) to model the tangential strain rate due to unresolved flow motions shows satisfying results in Section 4.4.3. LPF model is based on a Heaviside function for computing the efficiency function  $\Gamma$  and assuming that the cut-off length of the low-pass filter is equal to the laminar flame thickness  $\delta_L^0$ . Despite encouraging results, one way of improving this model would be to check the dependence of the cut-off length on Karlovitz number, based on the work of Gülder (1995).

Second, improvements of the models of displacement speed and stretch due to curvature could be proposed. The models proposed being strongly dependent on the values of the Markstein lengths, a further study of these lengths should be conducted. The assumption of two distinct Markstein lengths to differentiate effects of strain rate and curvature should be further analysed. Indeed, the *a posteriori* simulations in Chapter 5 question the relevance of this differentiation. Moreover, the correlations proposed must be verified using different fuels (from  $\text{H}_2$  and light hydrocarbons, to heavier fuels, like iso-octane). The effect of preferential diffusion on these Markstein lengths might also be evaluated using different equivalence ratios or different dilution rates. Nevertheless, this kind of studies is very expensive because 3D DNS for different Karlovitz numbers are needed for each fuel, each equivalence ratio and each dilution rate. Furthermore, as already pointed out the Markstein formalism might not be a suitable way to model the effect of turbulence on displacement speed and stretch due to curvature, despite encouraging results. Thus, future work could be dedicated to evaluate and develop other models,

for instance, by considering a non-linear relationship between stretch and displacement speed (Chen, 2011; Halter et al., 2010).

Finally, a key parameter to improve is the modelling of the probability density function (PDF) of curvature. As already pointed out, a Gaussian presumed PDF (Eq. 4.3.9) does not predict accurately curvature distribution unless modifying the variance. Thus, other functions should be studied as presumed PDF in future work.

## Toward SI engines application

To use the formalism presented in this thesis in SI engines applications, some steps need to be achieved. In the present study, the proposed model is evaluated against DNS using a Reynolds averaged Navier-Stokes (RANS) approach avoiding to explore the behaviour of the resolved closures. To investigate this aspect of the proposed model, simulation of spherical laminar flame is a simple test to verify the relevance of the resolved closures. This kind of simulation is the simplest approximation of a curved flame allowing to explore the effects of curvature and tangential strain rate due to sphericity, the effects of normal propagation and resolved transport, as reported in Fig. 6.2.2. These simulations allow to investigate the sensitivity to LES filter width of the resolved closures. The case of a spherical laminar flame is particularly interesting because the flames encountered in SI engines are generally spherical flames initially laminar.

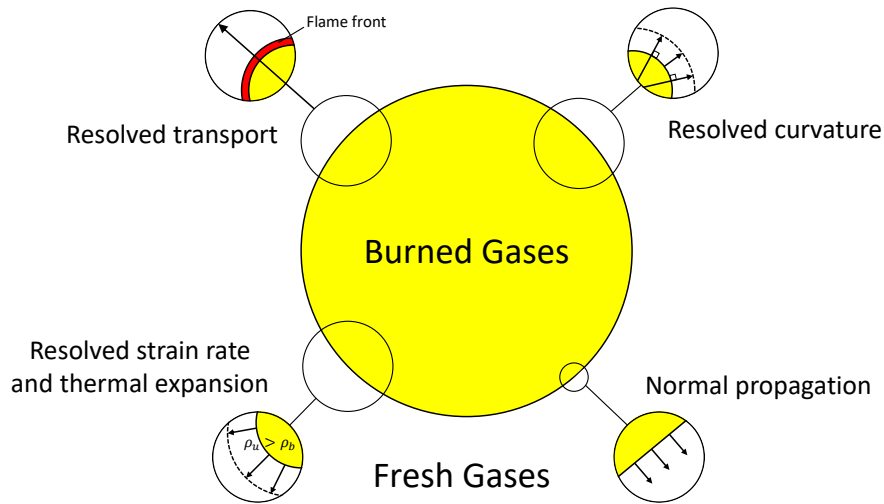


Figure 6.2.2: Schematic view of the physical mechanisms involved in the propagation of a spherical laminar flame. (Richard, 2005)

Then, the proposed model should be validated on 3D LES *a posteriori* analyses. These validations may be performed by extracting the quantities of interest following an LES procedure, similarly to the RANS method proposed in Section 4.2. In this future procedure, the domain should be discretized into cells instead of slices. The difficulty encountered in such procedure is the definition of the filter width, *i.e.*, the size of the cells. Indeed, it should be simultaneously

large enough to contain unresolved contributions and sufficiently thin to get a large number of cells in the LES mesh.

Then, the model should be tested on a LES of an actual engine. However, some sub-models for engine applications should be first verified compatible with the formalism proposed in the present study:

- The model used for the ignition phase in ECFM-LES model is based on imposing, at the ignition time  $t_{ign}$ , an initial profile of  $\bar{\Sigma}_{\tilde{c}}$  close to the spark plug (Richard et al., 2007). In this model, at the instant of spark timing  $t_{ign}$ , an initial spherical profile is imposed for the progress variable  $\tilde{c}$ . After time  $t_{ign}$ , the FSD has to be evaluated but cannot be given by the transport equation Eq. (1.5.29) as the flame front is not fully established. The FSD is then determined from a zero dimensional model (Richard, 2005; Richard et al., 2007) until the flame front is fully established and sufficiently resolved. Until then, a model for the evolution of the wrinkling of the flame kernel due to turbulent flow field combined with the zero dimensional model allows to evaluate the total flame surface of the flame kernel. This surface is then distributed as proposed by Boger et al. (1998). Finally, when the flame kernel is sufficiently large, the ECFM-LES model can be used to simulate the flame. The difficulty that can be faced with combining this ignition model with the formalism proposed in the present study lies in the transition phase. Indeed, with this iso-surface approach the time needed for the flame kernel to grow might be too long, leading to underestimation of the fuel consumption.
- The behaviour of the proposed model in this thesis should be evaluated in wall/flame interactions. One potential solution is to adapt the model developed by Bruneaux et al. (1997), as already done for ECFM-LES by Richard (2005).

When these adaptations are done, the complete model can be assessed using the data generated from bench measurements of a well known engine, for example an IFPEN engine. In a final step, this model should be evaluated using a modern downsized spark-ignition engine using EGR dilution.



# Appendix A

## Comparison of the convective schemes

As mentioned in Chapter 3, codes dedicated to direct numerical simulation (DNS) use convective scheme with high spatial orders, like S3D in (Wang et al., 2017) or NTMIX (Baum et al., 1995; Cuenot et al., 1997) with 8<sup>th</sup> and 6<sup>th</sup> orders, respectively. In the present study, the DNS computations were conducted using the AVBP code (Moureau et al., 2005). It solves the three-dimensional compressible Navier-Stokes equations on unstructured and hybrid grids. The AVBP numerical schemes are based on the cell-vertex method. Two convective schemes are available :

1. a finite-volume Lax-Wendroff type scheme (LW), which is 2<sup>nd</sup> order in time and space,
2. a two-steps Taylor-Galerkin type scheme (TTGC) (Colin and Rudgyard, 2000), which is 3<sup>rd</sup> order in time and space.

Because the order of TTGC scheme is larger than the one of LW scheme, the former seems to be a better choice than the latter for DNS with AVBP.

The present appendix is dedicated to the comparison of LW and TTGC schemes. First, the two schemes are presented in Section A.1 along with the impact of each scheme on computational cost. Then, the statistics resulting from simulations using LW or TTGC schemes are compared in Section A.2.

### A.1 Numerical schemes description

In this section the different convective schemes used in the AVBP code are presented after the brief description of the equations to be discretized in time and in space.

#### A.1.1 Equations and temporal discretization

The differential formulations of the Navier-Stokes (NS) equations presented in Chapter 1 can be written in the following compact form, which will be use for simplicity in the rest of this section:

$$\frac{\partial \mathbf{w}}{\partial t} + \nabla \cdot \mathbf{F} = s, \quad (\text{A.1.1})$$

where  $\mathbf{w} = (\rho, \rho\mathbf{u}, \rho E)$  is the vector of conserved variables,  $\mathbf{F}$  is the corresponding flux tensor and  $s$  is the source terms. The fluxes can be divided into an inviscid, convective part  $\mathbf{F}^i$  and a viscous part  $\mathbf{F}^v$  and expressed as:

$$\mathbf{F} = \mathbf{F}^i(\mathbf{w}) + \mathbf{F}^v(\mathbf{w}, \nabla\mathbf{w}) \quad (\text{A.1.2})$$

Note that viscous fluxes not only depends on  $\mathbf{w}$ , but also on its gradients  $\nabla\mathbf{w}$ .

Equation (A.1.1) has to be discretized in time and space in order to numerically solve it. The temporal scheme used is based on a N-step low storage Runge-Kutta (RK) scheme. It is expressed as follows:

$$\begin{aligned} \frac{\mathbf{w}_k^{(1)} - \mathbf{w}_k^n}{\alpha_1 \Delta t} &= -C_k(\mathbf{w}^n) \\ \frac{\mathbf{w}_k^{(2)} - \mathbf{w}_k^{(1)}}{\alpha_2 \Delta t} &= -C_k(\mathbf{w}^{(1)}) \\ &\vdots \\ \frac{\mathbf{w}_k^{n+1} - \mathbf{w}_k^{(N)}}{\alpha_N \Delta t} &= -C_k(\mathbf{w}^{(N-1)}) + D_k(\mathbf{w}^n) + S_k(\mathbf{w}^n), \end{aligned}$$

where  $\Delta t$  is the time step,  $\{\alpha_l | l \in N\}$  are real coefficients (for consistency,  $\alpha_N = 1$ ) and  $\mathbf{w}_k^n$  is the conservative variable vector taken at the mesh node  $k$  at instant  $t^n$ . The discrete operators  $C_k$ ,  $D_k$  and  $S_k$  are convection, molar and turbulent diffusion operators, and source terms, respectively. For  $N = 1$ , we get the classical explicit first-order Euler scheme.

In the AVBP code, the stability constraint for the convective schemes is a Courant-Friedrichs-Lewy (CFL) constraint based on the fastest waves of the flow, *i.e.*, acoustic waves:

$$\Delta t < \text{CFL} \frac{\min(\Delta x)}{\max|\mathbf{u}| + c}, \quad (\text{A.1.3})$$

where  $c$  is the speed of sound. The maximum value of CFL constant depends on the numerical scheme used.

## A.1.2 Spatial discretization

### Lax-Wendroff scheme

Lax-Wendroff scheme is a single step finite volume scheme. Its temporal integration is deduced from the RK scheme considering  $N = 1$ , leading to:

$$\frac{\mathbf{w}_k^{n+1} - \mathbf{w}_k^n}{\Delta t} = -C_k(\mathbf{w}^n) + D_k(\mathbf{w}^n) + S_k(\mathbf{w}^n). \quad (\text{A.1.4})$$

In this equation, the convective term  $C_k(\mathbf{w}^n)$  is written as:

$$C_k(\mathbf{w}^n) = \frac{1}{V_k} \sum_{j|k \in \Omega_j} V_{\Omega_j} D_{k,\Omega_j} C|_{\Omega_j}(\mathbf{w}^n), \quad (\text{A.1.5})$$

where  $V_k$  is the control volume associated with mesh node  $k$ ,  $\Omega_j$  designates a mesh cell,  $D_{k,\Omega_j}$  is a distribution matrix,  $C|_{\Omega_j}(\mathbf{w}^n)$  corresponds to the cell gradient operator applied to inviscid, convective fluxes  $\mathbf{F}^i$ :

$$C|_{\Omega_j}(\mathbf{w}^n) = \frac{1}{N_d V_{\Omega_j}} \sum_{l|l \in \Omega_j} \mathbf{F}_l^i \cdot d\mathbf{S}_l, \quad (\text{A.1.6})$$

where  $N_d$  is the number of dimensions,  $V_{\Omega_j}$  is the volume associated to mesh cell  $\Omega_j$  and  $d\mathbf{S}_l$  are the normal vectors to the surfaces of mesh cell  $\Omega_j$ . The distribution matrix allows to evaluate the first and second order terms of the numerical scheme:

$$D_{k,\Omega_j} = \frac{1}{n_v(\Omega_j)} \left( \mathbf{I} + \frac{n_v(\Omega_j)}{2N_d} \frac{\Delta t}{V_{\Omega_j}} \mathbf{A}_{\Omega_j} \cdot d\mathbf{S}_l \right), \quad (\text{A.1.7})$$

where  $n_v(\Omega_j)$  is the number of nodes of cell  $\Omega_j$  and  $\mathbf{A}_{\Omega_j}$  is the Jacobian flux tensor at the centre of cell  $\Omega_j$ .

### Taylor-Galerkin scheme

In the AVBP code, a finite element two-steps Taylor-Galerkin type scheme (TTGC) (Colin and Rudgyard, 2000) was developed for large eddy simulations (LES) focusing mainly on reducing the numerical dissipation of the smallest resolved scales. Finite element schemes in the AVBP code rely on the decomposition of conservative variables based on shape functions  $\phi_k$ :

$$\mathbf{W}^n(\mathbf{x}) = \sum_k \phi_k(\mathbf{x}) \mathbf{w}_k^n, \quad (\text{A.1.8})$$

where  $\mathbf{x}$  is the position vector. When mesh cells are triangles or tetrahedra, the shape functions are linear, while for all the other elements they are bilinear. TTGC scheme is then written using first and second order operators  $L(\mathbf{W}^n)$  and  $LL(\mathbf{W}^n)$ , respectively:

$$L(\mathbf{W}^n) = \sum_{j|k \in \Omega_j} L_k(\mathbf{W}^n)|_{\Omega_j}, \quad (\text{A.1.9})$$

$$LL(\mathbf{W}^n) = \sum_{j|k \in \Omega_j} LL_k(\mathbf{W}^n)|_{\Omega_j}. \quad (\text{A.1.10})$$

$$(\text{A.1.11})$$

When the elements are triangles or tetrahedra,  $L_k$  and  $LL_k$  are similar to the finite volume operators of LW scheme. However, for the bilinear elements, their expression is much more complex and needs to approximate residuals (Colin and Rudgyard, 2000).



### A.1.3 Direct numerical simulation set-up for convective scheme comparison

A comparison of the two schemes is given in Sections A.2 and A.3 to evaluate the benefit of one over the other by conducting twice the same set-up. Because the present study is dedicated to modelling flames in the thin reaction zone (TRZ) regime, the case used to compare both numerical scheme is selected in the TRZ regime and is case C (presented in Chapter 3). The chemical mechanism used in this comparison is the two-step Arrhenius mechanism with 6 species presented in Section 3.1.1. The numerical parameters of this case are reported in Table A.1.

Table A.1: The DNS set-up for the simulation C of the interaction between a planar flame and forced homogeneous isotropic turbulence. The Karlovitz number  $Ka$  and the Damköhler number  $Da$  are defined with Eqs. (1.3.11) and (1.3.10), respectively. The laminar flame thickness used to evaluate these numbers is the thermal laminar flame thickness  $\delta_L^0 = (T_b - T_u)/\max(|\nabla T|)$ .  $N_{cell}$  is the number of cells in the mesh used for simulating the flames.

Case	$l_t/\delta_L$	$u'/S_L^0$	$Ka$	$Da$	$Re_t$	$Le_{Fuel}$	$\delta_L^0/\Delta_x$	$\eta_k/\Delta_x$	$N_{cell}$
C	4.3	12.5	21.4	3.1	489.0	2.9	20	0.6	$83e^6$

First, the computational time for both LW and TTGC schemes are reported in Table A.2. The computation time for one iteration  $\tau_i$  is about 4 times larger using the TTGC scheme compared to the LW scheme. Thus, the benefit of LW scheme over TTGC is the computational economy, but TTGC is expected to be more accurate (with less spatial dissipation) because of its higher order. The rest of this appendix is dedicated to compare the results from both LW and TTGC schemes.

Table A.2: Computational characteristics of simulations LW and TTGC schemes.

Scheme	Physical time [ms]	Real elapsed time [h]	Computation time $\tau_i$ [s/iteration]	CPU time [hCPU]
LW	4.7	43	0.65	86713
TTGC	5.1	174	2.5	349785

## A.2 Comparison of the convective schemes

This section is dedicated to the comparison of the statistics of the flames resulting from the use of LW and TTGC schemes. Note that in this analysis the progress variable is computed from the fuel mass fraction:

$$c = \frac{Y_{fuel} - Y_{fuel}^b}{Y_{fuel}^u - Y_{fuel}^b}. \quad (A.2.1)$$

This definition explains the slight differences between the results presented in this appendix and those observed in Chapter 3, where the progress variable is computed as the reduced temperature.

### A.2.1 Temporal evolutions

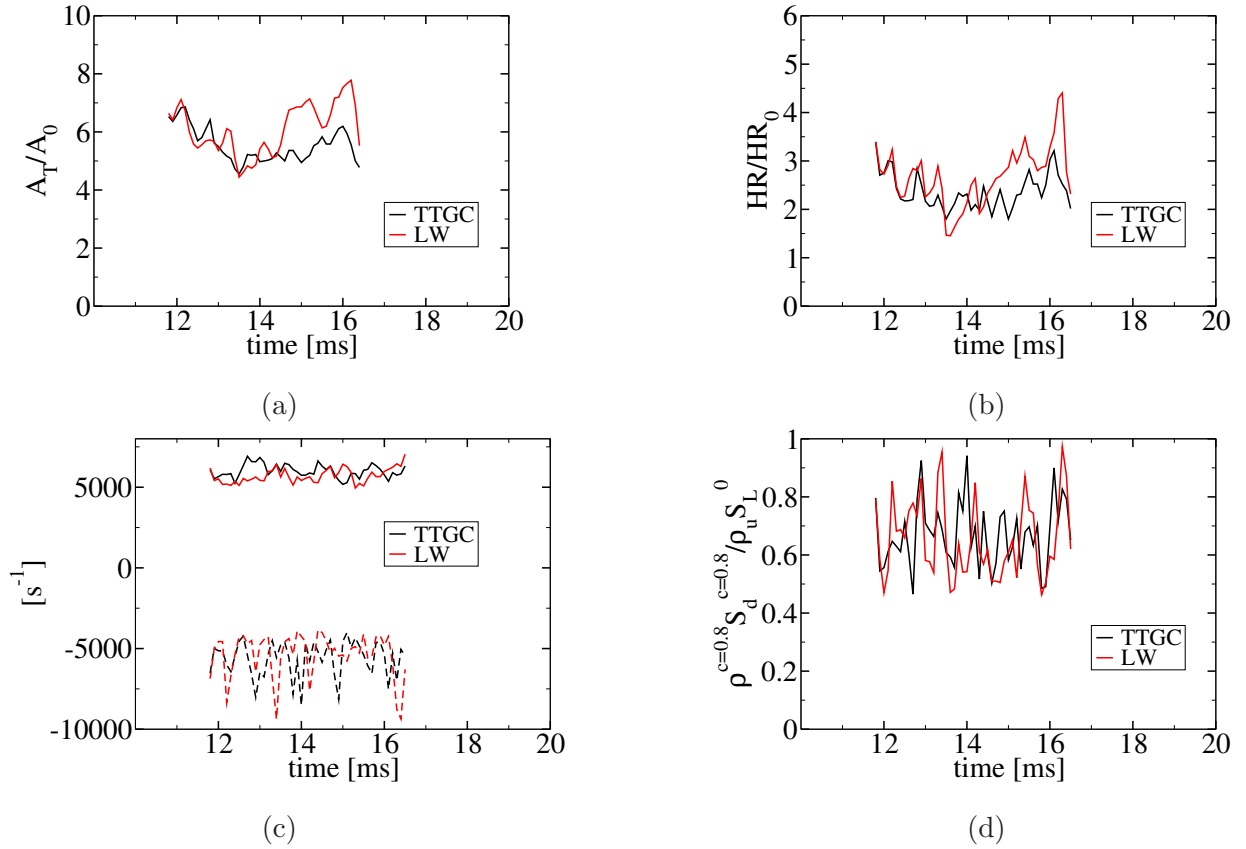


Figure A.2.1: Comparison of the overall results using TTGC scheme or LW scheme: (a) the temporal evolution of the generalized flame surface normalized with the laminar flame surface  $A_0 = L^2$ , (b) the temporal evolution of the heat release rate normalized with the heat release rate of the laminar flame  $HR_0$ , (c) the temporal evolution of the generalized tangential strain rate in solid lines and the stretch due to curvature in dashed lines, and (d) the temporal evolutions of the density weighted displacement speed at  $c = 0.8$  normalized with the density weighted laminar flame speed  $\rho_u S_L^0$ .

The temporal evolutions of some variables are compared in Fig. A.2.1. First, the flame surface normalized with the laminar flame surface of TTGC case in Fig. A.2.1a has a similar evolution as LW case. The latter has a time averaged flame surface only 9% higher than the flame surface of TTGC case. The heat release rate for both cases are also shown in Fig. A.2.1b. As for the flame surface the heat release rates are very similar, and their time averaged values differ by 13%. Moreover, the surface averaged stretch due to curvature, strain rate and displacement speed are compared. Figure A.2.1c shows the temporal evolutions of the surface averaged strain rate in solid lines and  $\langle S_d \kappa \rangle_s$  in dashed lines. These evolutions are similar for both TTGC and LW cases with a relative deviation of 6% on the time averaged strain rate and 5% on the time averaged stretch due to curvature. As for the previous variables, the displacement speed presents the same temporal evolution in Fig. A.2.1d with both TTGC and LW schemes. The relative deviation on the time averaged  $\langle S_d \rangle_s$  is 2%.

These observations suggest that the numerical scheme (LW or TTGC) has a weak impact on the statistics of the quantities of interest. However, the observations made present two main

drawbacks:

- the quantities displayed in Fig. A.2.1 are surface averaged variables, therefore, the impact of spatial dissipation for modelling is not highlighted,
- the temporal sample might be too small for a relevant comparison.

### A.2.2 Comparison of statistics of displacement speed on a progress variable iso-surface

Because the modelling approach chosen in this study is based on the analysis of the behaviour of an iso-surface of progress variable at  $c = 0.8$ , the comparison of the displacement speed from cases using LW and TTGC schemes is performed.

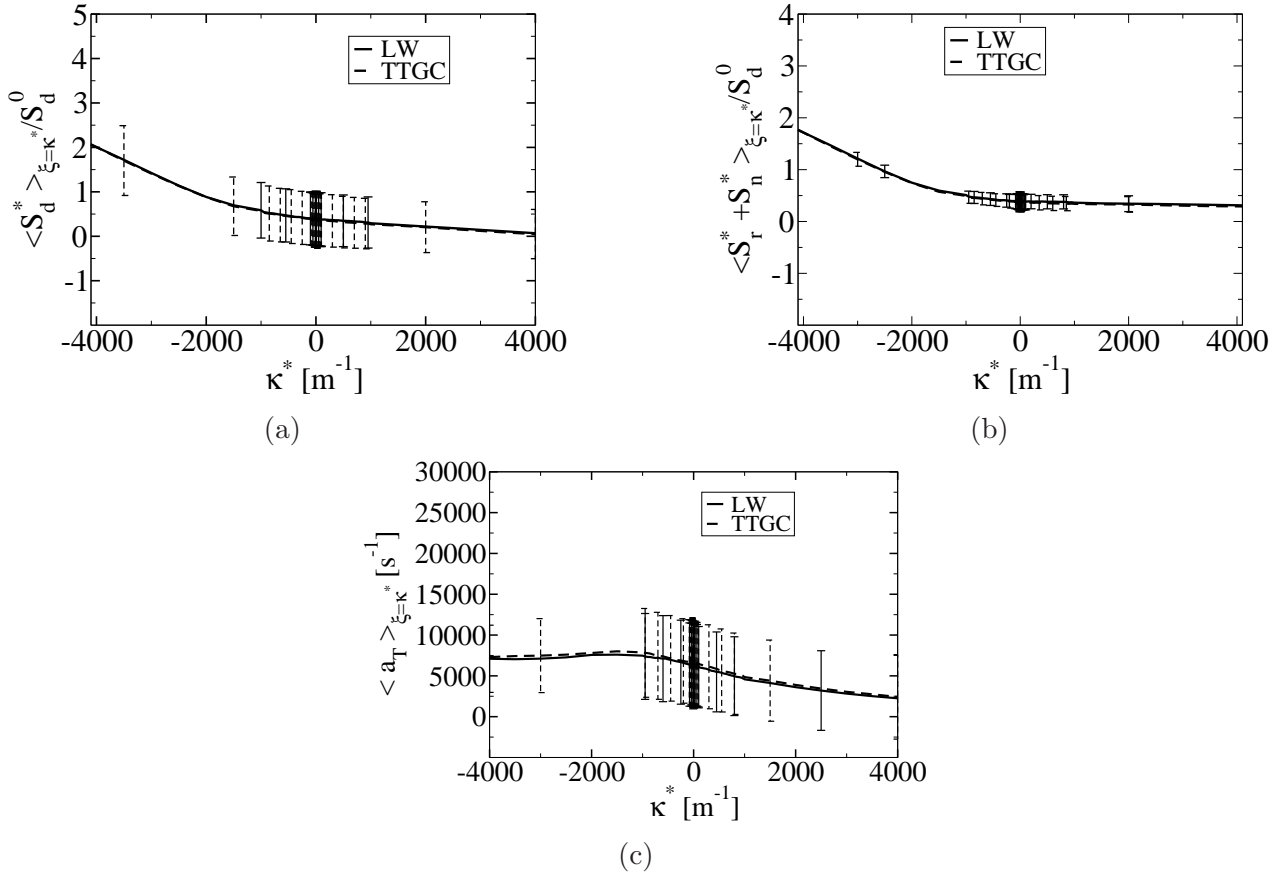


Figure A.2.2: Comparisons of the conditional mean of (a) displacement speed  $\langle S_d^*(\xi) \rangle_{\xi=\kappa^*}$  and (b) its components  $\langle S_r^* + S_n^*(\xi) \rangle_{\xi=\kappa^*}$ , normalized with the laminar flame speed at  $c = c^*$   $S_d^0$  as functions of  $\kappa^*$ . (c) Comparison of the conditional mean of tangential strain rate  $\langle a_T^*(\xi) \rangle_{\xi=\kappa^*}$  as function of  $\kappa^*$ . The error bars represent the standard deviation.

Figure A.2.2 compares the conditional means of displacement speed, its components  $\langle S_r^* + S_n^*(\xi) \rangle_{\xi=\kappa^*}$  and tangential strain rate conditioned on  $\kappa^*$  resulting from simulations using LW and TTGC schemes. The standard deviation is also displayed by error bars in the same figure. In Figs. A.2.2a to A.2.2c curves representing results from LW and TTGC simulations are almost superimposed, meaning that the convective scheme has almost no impact on the conditional

mean of the quantities of interest. Moreover, the standard deviations observed in these figures are very similar whether LW scheme or TTGC scheme is used. This suggest that the spatial dissipation does not impact significantly the statistics of the quantities of interest regarding the flame curvature  $\kappa^*$ .

A similar analysis is performed on the double conditioning on both curvature and strain rate conducted in Section 3.3.2. Figure A.2.3 shows this double conditioning resulting from simulations using LW and TTGC schemes. The joint probability density function (PDF) of curvature and strain rate is also plotted in this figure by black solid lines corresponding to 10% (outer line), 50% and 90% (inner line) of the maximum values of the joint PDF.

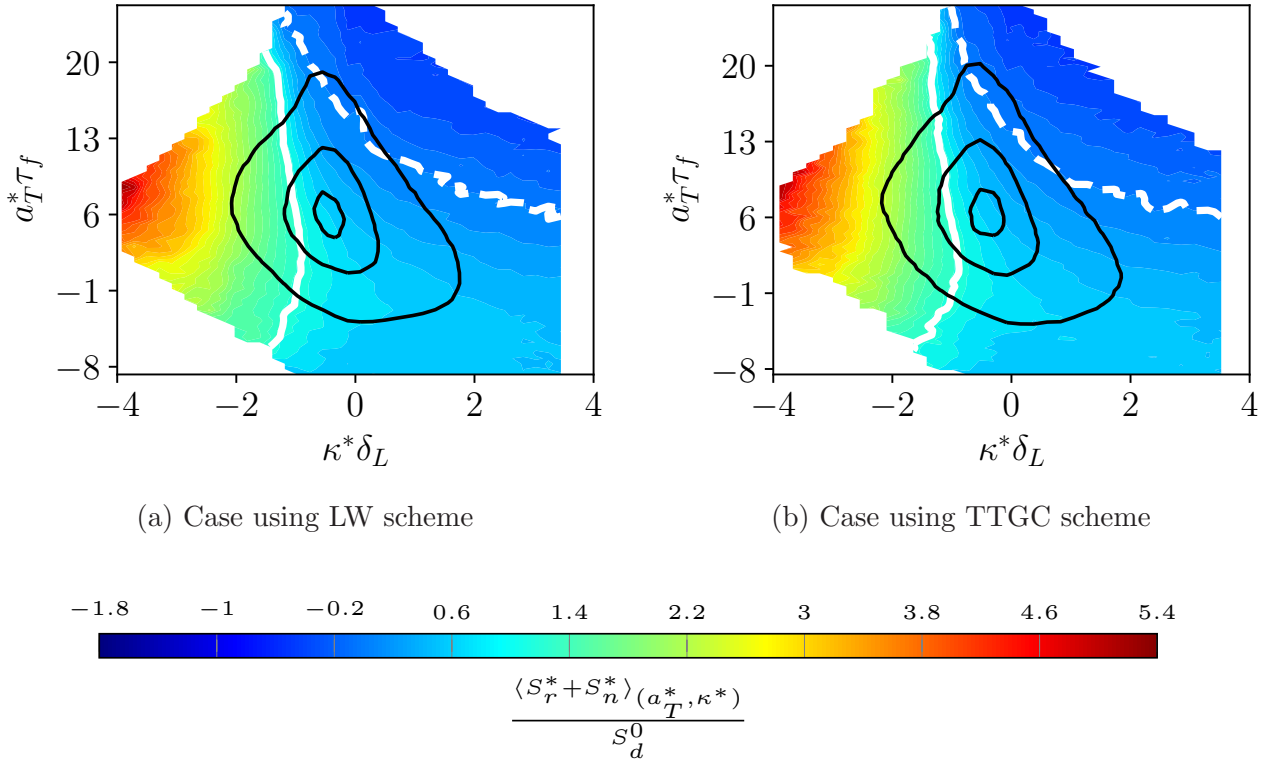


Figure A.2.3: Evolution of the conditional mean of  $\langle S_r^* + S_n^* \rangle_{(a_T^*, \kappa^*)}$  with  $a_T^*$  and  $\kappa^*$  for: (a) case C using LW scheme and (b) case C using TTGC scheme. Black lines are contours of the joint probability density function (PDF) of  $a_T^*$  and  $\kappa^*$  corresponding to 10% (outer line), 50% and 90% (inner line) of its maximum value. The solid white line is the iso-contour  $\langle S_r^* + S_n^* \rangle_{(a_T^*, \kappa^*)} = \rho_u S_L / \rho^*$  and the dashed white line is the iso-contour  $\langle S_r^* + S_n^* \rangle_{(a_T^*, \kappa^*)} = 0$ .

The joint PDFs displayed in Fig. A.2.3b are similar to those in Fig. A.2.3a. Pearson's correlation coefficient  $r_{a_T^*, \kappa^*}$  (Pearson, 1895), defined in Eq. (3.3.1), confirm the apparent similar joint PDFs resulting from LW and TTGC simulations. Indeed,  $r_{a_T^*, \kappa^*}$  equals  $-0.14$  and  $-0.16$  when LW and TTGC scheme are used, respectively. Figures A.2.3a and A.2.3b show similar dependency of  $\langle S_r^* + S_n^* \rangle_{(a_T^*, \kappa^*)}$  on both  $\kappa^*$  and  $a_T^*$  with very close magnitudes. These observations confirm the weak impact of the numerical schemes on the statistics of the quantities of interests regarding dependency on flame curvature and tangential strain rate.

### A.2.3 Comparison of statistics for Reynolds averaged Navier-Stokes modelling

The impact of the choice in numerical scheme on the statistics of the quantities of interest from a Reynolds averaged Navier-Stokes (RANS) point of view (see Section 4.2) is here investigated.

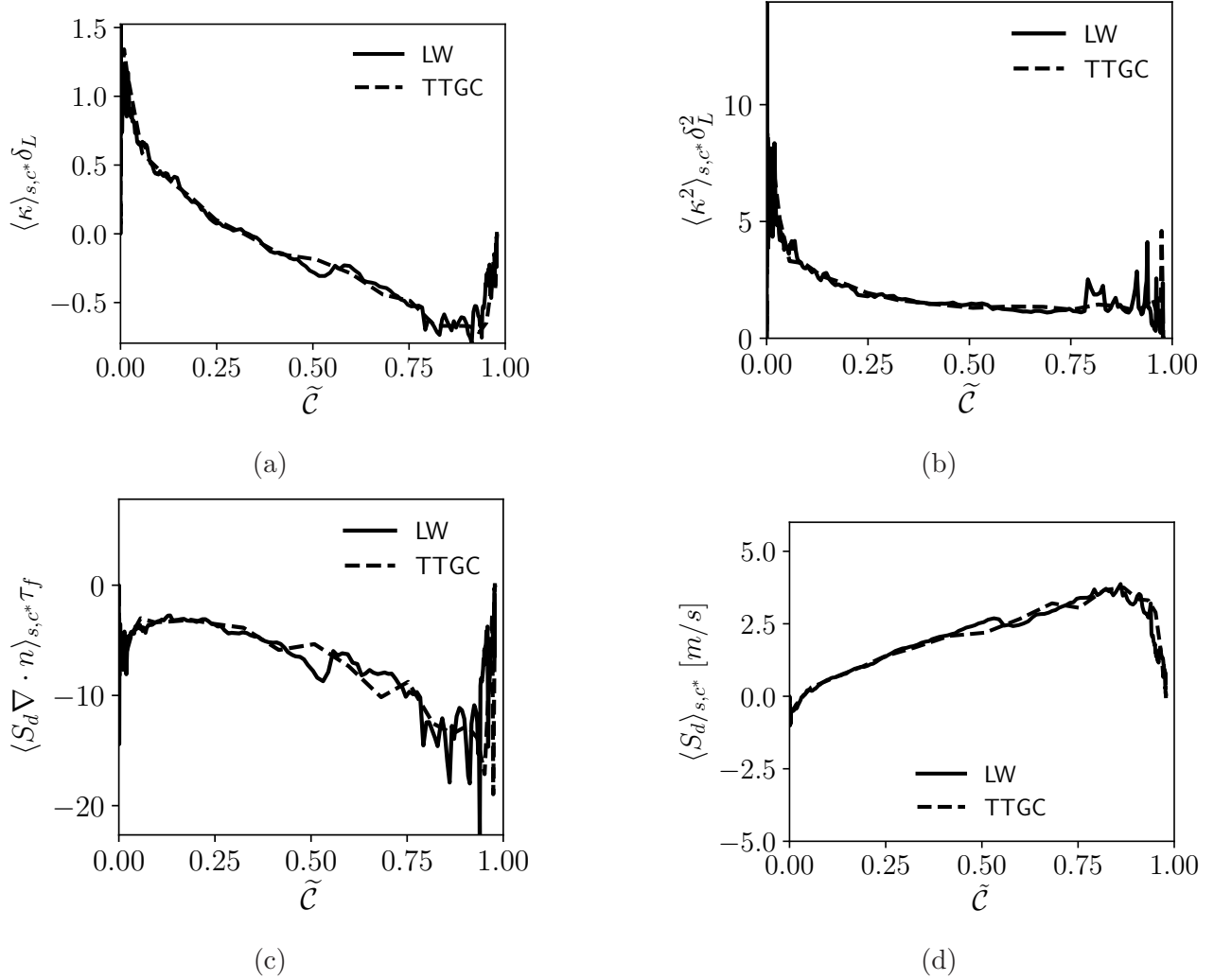


Figure A.2.4: Comparison of statistics as functions of  $\tilde{C}$  following the procedure presented in Section 4.2 from simulations using LW or TTGC scheme for: (a) curvature  $\langle \kappa \rangle_{s,c^*}$ , (b)  $\langle \kappa^2 \rangle_{s,c^*}$ , (c) stretch due to curvature  $\langle S_d \kappa \rangle_{s,c^*}$  and (d) displacement speed  $\langle S_d \rangle_{s,c^*}$ .

Figure A.2.4 compares the statistics of curvature and its variance, stretch due to curvature and displacement speed resulting from simulations using LW and TTGC schemes as functions of  $\tilde{C}$ . For each quantity, the curves of the extracted statistics resulting from the use of LW scheme are superimposed with the curves from TTGC simulation. This shows that the numerical scheme chosen has a weak impact on the statistics of the quantities of interest for *a priori* modelling.

## A.3 Conclusions

Even if the AVBP code was not developed for DNS, it has several numerical schemes of different order in space and time. In this appendix, simulations of turbulent flame with the same numerical set up, only differing from each other by the numerical scheme chosen, are conducted and compared. The comparison conducted shows that the statistics of the quantities of interest are weakly affected by the choice of the convective scheme. It also shows that the Lax-Wendrof scheme is much faster than the TTGC scheme. Thus, the former is preferred to the latter for the purpose of computational economy for all the study.



# Appendix B

## Discussion on turbulence forcing method

In the present study, the response of a statistically planar flame to a turbulent flow field has been study. As presented in Chapter 3, the simple case of homogeneous isotropic turbulence (HIT) is very dissipative, meaning that turbulent kinetic energy (TKE) decays with time. The more intense the turbulent flow field is, the faster TKE decays. This represents an issue for studying interactions between turbulence and a flame front because the flame does not have the time to adapt to turbulence therefore leading to unrealistic statistics.

To overcome this issue, different methods exist, reported in Chapter 3 and by Klein et al. (2017). Here, the use of volume forcing within the whole computational domain was chosen, in order to ensure a constant turbulent level, similarly to (Aspden et al., 2011a,b, 2015, 2016, 2017, 2019). However, even if this forcing method allows to offset the decay of TKE and maintain turbulence, this approach might lead to erroneous flame statistics because turbulence is forced in the fresh and burned gases.

In this appendix, we propose to study the impact of forcing turbulence in both the fresh and burned gases by limiting turbulence forcing to fresh gases only.

### B.1 Direct numerical simulation implementation

A spectral forcing method proposed by Eswaran and Pope (1988) is used in this study to maintain the turbulence characteristics. This method generates a stochastic time-evolving forcing vector  $\mathbf{f}$  used as a source term in the momentum conservation equation of the Navier-Stokes equations, as  $\rho\mathbf{f}$ . This stochastic forcing term introduces energy in the largest scales of the domain. A turbulent energy spectrum is established, with the largest scales cascading toward smaller scales and these being dissipated by viscosity. When the rate of energy introduced by the forcing technique equals the rate of dissipation, a statistically steady state is reached

In practice, Eswaran and Pope (1988) added a forcing acceleration in the momentum conservation equation of the Navier-Stokes equations in wavenumber space. According to them,



the dissipation rate  $\varepsilon$  can be estimated from forcing parameters as:

$$\varepsilon = \frac{4\tau_g\sigma_g^2 N_g}{1 + \tau_g (k_0^2 \varepsilon)^{1/3}}, \quad (\text{B.1.1})$$

where  $\sigma_g$  and  $\tau_g$  are a characteristic forcing acceleration and a characteristic forcing time, respectively. The latter controlled the time to reach a statistically steady state. Moreover, this method requires two other parameters: the size of the computational domain  $L$ , such that  $2\pi/L$  is the first forced wave number, and the number of forced modes  $N_g$ , which has been set to 92 from the works of Paoli and Shariff (2009).

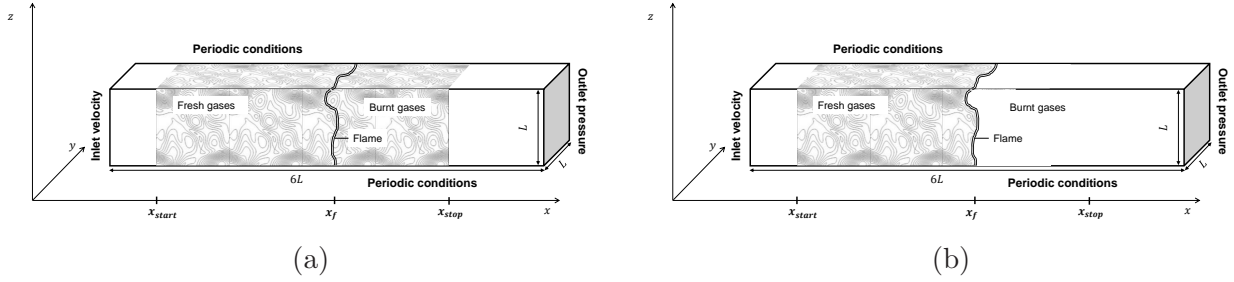


Figure B.1.1: Schematic view of the flow configuration of the DNS with: (a) turbulence forced in the whole domain and (b) turbulence forced only in the fresh gases.

With this forcing method, HIT is imposed in the volume defined in Fig. B.1.1a where the flame is contained. As already mentioned, it can be argued that the forcing term being artificial and imposed at the flame location, this approach can lead to erroneous flame statistics. Moreover, flames in engine spark-ignition (SI) engines propagate facing a turbulent flow in the fresh gases. Thus, to evaluate the impact of forcing turbulence in the fresh and burned gases and to get closer to conditions encountered in SI engines, additional simulations were performed conditioning the forcing source term with the progress variable (Eq. B.1.2), as suggested by Klein et al. (2017). In such a case the forcing is only active in the fresh gases as illustrated in Fig. B.1.1b, thus leading to the interaction of the flame with a more standard decaying turbulence.

$$\mathbf{f}_{FG} = \left(1 - \tanh\left(\frac{c}{c_{lim}}\right)\right) \mathbf{f}. \quad (\text{B.1.2})$$

Three of the four cases presented in Chapter 3 are used to investigate the effects of turbulence forcing in the whole domain (Fig. B.1.1). Cases A, C and D were selected to evaluate these effects in the flamelet and the thin reaction (TRZ) regime. These cases are performed with differential diffusion ( $Le_k \neq 1$ ) and the 2-step chemistry presented in Chapter 3. Cases A<sub>FG</sub>, C<sub>FG</sub> and D<sub>FG</sub> are performed with the same turbulence forcing parameters as A, C and D, but by forcing the turbulence only in the fresh gases.

All these cases are displayed in the Peters-Borghgi diagram in Fig. B.1.2, where plain and empty symbols represent cases with turbulence forced in the whole domain and cases with turbulence forced only in the fresh gases, respectively. Their numerical parameters are reported in Table B.1.

Table B.1: The DNS set-up for the simulations of the interaction between a planar flame and forced homogeneous isotropic turbulence. The Karlovitz number  $Ka$  and the Damköhler number  $Da$  are defined with Eqs. (1.3.11) and (1.3.10), respectively. The laminar flame thickness used to evaluate these numbers is the thermal laminar flame thickness  $\delta_L^0 = (T_b - T_u) / \max(|\nabla T|)$ .  $N_{cell}$  is the number of cells in the mesh used for simulating the flames.

Case	$l_t/\delta_L$	$u'/S_L^0$	$Ka$	$Da$	$Re_t$	$\delta_L^0/\Delta_x$	$\eta_k/\Delta_x$	$N_{cell}$
A	3.3	3.0	2.9	9.9	89.6	20	1.7	$83e^6$
C	4.3	12.5	21.4	3.1	489.0	20	0.6	$83e^6$
D	4.4	21.1	46.2	1.9	833.2	31	0.7	$254e^6$
A <sub>FG</sub>	3.5	3.4	3.4	9.1	106.6	20	1.6	$83e^6$
C <sub>FG</sub>	4.1	11.7	19.8	3.1	427.0	20	0.7	$83e^6$
D <sub>FG</sub>	4.2	22.7	52.6	1.7	858.2	31	0.6	$254e^6$

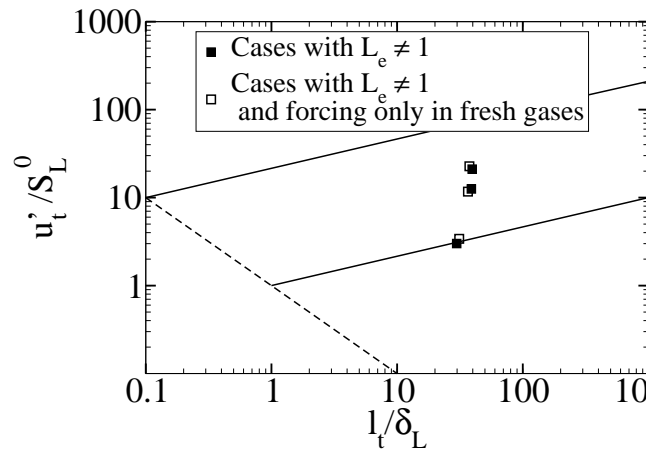


Figure B.1.2: Direct Numerical Simulations of High Karlovitz turbulent premixed flame.

## B.2 Flame surface analysis

In this section, the same analysis conducted in Chapter 3 is presented by comparing systematically cases A<sub>FG</sub>, C<sub>FG</sub> and D<sub>FG</sub> to cases A, C and D, respectively. The progress variable is defined as the reduced temperature, Eq. (1.1.12a).

### B.2.1 Analysis of the temporal evolution of flame surfaces

Figure B.2.1 shows the temporal evolution of the flame surface defined as  $\mathcal{A}_T(t) = \int_{\mathcal{V}} |\nabla c|(t) dV$ , with  $\mathcal{V}$  the whole domain. As expected, each case shows a transitory phase followed by a quasi steady-state with  $\mathcal{A}_T(t)$  oscillating around an average value. Note that the flame surface magnitudes are smaller when turbulence is only forced in the fresh gases, especially at high Karlovitz numbers. To verify that the flames are stationary, the temporal averaged rate of change of the flame surface  $(1/\mathcal{A}_T)d\mathcal{A}_T/dt$  was verified to be close to zero.

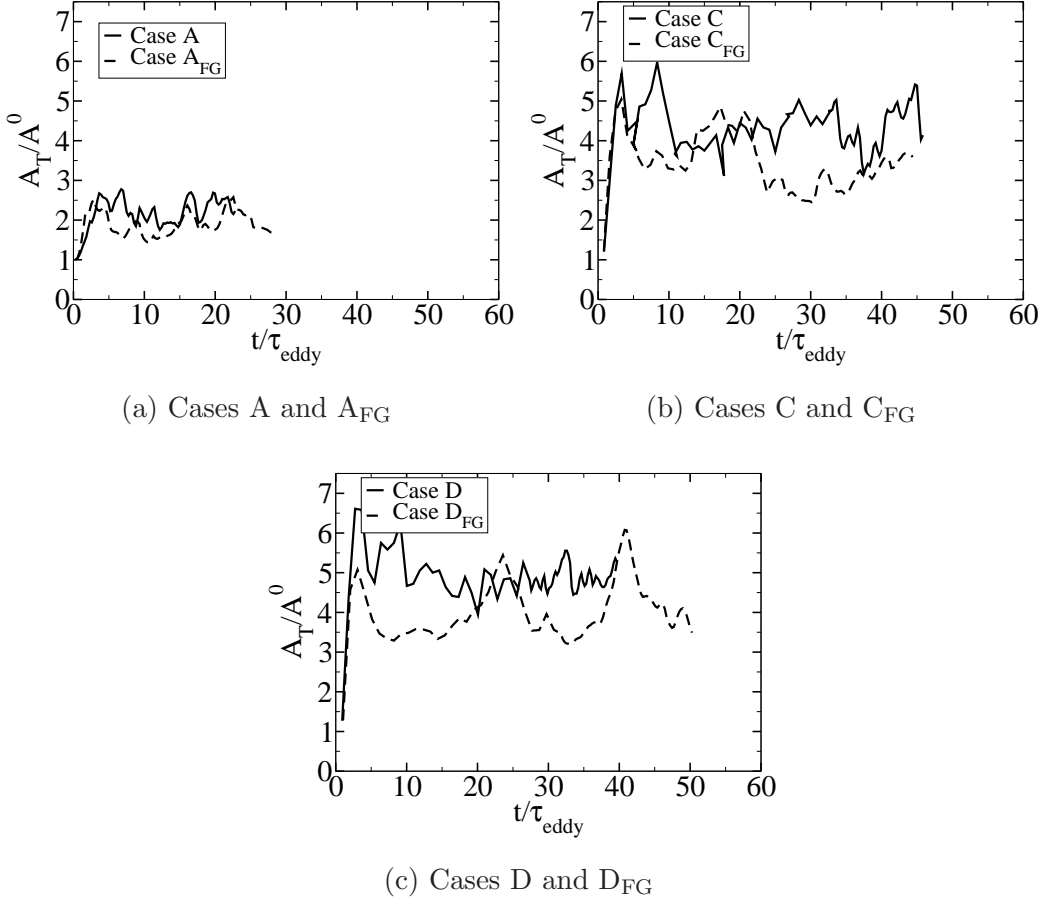


Figure B.2.1: Temporal evolution of the turbulent flame surface  $\mathcal{A}_T$  normalized with the laminar flame surface  $\mathcal{A}_0$  (a) for cases A and A<sub>FG</sub>, (b) for cases C and C<sub>FG</sub> and (c) for cases D and D<sub>FG</sub>.

## B.2.2 Analysis of the turbulent flame velocity and wrinkling

The effect of turbulence forcing is then investigated through the propagation speed  $S_T$  defined as:

$$S_T = \frac{1}{\rho_u \mathcal{A}_0} \int_V \dot{\omega}_c dV, \quad (\text{B.2.1})$$

where  $\dot{\omega}_c = \dot{\omega}'_T / (C_p(T_b - T_u))$  is the chemical source term with  $\dot{\omega}'_T$  the heat release rate,  $\rho_u$  the density of the fresh gases and  $\mathcal{A}_0$  the laminar flame surface corresponding to the y-z cross section of surface  $L^2$ . Moreover, as presented in Chapter 3, the increase of  $S_T$  is often attributed to the increase in the flame front surface  $\mathcal{A}_T$  by wrinkling. The proportionality between the increase of the propagation speed and the flame wrinkling  $\Xi = \mathcal{A}_T / \mathcal{A}_0$  is often quantified through the effect of the flame stretch using the stretch factor  $I_0$  (Eq. 3.2.3).

The evolutions of the flame wrinkling (circles) and propagation speed (triangles) are plotted as functions of  $Ka$  in Fig. B.2.2a for  $Le_k \neq 1$  cases with turbulence forced in the whole domain and only in the fresh gases in plain and empty symbols, respectively. Cases with turbulence forced only in the fresh gases present similar evolutions with  $Ka$  for  $\Xi$  and  $S_T/S_L^0$  as cases with turbulence forced in the whole domain in Fig. B.2.2a, but their magnitudes at high Karlovitz number are reduced by approximately 30% and 20% for cases C and D, respectively. Because

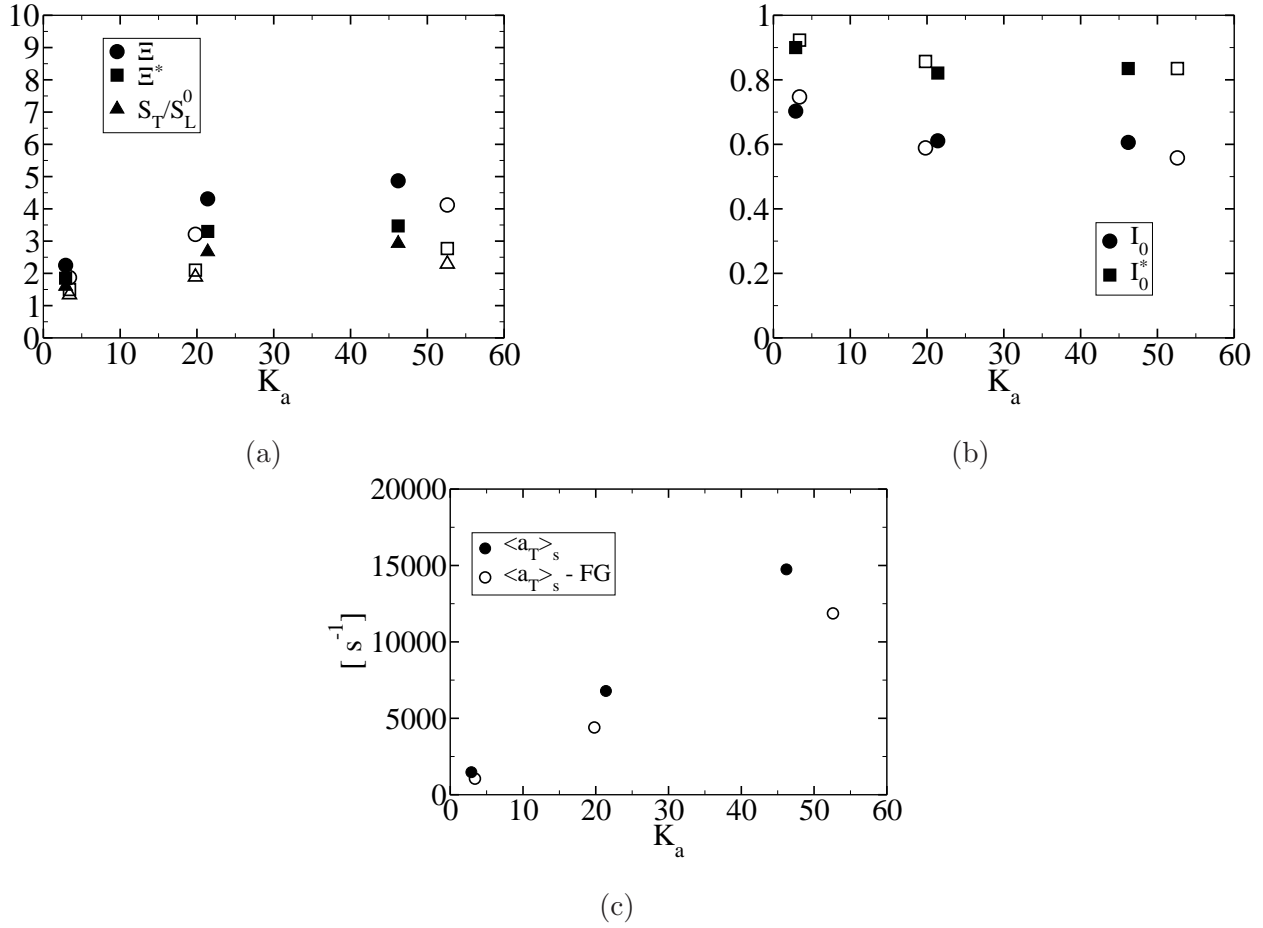


Figure B.2.2: Evolutions of (a)  $\Xi = \mathcal{A}_T/\mathcal{A}_0$ ,  $\Xi^* = \mathcal{A}_T^*/\mathcal{A}_0$  and  $S_T/S_L^0$ , (b) of the stretch factors  $I_0$  and  $I_0^*$ , and (c) of the surface averaged tangential strain rate  $\langle a_T \rangle_s$  with  $Ka$  for  $Le_k \neq 1$  cases with turbulence forced in the whole domain and only in the fresh gases with plain and empty symbols, respectively.

the stretch factors  $I_0$  are the same in Fig. B.2.2b, the difference observed for the wrinkling and the turbulent flame speed is due to the reduced turbulent intensity in the flame front leading to a reduced tangential strain rate as seen in Fig. B.2.2c.

The evolution of the wrinkling  $\Xi^*$  on an iso-surface  $c^* = 0.8$ , corresponding to the maximum reaction rate of the laminar flame (see Fig. B.2.3), is also plotted in Fig. B.2.2a. This wrinkling is defined as:

$$\Xi^* = \frac{\mathcal{A}_T^*}{\mathcal{A}_0}, \quad (\text{B.2.2})$$

where  $\mathcal{A}_T^*$  is the area of the iso-surface  $c^* = 0.8$ . In Fig B.2.2b, the stretch factor  $I_0^* = \langle \rho S_d \rangle_s^* / (\rho_u S_L^0)$  is also displayed.

Figure B.2.2a shows that  $\Xi^*$  (squares) present similar evolution with  $Ka$  when turbulence is only forced in the fresh gases (empty symbols) than cases with turbulence forcing in the whole domain (plain symbols). However, the former present magnitudes significantly smaller than the latter, down to a reduction of approximately 35% for cases C and C<sub>FG</sub>. As mentioned in Chapter 3, the values of  $\Xi^*$  are close to those of  $S_T/S_L^0$ , which reflects the fact that  $I_0^*$  is closer to unity than  $I_0$  as shown in Fig. B.2.2b. This suggests that the modelling approach chosen in the present study is not dependent on the turbulence forcing method.

### B.2.3 Analysis of the inner flame structure

To evaluate the effect of turbulence forcing method on the inner structure of the flame, the profile of the conditional mean of the chemical source term  $\dot{\omega}_c = \dot{\omega}'_T / (C_p(T_b - T_u))$  with the progress variable is plotted for each case in Fig. B.2.3.

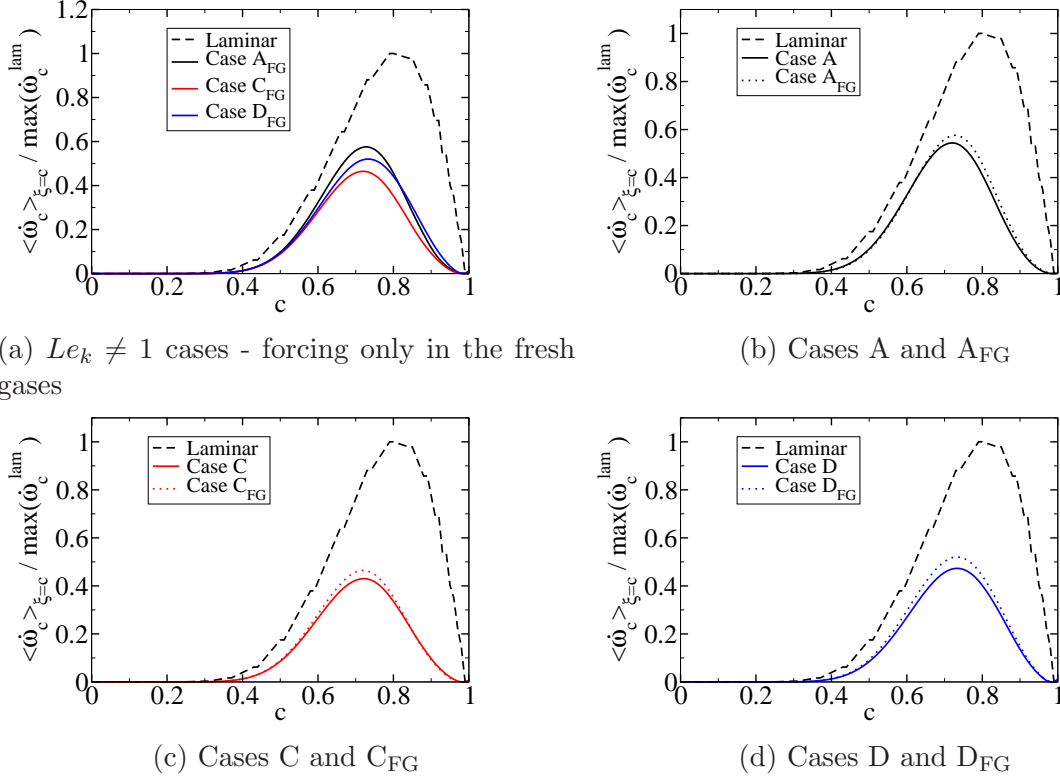


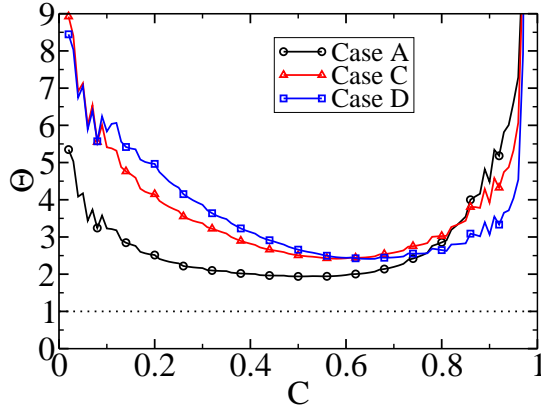
Figure B.2.3: Conditional mean of the chemical source term  $\langle \dot{\omega}_c(c) \rangle_{\xi=c}$  as a function of progress variable (a) for cases with  $Le_k = 1$  with turbulence forced only in the fresh gases. Comparisons of conditional mean of the chemical source term  $\langle \dot{\omega}_c(c) \rangle_{\xi=c}$  (b) for cases A and A<sub>FG</sub>, (c) for cases C and C<sub>FG</sub> and (d) for cases D and D<sub>FG</sub>.

Figure B.2.3 shows the conditional mean of the progress variable chemical source term  $\dot{\omega}_c$ , normalized by the peak chemical source term of the 1D laminar flame, as a function of the progress variable  $c$  for each case. As already mentioned in Chapter 3, the non-unity Lewis number cases with turbulence forced in the whole domain show a decrease of the chemical source term when  $Ka$  increases, from a maximum of 0.55 for case A (Fig. B.2.3b) down to 0.43 for case C (Fig. B.2.3c). However, when  $Ka$  increases further, the inverse tendency is observed with an increase of  $\dot{\omega}_c / \max(\dot{\omega}_c^{lam})$  up to 0.48 for case D (Fig. B.2.3d). The conditional means of the progress variable chemical source term for  $Le \neq 1$  cases with turbulence forced only in the fresh gases are plotted in Fig. B.2.3a, showing similar tendency with  $Ka$  than cases with turbulence forced in the whole domain. Indeed, from cases A<sub>FG</sub> to C<sub>FG</sub>, the maximum of  $\langle \dot{\omega}_c \rangle_{\xi=c} / \max(\dot{\omega}_c^{lam})$  decreases from 0.57 down to 0.46. When  $Ka$  increases further, the inverse tendency is observed with an increase of  $\dot{\omega}_c / \max(\dot{\omega}_c^{lam})$  up to 0.52 for case D<sub>FG</sub>. As mentioned in Chapter 3, the number of studied cases here is too low to provide a clear view on the evolution of this maximum as a function of  $Ka$ . These similar tendencies with increasing Karlovitz number confirms that the forcing turbulence does not impact the flame behaviour to turbulence.

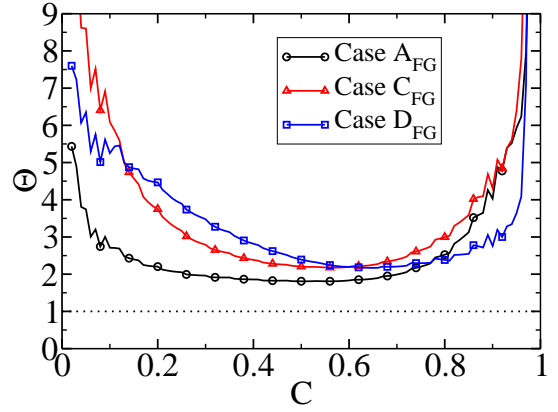
To quantify the apparent thickening of the flame, the thickening factor  $\Theta$  introduced by Aspden et al. (2019) is examined.:

$$\Theta = \frac{\langle |\nabla c|(\xi) \rangle_{\xi=c}^{ref}}{\langle |\nabla c|(\xi) \rangle_{\xi=c}}. \quad (\text{B.2.3})$$

$\langle |\nabla c|(\xi) \rangle_{\xi=c}$  is the mean value of the progress variable gradient conditioned on the progress variable value  $\xi$ . In this study the normalization is made using the gradient of the laminar flame.



(a)  $Le_k \neq 1$  cases - forcing in the whole domain



(b)  $Le_k \neq 1$  cases - forcing only in the fresh gases

Figure B.2.4: Thickening factor  $\Theta(c)$  (a) for cases with  $Le_k \neq 1$  with turbulence forcing in the whole domain and (b) for cases with  $Le_k \neq 1$  with turbulence forced only in the fresh gases.

In Fig. B.2.4, the evolution of  $\Theta$  with the progress variable is shown for non-unity Lewis number cases with turbulence forced in the whole domain. The same quantity is shown for non-unity Lewis number simulations with turbulence forced only in the fresh gases in Fig. B.2.4a. For both turbulence forcing methods, the resulting thickening factors are quite similar characterized by a thickening on the fresh ( $c < 0.3$ ) and burned ( $c > 0.7$ ) gases getting larger with an increase of the Karlovitz number. In the reaction zone ( $0.5 < c < 0.9$  as seen in Fig. B.2.3) the increase of the thickening compared to cases with the lowest  $Ka$  (cases A and A<sub>FG</sub>) is relatively low. These results seem to confirm that the inner structure of flames is weakly affected by the turbulent forcing method used in the simulations.

### B.3 Analysis of the displacement speed on an iso-surface

Because the modelling approach chosen in this study is based on the analysis of the behaviour of an iso-surface of progress variable at  $c = 0.8$ , this section is dedicated to the comparison of the displacement speed from cases with turbulence forced in the whole domain or only in the fresh gases.

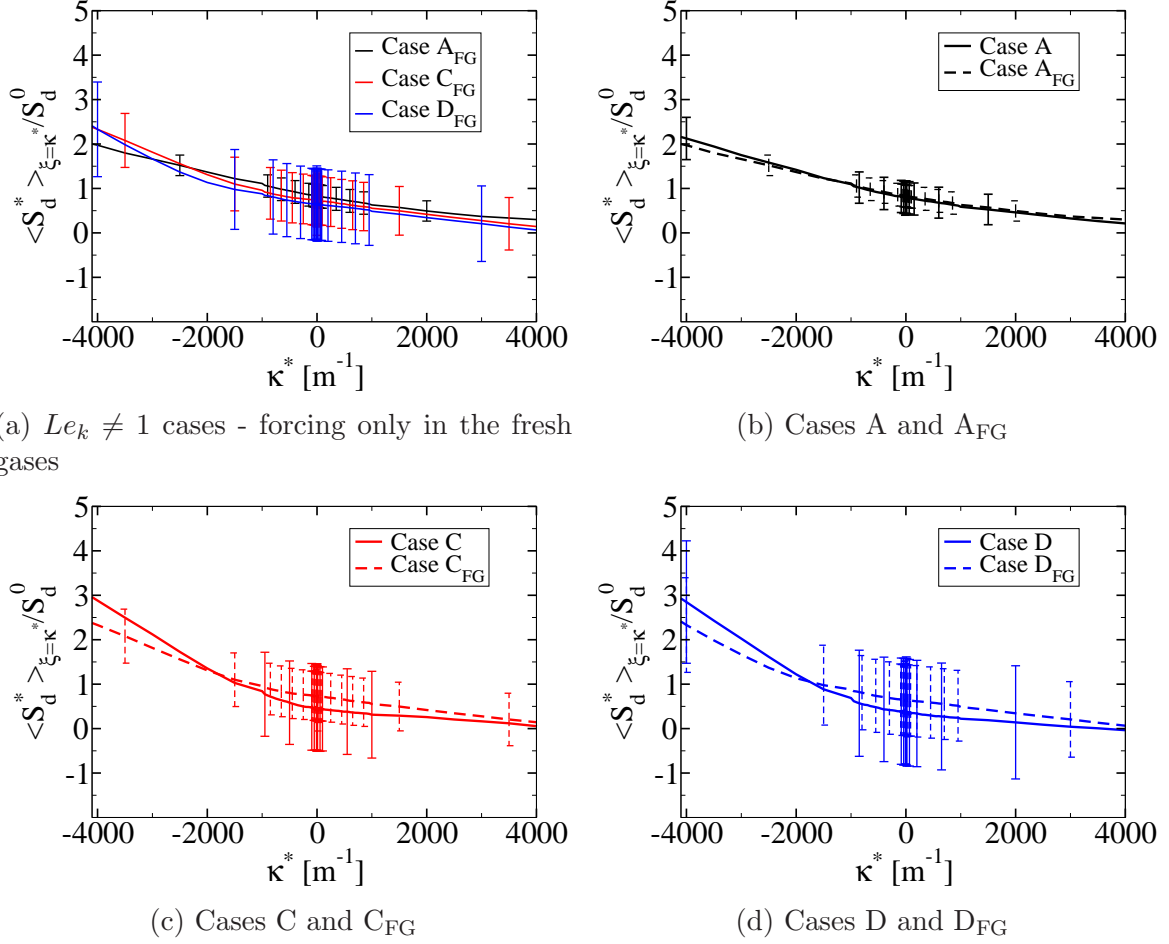


Figure B.3.1: Evolution of the conditional mean of displacement speed  $\langle S_d^*(\xi) \rangle_{\xi=\kappa^*}$ , normalized with the laminar flame speed at  $c = c^*$ ,  $S_d^0$ , with curvature  $\kappa^*$  (a) for  $Le_k \neq 1$  cases with turbulence forced only in the fresh gases. Comparisons of: (b) cases A and A<sub>FG</sub>, (c) cases C and C<sub>FG</sub>, and (d) cases D and D<sub>FG</sub>. The error bars represent the standard deviation.

### B.3.1 Analysis of conditional means with curvature

Figure B.3.1 presents the mean displacement speed  $\langle S_d^*(\xi) \rangle_{\xi=\kappa^*}$  conditioned on  $\kappa^*$ , the flame curvature. The displacement speed is normalized with  $S_d^0 = \rho_u S_L^0 / \rho^*$ , the displacement speed of the planar laminar flame at  $c = c^*$ . The standard deviation is also reported by error bars. As observed in Chapter 3, figure B.3.1a shows a negative correlation between displacement speed and curvature. Figures B.3.1b to B.3.1d compare the mean displacement speed resulting from simulations forcing turbulence in the whole domain and only in the fresh gases for each case. Cases A and A<sub>FG</sub> show very similar profiles with similar standard deviation. Similarly, cases at high Karlovitz numbers (Figs.B.3.1c and B.3.1d) show mean displacement speed weakly affected by the turbulence forcing method. However, for large Karlovitz numbers the standard deviations are slightly smaller when the turbulence is forced only in the fresh gases.

In Chapter 3, the focus is made on the conditional statistics of the different components of  $S_d^*$ , as defined in Eqs. (1.6.17) to (1.6.19). The thermal diffusivity  $D_{th}^*$  being the same between simulations with turbulence forced in the whole domain and those with turbulence forced only in the fresh gases, only the sum  $\langle S_r^* + S_n^* \rangle_{\xi=\kappa^*}$  is plotted as a function of curvature in Fig. B.3.2.

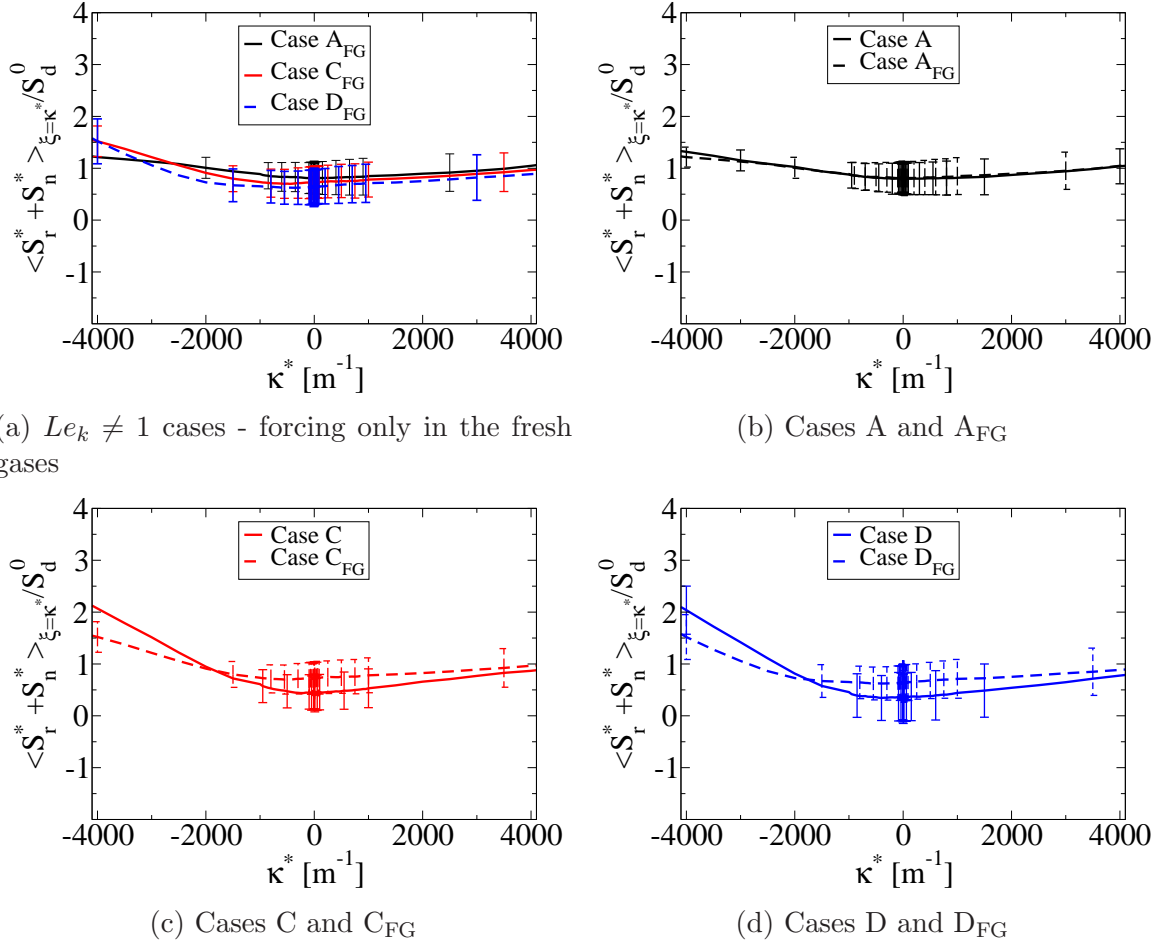


Figure B.3.2: Evolution of the conditional mean of displacement speed  $\langle S_r^* + S_n^*(\xi) \rangle_{\xi=\kappa^*}$ , normalized with the laminar flame speed at  $c = c^*$ ,  $S_d^0$ , with curvature  $\kappa^*$  (a) for  $Le_k \neq 1$  cases with turbulence forced only in the fresh gases. Comparisons of: (b) cases A and A<sub>FG</sub>, (c) cases C and C<sub>FG</sub>, and (d) cases D and D<sub>FG</sub>. The error bars represent the standard deviation.

As already observed for cases with turbulence forced in the whole domain (Chapter 3), the evolution of  $\langle S_r^* + S_n^* \rangle_{\xi=\kappa^*}$  in Fig. B.3.2a differs from  $\langle S_d^* \rangle_{\xi=\kappa^*}$  mainly for positive curvature where the correlation is positive between  $\langle S_r^* + S_n^* \rangle_{\xi=\kappa^*}$  and  $\kappa^*$ . The conclusions drawn for  $\langle S_d^* \rangle_{\xi=\kappa^*}$  are the same when  $\langle S_r^* + S_n^*(\xi) \rangle_{\xi=\kappa^*}$  resulting from the two forcing methods presented in Section B.1 are compared for each case in Figs. B.3.2b to B.3.2d.

As noticed for cases with turbulence forced in the whole domain in Chapter 3,  $\langle S_d^* \rangle_{\xi=\kappa^*} / S_d^0$  is not close to unity when  $\kappa^* = 0$ . Indeed,  $\langle S_d^* \rangle_{\xi=\kappa^*} / S_d^0$  ranges between 0.6 and 0.8. Figure B.3.3a shows that the mean tangential strain rate conditioned with curvature,  $\langle a_T^* \rangle_{\xi=\kappa^*}$ , is not zero at  $\kappa^* = 0$  as observed when turbulence is forced in the whole domain (Fig. B.3.3). Figures B.3.3b to B.3.3d compare the mean tangential strain rate resulting from the two forcing methods presented in Section B.1 for each case. These comparisons mainly show that forcing turbulence only in the fresh gases results to much smaller mean tangential strain rate with much smaller standard deviation.



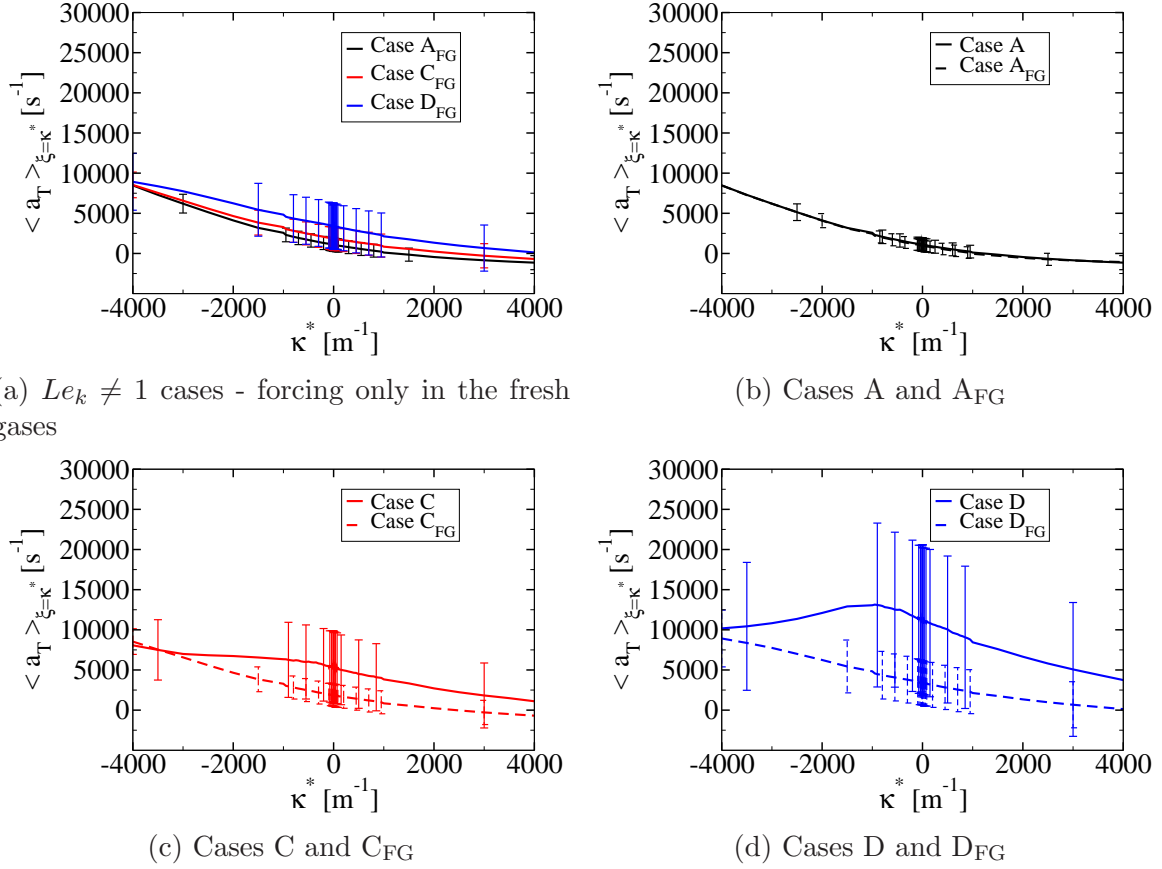


Figure B.3.3: Evolution of the conditional mean of tangential strain rate  $\langle a_T^*(\xi) \rangle_{\xi=\kappa^*}$  with curvature  $\kappa^*$  (a) for  $Le_k \neq 1$  cases with turbulence forced only in the fresh gases. Comparisons of: (b) cases A and A<sub>FG</sub>, (c) cases C and C<sub>FG</sub>, and (d) cases D and D<sub>FG</sub>. The error bars represent the standard deviation.

### B.3.2 Analysis of conditional means with strain rate and curvature

The double conditioning on both curvature and strain rate proposed in Chapter 3 is here analysed in term of impact of the turbulence forcing method. Figure B.3.4 shows this double conditioning for simulations with turbulence forced in the whole domain and only in the fresh gases. The joint probability density function (PDF) of curvature and strain rate is also plotted in this figure by black solid lines corresponding to 10% (outer line), 50% and 90% (inner line) of the maximum values of the joint PDF.

The joint PDFs displayed in Fig. B.3.4 suggest that  $a_T^*$  and  $\kappa^*$  are more correlated when the turbulence is only forced in the fresh gases. This can be quantified by evaluating Pearson's correlation coefficient (Pearson, 1895), defined in Eq. (3.3.1), and listed in Table B.2. As already

Table B.2: Pearson's correlation coefficient,  $r_{a_T^*, \kappa^*}$ , between strain rate  $a_T^*$  and curvature  $\kappa^*$  for the flames using the two forcing methods presented in Section B.1.

Case	A	C	D	A <sub>FG</sub>	C <sub>FG</sub>	D <sub>FG</sub>
$Ka$	2.9	21.4	46.2	3.4	19.8	52.6
$r_{a_T^*, \kappa^*}$	-0.65	-0.40	-0.28	-0.68	-0.60	-0.50

observed in Chapter 3, the correlation of  $a_T^*$  and  $\kappa^*$  is negative and decreases as  $Ka$  increases.

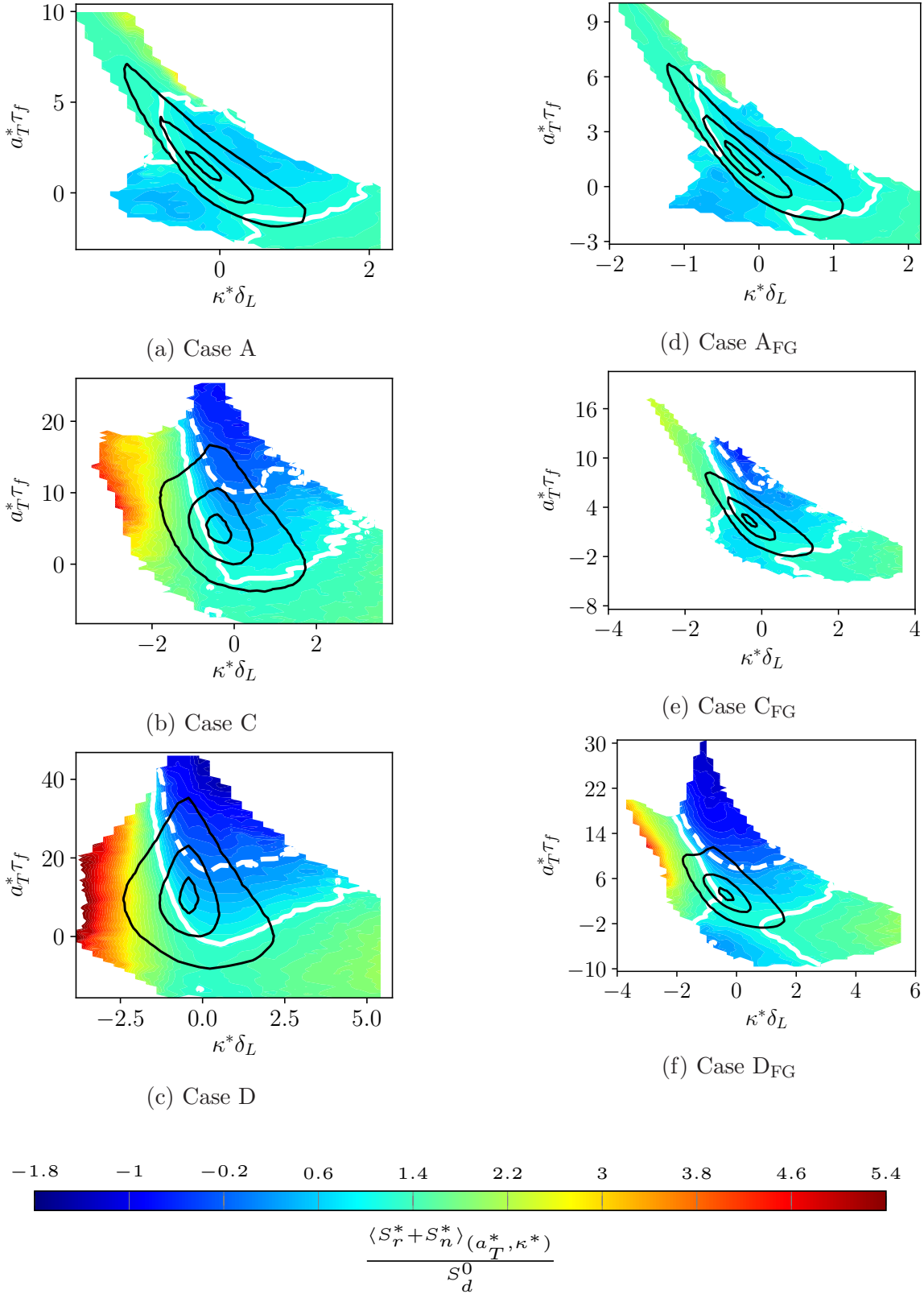


Figure B.3.4: Evolution of the conditional mean of  $\langle S_r^* + S_n^* \rangle_{(a_T^*, \kappa^*)}$  with  $a_T^*$  and  $\kappa^*$  for: (a) to (c) the cases with turbulence forced in the whole domain and (d) to (f) the cases with turbulence forced only in the fresh gases. Black lines are contours of the joint probability density function (PDF) of  $a_T^*$  and  $\kappa^*$  corresponding to 10% (outer line), 50% and 90% (inner line) of its maximum value. The solid white line is the iso-contour  $\langle S_r^* + S_n^* \rangle_{(a_T^*, \kappa^*)} = \rho_u S_L / \rho^*$  and the dashed white line is the iso-contour  $\langle S_r^* + S_n^* \rangle_{(a_T^*, \kappa^*)} = 0$ .

When the turbulence is forced only in the fresh gases, Pearson's correlation coefficients decrease compared to simulations with turbulence forced in the whole domain, showing that the correlation is stronger for cases A<sub>FG</sub> to D<sub>FG</sub>. Figures B.3.4d to B.3.4f show that the dependency of the displacement speed with strain rate and curvature of cases A<sub>FG</sub> to D<sub>FG</sub> is as complex as cases A to D. Note that the magnitudes of  $\langle S_r^* + S_n^* \rangle_{(a_T^*, \kappa^*)}$  of cases with turbulence forced only in the fresh gases are smaller than cases A to D, which confirms that the iso-surface  $c^* = 0.8$  interacts with less intense turbulence. In addition, when turbulence is forced only in the fresh gases, the evolutions of  $\langle S_r^* + S_n^* \rangle_{(a_T^*, \kappa^*)}$  seem similar to the lowest  $Ka$  cases. This observation is expected to impact the values of the effective Markstein lengths involved in Eq. (3.3.3).

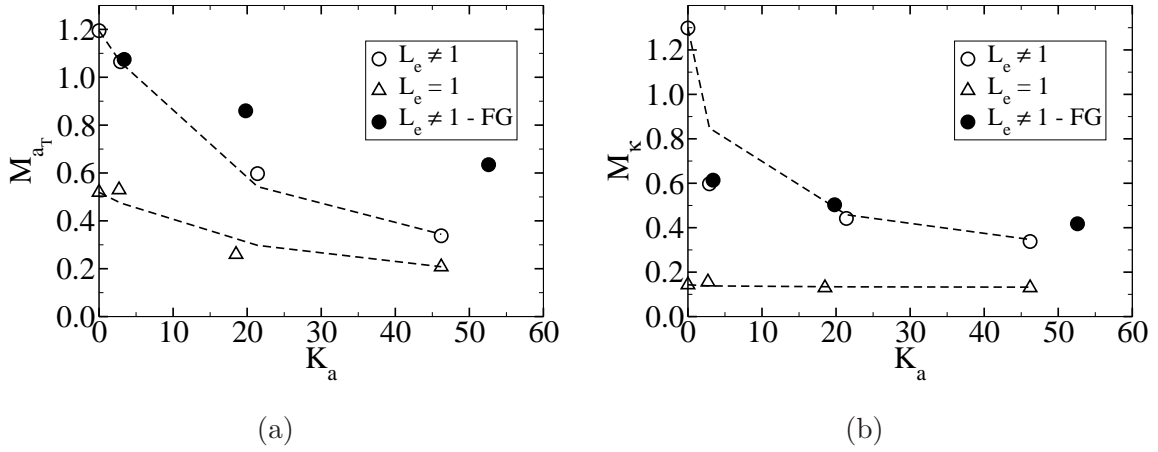


Figure B.3.5: Evolution of effective Markstein numbers with  $Ka$ : (a) for  $\mathcal{M}_{a_T} = \mathcal{L}_{a_T}/\delta_L$  and (b) for  $\mathcal{M}_\kappa = \mathcal{L}_\kappa/\delta_L$ . The values computed from stretched laminar flame and from the optimization methods are shown with dots and the dashed lines represent the models in Eqs. (3.3.5) and (3.3.6). Markstein numbers resulting from simulations with turbulence forcing in the whole domain are represented in empty symbols, while plain symbols are used for cases with turbulence forced only in the fresh gases.

The evolutions of  $\mathcal{M}_{a_T} = \mathcal{L}_{a_T}/\delta_L$  and  $\mathcal{M}_\kappa = \mathcal{L}_\kappa/\delta_L$  with turbulent intensity are plotted in Fig. B.3.5 for all cases. Markstein numbers resulting from simulations with turbulence forced in the whole domain are displayed in empty symbols, while plain symbols are used for simulations with turbulence forced only in the fresh gases. Figure B.3.5a shows that  $\mathcal{M}_{a_T}$  at low Karlovitz number is weakly affected by the forcing method, while at higher  $Ka$  Markstein numbers  $\mathcal{M}_{a_T}$  are much larger when turbulence is forced only in the fresh gases than in the whole domain. Indeed,  $\mathcal{M}_{a_T}$  for cases C<sub>FG</sub> and D<sub>FG</sub> are 43% and 85% larger than those for cases C and D. Thus, forcing turbulence only in the fresh gases results to weaker dependency of  $\mathcal{M}_{a_T}$  on  $Ka$ , illustrated by the smoother slope in Fig. B.3.5a. On the contrary, Fig. B.3.5a shows that  $\mathcal{M}_\kappa$  is weakly affected by the turbulence forcing method. Indeed, the maximum relative error is approximately 23% for cases D and D<sub>FG</sub>. These observations question the relevance of the use of the asymptotic theories for turbulent flames. As mentioned in Chapter 6, future work should be dedicated to a further investigation of these Markstein lengths and even to different approach for modelling the displacement speed.

## B.4 Statistics for *a priori* validation

This section is dedicated to investigate the impact of the turbulence forcing method on the statistics of the quantities of interest from a Reynolds Averaged Navier-Stokes (RANS) point of view (see Section 4.2).

### B.4.1 Statistics of curvature and its variance

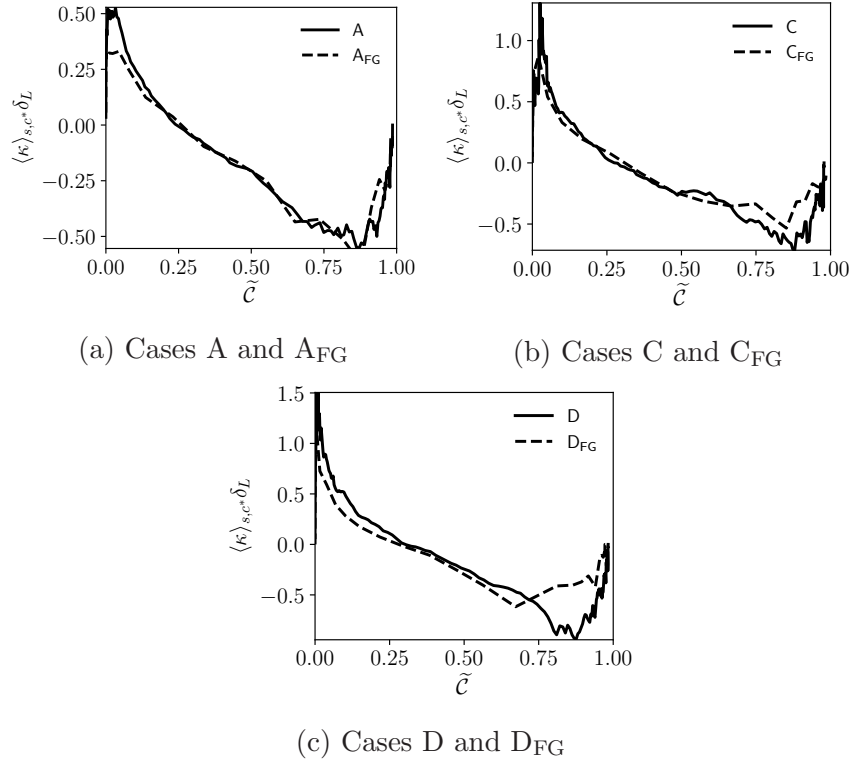


Figure B.4.1: Comparison of the profiles of curvature  $\langle \kappa \rangle_{s,c^*}$  by forcing the turbulence in the whole domain (solid lines) or in the fresh gases only (dashed lines).

Figure B.4.1 compares the curvature  $\langle \kappa \rangle_{s,c^*}$  extracted following the procedure presented in Section 4.2 resulting from simulations with turbulence forced in the whole domain and only in the fresh gases. For the lowest Karlovitz number (Fig. B.4.1a) the turbulence forcing method does not have a significant impact on the statistics of the curvature, as seen with the superimposition of the profiles of  $\langle \kappa \rangle_{s,c^*}$  of cases A and A<sub>FG</sub>. Figures B.4.1b and B.4.1c show that even for high  $Ka$  the impact of the turbulence forcing method is weak on the statistics of curvature. Note that at high Karlovitz the curvature on the burned gases side ( $\tilde{C} \geq 0.6$ ) is slightly reduced due to less intense turbulence, when turbulence is forced only in the fresh gases.

Figure B.4.2 compares the variance of curvature (through  $\langle \kappa^2 \rangle_{s,c^*}$ ) extracted following the procedure presented in Section 4.2 resulting from simulations with turbulence forced in the whole domain and only in the fresh gases. As for curvature in Fig. B.4.1a, the variance of curvature is not affected by the turbulence forcing method at low  $Ka$ , as observed in Fig. B.4.2a. However, for high Karlovitz numbers, even if the shape of curves are similar in Figs. B.4.1b

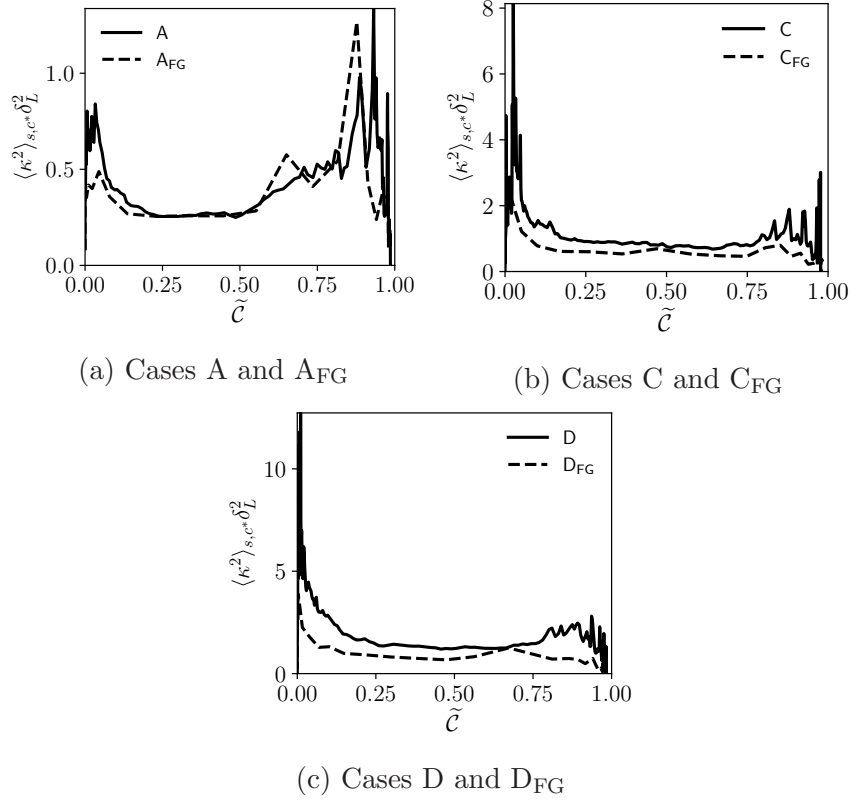


Figure B.4.2: Comparison of the profiles of  $\langle \kappa^2 \rangle_{s,c^*}$  by forcing the turbulence in the whole domain (solid lines) or in the fresh gases only (dashed lines).

and B.4.1c, the magnitudes of  $\langle \kappa^2 \rangle_{s,c^*}$  are significantly reduced when turbulence is forced only in the fresh gases, down to almost half the values encountered in cases C and D. This results from the less intense turbulence interacting with the iso-surface  $c = 0.8$  in cases C<sub>FG</sub> and D<sub>FG</sub>.

## B.4.2 Statistics of stretch due to curvature and displacement speed

Figure B.4.3 compares the stretch due to curvature ( $\langle S_d \kappa \rangle_{s,c^*}$ ) extracted following the procedure presented in Section 4.2 resulting from simulations with turbulence forced in the whole domain and only in the fresh gases. As for curvature and its variance, the stretch due to curvature is not affected by the turbulence forcing method at low  $Ka$ , as observed in Fig. B.4.3a. As  $\langle \kappa^2 \rangle_{s,c^*}$ , the stretch due to curvature is significantly affected for high Karlovitz number in Figs. B.4.3b and B.4.3c. Indeed, even if the shape of the profiles of  $\langle S_d \kappa \rangle_{s,c^*}$  are similar between cases with turbulence forced in the whole domain and only in the fresh gases, cases C<sub>FG</sub> and D<sub>FG</sub> present reduced stretch due to curvature, especially on the burned gases side, down to approximately half the values observed in cases C and D.

Figure B.4.4 compares the displacement speed ( $\langle S_d \rangle_{s,c^*}$ ) extracted following the procedure presented in Section 4.2 resulting from simulations with turbulence forced in the whole domain and only in the fresh gases. The profiles of displacement speed displayed in Fig. B.4.4 are weakly affected by the turbulence forcing method, except at high  $Ka$  for  $\tilde{c} \geq 0.6$  where  $\langle S_d \rangle_{s,c^*}$  is flattened for cases C<sub>FG</sub> and D<sub>FG</sub> compared to cases C and D.

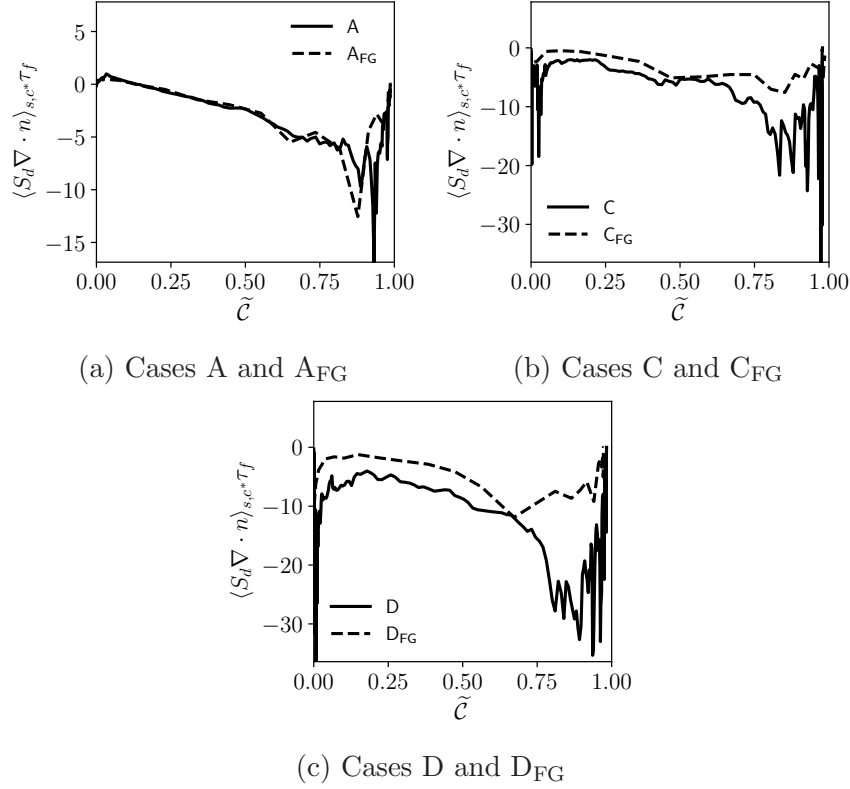


Figure B.4.3: Comparison of the profiles of the stretch due curvature  $\langle S_d \kappa \rangle_{s,c^*}$  by forcing the turbulence in the whole domain (solid lines) or in the fresh gases only (dashed lines).

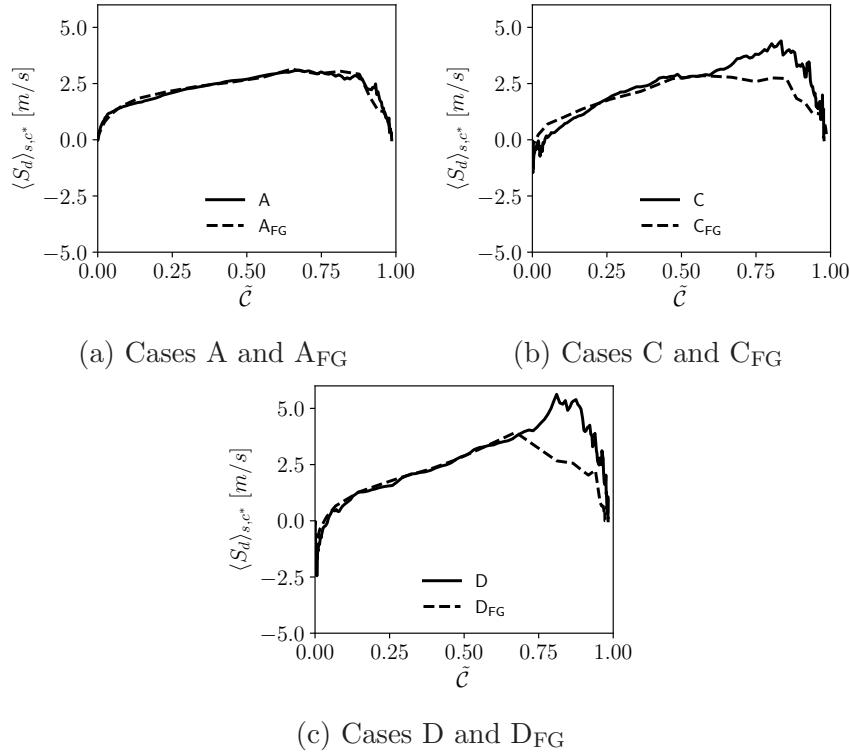


Figure B.4.4: Comparison of the profiles of the displacement speed  $\langle S_d \rangle_{s,c^*}$  by forcing the turbulence in the whole domain (solid lines) or in the fresh gases only (dashed lines).

## B.5 Conclusions

In this appendix, the turbulence forcing method has been modified to forced turbulence only in the fresh gases. Then, simulations were conducted using this modified turbulence forcing method to investigate the impact of this method on the statistics of the flame. The comparisons performed in this appendix show that the main effects of the turbulence forcing method are due to the less intense turbulence interacting with the flame. The consequence on a modelling point of view is a reduction of the magnitudes of the statistics of the quantities of interest. However, the tendencies observed remain almost unchanged, suggesting that the model proposed in this PhD thesis is still relevant.

# Appendix C

## Derivation of the fine grained flame surface density transport equation

As suggested in Chapter 3, it seems reasonable to evaluate the total chemical source term by modelling the behaviour of a specific  $c$  iso-surface. So, the modelling approach proposed is based on the definition of the progress variable  $\mathcal{C}$  and the associated flame surface density (FSD)  $\Sigma^*$  corresponding to the fine grained FSD introduced by Vervisch et al. (1995):

$$\mathcal{C} = \mathcal{H}(c - c^*), \quad (\text{C.1})$$

$$\Sigma^* = |\nabla \mathcal{C}| = |\nabla c| \delta(c - c^*), \quad (\text{C.2})$$

where  $\mathcal{H}(c)$  and  $\delta(c)$  are the Heaviside and the Dirac functions, respectively. This appendix is therefore dedicated to the derivation and filtering of transport equations for both variables.

Knudsen and Pitsch (2008) modified the balance equation of the progress variable (Eq. 1.1.13) presented in Section 1.1 using the variable defined in Eq. (C.1):

$$\frac{\partial \rho \mathcal{C}}{\partial t} + \nabla \cdot (\rho \mathbf{u} \mathcal{C}) = \rho S_d |\nabla \mathcal{C}|, \quad (\text{C.3})$$

Then, Eq. (C.3) is filtered using the large-eddy simulation (LES) filter  $G_\Delta$ :

$$\frac{\partial \bar{\rho} \tilde{\mathcal{C}}}{\partial t} + \nabla \cdot (\bar{\rho} \tilde{\mathbf{u}} \tilde{\mathcal{C}}) = - \underbrace{\nabla \cdot (\overline{\rho \mathbf{u} \mathcal{C}} - \bar{\rho} \tilde{\mathbf{u}} \tilde{\mathcal{C}})}_{T_1} + \underbrace{\langle \rho S_d \rangle_{s, c^*} \bar{\Sigma}^*}_{T_2}, \quad (\text{C.4})$$

where  $T_1$  is the unresolved transport term associated with turbulent flux, and  $\langle \cdot \rangle_{s, c^*}$  is the surface averaging operation on the iso-surface  $c = c^*$  defined as:

$$\langle Q \rangle_{s, c^*} = \frac{\overline{Q |\nabla c| \delta(c - c^*)}}{\bar{\Sigma}^*} = \frac{\int_V Q |\nabla c| \delta(c - c^*) G_\Delta(\mathbf{x} - \mathbf{x}') d\mathbf{x}'}{\int_V |\nabla c| \delta(c - c^*) G_\Delta(\mathbf{x} - \mathbf{x}') d\mathbf{x}'}, \quad (\text{C.5})$$

where  $Q$  is a quantity of interest.



As for the generalized approach of the coherent flame model (CFM), the surface density of the iso-surface  $c = c^*$  is evaluated through a transport equation. This equation is determined by first spatially deriving Eq. (C.3), leading to:

$$\frac{\partial}{\partial t} \left( \frac{\partial \mathcal{C}}{\partial x_j} \right) + u_i \frac{\partial}{\partial x_i} \left( \frac{\partial \mathcal{C}}{\partial x_j} \right) + \frac{\partial u_i}{\partial x_j} \frac{\partial \mathcal{C}}{\partial x_i} = \frac{\partial}{\partial x_j} (S_d |\nabla \mathcal{C}|), \quad (\text{C.6})$$

where subscript  $i$  and  $j$  correspond to the spatial directions. Eq. (C.7) is deduced from Eq. (C.6) by multiplying by  $\partial \mathcal{C} / \partial x_j$  and summing on the three spatial directions.

$$\frac{1}{2} \frac{\partial |\nabla \mathcal{C}|^2}{\partial t} + \frac{1}{2} u_i \frac{\partial |\nabla \mathcal{C}|^2}{\partial x_i} + \frac{\partial u_i}{\partial x_j} \frac{\partial \mathcal{C}}{\partial x_i} \frac{\partial \mathcal{C}}{\partial x_j} = \frac{\partial}{\partial x_j} (S_d |\nabla \mathcal{C}|) \frac{\partial \mathcal{C}}{\partial x_j}. \quad (\text{C.7})$$

The local normal vector of the iso-surface  $c = c^*$  pointing towards the reactants is defined as  $\mathbf{n}^* = -\nabla \mathcal{C} / |\nabla \mathcal{C}|$ . Because  $\nabla \mathcal{C} = \nabla [\mathcal{H}(c - c^*)] = (\nabla c) \delta(c - c^*)$ , we can write  $-\nabla \mathcal{C} / |\nabla \mathcal{C}| = -\nabla c / |\nabla c|$ . So, the local normal vector of the iso-surface  $c = c^*$  is equal to the local normal vector of the generalized surface.

$$\frac{\partial \mathcal{C}}{\partial x_i} = n_i |\nabla \mathcal{C}|, \quad (\text{C.8})$$

where  $n_i$  is the component along the spatial vector  $x_i$  of the normal vector  $\mathbf{n}$ .

When Eq. (C.8) is used, Eq. (C.7) becomes:

$$\frac{\partial |\nabla \mathcal{C}|}{\partial t} + u_i \frac{\partial |\nabla \mathcal{C}|}{\partial x_i} + n_i n_j |\nabla \mathcal{C}| \frac{\partial u_i}{\partial x_j} = -n_j \frac{\partial}{\partial x_j} (S_d |\nabla \mathcal{C}|). \quad (\text{C.9})$$

Reminding that  $\nabla \cdot (\mathbf{u} |\nabla \mathcal{C}|) = \mathbf{u} \cdot \nabla (|\nabla \mathcal{C}|) + |\nabla \mathcal{C}| \nabla \cdot \mathbf{u}$  and that  $\nabla \cdot (S_d \mathbf{n} |\nabla \mathcal{C}|) = \mathbf{n} \cdot \nabla (S_d |\nabla \mathcal{C}|) + S_d |\nabla \mathcal{C}| \nabla \cdot \mathbf{n}$ , Eq. (C.9) is written as follows:

$$\frac{\partial |\nabla \mathcal{C}|}{\partial t} + \nabla \cdot (\mathbf{u} |\nabla \mathcal{C}|) = (\nabla \cdot \mathbf{u} - \mathbf{n} \mathbf{n} : \nabla \mathbf{u}) |\nabla \mathcal{C}| + S_d \nabla \cdot \mathbf{n} |\nabla \mathcal{C}| - \nabla \cdot (S_d \mathbf{n} |\nabla \mathcal{C}|). \quad (\text{C.10})$$

Finally, the exact transport equation of FSD of iso-surface  $c = c^*$  given in Eq. (C.10) is filtered using the LES filter  $G_\Delta$ :

$$\begin{aligned} \frac{\partial \overline{\Sigma^*}}{\partial t} + \nabla \cdot (\tilde{\mathbf{u}} \overline{\Sigma^*}) = & - \underbrace{\nabla \cdot (\overline{\mathbf{u} \Sigma^*} - \tilde{\mathbf{u}} \overline{\Sigma^*})}_T + \underbrace{\langle \nabla \cdot \mathbf{u} - \mathbf{n} \mathbf{n} : \nabla \mathbf{u} \rangle_{s, c^*}}_S \overline{\Sigma^*} + \underbrace{\langle S_d \kappa \rangle_{s, c^*}}_C \overline{\Sigma^*} \\ & - \underbrace{\nabla \cdot (\langle S_d \mathbf{n} \rangle_{s, c^*} \overline{\Sigma^*})}_P, \end{aligned} \quad (\text{C.11})$$

where  $T$  is the unresolved transport term associated with turbulent flux,  $\langle a_T \rangle_{s, c^*} = \langle \nabla \cdot \mathbf{u} - \mathbf{n} \mathbf{n} : \nabla \mathbf{u} \rangle_{s, c^*}$  is the surface averaged tangential strain rate,  $\langle S_d \kappa \rangle_{s, c^*}$  is the surface averaged stretch due to curvature, where  $\kappa = \nabla \cdot \mathbf{n}$  is the curvature, and  $P$  is the normal propagation term.

# Appendix D

## Laminar stretched flames

In Chapter 3, Markstein lengths are introduced. These lengths are used to study the speeds of stretched flames following asymptotic theories, like the one proposed by Pelce and Clavin (1982). These studies suggest, that in the limit of small strain and curvature terms, stretch  $K$  is the unique parameter controlling the flame structure and therefore the displacement speed through a linear relationship:

$$\frac{S_d(c=0)}{S_L^0} = 1 - \frac{\mathcal{L}}{S_L^0} K, \quad (\text{D.1})$$

where  $\mathcal{L}$  is the Markstein length associated to the displacement speed on the fresh gases side. However, in Chapter 3, it is proposed to isolate strain and curvature effects leading to define two distinct Markstein lengths  $\mathcal{L}_{a_T}$  and  $\mathcal{L}_\kappa$ , as already proposed by Thiesset et al. (2017). These lengths lead to express the displacement as follows, by combining asymptotic theories and the displacement speed decomposition  $S_d = S_r + S_n - D\kappa$ :

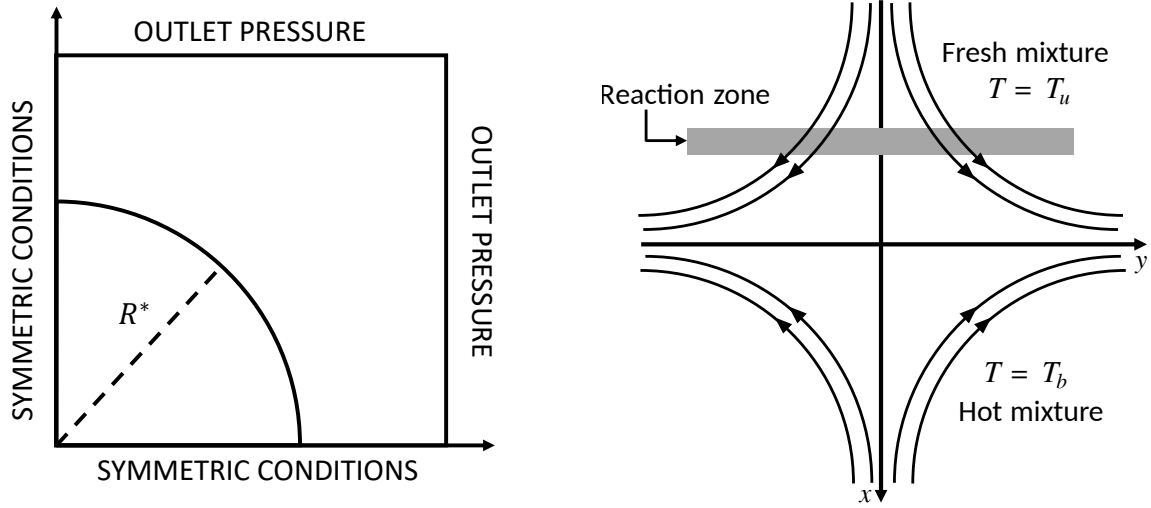
$$\frac{S_d}{S_L^0} = 1 - \frac{\mathcal{L}_{a_T}}{S_L^0} a_T - \frac{\mathcal{L}_\kappa}{S_L^0} S_d \kappa - D\kappa, \quad (\text{D.2})$$

where  $D$  is either species or thermal diffusivities. The main difficulty that appears in Eq. (D.2) is to simulate flames where  $a_T = 0$  and  $S_d \kappa \neq 0$  (and  $a_T \neq 0$  and  $S_d \kappa = 0$ ) to evaluate  $\mathcal{L}_\kappa$  (and  $\mathcal{L}_{a_T}$ ). In this study, we are interested in the displacement speed  $S_d^*$  on the iso-surface  $c = c^*$ , therefore the Markstein lengths should be evaluated at  $c = c^*$ .

Several techniques reported by Poinso and Veynante (2012) have been used to estimate a Markstein length. Two configurations allowing to isolate strain and curvature effects were chosen: a spherical laminar premixed flame for the effect of curvature (Fig. D.1a) and a counter-flow laminar premixed flame for the tangential strain rate (Fig. D.1b).

### D.1 Spherical laminar premixed flame

Using the AVBP-code, one 8<sup>th</sup> of a freely propagating spherical iso-octane/air premixed laminar flame is simulated (see Fig. D.1a). Two flames are compared, one with  $Le_k \neq 1$  for each species



(a) The spherical laminar stretched premixed flame (b) The stagnation point flame using a single counterflow flame

Figure D.1: Schematic view of laminar stretched flames.

and one with unity Lewis numbers. With this configuration, the flame stretch is computed as follows:

$$K^* = \frac{1}{\mathcal{A}^*} \frac{d\mathcal{A}^*}{dt} = \frac{2}{R^*} \frac{dR^*}{dt}, \quad (\text{D.1})$$

where  $\mathcal{A}^*$  is the area of the iso-surface  $c = c^*$ ,  $R^*$  is the radius of the spherical flame taken at  $c = c^*$ .

The displacement flame speed at  $c = c^*$  is computed as  $S_d^* = dR^*/dt$  and the curvature at  $c = c^*$  is  $\kappa^* = 2/R^*$ . Thus, the flame stretch is only due to curvature and equals  $S_d^*\kappa^*$  allowing to evaluate  $\mathcal{L}_\kappa$ .

The sum  $S_r^* + S_n^*$  at  $c = c^*$  is extracted from the spherical flame and plotted as a function of  $K^* = S_d^*\kappa^*$  in Fig. D.1. The dashed line in Fig. D.1, represents the linear relationship:  $S_r^* + S_n^* = S_d^0 - \mathcal{L}_\kappa K^*$ . The latter is fitted using a least-square method to best reproduce the evolution of  $S_r^* + S_n^*$  for low stretch. The arrows displayed in Fig. D.1 represent the temporal

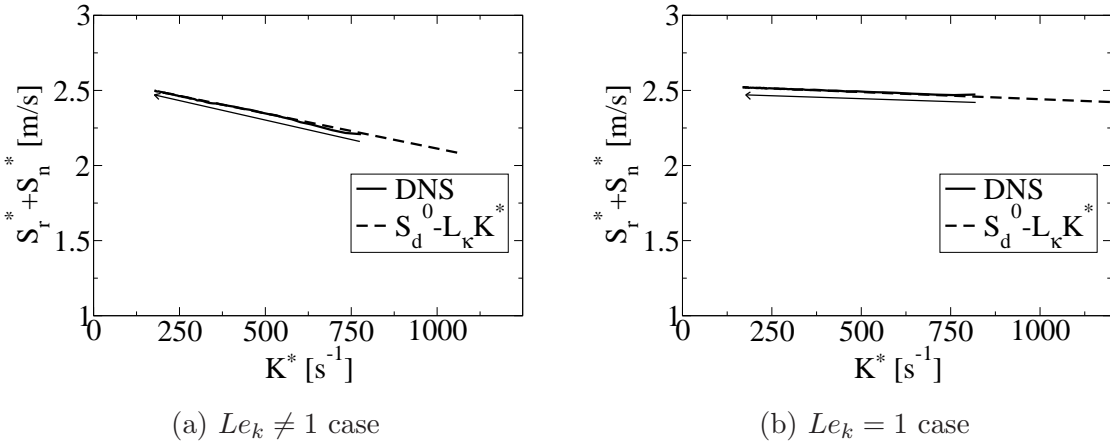


Figure D.1: Evolution of the sum  $S_r^* + S_n^*$  as a function of stretch  $K^*$  for spherical premixed flames for (a) non-unity Lewis numbers case and (b) unity Lewis numbers case.

evolution. Note that large curvatures correspond to the initial instants of the simulations. So, these values are not representative of the asymptotic theories explaining the slight discrepancies observed.

## D.2 Counter-flow laminar premixed flame

Using the open-source solver Cantera, a counter-flow iso-octane/air premixed flame is computed as described by Darabiha et al. (1986) and illustrated in Fig. D.1b. As for the spherical flames, both  $Le_k \neq 1$  and  $Le_k = 1$  flames are simulated. The flame stretch in this configuration is only due to tangential strain, *i.e.*,  $K = a_T$ . The stretch is computed as follows (Van Oijen, 2002):

$$K = \frac{1}{\rho} \frac{d\rho u}{dx}. \quad (\text{D.1})$$

$S_r^* + S_n^*$  at  $c = c^*$  is extracted and plotted as a function of  $K^*$  in Fig. D.1. The dashed line in Fig. D.1, represents the linear relationship:  $S_r^* + S_n^* = S_d^0 - \mathcal{L}_{a_T} K^*$ . The latter is fitted with a least square method to best reproduce the evolution of  $S_r^* + S_n^*$  for low stretch.

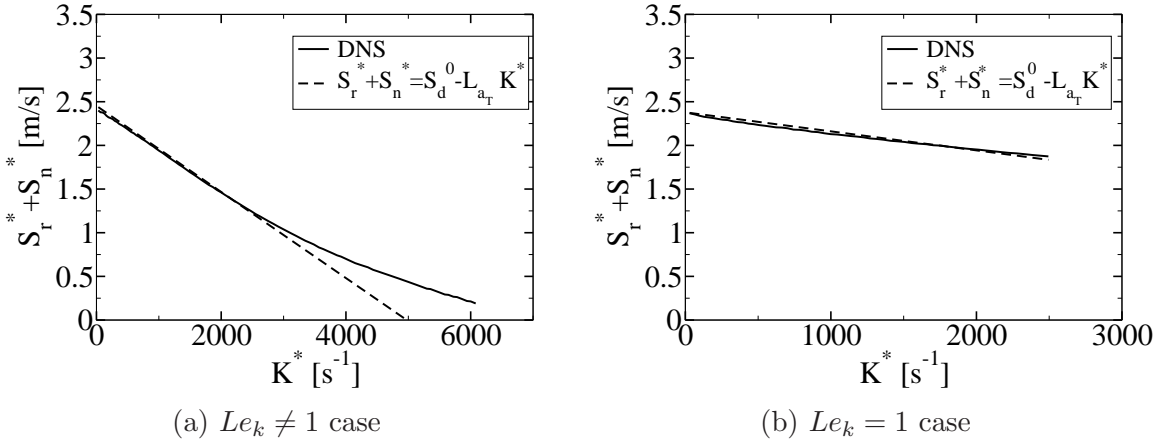


Figure D.1: Evolution of the sum  $S_r^* + S_n^*$  as a function of stretch  $K^*$  for counterflow premixed flames for (a) non-unity Lewis numbers case and (b) unity Lewis numbers case.



# Appendix E

## Closure of the term due to heat release in the tangential strain rate

In Chapter 4, the tangential strain rate  $\langle a_T \rangle_{s,c^*}$  is decomposed, following the work of Hawkes and Cant (2000), as:

$$\langle a_T \rangle_{s,c^*} = \underbrace{\nabla \cdot \tilde{\mathbf{u}} - \langle \mathbf{nn} \rangle_{s,c^*} : \nabla \tilde{\mathbf{u}}}_{\langle A_T \rangle_{s,c^*}} + \langle a_T \rangle_{s,c^*}^{sgs} + S_{hr}, \quad (\text{E.1})$$

where  $\langle A_T \rangle_{s,c^*}$  is the tangential strain rate due to the resolved flow motions,  $\langle a_T \rangle_{s,c^*}^{sgs}$  is the tangential strain rate due to unresolved flow motions and  $S_{hr}$  is a term that accounts for the effects of heat release. The latter is then combined with the stretch due to curvature caused by the resolved flow motions  $\langle S_d \kappa \rangle_{s,c^*}^{res}$ . The present appendix is therefore dedicated to derive an expression for the term  $S_{hr}$  involved in Eq. (E.1).

To derive the surface averaged tangential strain rate  $\langle a_T \rangle_{s,c^*} = \langle \nabla \cdot \mathbf{u} - \mathbf{nn} : \nabla \mathbf{u} \rangle_{s,c^*}$ , the velocity field is decomposed into a surface averaged component  $\langle \mathbf{u} \rangle_{s,c^*}$  and associated fluctuations  $\mathbf{v}''$ :

$$\mathbf{u} = \langle \mathbf{u} \rangle_{s,c^*} + \mathbf{v}''. \quad (\text{E.2})$$

In this equation the surface averaged component is decomposed as presented in Section 4.4.1:

$$\langle \mathbf{u} \rangle_{s,c^*} = \tilde{\mathbf{u}} + \langle \mathbf{u}'' \rangle_{s,c^*}, \quad (\text{E.3})$$

where  $\langle \mathbf{u}'' \rangle_{s,c^*}$  is a term due to thermal expansion expressed as presented in Section 4.4.1:

$$\langle \mathbf{u}'' \rangle_{s,c^*} = \left( \frac{\rho_u}{\bar{\rho}} - \frac{\rho_u}{\rho^*} \right) S_L^0 \langle \mathbf{n} \rangle_{s,c^*}. \quad (\text{E.4})$$

In this equation,  $\rho_u$  and  $\rho^*$  are the densities of the fresh gases and taken at  $c = c^*$ , respectively,  $\bar{\rho}$  is the filtered gas density,  $S_L^0$  is the laminar flame speed and  $\langle \mathbf{n} \rangle_{s,c^*} = -\nabla \bar{C} / \bar{\Sigma}^*$  is the surface averaged normal vector to the iso-surface  $c = c^*$  pointing toward the fresh gases.

Thus, combining Eqs. (E.2), (E.3) and (E.4) in the definition of the tangential strain rate

leads to:

$$\begin{aligned}
\langle a_T \rangle_{s,c^*} = & \underbrace{\langle \nabla \cdot \tilde{\mathbf{u}} \rangle_{s,c^*} - \langle \mathbf{nn} : \nabla \tilde{\mathbf{u}} \rangle_{s,c^*}}_{\langle A_T \rangle_{s,c^*}} + \underbrace{\langle \nabla \cdot \mathbf{v}'' \rangle_{s,c^*} - \langle \mathbf{nn} : \nabla \mathbf{v}'' \rangle_{s,c^*}}_{\langle a_T \rangle_{s,c^*}^{sgs}} \\
& + \underbrace{\nabla \cdot \left[ \left( \frac{\rho_u}{\bar{\rho}} - \frac{\rho_u}{\rho^*} \right) S_L^0 \langle \mathbf{n} \rangle_{s,c^*} \right] - \left\langle \mathbf{nn} : \nabla \left[ \left( \frac{\rho_u}{\bar{\rho}} - \frac{\rho_u}{\rho^*} \right) S_L^0 \langle \mathbf{n} \rangle_{s,c^*} \right] \right\rangle_{s,c^*}}_{S_{hr}}. \tag{E.5}
\end{aligned}$$

In this equation, the expression of  $S_{hr}$  should be simplified. In the simple case of a laminar flame, the surface averaged normal vector equals the unit normal vector:  $\langle \mathbf{n} \rangle_{s,c^*} = \bar{\mathbf{n}} = \mathbf{n}$ . Therefore,  $S_{hr}$  can be expanded as follows, by introducing the notation  $U_{hr} = (\rho_u/\bar{\rho} - \rho_u/\rho^*)S_L^0$ :

$$\nabla \cdot (U_{hr} \mathbf{n}) - \mathbf{nn} : \nabla (U_{hr} \mathbf{n}) = U_{hr} \frac{\partial n_i}{\partial x_i} + n_i \frac{\partial U_{hr}}{\partial x_i} - n_i n_j \left[ U_{hr} \frac{\partial n_i}{\partial x_j} + n_i \frac{\partial U_{hr}}{\partial x_j} \right] \tag{E.6}$$

$$= U_{hr} \frac{\partial n_i}{\partial x_i} + n_i \frac{\partial U_{hr}}{\partial x_i} - n_j U_{hr} \frac{\partial n_i^2}{\partial x_j} - n_i^2 n_j \frac{\partial U_{hr}}{\partial x_j} \tag{E.7}$$

$$= U_{hr} \frac{\partial n_i}{\partial x_i}, \tag{E.8}$$

because  $\sum n_i^2 = 1$ . This demonstration is only valid for the specific case of a laminar flame. When a turbulent flame is considered, the equality  $\langle \mathbf{n} \rangle_{s,c^*} = \mathbf{n}$  is no longer valid and some additional terms appear. However, by neglecting these additional terms a similar expression for  $S_{hr}$  as the one proposed by Hawkes and Cant (2000) is derived:

$$S_{hr} = \left( \frac{\rho_u}{\bar{\rho}} - \frac{\rho_u}{\rho^*} \right) S_L^0 \nabla \cdot \langle \mathbf{n} \rangle_{s,c^*}. \tag{E.9}$$

# Appendix F

## Synthèse en français

Ce manuscrit est consacré à la modélisation de la combustion turbulente dans le contexte des moteurs à fort taux d'EGR (Exhaust Gas Recirculation). La diminution recherchée du volume de la chambre de combustion conduit à des phénomènes de cliquetis et super-cliquetis, qui peuvent être améliorés par une dilution par EGR à hauteur de 20 à 30%. Le régime de combustion ne peut plus alors être considéré de type flammelette et est situé dans le diagramme de Borghi-Peters dans le régime TRZ (Thin Reaction Zone) caractérisé par des nombres de Karlovitz importants. Dans ce régime la flamme peut être décomposée en deux zones : une première fortement déformée et épaissie par la turbulence et une deuxième, où se situe le maximum du dégagement de chaleur, conservant des caractéristiques proches d'une flammelette.

Dans cette thèse, on s'attache à l'adaptation de l'approche FSD (Flame Surface Density) pour ce régime TRZ. Cette démarche est appuyée par des simulations numériques directes (DNS) représentatives des conditions recherchées. Les modèles existants sont évalués et des modifications sont proposées pour ce régime à haut Karlovitz. Une validation de l'approche sur une configuration monodimensionnelle est aussi menée.

Ce document, rédigé en anglais, se décompose en six chapitres. Des conclusions partielles sont présentes à la fin des chapitres et reviennent sur les points essentiels, jalonnant la progression.

Après une très courte introduction, le chapitre 1 propose une revue des modélisations existantes pour la combustion prémélangée dans les moteurs à allumage commandé. Les concepts de base de la combustion turbulente sont rappelés ainsi que le diagramme de Borghi-Peter permettant une classification des différents régimes de combustion. Les trois approches DNS, RANS et LES sont introduites. Une description des modélisations pour la combustion turbulente prémélangée (TFLES, Gequation, FSD) est menée avec l'accent sur le modèle FSD (Flame Surface Density) qui sera celui retenu dans la suite. Le chapitre s'achève sur les objectifs précis du travail :

1. adapter l'approche FSD au régime TRZ,
2. modéliser le taux de contrainte tangentielle,
3. modéliser la relation courbure/étirement



#### 4. introduire la diffusion différentielle.

Le chapitre 2 présente une première série de DNS bi-dimensionnelles. La configuration est celle d'une flamme plane d'iso-octane à la stoechiométrie en interaction avec une paire de tourbillons. La cinétique est à 2 étapes. Trente-huit simulations ont été effectuées variant les propriétés des tourbillons, la dilution et le nombre de Lewis du fuel. Le Karlovitz varie donc de 3 à 250. Ces DNS ont pour but principal de caractériser le taux de contrainte tangentielle et d'en étudier la modélisation. Trois modèles existants sont confrontés aux résultats de la DNS et un quatrième est proposé hybridant les approches de Charlette et al. (2002a) et Bougrine et al. (2014). Cette dernière version est la plus représentative des 28 cas non-dilués avec et sans diffusion différentielle (un fit des 6 paramètres du modèle est effectué pour représenter au mieux les DNS). La validation de la modélisation sur les cas dilués n'est pas abordée parce que la dilution présente peu d'influence dans le cadre d'une simulation bidimensionnelle.

Une configuration plus générale est abordée dans le chapitre suivant où une base de données de DNS de flamme plane interagissant avec une turbulence forcée est construite. Le carburant est toujours l'iso-octane et en sus de la cinétique à 2 étapes du chapitre précédent, une cinétique avec 18 espèces transportées et 13 en QSS (Quasi Steady State) est introduite. Au total, 9 cas sont traités incluant ou non la diffusion différentielle, variant les propriétés de la turbulence, un cas contient une dilution par EGR et un cas est effectué avec la chimie semi-détaillée. Comme dans le chapitre précédent, la dilution est faite avec des produits froids, ce qui ne correspond pas aux conditions réelles. Pour ces DNS, un schéma au second ordre est retenu. Une comparaison avec un schéma au troisième ordre est effectuée (Annexe A), montrant assez peu de différence entre les résultats. Les résultats de la DNS ne retrouvent pas l'évolution de la vitesse de flamme turbulente ( $S_T$ ) telle que dans des expériences de la littérature. L'influence forte du Lewis non unitaire est mise en évidence. Une formulation est proposée pour la vitesse de déplacement de l'iso-surface correspond au maximum du dégagement de chaleur dans la flamme laminaire. Deux longueurs de Markstein sont introduites correspondant respectivement au taux d'étirement et à la courbure. Une fermeture est proposée tenant compte du nombre de Karlovitz.

Le quatrième chapitre s'attache à la construction d'un modèle complet de type CFM (Coherent Flame Model) adapté aux spécificités de la combustion turbulente dans le régime TRZ. Des fermetures sont proposées et évaluées a priori sur la base de données construite au chapitre précédent, pour tous les termes. Le contexte RANS est conservé car plus simple à mettre en œuvre pour la validation a priori des fermetures. En revanche, à ce stade aucune preuve n'est apportée sur la validité de la modélisation finale dans une approche filtrée. Une nouvelle variable est introduite,  $\mathcal{C}$ , qui prend la valeur 0 pour une variable de progrès inférieure à  $c^*$  (ici choisie égale à 0.8) et la valeur 1 pour une variable de progrès supérieure à 0.8. Cette transformation permet de s'affranchir de la partie de la flamme dont la structure est altérée par la turbulence. À l'équation de transport pour  $\mathcal{C}$ , est associée l'équation de transport de la surface de flamme à  $c^*$ . Au total, 6 termes nécessitent d'être fermés par un modèle. Dans ce chapitre, sont notamment proposées des fermetures pour la vitesse de déplacement  $\langle S_d \rangle_{s,c^*}$  et l'étirement lié à la courbure  $\langle S_d \kappa \rangle_{s,c^*}$ . Ces deux fermetures reposent sur l'intégration de la

formulation proposée dans la chapitre précédent (faisant intervenir des longueurs de Markstein) sur l'ensemble des courbures possibles à travers une PDF (Probability Density Function) présumée de la distribution de  $\kappa$ .

Dans le dernier chapitre, une validation a priori est entreprise. Une série de flammes turbulentes mono dimensionnelles sont simulées correspondant aux solutions RANS de la base de données DNS. Pour ce faire, la modélisation développée dans les 2 chapitres précédents est implémentée dans AVBP. La comparaison de ces simulations 1D avec les statistiques issues de la DNS sont globalement très bonnes exceptés pour les cas à Lewis unitaire et bas Karlovitz. Même si ce point mériterait d'être parfaitement compris, la modélisation remplit son rôle pour les cas réalistes à Lewis non unitaire et les hauts Karlovitz. Une courte discussion sur l'application de cette modélisation à la LES des moteurs est menée mais sans mise en œuvre.



# List of Figures

1	Diagram of anthropogenic emissions focusing on the transport sector . . . . .	i
2	The impact of variation of exhaust gas recirculation (EGR) rate on the engine: (a) the evolution of combustion duration with EGR rate, (b) the evolution of fluctuations of indicated mean effective pressure (IMEP) with EGR rate and (c) the evolution of the exhaust gas temperature with EGR rate. (Francqueville and Michel, 2014) . . . . .	ii
3	OH-planar Laser induced fluorescence (PLIF) images at 0.5 MPa and 573K: (a) EGR rate = 0% and $u'_t/S_L^0 = 3$ , (b) EGR rate = 14% and $u'_t/S_L^0 = 3$ , and (c) EGR rate = 7% and $u'_t/S_L^0 \approx 0$ . (Kobayashi et al., 2007) . . . . .	iii
4	Evolution of laminar burning velocity (expressed in cm/s unlike displayed in the original figure), using the PREMIX code (CHEMKIN package), versus burnt mass fraction for all conditions. (Mounaïm-Rousselle et al., 2013) . . . . .	iv
5	Comparison of combustion traces in Peters-Borghgi diagram, $\blacklozenge$ 10% EGR, $\blacklozenge$ 15% EGR, $\blacklozenge$ 20% EGR, $\blacklozenge$ 25% EGR, $\blacklozenge$ 30% EGR. Cross symbols indicate the conditions at the spark timing, while diamond symbols represent the conditions as a function of fresh gas consumption. Diagram from from (Mounaïm-Rousselle et al., 2013). . . . .	v
1.2.1	Propagation of a laminar premixed flame in a duct. (Richard, 2005). . . . .	4
1.2.2	Spatial profiles of normalized temperature, normalized fuel mass fraction and the normalized reaction rate of a steady 1D laminar premixed flame. . . . .	4
1.3.1	Turbulence spectrum . . . . .	8
1.3.2	Combustion regimes using Peters-Borghgi diagram (Peters, 1999) . . . . .	10
1.3.3	Operating domain of a IFPEN's SI engine burning gasoline at different engine speeds and loads, from the work of Bougrine (2012). . . . .	11
1.4.1	Turbulence spectrum with resolution methods domain . . . . .	12
1.5.1	Flame front and $G$ field (Poinso and Veynante, 2012) . . . . .	20
1.5.2	Schematic iso-surface $c = c^*$ . A flame surface density $\bar{\Sigma}^*$ and a surface averaged reaction rate $\langle \rho S_d \rangle_s^*$ are associated with each iso-surface. The generalized flame surface density and the generalized surface averaged reaction rate $\langle \rho S_d \rangle_s$ allow to take into account all the iso-surfaces in the flame front. (Richard, 2005) . . .	22
1.6.1	Transport of preheated material from a region of thickness $\delta_L$ , the flame thick- ness, by an eddy of size $l_n$ during half a turnover time. (Peters, 1999) . . . . .	29

1.6.2	Some studies of high Karlovitz turbulent premixed flames: $\blacklozenge$ experiments by Gülder (2007) and Yuen and Gülder (2013), $\blacksquare$ experiments by Wabel et al. (2017), $\square$ DNS by Ahmed et al. (2019), $\diamond$ DNS by Aspden et al. (2011a,b, 2015, 2016, 2017, 2019), $\triangle$ DNS by Han and Huh (2009), $\triangleright$ DNS by Hawkes and Chen (2005), $\nabla$ DNS by Nivarti and Cant (2017), $*$ DNS by Poludnenko and Oran (2010, 2011), and $+$ DNS by Lapointe and Blanquart (2017; 2015) and Savard et al. (2014; 2015; 2017; 2015).	30
1.6.3	Integrated flame surface density data. Also shown are the experimentally determined turbulent burning velocities evaluated at $\bar{c} = 0.5$ (full circles) and $\bar{c} = 0.05$ (full squares). Two dotted-dashed straight lines are approximate linear fits to experimental turbulent burning velocity data. Empty circles represent the product of $J_0$ , defined in Eq. (1.6.7) and integrated flame surface density. (Gülder, 2007)	31
1.6.4	Mean flamelet velocity, $S_{T,F}$ in red symbols, compared to global consumption speed based on $\bar{c} = 0.5$ , $S_{T,1}$ in black symbols. (Wabel et al., 2017)	33
1.6.5	Measured disparity $(S_T/S_L^0)/(\mathcal{A}_T/\mathcal{A}_L)$ in the profiles of burning velocity enhancement and flame surface area enhancement as observed in experiments (Wabel et al., 2017; Yuen and Gülder, 2013) (symbols) and the enhancement factor (solid line) obtained from a numerical evaluation of $(1 + \Delta D/D)^{1/2}$ . Also shown is the leading-order term $Ka^{1/3}$ (dashed line). (Nivarti et al., 2018)	34
1.6.6	Evolution of $S_T/S_L^0$ and $\mathcal{A}_T/\mathcal{A}_L$ with the velocity ratio $u'/S_L^0$ from two DNS studies (Ahmed et al., 2019; Nivarti and Cant, 2017).	35
1.6.7	Iso-surfaces of fuel mass fraction, the values of which are 0.05 (red), 0.6 (green) and 0.95 (blue). The red and green iso-surfaces bound the flamelet reaction zone. The green and blue iso-surfaces bound the preheat zone. $z_{0,min}$ and $z_{1,max}$ mark the flame brush bounds. (Poludnenko and Oran, 2010, 2011)	35
1.6.8	Thickening factor $\Theta(c)$ as a function of the normalized temperature (a) for $\text{CH}_4$ and (b) for $\text{H}_2$ . (Aspden et al., 2019)	36
1.6.9	Joint probability density function (PDF) and conditional mean $\langle Y T \rangle$ (in black solid line) of $\text{C}_2\text{H}_4$ mass fraction vs temperature (a) from the unity Lewis number and (b) from the non-unity Lewis number. Dashed lines are flamelet solutions for non-unity Lewis number in blue and for unity Lewis number in orange. (Savard et al., 2015)	37
1.6.10	Conditional mean of fuel consumption $\langle \dot{\omega}_F T \rangle$ and heat release $\langle \dot{\omega}_T T \rangle$ corresponding to temperature of peak source term using data from (Lapointe et al., 2015). The values are normalized by the corresponding laminar flame.	38
1.6.11	Conditional means of normalized fuel consumption rate for non-unity Lewis number simulations. The fuel consumption rates are normalized by the peak value in the corresponding laminar flame. (Lapointe et al., 2015)	39

1.6.1	Stretch rate due to curvature, $S_d \nabla \cdot \mathbf{n}$ , and models versus time - normalized by the eddy turnover time of integral scale $\tau_e$ , for methane-air premixed flame: for (a) $Ka = 30$ , for (b) $Ka = 165$ and for (c) $Ka = 290$ . (Hawkes and Chen, 2005)	41
1.6.1	(a) Response of reaction related speed $V_r = S_r$ normalized with $S_L^0$ to strain. (Trisjono et al., 2016) (b) The axial evolution of the integrated generalized surface averaged curvature stretch term: $T_0 = \langle S_d \nabla \cdot \mathbf{n} \rangle$ ; $T_1 = \langle (S_r + S_n) \nabla \cdot \mathbf{n} \rangle$ ; $T_2 = -\langle D(\nabla \cdot \mathbf{n})^2 \rangle$ ; $T_3 = \langle S_d \rangle \langle \nabla \cdot \mathbf{n} \rangle$ ; $T_4 = \langle S_d \nabla \cdot \mathbf{n} \rangle - \langle S_d \rangle \langle \nabla \cdot \mathbf{n} \rangle$ . (Wang et al., 2017)	42
2.1.1	Initial geometry of the flame-vortex interaction (Candel and Poinso, 1990). A pair of counter-rotating vortices, of radius $r$ and velocity $u'_r$ , is initially located at a distance $l'$ from the flame front. The centres of the two vortices are at a distance $l$ from each other.	48
2.1.2	An example of the temporal evolution of the total heat release during a flame-vortex interaction ( $u'_r/S_L^0 = 28$ and $r_c/\delta_L^0 = 5$ ). (Meneveau and Poinso, 1991)	49
2.1.3	Diagram presenting the range of operating conditions from the works of Colin et al. (2000), Bougrine et al. (2014) and from this study with grey, blue and orange areas, respectively.	50
2.1.4	DNS configuration of flame-vortex interactions. A pair of counter-rotating vortices interacts with an initially planar premixed flame. (a) the schematic configuration of the initial solution. (b) The schematic configuration corresponding to the moment when the flame stretch is evaluated.	52
2.1.5	Evolution of the normalized enstrophy $\mathcal{E}/\mathcal{E}_{t=0}$ , with $\mathcal{E}_{t=0}$ the initial enstrophy, against time normalized with the eddy turnover time $\tau_{eddy}$ for: (a) vortices with the same velocity ratio, $u'_r/S_L^0 = 1$ and (b) vortices with the same size $r/\delta_L = 2$ .	53
2.2.1	Comparison of the efficiency functions computed from a stretch rate defined using the generalized flame surface (■) and using an iso-surface at $c^* = 0.8$ (□), for the velocity ratios: (a) $u'/S_L^0 = 1$ , (b) $u'/S_L^0 = 8.7$ and (c) $u'/S_L^0 = 17$ .	56
2.2.2	Comparison of the efficiency functions computed from a stretch defined with $(1/\mathcal{A})d\mathcal{A}/dt$ and with $(1/Q)dQ/dt$ , for the velocity ratios: (a) $u'/S_L^0 = 1$ , (b) $u'/S_L^0 = 8.7$ and (c) $u'/S_L^0 = 17$ .	57
2.2.3	The balance on the flame stretch terms normalized with the flame time $\tau_F = \delta_L/S_L^0$ , allowing evaluations of the roles of the strain rate $\langle a_T \rangle_s$ and the stretch due to curvature $\langle S_d \kappa \rangle_s$ , for the velocity ratios: (a) $u'/S_L^0 = 1$ , (b) $u'/S_L^0 = 8.7$ and (c) $u'/S_L^0 = 17$ .	58
2.2.4	Comparison of the efficiency functions computed from the stretch $K_r$ (Eq. 2.1.5) and from the tangential strain rate $\langle a_T \rangle_s$ (Eq. 2.1.14) for the velocity ratios: (a) $u'/S_L^0 = 1$ , (b) $u'/S_L^0 = 8.7$ and (c) $u'/S_L^0 = 17$ .	59
2.3.1	Comparison of the efficiency functions computed from unity Lewis numbers, non unity Lewis numbers and diluted cases for the following velocity ratios: (a) $u'/S_L^0 = 1$ , (b) $u'/S_L^0 = 8.7$ and (c) $u'/S_L^0 = 17$ .	60

2.3.2 Evolutions of the efficiency functions with $r/\delta_L$ from the DNS compared to Cant's model, Bougrine's model (Bougrine et al., 2014), Charlette's model (Charlette et al., 2002a) and the proposed model (Eq. 2.3.5) for the following velocity ratios: (a) $u'/S_L^0 = 1$ , (b) $u'/S_L^0 = 8.7$ and (c) $u'/S_L^0 = 17$ . (d) Comparisons of the efficiencies from the different velocity ratios for $Le_k \neq 1$ cases. . . . .	62
2.3.3 Comparisons between effective tangential strain rate from DNS ( $\langle a_T \rangle_s$ ) from the 28 non-diluted flames of Table 2.2 and from several $C_r$ functions following Eq. (2.1.14): (a) Cant et al. (1991), (b) Charlette et al. (2002a), (c) Bougrine et al. (2014) and (d) Present work (Eq. 2.3.5). . . . .	64
3.1.1 Schematic view of the flow configuration of the DNS with turbulence forced in a defined volume including fresh and burnt gases. The turbulence is forced between $x_{start}$ and $x_{stop}$ . The domain width is $L_y = L_z = L$ and the domain length is $L_x = 6L$ . The position of the flame front on this view is given by $x_f$ . . . . .	68
3.1.2 Comparisons of the one dimensional laminar flames spatial profiles of (a) progress variable and (b) velocity centred on $c = 0.5$ . . . . .	71
3.1.3 The temporal evolution of the turbulent kinetic energy $k$ normalized by its initial value $k_0$ for three different turbulent intensities. Two of these cases correspond to turbulent flows encountered in the TRZ regime. The time in x-axis is normalized with the characterized time of the flame $\tau_f = \delta_L^0/S_L^0$ . . . . .	72
3.1.4 Direct Numerical Simulations of High Karlovitz turbulent premixed flame. . . . .	75
3.2.1 Two-dimensional slices in x-y mid-plane of the flames coloured with the heat release rate and with contours of the progress variable (white lines), defined as the reduced temperature: (a) to (c) for unity Lewis number cases and (d) to (f) for non-unity Lewis number cases. . . . .	78
3.2.2 Temporal evolution of the turbulent flame surface $\mathcal{A}_T$ normalized with the laminar flame surface $\mathcal{A}_0$ (a) for cases with $Le_k \neq 1$ , (b) for cases with $Le_k = 1$ . . . . .	79
3.2.3 Evolutions of $\Xi = \mathcal{A}_T/\mathcal{A}_0$ , $\Xi^* = \mathcal{A}_T^*/\mathcal{A}_0$ and $S_T/S_L^0$ with $Ka$ , (a) for $Le_k \neq 1$ cases, (b) for cases with $Le_k = 1$ and (c) Evolution of the stretch factor $I_0$ . Dashed symbols are used for case C-EGR. . . . .	80
3.2.4 Conditional mean of the chemical source term $\langle \dot{\omega}_c(c) \rangle_{\xi=c}$ as a function of progress variable: (a) for cases with $Le_k = 1$ , and (b) for $Le_k \neq 1$ cases. Dotted lines are used to represent flames diluted with burned gases. . . . .	81
3.2.5 Thickening factor $\Theta(c)$ (a) for cases with $Le_k = 1$ , and (b) for $Le_k \neq 1$ cases. Dotted lines are used to represent flames diluted with burned gases. . . . .	83
3.2.6 The evolution $\Omega_{c^*}$ , $\langle \rho S_d \rangle_s^*$ and $\mathcal{A}_T^*$ normalized by $\Omega_{tot}$ , $\langle \rho S_d \rangle_s$ and $\mathcal{A}_T$ , respectively, and $I_0^*$ as functions of the progress variable for case C. . . . .	85

- 3.2.7 Evolutions of  $\langle K \rangle_s^* = (1/\mathcal{A}_T^*) (d\mathcal{A}_T^*/dt) = \langle a_T \rangle_s^* + \langle S_d \kappa \rangle_s^*$ ,  $\langle a_T \rangle_s^* = \langle \nabla \cdot \mathbf{u} - \mathbf{n} \mathbf{n} : \nabla \mathbf{u} \rangle_s^*$  and  $\langle S_d \kappa \rangle_s^* = \langle S_d \nabla \cdot \mathbf{n} \rangle_s^*$ , where  $\mathbf{n} = -\nabla c / |\nabla c|$  is the local normal vector to the flame,  $\mathbf{u}$  is the flow velocity and  $\langle \rangle_s^*$  is the surface averaging operator defined with Eq. (3.1.11): (a) for cases with  $Le_k \neq 1$  and (b) for cases with  $Le_k = 1$ . Dashed symbols are used for case C-EGR. . . . . 86
- 3.2.8 Evolutions of: (a) area of the iso-surface  $c^* = 0.8$  normalized with the laminar flame surface and (b) the stretch factor  $I_0^* = \langle \rho S_d \rangle_s^* / (\rho_u S_L^0)$ . Non-unity Lewis number cases, unity Lewis number cases and cases with turbulence forced only in the fresh gases are plotted in square, circle and cross symbols, respectively. . . 86
- 3.3.1 Evolution of the conditional mean of displacement speed  $\langle S_d^*(\xi) \rangle_{\xi=\kappa^*}$ , normalized with the laminar flame speed at  $c = c^*$ ,  $S_d^0$ , with curvature  $\kappa^*$ : (a) for cases with  $Le_k = 1$  and (b) for  $Le_k \neq 1$  cases. The error bars represent the standard deviation. . . . . 88
- 3.3.2 Evolution of the conditional mean of the components of the displacement speed, normalized with the laminar flame speed at  $c = c^*$ ,  $S_d^0$ , with curvature  $\kappa^*$ : (a)  $\langle -D_{th}^* \kappa(\xi) \rangle_{\xi=\kappa^*}$  for all the cases (b)  $\langle S_r^* + S_n^*(\xi) \rangle_{\xi=\kappa^*}$  for cases with  $Le_k \neq 1$  and (c)  $\langle S_r^* + S_n^*(\xi) \rangle_{\xi=\kappa^*}$  for cases with  $Le_k = 1$ . The error bars represent the standard deviation. . . . . 89
- 3.3.3 Evolution of the conditional mean of tangential strain rate  $\langle a_T^*(\xi) \rangle_{\xi=\kappa^*}$  with curvature  $\kappa^*$ : (a) for cases with  $Le_k \neq 1$  and (b) for cases with  $Le_k = 1$ . The error bars represent the standard deviation. . . . . 90
- 3.3.4 Evolution of the conditional mean of  $\langle S_r^* + S_n^* \rangle_{(a_T^*, \kappa^*)}$  with  $a_T^*$  and  $\kappa^*$  for: (a) to (c) the cases with  $Le_k \neq 1$  and (d) to (f) the cases with  $Le_k = 1$ . Black lines are contours of the joint probability density function (PDF) of  $a_T^*$  and  $\kappa^*$  corresponding to 10% (outer line), 50% and 90% (inner line) of its maximum value. The solid white line is the iso-contour  $\langle S_r^* + S_n^* \rangle_{(a_T^*, \kappa^*)} = \rho_u S_L / \rho^*$  and the dashed white line is the iso-contour  $\langle S_r^* + S_n^* \rangle_{(a_T^*, \kappa^*)} = 0$ . . . . . 91
- 3.3.5 Evolution of effective Markstein numbers with  $Ka$ : (a) for  $\mathcal{M}_{a_T} = \mathcal{L}_{a_T} / \delta_L^0$  and (b) for  $\mathcal{M}_\kappa = \mathcal{L}_\kappa / \delta_L^0$ . The values computed from stretched laminar flame and from the optimization methods are shown with dots and the dashed lines represent the models in Eqs. (3.3.5) and (3.3.6). . . . . 93
- 3.3.6 Evolution of  $\langle S_r^* + S_n^* \rangle_{(a_T^*, \kappa^*)}$  from DNS and predicted by Eq. (3.3.2) with  $a_T^*$  at fixed  $\kappa^*$  values for: (a) to (c) the cases with  $Le_k \neq 1$  and (d) to (f) the cases with  $Le_k = 1$ . The values of  $\kappa^*$  chosen correspond to the maxima of joint PDF. The PDF of  $a_T^*$  is shown in grey dot lines. . . . . 95
- 3.3.7 Evolution of  $\langle S_r^* + S_n^* \rangle_{(a_T^*, \kappa^*)}$  from DNS and predicted by Eq. (3.3.2) with  $\kappa^*$  at fixed  $a_T^*$  values for: (a) to (c) the cases with  $Le_k \neq 1$  and (d) to (f) the cases with  $Le_k = 1$ . The values of  $a_T^*$  chosen correspond to the maxima of joint PDF. The PDF of  $\kappa^*$  is shown in grey dot lines. . . . . 96



3.3.8 Evolution of the effective Markstein numbers with $Ka$ : (a) for $\mathcal{M}_{aT} = \mathcal{L}_{aT}/\delta_L^0$ and (b) for $\mathcal{M}_\kappa = \mathcal{L}_\kappa/\delta_L^0$ . The values computed from stretched laminar flame and from the optimization methods are shown with symbols, the dashed lines represent the models in Eqs. (3.3.5) and (3.3.6) and the solid lines correspond to the model in Eq. (3.3.7). . . . .	97
4.2.1 Schematic view of the post-processing method. . . . .	102
4.3.1 Comparison of the source terms involved in Eq. (4.1.5) as functions of $\tilde{\mathcal{C}}$ . $T_1$ is the unresolved transport term $\nabla \cdot (\overline{\rho \mathbf{u} \mathcal{C}} - \bar{\rho} \tilde{\mathbf{u}} \tilde{\mathcal{C}})$ and $T_2$ is the propagation term $\langle \rho S_d \rangle_{s,c^*} \bar{\Sigma}^*$ . . . . .	103
4.3.2 Comparison $T_1 = \nabla \cdot (\overline{\rho \mathbf{u} \mathcal{C}} - \bar{\rho} \tilde{\mathbf{u}} \tilde{\mathcal{C}})$ extracted from the DNS with both the simple gradient model (Eq. 4.3.1) and the model including the thermal expansion (Eq. 4.3.6) as functions of $\tilde{\mathcal{C}}$ for: (a) to (c) the cases with $Le_k \neq 1$ and (d) to (f) the cases with $Le_k = 1$ . . . . .	105
4.3.3 Probability density function (PDF) of $\kappa$ in solid line compared to a presumed Gaussian PDF, defined in Eq. (4.3.9) in dashed line: (a) for $\tilde{\mathcal{C}} = 0.2$ , (b) for $\tilde{\mathcal{C}} = 0.5$ and (c) for $\tilde{\mathcal{C}} = 0.8$ . The vertical dotted line represents the value of $\kappa$ where $1 + \mathcal{L}_\kappa \kappa$ is zero for the case C (for the case C <sub>1</sub> this value is approximately $-20000 \text{ m}^{-1}$ ). . . . .	107
4.3.4 Probability density function (PDF) of $\kappa$ in solid line compared to presumed PDF for case C: (a) for $\tilde{\mathcal{C}} = 0.2$ , (b) for $\tilde{\mathcal{C}} = 0.5$ and (c) for $\tilde{\mathcal{C}} = 0.8$ . The presumed PDF tested are the Gaussian presumed PDF defined in Eq. (4.3.9) using the variance of curvature extracted from DNS (Eq. 4.3.10) and using half the variance (Eq. 4.3.11) in red and blue dashed lines, respectively. . . . .	108
4.3.5 Comparison of the model for the curvature $\langle \kappa \rangle_{s,c^*}$ given in Eq. (4.3.13) with the data from the DNS versus $\tilde{\mathcal{C}}$ for : (a) to (c) the cases with $Le_k \neq 1$ and (d) to (f) the cases with $Le_k = 1$ . Dashed line in (b) represents the curvature extracted from the simulation using ARC mechanism (case C-ARC). . . . .	109
4.3.6 Comparison of the model for $\langle \kappa^2 \rangle_{s,c^*}$ (Eq.4.3.15) with the data from the DNS and the model proposed by Hawkes et al. (2009) (Eq. 4.3.14) versus $\tilde{\mathcal{C}}$ for: (a) to (c) the cases with $Le_k \neq 1$ and (d) to (f) the cases with $Le_k = 1$ . Dashed line in (b) represents $\langle \kappa^2 \rangle_{s,c^*}$ extracted from the simulation using ARC mechanism (case C-ARC). . . . .	110
4.3.7 Comparison of the displacement speed $\langle S_d \rangle_{s,c^*}$ for the proposed model (Eq. 4.3.8) with the DNS versus $\tilde{\mathcal{C}}$ for: (a) to (c) cases with $Le_k \neq 1$ and (d) to (f) cases with $Le_k = 1$ . Plain symbols and dashed line represent predictions from Eq. (4.3.8) using Markstein lengths fitted from the DNS. Black dashed line represents $\langle S_d \rangle_{s,c^*}$ extracted from the simulation using ARC mechanism (case C-ARC). . . . .	112

4.3.8 Comparison of the displacement speed $\langle S_d \rangle_{s,c^*}$ for the proposed models in Eqs. (4.3.8) and (4.3.16) with the DNS versus $\tilde{\mathcal{C}}$ for: (a) to (c) cases with $Le_k \neq 1$ and (d) to (f) cases with $Le_k = 1$ . Plain symbols and dashed line represent predictions from Eqs. (4.3.8) and (4.3.16) using Markstein lengths fitted from the DNS. Black dashed line represents $\langle S_d \rangle_{s,c^*}$ extracted from the simulation using ARC mechanism (case C-ARC). . . . .	113
4.4.1 Comparison of the source terms involved in Eq. (3.2.14) as functions of $\tilde{\mathcal{C}}$ . $T$ is the unresolved transport term $\nabla \cdot (\overline{\mathbf{u}\Sigma^*} - \tilde{\mathbf{u}}\overline{\Sigma^*})$ , $S$ is the source term related to tangential strain rate and $C$ is the source term related to stretch due to curvature $\langle S_d \kappa \rangle_{s,c^*}$ and $P$ is the normal propagation term $\nabla \cdot (\langle S_d \mathbf{n} \rangle_{s,c^*} \overline{\Sigma^*})$ . . . . .	115
4.4.2 Comparison $T = \nabla \cdot (\overline{\mathbf{u}\Sigma^*} - \tilde{\mathbf{u}}\overline{\Sigma^*})$ extracted from the DNS with the models given in Eqs. (4.4.1) and (4.4.6) as functions of $\tilde{\mathcal{C}}$ for: (a) to (c) the cases with $Le_k \neq 1$ and (d) to (f) the cases with $Le_k = 1$ . . . . .	117
4.4.3 Comparison of $\langle S_d \mathbf{n} \rangle_{s,c^*} \overline{\Sigma^*}$ extracted from the DNS with the models given by Eqs. (4.4.8) and (4.4.10) as functions of $\tilde{\mathcal{C}}$ for: (a) to (c) the cases with $Le_k \neq 1$ and (d) to (f) the cases with $Le_k = 1$ . . . . .	119
4.4.4 Evolutions of the tangential strain rate due to resolved flow motions $\langle A_T \rangle_{s,c^*}$ in Eq. (4.4.12) with the filtered progress variable $\tilde{\mathcal{C}}$ for: (a) to (c) the cases with $Le_k \neq 1$ and (d) to (f) the cases with $Le_k = 1$ . . . . .	121
4.4.5 Tangential strain rate $\langle a_T \rangle_s^* = \langle a_T \rangle_{s,c^*}^{sgs}$ from DNS compared to Bougrine's model (Bougrine et al., 2014), Cant's model (Cant et al., 1991), Charlette's model (Charlette et al., 2002a), HK <sub>2D</sub> (Eq. 2.3.5) and LPF models (Eq. 4.4.20): (a) for cases with $Le_k \neq 1$ and (b) for cases with $Le_k = 1$ . . . . .	124
4.4.6 Tangential strain rate $\langle a_T \rangle_s^* = \langle a_T \rangle_{s,c^*}^{sgs}$ from DNS compared to Bougrine's model (Bougrine et al., 2014), Cant's model (Cant et al., 1991), Charlette's model (Charlette et al., 2002a), HK <sub>2D</sub> (Eq. 2.3.5) and LPF model (Eq. 4.4.20): (a) for cases with $Le_k \neq 1$ and (b) for cases with $Le_k = 1$ . Each model is tuned to fit the lowest Karlovitz number case. . . . .	126
4.4.7 Comparison of the stretch due to curvature $\langle S_d \kappa \rangle_{s,c^*}$ normalized with the chemical time $\tau_f = \delta_L^0 / S_L^0$ for Katragadda's model (Katragadda et al., 2014a) and the proposed model (Eq. 4.4.24) with the DNS versus $\tilde{\mathcal{C}}$ for : (a) to (c) cases with $Le_k \neq 1$ and (d) to (f) cases with $Le_k = 1$ . Plain symbols and dashed line represent predictions from Eq. (4.4.24) using Markstein lengths fitted from the DNS in (a). Black dashed line represents $\langle S_d \kappa \rangle_{s,c^*}$ extracted from the simulation using ARC mechanism (case C-ARC). . . . .	128
4.5.1 Evolutions of $\overline{\mathcal{C}}$ as a function of $\tilde{\mathcal{C}}$ for: (a) non-unity Lewis numbers cases and (b) unity Lewis numbers cases. The BML relationship is plotted in dashed line. The model proposed by Chakraborty and Cant (2011) is plotted in dotted lines. . . . .	130
4.5.2 Schematic explanation for the determination of $\overline{\mathcal{C}}$ from $\Sigma^+$ and $\tilde{\mathcal{C}}$ . . . . .	131

4.5.3 Schematic view of the look-up tables for the determination of $\bar{\mathcal{C}}$ from $\Sigma^+$ and $\tilde{\mathcal{C}}$ :	
(a) $\Sigma^+$ versus $\tilde{\mathcal{C}}$ and $\Delta_0$ and (b) $\bar{\mathcal{C}}$ versus $\tilde{\mathcal{C}}$ and $\Delta_0$ . . . . .	132
4.5.4 Comparisons of the profiles of filtered progress variable $\bar{\mathcal{C}}$ extracted from DNS (solid lines), from the FLF-PDF based model using the laminar flame thickness in Eq. (4.5.8) (dotted lines) and from the FLF-PDF based model using the effective flame thickness $\delta_L^{eff}$ in Eq. (4.5.8) (dashed lines) for: (a) $Le_k \neq 1$ cases and (b) $Le_k = 1$ cases. . . . .	132
5.1.1 Schematic view of the flow configuration of <i>a posteriori</i> simulations. . . . .	137
5.2.1 Evolutions of the predictions of $S_T/S_L^0$ compared to DNS for: (a) $Le_k \neq 1$ cases and (c) for $Le_k = 1$ cases. (b) and (d) show a focus on the versions of HK model and DNS. . . . .	139
5.2.2 Predictions of the spatial profile of propagation term $\langle \rho S_d \rangle_{s,c^*} \bar{\Sigma}^*$ centred on $\tilde{\mathcal{C}} = 0.5$ from the proposed model compared to ECFM-LES model and DNS, for :(a) to (d) cases with $Le_k \neq 1$ and (e) to (g) cases with $Le_k = 1$ . . . . .	141
5.2.3 Predictions of the spatial profile of $\tilde{\mathcal{C}}$ centred on the spatial location corresponding to $\tilde{\mathcal{C}} = 0.5$ from the proposed model compared to ECFM-LES model and DNS, for :(a) to (d) cases with $Le_k \neq 1$ and (e) to (g) cases with $Le_k = 1$ . . . . .	143
5.2.4 Predictions of the spatial profile of FSD $\bar{\Sigma}^*$ centred on the spatial location corresponding to $\tilde{\mathcal{C}} = 0.5$ from the proposed model compared to ECFM-LES model and DNS, for :(a) to (d) cases with $Le_k \neq 1$ and (e) to (g) cases with $Le_k = 1$ . . . . .	144
5.3.1 Predictions of $\bar{\mathcal{C}}$ from the proposed model as functions of $\tilde{\mathcal{C}}$ compared to ECFM-LES model and DNS, for :(a) to (d) cases with $Le_k \neq 1$ and (e) to (g) cases with $Le_k = 1$ . . . . .	146
5.3.2 Predictions of $\langle \kappa \rangle_{s,c^*}$ from the proposed model as functions of $\tilde{\mathcal{C}}$ compared to DNS, for :(a) to (d) cases with $Le_k \neq 1$ and (e) to (g) cases with $Le_k = 1$ . . . . .	148
5.3.3 Predictions of $\langle \kappa^2 \rangle_{s,c^*}$ from the proposed model as functions of $\tilde{\mathcal{C}}$ compared to DNS, for :(a) to (d) cases with $Le_k \neq 1$ and (e) to (g) cases with $Le_k = 1$ . . . . .	149
5.3.4 Predictions of $\langle S_d \kappa \rangle_{s,c^*}$ from the proposed model as functions of $\tilde{\mathcal{C}}$ compared to DNS, for :(a) to (d) cases with $Le_k \neq 1$ and (e) to (g) cases with $Le_k = 1$ . . . . .	151
5.3.5 Predictions of $\langle S_d \rangle_{s,c^*}$ from the proposed model as functions of $\tilde{\mathcal{C}}$ compared to DNS, for :(a) to (d) cases with $Le_k \neq 1$ and (e) to (g) cases with $Le_k = 1$ . . . . .	152
5.4.1 Spatial profiles of FSD $\bar{\Sigma}^*$ and $\bar{\Sigma}^*_{\tilde{\mathcal{C}}}$ (Eq. 5.4.4) centred on $\tilde{\mathcal{C}} = 0.5$ extracted from the DNS for (a) to (d) cases with $Le_k \neq 1$ . . . . .	155
5.4.2 Evolution of the predictions of $S_T/S_L^0$ when the transported FSD is $\bar{\Sigma}^*_{\tilde{\mathcal{C}}}$ compared to DNS and to HK $_{\gamma}^{1L}$ model using $\bar{\Sigma}^*$ as the transported FSD. . . . .	156
5.4.3 Predictions of the spatial profile of FSD $\bar{\Sigma}^*$ centred on $\tilde{\mathcal{C}} = 0.5$ when the transported FSD is $\bar{\Sigma}^*_{\tilde{\mathcal{C}}}$ compared to DNS and HK $_{\gamma}^{1L}$ model using $\bar{\Sigma}^*$ as the transported FSD, for (a) to (d) cases with $Le_k \neq 1$ . . . . .	157
5.4.4 Evolutions of total, resolved and sub-grid scale tangential strain rate with the filtered progress variable $\tilde{\mathcal{C}}$ for (a) to (c) the cases with $Le_k \neq 1$ . . . . .	158

5.4.5 Schematic view of the flame front using two progress variable iso-surfaces at $c^0$ and $c^*$ . . . . .	159
5.4.6 Comparison of the tangential strain rates $\langle a_T \rangle_{s,c^*}$ and $\langle a_T \rangle_{s,c^0}$ with the corrective strain rate $(\langle a_T \rangle_{s,c^*} - \langle a_T \rangle_{s,c^0})$ and the modelled corrective strain rate $(S_{d,c^0}^0 - S_{d,c^*}^0) \langle \kappa \rangle_{s,c^*}$ , for: (a) case A and (b) case C. . . . .	160
6.2.1 Schematic view of pulsed interactions flame-vortex: (a) Initial configuration with the creation of the first pair of vortices and (b) creation of the $n^{\text{th}}$ pair of vortices after $n\tau$ , where $\tau$ is the period to be defined. . . . .	167
6.2.2 Schematic view of the physical mechanisms involved in the propagation of a spherical laminar flame. (Richard, 2005) . . . . .	168
A.2.1 Comparison of the overall results using TTGC scheme or LW scheme: (a) the temporal evolution of the generalized flame surface normalized with the laminar flame surface $\mathcal{A}_0 = L^2$ , (b) the temporal evolution of the heat release rate normalized with the heat release rate of the laminar flame $HR_0$ , (c) the temporal evolution of the generalized tangential strain rate in solid lines and the stretch due to curvature in dashed lines, and (d) the temporal evolutions of the density weighted displacement speed at $c = 0.8$ normalized with the density weighted laminar flame speed $\rho_u S_L^0$ . . . . .	175
A.2.2 Comparisons of the conditional mean of (a) displacement speed $\langle S_d^*(\xi) \rangle_{\xi=\kappa^*}$ and (b) its components $\langle S_r^* + S_n^*(\xi) \rangle_{\xi=\kappa^*}$ , normalized with the laminar flame speed at $c = c^*$ $S_d^0$ as functions of $\kappa^*$ . (c) Comparison of the conditional mean of tangential strain rate $\langle a_T^*(\xi) \rangle_{\xi=\kappa^*}$ as function of $\kappa^*$ . The error bars represent the standard deviation. . . . .	176
A.2.3 Evolution of the conditional mean of $\langle S_r^* + S_n^* \rangle_{(a_T^*, \kappa^*)}$ with $a_T^*$ and $\kappa^*$ for: (a) case C using LW scheme and (b) case C using TTGC scheme. Black lines are contours of the joint probability density function (PDF) of $a_T^*$ and $\kappa^*$ corresponding to 10% (outer line), 50% and 90% (inner line) of its maximum value. The solid white line is the iso-contour $\langle S_r^* + S_n^* \rangle_{(a_T^*, \kappa^*)} = \rho_u S_L / \rho^*$ and the dashed white line is the iso-contour $\langle S_r^* + S_n^* \rangle_{(a_T^*, \kappa^*)} = 0$ . . . . .	177
A.2.4 Comparison of statistics as functions of $\tilde{\mathcal{C}}$ following the procedure presented in Section 4.2 from simulations using LW or TTGC scheme for: (a) curvature $\langle \kappa \rangle_{s,c^*}$ , (b) $\langle \kappa^2 \rangle_{s,c^*}$ , (c) stretch due to curvature $\langle S_d \kappa \rangle_{s,c^*}$ and (d) displacement speed $\langle S_d \rangle_{s,c^*}$ . . . . .	178
B.1.1 Schematic view of the flow configuration of the DNS with: (a) turbulence forced in the whole domain and (b) turbulence forced only in the fresh gases. . . . .	182
B.1.2 Direct Numerical Simulations of High Karlovitz turbulent premixed flame. . . . .	183
B.2.1 Temporal evolution of the turbulent flame surface $\mathcal{A}_T$ normalized with the laminar flame surface $\mathcal{A}_0$ (a) for cases A and A <sub>FG</sub> , (b) for cases C and C <sub>FG</sub> and (c) for cases D and D <sub>FG</sub> . . . . .	184

B.2.2	Evolutions of (a) $\Xi = \mathcal{A}_T/\mathcal{A}_0$ , $\Xi^* = \mathcal{A}_T^*/\mathcal{A}_0$ and $S_T/S_L^0$ , (b) of the stretch factors $I_0$ and $I_0^*$ , and (c) of the surface averaged tangential strain rate $\langle a_T \rangle_s$ with $Ka$ for $Le_k \neq 1$ cases with turbulence forced in the whole domain and only in the fresh gases with plain and empty symbols, respectively. . . . .	185
B.2.3	Conditional mean of the chemical source term $\langle \dot{\omega}_c(c) \rangle_{\xi=c}$ as a function of progress variable (a) for cases with $Le_k = 1$ with turbulence forced only in the fresh gases. Comparisons of conditional mean of the chemical source term $\langle \dot{\omega}_c(c) \rangle_{\xi=c}$ (b) for cases A and A <sub>FG</sub> , (c) for cases C and C <sub>FG</sub> and (d) for cases D and D <sub>FG</sub> . . . . .	186
B.2.4	Thickening factor $\Theta(c)$ (a) for cases with $Le_k \neq 1$ with turbulence forcing in the whole domain and (b) for cases with $Le_k \neq 1$ with turbulence forced only in the fresh gases. . . . .	187
B.3.1	Evolution of the conditional mean of displacement speed $\langle S_d^*(\xi) \rangle_{\xi=\kappa^*}$ , normalized with the laminar flame speed at $c = c^*$ , $S_d^0$ , with curvature $\kappa^*$ (a) for $Le_k \neq 1$ cases with turbulence forced only in the fresh gases. Comparisons of: (b) cases A and A <sub>FG</sub> , (c) cases C and C <sub>FG</sub> , and (d) cases D and D <sub>FG</sub> . The error bars represent the standard deviation. . . . .	188
B.3.2	Evolution of the conditional mean of displacement speed $\langle S_r^* + S_n^*(\xi) \rangle_{\xi=\kappa^*}$ , normalized with the laminar flame speed at $c = c^*$ , $S_d^0$ , with curvature $\kappa^*$ (a) for $Le_k \neq 1$ cases with turbulence forced only in the fresh gases. Comparisons of: (b) cases A and A <sub>FG</sub> , (c) cases C and C <sub>FG</sub> , and (d) cases D and D <sub>FG</sub> . The error bars represent the standard deviation. . . . .	189
B.3.3	Evolution of the conditional mean of tangential strain rate $\langle a_T^*(\xi) \rangle_{\xi=\kappa^*}$ with curvature $\kappa^*$ (a) for $Le_k \neq 1$ cases with turbulence forced only in the fresh gases. Comparisons of: (b) cases A and A <sub>FG</sub> , (c) cases C and C <sub>FG</sub> , and (d) cases D and D <sub>FG</sub> . The error bars represent the standard deviation. . . . .	190
B.3.4	Evolution of the conditional mean of $\langle S_r^* + S_n^* \rangle_{(a_T^*, \kappa^*)}$ with $a_T^*$ and $\kappa^*$ for: (a) to (c) the cases with turbulence forced in the whole domain and (d) to (f) the cases with turbulence forced only in the fresh gases. Black lines are contours of the joint probability density function (PDF) of $a_T^*$ and $\kappa^*$ corresponding to 10% (outer line), 50% and 90% (inner line) of its maximum value. The solid white line is the iso-contour $\langle S_r^* + S_n^* \rangle_{(a_T^*, \kappa^*)} = \rho_u S_L / \rho^*$ and the dashed white line is the iso-contour $\langle S_r^* + S_n^* \rangle_{(a_T^*, \kappa^*)} = 0$ . . . . .	191
B.3.5	Evolution of effective Markstein numbers with $Ka$ : (a) for $\mathcal{M}_{a_T} = \mathcal{L}_{a_T} / \delta_L$ and (b) for $\mathcal{M}_\kappa = \mathcal{L}_\kappa / \delta_L$ . The values computed from stretched laminar flame and from the optimization methods are shown with dots and the dashed lines represent the models in Eqs. (3.3.5) and (3.3.6). Markstein numbers resulting from simulations with turbulence forcing in the whole domain are represented in empty symbols, while plain symbols are used for cases with turbulence forced only in the fresh gases. . . . .	192

B.4.1	Comparison of the profiles of curvature $\langle \kappa \rangle_{s,c^*}$ by forcing the turbulence in the whole domain (solid lines) or in the fresh gases only (dashed lines). . . . .	193
B.4.2	Comparison of the profiles of $\langle \kappa^2 \rangle_{s,c^*}$ by forcing the turbulence in the whole domain (solid lines) or in the fresh gases only (dashed lines). . . . .	194
B.4.3	Comparison of the profiles of the stretch due curvature $\langle S_d \kappa \rangle_{s,c^*}$ by forcing the turbulence in the whole domain (solid lines) or in the fresh gases only (dashed lines). . . . .	195
B.4.4	Comparison of the profiles of the displacement speed $\langle S_d \rangle_{s,c^*}$ by forcing the turbulence in the whole domain (solid lines) or in the fresh gases only (dashed lines). . . . .	195
D.1	Schematic view of laminar stretched flames. . . . .	200
D.1	Evolution of the sum $S_r^* + S_n^*$ as a function of stretch $K^*$ for spherical premixed flames for (a) non-unity Lewis numbers case and (b) unity Lewis numbers case. .	200
D.1	Evolution of the sum $S_r^* + S_n^*$ as a function of stretch $K^*$ for counterflow premixed flames for (a) non-unity Lewis numbers case and (b) unity Lewis numbers case. .	201



# List of Tables

1.1	The most common correction functions taking into account the ability of the turbulent eddies at scale $r_c = \pi/k$ to stretch the flame. $u_c$ is the characteristic velocity of the turbulent eddies at scale $r_c$ . . . . .	27
1.2	Parameters of the simulations conducted in (Lapointe et al., 2015). $Ka$ is the Karlovitz number in the unburnt gases computed as $Ka = (\delta_L^0/S_L^0)\sqrt{u_t^3/(\nu l_t)}$ . . . . .	37
2.1	Arrhenius parameters for the $C_8H_{18}$ 2-step mechanism. . . . .	51
2.2	The DNS set-up of the flame-vortex interactions . . . . .	55
2.3	Deviation of the efficiency $C_r$ for each pair of vortices using $a_T^r$ instead of $K_r$ . . . . .	60
2.4	Fitted parameters of the proposed efficiency function. . . . .	63
2.5	Mean error on the effective tangential strain rate (Eq. 2.3.7) for the 28 non-diluted flames of Table 2.2. . . . .	63
3.1	Arrhenius parameters for the $C_8H_{18}$ 2-step mechanism. . . . .	70
3.2	ISOOC18 scheme: 18 transported species, and 13 as QSS species to compute source terms. . . . .	70
3.3	Schmidt number of each species of the two-step mechanism for $Le_k \neq 1$ and $Le_k = 1$ cases. The Prandtl number is $Pr = 0.69$ . . . . .	71
3.4	Laminar flame velocity $S_L^0 = -(1/\rho_u Y_F^u) \int_{-\infty}^{+\infty} \dot{\omega}_F dx$ , where $\dot{\omega}_F$ , $\rho_u$ and $Y_F^u$ are the local fuel reaction rate, the density and the fuel mass fraction in the fresh gases, respectively, and thermal diluted laminar flame thickness $\delta_L^0 = (T_b - T_u)/\max( \nabla T )$ for the different flames simulated. . . . .	72
3.5	The DNS set-up for the simulations of the interaction between a planar flame and forced homogeneous isotropic turbulence. The Karlovitz number $Ka$ and the Damköhler number $Da$ are defined with Eqs. (1.3.11) and (1.3.10), respectively. The laminar flame thickness used to evaluate these numbers is the thermal laminar flame thickness $\delta_L^0 = (T_b - T_u)/\max( \nabla T )$ . $N_{cell}$ is the number of cells in the mesh used for simulating the flames. . . . .	75
3.6	Characteristic times for each simulations. . . . .	77
3.7	Pearson's correlation coefficient, $r_{a_T^*, \kappa^*}$ , between strain rate $a_T^*$ and curvature $\kappa^*$ for the flames presented in this paper. . . . .	90
3.8	Fitted parameters for modelling the Markstein numbers with Eqs.(3.3.5) and (3.3.6). . . . .	94



4.1	Estimated values of the efficiency function $\alpha$ using ITNFS model (Meneveau and Poinso, 1991) and of $N_B$ defined in Eq. (4.3.7) for each case. . . . .	104
4.2	The efficiency functions of the models compared to the DNS. . . . .	123
4.3	Tuned model parameter $\alpha_{a_T}$ for each model. . . . .	125
4.4	Segregation factor involved in Eq. (4.5.5) fitted to best reproduce $\bar{\mathcal{C}}$ of each DNS. . . . .	130
5.1	Tuned model parameter $\alpha_{a_T}$ for each model. . . . .	136
5.2	Set-up for the simulations of one-dimensional turbulent flame. . . . .	137
5.3	The different models characteristics . . . . .	138
A.1	The DNS set-up for the simulation C of the interaction between a planar flame and forced homogeneous isotropic turbulence. The Karlovitz number $Ka$ and the Damköhler number $Da$ are defined with Eqs. (1.3.11) and (1.3.10), respectively. The laminar flame thickness used to evaluate these numbers is the thermal laminar flame thickness $\delta_L^0 = (T_b - T_u) / \max( \nabla T )$ . $N_{cell}$ is the number of cells in the mesh used for simulating the flames. . . . .	174
A.2	Computational characteristics of simulations LW and TTGC schemes. . . . .	174
B.1	The DNS set-up for the simulations of the interaction between a planar flame and forced homogeneous isotropic turbulence. The Karlovitz number $Ka$ and the Damköhler number $Da$ are defined with Eqs. (1.3.11) and (1.3.10), respectively. The laminar flame thickness used to evaluate these numbers is the thermal laminar flame thickness $\delta_L^0 = (T_b - T_u) / \max( \nabla T )$ . $N_{cell}$ is the number of cells in the mesh used for simulating the flames. . . . .	183
B.2	Pearson's correlation coefficient, $r_{a_T^*, \kappa^*}$ , between strain rate $a_T^*$ and curvature $\kappa^*$ for the flames using the two forcing methods presented in Section B.1. . . . .	190

# Bibliography

- R. G. Abdel-Gayed, K. J. Al-Khishali, D. Bradley, and P. Gray. Turbulent burning velocities and flame straining in explosions. *Proceedings of the Royal Society of London. A. Mathematical and Physical Sciences*, 391(1801):393–414, feb 1984. doi: 10.1098/rspa.1984.0019. URL <https://doi.org/10.1098/rspa.1984.0019>. 9
- R. G. Abdel-Gayed, D. Bradley, and F.-K. Lung. Combustion regimes and the straining of turbulent premixed flames. *Combustion and Flame*, 76(2):213–218, 1989. 9
- U. Ahmed, N. Chakraborty, and M. Klein. Insights into the bending effect in premixed turbulent combustion using the flame surface density transport. *Combustion Science and Technology*, 191(5-6):898–920, mar 2019. doi: 10.1080/00102202.2019.1577241. URL <https://doi.org/10.1080/00102202.2019.1577241>. 30, 33, 34, 35, 79, 81, 210
- C. Angelberger, D. Veynante, F. Egolfopoulos, and T. Poinso. Large eddy simulations of combustion instabilities in premixed flames. In *Proceedings of the Summer Program, Center for Turbulence Research, Stanford*, pages 61–82. Citeseer, 1998. 18
- A. J. Aspden, M. S. Day, and J. Bell. Lewis number effects in distributed flames. *Proceedings of the Combustion Institute*, 33(1):1473–1480, 2011a. doi: 10.1016/j.proci.2010.05.095. URL <https://doi.org/10.1016/j.proci.2010.05.095>. 30, 35, 45, 68, 73, 77, 181, 210
- A. J. Aspden, M. S. Day, and J. B. Bell. Turbulence–flame interactions in lean premixed hydrogen: transition to the distributed burning regime. *Journal of Fluid Mechanics*, 680: 287–320, may 2011b. doi: 10.1017/jfm.2011.164. URL <https://doi.org/10.1017/jfm.2011.164>. 30, 35, 45, 68, 73, 77, 80, 81, 181, 210
- A. J. Aspden, M. S. Day, and J. Bell. Turbulence-chemistry interaction in lean premixed hydrogen combustion. *Proceedings of the Combustion Institute*, 35(2):1321–1329, 2015. doi: 10.1016/j.proci.2014.08.012. URL <https://doi.org/10.1016/j.proci.2014.08.012>. 30, 35, 45, 68, 73, 77, 181, 210
- A. J. Aspden, M. S. Day, and J. Bell. Three-dimensional direct numerical simulation of turbulent lean premixed methane combustion with detailed kinetics. *Combustion and Flame*, 166: 266–283, apr 2016. doi: 10.1016/j.combustflame.2016.01.027. URL <https://doi.org/10.1016/j.combustflame.2016.01.027>. 30, 35, 36, 45, 68, 73, 77, 181, 210

- A. J. Aspden, J. Bell, M. S. Day, and F. Egolfopoulos. Turbulence–flame interactions in lean premixed dodecane flames. *Proceedings of the Combustion Institute*, 36(2):2005–2016, 2017. doi: 10.1016/j.proci.2016.07.068. URL <https://doi.org/10.1016/j.proci.2016.07.068>. 30, 35, 45, 68, 73, 77, 181, 210
- A. J. Aspden, M. S. Day, and J. B. Bell. Towards the distributed burning regime in turbulent premixed flames. *Journal of Fluid Mechanics*, 871:1–21, may 2019. doi: 10.1017/jfm.2019.316. URL <https://doi.org/10.1017/jfm.2019.316>. 30, 35, 36, 45, 68, 73, 77, 82, 83, 181, 187, 210
- G. Batley, A. McIntosh, and J. Brindley. The baroclinic effect in combustion. *Mathematical and Computer Modelling*, 24(8):165–176, oct 1996. doi: 10.1016/0895-7177(96)00148-3. URL [https://doi.org/10.1016/0895-7177\(96\)00148-3](https://doi.org/10.1016/0895-7177(96)00148-3). 9
- M. Baum, T. Poinso, and D. Thévenin. Accurate boundary conditions for multicomponent reactive flows. *Journal of Computational Physics*, 116(2):247–261, feb 1995. doi: 10.1006/jcph.1995.1024. URL <https://doi.org/10.1006/jcph.1995.1024>. 171
- O. Benoit, P. Luszcz, Y. Drouvin, T. Kayashima, P. Adomeit, A. Brunn, S. Jay, K. Truffin, and C. Angelberger. Study of ignition processes of a lean burn engine using large-eddy simulation. In *SAE Technical Paper Series*. SAE International, dec 2019. doi: 10.4271/2019-01-2209. URL <https://doi.org/10.4271/2019-01-2209>. i
- R. J. Blint. The relationship of the laminar flame width to flame speed. *Combustion Science and Technology*, 49(1-2):79–92, sep 1986. doi: 10.1080/00102208608923903. URL <https://doi.org/10.1080/00102208608923903>. 6
- M. Boger, D. Veynante, H. Boughanem, and A. Trouvé. Direct numerical simulation analysis of flame surface density concept for large eddy simulation of turbulent premixed combustion. *Symposium (International) on Combustion*, 27(1):917–925, jan 1998. doi: 10.1016/s0082-0784(98)80489-x. URL [https://doi.org/10.1016/s0082-0784\(98\)80489-x](https://doi.org/10.1016/s0082-0784(98)80489-x). 17, 21, 22, 23, 24, 169
- M. M. Boger. *Modélisation de sous-maille pour la simulation aux grandes échelles de la combustion turbulente prémélangée*. PhD thesis, Ecole centrale de Paris, 2000. URL <http://www.theses.fr/2000ECAP0904>. 17, 21, 22, 23, 24, 102
- A. Bonhomme, L. Selle, and T. Poinso. Curvature and confinement effects for flame speed measurements in laminar spherical and cylindrical flames. *Combustion and Flame*, 160(7):1208–1214, jul 2013. doi: 10.1016/j.combustflame.2013.02.003. URL <https://doi.org/10.1016/j.combustflame.2013.02.003>. 51, 69
- R. Borghi. On the structure and morphology of turbulent premixed flames. In *Recent Advances in the Aerospace Sciences*, pages 117–138. Springer US, 1985. doi: 10.1007/978-1-4684-4298-4.7. URL <https://doi.org/10.1007/978-1-4684-4298-4.7>. 9

- S. Bougrine. *0-dimensional modeling of the combustion of alternative fuels in spark ignition engines*. PhD thesis, Ecole Centrale Paris, June 2012. URL <https://tel.archives-ouvertes.fr/tel-00740654>. 11, 209
- S. Bougrine, S. Richard, O. Colin, and D. Veynante. Fuel composition effects on flame stretch in turbulent premixed combustion: Numerical analysis of flame-vortex interaction and formulation of a new efficiency function. *Flow, Turbulence and Combustion*, 93(2):259–281, jun 2014. doi: 10.1007/s10494-014-9546-4. URL <https://doi.org/10.1007/s10494-014-9546-4>. 18, 27, 47, 49, 50, 52, 54, 61, 62, 63, 64, 123, 124, 125, 126, 137, 164, 165, 206, 211, 212, 215
- J. Boussinesq. *Théorie de l'écoulement tourbillonnant et tumultueux des liquides dans les lits rectilignes a grande section*, volume 1. Gauthier-Villars, 1897. 14
- F. Bozza, V. D. Bellis, D. Tufano, E. Malfi, C. Müller, and K. Habermann. A quasi-dimensional model of pre-chamber spark-ignition engines. In *SAE Technical Paper Series*. SAE International, apr 2019. doi: 10.4271/2019-01-0470. URL <https://doi.org/10.4271/2019-01-0470>. i
- K. Bray and J. Moss. A unified statistical model of the premixed turbulent flame. *Acta Astronautica*, 4(3-4):291–319, mar 1977. doi: 10.1016/0094-5765(77)90053-4. URL [https://doi.org/10.1016/0094-5765\(77\)90053-4](https://doi.org/10.1016/0094-5765(77)90053-4). 15, 129
- G. Bruneaux, T. Poinso, and J. H. Ferziger. Premixed flame-wall interaction in a turbulent channel flow: budget for the flame surface density evolution equation and modelling. *Journal of Fluid Mechanics*, 349:191–219, oct 1997. doi: 10.1017/s0022112097006769. URL <https://doi.org/10.1017/s0022112097006769>. 169
- T. Butler and P. O'Rourke. A numerical method for two dimensional unsteady reacting flows. *Symposium (International) on Combustion*, 16(1):1503–1515, jan 1977. doi: 10.1016/s0082-0784(77)80432-3. URL [https://doi.org/10.1016/s0082-0784\(77\)80432-3](https://doi.org/10.1016/s0082-0784(77)80432-3). 17
- S. M. Candel and T. J. Poinso. Flame stretch and the balance equation for the flame area. *Combustion Science and Technology*, 70(1-3):1–15, mar 1990. doi: 10.1080/00102209008951608. URL <https://doi.org/10.1080/00102209008951608>. 24, 47, 48, 164, 211
- R. Cant, S. Pope, and K. Bray. Modelling of flamelet surface-to-volume ratio in turbulent premixed combustion. *Symposium (International) on Combustion*, 23(1):809–815, jan 1991. doi: 10.1016/s0082-0784(06)80334-6. URL [https://doi.org/10.1016/s0082-0784\(06\)80334-6](https://doi.org/10.1016/s0082-0784(06)80334-6). 61, 63, 64, 111, 120, 122, 124, 126, 212, 215
- N. Chakraborty and R. Cant. Influence of Lewis number on strain rate effects in turbulent premixed flame propagation. *International Journal of Heat and Mass Transfer*, 49(13-14):2158–2172, jul 2006. doi: 10.1016/j.ijheatmasstransfer.2005.11.025. URL <https://doi.org/10.1016/j.ijheatmasstransfer.2005.11.025>. 43, 45, 51, 92, 163

- N. Chakraborty and R. Cant. Effects of Lewis number on flame surface density transport in turbulent premixed combustion. *Combustion and Flame*, 158(9):1768–1787, sep 2011. doi: 10.1016/j.combustflame.2011.01.011. URL <https://doi.org/10.1016/j.combustflame.2011.01.011>. 43, 45, 51, 92, 130, 131, 163, 215
- N. Chakraborty and R. S. Cant. Effects of strain rate and curvature on surface density function transport in turbulent premixed flames in the thin reaction zones regime. *Physics of Fluids*, 17(6):065108, jun 2005a. doi: 10.1063/1.1923047. URL <https://doi.org/10.1063/1.1923047>. 43, 45, 51, 90, 163
- N. Chakraborty and R. S. Cant. Influence of Lewis number on curvature effects in turbulent premixed flame propagation in the thin reaction zones regime. *Physics of Fluids*, 17(10):105105, 2005b. doi: 10.1063/1.2084231. URL <https://doi.org/10.1063/1.2084231>. 43, 45, 51, 92, 163
- N. Chakraborty and M. Klein. Influence of Lewis number on the surface density function transport in the thin reaction zone regime for turbulent premixed flames. *Physics of Fluids*, 20(6):065102, jun 2008. doi: 10.1063/1.2919129. URL <https://doi.org/10.1063/1.2919129>. 43, 45, 52, 163
- F. Charlette, C. Meneveau, and D. Veynante. A power-law flame wrinkling model for LES of premixed turbulent combustion part i: non-dynamic formulation and initial tests. *Combustion and Flame*, 131(1-2):159–180, oct 2002a. doi: 10.1016/s0010-2180(02)00400-5. URL [https://doi.org/10.1016/s0010-2180\(02\)00400-5](https://doi.org/10.1016/s0010-2180(02)00400-5). 18, 23, 26, 27, 45, 47, 48, 49, 54, 61, 62, 63, 64, 122, 123, 124, 126, 164, 165, 206, 212, 215
- F. Charlette, C. Meneveau, and D. Veynante. A power-law flame wrinkling model for LES of premixed turbulent combustion part II: dynamic formulation. *Combustion and Flame*, 131(1-2):181–197, oct 2002b. doi: 10.1016/s0010-2180(02)00401-7. URL [https://doi.org/10.1016/s0010-2180\(02\)00401-7](https://doi.org/10.1016/s0010-2180(02)00401-7). 23, 24
- C. Chen, P. Pal, M. Ameen, D. Feng, and H. Wei. Large-eddy simulation study on cycle-to-cycle variation of knocking combustion in a spark-ignition engine. *Applied Energy*, 261:114447, mar 2020. doi: 10.1016/j.apenergy.2019.114447. URL <https://doi.org/10.1016/j.apenergy.2019.114447>. ii
- Z. Chen. On the extraction of laminar flame speed and Markstein length from outwardly propagating spherical flames. *Combustion and Flame*, 158(2):291–300, feb 2011. doi: 10.1016/j.combustflame.2010.09.001. URL <https://doi.org/10.1016/j.combustflame.2010.09.001>. 168
- O. Colin and M. Rudgyard. Development of high-order Taylor–Galerkin schemes for LES. *Journal of Computational Physics*, 162(2):338–371, aug 2000. doi: 10.1006/jcph.2000.6538. URL <https://doi.org/10.1006/jcph.2000.6538>. 51, 68, 171, 173

- O. Colin, F. Ducros, D. Veynante, and T. Poinso. A thickened flame model for large eddy simulations of turbulent premixed combustion. *Physics of Fluids*, 12(7):1843–1863, jul 2000. doi: 10.1063/1.870436. URL <https://doi.org/10.1063/1.870436>. 18, 26, 27, 47, 50, 52, 53, 54, 164, 211
- B. Cuenot, B. Bedat, and A. Corjon. *Ntmix3d user’s guide, preliminary version 1.0*, 1997. 171
- G. Damköhler. Influence of turbulence on the velocity flames in gas mixtures. *Z. Elektrochem*, 46:601–626, 1940. 9
- N. Darabiha, S. Candel, and F. Marble. The effect of strain rate on a premixed laminar flame. *Combustion and Flame*, 64(2):203–217, may 1986. doi: 10.1016/0010-2180(86)90057-x. URL [https://doi.org/10.1016/0010-2180\(86\)90057-x](https://doi.org/10.1016/0010-2180(86)90057-x). 201
- L. de Goey, T. Plessing, R. Hermanns, and N. Peters. Analysis of the flame thickness of turbulent flamelets in the thin reaction zones regime. *Proceedings of the Combustion Institute*, 30(1):859–866, jan 2005. doi: 10.1016/j.proci.2004.08.016. URL <https://doi.org/10.1016/j.proci.2004.08.016>. 30, 32, 45, 164
- N. Doan, N. Swaminathan, and N. Chakraborty. Multiscale analysis of turbulence-flame interaction in premixed flames. *Proceedings of the Combustion Institute*, 36(2):1929–1935, 2017. doi: 10.1016/j.proci.2016.07.111. URL <https://doi.org/10.1016/j.proci.2016.07.111>. 48
- J. F. Driscoll, J. H. Chen, A. W. Skiba, C. D. Carter, E. R. Hawkes, and H. Wang. Premixed flames subjected to extreme turbulence: Some questions and recent answers. *Progress in Energy and Combustion Science*, 76:100802, jan 2020. doi: 10.1016/j.pecs.2019.100802. URL <https://doi.org/10.1016/j.pecs.2019.100802>. 29, 30, 33, 37, 79
- C. Duwig, K. Nogenmyr, C. Chan, and M. J. Dunn. Large eddy simulations of a piloted lean premix jet flame using finite-rate chemistry. *Combustion Theory and Modelling*, 15(4):537–568, aug 2011. doi: 10.1080/13647830.2010.548531. URL <https://doi.org/10.1080/13647830.2010.548531>. 44
- V. Eswaran and S. Pope. An examination of forcing in direct numerical simulations of turbulence. *Computers & Fluids*, 16(3):257–278, jan 1988. doi: 10.1016/0045-7930(88)90013-8. URL [https://doi.org/10.1016/0045-7930\(88\)90013-8](https://doi.org/10.1016/0045-7930(88)90013-8). 73, 181
- A. Felden, E. Riber, and B. Cuenot. Impact of direct integration of analytically reduced chemistry in LES of a sooting swirled non-premixed combustor. *Combustion and Flame*, 191:270–286, may 2018. doi: 10.1016/j.combustflame.2018.01.005. URL <https://doi.org/10.1016/j.combustflame.2018.01.005>. 70
- A. Felden, P. Pepiot, L. Esclapez, E. Riber, and B. Cuenot. Including analytically reduced chemistry (ARC) in CFD applications. *Acta Astronautica*, 158:444–459, may 2019. doi: 10.1016/j.actaastro.2019.03.035. URL <https://doi.org/10.1016/j.actaastro.2019.03.035>. 70



- L. Francqueville and J.-B. Michel. On the effects of EGR on spark-ignited gasoline combustion at high load. *SAE International Journal of Engines*, 7(4):1808–1823, oct 2014. doi: 10.4271/2014-01-2628. URL <https://doi.org/10.4271/2014-01-2628>. ii, iv, 209
- F. Gao and E. O’Brien. A large-eddy simulation scheme for turbulent reacting flows. *Physics of Fluids A: Fluid Dynamics*, 5(6):1282–1284, jun 1993. doi: 10.1063/1.858617. URL <https://doi.org/10.1063/1.858617>. 22
- F. C. Gouldin. An application of fractals to modeling premixed turbulent flames. *Combustion and Flame*, 68(3):249–266, jun 1987. doi: 10.1016/0010-2180(87)90003-4. URL [https://doi.org/10.1016/0010-2180\(87\)90003-4](https://doi.org/10.1016/0010-2180(87)90003-4). 31
- F. C. Gouldin, K. N. C. Bray, and J.-Y. Chen. Chemical closure model for fractal flamelets. *Combustion and Flame*, 77(3-4):241–259, sep 1989. doi: 10.1016/0010-2180(89)90132-6. URL [https://doi.org/10.1016/0010-2180\(89\)90132-6](https://doi.org/10.1016/0010-2180(89)90132-6). 23
- Ö. Gülder. Inner cutoff scale of flame surface wrinkling in turbulent premixed flames. *Combustion and Flame*, 103(1-2):107–114, oct 1995. doi: 10.1016/0010-2180(95)00073-f. URL [https://doi.org/10.1016/0010-2180\(95\)00073-f](https://doi.org/10.1016/0010-2180(95)00073-f). 125, 167
- Ö. L. Gülder. Contribution of small scale turbulence to burning velocity of flamelets in the thin reaction zone regime. *Proceedings of the Combustion Institute*, 31(1):1369–1375, jan 2007. doi: 10.1016/j.proci.2006.07.189. URL <https://doi.org/10.1016/j.proci.2006.07.189>. 30, 31, 32, 34, 45, 79, 164, 210
- Ö. L. Gülder and G. J. Smallwood. Flame surface densities in premixed combustion at medium to high turbulence intensities. *Combustion Science and Technology*, 179(1-2):191–206, jan 2007. doi: 10.1080/00102200600808722. URL <https://doi.org/10.1080/00102200600808722>. vi, 32, 79, 81
- F. Halter, C. Chauveau, I. Gökalp, and D. Veynante. Analysis of flame surface density measurements in turbulent premixed combustion. *Combustion and Flame*, 156(3):657–664, mar 2009. doi: 10.1016/j.combustflame.2008.11.016. URL <https://doi.org/10.1016/j.combustflame.2008.11.016>. 31
- F. Halter, T. Tahtouh, and C. Mounaïm-Rousselle. Nonlinear effects of stretch on the flame front propagation. *Combustion and Flame*, 157(10):1825–1832, oct 2010. doi: 10.1016/j.combustflame.2010.05.013. URL <https://doi.org/10.1016/j.combustflame.2010.05.013>. 168
- I. Han and K. Y. Huh. Effects of the Karlovitz number on the evolution of the flame surface density in turbulent premixed flames. *Proceedings of the Combustion Institute*, 32(1):1419–1425, 2009. doi: 10.1016/j.proci.2008.07.041. URL <https://doi.org/10.1016/j.proci.2008.07.041>. 30, 43, 45, 88, 90, 210

- E. Hawkes and R. Cant. A flame surface density approach to large-eddy simulation of premixed turbulent combustion. *Proceedings of the Combustion Institute*, 28(1):51–58, jan 2000. doi: 10.1016/s0082-0784(00)80194-0. URL [https://doi.org/10.1016/s0082-0784\(00\)80194-0](https://doi.org/10.1016/s0082-0784(00)80194-0). 24, 25, 118, 120, 129, 133, 165, 203, 204
- E. R. Hawkes and J. H. Chen. Evaluation of models for flame stretch due to curvature in the thin reaction zones regime. *Proceedings of the Combustion Institute*, 30(1):647–655, jan 2005. doi: 10.1016/j.proci.2004.08.106. URL <https://doi.org/10.1016/j.proci.2004.08.106>. 30, 40, 41, 43, 88, 90, 163, 210, 211
- E. R. Hawkes, R. Sankaran, O. Colin, and J. H. Chen. An analysis of the flame surface density transport equation using direct numerical simulation of a methane-air jet flame. In *Proceedings of The Australian Combustion Symposium*. The University of Queensland, Brisbane, 2009. 108, 110, 111, 214
- J. Heywood. *Internal combustion engine fundamentals*. McGraw-Hill, New York, 1988. ISBN 9780070286375. 7
- W. Jones and B. Launder. The prediction of laminarization with a two-equation model of turbulence. *International Journal of Heat and Mass Transfer*, 15(2):301–314, feb 1972. doi: 10.1016/0017-9310(72)90076-2. URL [https://doi.org/10.1016/0017-9310\(72\)90076-2](https://doi.org/10.1016/0017-9310(72)90076-2). 14
- M. Katragadda and N. Chakraborty. Modelling of the curvature term of the flame surface density transport equation for large eddy simulations. *Journal of Combustion*, 2012:1–12, 2012. doi: 10.1155/2012/915482. URL <https://doi.org/10.1155/2012/915482>. 43
- M. Katragadda, S. P. Malkeson, and N. Chakraborty. Modelling of the curvature term in the flame surface density transport equation: A direct numerical simulations based analysis. *International Journal of Spray and Combustion Dynamics*, 6(2):163–198, jun 2014a. doi: 10.1260/1756-8277.6.2.163. URL <https://doi.org/10.1260/1756-8277.6.2.163>. 43, 127, 128, 163, 215
- M. Katragadda, S. P. Malkeson, and N. Chakraborty. Modelling of the tangential strain rate term in the flame surface density transport equation in the context of Reynolds averaged navier stokes simulations: A direct numerical simulation analysis. *Mathematical Problems in Engineering*, 2014:1–15, 2014b. doi: 10.1155/2014/927408. URL <https://doi.org/10.1155/2014/927408>. 43
- A. R. Kerstein, W. T. Ashurst, and F. A. Williams. Field equation for interface propagation in an unsteady homogeneous flow field. *Physical Review A*, 37(7):2728–2731, apr 1988. doi: 10.1103/physreva.37.2728. URL <https://doi.org/10.1103/physreva.37.2728>. 19
- M. Klein, N. Chakraborty, and S. Ketterl. A comparison of strategies for direct numerical simulation of turbulence chemistry interaction in generic planar turbulent premixed flames. *Flow*,



- Turbulence and Combustion*, 99(3-4):955–971, aug 2017. doi: 10.1007/s10494-017-9843-9. URL <https://doi.org/10.1007/s10494-017-9843-9>. 73, 74, 181, 182
- E. Knudsen and H. Pitsch. A dynamic model for the turbulent burning velocity for large eddy simulation of premixed combustion. *Combustion and Flame*, 154(4):740–760, sep 2008. doi: 10.1016/j.combustflame.2008.05.024. URL <https://doi.org/10.1016/j.combustflame.2008.05.024>. 87, 100, 197
- H. Kobayashi, H. Hagiwara, H. Kaneko, and Y. Ogami. Effects of CO<sub>2</sub> dilution on turbulent premixed flames at high pressure and high temperature. *Proceedings of the Combustion Institute*, 31(1):1451–1458, jan 2007. doi: 10.1016/j.proci.2006.07.159. URL <https://doi.org/10.1016/j.proci.2006.07.159>. iii, v, 36, 209
- A. Kolmogorov. Local structure of turbulence in incompressible liquid for very large Reynolds numbers. *C.r. Koklaly acad.Sci. URSS*, 30:299–303, 1940. 7
- K. Kuo. *Principles of combustion*. John Wiley, Hoboken, NJ, 2005. ISBN 978-0-471-04689-9. 15
- C. Lacour and C. Pera. An experimental database dedicated to the study and modelling of cyclic variability in spark-ignition engines with LES. In *SAE Technical Paper Series*. SAE International, apr 2011. doi: 10.4271/2011-01-1282. URL <https://doi.org/10.4271/2011-01-1282>. 7
- C. Lapeyre, L. Selle, B. Bédard, and T. Poinso. Stretched flame DNS with analytical chemistries, for methane and iso-octane premixed configurations. Technical report, Idylle ANR report, 2016. URL <https://claipayre.github.io/research/>. 70
- S. Lapointe and G. Blanquart. A priori filtered chemical source term modeling for LES of high Karlovitz number premixed flames. *Combustion and Flame*, 176:500–510, feb 2017. doi: 10.1016/j.combustflame.2016.11.015. URL <https://doi.org/10.1016/j.combustflame.2016.11.015>. 30, 36, 37, 45, 52, 92, 210
- S. Lapointe, B. Savard, and G. Blanquart. Differential diffusion effects, distributed burning, and local extinctions in high Karlovitz premixed flames. *Combustion and Flame*, 162(9):3341–3355, sep 2015. doi: 10.1016/j.combustflame.2015.06.001. URL <https://doi.org/10.1016/j.combustflame.2015.06.001>. 30, 36, 37, 38, 39, 45, 49, 52, 67, 70, 77, 80, 81, 82, 92, 210, 221
- B. Launder and D. Spalding. Mathematical models of turbulence. 53, 01 1972. 136
- T. Leung, N. Swaminathan, and P. A. Davidson. Geometry and interaction of structures in homogeneous isotropic turbulence. *Journal of Fluid Mechanics*, 710:453–481, aug 2012. doi: 10.1017/jfm.2012.373. URL <https://doi.org/10.1017/jfm.2012.373>. 48

- M. D. Lorenzo, P. Brequigny, F. Foucher, and C. Mounaïm-Rousselle. New one shot engine validation based on aerodynamic characterization and preliminary combustion tests. *Flow, Turbulence and Combustion*, jun 2020. doi: 10.1007/s10494-020-00185-3. URL <https://doi.org/10.1007/s10494-020-00185-3>. 7
- S. K. Mahendar, N. Giramondi, V. Venkataraman, and A. C. Erlandsson. Numerical investigation of increasing turbulence through piston geometries on knock reduction in heavy duty spark ignition engines. In *SAE Technical Paper Series*. SAE International, dec 2019. doi: 10.4271/2019-01-2302. URL <https://doi.org/10.4271/2019-01-2302>. 7
- F. E. Marble and J. E. Broadwell. The coherent flame model for turbulent chemical reactions. Technical report, Purdue Univ Lafayette In Project Squidheadquarters, 1977. 15, 24
- M. Matalon and F. Creta. The “turbulent flame speed” of wrinkled premixed flames. *Comptes Rendus Mécanique*, 340(11-12):845–858, nov 2012. doi: 10.1016/j.crme.2012.10.031. URL <https://doi.org/10.1016/j.crme.2012.10.031>. 29
- M. Matalon and B. J. Matkowsky. Flames as gasdynamic discontinuities. *Journal of Fluid Mechanics*, 124(-1):239, nov 1982. doi: 10.1017/s0022112082002481. URL <https://doi.org/10.1017/s0022112082002481>. 29, 31, 92
- C. Meneveau and T. Poinso. Stretching and quenching of flamelets in premixed turbulent combustion. *Combustion and Flame*, 86(4):311–332, sep 1991. doi: 10.1016/0010-2180(91)90126-v. URL [https://doi.org/10.1016/0010-2180\(91\)90126-v](https://doi.org/10.1016/0010-2180(91)90126-v). 18, 26, 27, 47, 48, 49, 52, 54, 64, 104, 164, 166, 211, 222
- M. Metghalchi and J. C. Keck. Burning velocities of mixtures of air with methanol, isooctane, and indolene at high pressure and temperature. *Combustion and Flame*, 48:191–210, jan 1982. doi: 10.1016/0010-2180(82)90127-4. URL [https://doi.org/10.1016/0010-2180\(82\)90127-4](https://doi.org/10.1016/0010-2180(82)90127-4). 6
- C. Mounaïm-Rousselle, L. Landry, F. Halter, and F. Foucher. Experimental characteristics of turbulent premixed flame in a boosted spark-ignition engine. *Proceedings of the Combustion Institute*, 34(2):2941–2949, jan 2013. doi: 10.1016/j.proci.2012.09.008. URL <https://doi.org/10.1016/j.proci.2012.09.008>. iv, v, 13, 17, 209
- V. Moureau, G. Lartigue, Y. Sommerer, C. Angelberger, O. Colin, and T. Poinso. Numerical methods for unsteady compressible multi-component reacting flows on fixed and moving grids. *Journal of Computational Physics*, 202(2):710–736, jan 2005. doi: 10.1016/j.jcp.2004.08.003. URL <https://doi.org/10.1016/j.jcp.2004.08.003>. 51, 68, 171
- V. Moureau, P. Domingo, and L. Vervisch. From large-eddy simulation to direct numerical simulation of a lean premixed swirl flame: Filtered laminar flame-PDF modeling. *Combustion and Flame*, 158(7):1340–1357, jul 2011. doi: 10.1016/j.combustflame.2010.12.004. URL <https://doi.org/10.1016/j.combustflame.2010.12.004>. 131, 134, 165

- S. Mouriaux, O. Colin, and D. Veynante. Adaptation of a dynamic wrinkling model to an engine configuration. *Proceedings of the Combustion Institute*, 36(3):3415–3422, 2017. doi: 10.1016/j.proci.2016.08.001. URL <https://doi.org/10.1016/j.proci.2016.08.001>. 24
- C. Mueller. Vorticity generation and attenuation as vortices convect through a premixed flame. *Combustion and Flame*, 112(3):342–346, feb 1998. doi: 10.1016/s0010-2180(97)00122-3. URL [https://doi.org/10.1016/s0010-2180\(97\)00122-3](https://doi.org/10.1016/s0010-2180(97)00122-3). 9
- G. Nivarti and S. Cant. Direct numerical simulation of the bending effect in turbulent premixed flames. *Proceedings of the Combustion Institute*, 36(2):1903–1910, 2017. doi: 10.1016/j.proci.2016.07.076. URL <https://doi.org/10.1016/j.proci.2016.07.076>. 30, 33, 34, 35, 79, 81, 210
- G. V. Nivarti, R. S. Cant, and S. Hochgreb. Reconciling turbulent burning velocity with flame surface area in small-scale turbulence. *Journal of Fluid Mechanics*, 858, nov 2018. doi: 10.1017/jfm.2018.841. URL <https://doi.org/10.1017/jfm.2018.841>. 32, 33, 34, 79, 81, 88, 210
- J. A. V. Oijen, R. J. M. Bastiaans, G. R. A. Groot, and L. P. H. de Goey. Direct numerical simulations of premixed turbulent flames with reduced chemistry: Validation and flamelet analysis. *Flow, Turbulence and Combustion*, 75(1-4):67–84, dec 2005. doi: 10.1007/s10494-005-8592-3. URL <https://doi.org/10.1007/s10494-005-8592-3>. vi
- P. O'Rourke and F. Bracco. Two scaling transformations for the numerical computation of multidimensional unsteady laminar flames. *Journal of Computational Physics*, 33(2):185–203, nov 1979. doi: 10.1016/0021-9991(79)90015-9. URL [https://doi.org/10.1016/0021-9991\(79\)90015-9](https://doi.org/10.1016/0021-9991(79)90015-9). 17
- R. Paoli and K. Shariff. Turbulent condensation of droplets: Direct simulation and a stochastic model. *Journal of the Atmospheric Sciences*, 66(3):723–740, mar 2009. doi: 10.1175/2008jas2734.1. URL <https://doi.org/10.1175/2008jas2734.1>. 73, 74, 182
- K. Pearson. VII. note on regression and inheritance in the case of two parents. *Proceedings of the Royal Society of London*, 58(347-352):240–242, dec 1895. doi: 10.1098/rspl.1895.0041. URL <https://doi.org/10.1098/rspl.1895.0041>. 90, 177, 190
- P. Pelce and P. Clavin. Influence of hydrodynamics and diffusion upon the stability limits of laminar premixed flames. *Journal of Fluid Mechanics*, 124(-1):219, nov 1982. doi: 10.1017/s002211208200247x. URL <https://doi.org/10.1017/s002211208200247x>. 29, 199
- P. Pepiot-Desjardins and H. Pitsch. An efficient error-propagation-based reduction method for large chemical kinetic mechanisms. *Combustion and Flame*, 154(1-2):67–81, jul 2008. doi: 10.1016/j.combustflame.2007.10.020. URL <https://doi.org/10.1016/j.combustflame.2007.10.020>. 70
- N. Peters. The turbulent burning velocity for large-scale and small-scale turbulence. *Journal of Fluid Mechanics*, 384:107–132, apr 1999. doi: 10.1017/s0022112098004212. URL <https://doi.org/10.1017/s0022112098004212>. URL <https://doi.org/10.1017/s0022112098004212>.

//doi.org/10.1017/s0022112098004212. v, 9, 10, 20, 28, 29, 30, 32, 36, 37, 39, 40, 42, 43, 45, 84, 163, 209

- H. Pitsch. A consistent level set formulation for large-eddy simulation of premixed turbulent combustion. *Combustion and Flame*, 143(4):587–598, dec 2005. doi: 10.1016/j.combustflame.2005.08.031. URL <https://doi.org/10.1016/j.combustflame.2005.08.031>. 20
- T. Poinso and S. Lele. Boundary conditions for direct simulations of compressible viscous flows. *Journal of Computational Physics*, 101(1):104–129, jul 1992. doi: 10.1016/0021-9991(92)90046-2. URL [https://doi.org/10.1016/0021-9991\(92\)90046-2](https://doi.org/10.1016/0021-9991(92)90046-2). 69, 137
- T. Poinso and D. Veynante. *Theoretical and numerical combustion*. T. Poinso, S.I, 2012. ISBN 9782746639904. 1, 2, 5, 8, 12, 15, 16, 17, 20, 23, 114, 199, 209
- T. Poinso, D. Veynante, and S. Candel. Diagrams of premixed turbulent combustion based on direct simulation. *Symposium (International) on Combustion*, 23(1):613–619, jan 1991. doi: 10.1016/s0082-0784(06)80308-5. URL [https://doi.org/10.1016/s0082-0784\(06\)80308-5](https://doi.org/10.1016/s0082-0784(06)80308-5). 47, 164
- A. Poludnenko and E. Oran. The interaction of high-speed turbulence with flames: Global properties and internal flame structure. *Combustion and Flame*, 157(5):995–1011, may 2010. doi: 10.1016/j.combustflame.2009.11.018. URL <https://doi.org/10.1016/j.combustflame.2009.11.018>. 30, 34, 35, 45, 210
- A. Poludnenko and E. Oran. The interaction of high-speed turbulence with flames: Turbulent flame speed. *Combustion and Flame*, 158(2):301–326, feb 2011. doi: 10.1016/j.combustflame.2010.09.002. URL <https://doi.org/10.1016/j.combustflame.2010.09.002>. 30, 34, 35, 45, 210
- S. Pope. PDF methods for turbulent reactive flows. *Progress in Energy and Combustion Science*, 11(2):119–192, 1985. doi: 10.1016/0360-1285(85)90002-4. URL [https://doi.org/10.1016/0360-1285\(85\)90002-4](https://doi.org/10.1016/0360-1285(85)90002-4). 15
- S. Pope. The evolution of surfaces in turbulence. *International Journal of Engineering Science*, 26(5):445–469, jan 1988. doi: 10.1016/0020-7225(88)90004-3. URL [https://doi.org/10.1016/0020-7225\(88\)90004-3](https://doi.org/10.1016/0020-7225(88)90004-3). 15, 24
- L. Prandtl. 7. bericht über untersuchungen zur ausgebildeten turbulenz. *ZAMM - Journal of Applied Mathematics and Mechanics / Zeitschrift für Angewandte Mathematik und Mechanik*, 5(2):136–139, 1925. doi: 10.1002/zamm.19250050212. URL <https://doi.org/10.1002/zamm.19250050212>. 14
- R. G. Prucka, T. kyung Lee, Z. Filipi, and D. N. Assanis. Turbulence intensity calculation from cylinder pressure data in a high degree of freedom spark-ignition engine. In *SAE Technical Paper Series*. SAE International, apr 2010. doi: 10.4271/2010-01-0175. URL <https://doi.org/10.4271/2010-01-0175>. 7

- S. Richard. *Simulation aux grandes échelles de la combustion dans les moteurs à allumage commandé*. PhD thesis, Ecole Centrale des Arts et Manufactures, 2005. 4, 16, 19, 21, 22, 24, 25, 27, 115, 129, 134, 154, 168, 169, 209, 217
- S. Richard, O. Colin, O. Vermorel, A. Benkenida, C. Angelberger, and D. Veynante. Towards large eddy simulation of combustion in spark ignition engines. *Proceedings of the Combustion Institute*, 31(2):3059–3066, jan 2007. doi: 10.1016/j.proci.2006.07.086. URL <https://doi.org/10.1016/j.proci.2006.07.086>. 21, 24, 25, 26, 27, 28, 99, 102, 103, 115, 137, 138, 150, 153, 154, 156, 157, 165, 169
- G. Rymer. *Analyse et modélisation du taux de réaction moyen et des mécanismes de transport en combustion turbulente prémélangée*. PhD thesis, Ecole centrale de Paris, 2001. 24, 103, 107, 108, 115, 116, 134, 147, 153, 154
- R. Sankaran, E. R. Hawkes, C. S. Yoo, and J. H. Chen. Response of flame thickness and propagation speed under intense turbulence in spatially developing lean premixed methane–air jet flames. *Combustion and Flame*, 162(9):3294–3306, sep 2015. doi: 10.1016/j.combustflame.2015.05.019. URL <https://doi.org/10.1016/j.combustflame.2015.05.019>. 43, 45, 88, 90
- B. Savard and G. Blanquart. An a priori model for the effective species Lewis numbers in premixed turbulent flames. *Combustion and Flame*, 161(6):1547–1557, jun 2014. doi: 10.1016/j.combustflame.2013.12.014. URL <https://doi.org/10.1016/j.combustflame.2013.12.014>. 30, 37, 39, 45, 52, 68, 70, 73, 77, 92, 93, 94, 163, 210
- B. Savard and G. Blanquart. Broken reaction zone and differential diffusion effects in high Karlovitz n-c7h16 premixed turbulent flames. *Combustion and Flame*, 162(5):2020–2033, may 2015. doi: 10.1016/j.combustflame.2014.12.020. URL <https://doi.org/10.1016/j.combustflame.2014.12.020>. 30, 37, 45, 49, 52, 67, 68, 70, 73, 77, 78, 80, 81, 92, 210
- B. Savard and G. Blanquart. Effects of dissipation rate and diffusion rate of the progress variable on local fuel burning rate in premixed turbulent flames. *Combustion and Flame*, 180:77–87, jun 2017. doi: 10.1016/j.combustflame.2017.02.025. URL <https://doi.org/10.1016/j.combustflame.2017.02.025>. 30, 37, 45, 52, 68, 70, 73, 77, 78, 92, 210
- B. Savard, B. Bobbitt, and G. Blanquart. Structure of a high Karlovitz n-c7h16 premixed turbulent flame. *Proceedings of the Combustion Institute*, 35(2):1377–1384, 2015. doi: 10.1016/j.proci.2014.06.133. URL <https://doi.org/10.1016/j.proci.2014.06.133>. 30, 37, 45, 49, 52, 67, 70, 80, 81, 92, 210
- J. Smagorinsky. General circulation experiments with the primitive equations. *Monthly Weather Review*, 91(3):99–164, mar 1963. doi: 10.1175/1520-0493(1963)091<0099:gcewtp>2.3.co;2. URL [https://doi.org/10.1175/1520-0493\(1963\)0913C00993Agcewtp3E2.3.co3B2](https://doi.org/10.1175/1520-0493(1963)0913C00993Agcewtp3E2.3.co3B2). 16

- D. B. Spalding. Development of the eddy-break-up model of turbulent combustion. *Symposium (International) on Combustion*, 16(1):1657–1663, jan 1977. doi: 10.1016/s0082-0784(77)80444-x. URL [https://doi.org/10.1016/s0082-0784\(77\)80444-x](https://doi.org/10.1016/s0082-0784(77)80444-x). 15
- F. Tagliante, T. Poinso, L. M. Pickett, P. Pepiot, L. marie Malbec, G. Bruneaux, and C. Angelberger. A conceptual model of the flame stabilization mechanisms for a lifted diesel-type flame based on direct numerical simulation and experiments. *Combustion and Flame*, 201: 65–77, mar 2019. doi: 10.1016/j.combustflame.2018.12.007. URL <https://doi.org/10.1016/j.combustflame.2018.12.007>. 68
- F. Thiesset, F. Halter, C. Bariki, C. Lapeyre, C. Chauveau, I. Gökalp, L. Selle, and T. Poinso. Isolating strain and curvature effects in premixed flame/vortex interactions. *Journal of Fluid Mechanics*, 831:618–654, oct 2017. doi: 10.1017/jfm.2017.641. URL <https://doi.org/10.1017/jfm.2017.641>. 199
- P. Trisjono, K. Kleinheinz, E. R. Hawkes, and H. Pitsch. Modeling turbulence–chemistry interaction in lean premixed hydrogen flames with a strained flamelet model. *Combustion and Flame*, 174:194–207, dec 2016. doi: 10.1016/j.combustflame.2016.07.008. URL <https://doi.org/10.1016/j.combustflame.2016.07.008>. 42, 45, 163, 211
- A. Trouvé and T. Poinso. The evolution equation for the flame surface density in turbulent premixed combustion. *Journal of Fluid Mechanics*, 278:1–31, nov 1994. doi: 10.1017/s0022112094003599. URL <https://doi.org/10.1017/s0022112094003599>. 15, 24, 28, 107
- J. Van Oijen. *Flamelet-generated manifolds: development and application to premixed laminar flames*. Technische Universiteit Eindhoven, Eindhoven, 2002. ISBN 90-386-3053-0. 201
- L. Vervisch, E. Bidaux, K. N. C. Bray, and W. Kollmann. Surface density function in premixed turbulent combustion modeling, similarities between probability density function and flame surface approaches. *Physics of Fluids*, 7(10):2496–2503, oct 1995. doi: 10.1063/1.868693. URL <https://doi.org/10.1063/1.868693>. 21, 87, 197
- D. Veynante and T. Poinso. Reynolds averaged and large eddy simulation modeling for turbulent combustion. In *New Tools in Turbulence Modelling*, pages 105–140. Springer Berlin Heidelberg, 1997. doi: 10.1007/978-3-662-08975-0.5. URL <https://doi.org/10.1007/978-3-662-08975-0.5>. 9, 18
- D. Veynante and L. Vervisch. Turbulent combustion modeling. *Progress in Energy and Combustion Science*, 28(3):193–266, mar 2002. doi: 10.1016/s0360-1285(01)00017-x. URL [https://doi.org/10.1016/s0360-1285\(01\)00017-x](https://doi.org/10.1016/s0360-1285(01)00017-x). 15, 16, 24
- D. Veynante, J. Piana, J. Duclos, and C. Martel. Experimental analysis of flame surface density models for premixed turbulent combustion. *Symposium (International) on Combustion*, 26



- (1):413–420, jan 1996. doi: 10.1016/s0082-0784(96)80243-8. URL [https://doi.org/10.1016/s0082-0784\(96\)80243-8](https://doi.org/10.1016/s0082-0784(96)80243-8). 28
- D. Veynante, A. Trouvé, K. N. C. Bray, and T. Mantel. Gradient and counter-gradient scalar transport in turbulent premixed flames. *Journal of Fluid Mechanics*, 332:263–293, feb 1997. doi: 10.1017/s0022112096004065. URL <https://doi.org/10.1017/s0022112096004065>. 104
- D. Veynante, G. Lodato, P. Domingo, L. Vervisch, and E. R. Hawkes. Estimation of three-dimensional flame surface densities from planar images in turbulent premixed combustion. *Experiments in Fluids*, 49(1):267–278, mar 2010. doi: 10.1007/s00348-010-0851-y. URL <https://doi.org/10.1007/s00348-010-0851-y>. 31
- T. M. Wabel, A. W. Skiba, and J. F. Driscoll. Turbulent burning velocity measurements: Extended to extreme levels of turbulence. *Proceedings of the Combustion Institute*, 36(2):1801–1808, 2017. doi: 10.1016/j.proci.2016.08.013. URL <https://doi.org/10.1016/j.proci.2016.08.013>. 30, 32, 33, 34, 79, 164, 210
- G. Wang, M. Boileau, and D. Veynante. Implementation of a dynamic thickened flame model for large eddy simulations of turbulent premixed combustion. *Combustion and Flame*, 158(11):2199–2213, nov 2011. doi: 10.1016/j.combustflame.2011.04.008. URL <https://doi.org/10.1016/j.combustflame.2011.04.008>. 23
- H. Wang, E. R. Hawkes, J. H. Chen, B. Zhou, Z. Li, and M. Aldén. Direct numerical simulations of a high Karlovitz number laboratory premixed jet flame – an analysis of flame stretch and flame thickening. *Journal of Fluid Mechanics*, 815:511–536, feb 2017. doi: 10.1017/jfm.2017.53. URL <https://doi.org/10.1017/jfm.2017.53>. 42, 43, 45, 90, 163, 171, 211
- F. T. Yuen and Ö. L. Gülder. Turbulent premixed flame front dynamics and implications for limits of flamelet hypothesis. *Proceedings of the Combustion Institute*, 34(1):1393–1400, jan 2013. doi: 10.1016/j.proci.2012.06.167. URL <https://doi.org/10.1016/j.proci.2012.06.167>. 30, 32, 34, 45, 164, 210